Hydrogen Bond Phase-Transfer Catalysis for Nucleophilic Fluorination – Design of a New Peptidic Scaffold



A thesis submitted to the Board of the Faculty of Physical Sciences, in partial fulfilment of the requirements for the degree of Doctor of Philosophy at the University of Oxford

Gabija Poskaite

Merton College
University of Oxford
Hilary Term 2026

Author's Declaration

The work presented in this thesis was conducted under the supervision of Prof. Véronique Gouverneur at the Department of Chemistry, University of Oxford. All of the work is my own, unless otherwise stated, and has not been submitted for any other degree at this or any other university.



Gabija Poškaitė

April 2026

Table of Contents

Chapter I: Introduction....1

1.1. Organofluorine chemistry....1

1.1.1. Applications of organofluorine compounds....1
1.1.2. C−F bond properties....3
1.1.2.1. Pharmacological properties....4
1.1.2.2. Conformational properties....7
1.1.2.3. F···H hydrogen bonding....11

1.2. Alkali metal fluorides in organic synthesis....15

1.2.1. Overview of fluorinating reagents....15
1.2.2. Challenges in fluorination with alkali metal fluorides....17
1.2.2.1. Solubilisation via cationic phase-transfer....19
1.2.2.2. Reactivity modulation via hydrogen-bonding....21

1.2.3. Fluoride complexes in asymmetric catalysis....24
1.2.4. Asymmetric nucleophilic fluorination using alkali metal fluorides....26

1.3. Biochemistry of fluorine....30

1.3.1. Protein-fluoride binding....30
1.3.2. Enzymatic fluorination....33
1.3.3. Defluorination....36

1.4. Peptide catalysis....38

1.4.1. Asymmetric catalysis with amino acids and short peptides....39
1.4.2. Secondary structures in peptide catalysis....44
1.4.3. Peptide-based catalysts for halogenation....46

1.5. Thesis outline....48

1.6. References....49

Chapter II: Synthesis, structure and fluoride binding of peptides....61

2.1. Introduction....61

2.1.1. Peptides for fluoride binding....61
2.1.2. β-Turn peptides....64

2.2. Results and discussion....67

2.2.1. Peptide β-turns for fluoride binding....67
2.2.1.1. Selection and synthesis of tetrapeptides....67
2.2.1.2. Conformation in solution phase....68
2.2.1.3. Conformation in solid state....72
2.2.1.4. Complexation with TBAF(H_2O)$_3$: NMR titrations....75

2.2.2. Urea-peptide hybrids for fluoride binding....81
2.2.2.1. Synthesis of ureido-peptide library....81
2.2.2.2. Conformational properties in solution....84
2.2.2.3. X-ray structures of ureido-peptides....93
2.2.2.4. Complexation with TBAF(H_2O)$_3$....97
2.2.2.5. Residue specific binding....100

2.3. Conclusions....105

2.4. References....107

Chapter III: Peptides as hydrogen bonding phase-transfer catalysts for fluorination 113

3.1. Introduction 113

3.1.1. Peptide-alkali metal interactions 115
3.1.2. Hydrogen-bonding phase-transfer catalysis for cyclic β-fluoroamines 118

3.2. Results and discussion 120

3.2.1. Peptide complexation with CsF 120
*3.2.1.1. Tetrapeptide **2b** complexation with CsF 120*
3.2.1.2. Ureido-peptides binding with CsF 124

3.2.2. Peptide catalysts for nucleophilic fluorination via HB-PTC 127
*3.2.2.1. Screening of catalysts **2a–s** 127*
3.2.2.2. Catalyst degradation 133

3.2.3. Optimisation for asymmetric fluorination with CsF 136
3.2.3.1. Catalyst optimisation 136
3.2.3.2. Optimisation of reaction conditions 139
3.2.3.3. Reaction scope 146

3.2.4. Peptide catalyst **3.3j** binding with CsF 150
3.2.4.1. NMR studies 150
3.2.4.2. Cesium chelation 152
3.2.4.3. Computational investigations 156

3.3. Conclusion 158

3.4. References 160

Chapter IV: Summary and outlook 163

4.1. Summary 163

4.2. Future work 165

4.3. References 169

Chapter V: Experimental 171

5.1. General information 171

5.2. Catalyst synthesis and characterisation 173

5.2.1. General procedures for catalyst assembly 173
5.2.2. Exemplary synthesis I: **3.3j** 175
5.2.3. Exemplary synthesis II: **2r** 180
5.2.4. Synthesis of novel building blocks 184
5.2.4.1. Amino acid derivatives 184
5.2.4.2. Isocyanates and anilines 187

5.2.5. Catalyst characterisation 193
5.2.5.1. Peptides described in chapter II 193
5.2.5.2. Peptides described in chapter III 204

5.3. Substrate synthesis and characterisation 212

5.3.1. β-Aminoalcohols 212
5.3.2. β-Bromoamines 214

5.4. Fluorination under HB-PTC 216

5.4.1. General procedures 216
5.4.2. Characterisation of products 218

5.5. NMR studies 225

5.5.1. ^{1}H and ^{13}C NMR spectra assignments and NOESY correlations 225
5.5.2. Method for *A*-value determination 264
5.5.3. NMR titrations of peptides **2a**−**r** and **3.3j** 265
5.5.3.1. Methodology *265*
5.5.3.2. Titration profiles *270*

5.5.4. ^{19}F–^{1}H HOESY NMR for **2d**:TBAF$(H_2O)_3$ and **3.3j**:TBAF$(H_2O)_3$ 279
5.5.5. Peptide-CsF complexes: low temperature NMR 280
*5.5.5.1. **2b**−CsF complex* *280*
*5.5.5.2. **2c**–CsF and **2d**–CsF complexes* *282*
*5.5.5.3. **2k**, **2l**, **2i** and **2h** complexation with CsF* *284*
*5.5.5.4. **3.3j**–CsF complex* *289*

5.5.6. $CsBAr^{F}_{4}$ complexation 292
5.5.6.1. Preparation of cesium tetrakis[3,5-bis(trifluoromethyl)phenyl]borate *292*
5.5.6.2. NMR investigations *293*

5.6. Computational methods 295

5.7. Crystallographic information 297

5.8. References 301

Abstract

Chapter I introduces the fundamental principles of organofluorine chemistry, highlighting the unique physicochemical properties of the C–F bond and the hydrogen-bonding behaviour of fluoride. The challenges of nucleophilic fluorination with alkali metal fluorides are discussed alongside phase-transfer and hydrogen-bonding strategies for asymmetric fluoride delivery. The chapter further explores the biochemistry of fluorine and surveys peptide-based asymmetric catalysis, establishing the conceptual foundation for peptide–fluoride catalytic systems and drawing attention to the limited development of peptide-mediated halogenation.

Chapter II focuses on the design and structural evaluation of a series of β-turn tetrapeptides and ureido-peptide hybrids for fluoride binding through hydrogen-bonding interactions. These scaffolds were characterised in solution and in the solid state, enabling identification of key conformational features governing their hydrogen-bonding ability. Subsequent complexation studies with tetrabutylammonium fluoride demonstrated that backbone amide NH groups function as effective hydrogen-bond donors, with their binding ability attributed to conformational effects. Residue-specific binding analyses further established structure–binding relationships to guide catalyst development.

Chapter III explores the application of peptides in hydrogen-bonding phase-transfer catalysis using cesium fluoride (CsF). The designed peptide library was shown to solubilise CsF through fluoride and alkali metal chelation, enabling fluoride transfer under catalytic conditions. Using structural insights described in Chapter II, the first peptide-mediated enantioselective fluorination protocol for cyclic β-bromoamines is disclosed. Finally, the implications for peptide–fluoride complexation upon replacing $TBAF(H_2O)_3$ with CsF are further explored through detailed NMR studies and computational modelling.

Chapter IV summarises the key findings and outlines future directions for peptide–fluoride chemistry, including opportunities in catalytic strategies and broader applications.

Chapter V contains full experimental procedures, characterisation data for compounds described in Chapters II and III, and detailed NMR, computational and crystallographic methodologies.

Acknowledgements

I would like to begin by expressing my heartfelt gratitude to Prof. Véronique Gouverneur for giving me the opportunity to join her research group and for her support. Her passion for science has been truly inspiring, and it is something I will carry with me in the years to come. I am especially thankful for the many discussions, her guidance throughout a challenging project, and the way she nurtured my independence as a researcher.

Also, I would like to thank the collaborators and university staff who made this research possible. Prof. Robert Paton, along with Dr. Mihai V. Popescu and Dr. Zijun Chen, for their excellent computational work. To the NMR staff – Dr. Nader Amin, Dr. Coral Mycroft and Dr. Harry Mackenzie – for all the NMR support, for the many instrument booking exceptions, and to Mike for his 'interesting' music selection that helped make titration days go faster (or slower). I am also very grateful to the crystallography team, particularly Dr. Amber Thompson and Dr. Agamemnon Crumpton, for their training, patience, and support in solving crystal structures.

Furthermore, I would like to sincerely thank all the members of the VG group for their support, suggestions, and friendship. I had the pleasure to work with truly exceptional scientists and fantastic people, all of whom have contributed to my journey to become a better chemist and person. In particular, I would like to extend my gratitude to Dr. Thomas Schlatzer and Dr. Francesco Ibba, who have contributed enormously to this work, for their patience and their attempts to teach me some practical chemistry, even though I am still a liability for the laboratory glassware… To Dr. Thomas Hohmann and Dr. Thomas Schlatzer for proofreading and insightful conversations. Also, I was fortunate to work with many young chemists – Jess, Rob, Boll, Ivan and Mikolaj – thank you for exploring all the impossible ideas in the realm of peptide catalysis and for making me a better teacher.

Last but not least, I would like to thank my lunch, coffee, and boardgame friends, who have made this journey unforgettable. To Chiara, Thomas H. and Alan, my dear (coffee) friends, for being there when it was tough. To Thomas S. for all the discussions, social events and for pretending

to like boardgames. To Immo and Sophia for actually loving boardgames (and everything else) – you are truly an inspiration! To Chris for his wisdom and advice.

My warmest *Ačiū* and *Kiitos* go to my family, who have always encouraged and believed in me. Thank you to my dad for celebrating my successes, reading my papers and theses, and, of course, showing them to everyone he meets. And to my mum for being there when it gets tough. Also, to my new in-law family for their support and stunning office views during the Christmas break while I was working on this thesis.

And finally, to Emil for being there through it all.

Abbreviations and Acronyms (alphabetical)

The three-letter abbreviations in accord with the *IUPAC-IUB* were used for proteinogenic amino acids.

1,2-DCE	1,2-dichloroethane
18-crown-6	1,4,7,10,13,16-hexaoxacyclooctadecane
^{18}F-FDG	[^{18}F]2-fluoro-2-deoxy-D-glucose
2-Nal	(*S*)-2-naphthylalanine
5'-FDA	5'-fluoro-5'-deoxyadenosine
A	solute hydrogen-bond acidity value
Acbc	1-aminocyclobutane-1-carboxylic acid
Ac-CoA	acetyl coenzyme A
Acpc	1-aminocyclopropane-1-carboxylic acid
ADP	adenosine-5'-diphosphate
Aib	α-aminoisobutyric acid
APC	*trans*-(3*R*,4*S*)-4-aminopyrrolidine carboxylic acid
aq.	aqueous
BAr^F_4	*tetrakis*[3,5-*bis*(trifluoromethyl)phenyl]borate
BDE	bond dissociation energy (in kcal mol^{-1})
BINAM	1,1'-binaphthyl-2,2'-diamine
Boc	*tert*-butyloxycarbonyl
Cat K	cathepsin K
Cat. deg.	catalyst degradation
Cbz	benzyloxycarbonyl
CFC	chlorofluorocarbon
COSY	homonuclear correlation spectroscopy
d	delay (in s)
d.r.	diastereomeric ratio
DEPT	distortionless enhancement by polarisation transfer
dfp	(*S*)-4,4-difluoroproline
DFT	density functional theory
DHAP	dihydroxyacetone phosphate
Dmaa	β-dimethylaminoalanine
DIPEA	*N*,*N*-diisopropylethylamine
DMF	*N*,*N*-dimethylformamide
dmp	(*S*)-5,5-dimethylproline
DMSO	dimethyl sulfoxide
DS	number of dummy scans
e.g.	*exempli gratia* (for example)
e.r.	enantiomeric ratio
E°	oxidation potential
E2	bimolecular elimination
EDC	1-ethyl-3-(3-dimethylaminopropyl)carbodiimide
equiv.	equivalents
ESI	electrospray ionization
et al.	*et alia* (and others)

FAc	fluoroacetate
FDP	fructose-1,6-diphosphate
Flp	(2*S*,4*R*)-4-fluoroproline
flp	(2*S*,4*S*)-4-fluoroproline
G	Gibbs free energy (in kcal mol^{-1})
GC	gas chromatography
GOAT	global optimiser algorithm
HBA	hydrogen bond acceptor
HBD	hydrogen bond donor
H-bond	hydrogen bond
H-bonding	hydrogen bonding
HB-PTC	hydrogen-bonding phase-transfer catalysis
HMBC	heteronuclear multiple bond correlation
HOBt	1-hydroxybenzotriazole
HOESY	$^{1}H–^{19}F$ heteronuclear Overhauser spectroscopy
HPLC	high-performance liquid chromatography
HRMS	high-resolution mass spectrometry
HSQC	heteronuclear single bond correlation
HTE	high-throughput experimentation
Hyp	(2*S*,4*R*)-4-hydroxyproline
I	nuclear spin quantum number
i.e.	*id est* (in other words)
IC_{50}	half maximal inhibitory concentration
IR	infra-red
J	scalar coupling (in Hz)
K_a	association constant (binding affinity; in M)
K_i	inhibitor dissociation constant (potency of inhibition; in M)
K_m	Michaelis constant (in M)
KSP	kinesin spindle protein
LC	liquid chromatography
MDR	multidrug resistance
MF	alkali metal fluoride (LiF, NaF, KF, RbF, or CsF)
ML	machine-learning
MS	mass spectrometry
MSD	mean square deviation
n.a.	not applicable
n.d.	not determined
NAG	*N*-acetyl-L-glutamate
NCI	non-covalent interaction
NFSI	*N*-fluorobenzenesulfonimide
NMR	nuclear magnetic resonance
nOe	nuclear Overhauser effect
NOESY	nuclear Overhauser effect spectroscopy
NS	number of scans
o1p	spectrum offset, centre of spectrum (in ppm)
o2p	selection of second nuclei (in ppm)

PDB	protein data bank
Phe(*p*-NH_2)	(*S*)-2-amino-3-(4-aminophenyl)propanoic acid
Phe(*p*-NMe_2)	(*S*)-2-amino-3-(4-(dimethylamino)phenyl)propanoic acid
Phe(*p*-NO_2)	(*S*)-2-amino-3-(4-nitrophenyl)propanoic acid
pK_a	acid dissociation constant, $-\log_{10}$
PMB	*para*-methoxybenzyl
ppm	parts per million
Pro(5*R*-*t*-Bu)	(2*S*,5*R*)-5-(*tert*-butyl)pyrrolidine-2-carboxylic acid
Pro(5*S*-*t*-Bu)	(2*S*,5*S*)-5-(*tert*-butyl)pyrrolidine-2-carboxylic acid
PT	phase-transfer
PTFE	polytetrafluoroethylene
q	quantitative (refers to NMR methods)
r.t.	room temperature
RMSD	root mean square deviation
rpm	revolutions per minute
SAM	*S*-adenosylmethionine
S_EAr	electrophilic aromatic substitution
SI	spectrum data size
S_N2	bimolecular nucleophilic substitution
SW	spectral window (in ppm)
$t_{1/2}$	half-life (in h)
TBA^+	tetra-*n*-butylammonium (*n*-Bu_4N^+)
TCA	trichloroacetic acid/trichloroacetate
TD	time domain points
TFA	trifluoroacetic acid/trifluoroacetate
THF	tetrahydrofuran
TLC	thin-layer chromatography
T_m	thermal stability
UV-Vis	ultraviolet-visible
v.	*vide* (refer to)
v/v	volume/volume
α-Me-Pro	(*S*)-2-methylproline
δ	chemical shift (in ppm)
$\Delta\delta_{max}$	limiting chemical shift value (in ppm)
ε_r	dielectric constant
ν	wavenumber (in cm^{-1})
τ_m	mixing time (in ms)
χ^p	Pauling electronegativity

Chapter I

Introduction

1.1. Organofluorine chemistry

1.1.1. Applications of organofluorine compounds

Over the past century, fluorinated compounds have made a profound contribution to modern society, particularly through their applications in material science,[1] pharmaceuticals,[2] and agrochemicals.[3] The beginning of organofluorine industry is closely associated with the introduction of chlorofluorocarbon (CFC) refrigerants (*e.g.* Freon®)[4] and fluoropolymer materials such as polytetrafluoroethylene (PTFE or Teflon®;[5] **Figure 1.1.1**) in the 1930-40s.[6] Owning to their favourable physiochemical properties, CFCs were produced on an enormous scale (exceeding one million metric tons annually in 1960−80s),[7] for use as refrigerants, propellants, solvents, and blowing agents. However, as it was discovered that CFCs exhibit destructive effects on the ozone layer, they have been replaced with alternative fluorocarbons (*e.g.* hydrofluoroolefins).[8] In parallel, PTFE has become one of the most widely recognised fluoropolymer materials, valued for its exceptional non-stick and chemical-resistant properties, enabling applications ranging from cookware coatings to industrial materials and soil- and stain-resistant textile treatments.[1]

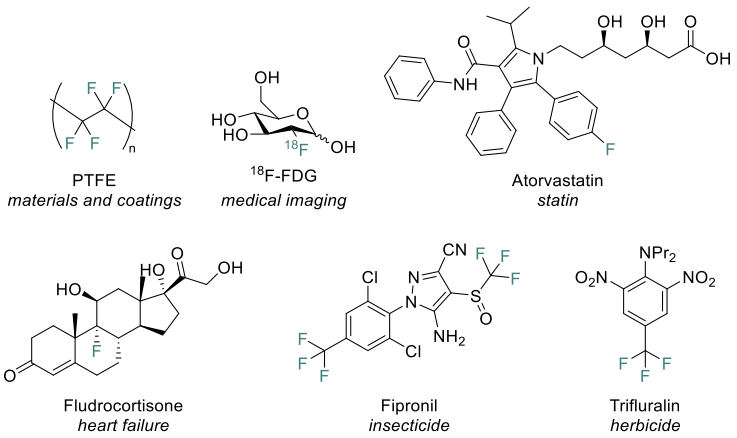

Figure 1.1.1. Examples of organofluorine compounds.

The expansion of organofluorine chemistry into the life sciences began in the 1950s with the discovery of the first fluorinated pharmaceutical, fludrocortisone,[9] which demonstrated the profound impact of fluorine substitution on biological activity (**Figure 1.1.1**). Since then, fluorine incorporation has led to the discovery of many essential[10] and blockbuster[2,11] medicines. Among many, the cholesterol-lowering atorvastatin (Lipitor®; **Figure 1.1.1**)[12] is the most profitable drug of all time (based on patent lifetime) and is consistently the most prescribed drug in the USA.[2,13] The strategic fluorine substitution has also been a cornerstone in design of agrochemicals, such as insecticide fipronil[14] and herbicide trifluralin[15] (**Figure 1.1.1**). In addition, ^{18}F-labelled compounds have found widespread application in medical imaging, particularly positron emission tomography, with [^{18}F]2-fluoro-2-deoxy-D-glucose (^{18}F-FDG; **Figure 1.1.1**) being the most extensively used radiotracer, now routinely applied beyond its original use in oncology.[16]

Consequently, it was accounted that 18% of newly approved pharmaceuticals (1991–2019) and 53% of registered agrochemicals (1998–2020) contain at least one fluorine atom.[3,17] This prevalence continues to increase: during the final five years of these periods, 35% of newly registered medicines and 67% of agrochemicals were organofluorine. The steady increase in fluorinated organic compounds has been attributed to their superior biological efficacy compared to non-fluorinated counterparts and development of new fluorination and trifluoromethylation methodologies in the last 20 years (*v.* Section 1.2.1).[18] Nevertheless, fluorine incorporation can remain costly, particularly on scale, highlighting the ongoing need for affordable, safe, and sustainable fluorination methods.

1.1.2. C−F bond properties

Strategic incorporation of fluorine into organic molecules can alter their physicochemical, conformational, and pharmacological properties. The unique properties of organofluorine compounds stem from the small size of fluorine (van der Waals radius = 1.47 Å; second smallest among the elements)[19] and its exceptionally high electronegativity ($\chi_P = 3.98$),[20] making it the most strongly electron-withdrawing element in the periodic table (**Table 1.1.1**). As a consequence, the corresponding C–F bond is highly polarised. In combination with optimal valence orbital energy matching between carbon and fluorine ($2s_{(C)} = -19.4$ eV *versus* $2p_{(F)} = -18.9$ eV), this polarity results in the strongest known carbon single bond (C–F), with a bond dissociation energy (BDE) of approximately 105 kcal mol^{-1} (**Table 1.1.1**).[21]

Table 1.1.1. Properties of H, O and F elements and their bond to carbon strengths.[19-21]

Atom	van der Waals radius (Å)	Pauling electronegativity (χ_P)	C−X BDE (kcal mol^{-1})
H	1.20	2.20	98
F	1.47	3.98	105
O	1.52	3.44	84
C	1.70	2.55	83
Cl	1.74	3.16	79

Building on these fundamental properties, the following sections explore how fluorine substitution is harnessed to tune molecular properties. In medicinal chemistry, the strength of the C–F bond is used to enhance metabolic stability, while the extreme electronegativity of fluorine enables modulation of acidity of neighbouring functional groups (*v.* Section 1.1.2.1).[22] In addition, the low-lying antibonding orbital of the C–F bond (σ^*_{CF}) underpins a range of stereoelectronic effects, including dipole–dipole and charge–dipole interactions as well as hyperconjugation (*v.* Section 1.1.2.2).[22-23] Owing to its small size, fluorine is often considered a biological isostere of hydrogen and hydroxy groups, allowing these electronic effects to be introduced with minimal steric perturbation. Substitution of fluorine for OH, C=O or H can also alter hydrogen-bonding (H-bonding) behaviour: fluorine functions only as a weak hydrogen-bond acceptor and not as donor (*v.* Section 1.1.2.3).[24] This section also addresses H-bonding involving ionic fluoride, which has been widely exploited in nucleophilic fluorination reactions.

1.1.2.1. Pharmacological properties

The introduction of fluorine has become a common strategy in drug design to enhance pharmacological properties such as lipophilicity, basicity, binding affinity and metabolic stability.[22b] Fluorine substitution can decrease the Brønsted basicity of neighbouring functional groups as a result of fluorine's strong inductive electron-withdrawing effect. In linear aliphatic systems, the influence of successive fluorine substitution to the acid dissociation constant (pK_a) of adjacent functionalities (*e.g.* COOH, OH, NH_2) is additive (**Table 1.1.2**). For example, experimentally each β-fluorine substitution in ethylamine reduces the pK_a by ~1.7. This effect is attenuated with increasing distance from the functional group, resulting in ΔpK_a values of approximately −0.7, −0.3 and −0.1 for fluorine substitution at the γ, δ and ε positions, respectively.[24] In a similar manner, cyclic amines are also influenced by fluorine substitution with additive effects, as exemplified by the pK_a variation of the mono and difluorinated piperidines (**Figure 1.1.2**).[22b,25]

Table 1.1.2. Effect of fluorination on the pK_a (in water at 20 °C) of common carboxylic acids, alcohols and amines.[22b,24]

Carboxylic acid	pK_a	Alcohol	pK_a	Amine	pK_a[a]	Amine	pK_a[a]
CH_3CO_2H	4.8	$(CH_3)_2CHOH$	17.1	$CH_3CH_2NH_2$	10.7	$CH_2F(CH_2)_2NH_2$	9.9
CH_2FCO_2H	2.6	CF_3CH_2OH	12.4	$CH_2FCH_2NH_2$	9.0	$CF_3(CH_2)_2NH_2$	8.7
CHF_2CO_2H	1.3	$(CF_3)_2CHOH$	9.3	$CHF_2CH_2NH_2$	7.3	$CH_3(CH_2)_3NH_2$	10.7
CF_3CO_2H	0.5	$(CF_3)_3OH$	5.4	$CF_3CH_2NH_2$	5.7	$CF_3(CH_2)_3NH_2$	9.7

[a]of conjugate acid

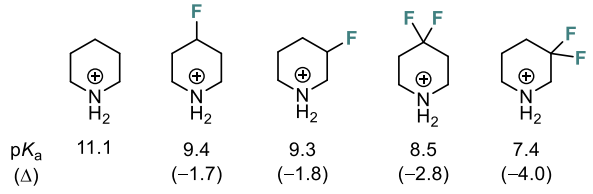

Figure 1.1.2. pK_a values (in water at 20 °C) of cyclic mono and difluorinated piperidines.[22b]

Modulating the pK_a of basic functionalities through fluorine substitution is a well-established and reported strategy in medicinal chemistry shown to achieve improved distribution and bioavailability of drug compounds and can have downstream effects on potency, selectivity, toxicity, and pharmacokinetic properties. An illustrative example of fluorine incorporation to tune

pK_a was reported during the development of kinesin spindle protein (KSP) inhibitors for the treatment of taxane-refractory solid tumours (**Figure 1.1.3**).[26] The initial lead compound **1.1.1** exhibited undesirable P-glycoprotein affinity, as reflected by a multidrug resistance (MDR) ratio of 21, while only compounds with MDR ratios below 10 were considered acceptable for further development. During the study, it was established that moderating the basicity of the piperidine nitrogen to a target pK_a range of 6.5–8.0 (in water) was necessary to reduce P-glycoprotein-mediated efflux in tumor cells and maintaining KSP potency. Fluorine substitution at the 3-position of the piperidine ring proved effective in achieving this modulation, with the effect on the pK_a of the heterocyclic nitrogen depending on whether the fluorine substituent adopted an axial (**1.1.2**) or equatorial (**1.1.3**) orientation. In both cases, fluorination resulted in reduced basicity (pK_a = 6.6 and 7.6 in water, respectively) and acceptable MDR ratios (2.4 and 4.5, respectively). Notably, the axial fluorinated isomer **1.1.2** displayed superior potency (half maximal inhibitory concentration; IC_{50} = 2.2 nM) and was ultimately selected for evaluation in a phase I clinical trial.

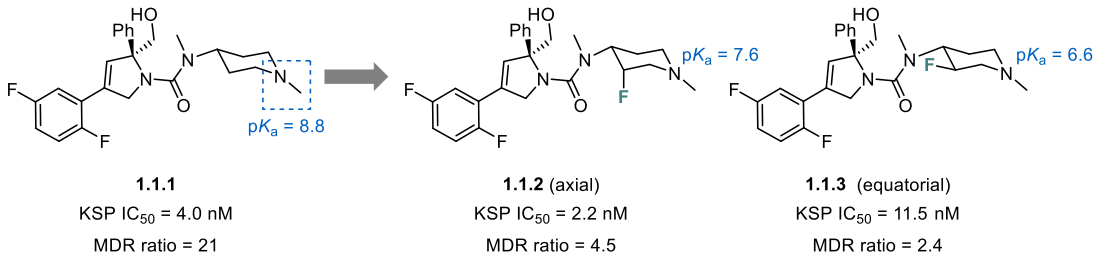

Figure 1.1.3. Effect of fluorine substitution in **1.1.1**–**1.1.3** on pK_a, P-glycoprotein affinity and KSP IC_{50}.[26]

Fluorine incorporation can also be fruitful in generation of bioisosteres by altering the physical and electronic properties of functional groups. For example, trifluoroethylamine ($CF_3CH_2NH_2$) is sufficiently basic to function as an amide isostere in drug discovery.[27] This strategy was utilised by Merck during the development of Odanacatib (**1.1.4**), a highly selective cathepsin K (Cat K) inhibitor investigated for the treatment of osteoporosis (**Figure 1.1.4**).[28] In early development stages, X-ray crystallography of dipeptide **1.1.5** bound to Cat K revealed that one amide formed a single H-bond with Gly-66, while its corresponding carbonyl group was solvent-exposed. Replacement of this amide with a trifluoroethylamine group yielded a neutral, mildly basic NH

moiety that retained H-bonding capability.[29] The resulting compound **1.1.6** displayed extremely high potency ($IC_{50} \leq 0.005$ nM) and improved selectivity relative to its amide analogue. Crystallographic studies further revealed that the (*S*)-diastereomer at the CF_3-substituted stereocentre of **1.1.6** was more potent, while the (*R*)-diastereomer displayed 1000-fold lower potency. However, compound 1.1.6 still suffered from poor metabolic stability (half-life; $t_{1/2}$ = 2 h).

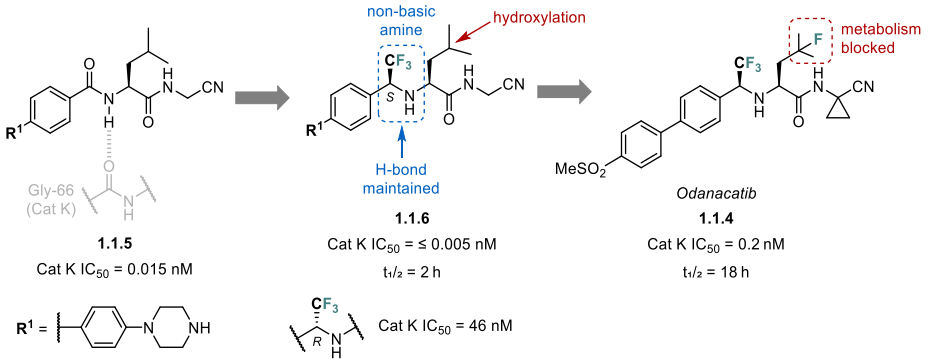

Figure 1.1.4. Effect of fluorine substitution in Odanacatib on binding affinity to Cat K and metabolic stability.[28-29]

This limitation is particularly important, as low metabolic stability is a major challenge in drug development, since rapid biotransformation can limit the efficacy, duration of action, and safety of drugs. A common strategy to address this issue is fluorine substitution to block metabolically labile sites.[30] In the case of Odanacatib, two key metabolic liabilities were addressed through fluorine incorporation, yielding a compound with high potency (IC_{50} = 0.2 nM) and improved metabolic stability ($t_1/_2$ = 18 h).[28] Fluorination of the leucine residue blocked hydroxylative metabolism, while the trifluoroethylamine group conferred resistance to proteolytic degradation, ultimately enabling Odanacatib to progress to phase III clinical trials (**Figure 1.1.4**).

1.1.2.2. Conformational properties

Beyond its impact on physiochemical properties, fluorine substitution can exert a pronounced influence on molecular conformation through electrostatic and stereoelectronic effects. The strong polarisation of the C–F bond gives rise to a large dipole moment, enabling favourable electrostatic (dipole–dipole and charge–dipole) interactions with nearby electropositive centres. Within a molecule, dipole-dipole interactions impose conformational bias, as dipoles tend to adopt orientations that minimise unfavourable electrostatic repulsion. For example, in 1,3-difluoropropane, repulsion between the two C–F dipoles favours an antiperiplanar conformation by approximately 3 kcal mol^{-1} (**Figure 1.1.5a**).[31] The magnitude of this effect decreases with decreasing dipole moment.[21] Accordingly, α-fluorocarbonyl compounds exhibit a strong preference for an anti-planar C–F/carbonyl arrangement. This conformational preference is particularly pronounced in α-fluoroamides (~7.5 kcal mol^{-1} for α-fluoroacetamide), but decreases progressively, reaching ~1.7 kcal mol^{-1} in α-fluoroacetylaldehyde (**Figure 1.1.5b**).[32]

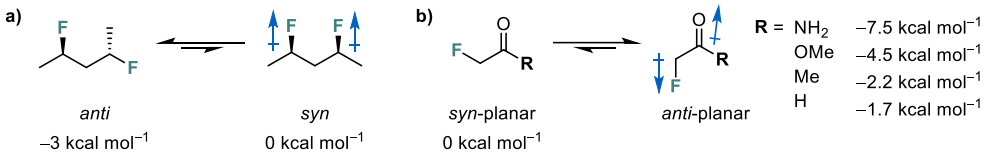

Figure 1.1.5. Calculated energy differences for conformers illustrating dipole-driven conformational preferences in a) 1,3-difluoropropane[31] and b) selected α-fluorocarbonyl compounds[32].

Intermolecular dipole-dipole interactions involving C–F have also been reported for small molecules and protein-ligand systems.[33] In 2007, the Protein Data Bank (PDB)[34] search by Müller *et al.* have identified 20 C–F···C=O and 11 C–F···H-N interactions involving fluorinated drugs (mostly aryl fluorides) and their protein targets (**Figure 1.1.6a**).[35] The C–F···C=O interactions adopt an orthogonal geometry, consistent with the C–F bond dipole approaching amide carbonyls along a Bürgi–Dunitz–type trajectory ($70° \leq \theta \leq 110°$). Dipolar C–F···C=O interactions were first identified by Olsen *et al.* during a fluorine scan of tricyclic thrombin inhibitors.[36] In this study, the *para*-fluorinated inhibitor **1.1.7** exhibited significantly enhanced inhibition of thrombin compared to the corresponding non-fluorinated analogue (the inhibitor dissociation constant, K_i = 0.056 *versus* 0.31 μM ; **Figure 1.1.6b**).

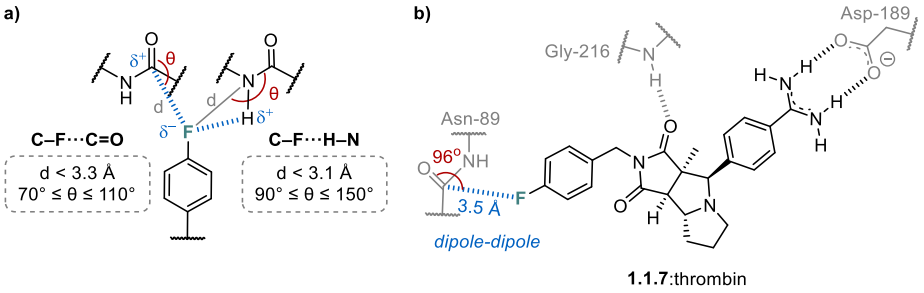

Figure 1.1.6. a) Dipole–dipole interactions between amides and C–F.[35] b) *Para*-fluorobenzyl containing inhibitor **1.1.7** in the active site of thrombin (in *grey*).[36]

Electrostatic interactions involving the C–F bond are strongly enhanced in the presence of a neighbouring formal charge, giving rise to pronounced charge–dipole stabilisation. This effect was first observed in 3-fluoropiperidinium ring systems, which exhibit a strong axial preference for fluorine (by 5.4 kcal mol^{-1}), whereas neutral 3-fluoropiperidine preferentially adopts conformations with equatorial fluorine (**Figure 1.1.7a**).[37] Strong *gauche* preferences are likewise observed for protonated fluoroethylamine and fluoroethanol with short C–F···H–X$^+$ (X = N, O) distances (**Figure 1.1.7b**).[38] Although these contacts are sometimes described as weak H-bonds, the persistence of a pronounced *gauche* preference in the fluoroethylpyridinium cation,[39] which cannot engage in intramolecular H-bonding, provides clear evidence that charge–dipole interactions dominate the conformational preference.

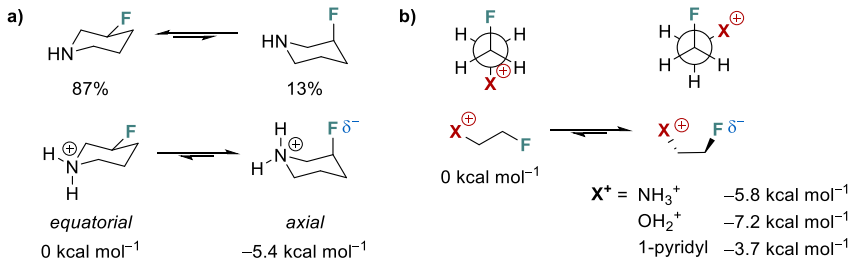

Figure 1.1.7. Charge–dipole interactions in a) 3-fluoropiperidinium,[37] and b) $[CH_2XCH_2F]^+$ cations[38-39].

In addition to electrostatic interactions, fluorine substitution can influence molecular conformation through stereoelectronic effects. Early vibrational spectroscopic studies of 1,2-difluoroethane by Klaboe and Nielsen suggested that the anti-periplanar (*anti*, ~180°) and syn-clinal (*gauche*, ~60°) conformers were of comparable stability in the gas phase.[40] Subsequent experimental and computational studies, however, established a preference for the *gauche* conformer by approximately 0.5–0.9 kcal mol^{-1}.[41] This unprecedented conformational preference

could not be readily rationalised based on simple electrostatic arguments, which would favour the antiperiplanar arrangement. Instead, the *gauche* conformer is stabilised by two reinforcing hyperconjugative interactions between electron-rich C–H σ-bonds and the low-lying antibonding C–F orbitals ($\sigma_{C–H} \rightarrow \sigma^*_{C–F}$; **Figure 1.1.8a**). This gauche effect is very general since the vacant, low-laying $\sigma^*_{C–F}$ orbital can accept electron density from well aligned electron-rich σ-bonds,[38,42] π-systems,[43] or lone pairs[44] ($\pi \rightarrow \sigma^*$, and $n \rightarrow \sigma^*$, respectively). A related stereoelectronic effect is observed in 2-fluoropyran,[44b] where the axial conformer is favoured by approximately 2.9 kcal mol^{-1} due to $n \rightarrow \sigma^*$ hyperconjugation between the ring oxygen lone pair and the σ*(C–F) orbital, giving rise to the anomeric effect (**Figure 1.1.8b**).

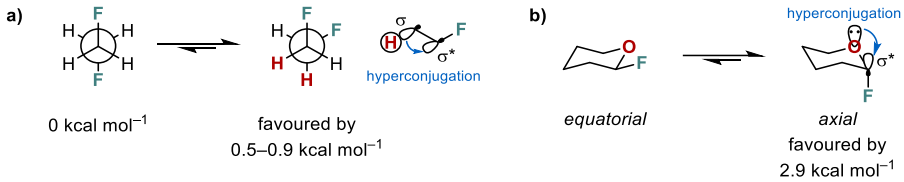

Figure 1.1.8. Conformational bias through hyperconjugation: a) the gauche effect ($\sigma_{C–H} \rightarrow \sigma^*_{C–F}$),[41] and b) the anomeric effect ($n_O \rightarrow \sigma^*_{C–F}$)[44b].

Some of the most illustrative examples of exploiting the C–F bond as a conformational control element arise from studies on peptides and proteins. In particular, the F–C–C–N gauche effect has been used to elucidate the role of (2*S*,4*R*)-4-hydroxyproline (Hyp) in the formation and stability of the collagen triple helix.[45] Each polypeptide chain of this fibrous protein is composed of approximately 300 repeating Xaa–Yaa–Gly units, where Xaa is frequently Pro and Yaa is commonly Hyp.[46] Collagen stability was long attributed to an extensive H-bonding network involving the hydroxy groups of Hyp residues and bridging water molecules. This hypothesis was challenged by Raines and co-workers by the incorporation of (2*S*,4*R*)-4-fluoroproline (Flp) and (2*S*,4*S*)-4-fluoroproline (flp) into collagen-mimetic $(Pro–Yaa–Gly)_n$ peptides.[45a,c] Flp-containing $(Pro–Yaa–Gly)_7$ peptide exhibited increased thermal stability (T_m = 45 °C), while flp-containing peptide was markedly destabilised (T_m < 2 °C), relative to the Hyp-containing analogue (T_m = 36 °C; **Figure 1.1.9a**).[45a] These trends excluded H-bonding as the stabilising interaction, since C–F bonds do not engage in strong H-bonding interactions (*v.* Section 1.1.2.3).

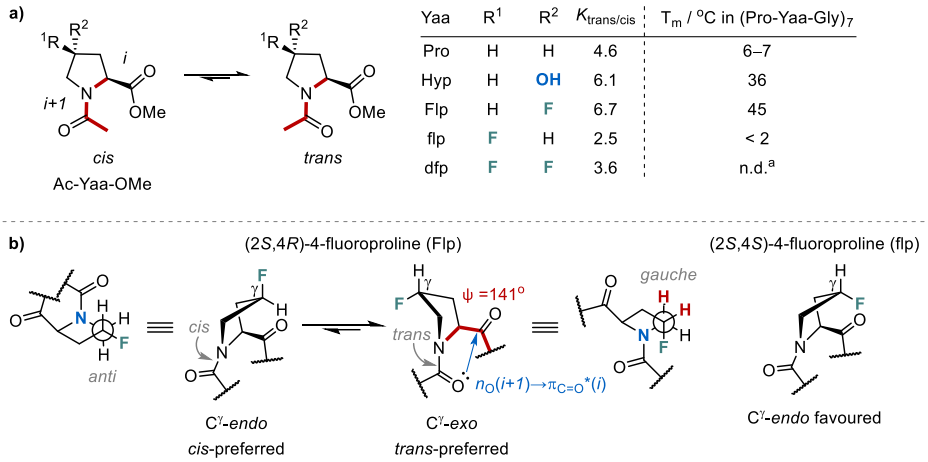

Figure 1.1.9. a) Fluorine substitution of proline effect on the thermal stability of collagen mimetic peptide and $K_{trans/cis}$ (in D_2O, 25 °C), and b) conformational preference of 4(*R*)- and 4(*S*)-substitued proline residues.[45a,47] [a]n.d. = not determined; poorly soluble in H_2O, see ref[45b].

Further analysis showed that substitution with an electronegative atom at Cγ strongly influences several properties, including nitrogen basicity (pK_a (of conjugate acid): Flp = 9.2; Hyp = 9.7; Pro = 10.8),[48] residue hydrophobicity,[45b] prolyl *cis–trans* isomerisation, and pyrrolidine ring puckering.[45a,47] Crucially, both Flp and flp experience a stereoelectronic gauche effect between fluorine and the β-nitrogen. However, their opposite stereochemistry at Cγ enforces distinct ring conformations, namely Cγ-*exo* and Cγ-*endo* puckers, respectively (**Figure 1.1.9b**). This divergence in ring puckering has direct consequences for peptide backbone geometry. When incorporated into a peptide, Flp strongly favours the *trans*-prolyl amide configuration, as this geometry allows a favourable $n_O(i+1)\rightarrow\pi_{C=O}^*(i)$ interaction between consecutive carbonyls (**Figure 1.1.9b**).[47] This arrangement corresponds to a $\psi(i) = 141°$, closely matching the $\psi(i) \approx 150°$ required for formation of the right-handed collagen triple helix,[49] thereby reducing the entropic penalty associated with folding. In contrast, flp exhibits a strong preference for the Cγ-*endo* pucker and consequently destabilises the *trans* amide, leading to reduced collagen stability.

Additional studies using (*S*)-4,4-difluoroproline (dfp),[45b] which exhibits Cγ-*endo*/*exo* and *cis*-*trans* populations similar to those of Pro, resulted in thermal stabilities comparable to Pro at the Yaa position. This confirmed that collagen stabilisation arises from stereoelectronic effects rather than changes in basicity or hydrophobicity.

1.1.2.3. F···H hydrogen bonding

Hydrogen bonds (H-bonds) are $n_A \rightarrow \sigma^*_{XH}$ interactions, where n_A represents the electron lone pair of the hydrogen bond acceptor (HBA) and σ^*_{XH} the unfilled antibonding molecular orbital of the hydrogen bond donor (HBD).[50] H-bonds were classified by Jeffrey into three categories (strong, moderate and weak) based on strength (BDE, in the gas-phase) and directionality (θ; **Table 1.1.3**).[50a] X-ray diffraction and NMR spectroscopy are among the most popular techniques to study H-bonding in solid and solution states.[50b,c] In the solid state, both methods can be used as complementary tools to each other.[51] However, the comparison between conformations observed in solid and solution states should be taken with caution, since solute-solvent interactions and packing effects can significantly alter the observed H-bonding network.[52] NMR spectroscopy is particularly suitable to study H-bonding interactions in solution, offering a range of observables: chemical shifts (δ), scalar couplings (*J*), relaxation rates, and nuclear Overhauser effects (nOe).[50c] In particular, deshielding of proton resonances is associated with increasing H-bond strength (**Table 1.1.3**).[50a,53] The covalent character of H-bond also allows for observation of through-bond scalar couplings between proton and HBA ($^hJ_{HA}$, where subscript *h* denotes H-bonding).[54]

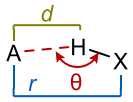

Table 1.1.3. Properties of H-Bonds.[50a,b] (X–H = donor, A = acceptor)

	Strong	**Moderate**	**Weak**
nature of bonding	mostly covalent	mostly electrostatic	electrostatic
H-bond length (*d*, Å)	1.2–1.5	1.5–2.2	2.2−3.2
A−X (*r*, Å)	2.2−2.5	2.5−3.2	> 3.2
BDE (kcal mol^{-1})	15–40	4–15	1–4
bond angle (θ, °)	170–180	130−180	90−150
δ ^{1}H (ppm)	14–22	< 14	-

Strong H-bonds (BDE = 15–40 kcal mol^{-1}, in the gas phase) display mostly covalent character and are of linear geometry (θ ≈ 175º). Examples of strong H-bonding generally involve non-organic complexes, with bifluoride anion (HF_2^-) recognised as the strongest H-bond known[50b,55] (calculated BDE = 39 kcal mol^{-1}, in the gas-phase)[56]. Single-crystal and neutron diffraction studies of KHF_2 revealed a symmetric $[F\cdots H\cdots F]^-$ complex with *d*(H−F) = 133 ppm.[57] In some cases, the symmetry was susceptible to change in countercation.[58] In solution state, early NMR spectroscopic investigations[59] of soluble $TBA^+HF_2^-$ (TBA^+ = tetra-*n*-butylammonium) indicated

a symmetric [F···H···F]⁻ complex as a doublet at δ ^{19}F = −153.8 ppm with $^{1h}J_{HF}$ = 123 Hz (in CD_2Cl_2 at 217 K). Additionally, dynamic mixtures in solution were highlighted, but not characterised. Shenderovich *et al.* investigated TBA⁺[F(HF)]⁻ via Density Functional Theory (DFT) calculations and NMR spectroscopy in liquefied freon (CDF_3/$CDClF_2$ 1:2) at low temperatures (120−130 K) to slowdown interconversion between species.[60] At 120 K, $[F(HF)_n]^-$ (n = 1−4) clusters were observed depending on HF/TBAF equivalence used (1:1 to 2:1 ratio). All clusters were fully characterised via NMR spectroscopy providing increasing $^{1}J_{HF}$ (124−480 Hz) and decreasing $^{1h}J_{FH}$ (124−10 Hz) with each addition of HF, indicating shifting of corresponding protons towards terminal fluorine atoms (**Figure 1.1.10**). Also, δ ^{1}H and δ ^{19}F(central) were inversely proportional to the coordination number of the central fluoride, indicating increasing H-bond length. This NMR investigation of $[F(HF)_n]^-$ (n = 1−4) clusters illustrates the range of strong to weak H-bonds involving F⁻. Other examples of NMR investigations of strong H-bonds were reported for F⁻ with acetate and pyridine derivatives.[61]

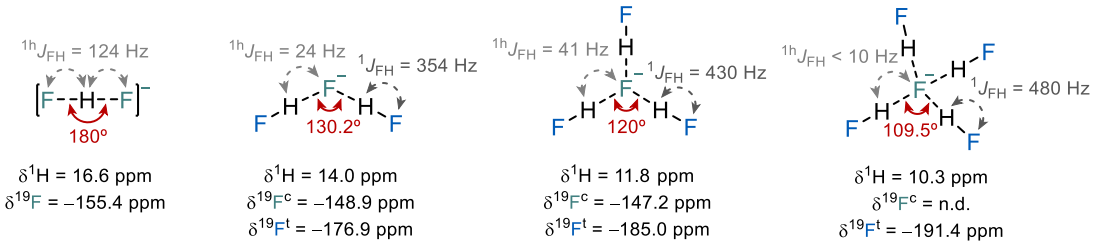

Figure 1.1.10. Key NMR parameters of $[F(HF)_n]^-$ (n = 1−4) clusters in CDF_3/$CDClF_2$ 1:2 at 120−130 K. Bond angles (in red) from DFT calculations.[60] F^c – central fluorine, F^t – terminal fluorine(s), n.d. = not determined.

Medium H-bonds are mostly electrostatic with BDE = 4−15 kcal mol⁻¹ (in the gas-phase) and a wider range of geometries (θ = 130–180°), which is commonly encountered in organic chemistry (C=O···HX, where X = N or O). Stable anion-receptor interactions involving H-bonds with F⁻ belong to this category as well.[62] Pupo *et al.* have reported intermediate strength H-bonds between F⁻ and a monoalkylated BINAM-derived (BINAM = 1,1'-binaphthyl-2,2'-diamine) *bis*-urea **1.1.7** – a catalyst designed for nucleophilic fluorination using CsF (*v.* Section 1.2.4).[62f] In solid state, TBA⁺[**1.1.7**:F⁻] complex displayed three NH···F interactions featuring *r*(N···F⁻) = 2.66, 2.67 and 2.69 Å (for NH(a−c), respectively), and an additional contact between the *ortho*-aromatic carbon (*o*-ArC) and fluoride (3.06 Å; **Figure 1.1.11a**). Subsequent spectroscopic investigations[62g]

showcased tridentate binding mode of **1.1.7** to TBAF$(H_2O)_3$ in CD_2Cl_2 with slightly more varied H-bonding strengths as demonstrated by δ ^{1}H(a−c) = 12.84, 12.21, 10.51 ppm and $^{1h}J_{HF}$ = 61, 51, 34 Hz, respectively (**Figure 1.1.11a**). Obtained relative H-bonding distances via quantitative ^{19}F–^{1}H heteronuclear Overhauser effect spectroscopy (qHOESY) confirmed elongated *d*(NH(b)···F$^-$) and *d*(*o*-ArH)···F$^-$) contacts in solution compared to the solid-state structure. The study culminated in the investigations of 12 related BINAM *bis*-urea catalysts showcasing a positive correlation between individual δ ^{1}H and $^{1h}J_{FH}$ for NH(b) and NH(c) (**Figure 1.1.11b**).

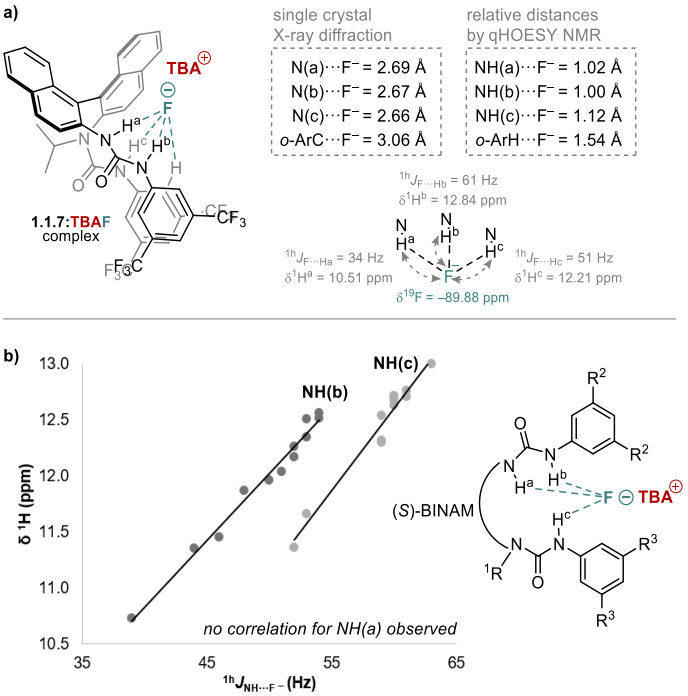

Figure 1.1.11. a) Single crystal X-ray and solution state NMR (in CD_2Cl_2, 298 K) investigations of **1.1.7**:TBAF complex. b) Linear correlation between δ^{1}H and $^{1h}J_{FH}$ for BINAM *bis*-urea catalysts with TBAF.[62f,g]

Weak H-bonds (BDE = 1–4 kcal/mol, in the gas-phase) arise from predominantly electrostatic interaction. The H-bonding interactions of organofluorine compounds (C−F···H) represent this category. Organic fluorine is a weak HBA, due to poor polarizability of lone pairs of fluorine.[21] Historically, H-bonding of C−F has been controversial, particularly due to limitations of crystallographic techniques to study weak non-covalent interactions (NCIs); single crystal X-ray is unsuitable to locate H-atoms, and weak H-bonding is difficult to distinguish from incidental, multipolar or dispersive interactions exclusively based on geometric criteria.[52c,63] Numerous screenings[52c] of the Cambridge Structural Database[64] and the PDB for CF···HX interactions

(where X = C, O, S, or N) indicate that such H-bonds are generally weak (r(F···H) > 2.0 Å) and not strongly directional (θ = 180−90°).[63a,65] Accordingly, classification of some types of CF···H interactions are still disputable. For example, Müller *et al.*,[35] have concluded that eleven C−F···H−N (backbone amide) contacts from the PDB with d(F···N) < 3.1 Å and θ ≥ 150° were more consistent with antiparallel dipole-dipole rather than H-bonding interactions, based on elongated distances.

Spectroscopic methods and computational studies have shown success in unequivocally establishing the presence of C−F···H−X (where X = C, O, or N) H-bonds.[52c] NMR spectroscopy allows these weak contacts to be probed in various media, however H-bonding is generally detectable in aprotic solvents, and suppressed by strong solute-solvent interactions in polar environments. The presence of $^{1h}J_{HF}$ scalar coupling is regarded as indisputable proof of H-bonding, which is observed if the H-bond is strong or rigid (*e.g.* intramolecular H-bond or part of a network of interactions). The earliest examples of $^{1h}J_{HF}$ couplings for organofluorine compounds were reported for intramolecular H-bonds involving C(sp^3)F···HX (X = S, O and N) as $^{h}J_{HF}$ = 2.0, 4.8 and 11.5 Hz, respectively (in CCl_4 or $CDCl_3$; **Figure 1.1.12**).[66] In all cases, the presence of $^{h}J_{HF}$ (referred to as 'through-space') coupling rather than long-range coupling was proven by acquiring NMR spectra in dimethyl sulfoxide-d_6 (DMSO-d_6), indicating disappearance of $^{h}J_{HF}$ and downfield δ ^{1}H due to interactions with the solvent.

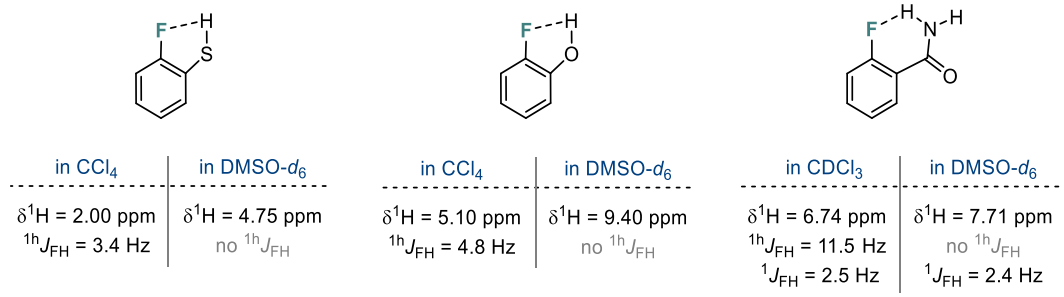

Figure 1.1.12. Selected examples of spectroscopic evidence for C–F···H–X (X = S, O, N) H-bonding.[66b,c]

1.2. Alkali metal fluorides in organic synthesis

1.2.1. Overview of fluorinating reagents

Fluorine naturally is found in the form of the minerals cryolite (Na_3AlF_6), fluorite (CaF_2) and fluorapatite ($Ca_5(PO_4)_3F$), but only CaF_2 is exploited in the fluorochemical supply chain.[67] Cryolite reserves were exhausted in the late 1980s,[68] while fluorapatite is currently used in the production of phosphoric acid, resulting in fluorosilicic acid (H_2SiF_6) as a waste by-product.[69] Industrially fluorochemical production commences by the treatment of acid-grade fluorite (>97% CaF_2) with sulfuric acid under harsh conditions (> 300 °C, **Scheme 1.2.1**) to produce anhydrous HF – a process first described by Scheele in 1771.[70] HF is then utilised for industrial production of all fluorochemicals including organofluorine compounds,[18] which were discussed in Section 1.1.1. HF in gaseous and aqueous forms is highly toxic and corrosive.[71] Hence, handling HF on a large scale requires specialised expertise, and due to stringent transportation regulations, HF is generally consumed at the production site.[72] Understandably, direct use of HF is restricted in both, industry and academia. Consequently, a range of fluorinating reagents have been prepared from HF (nucleophilic and electrophilic) to address safety concerns and to diversify the reactivity profile.

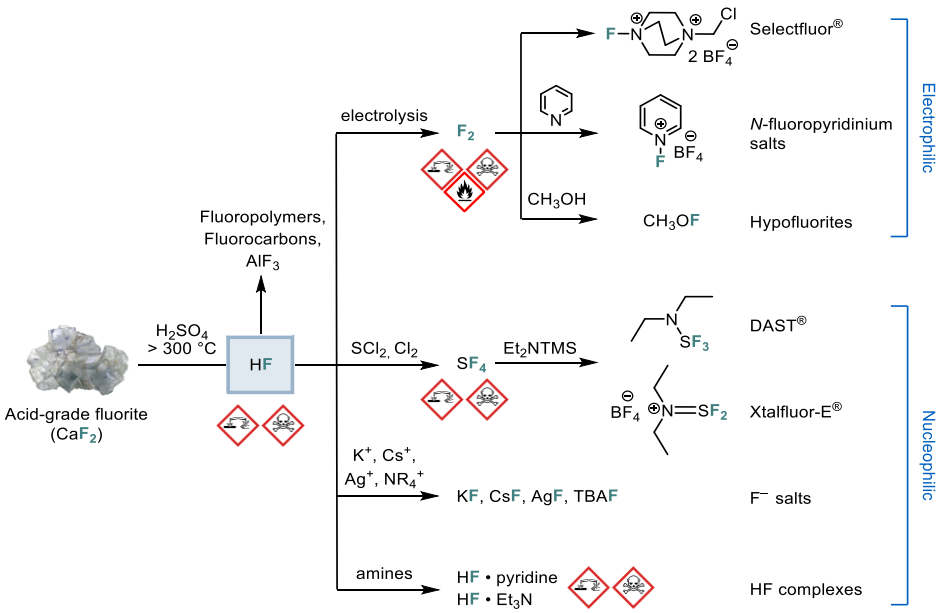

Scheme 1.2.1. Production of fluorinating reagents. Adapted from ref[67].

Many fluorinating reagents are prepared from F_2 and SF_4 gasses. The F_2 gas is produced via electrolysis of anhydrous HF, following a modified procedure first reported by Moissan in 1886 (Nobel prize 1906).[73] Many preparations of SF_4 gas have been disclosed, all including oxidation of sulfur or sulfur chlorides and HF, F_2 or alkali metal fluorides (NaF or KF) as a fluorine source.[74] The HF-derived toxic F_2 and corrosive SF_4 gases can be converted to many electrophilic N-F (*e.g.* 1-chloromethyl-4-fluoro-1,4-diazoniabicyclo[2.2.2]octane *bis*(tetrafluoroborate) (Selectfluor®), *N*-fluorobenzenesulfonimide (NFSI), *N*-fluoropyridinium salts)[75] and nucleophilic S-F (*e.g.* diethylaminosulfur trifluoride (DAST®), diethylaminodifluorosulfinium tetrafluoroborate (XtalFluor-E®))[76] fluorinating reagents of tailored reactivity (**Scheme 1.2.1**). Even though both classes of these reagents have had a transformative impact on organic synthesis, their use is not without significant drawbacks. First, since the synthesis of such reagents is reliant on handling and storage of hazardous gases, they are more expensive to produce than reagents directly derived from HF. Moreover, the highly oxidising nature of electrophilic reagents, while beneficial in some cases, can be incompatible with highly functionalised substrates. Deoxyfluorination reagents similarly feature limited functional group tolerance, but also suffer from elimination side products and thermal instability. From a sustainability perspective, the large molecular weight of many specialised fluorinating reagents and the use of BF_4^- and PF_6^- counter anions lead to poor atom economy.

Alkali metal fluorides (MFs = LiF, NaF, KF, RbF, and CsF) are prepared by neutralising HF with the corresponding hydroxides or carbonates. These nucleophilic reagents are easy-to-handle, relatively cheap and environmentally friendly compared to reagents discussed above. Moreover, the use of [^{18}F]MFs is particularly attractive for the preparation of medicinally relevant targets for PET imaging due to ease of handling, high specific activity and ease of generation compared to other ^{18}F-labeled fluorinating reagents.[77]

1.2.2. Challenges in fluorination with alkali metal fluorides

The use of alkali metal fluoride salts in organic synthesis is limited due to their high hygroscopicity and poor solubility in organic solvents,[79] which can be traced back to F^- being the most densely charged monovalent anion (charge density = 24 C mm^{-3})[78]. Fluoride forms very strong ionic bonds with alkali metal cations, and the resulting lattice energy increases as the cation charge density increases, where CsF is the weakest bound in the alkali metal fluoride series (**Table 1.2.1**). The lattice energy also governs solubility and hygroscopicity of MFs, being inversely proportional, with CsF the most water-soluble, but also the most challenging alkali metal fluoride to handle due to its hygroscopicity. On the other hand, LiF and NaF are not used in fluorination chemistry due to their poor solubility.[72]

Table 1.2.1. Lattice energy and aqueous solubility of alkali metal fluoride salts.[78]

Fluoride salt	Lattice energy (kcal mol^{-1})	Cation charge density (C mm^{-3})	Solubility (g/100 g H_2O)
LiF	251	52	0.134
NaF	222	24	4.13
KF	198	11	102
RbF	190	8	300
CsF	181	6	573

The high hygroscopicity of MF salts is a result of F^- engaging in strong H-bonds to any available HBDs such as water or alcohols, which in turn lowers F^- nucleophilicity.[55] H-bonding can suppress the reactivity of fluoride to the extent that HBDs such as carboxylic acids have been reported to act as nucleophiles instead.[80] On the other hand, in the desolvated state, 'naked' F^- exhibits dual reactivity as both – a strong nucleophile and base.[81] Aqueous HF is a weak acid (pK_a(HF) = 3.2,[82] in H_2O), while 'naked' fluoride in DMSO is a base strong enough to deprotonate the solvent (pK_a(DMSO) = 35.1,[83] in DMSO).[81b]

The basicity of fluoride restricts its synthetic utility because it promotes various side reactions, such as elimination of alkyl halides to form alkenes or hydrolysis facilitated by the generation of hydroxide (**Scheme 1.2.2**, *top*). In *N*,*N*-dimethylformamide (DMF), a polar aprotic solvent, CsF is sufficiently soluble to undergo a bimolecular nucleophilic substitution (S_N2) of alkyl mesylate

1.2.1 to afford alkyl fluoride **1.2.2a** in 48% yield (**Scheme 1.2.2**, *bottom*).[84] Fluoride also displays its basic character as illustrated by the formation of alkene **1.2.2b** (8%) and alcohol **1.2.2c** (9%) by-products via bimolecular elimination (E2). Meanwhile, in a polar protic solvent – MeOH, in which CsF is fully soluble under reaction conditions, a less reactive F^- species is generated, resulting in only 20% of fluorinated product, and no signs of elimination product. The formation of ether **1.2.2d** (43%) can be attributed to competitive nucleophilicity of the solvent.[85] These examples perfectly illustrate the challenge in controlling the selectivity and reactivity of F^-.

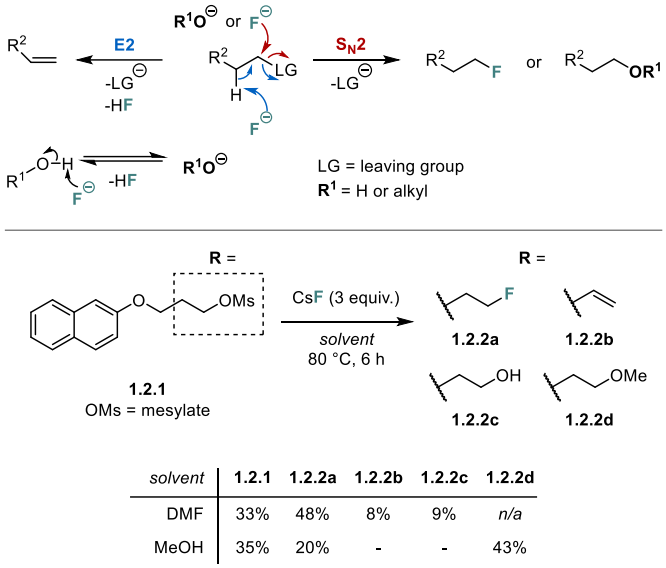

solvent	**1.2.1**	**1.2.2a**	**1.2.2b**	**1.2.2c**	**1.2.2d**
DMF	33%	48%	8%	9%	*n/a*
MeOH	35%	20%	-	-	43%

Scheme 1.2.2. Dual reactivity of fluoride as a base and a nucleophile.[84-85]

The following sub-sections describe strategies for generating a more soluble and more controllable fluoride anion using MFs by weakening the ionic interactions between the counter cation and fluoride.

1.2.2.1. *Solubilisation via cationic phase-transfer*

A common strategy to improve the solubility of MFs involve sequestration of the metal counter-cation, or the use of organic counter-cations (**Scheme 1.2.3**, *top*). The work of Liotta and Harris have demonstrated the use of 18-crown-6 (1,4,7,10,13,16-hexaoxacyclooctadecane) for solubilisation of KF and subsequent fluorination in MeCN or benzene.[81a] The fluorination of a primary benzylic bromide without 18-crown-6 in MeCN resulted in < 5% fluorination yield, which upon addition of ether increased to quantitative product formation (**Scheme 1.2.3**, *conditions A*). However, since the chelation by 18-crown-6 to potassium cation results in a highly activated fluoride source, the fluorinations of secondary and tertiary bromides suffered from high degrees of elimination. Since the first report, a wide range of organic molecules containing Lewis basic sites have been developed for cation-binding phase-transfer (PT) of MFs, *e.g.* cryptands,[86] polyethylene glycols[87] and ionic liquids[88].

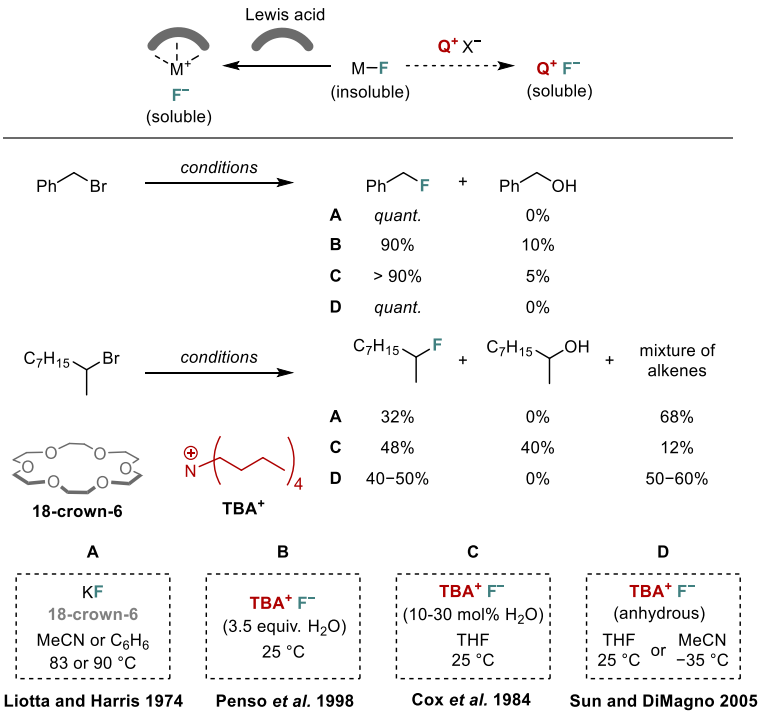

Scheme 1.2.3. Lewis base and onium (Q) salt mediated solid-liquid phase-transfer of F^-.[81a,89]

As an alternative to metal chelation for weakening M−F ionic bond, many weakly coordinating organic counter-cations have been developed for cation-directed PT, *e.g.* quaternary ammonium[90] or phosphonium salts.[91] TBAF, which is highly soluble in apolar solvents, is by far the most

commonly used ammonium salt. It is commercially available as a stable trihydrate ($TBAF(H_2O)_3$) salt due to its hygroscopicity and its tendency to undergo thermal decomposition via Hofmann elimination[92]. $TBAF(H_2O)_3$ can be used as a mild fluorinating reagent, however, due to the presence of water, it acts as a hydrolysing agent too.[89a] The reaction with benzyl bromide afforded 10% of benzyl alcohol in addition to fluorinated product (**Scheme 1.2.3**, *conditions B*). Cox *et al.* have reported a mild protocol for reducing the water content of $TBAF(H_2O)_3$ to 10−30 mol% in tetrahydrofuran (THF).[89b] This reagent showed improved reactivity compared to TBAF trihydrate, however, the small water content still resulted in alcohol by-product formation (**Scheme 1.2.3**, *conditions C*). A truly anhydrous TBAF can be generated *in situ* via a method described by Sun and DiMigano.[89c] As with the KF/18-crown-6 system, the use of anhydrous TBAF with 2-bromononane (*i.e.* secondary bromide) results in significant alkene formation owing to the generation of a highly basic F^- species (**Scheme 1.2.3**, *conditions D*). Despite advances in fluoride salt solubilisation via PT, enhanced fluoride reactivity often comes at the expense of reduced chemoselectivity.

1.2.2.2. Reactivity modulation via hydrogen-bonding

H-bonding has been invoked to attenuate fluoride reactivity and, consequently, protic solvents were deemed unsuitable for S_N2 fluorination.[55,93] This view was challenged in 1994, when Yonezawa and co-workers investigated the reactivity of TBAF-alcohol complexes in a model S_N2 reaction with benzyl bromide. The study demonstrated a direct correlation between reaction rate and the steric bulk of the alcohol used (*t*-BuOH ≫ *i*-PrOH > *n*-BuOH ~ *n*-PrOH > H_2O).[94] This was the first example of using H-bonding to probe fluoride reactivity. The following studies by the Chi group have translated the concept of using bulky alcohols for fluorinations with alkali metal fluorides (CsF and RbF).[84-85] It was shown that alcohol-mediated fluorination of mesylate **1.2.1** with CsF did not afford any alkene, but rather an ether by-product **1.2.2d** (**Scheme 1.2.4a**). Also, the reactivity of fluoride and selectivity against formation of the ether by-product improved as the steric hindrance of the alcohols increased from *n*- to *tert*-alcohols. The equivalent reactivity profile was observed for TBAF(*t*-BuOH)$_4$ and CsF in *t*-BuOH, which suggested a soluble dissociated Cs^+ F^- complex. Moreover, significantly reduced elimination by-product formation was observed when base-labile substrates, for example **1.2.3**, were subjected to CsF/*t*-BuOH or TBAF/*t*-BuOH conditions, indicating significantly reduced Brønsted basicity of fluoride (**Scheme 1.2.4a**).[95]

In 2015, Engle *et al.* investigated the influence of alcohol H-bonding denticity on fluoride reactivity.[96] A range of TBAF(ROH)$_n$ complexes were crystallised exhibiting di- to tetradentate coordination modes to fluoride. It was observed that the coordination number of fluoride affected the chemoselectivity of the model reaction with alkyl bromide **1.2.4** (**Scheme 1.2.4b**). The reaction outcome was more selective (S_N2 *versus* E2) as coordination number increased, but this resulted in a reduced reaction rate.

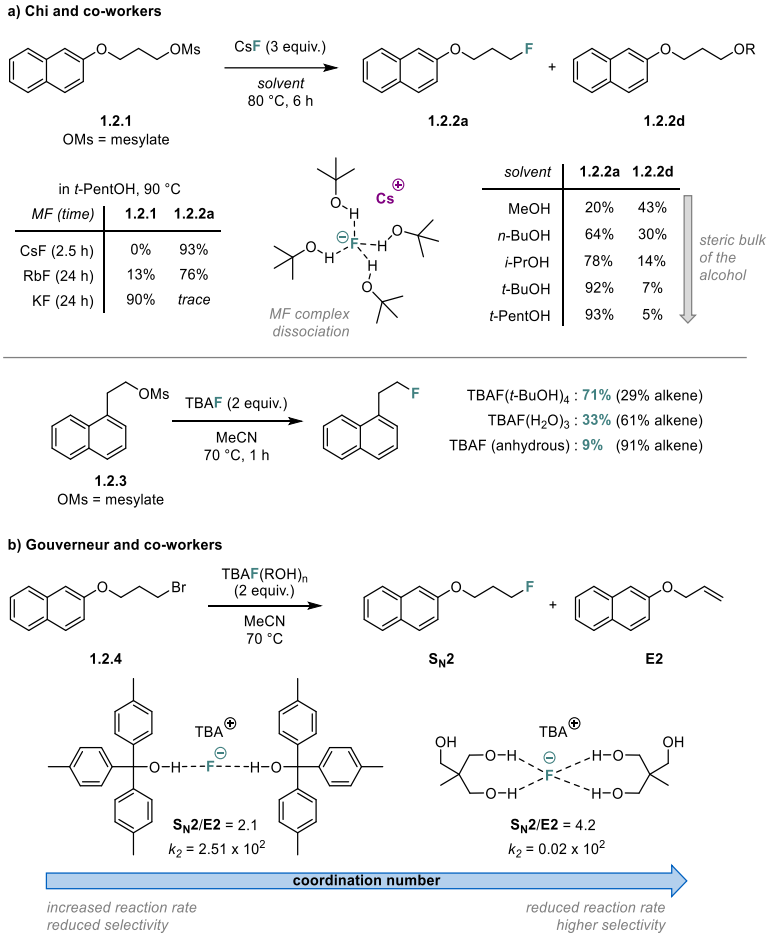

Scheme 1.2.4. Alcohol mediated nucleophilic fluorination.[84-85,95-96] k_2 = second-order rate constant (in M^{-1} s^{-1}).

The follow-up investigations by the Gouverneur group have demonstrated that the reactivity of fluoride can also be modulated by the strength of the H-bonds.[97] A range of 1,3-diarylureas with aryl substituents of varying electronic properties were complexed and crystallised with TBAF. The resulting TBAF(urea)$_2$ complexes exhibited lower reactivity but significantly improved selectivity compared to the previously studied TBAF-alcohol complexes or commercially available TBAF(H_2O)$_3$ (**Scheme 1.2.5**, *top*). The binding and kinetic studies suggested that the 1:1 urea–fluoride complex was the reactive species in solution, while the 2:1 urea–fluoride coordination mode predominates in the solid state. UV-Vis titrations revealed that the 1:1 TBAF-urea binding constants (log($K_{a\ (1:1\ TBAF\text{-}3H2O)}$ in MeCN) increase with the electron-withdrawing nature of *para*-substituents on the urea aryl ring, consistent with enhanced acidity of the urea NH protons. Using more acidic urea in the model reaction resulted in a reduced reaction rate, consistent with a more deactivated F^- species. The *para*-trifluoromethyl substituted 1,3-diarylurea (**1.2.5**) was also shown

to act as a catalyst for the solubilisation of CsF which is poorly soluble in MeCN – an early proof of concept that ureas can act as PT catalysts for alkali metal fluorides (**Scheme 1.2.5**, *bottom*).

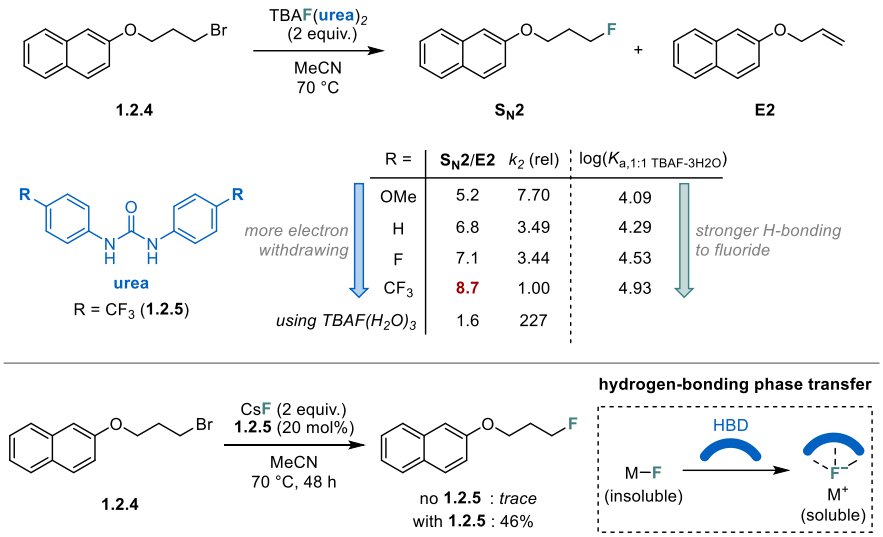

Scheme 1.2.5. Tuneable H-bonding strength for nucleophilic fluorination.[97] $K_{a\ (1:1\ TBAF\text{-}3H2O)}$ measured in MeCN.

1.2.3. Fluoride complexes in asymmetric catalysis

The strategies described in Sections 1.2.2.1 and 1.2.2.2 for controlling fluoride reactivity via cation phase transfer or anion binding offer opportunities to generate chiral fluoride complexes for asymmetric catalysis. The early reports of such chiral complexes were used for fluoride ion catalysed processes rather than for nucleophilic fluorination. The first example of alkali metal fluoride PT using a *chiral* quaternary ammonium salt was reported in 1978 by Colonna *et al.*[98] In this instance, KF was used as a base for the Michael addition of nitromethane to chalcone affording modest enantioselectivity (61:39 enantiomeric ratio (*e.r.*).; **Scheme 1.2.6**, *top*). Two decades later, Maruoka and co-workers showcased the asymmetric variant of a fluoride ion catalysed Mukaiyama-type aldol[99] using KF as a catalyst; the solubilisation of F^- was facilitated by the chiral ammonium salt – **1.2.6** (**Scheme 1.2.6**, *bottom*).[100] The hydrogen sulphate counter anion of **1.2.6** was shown to be crucial for *in situ* preparation of ammonium fluoride through the formation of a less soluble $KHSO_4$.

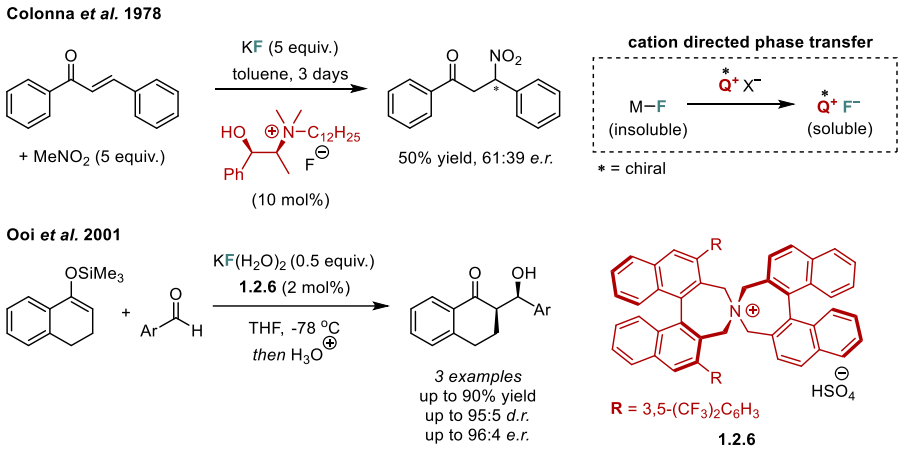

Scheme 1.2.6. Chiral ammonium salt catalysed phase-transfer of KF.[98,100] *d.r.* = diastereomeric ratio.

The Song group reported a chiral, cation-binding phase-transfer strategy for MFs using a BINOL-based bis(hydroxyl) polyether catalyst (**1.2.7**; BINOL = 1,1'-bi-2-naphthol; **Scheme 1.2.7**).[101] Activation and solubilisation of KF were achieved through synergistic interactions involving coordination of K^+ by the polyether chain and H-bonding between F^- and the BINOL hydroxy group. This binding mode is reminiscent of previously reported achiral polyethylene glycol-catalysed fluorinations with MFs, where a glycol OH group was proposed to activate the

incoming electrophile.[87] X-ray crystallographic studies further revealed an additional unprecedented interaction between K^+ and halogen substituents on the BINOL framework. The resulting chiral **1.2.7**:KF complex enabled kinetic resolution of secondary silyl alcohols via nucleophilic fluorodesilylation (Si–F bond formation), but has not yet been extended to C–F bond formation.

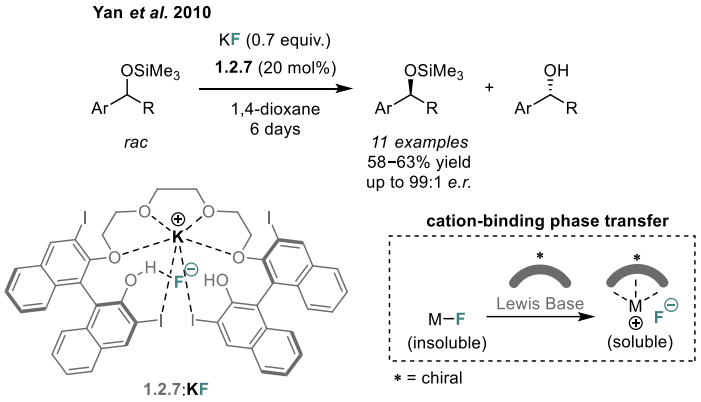

Scheme 1.2.7. Phase-transfer of KF via chiral cation binding catalysis for asymmetric desilylation.[101]

The pioneering work by Jacobsen in the field of anion-binding catalysis has demonstrated the ability for chiral HBD catalysts to activate electrophiles by halide abstraction.[102] In this context, fluoride is complicated due to the strength of the C−F bond. However, in a rare example, Jacobsen and co-workers have demonstrated that thiourea catalyst **1.2.8** can abstract F^- from acyl fluorides to facilitate asymmetric acyl transfer (**Scheme 1.2.8**).[103] The halogen abstraction generates an activated ion pair between the chiral **1.2.8**:F^- complex and an acylated amino pyridinium co-catalyst. Fluoride acts as a desilylating reagent of silyl enol acetals, however, is not involved in the enantiodetermining step of the C−C bond formation.

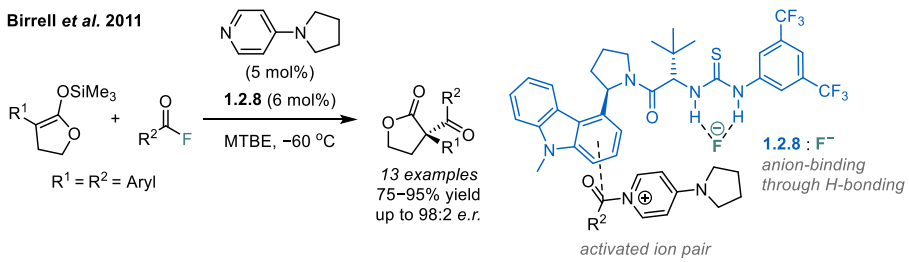

Scheme 1.2.8. Catalytic fluoride anion abstraction by hydrogen bond donor.[102]
MTBE = methyl *tert*-butyl ether.

1.2.4. Asymmetric nucleophilic fluorination using alkali metal fluorides

In 2018 Gouverneur and co-workers have reported the first example of organocatalytic asymmetric nucleophilic fluorination using alkali metal fluorides.[62f] The group has optimised axially chiral *bis*-urea **1.1.7** derived from BINAM for desymmetrisation of stilbene-derived episulfonium ions using CsF in up to 98% yield and 97:3 *e.r.* (**Scheme 1.2.9**). The urea moiety was designed to solubilise and activate CsF, which otherwise is insoluble in 1,2-difluorobenzene. Extensive X-ray and NMR investigations have confirmed that BINAM *bis*-urea catalysts form soluble CsF:urea complexes in solution through H-bonding.[62f,g] Highly electrophilic β-bromosulfide substrates were chosen for the asymmetric C-F bond formation, which *in situ* auto-ionise into reactive *meso*-episulfonium ions that can subsequently engage in ion-pairing. The proposed ion-pair is reminiscent of nucleophilic fluorination of the corresponding sulfonium electrophile in nature by fluorinase (**Scheme 1.2.9** and *v.* Section 1.3.2).

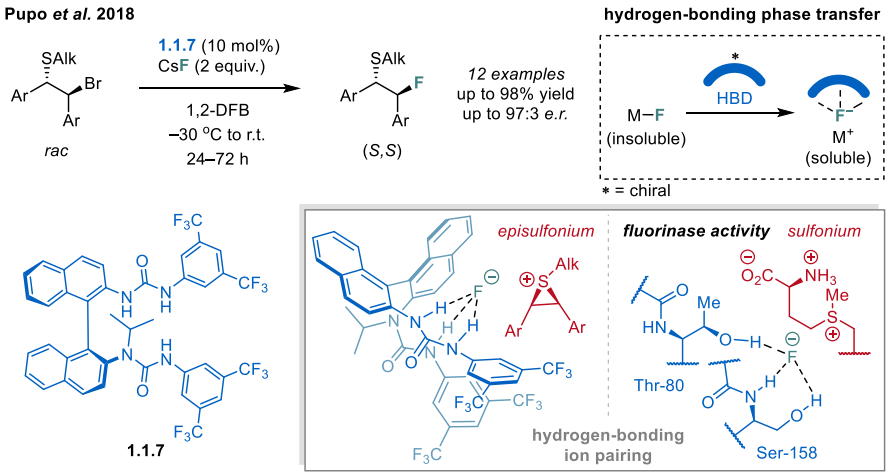

Scheme 1.2.9. Asymmetric fluorination of β-bromosulfides via HP-PTC using CsF.[62f] 1,2-DFB = 1,2-difluorobenzene.

Since the first disclosure, the concept of hydrogen-bonding phase-transfer catalysis (HB-PTC) with MF salts for asymmetric fluorination has been applied to a range of highly electrophilic substrate classes. In 2019, Pupo *et al.* have disclosed the enantioselective synthesis of pharmaceutically relevant β-fluoroamines through desymmetrisation of *in situ* formed *meso*-aziridinium ions (**Scheme 1.2.10**).[104] Using catalyst **1.2.9**, the stilbene-derived β-chloroamines were fluorinated in excellent enantioselectivities (up to 96:4 *e.r.*), while a few examples of aliphatic products from corresponding β-bromoamines were afforded in up to 85:5 *e.r.*. The method was

shown to be compatible with CsF and KF, the latter being cheaper, yet more demanding F^- source (lattice energy, 181 *versus* 198 kcal mol^{-1},[78] respectively).

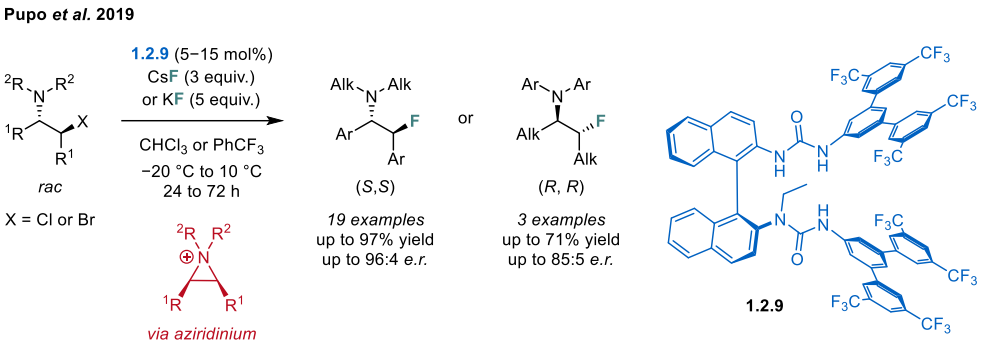

Scheme 1.2.10. HP-PTC using KF for asymmetric fluorination of β-haloamines.[104]

In 2020, Roagna *et al.* demonstrated asymmetric fluorination of pre-formed azetidinium triflate salts.[105] Although ammonium salts are known to facilitate cation-directed PT of CsF (*v.* Section 1.2.2.1), the *bis*-urea catalyst **1.1.7** outcompeted the non-stereoselective background reactivity to afford enantioenriched γ-fluoroamines in up to 99% yield and 97:3 *e.r.* (**Scheme 1.2.11a**, *top*). Fluorination of model substrate **1.2.10** using *in situ* prepared **1.1.7**:TBAF provided the fluorinated product in analogous enantioenrichment yet in lower yield (96:4 *e.r.*, 30% yield) in comparison to using CsF and 10 mol% of (*S*)-**1.1.7** (96:4 *e.r.*, >95% yield; **Scheme 1.2.11a**, *bottom*). These results indicate the formation of **1.1.7**:F^- species and no contributions of Cs^+ in the enantiodetermining step. The reduced conversion was attributed to the water content of **1.1.7**:TBAF, which was prepared from TBAF$(H_2O)_3$.

Work by Sun and co-workers demonstrated that HB-PTC for asymmetric nucleophilic fluorination is not limited to BINAM *bis*-urea based HDB catalysts. A squaramide-derived chiral catalyst **1.2.11** was developed for enantioconvergent fluorination of α-keto sulfonium salts – a substrate class prone to racemisation (**Scheme 1.2.11b**).[62i] It was suggested that the squaramide catalyst was bringing both of the reactants into solution via formation of ion pair, since the sulfonium substrate and CsF were insoluble in mesitylene. Additionally, RbF was shown to be a competent F^- source, but no successful fluorination was achieved with KF or less reactive alkali metal fluorides.

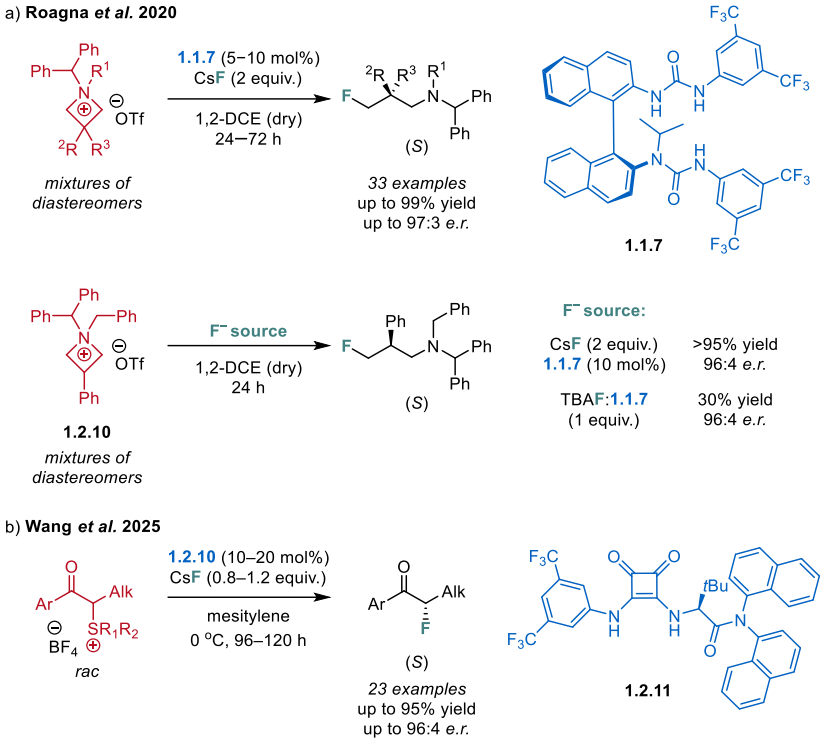

Scheme 1.2.11. Pre-formed ionic substrates for fluorination with CsF under HB-PTC.[62i,105] 1,2-DCE = dichloroethane, OTf = triflate.

All the examples discussed highlight the reliance on the generation of chiral ion pair between HBD-bound fluoride and ionic substrate. Dooley *et al.* showed that even though HBD catalyst **1.1.7** is sufficient to solubilise CsF, solubilisation of KF requires both, HBD and onium salt (**Scheme 1.2.12**, *top*).[62h] Using a neutral substrate, benzyl bromide, no fluorination was observed with either CsF or KF in the presence of phosphonium additive in toluene at elevated temperatures. In contrast, the synergy of HBD catalyst **1.1.7** and the onium additive afforded fluorinated products in 34% and 55% yields using KF and CsF, respectively. This work culminated in the characterisation of *in situ* formed ternary HBD-onium-fluoride complexes derived from KF. The concept was applied for enantioconvergent nucleophilic substitution of benzylic bromides and α-bromoketones using chiral BINAM *bis*-urea catalysts (**Scheme 1.2.12**, *bottom*). The in-depth mechanistic investigations also indicated that both catalysts, onium salt and HBD, are involved in substrate racemisation.

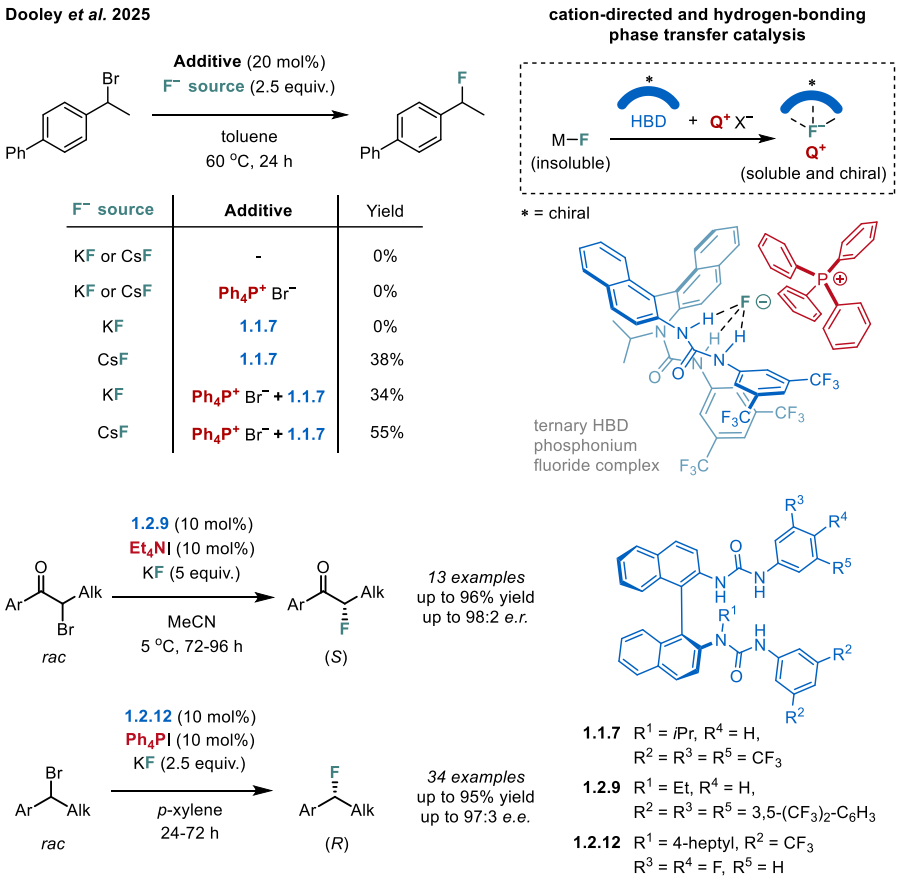

Scheme 1.2.12. Solubilisation KF using two-catalyst system for asymmetric fluorination of neutral substrates.[62h]

1.3. Biochemistry of fluorine

1.3.1. Protein-fluoride binding

Even though fluorine is the 13th most abundant element in the Earth's crust, compared to the other halogens (20th, 62nd, and 64th for Cl^-, Br^-, and I^-, respectively), fluoride appears to be relatively rare in nature. In the PDB there are currently only 94 entries containing fluoride as a ligand, with close to 20,000 for chloride, 688 for bromide, and 1,200 for iodide. This is in part a consequence of the low abundance of fluoride in seawater (1.3 ppm for fluoride in contrast to 19,000 ppm for chloride),[106] which arises from the low solubility of CaF_2 (16 $mg \cdot kg^{-1}$ in water at 25 °C).[78] The biochemistry of fluoride mainly features protein inhibition, either directly through binding or indirectly as a transmembrane proton carrier,[107] and is associated with a range of disorders in a concentration-dependent manner.[108] In contrast to other anions, fluoride does not bind to typical anion-binding sites formed by the main-chain NH groups.[109] Instead, the main mechanisms of F^--mediated protein inhibition are: 1) binding to metal centres of metalloenzymes (*e.g.* transition metals in peroxidases and ureases: Fe, Cu, Mn, Ni; or alkali metals in enolases and phosphatases: Mg^{2+}, Ca^{2+}), and 2) complexation with metals to mimic substrates.[107b] Since approximately 25–50% of proteins rely on metals for their activity, there are numerous potential targets for fluoride.[110]

In terms of metalloenzyme-fluoride binding, enolase, which catalyses the penultimate step of glycolysis by converting 2-phosphoglycerate to phosphoenolpyruvate, is by far the most extensively studied enzyme. The initially accidental crystallisation of the enolase-fluoride complex by Warburg and Christian,[111] followed by subsequent crystallographic studies[107b,112] revealed two fluoride anions bound to a magnesium-phosphate complex in the active site, occupying the carboxylate binding site of the native substrate (**Figure 1.3.1a**). Heme-containing enzymes that bind to fluoride (as a proxy for H_2O_2) represent another well-documented example. One of the early crystal structures of heme-fluoride complexes was reported in 1984 for cytochrome *c* peroxidase.[113] In addition to the anticipated direct iron-fluoride binding, another interaction involving distal His-52 as an H-bond acceptor was identified (**Figure 1.3.1b**). The authors

postulated that, due to this H-bonding interaction, peroxidases preferentially bind to HX ligands rather than X^-.

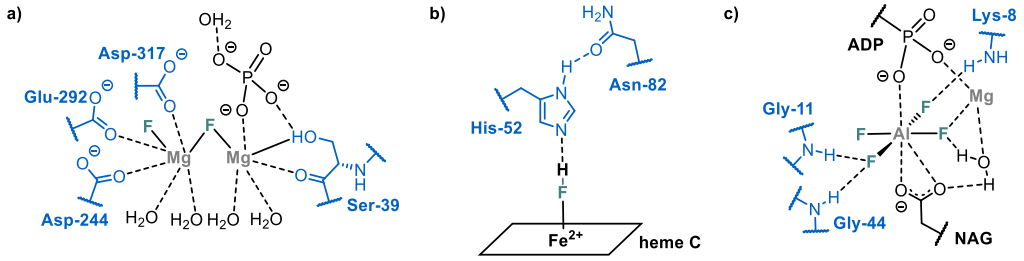

Figure 1.3.1. Examples of metal-fluoride inhibition: a) enolase inhibition, adapted from pdb: 2AKZ,[114] b) cytochrome *c* peroxidase inhibition,[113] and c) *N*-acetyl-L-glutamate kinase inhibition, adapted from pdb: 1OH9.[115]

Fluoride tends to complex not only with metalloenzymes, but also with other naturally occurring metals, and the resulting complexes can subsequently interact with enzymes. The most toxic complexes, aluminium and beryllium fluorides ($AlF_{3,4}$ and $BeF_{3,4}$), are isomorphous to phosphate and consequently inhibit numerous phosphoryl-transfer enzymes, including kinases and adenosine and guanosine triphosphatases.[116] The crystallisation of *N*-acetyl-L-glutamate (NAG) kinase with $MgCl_2$, adenosine-5'-diphosphate (ADP), $AlCl_3$ and NaF revealed an active site complexed with an Mg^{2+}-ADP-AlF_4^- cluster – a transition-state analogue responsible for NAG kinase inhibition (**Figure 1.3.1c**).[117] In the complex, the Al^{3+} is octahedrally coordinated with four equatorial F^-, one of which is exposed to solvent, while another is bound to Mg^{2+}. The remaining two F^- are hydrogen-bonded to the enzyme via the side chain of Lys-8, and the amide protons of Gly-44 and Gly-11.

To tackle fluoride toxicity described above, some classes of organisms have developed transport systems to control fluoride concentration. These include Fluc proteins (found in prokaryotes and lower eukaryotes)[118] and CLC^F proteins (found in bacterial species)[119]. Fluc is an electrodiffusive fluoride-specific channel consisting of a homodimer in which both subunits consist of four α-helices (α^{1-4}; **Figure 1.3.2a**). The crystal structure of the Fluc channel from *Bordetella pertussis* with NaF suggested that the homodimer contains two identical narrow pores for anion conduction, which are highly size-selective for F^- over Cl^- (the architecture of one of the pores is shown in **Figure 1.3.2b**).[120] Two potential fluoride binding sites were also identified from X-ray

structures, but due to limitations of the technique, F^- could not be distinguished from H_2O. From these crystal structures it was proposed that the F^- conductivity is aided by H-bonding interactions with the side chain of Asn-43 in α^2, and the conserved Ser-108 and Ser-112 in α^2 (**Figure 1.3.2b**). In addition, two edge-on interactions between the aromatic rings of Phe-82 and Phe-85 in α^3 with the anion were identified, which is rather unusual in proteins.[121] Subsequent extensive NMR investigations revealed that site-1 is only a transient binding site for fluoride, which is replaced by H_2O once fluoride moves to site-2 – the resting site (**Figure 1.3.2c**).[122] Notably, sites 1 and 2 only contain the desolvated anion, however, the exact mechanism of fluoride dehydration remains unclear.

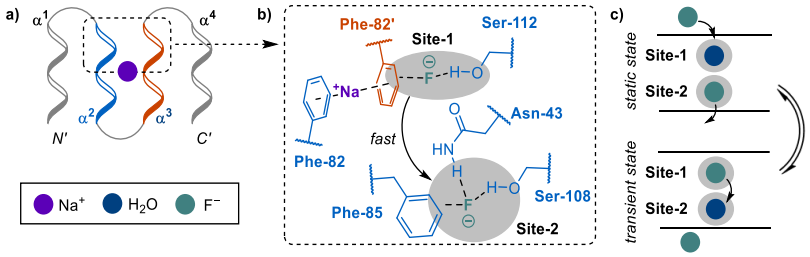

Figure 1.3.2. Two F^-/H_2O binding sites in electrodiffusive Fluc channel. For clarity, only one pore is shown.[120-122]

The other major class of F^- transporting proteins, so-called CLC^F, is a subfamily of CLC (chloride channels and transporters) that couple F^- efflux to a proton gradient.[119] The selectivity of these transporters for F^- over Cl^- is also extremely high, but due to the lack of high-resolution structures of CLC^F, the fluoride binding sites and the rationale behind anion selectivity have not yet been characterised.[123]

1.3.2. Enzymatic fluorination

Regarding the organic fluoride, there are 20 fluorinated natural products reported to date (**Figure 1.3.3**),[124] in stark contrast of approximately 8,000 characterised naturally occurring organohalogen compounds.[125] The biosynthesis of most halocarbons proceeds via an oxidative mechanism by hydrogen peroxide (H_2O_2) dependent haloperoxidases.[126] The electronegativity of fluorine results in a very high oxidation potential (E° = 2.87 V), which is higher than the respective value of H_2O_2 (E° = 1.76 V), making enzymatic oxidative halogenation pathway for C–F bond formation unfeasable.[127] Therefore, fluoride incorporation in nature is limited to nucleophilic substitution, which requires an enzyme evolved for dehydration of the fluoride anion (ΔG_{hyd}^{298}(calc.) = –104.2 ± 0.7 kcal mol^{-1})[128], since fully hydrated F^- is a poor nucleophile (*v.* Section 1.2.2).

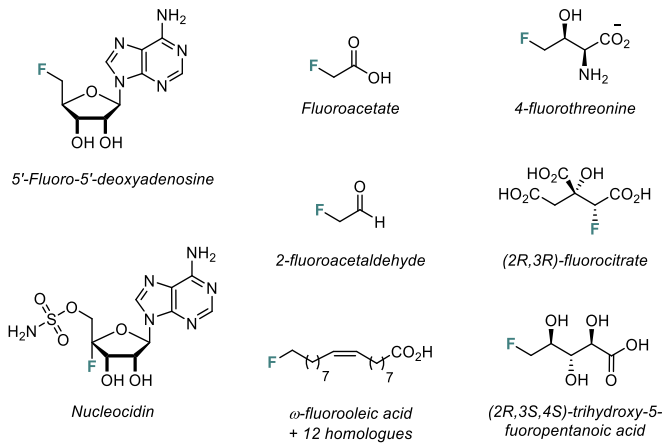

Figure 1.3.3. Biogenic organofluorine compounds.[124]

In 2002, O'Hagan reported a naturally occurring enzyme, called fluorinase or 5'-fluoro-5'-deoxyadenosine (5'-FDA) synthase, capable of catalysing the formation of C–F in the strains of bacterium *Strepomyces cattleya*.[129] The isolated enzyme facilitated the nucleophilic substitution of *S*-adenosylmethionine (SAM) with fluoride (F^-; from aqueous NaF) to generate 5'-FDA and L-methionine. The rare activity of fluorinase has sought extensive structural and mechanistic investigations.[130] The enzyme exhibits a very low turnover rate (10^{-3} s^{-1}), compared to the average turnover rates of enzymes (10^3–10^7 s^{-1}), which is associated with the high activation energy to compensate for desolvation of fluoride. Fluorinase achieves desolvation of F^- by a carefully orchestrated H-bonding network (**Scheme 1.3.1**). First, fluoride weakly binds to the

enzyme (Michaelis constant, K_m ~ 10 mM) via bidentate H-bonding with Ser-158, which results in partial F^- dehydration. Binding with SAM (K_m ~ 20 μM) facilitates full dehydration and formation of additional F^- H-bond contact with fluorinase – Thr-80. Based on deuterium-labelling experiments, the subsequent fluorine incorporation proceeds via S_N2 mechanism with inversion of configuration, which is rather uncommon in enzymatic catalysis.[130b,131]

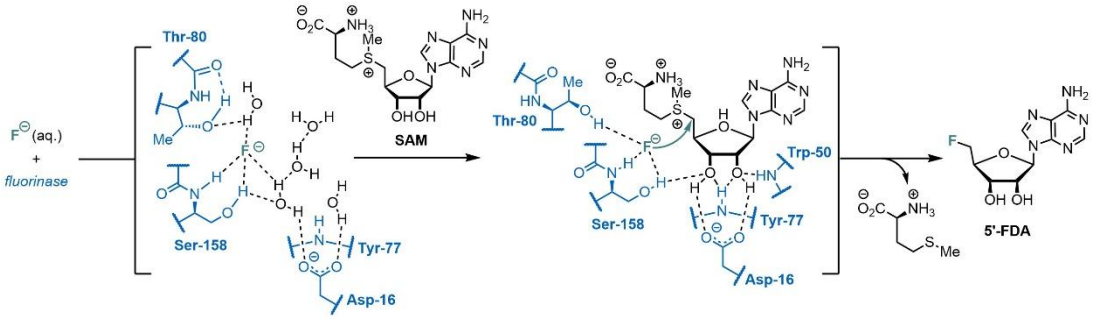

Scheme 1.3.1. Mechanism of the fluorinase enzymatic fluorination.[129-130]

Fluorinase, and its six later discovered homologues,[132] is still the only known natural biosynthetic route to forming C–F bonds. Notably, 5'-FDA is considered as the precursor for all biogenic organofluorine compounds in **Figure 1.3.3** through 2-fluoroacetaldehyde, except for nucleocidin.[133] The biochemical mechanism of C–F bond formation in nucleocidin, an antibiotic produced by bacterium *Strepomyces calvis*, still remains unknown, but is suggestive of an alternative fluorinating enzyme.[134]

Fluorinations catalysed by non-native enzymes remain scarce too.[127,135] In 2001, Withers and co-workers reported that six active site mutants of the two retaining glycosidases *Agrobacterium sp.* β-glucosidase (Abg) and *Cellulomonas fimi* β-mannosidase (Man2A) could form α- and β-glycosyl fluorides (**1.3.2**) under biological conditions using aqueous KF (**Scheme 1.3.2**).[127] The respective fluorinated intermediates would then act as glycosyl donors in transglycosylation with the corresponding substrate (**1.3.1**). The exact state of fluoride water solvation and interactions with glycosidases during the nucleophilic fluorination event were not elucidated.

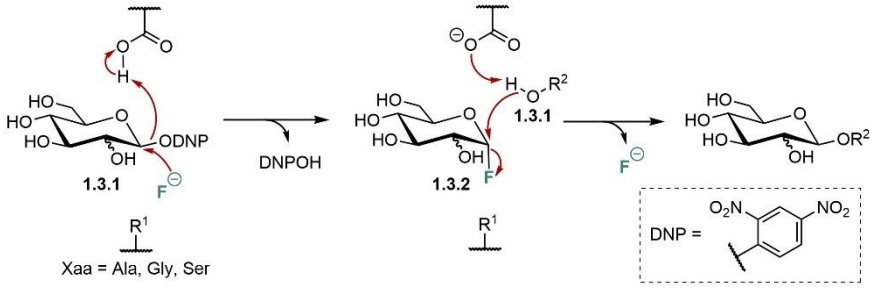

Scheme 1.3.2. Mutated Abg/Man2A catalysing nucleophilic fluorination of 2,4-dinitrophenyl (DNP) β-glucoside/mannoside, and subsequent transglycosylation.[127]

In 2024, two examples of engineered nonheme iron enzymes, a variant of (*S*)-2-hydroxypropylphosphonate epoxidase (*Sv*HppE-Fluor) and a variant of 1-aminocyclopropane-1-carboxylic acid oxidase ($ACCO_{CHF}$), emerged for asymmetric fluorination via an unprecedented biocatalytic radical-mediated fluorine atom transfer (**Scheme 1.3.3**).[135] Albeit, the ion mediated C–H fluorination via N–F activation has been reported previously,[136] this work was the first example of asymmetric radical C–H fluorination.

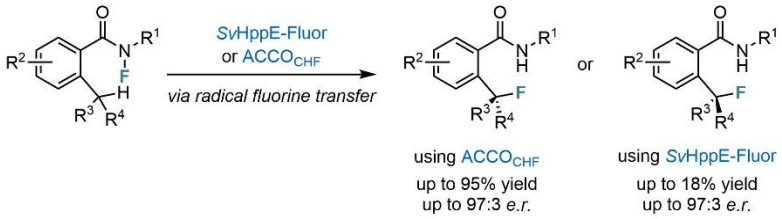

Scheme 1.3.3. Bioengineered asymmetric radical C(sp^3)–H fluorination.[135]

1.3.3. Defluorination

Most of the fluorinated natural products shown in **Figure 1.3.3** are acids that are known to be toxic and presumably were produced as a defence strategy. For example, fluoroacetate (FAc), the most common biogenic organofluorine compound, is produced by numerous plants as a defence mechanism against grazing and is one of the most toxic poisons to mammals.[137] Consequently, nature has evolved a few classes of enzymes (FAc dehalogenases,[138] L-2-haloacid dehalogenases,[139] and FAc-specific defluorinases[140]) to tackle cytotoxic FAc and its derivatives[78] (**Scheme 1.3.4**). There is also an array of reductive enzymes and redox metalloenzymes that utilise native or engineered pathways to catabolise other organofluorines arising from industrial contamination (*e.g.* aromatics), but they will not be covered in this section.[141]

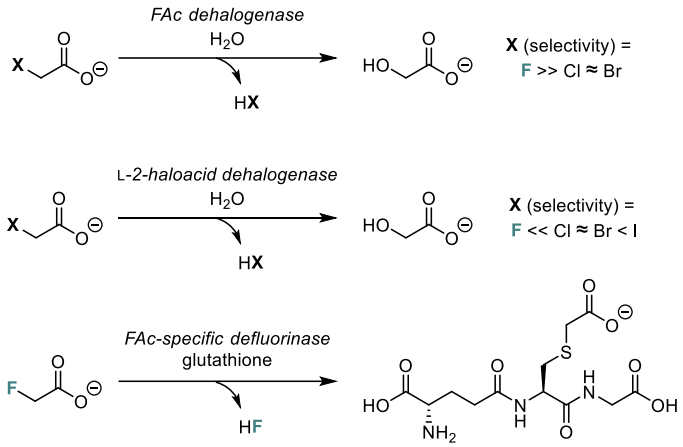

Scheme 1.3.4. Native enzymatic defluorination of fluoroacetate.[138-140]

The most studied enzyme, fluoroacetate dehalogenase from *Burkholderia sp.* FA1, was first described in 1965 by Goldman,[138a] but its catalytic triad Asp-His-Asp was only identified in 2009 via X-ray crystallography (**Scheme 1.3.5**).[142] Further mechanistic investigations[143] confirmed that fluoride is displaced via an S_N2 attack of Asp-104 to the C^{α} of FAc forming a covalent enzyme-glycolyl intermediate. Following, the hydrolysis of this intermediate is facilitated by the His-271 and Asp-128 forming a glycolic acid. During the fluoride displacement event, His-149, Trp-150, and Tyr-212 residues are involved in H-bonding to F^-, which results in a reduction of the activation energy. Haloacid dehalogenases have been shown to proceed via an identical

mechanism, albeit the absence of sequence similarities and inverse selectivity for other halogens (Cl, Br and I).[139b]

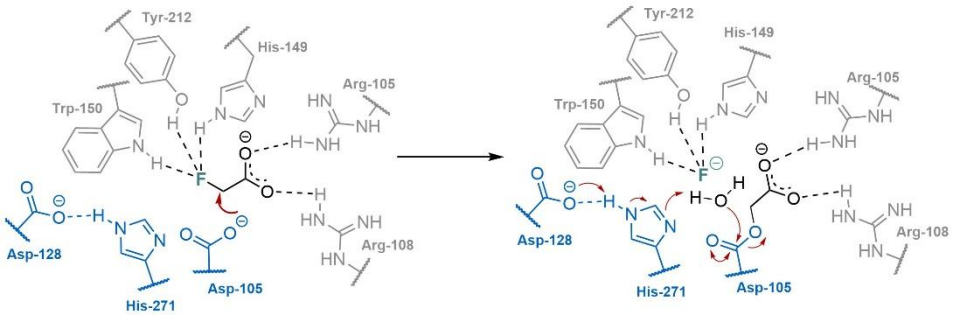

Scheme 1.3.5. Hydrolytic mechanism of fluoroacetate dehalogenase with a catalytic triad highlighted in blue.[138a,142-143]

The catalytic defluorination by fluoroacetate-specific defluorinases, which are only found in mammals, is different from hydrolases described above.[144] The enzymes are known to be glutathione-dependant and represent a new class of dehalogenases, but mechanistic detail still requires further investigation.

1.4. Peptide catalysis

Over the past century, significant advances have been made in understanding protein function, enabling chemists to exploit their remarkable efficiency in chemical synthesis.[145] The secondary and tertiary structures of large proteins have been ingeniously mimicked through advances in *de novo* protein design[146] or *directed evolution*[147] in order to develop enzymes with non-native activities. The latter was recognised with the Nobel Prize (Chemistry) in 2018 to Frances H. Arnold. Alongside, synthetic chemists have attempted to mimic enzymes by utilising amino acids as ligands for transition metals, organocatalysts for asymmetric synthesis and as multifunctional catalysts for hydrolysis/transesterification.[148] This section will cover key concepts in metal-free amino acid and small to medium peptide-based catalysts (< 20 amino acids) for asymmetric transformations, a key subset of the wider field of organocatalysis. The first two sections focus on strategies to enforce conformational restraint used for the construction of selective reaction sites: cyclic and β-turn based short peptides (*v.* Section 1.4.1), and secondary structures of medium length peptides (*v.* Section 1.4.2). Also, the breath of peptide-catalysed asymmetric transformations will be explored in Section 1.4.1, with methods for halogenations covered in Section 1.4.3.

1.4.1. Asymmetric catalysis with amino acids and short peptides

Although organic molecules have been used as catalysts for almost two centuries, their application in enantioselective catalysis has only surged in the late 20th century. The start of the asymmetric organocatalysis could be attributed to the use of a privileged amino acid – L-proline. The most renowned example was reported in early 1970s by two groups, Hajos and Parrish,[149] and Wiechert *et al.*,[150] where Pro was employed for intramolecular aldol reaction to access ketols **1.4.1** and **1.4.2** (**Scheme 1.4.1a**). In 2001, Barbas III and List showcased an intermolecular version of Pro catalysed asymmetric aldol between acetone and a range of aldehydes (**Scheme 1.4.1b**).[151] The enantioselectivity was governed by Zimmerman-Traxler transition state between enamine (from proline and acetone condensation) and aldehyde. The concept was inspired by the Hajos−Eder−Sauer−Wiechert reaction and the extensive work by Barbas *et al.* on type 1 fructose-1,6-diphosphate (FDP) aldolase activity (**Scheme 1.4.1c**).[152] In nature, the enzyme catalyses aldol addition of dihydroxyacetone phosphate (DHAP) and glyceraldehyde 3-phosphate. Instead of Pro, type I aldolases utilise side chain of Lys residue and DHAP to generate a Schiff-base, which tautomerizes to the reactive enamine. Interestingly, for beforementioned proline-catalysed aldol reported by List *et al.*, other primary amine and secondary amine containing amino acids were shown to be ineffective. Since then, the use of proline, its derivatives, and other small cyclic secondary amine based organocatalysts have flourished into a field of its own and was recently acknowledged with the 2021 Nobel Prize in chemistry.

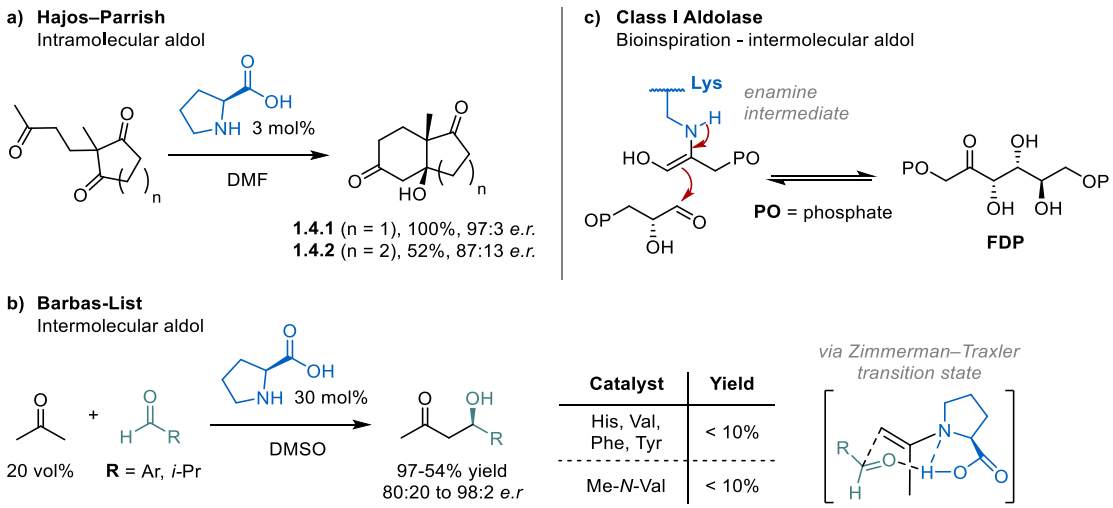

Scheme 1.4.1. Class I aldolase inspired proline-catalysed intra- and intermolecular aldol.[149-152]

In comparison to single amino acids, the structural diversity available with short peptide sequences, makes them promising for the development of a broad spectrum of organic catalysts with tunable structural and electronic properties. The first examples of asymmetric short peptide catalysis was reported in 1981 by Inoue and Oku for enantioselective hydrocyanation of benzaldehyde employing cyclic dipeptide cyclo(His-Phe) (**1.4.3**; **Scheme 1.4.2a**).[153] This catalyst was designed as a small molecule mimic to naturally occurring enzyme – D-oxynitrilase.[154] Many isoforms of the enzyme exists, but the active site always contains HBD–histidine–acid triad. Typical mechanism proceeds via H-bonding activation of aldehyde (*e.g.* with alcohol or thiol functionalities), followed by stereospecific nucleophilic attack of CN^- (**Scheme 1.4.2b**).[155] Even though mechanism of hydrocyanation using synthetic peptide **1.4.3** still remains elusive, it is known that reaction displays 2nd order kinetics with respect to catalyst.[156] One His residue is thought to engage in H-bonding to aldehyde, with another acting as a base catalyst, drawing many similarities to the native enzymatic process. Since linear analogue Cbz-Phe-His-OMe (**1.4.4**) had achieved no enantiocontrol compared to cyclic **1.4.3** (95:5 *e.r.*), it was postulated that stereocontrol of the reaction is reliant on structural rigidity of the 2,5-piperazinedione ring.[157]

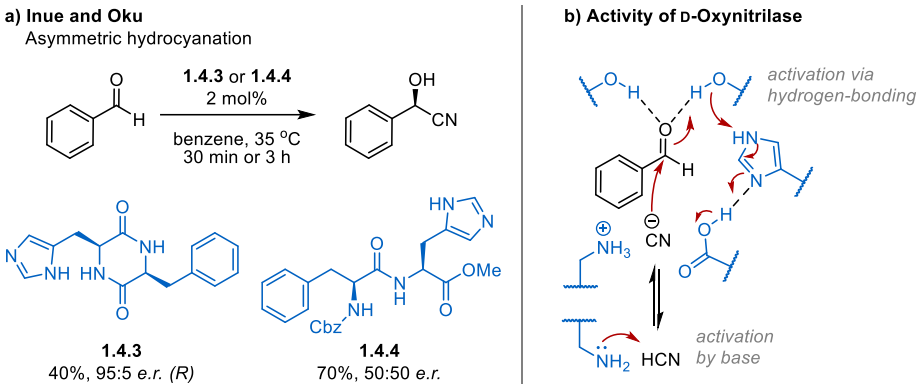

Scheme 1.4.2. Cyclic dipeptides for asymmetric hydrocyanation inspired by D-oxynitrilase.[153,155,157] Cbz = benzyloxycarbonyl.

In late 20th short linear peptides were considered unsuitable for catalysis; their flexibility in solution was regarded as disadvantage for achieving high enantioselectivities. In 1998, the seminal work by Miller *et al.* have demonstrated that short linear peptides are more than capable catalysts for asymmetric transformations.[158] In one of the early studies by the group, tetrapeptide **1.4.5** containing alkylated histidine (His(Me)) residue was discovered for the kinetic resolutions of

amino alcohol *rac*-**1.4.6** (58% yield, 99:1 *e.r.*; **Scheme 1.4.3a**). The peptide was proposed as an alternative to acetyltransferase enzymes, which employ acetyl coenzyme A (Ac-CoA)[159] for acetylation of biologically relevant amines and alcohols.[160] The key active residue in **1.4.5** was designed to contain substructure of known nucleophilic catalyst for acetyl-transfer in organic synthesis – *N*-methylimidazole.[161] The success of **1.4.5** was attributed to the formation of proline-induced non-regular secondary structure, a type II' β-hairpin, which was responsible for the rigidity of the short-peptide. The (*R*,*R*)-**1.4.6** chiral recognition was proposed to be facilitated by the H-bonding with amino acid at the heart of the β-turn – α-aminoisobutyric acid (Aib). Alongside, work by Toniolo *et al.* on Pro-Xaa motif (where Xaa = α,α-disubstituted amino acid) has demonstrated that β-turn conformation can be fine-tuned by varying Xaa substitution pattern.[162] Later studies by the Miller group have identified a range of covalent functional handles in place of His(Me), for example, Asp for oxidations, Cys for hydrogen atom transfer, and phosphothreonine for reductions (**Scheme 1.4.3b**).[163] This work has established a very modular peptide-based platform and has laid the foundations for the field of asymmetric peptide catalysis.

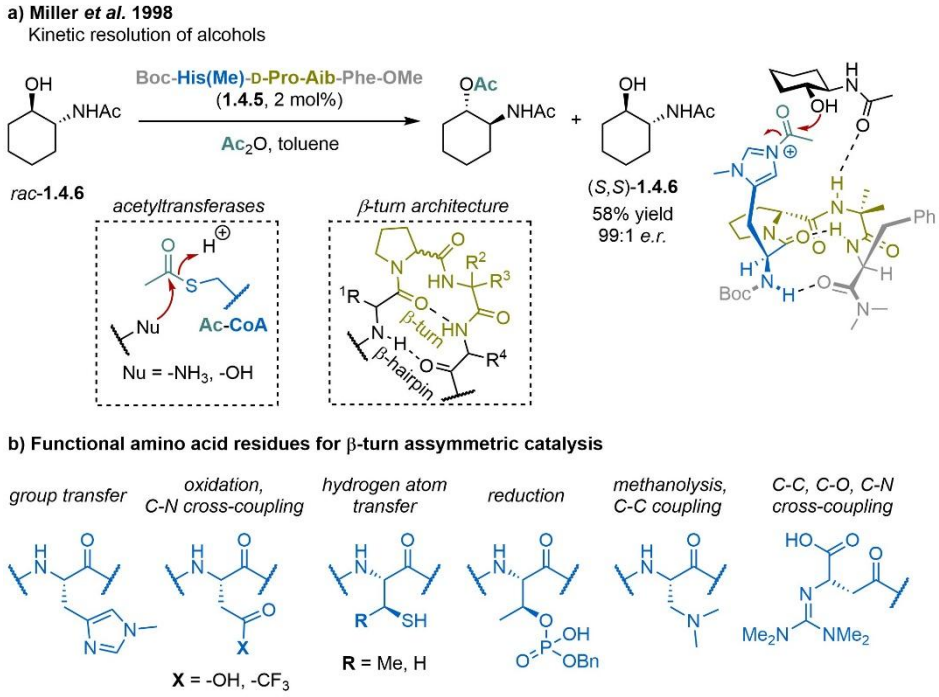

Scheme 1.4.3. A β-turn containing short-peptide catalyst for asymmetric transformation. a) Asymmetric acyl transfer with His(Me) residue,[158,160] and b) examples of functional handles for asymmetric peptide catalysis.[163]

Another approach in peptide-catalysis features substrate activation via enamine/iminium formation (covalent catalysis), which draws inspiration from early work on asymmetric proline catalysis described previously.[164] The concept of peptide-catalysts bearing *N*-terminal prolyl residues has been explored already in 2003 for aldol reaction by the groups of Reymond[165] and List[166], but the methods described achieved only moderate enantioselectivities. The first successful asymmetric approach was demonstrated by the Gong *et al.*[167] using the tetrapeptide catalyst H-Pro-(Phe)$_3$-OMe (**1.4.7**) for aldol between hydroxyacetone and aromatic aldehydes (**Scheme 1.4.4**). Catalyst **1.4.7** achieved not only excellent stereoselectivities (up to 98:2 *e.r.*) but also an opposite regioselectivity compared to L-proline[168] (1,4- *versus* 1,2-diol, respectively), highlighting the potential of tuneable selectivity in peptide catalysis. The *N*-terminal amine catalysis is not only limited to proline derivatives; other primary amino acids can also be utilised, offering a wide range of modularity.[169] Nowadays, peptide-based primary/secondary amine catalysts have been extended to other C−C bond forming reactions via enamine (*e.g.* Mannich and 1,4 addition) and iminium formation (*e.g.* cycloaddition and Friedel-Crafts).[163]

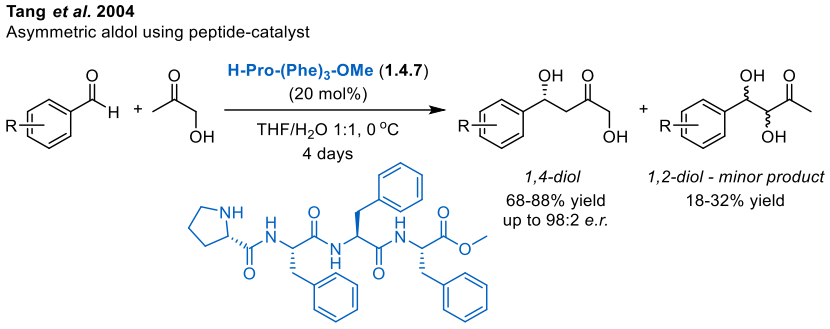

Scheme 1.4.4. *N*-Terminal prolyl-peptides for asymmetric aldol.[167]

In contrast to Miller's tuneable design of β-turn peptides containing Pro-Xaa motif (where Xaa = α,α-dialkylated amino acid, **Scheme 1.4.3**), the work of Wennemers *et al.* has established another modular peptide-based platform. In 2005, through combinatorial screening the group has discovered a tripeptide H-Pro-Pro-Asp-NH$_2$ (**1.4.8**) for the aldol reaction between acetone and aldehydes (**Scheme 1.4.5a**).[170] At that time **1.4.8** was the most efficient peptide for enamine catalysis requiring only 1 mol% catalyst loading to achieve quantitative yield in only 4 hours. Following studies have established a general H-Pro-Pro-Xaa motif, where Xaa = acidic amino

acid, for 1,2- and 1,4- additions with a diverse substrate scope accessed by fine-tuning the catalyst to address the steric and stereoelectronic properties of the substrates (**Scheme 1.4.5b**).[163a,171] The structural design of the peptide sequence relies on the formation of a β-turn induced by two consecutive prolines.[172]

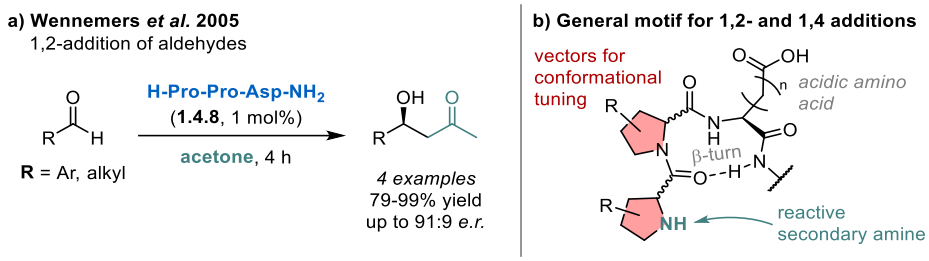

Scheme 1.4.5. Enamine catalysis using H-Pro-Pro-Xaa scaffold.[163a,170-171]

1.4.2. Secondary structures in peptide catalysis

For catalysis a well-defined peptide conformation is crucial for reactivity and selectivity. Inducing β-turns has been shown to be particularly successful in short peptide catalysis (*v.* Section 1.4.1). Meanwhile, for medium sized peptides (up to 50 amino acids) helices have been established as privileged motifs to enforce rigidity. In 1980, Juliá *et al.* have reported catalytic asymmetric epoxidation of chalcone (**1.4.10**) using poly-L-alanine (H-(Ala)$_{10}$-NHBu, **1.4.9c**; **Scheme 1.4.6**).[173] Later studies by Juliá and Colonna and their co-workers have investigated varying lengths of polypeptide (H-(Ala)$_n$-NHBu, where n = 5−30; **1.4.9a−d**) for the transformation and found that polymers of increasing length provided superior yields and enantioselectivities.[174] The H-(Ala)$_{30}$-NHBu (**1.4.9d**) provided epoxide **1.4.11** in 96% yield and 98:2 *e.r.*, while the shortest polymer H-(Ala)$_5$-NHBu (**1.4.9a**) afforded product only in trace yield and 56:44 *e.r.* (**Scheme 1.4.6**). The selectivity was associated with longer polymers having increased propensity to form α-helices.

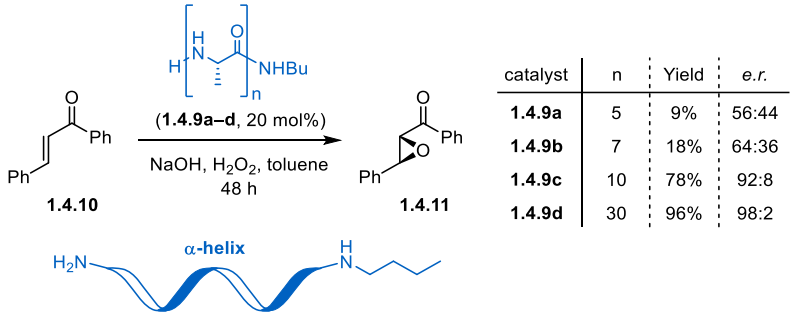

catalyst	n	Yield	*e.r.*
1.4.9a	5	9%	56:44
1.4.9b	7	18%	64:36
1.4.9c	10	78%	92:8
1.4.9d	30	96%	98:2

Scheme 1.4.6. Asymmetric Juliá-Colonna epoxidation with α-helix motif.[173-174]

The seminal work of Juliá and Colonna has led to a development of a wide range of peptide catalysts with secondary frameworks, most often featuring helices.[175] The designed peptide scaffolds can even contain multiple secondary structural motifs. For example, Kudo *et al.* have demonstrated a concept of combining α-helix and β-turn segments for asymmetric reduction of α,β-unsaturated aldehydes using Hantzsch ester (**Scheme 1.4.7a**).[176] The optimised peptide **1.4.12** contained Pro-D-Pro-Aib induced β-turn, reminiscent of work by Wennemers and Miller groups (*v.* Section 1.4.1), and a poly-Leu tether inspired by Juliá-Colonna epoxidation[177] – both components were shown to be crucial for enantioinduction. Installing peptide to polyethyleneglycol grafted on polystyrene resin support[178] allowed for a direct use of **1.4.12** after

solid-phase synthesis and an easy recovery of **1.4.12** by filtration post-catalysis. The resin support was inconsequential for the hydrogenation yield or enantioselectivity.

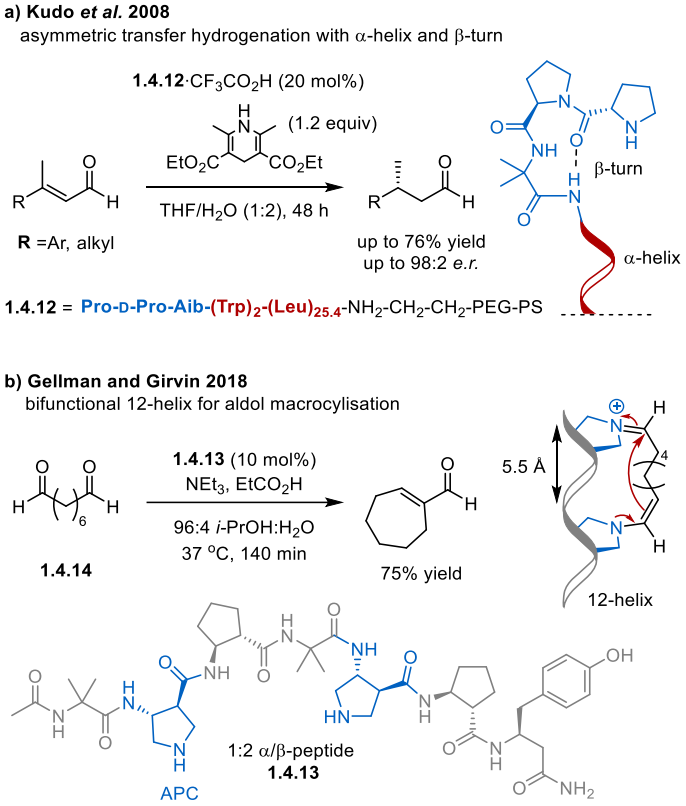

Scheme 1.4.7. Examples of secondary structures in peptide-catalysis.[176,179] PEG-PS = polyethyleneglycol grafted on polystyrene.

The development of unnatural amino acids has allowed for design of non-native architectures beyond α-helixes. Gellman and Girvin have demonstrated that oligomer **1.4.13** which contains a 1:2 mix of α- and β-amino acids can form a *i,i+3* 12-helix which enables an effective aldol macrocyclisation of dialdehyde **1.4.14** (**Scheme 1.4.7b**).[179] The bifunctional catalyst could activate both, electrophile and nucleophile, via a reactive dyad consisting of two *trans*-(3*R*,4*S*)-4-aminopyrrolidine carboxylic acid (APC) units. The 12-helix conformation assured the proximity of the groves in comparison to a typical all β-peptide *i,i+3* helix (pitch of 5.5 Å *versus* 6.6 Å). In addition, 12-helix was shown to contain ~3 residues per turn, compared to ~3.6 for α-helix or ~2.5 for pure β backbone, affording a nearly perfect angular alignment of the APC pyrrolidine rings.[180] The proximity-induced reactivity was also reported using an α-helix framework by Kinghorn *et al.*[181]

1.4.3. Peptide-based catalysts for halogenation

Despite a wide range of transformations catalysed by peptides: oxidations/reductions, hydrolysis/transesterification, C−C bond formations, and group transfers (*e.g.* acyl, phosphoryl and sulfonyl),[163] peptide-catalysed halogenations are uncommon and limited to electrophilic chemistry. Miller *et al.* has reported a range of linear peptides for atroposelective and site-selective bromination via electrophilic aromatic substitution (S_EAr).[182] The first disclosure of tripeptide **1.4.14** for dynamic kinetic resolutions of biphenol atropisomers was made in 2010.[182c] During the study it was observed that carboxylate functionality on the substrate is crucial for enantioselectivity, as it would form one of the key H-bonding contacts to the peptide via β-dimethylaminoalanine (Dmaa) residue (**Scheme 1.4.8a**). The ensuing examples of peptide-catalysed S_EAr brominations by the Miller group focused on expanding the methodology to site-selective bromination of complex natural products, desymmetrisation of bi-aryls, and to expand a substrate scope for atroposelective bromination. All the disclosures feature a comparable mode of action of the catalyst – the tertiary amine handle is responsible for chiral recognition via H-bonding with the pre-installed functional groups of the substrate (*i.e.* alcohol or carbonyl). Based on literature precedence by Demark and Burk,[183] the delivery of the bromonium (Br^+) was postulated to proceed via proximal Lewis basic carbonyls, however no experimental evidence of Br^+--O=C interaction was secured by the Miller group.

On the other hand, recently, Maji and co-workers disclosed a methionine containing peptide **1.4.15** for site-selective S_EAr chlorination, where S--Cl^+ formation was deemed crucial for the chlorination step (**Scheme 1.4.8b**).[184] The method was successfully applied for site-selective *ortho*-directed chlorination of Tyr residues in functionalised oligopeptide sequences and of various aryl motifs in drug molecules (*ortho*/*para*-directed by pre-installed functional groups). For chlorination, very low catalyst loading (0.5 mol%) could be used, which is uncommon for peptide-catalysed processes.

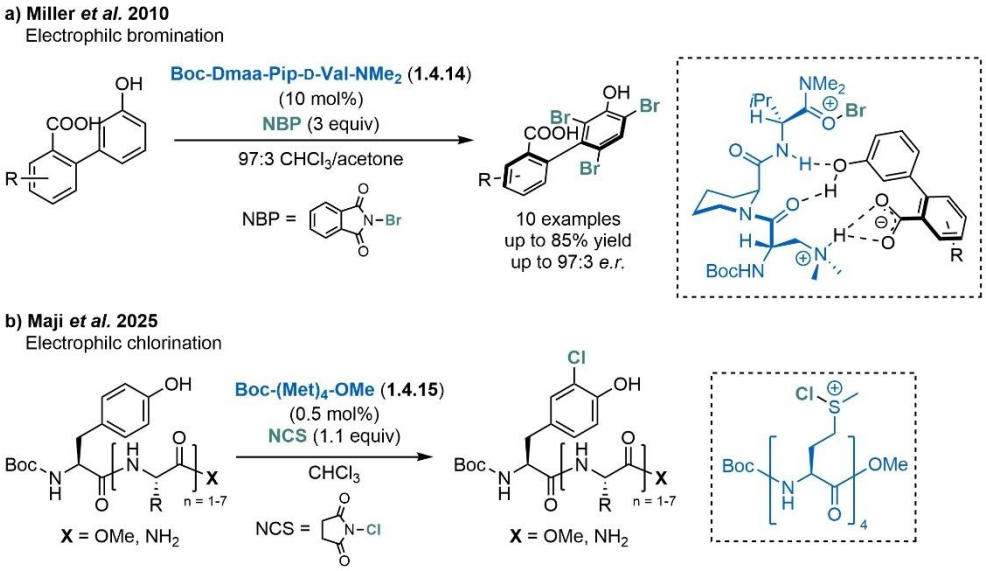

Scheme 1.4.8. Halogenations catalysed by peptides.[182c,184]

Meanwhile, the extension to peptide-catalysed fluorinations remains underexplored, even though the reactivity of fluorinase has been elucidated two decades ago. Although the fluorinase established that fluoride can be selectively activated within a defined hydrogen-bonding environment, analogous synthetic peptide systems have not been pursued.

1.5. Thesis outline

The incorporation of fluorine modulates many parameters of compounds including conformational bias, metabolic stability and H-bonding propensity. An ever-growing demand of organofluorine compounds has contributed to the development of countless nucleophilic and electrophilic fluorinating reagents over the last 50 years. And yet, the development of nucleophilic fluorination strategies, particularly using alkali metal fluorides, has been explored in a lesser extent compared to the electrophilic methods, despite their enormous potential and the low cost of the corresponding reagents. Additionally, stereoselective C–F bond formation remains one of the biggest challenges in developing fluorination methods.

In this context, organocatalysis represents a powerful and a green solution to this problem. This chapter highlighted how solubility and reactivity of MFs can be controlled via H-bonding. Gouverneur group has showcased that merging the H-bonding and PT activation modes of KF and CsF could be utilised for the construction of chiral C–F bonds using BINAM *bis*-urea catalysts. To expand the HP-PTC methodology beyond privileged BINAM scaffolds for enantioinduction, the development of a naturally chiral peptide-based fluorinating platform would be a highly attractive advance.

In nature, H-bonding plays a key role in enzyme mediated fluorination and defluorination processes, hinting at the potential of peptides for fluoride delivery. To date, the nucleophilic fluorination catalysed by peptides is entirely unknown, highlighting the difficulty of this objective. This work therefore aims to establish fundamental design principles for peptide–fluoride interactions and to translate these insights into catalytic applications. Chapter II investigates the ability of structurally defined peptide scaffolds to bind fluoride through hydrogen bonding, with particular emphasis on how conformation and backbone organisation influence binding strength and mode of interaction. Building on these findings, Chapter III explores the application of peptides in hydrogen-bonding phase-transfer catalysis (HB-PTC), focusing on their capacity to solubilise CsF and enable asymmetric fluorination reactions.

1.6. References

(1) Banks, R. E.; Smart, B. E.; Tatlow, J. C. *Organofluorine Chemistry, Principles and Commercial Applications*; Springer New York, NY, 1994.

(2) Han, J.; Remete, A. M.; Dobson, L. S.; Kiss, L.; Izawa, K.; Moriwaki, H.; Soloshonok, V. A.; O'Hagan, D. Next generation organofluorine containing blockbuster drugs. *J. Fluor. Chem.* **2020**, *239*, 109639.

(3) Ogawa, Y.; Tokunaga, E.; Kobayashi, O.; Hirai, K.; Shibata, N. Current Contributions of Organofluorine Compounds to the Agrochemical Industry. *iScience* **2020**, *23* (9), 101467.

(4) (a) Midgley Jr., T.; Henne, A. L. Organic fluorides as refrigerants. *Ind. Eng. Chem. Res.* **1930**, *22* (5), 542–545; (b) Wilkens, D. H.; Alexander, Y. M. Organic fluorine compound. US2005706A, 1935.

(5) Plunkett, R. J. Tetrafluoroethylene polymers. US2230654A, 1939.

(6) Banks, R. E.; Tatlow, J. C. Organofluorine Chemistry: Nomenclature and Historical Landmarks. In *Organofluorine Chemistry: Principles and Commercial Applications*, Banks, R. E., Smart, B. E., Tatlow, J. C. Eds.; Springer US, 1994, 1–24.

(7) Elkins, J. W. Chlorofluorocarbons (CFCs). In *Environ. Geol.*, Springer Netherlands, 1999, 78–80.

(8) Rao, V. N. M. Alternatives to Chlorofluorocarbons (CFCs). In *Organofluorine Chemistry: Principles and Commercial Applications*, Banks, R. E., Smart, B. E., Tatlow, J. C. Eds.; Springer US, 1994, 159–175.

(9) (a) Fried, J.; Sabo, E. F. 9α-Fluoro Derivatives of Cortisone and Hydrocortisone. *J. Am. Chem. Soc.* **1954**, *76* (5), 1455–1456; (b) Fried, J.; Sabo, E. F. Synthesis of 17α-hydroxycorticoster-one and its 9α-halo derivatives from 11-epi-17α-hydroxycorticosterone. *J. Am. Chem. Soc.* **1953**, *75* (9), 2273–2274.

(10) *The selection and use of essential medicines, 2025: WHO Model List of Essential Medicines, 24th list*. World Health Organization, 2025.

(11) O'Hagan, D. Fluorine in health care: Organofluorine containing blockbuster drugs. *J. Fluor. Chem.* **2010**, *131* (11), 1071–1081.

(12) (a) Roth, B. D. The Discovery and Development of Atorvastatin, A Potent Novel Hypolipidemic Agent. In *Progress in Medicinal Chemistry*, King, F. D., Oxford, A. W., Reitz, A. B., Dax, S. L. Eds.; Vol. 40; Elsevier, 2002, 1–22; (b) Roth, B. D. Trans-6-[2-(3- or 4-carboxamido-substituted pyrrol-1-yl)alkyl]-4-hydroxypyran-2-one inhibitors of cholesterol synthesis. US4681893A, 1986.

(13) The Top 200 of 2023. ClinCalc DrugStats Database. https://clincalc.com/DrugStats/Top200Drugs.aspx (accessed 7/10/2025).

(14) (a) Moffat, A. S. New Chemicals Seek to Outwit Insect Pests. *Science* **1993**, *261* (5121), 550–551; (b) Rauh, J. J.; Lummis, S. C. R.; Sattelle, D. B. Pharmacological and biochemical properties of insect GABA receptors. *Trends Pharmacol. Sci.* **1990**, *11* (8), 325–329.

(15) (a) HAMILTON, K. C.; ARLE, H. F. Preplant applicationis of herbicides in cotton. *Res. Prog. Rept. WWCC* **1963**, 49–50; (b) Epp, J. B.; Schmitzer, P. R.; Crouse, G. D. Fifty years of herbicide research: comparing the discovery of trifluralin and halauxifen-methyl. *Pest Manage. Sci.* **2018**, *74* (1), 9–16.

(16) (a) Coe, E. L. Inhibition of glycolysis in ascites tumor cells preincubated with 2-deoxy-2-fluoro-d-glucose. *Biochim. Biophys. Acta Gen. Subj.* **1972**, *264* (2), 319–327; (b) Som, P.; Atkins, H. L.; Bandoypadhyay, D.; Fowler, J. S.; MacGregor, R. R.; Matsui, K.; Oster, Z. H.; Sacker, D. F.; Shiue, C. Y.; Turner, H.; Wan, C. N.; Wolf, A. P.; Zabinski, S. V. A Fluorinated Glucose Analog, 2-fluoro-2-deoxy-D-glucose (F-18): Nontoxic Tracer for Rapid Tumor Detection. *J. Nucl. Med.* **1980**, *21* (7), 670; (c) Phelps, M. E.; Huang, S. C.; Hoffman, E. J.; Selin, C.; Sokoloff, L.; Kuhl, D. E. Tomographic measurement of local cerebral glucose metabolic rate in humans with (F-18)2-fluoro-2-deoxy-D-glucose: Validation of method. *Ann. Neurol.* **1979**, *6* (5), 371–388.

(17) Inoue, M.; Sumii, Y.; Shibata, N. Contribution of Organofluorine Compounds to Pharmaceuticals. *ACS Omega* **2020**, *5* (19), 10633–10640.

(18) Britton, R.; Gouverneur, V.; Lin, J.-H.; Meanwell, M.; Ni, C.; Pupo, G.; Xiao, J.-C.; Hu, J. Contemporary synthetic strategies in organofluorine chemistry. *Nat. Rev. Methods Primers* **2021**, *1* (1), 47.

(19) Bondi, A. van der Waals Volumes and Radii. *J. Phys. Chem.* **1964**, *68* (3), 441–451.

(20) Pauling, L. *The Nature of the Chemical Bond and the Structure of Molecules and Crystals: An Introduction to Modern Structural Chemistry*; Cornell University Press, 1939.

(21) O'Hagan, D. Understanding organofluorine chemistry. An introduction to the C–F bond. *Chem. Soc. Rev.* **2008**, *37* (2), 308–319.

(22) (a) Purser, S.; Moore, P. R.; Swallow, S.; Gouverneur, V. Fluorine in medicinal chemistry. *Chem. Soc. Rev.* **2008**, *37* (2), 320–330; (b) Gillis, E. P.; Eastman, K. J.; Hill, M. D.; Donnelly, D. J.; Meanwell, N. A. Applications of Fluorine in Medicinal Chemistry. *J. Med. Chem.* **2015**, *58* (21), 8315–8359.

(23) (a) Zimmer, L. E.; Sparr, C.; Gilmour, R. Fluorine Conformational Effects in Organocatalysis: An Emerging Strategy for Molecular Design. *Angew. Chem., Int. Ed.* **2011**, *50* (50), 11860–11871; (b) Cahard, D.; Bizet, V. The influence of fluorine in asymmetric catalysis. *Chem. Soc. Rev.* **2014**, *43* (1), 135–147.

(24) Morgenthaler, M.; Schweizer, E.; Hoffmann-Röder, A.; Benini, F.; Martin, R. E.; Jaeschke, G.; Wagner, B.; Fischer, H.; Bendels, S.; Zimmerli, D.; Schneider, J.; Diederich, F.; Kansy, M.; Müller, K. Predicting and Tuning Physicochemical Properties in Lead Optimization: Amine Basicities. *ChemMedChem* **2007**, *2* (8), 1100–1115.

(25) Melnykov, K. P.; Tavlui, O.; Skreminskiy, A.; Kuchkovska, Y. O.; Grygorenko, O. O. Impact of Fluoroalkyl Substituents on the Physicochemical Properties of Saturated Heterocyclic Amines. *Chem. – Eur. J.* **2022**, *28* (55), e202201601.

(26) Cox, C. D.; Coleman, P. J.; Breslin, M. J.; Whitman, D. B.; Garbaccio, R. M.; Fraley, M. E.; Buser, C. A.; Walsh, E. S.; Hamilton, K.; Schaber, M. D.; Lobell, R. B.; Tao, W.; Davide, J. P.; Diehl, R. E.; Abrams, M. T.; South, V. J.; Huber, H. E.; Torrent, M.; Prueksaritanont, T.; Li, C.; Slaughter, D. E.; Mahan, E.; Fernandez-Metzler, C.; Yan, Y.; Kuo, L. C.; Kohl, N. E.; Hartman, G. D. Kinesin Spindle Protein (KSP) Inhibitors. 9. Discovery of (2*S*)-4-(2,5-Difluorophenyl)-*N*-[(3*R*,4*S*)-3-fluoro-1-methylpiperidin-4-yl]-2-(hydroxymethyl)-*N*-methyl-2-phenyl-2,5-dihydro-1*H*-pyrrole-1-carboxamide (MK-0731) for the Treatment of Taxane-Refractory Cancer. *J. Med. Chem.* **2008**, *51* (14), 4239–4252.

(27) (a) Sani, M.; Volonterio, A.; Zanda, M. The Trifluoroethylamine Function as Peptide Bond Replacement. *ChemMedChem* **2007**, *2* (12), 1693–1700; (b) Jagodzinska, M.; Huguenot, F.; Candiani, G.; Zanda, M. Assessing the Bioisosterism of the Trifluoromethyl Group with a Protease Probe. *ChemMedChem* **2009**, *4* (1), 49–51.

(28) Gauthier, J. Y.; Chauret, N.; Cromlish, W.; Desmarais, S.; Duong, L. T.; Falgueyret, J.-P.; Kimmel, D. B.; Lamontagne, S.; Léger, S.; LeRiche, T.; Li, C. S.; Massé, F.; McKay, D. J.; Nicoll-Griffith, D. A.; Oballa, R. M.; Palmer, J. T.; Percival, M. D.; Riendeau, D.; Robichaud, J.; Rodan, G. A.; Rodan, S. B.; Seto, C.; Thérien, M.; Truong, V.-L.; Venuti, M. C.; Wesolowski, G.; Young, R. N.; Zamboni, R.; Black, W. C. The discovery of odanacatib (MK-0822), a selective inhibitor of cathepsin K. *Bioorg. Med. Chem. Lett.* **2008**, *18* (3), 923–928.

(29) (a) Black, W. C.; Bayly, C. I.; Davis, D. E.; Desmarais, S.; Falgueyret, J.-P.; Léger, S.; Li, C. S.; Massé, F.; McKay, D. J.; Palmer, J. T.; Percival, M. D.; Robichaud, J.; Tsou, N.; Zamboni, R. Trifluoroethylamines as amide isosteres in inhibitors of cathepsin K. *Bioorg. Med. Chem. Lett.* **2005**, *15* (21), 4741–4744; (b) Li, C. S.; Deschenes, D.; Desmarais, S.; Falgueyret, J.-P.; Gauthier, J. Y.; Kimmel, D. B.; Léger, S.; Massé, F.; McGrath, M. E.; McKay, D. J.; Percival, M. D.; Riendeau, D.; Rodan, S. B.; Thérien, M.; Truong, V.-L.; Wesolowski, G.; Zamboni, R.; Black, W. C. Identification of a potent and selective non-basic cathepsin K inhibitor. *Bioorg. Med. Chem. Lett.* **2006**, *16* (7), 1985–1989.

(30) (a) Johnson, B. M.; Shu, Y.-Z.; Zhuo, X.; Meanwell, N. A. Metabolic and Pharmaceutical Aspects of Fluorinated Compounds. *J. Med. Chem.* **2020**, *63* (12), 6315–6386; (b) Bhattarai, P.; Trombley, T. A.; Altman, R. A. Metabolic Stability of Fluorinated Small Molecules: A Physical Organic Chemistry Perspective. *J. Med. Chem.* **2026**, *69* (3), 1916–1941.

(31) Wu, D.; Tian, A.; Sun, H. Conformational Properties of 1,3-Difluoropropane. *J. Phys. Chem. A* **1998**, *102* (48), 9901–9905.

(32) (a) Phan, H. V.; Durig, J. R. Conformational stability, structural parameters, and vibrational frequencies from ab initio calculations on fluoroacetaldehyde. *J. Mol. Struct.: THEOCHEM* **1990**, *209* (3), 333–347; (b) W. Banks, J.; S. Batsanov, A.; A. K. Howard, J.; O'Hagan, D.; S. Rzepa, H.; Martin-Santamaria, S. The preferred conformation of α-fluoroamides. *J. Chem. Soc., Perkin Trans. 2* **1999**, (11), 2409–2411; (c) van der Veken, B. J.; Truyen, S.; Herrebout, W. A.; Watkins, G. Vibrational conformational analysis of methyl fluoroacetate and methyl difluoroacetate. *J. Mol. Struct.* **1993**, *293*, 55–58; (d) Abraham, R. J.; Jones, A. D.; Warne, M. A.; Rittner, R.; Tormena, C. F. Conformational analysis. Part 27. NMR, solvation and theoretical investigation of conformational isomerism in fluoro- and 1,1-difluoro-acetone. *J. Chem. Soc., Perkin Trans. 2* **1996**, (4), 533–539.

(33) Paulini, R.; Müller, K.; Diederich, F. Orthogonal Multipolar Interactions in Structural Chemistry and Biology. *Angew. Chem., Int. Ed.* **2005**, *44* (12), 1788–1805.

(34) Berman, H. M.; Westbrook, J.; Feng, Z.; Gilliland, G.; Bhat, T. N.; Weissig, H.; Shindyalov, I. N.; Bourne, P. E. The Protein Data Bank. *Nucleic Acids Res.* **2000**, *28* (1), 235–242.

(35) Müller, K.; Faeh, C.; Diederich, F. Fluorine in Pharmaceuticals: Looking Beyond Intuition. *Science* **2007**, *317* (5846), 1881–1886.

(36) Olsen, J. A.; Banner, D. W.; Seiler, P.; Obst Sander, U.; D'Arcy, A.; Stihle, M.; Müller, K.; Diederich, F. A Fluorine Scan of Thrombin Inhibitors to Map the Fluorophilicity/Fluorophobicity of an Enzyme Active Site: Evidence for C–F···C=O Interactions. *Angew. Chem., Int. Ed.* **2003**, *42* (22), 2507–2511.

(37) (a) Lankin, D. C.; Chandrakumar, N. S.; Rao, S. N.; Spangler, D. P.; Snyder, J. P. Protonated 3-fluoropiperidines: an unusual fluoro directing effect and a test for quantitative theories of solvation. *J. Am. Chem. Soc.* **1993**, *115* (8), 3356–3357; (b) Sun, A.; Lankin, D. C.; Hardcastle, K.; Snyder, J. P. 3-Fluoropiperidines and *N*-Methyl-3-fluoropiperidinium Salts: The Persistence of Axial Fluorine. *Chem. – Eur. J.* **2005**, *11* (5), 1579–1591.

(38) Briggs, C. R. S.; Allen, M. J.; O'Hagan, D.; Tozer, D. J.; Slawin, A. M. Z.; Goeta, A. E.; Howard, J. A. K. The observation of a large gauche preference when 2-fluoroethylamine and 2-fluoroethanol become protonated. *Org. Biomol. Chem.* **2004**, *2* (5), 732–740.

(39) Gooseman, N. E. J.; O'Hagan, D.; Peach, M. J. G.; Slawin, A. M. Z.; Tozer, D. J.; Young, R. J. An Electrostatic *Gauche* Effect in β-Fluoro- and β-Hydroxy-*N*-ethylpyridinium Cations. *Angew. Chem., Int. Ed.* **2007**, *46* (31), 5904–5908.

(40) Klaboe, P.; Nielsen, J. R. Infrared and Raman Spectra of Fluorinated Ethanes. XIII. 1,2-Difluoroethane. *J. Chem. Phys.* **1960**, *33* (6), 1764–1774.

(41) Thiehoff, C.; Rey, Y. P.; Gilmour, R. The Fluorine Gauche Effect: A Brief History. *Isr. J. Chem.* **2017**, *57* (1–2), 92–100.

(42) (a) Wiberg, K. B.; Murcko, M. A.; Laidig, K. E.; MacDougall, P. J. Origin of the Gauche Effect in substituted ethanes and ethenes. *J. Phys. Chem.* **1990**, *94* (18), 6956–6959; (b) O'Hagan, D.; Bilton, C.; Howard, J. A. K.; Knight, L.; Tozer, D. J. The preferred conformation of *N*-β-fluoroethylamides. Observation of the fluorine amide *gauche* effect. *J. Chem. Soc., Perkin Trans. 2* **2000**, (4), 605–607; (c) Briggs, C. R. S.; O'Hagan, D.; Rzepa, H. S.; Slawin, A. M. Z. Solid state and theoretical evaluation of β-fluoroethyl esters indicate a fluorine-ester *gauche* effect. *J. Fluor. Chem.* **2004**, *125* (1), 19–25.

(43) (a) Schaefer, T.; Schurko, R. W.; Sebastian, R.; Hruska, F. E. Experimental and theoretical assessments of the substituent and medium dependence of the internal rotational potentials in benzyl fluoride. 3,5-Difluorobenzyl fluoride and 4-fluorobenzyl fluoride. *Can. J. Chem.* **1995**, *73* (6), 816–825; (b) Tozer, D. J. The conformation and internal rotational barrier of benzyl fluoride. *Chem. Phys. Lett.* **1999**, *308* (1), 160–164.

(44) (a) Irwin, J. J.; Ha, T.-K.; Dunitz, J. D. Stereoelectronic Aspects of the Anomeric Effect in Fluoromethylamine. *Helv. Chim. Acta* **1990**, *73* (7), 1805–1817; (b) Trapp, M. L.; Watts, J. K.; Weinberg, N.; Pinto, B. M. Component analysis of the X-C-Y anomeric effect (X = O, S; Y = F, OMe, NHMe) by DFT molecular orbital calculations and natural bond orbital analysis. *Can. J. Chem.* **2006**, *84* (4), 692–701.

(45) (a) Bretscher, L. E.; Jenkins, C. L.; Taylor, K. M.; DeRider, M. L.; Raines, R. T. Conformational Stability of Collagen Relies on a Stereoelectronic Effect. *J. Am. Chem. Soc.* **2001**, *123* (4), 777–778; (b) Shoulders, M. D.; Kamer, K. J.; Raines, R. T. Origin of the stability conferred upon collagen by fluorination. *Bioorg. Med. Chem. Lett.* **2009**, *19* (14), 3859–3862; (c) Holmgren, S. K.; Taylor, K. M.; Bretscher, L. E.; Raines, R. T. Code for collagen's stability deciphered. *Nature* **1998**, *392* (6677), 666–667.

(46) Jenkins, C. L.; Raines, R. T. Insights on the conformational stability of collagen. *Nat. Prod. Rep.* **2002**, *19* (1), 49–59.

(47) DeRider, M. L.; Wilkens, S. J.; Waddell, M. J.; Bretscher, L. E.; Weinhold, F.; Raines, R. T.; Markley, J. L. Collagen Stability: Insights from NMR Spectroscopic and Hybrid Density Functional Computational Investigations of the Effect of Electronegative Substituents on Prolyl Ring Conformations. *J. Am. Chem. Soc.* **2002**, *124* (11), 2497–2505.

(48) Eberhardt, E. S.; Panasik, N.; Raines, R. T. Inductive Effects on the Energetics of Prolyl Peptide Bond Isomerization: Implications for Collagen Folding and Stability. *J. Am. Chem. Soc.* **1996**, *118* (49), 12261–12266.

(49) Bella, J.; Eaton, M.; Brodsky, B.; Berman, H. M. Crystal and Molecular Structure of a Collagen-Like Peptide at 1.9 Å Resolution. *Science* **1994**, *266* (5182), 75–81.

(50) (a) Jeffrey, G. A. *An Introduction to Hydrogen Bonding*; Oxford University Press, 1997; (b) Steiner, T. The Hydrogen Bond in the Solid State. *Angew. Chem., Int. Ed.* **2002**, *41* (1), 48–76; (c) Dračínský, M. NMR spectroscopy studies of hydrogen bonding. *Coord. Chem. Rev.* **2026**, *549*, 217284.

(51) Siskos, M. G.; Choudhary, M. I.; Gerothanassis, I. P. Hydrogen Atomic Positions of O–H···O Hydrogen Bonds in Solution and in the Solid State: The Synergy of Quantum Chemical Calculations with ^{1}H-NMR Chemical Shifts and X-ray Diffraction Methods. *Molecules* **2017**, *22* (3), 415.

(52) (a) Vibhute, A. M.; Gonnade, R. G.; Swathi, R. S.; Sureshan, K. M. Strength from weakness: opportunistic CH···O hydrogen bonds differentially dictate the conformational fate in solid and solution states. *Chem. Commun.* **2012**, *48* (5), 717–719; (b) Carlon, A.; Ravera, E.; Andrałojć, W.; Parigi, G.; Murshudov, G. N.; Luchinat, C. How to tackle protein structural data from solution and solid state: An integrated approach. *Prog. Nucl. Magn. Reson. Spectrosc.* **2016**, *92-93*, 54–70; (c) Schneider, H.-J.

Hydrogen bonds with fluorine. Studies in solution, in gas phase and by computations, conflicting conclusions from crystallographic analyses. *Chem. Sci.* **2012**, *3* (5), 1381–1394.

(53) (a) Siskos, M. G.; Tzakos, A. G.; Gerothanassis, I. P. Accurate *ab initio* calculations of O–H···O and O–H···⁻O proton chemical shifts: towards elucidation of the nature of the hydrogen bond and prediction of hydrogen bond distances. *Org. Biomol. Chem.* **2015**, *13* (33), 8852–8868; (b) Herschlag, D.; Pinney, M. M. Hydrogen Bonds: Simple after All? *Biochemistry* **2018**, *57* (24), 3338–3352.

(54) (a) Cordier, F.; Rogowski, M.; Grzesiek, S.; Bax, A. Observation of Through-Hydrogen-Bond $^{2h}J_{HC'}$ in a Perdeuterated Protein. *J. Magn. Reson.* **1999**, *140* (2), 510–512; (b) Pervushin, K.; Ono, A.; Fernández, C.; Szyperski, T.; Kainosho, M.; Wüthrich, K. NMR scalar couplings across Watson–Crick base pair hydrogen bonds in DNA observed by transverse relaxation-optimized spectroscopy. *PNAS* **1998**, *95* (24), 14147–14151.

(55) Emsley, J. Very strong hydrogen bonding. *Chem. Soc. Rev.* **1980**, *9* (1), 91–124.

(56) Larson, J. W.; McMahon, T. B. Gas-phase bihalide and pseudobihalide ions. An ion cyclotron resonance determination of hydrogen bond energies in XHY^- species (X, Y = F, Cl, Br, CN). *Inorg. Chem.* **1984**, *23* (14), 2029–2033.

(57) (a) Bozorth, R. M. The crystal structure of potassium hydrogen fluoride. *J. Am. Chem. Soc.* **1923**, *45* (9), 2128–2132; (b) Peterson, S. W.; Levy, H. A. A Single Crystal Neutron Diffraction Determination of the Hydrogen Position in Potassium Bifluoride. *J. Chem. Phys.* **1952**, *20* (4), 704–707.

(58) Rogers, M. T.; Helmholz, L. A Redetermination of the Parameters in Ammonium Bifluoride. *J. Am. Chem. Soc.* **1940**, *62* (6), 1533–1536.

(59) (a) Fujiwara, F. Y.; Martin, J. S. Heterobihalide ions. Nuclear magnetic resonance spectroscopy of strong hydrogen bonds. *J. Am. Chem. Soc.* **1974**, *96* (25), 7625–7631; (b) Christe, K. O.; Wilson, W. W. Nuclear magnetic resonance spectrum of the fluoride anion. *J. Fluor. Chem.* **1990**, *46* (2), 339–342; (c) Rieux, C.; Langlois, B.; Gallo, R. Le «fluorure nu»: mythe ou réalité. *C. R. Acad. Sci. Ser. IIb* **1990**, *310*, 25–30.

(60) Shenderovich, I. G.; Smirnov, S. N.; Denisov, G. S.; Gindin, V. A.; Golubev, N. S.; Dunger, A.; Reibke, R.; Kirpekar, S.; Malkina, O. L.; Limbach, H.-H. Nuclear magnetic resonance of hydrogen bonded clusters between F^- and $(HF)_n$: Experiment and theory. *Ber. Bunsenges. Phys. Chem.* **1998**, *102* (3), 422–428.

(61) Alkorta, I.; Elguero, J.; Denisov, G. S. A review with comprehensive data on experimental indirect scalar NMR spin–spin coupling constants across hydrogen bonds. *Magn. Reson. Chem.* **2008**, *46* (7), 599–624.

(62) (a) A. Gale, P.; L. Sessler, J.; Král, V. Calixpyrroles. *Chem. Commun.* **1998**, (1), 1–8; (b) Clarke, H. J.; Howe, E. N. W.; Wu, X.; Sommer, F.; Yano, M.; Light, M. E.; Kubik, S.; Gale, P. A. Transmembrane Fluoride Transport: Direct Measurement and Selectivity Studies. *J. Am. Chem. Soc.* **2016**, *138* (50), 16515–16522; (c) Woods, C. J.; Camiolo, S.; Light, M. E.; Coles, S. J.; Hursthouse, M. B.; King, M. A.; Gale, P. A.; Essex, J. W. Fluoride-Selective Binding in a New Deep Cavity Calix[4]pyrrole: Experiment and Theory. *J. Am. Chem. Soc.* **2002**, *124* (29), 8644–8652; (d) Kang, S. O.; Day, V. W.; Bowman-James, K. Fluoride: Solution- and Solid-State Structural Binding Probe. *J. Org. Chem.* **2010**, *75* (2), 277–283; (e) Kang, S. O.; VanderVelde, D.; Powell, D.; Bowman-James, K. Fluoride-Facilitated Deuterium Exchange from DMSO-d_6 to Polyamide-Based Cryptands. *J. Am. Chem. Soc.* **2004**, *126* (39), 12272–12273; (f) Pupo, G.; Ibba, F.; Ascough, D. M. H.; Vicini, A. C.; Ricci, P.; Christensen, K. E.; Pfeifer, L.; Morphy, J. R.; Brown, J. M.; Paton, R. S.; Gouverneur, V. Asymmetric nucleophilic fluorination under hydrogen bonding phase-transfer catalysis. *Science* **2018**, *360* (6389), 638–642; (g) Ibba, F.; Pupo, G.; Thompson, A. L.; Brown, J. M.; Claridge, T. D. W.; Gouverneur, V. Impact of Multiple Hydrogen Bonds with Fluoride on Catalysis: Insight from NMR Spectroscopy. *J. Am. Chem. Soc.* **2020**, *142* (46), 19731–19744; (h) Dooley, C.; Ibba, F.; Botlik, B. B.; Palladino, C.; Goult, C. A.; Gao, Y.; Lister, A.; Paton, R. S.; Lloyd-Jones, G. C.; Gouverneur, V. Enantioconvergent nucleophilic substitution via synergistic phase-transfer catalysis. *Nat. Catal.* **2025**, *8* (2), 107–115; (i) Wang, B.; Fan, S.; Zhang, C.; Sun, J. Catalytic Enantioselective α-Fluorination of Ketones with CsF. *J. Am. Chem. Soc.* **2025**, *147* (12), 10059–10065.

(63) (a) Howard, J. A. K.; Hoy, V. J.; O'Hagan, D.; Smith, G. T. How good is fluorine as a hydrogen bond acceptor? *Tetrahedron* **1996**, *52* (38), 12613–12622; (b) Dunitz, J. D.; Taylor, R. Organic Fluorine Hardly Ever Accepts Hydrogen Bonds. *Chem. – Eur. J.* **1997**, *3* (1), 89–98.

(64) Groom, C. R.; Bruno, I. J.; Lightfoot, M. P.; Ward, S. C. The Cambridge Structural Database. *Acta Crystallogr. Sect. B* **2016**, *72* (2), 171–179.

(65) Carosati, E.; Sciabola, S.; Cruciani, G. Hydrogen Bonding Interactions of Covalently Bonded Fluorine Atoms: From Crystallographic Data to a New Angular Function in the GRID Force Field. *J. Med. Chem.* **2004**, *47* (21), 5114–5125.

(66) (a) Fritz, H.; Winkler, T. Weitreichende Kopplung zwischen Protonen und Fluor in 2-Fluorbenzamiden. *Helv. Chim. Acta* **1974**, *57* (3), 836–839; (b) Kobayashi, T.; Hirota, M. Through-space H–^{19}F spin–spin coupling and intramolecular hydrogen bonding in *o*-fluoro-phenol and -benzenethiol. *Chem. Lett.* **1972**, *1* (10), 975–979; (c) Fritz, H.; Winkler, T.; Küng, W. Weitreichende Kernspin-Kopplungen in 2-Fluorbenzamiden II. [^{15}N]-2-Fluorbenzamid. *Helv. Chim. Acta* **1975**, *58* (6), 1822–1824.

(67) Harsanyi, A.; Sandford, G. Organofluorine chemistry: applications, sources and sustainability. *Green Chem.* **2015**, *17* (4), 2081–2086.

(68) Christiansen, F. G. Greenland mineral exploration history. *Mineral Economics* **2022**.

(69) Will, R. K. The Benefits of Isolating & Utilizing Fluorine from Phosphate Operations. *Procedia Engineering* **2016**, *138*, 267–272.

(70) Scheele, C. W. Undersökning om fluss-spat och dess syra. *Kongl. Vetensk. Acad. Handl.* **1771**, 120–138.

(71) Özcan, M.; Allahbeickaraghi, A.; Dündar, M. Possible hazardous effects of hydrofluoric acid and recommendations for treatment approach: a review. *Clin. Oral Investig.* **2012**, *16* (1), 15–23.

(72) Jean Aigueperse; Paul Mollard; Didier Devilliers; Marius Chemla; Robert Faron; René Romano; Cuer, J. P. Fluorine Compounds, Inorganic. In *Ullmann's Encyclopedia of Industrial Chemistry*, Wiley-VCH, 2016.

(73) Moissan, H. Action d'un courant électrique sur l'acide fluorhydrique anhydre. *C. R. Acad. Sci.* **1886**, 1543–1544.

(74) (a) Appel, R.; Gilak, A. Process for the production of sulfur tetrafluoride. US3950498A, 1976; (b) Becher, W.; Massonne, J.; Pohlmeyer, W. Production of sulfur tetrafluoride from sulfur chlorides and fluorine. US3848064A, 1972; (c) Winter, R.; Cook, P. W. A simplified and efficient bromine-facilitated SF_4-preparation method. *J. Fluor. Chem.* **2010**, *131* (7), 780–783; (d) Tullock, C. W.; Fawcett, F. S.; Smith, W. C.; Coffman, D. D. The Chemistry of Sulfur Tetrafluoride. I. The Synthesis of Sulfur Tetrafluoride. *J. Am. Chem. Soc.* **1960**, *82* (3), 539–542.

(75) (a) Umemoto, T.; Kawada, K.; Tomita, K. *N*-fluoropyridinium triflate and its derivatives: Useful fluorinating agents. *Tetrahedron Lett.* **1986**, *27* (37), 4465–4468; (b) Umemoto, T.; Harasawa, K.; Tomizawa, G.; Kawada, K.; Tomita, K. Syntheses and Properties of *N*-Fluoropyridinium Salts. *Bull. Chem. Soc. Jpn.* **2006**, *64* (4), 1081–1092; (c) Banks, R. E. Selectfluor™ reagent F-TEDA-BF_4 in action: tamed fluorine at your service. *J. Fluor. Chem.* **1998**, *87* (1), 1–17; (d) Differding, E.; Ofner, H. *N*-Fluorobenzenesulfonimide: A Practical Reagent For Electrophilic Fluorinations. *Synlett* **1991**, *1991* (03), 187–189.

(76) (a) L'Heureux, A.; Beaulieu, F.; Bennett, C.; Bill, D. R.; Clayton, S.; LaFlamme, F.; Mirmehrabi, M.; Tadayon, S.; Tovell, D.; Couturier, M. Aminodifluorosulfinium Salts: Selective Fluorination Reagents with Enhanced Thermal Stability and Ease of Handling. *J. Org. Chem.* **2010**, *75* (10), 3401–3411; (b) Middleton, W. J. New fluorinating reagents. Dialkylaminosulfur fluorides. *J. Org. Chem.* **1975**, *40* (5), 574–578.

(77) Lee, J.-W.; Oliveira, M. T.; Jang, H. B.; Lee, S.; Chi, D. Y.; Kim, D. W.; Song, C. E. Hydrogen-bond promoted nucleophilic fluorination: concept, mechanism and applications in positron emission tomography. *Chem. Soc. Rev.* **2016**, *45* (17), 4638–4650.

(78) Haynes, W. M. *CRC Handbook of Chemistry and Physics*; 97th ed., CRC Press, 2016.

(79) Wynn, D. A.; Roth, M. M.; Pollard, B. D. The solubility of alkali-metal fluorides in non-aqueous solvents with and without crown ethers, as determined by flame emission spectrometry. *Talanta* **1984**, *31* (11), 1036–1040.

(80) Sasson, Y.; Mushkin, N.; Abu, E.; Negussie, S.; Dermeik, S.; Zoran, A. Fluoride Anion as a Base and a Nucleophile in Phase-Transfer Catalysis of Uncharged Species. In *Phase-Transfer Catalysis*, Vol. 659; American Chemical Society, 1997, 148–162.

(81) (a) Liotta, C. L.; Harris, H. P. Chemistry of naked anions. I. Reactions of the 18-crown-6 complex of potassium fluoride with organic substrates in aprotic organic solvents. *J. Am. Chem. Soc.* **1974**, *96* (7), 2250–2252; (b) Clark, J. H. Fluoride ion as a base in organic synthesis. *Chem. Rev.* **1980**, *80* (5), 429–452.

(82) Bordwell, F. G. Equilibrium acidities in dimethyl sulfoxide solution. *Acc. Chem. Res.* **1988**, *21* (12), 456–463.

(83) Matthews, W. S.; Bares, J. E.; Bartmess, J. E.; Bordwell, F. G.; Cornforth, F. J.; Drucker, G. E.; Margolin, Z.; McCallum, R. J.; McCollum, G. J.; Vanier, N. R. Equilibrium acidities of carbon acids. VI. Establishment of an absolute scale of acidities in dimethyl sulfoxide solution. *J. Am. Chem. Soc.* **1975**, *97* (24), 7006–7014.

(84) Kim, D. W.; Ahn, D.-S.; Oh, Y.-H.; Lee, S.; Kil, H. S.; Oh, S. J.; Lee, S. J.; Kim, J. S.; Ryu, J. S.; Moon, D. H.; Chi, D. Y. A New Class of S_N2 Reactions Catalyzed by Protic Solvents: Facile Fluorination for Isotopic Labeling of Diagnostic Molecules. *J. Am. Chem. Soc.* **2006**, *128* (50), 16394–16397.

(85) Kim, D. W.; Jeong; Lim, S. T.; Sohn, M.-H.; Katzenellenbogen, J. A.; Chi, D. Y. Facile Nucleophilic Fluorination Reactions Using *tert*-Alcohols as a Reaction Medium: Significantly Enhanced Reactivity of Alkali Metal Fluorides and Improved Selectivity. *J. Org. Chem.* **2008**, *73* (3), 957–962.

(86) Gross, M.; Peter, F. New method for fluorination of organic compounds. *Bull. Soc. Chim. Fr.* **1975**, 871–874.

(87) Lee, J. W.; Yan, H.; Jang, H. B.; Kim, H. K.; Park, S.-W.; Lee, S.; Chi, D. Y.; Song, C. E. Bis-Terminal Hydroxy Polyethers as All-Purpose, Multifunctional Organic Promoters: A Mechanistic Investigation and Applications. *Angew. Chem., Int. Ed.* **2009**, *48* (41), 7683–7686.

(88) Kim, D. W.; Song, C. E.; Chi, D. Y. New Method of Fluorination Using Potassium Fluoride in Ionic Liquid: Significantly Enhanced Reactivity of Fluoride and Improved Selectivity. *J. Am. Chem. Soc.* **2002**, *124* (35), 10278–10279.

(89) (a) Albanese, D.; Landini, D.; Penso, M. Hydrated Tetrabutylammonium Fluoride as a Powerful Nucleophilic Fluorinating Agent. *J. Org. Chem.* **1998**, *63* (25), 9587–9589; (b) Cox, D. P.; Terpinski, J.; Lawrynowicz, W. "Anhydrous" tetrabutylammonium fluoride: a mild but highly efficient source of nucleophilic fluoride ion. *J. Org. Chem.* **1984**, *49* (17), 3216–3219; (c) Sun, H.; DiMagno, S. G. Anhydrous Tetrabutylammonium Fluoride. *J. Am. Chem. Soc.* **2005**, *127* (7), 2050–2051.

(90) Fowler, D. L.; Loebenstein, W. V.; Pall, D. B.; Kraus, C. A. Some Unusual Hydrates of Quaternary Ammonium Salts. *J. Am. Chem. Soc.* **1940**, *62* (5), 1140–1142.

(91) Richman, J. E.; Flay, R. B. Phosphonium fluoride salts. *J. Am. Chem. Soc.* **1981**, *103* (17), 5265–5265.

(92) Sharma, R. K.; Fry, J. L. Instability of anhydrous tetra-*n*-alkylammonium fluorides. *J. Org. Chem.* **1983**, *48* (12), 2112–2114.

(93) J. Adams, D.; H. Clark, J. Nucleophilic routes to selectively fluorinated aromatics. *Chem. Soc. Rev.* **1999**, *28* (4), 225–231.

(94) Yonezawa, T.; Sakamoto, Y.; Nogawa, K. Preparation of Tetrabutylammonium Fluoride–Alcohol Adducts as Fluorination Agents. JP06316551A, 1994.

(95) Kim, D. W.; Jeong, H.-J.; Lim, S. T.; Sohn, M.-H. Tetrabutylammonium Tetra(*tert*-Butyl Alcohol)-Coordinated Fluoride as a Facile Fluoride Source. *Angew. Chem., Int. Ed.* **2008**, *47* (44), 8404–8406.

(96) Engle, K. M.; Pfeifer, L.; Pidgeon, G. W.; Giuffredi, G. T.; Thompson, A. L.; Paton, R. S.; Brown, J. M.; Gouverneur, V. Coordination diversity in hydrogen-bonded homoleptic fluoride–alcohol complexes modulates reactivity. *Chem. Sci.* **2015**, *6* (9), 5293–5302.

(97) Pfeifer, L.; Engle, K. M.; Pidgeon, G. W.; Sparkes, H. A.; Thompson, A. L.; Brown, J. M.; Gouverneur, V. Hydrogen-Bonded Homoleptic Fluoride–Diarylurea Complexes: Structure, Reactivity, and Coordinating Power. *J. Am. Chem. Soc.* **2016**, *138* (40), 13314–13325.

(98) Colonna, S.; Hiemstra, H.; Wynberg, H. Asymmetric induction in the base-catalysed Michael addition of nitromethane to chalcone. *J. Chem. Soc., Chem. Commun.* **1978**, (6), 238–239.

(99) Nakamura, E.; Shimizu, M.; Kuwajima, I.; Sakata, J.; Yokoyama, K.; Noyori, R. Fluoride ion catalyzed aldol reaction between enol silyl ethers and carbonyl compounds. *J. Org. Chem.* **1983**, *48* (7), 932–945.

(100) Ooi, T.; Doda, K.; Maruoka, K. Distinct Advantage of the in Situ Generation of Quaternary Ammonium Fluorides under Phase-Transfer Conditions toward Catalytic Asymmetric Synthesis. *Org. Lett.* **2001**, *3* (9), 1273–1276.

(101) Yan, H.; Jang, H. B.; Lee, J.-W.; Kim, H. K.; Lee, S. W.; Yang, J. W.; Song, C. E. A Chiral-Anion Generator: Application to Catalytic Desilylative Kinetic Resolution of Silyl-Protected Secondary Alcohols. *Angew. Chem., Int. Ed.* **2010**, *49* (47), 8915–8917.

(102) (a) Taylor, M. S.; Jacobsen, E. N. Highly Enantioselective Catalytic Acyl-Pictet−Spengler Reactions. *J. Am. Chem. Soc.* **2004**, *126* (34), 10558–10559; (b) Brak, K.; Jacobsen, E. N. Asymmetric Ion-Pairing Catalysis. *Angew. Chem., Int. Ed.* **2013**, *52* (2), 534–561; (c) Ford, D. D.; Lehnherr, D.; Kennedy, C. R.; Jacobsen, E. N. Anion-Abstraction Catalysis: The Cooperative Mechanism of α-Chloroether Activation by Dual Hydrogen-Bond Donors. *ACS Catal.* **2016**, *6* (7), 4616–4620.

(103) Birrell, J. A.; Desrosiers, J.-N.; Jacobsen, E. N. Enantioselective Acylation of Silyl Ketene Acetals through Fluoride Anion-Binding Catalysis. *J. Am. Chem. Soc.* **2011**, *133* (35), 13872–13875.

(104) Pupo, G.; Vicini, A. C.; Ascough, D. M. H.; Ibba, F.; Christensen, K. E.; Thompson, A. L.; Brown, J. M.; Paton, R. S.; Gouverneur, V. Hydrogen Bonding Phase-Transfer Catalysis with Potassium Fluoride: Enantioselective Synthesis of β-Fluoroamines. *J. Am. Chem. Soc.* **2019**, *141* (7), 2878–2883.

(105) Roagna, G.; Ascough, D. M. H.; Ibba, F.; Vicini, A. C.; Fontana, A.; Christensen, K. E.; Peschiulli, A.; Oehlrich, D.; Misale, A.; Trabanco, A. A.; Paton, R. S.; Pupo, G.; Gouverneur, V. Hydrogen Bonding Phase-Transfer Catalysis with Ionic Reactants: Enantioselective Synthesis of γ-Fluoroamines. *J. Am. Chem. Soc.* **2020**, *142* (33), 14045–14051.

(106) Harper, D. B.; O'Hagan, D. The fluorinated natural products. *Nat. Prod. Rep.* **1994**, *11*, 123–133.

(107) (a) Eisenberg, A. D.; Marquis, R. E. Enhanced Transmembrane Proton Conductance in *Streptococcus mutans* GS-5 Due to Ionophores and Fluoride. *Antimicrob. Agents Chemother.* **1981**, *19* (5), 807–812; (b) Marquis, R. E.; Clock, S. A.; Mota-Meira, M. Fluoride and organic weak acids as modulators of microbial physiology. *FEMS Microbiology Reviews* **2003**, *26* (5), 493–510.

(108) Pal, P.; Jha, N. K.; Pal, D.; Jha, S. K.; Anand, U.; Gopalakrishnan, A. V.; Dey, A.; Mukhopadhyay, P. K. Molecular basis of fluoride toxicities: Beyond benefits and implications in human disorders. *G&D* **2023**, *10* (4), 1470–1493.

(109) (a) Watson, J. D.; Milner-White, E. J. A novel main-chain anion-binding site in proteins: the nest. A particular combination of φ,ψ values in successive residues gives rise to anion-binding sites that occur commonly and are found often at functionally important regions. *J. Mol. Biol.* **2002**, *315* (2), 171–182; (b) Denessiouk, K. A.; Johnson, M. S.; Denesyuk, A. I. Novel C°NN Structural Motif for Protein Recognition of Phosphate Ions. *J. Mol. Biol.* **2005**, *345* (3), 611–629.

(110) (a) Thomson, A. J.; Gray, H. B. Bio-inorganic chemistry. *Curr. Opin. Chem. Biol.* **1998**, *2* (2), 155–158; (b) Waldron, K. J.; Robinson, N. J. How do bacterial cells ensure that metalloproteins get the correct metal? *Nat. Rev. Microbiol.* **2009**, *7* (1), 25–35.

(111) O., W.; W., C. Isolation and Crystallization of Enolase. *Biochem Zeitschrift* **1941**, *310*, 384–421.

(112) Qin, J.; Chai, G.; Brewer, J. M.; Lovelace, L. L.; Lebioda, L. Fluoride Inhibition of Enolase: Crystal Structure and Thermodynamics. *Biochemistry* **2006**, *45* (3), 793–800.

(113) Edwards, S. L.; Poulos, T. L.; Kraut, J. The Crystal Structure of Fluoride-inhibited Cytochrome *c* Peroxidase. *J. Biol. Chem.* **1984**, *259* (21), 12984–12988.

(114) Qin, J.; Chai, G.; Brewer, J. M.; Lovelace, L. L. Fluoride Inhibition of Enolase: Crystal Structure of the Inhibitory Complex. **2005**, PDB: 2AKZ.

(115) Gil-Ortiz, F.; Ramon-Maiques, S.; Fita, I.; Rubio, V. Acetylglutamate kinase from *Escherichia coli* complexed with MgADP, *N*-acetyl-l-glutamate and the transition-state mimic AlF_4^-. **2003**, PDB: 1OH9.

(116) Li, L. The Biochemistry and Physiology of Metallic Fluoride: Action, Mechanism, and Implications. *Crit. Rev. Oral Biol. Med.* **2003**, *14* (2), 100–114.

(117) Gil-Ortiz, F.; Ramón-Maiques, S.; Fita, I.; Rubio, V. The Course of Phosphorus in the Reaction of *N*-Acetyl-l-glutamate Kinase, Determined from the Structures of Crystalline Complexes, Including a Complex with an AlF_4^- Transition State Mimic. *J. Mol. Biol.* **2003**, *331* (1), 231–244.

(118) Stockbridge, R. B.; Robertson, J. L.; Kolmakova-Partensky, L.; Miller, C. A family of fluoride-specific ion channels with dual-topology architecture. *eLife* **2013**, *2*, e01084.

(119) Stockbridge, R. B.; Lim, H.-H.; Otten, R.; Williams, C.; Shane, T.; Weinberg, Z.; Miller, C. Fluoride resistance and transport by riboswitch-controlled CLC antiporters. *PNAS* **2012**, *109* (38), 15289–15294.

(120) Stockbridge, R. B.; Kolmakova-Partensky, L.; Shane, T.; Koide, A.; Koide, S.; Miller, C.; Newstead, S. Crystal structures of a double-barrelled fluoride ion channel. *Nature* **2015**, *525* (7570), 548–551.

(121) Philip, V.; Harris, J.; Adams, R.; Nguyen, D.; Spiers, J.; Baudry, J.; Howell, E. E.; Hinde, R. J. A Survey of Aspartate−Phenylalanine and Glutamate−Phenylalanine Interactions in the Protein Data Bank: Searching for Anion−π Pairs. *Biochemistry* **2011**, *50* (14), 2939–2950.

(122) Zhang, J.; Song, D.; Schackert, F. K.; Li, J.; Xiang, S.; Tian, C.; Gong, W.; Carloni, P.; Alfonso-Prieto, M.; Shi, C. Fluoride permeation mechanism of the Fluc channel in liposomes revealed by solid-state NMR. *Sci. Adv.* **2023**, *9* (34), eadg9709.

(123) Brammer, A. E.; Stockbridge, R. B.; Miller, C. F^-/Cl^- selectivity in CLCF-type F^-/H^+ antiporters. *J. Gen. Physiol.* **2014**, *144* (2), 129–136.

(124) Chan, K. K. J.; O'Hagan, D. The Rare Fluorinated Natural Products and Biotechnological Prospects for Fluorine Enzymology. In *Methods Enzymol.*, Hopwood, D. A. Ed.; Vol. 516; Academic Press, 2012, 219–235.

(125) Gribble, G. W. Naturally Occurring Organohalogen Compounds—A Comprehensive Review. In *Naturally Occurring Organohalogen Compounds*, Kinghorn, A. D., Falk, H., Gibbons, S., Asakawa, Y., Liu, J.-K., Dirsch, V. M. Eds.; Springer Nature Switzerland, 2023, 1–546.

(126) Neumann, C. S.; Fujimori, D. G.; Walsh, C. T. Halogenation Strategies In Natural Product Biosynthesis. *Chemistry & Biology* **2008**, *15* (2), 99–109.

(127) Zechel, D. L.; Reid, S. P.; Nashiru, O.; Mayer, C.; Stoll, D.; Jakeman, D. L.; Warren, R. A. J.; Withers, S. G. Enzymatic Synthesis of Carbon−Fluorine Bonds. *J. Am. Chem. Soc.* **2001**, *123* (18), 4350–4351.

(128) Zhan, C.-G.; Dixon, D. A. Hydration of the Fluoride Anion: Structures and Absolute Hydration Free Energy from First-Principles Electronic Structure Calculations. *J. Phys. Chem. A* **2004**, *108* (11), 2020–2029.

(129) O'Hagan, D.; Schaffrath, C.; Cobb, S. L.; Hamilton, J. T. G.; Murphy, C. D. Biosynthesis of an organofluorine molecule. *Nature* **2002**, *416* (6878), 279–279.

(130) (a) Dong, C.; Huang, F.; Deng, H.; Schaffrath, C.; Spencer, J. B.; O'Hagan, D.; Naismith, J. H. Crystal structure and mechanism of a bacterial fluorinating enzyme. *Nature* **2004**, *427* (6974), 561–565; (b) Cadicamo, C. D.; Courtieu, J.; Deng, H.; Meddour, A.; O'Hagan, D. Enzymatic Fluorination in *Streptomyces cattleya* Takes Place with an Inversion of Configuration Consistent with an S_N2 Reaction Mechanism. *ChemBioChem* **2004**, *5* (5), 685–690; (c) Senn, H. M.; O'Hagan, D.; Thiel, W. Insight into Enzymatic C−F Bond Formation from QM and QM/MM Calculations. *J. Am. Chem. Soc.* **2005**, *127* (39), 13643–13655.

(131) O'Hagan, D.; Schmidberger, J. W. Enzymes that catalyse S_N2 reaction mechanisms. *Nat. Prod. Rep.* **2010**, *27* (6), 900–918.

(132) (a) Deng, H.; Ma, L.; Bandaranayaka, N.; Qin, Z.; Mann, G.; Kyeremeh, K.; Yu, Y.; Shepherd, T.; Naismith, J. H.; O'Hagan, D. Identification of Fluorinases from *Streptomyces* sp MA37, *Norcardia brasiliensis*, and *Actinoplanes* sp N902-109 by Genome Mining. *ChemBioChem* **2014**, *15* (3), 364–368; (b) Ma, L.; Li, Y.; Meng, L.; Deng, H.; Li, Y.; Zhang, Q.; Diao, A. Biological fluorination from the sea: discovery of a SAM-dependent nucleophilic fluorinating enzyme from the marine-derived bacterium *Streptomyces xinghaiensis* NRRL B24674. *RSC Adv.* **2016**, *6* (32), 27047–27051; (c) Sooklal, S. A.; De Koning, C.; Brady, D.; Rumbold, K. Identification and characterisation of a fluorinase from *Actinopolyspora mzabensis*. *Protein Expr. Purif.* **2020**, *166*, 105508; (d) Feng, X.; Cao, Y.; Liu, W.; Xian, M. Identification of Two Novel Fluorinases From *Amycolatopsis* sp. CA-128772 and *Methanosaeta* sp. PtaU1.Bin055 and a Mutant With Improved Catalytic Efficiency With Native Substrate. *Front. Bioeng. Biotechnol.* **2022**, *10*.

(133) Walker, M. C.; Chang, M. C. Y. Natural and engineered biosynthesis of fluorinated natural products. *Chem. Soc. Rev.* **2014**, *43* (18), 6527–6536.

(134) Motter, J.; Benckendorff, C. M. M.; Westarp, S.; Sunde-Brown, P.; Neubauer, P.; Kurreck, A.; Miller, G. J. Purine nucleoside antibiotics: recent synthetic advances harnessing chemistry and biology. *Nat. Prod. Rep.* **2024**, *41* (6), 873–884.

(135) (a) Zhao, L.-P.; Mai, B. K.; Cheng, L.; Gao, F.; Zhao, Y.; Guo, R.; Wu, H.; Zhang, Y.; Liu, P.; Yang, Y. Biocatalytic enantioselective C(sp^3)–H fluorination enabled by directed evolution of non-haem iron enzymes. *Nat. Synth.* **2024**, *3* (8), 967–975; (b) Zhao, Q.; Chen, Z.; Soler, J.; Chen, X.; Rui, J.; Ji, N. T.; Yu, Q. E.; Yang, Y.; Garcia-Borràs, M.; Huang, X. Engineering non-haem iron enzymes for enantioselective C(sp^3)–F bond formation via radical fluorine transfer. *Nat. Synth.* **2024**, *3* (8), 958–966.

(136) Groendyke, B. J.; AbuSalim, D. I.; Cook, S. P. Iron-Catalyzed, Fluoroamide-Directed C–H Fluorination. *J. Am. Chem. Soc.* **2016**, *138* (39), 12771–12774.

(137) O'Hagan, D.; B. Harper, D. Fluorine-containing natural products. *J. Fluor. Chem.* **1999**, *100* (1), 127–133.

(138) (a) Goldman, P. The Enzymatic Cleavage of the Carbon-Fluorine Bond in Fluoroacetate. *J. Biol. Chem.* **1965**, *240* (8), 3434–3438; (b) Khusnutdinova, A. N.; Batyrova, K. A.; Brown, G.; Fedorchuk, T.; Chai, Y. S.; Skarina, T.; Flick, R.; Petit, A.-P.; Savchenko, A.; Stogios, P.; Yakunin, A. F. Structural insights into hydrolytic defluorination of difluoroacetate by microbial fluoroacetate dehalogenases. *FEBS J.* **2023**, *290* (20), 4966–4983.

(139) (a) Chan, P. W. Y.; Chakrabarti, N.; Ing, C.; Halgas, O.; To, T. K. W.; Wälti, M.; Petit, A.-P.; Tran, C.; Savchenko, A.; Yakunin, A. F.; Edwards, E. A.; Pomès, R.; Pai, E. F. Defluorination Capability of l-2-Haloacid Dehalogenases in the HAD-Like Hydrolase Superfamily Correlates with Active Site Compactness. *ChemBioChem* **2022**, *23* (1), e202100414; (b) Chan, W. Y.; Wong, M.; Guthrie, J.; Savchenko, A. V.; Yakunin, A. F.; Pai, E. F.; Edwards, E. A. Sequence- and activity-based screening of microbial genomes for novel dehalogenases. *Microb. Biotechnol.* **2010**, *3* (1), 107–120.

(140) Soiefer, A. I.; Kostyniak, P. J. Purification of a fluoroacetate-specific defluorinase from mouse liver cytosol. *J. Biol. Chem.* **1984**, *259* (17), 10787–10792.

(141) (a) Fetzner, S.; Lingens, F. Bacterial dehalogenases: biochemistry, genetics, and biotechnological applications. *Microbiol. Rev.* **1994**, *58* (4), 641–685; (b) Murphy, C. D. Biodegradation and

biotransformation of organofluorine compounds. *Biotechnol. Lett* **2010**, *32* (3), 351–359; (c) Wang, Y.; Liu, A. Carbon–fluorine bond cleavage mediated by metalloenzymes. *Chem. Soc. Rev.* **2020**, *49* (14), 4906–4925; (d) Natarajan, R.; Azerad, R.; Badet, B.; Copin, E. Microbial cleavage of CF bond. *J. Fluor. Chem.* **2005**, *126* (4), 424–435.

(142) Jitsumori, K.; Omi, R.; Kurihara, T.; Kurata, A.; Mihara, H.; Miyahara, I.; Hirotsu, K.; Esaki, N. X-Ray Crystallographic and Mutational Studies of Fluoroacetate Dehalogenase from *Burkholderia* sp. Strain FA1. *J. Bacteriol.* **2009**, *191* (8), 2630–2637.

(143) (a) Kamachi, T.; Nakayama, T.; Shitamichi, O.; Jitsumori, K.; Kurihara, T.; Esaki, N.; Yoshizawa, K. The Catalytic Mechanism of Fluoroacetate Dehalogenase: A Computational Exploration of Biological Dehalogenation. *Chem. – Eur. J.* **2009**, *15* (30), 7394–7403; (b) Chan, P. W. Y.; Yakunin, A. F.; Edwards, E. A.; Pai, E. F. Mapping the Reaction Coordinates of Enzymatic Defluorination. *J. Am. Chem. Soc.* **2011**, *133* (19), 7461–7468.

(144) (a) Tu, L. Q.; Chen, Y. Y.; Wright, P. F. A.; Rix, C. J.; Bolton-Grob, R.; Ahokas, J. T. Characterization of the fluoroacetate detoxication enzymes of rat liver cytosol. *Xenobiotica* **2005**, *35* (10-11), 989–1002; (b) Tu, L. Q.; Wright, P. F. A.; Rix, C. J.; Ahokas, J. T. Is fluoroacetate-specific defluorinase a glutathione *S*-transferase? *Comp. Biochem. Physiol. C, Toxicol. Pharmacol.* **2006**, *143* (1), 59–66.

(145) Reisenbauer, J. C.; Sicinski, K. M.; Arnold, F. H. Catalyzing the future: recent advances in chemical synthesis using enzymes. *Curr. Opin. Chem. Biol.* **2024**, *83*, 102536.

(146) Kortemme, T. *De novo* protein design - From new structures to programmable functions. *Cell* **2024**, *187* (3), 526–544.

(147) Wang, Y.; Xue, P.; Cao, M.; Yu, T.; Lane, S. T.; Zhao, H. Directed Evolution: Methodologies and Applications. *Chem. Rev.* **2021**, *121* (20), 12384–12444.

(148) (a) Akagawa, K. 19 - Catalysis by peptides. In *Peptide Applications in Biomedicine, Biotechnology and Bioengineering*, Koutsopoulos, S. Ed.; Woodhead Publishing, 2018, 513–564; (b) Deuss, P. J.; den Heeten, R.; Laan, W.; Kamer, P. C. J. Bioinspired Catalyst Design and Artificial Metalloenzymes. *Chem. – Eur. J.* **2011**, *17* (17), 4680–4698.

(149) Hajos, Z. G.; Parrish, D. R. Asymmetric synthesis of bicyclic intermediates of natural product chemistry. *J. Org. Chem.* **1974**, *39* (12), 1615–1621.

(150) Eder, U.; Sauer, G.; Wiechert, R. New Type of Asymmetric Cyclization to Optically Active Steroid CD Partial Structures. *Angew. Chem. Int. Ed. Engl.* **1971**, *10* (7), 496–497.

(151) List, B.; Lerner, R. A.; Barbas, C. F. Proline-Catalyzed Direct Asymmetric Aldol Reactions. *J. Am. Chem. Soc.* **2000**, *122* (10), 2395–2396.

(152) (a) Wagner, J.; Lerner, R. A.; Barbas, C. F. Efficient Aldolase Catalytic Antibodies That Use the Enamine Mechanism of Natural Enzymes. *Science* **1995**, *270* (5243), 1797–1800; (b) Barbas, C. F.; Heine, A.; Zhong, G.; Hoffmann, T.; Gramatikova, S.; Björnestedt, R.; List, B.; Anderson, J.; Stura, E. A.; Wilson, I. A.; Lerner, R. A. Immune Versus Natural Selection: Antibody Aldolases with Enzymic Rates But Broader Scope. *Science* **1997**, *278* (5346), 2085–2092.

(153) Oku, J.-i.; Inoue, S. Asymmetric cyanohydrin synthesis catalysed by a synthetic cyclic dipeptide. *J. Chem. Soc., Chem. Commun.* **1981**, (5), 229–230.

(154) Becker, W.; Pfeil, E. Continuous Synthesis of Optically Activa α-Hydroxynitriles. *J. Am. Chem. Soc.* **1966**, *88* (18), 4299–4300.

(155) Dadashipour, M.; Asano, Y. Hydroxynitrile Lyases: Insights into Biochemistry, Discovery, and Engineering. *ACS Catal.* **2011**, *1* (9), 1121–1149.

(156) Shvo, Y.; Gal, M.; Becker, Y.; Elgavi, A. Asymmetric hydrocyanation of aldehydes with cyclo-dipeptides: A new mechanistic approach. *Tetrahedron Asymm.* **1996**, *7* (3), 911–924.

(157) Oku, J.-i.; Ito, N.; Inoue, S. Asymmetric cyanohydrin synthesis catalyzed by synthetic dipeptides, 2. *Makromol. Chem.* **1982**, *183* (3), 579–586.

(158) (a) Miller, S. J.; Copeland, G. T.; Papaioannou, N.; Horstmann, T. E.; Ruel, E. M. Kinetic Resolution of Alcohols Catalyzed by Tripeptides Containing the *N*-Alkylimidazole Substructure. *J. Am. Chem. Soc.* **1998**, *120* (7), 1629–1630; (b) Copeland, G. T.; Jarvo, E. R.; Miller, S. J. Minimal Acylase-Like Peptides. Conformational Control of Absolute Stereospecificity. *J. Org. Chem.* **1998**, *63* (20), 6784–6785.

(159) Baddiley, J.; Thain, E. M.; Novelli, G. D.; Lipmann, F. Structure of Coenzyme A. *Nature* **1953**, *171* (4341), 76–76.

(160) Wang, Y.; Yang, H.; Geerts, C.; Furtos, A.; Waters, P.; Cyr, D.; Wang, S.; Mitchell, G. A. The multiple facets of acetyl-CoA metabolism: Energetics, biosynthesis, regulation, acylation and inborn errors. *Mol. Genet. Metab.* **2023**, *138* (1), 106966.

(161) Guibé-Jampel, E.; Bram, G.; Vilkas, M. *Bull. Soc. Chim. Fr.* **1973**, 1021−1027.

(162) Toniolo, C.; Crisma, M.; Formaggio, F.; Peggion, C. Control of peptide conformation by the Thorpe-Ingold effect (C^{α}-tetrasubstitution). *Pept. Sci.* **2001**, *60* (6), 396–419.

(163) (a) Metrano, A. J.; Chinn, A. J.; Shugrue, C. R.; Stone, E. A.; Kim, B.; Miller, S. J. Asymmetric Catalysis Mediated by Synthetic Peptides, Version 2.0: Expansion of Scope and Mechanisms. *Chem. Rev.* **2020**, *120* (20), 11479–11615; (b) Davie, E. A. C.; Mennen, S. M.; Xu, Y.; Miller, S. J. Asymmetric Catalysis Mediated by Synthetic Peptides. *Chem. Rev.* **2007**, *107* (12), 5759–5812.

(164) List, B. Proline-catalyzed asymmetric reactions. *Tetrahedron* **2002**, *58* (28), 5573–5590.

(165) Kofoed, J.; Nielsen, J.; Reymond, J.-L. Discovery of new peptide-Based catalysts for the direct asymmetric aldol reaction. *Bioorg. Med. Chem. Lett.* **2003**, *13* (15), 2445–2447.

(166) Martin, H. J.; List, B. Mining Sequence Space for Asymmetric Aminocatalysis: *N*-Terminal Prolyl-Peptides Efficiently Catalyze Enantioselective Aldol and Michael Reactions. *Synlett* **2003**, *2003* (12), 1901–1902.

(167) Tang, Z.; Yang, Z.-H.; Cun, L.-F.; Gong, L.-Z.; Mi, A.-Q.; Jiang, Y.-Z. Small Peptides Catalyze Highly Enantioselective Direct Aldol Reactions of Aldehydes with Hydroxyacetone: Unprecedented Regiocontrol in Aqueous Media. *Org. Lett.* **2004**, *6* (13), 2285–2287.

(168) Notz, W.; List, B. Catalytic Asymmetric Synthesis of *anti*-1,2-Diols. *J. Am. Chem. Soc.* **2000**, *122* (30), 7386–7387.

(169) (a) Tsogoeva, S. B.; Wei, S. (*S*)-Histidine-based dipeptides as organic catalysts for direct asymmetric aldol reactions. *Tetrahedron Asymm.* **2005**, *16* (11), 1947–1951; (b) Zou, W.; Ibrahem, I.; Dziedzic, P.; Sundén, H.; Córdova, A. Small peptides as modular catalysts for the direct asymmetric aldol reaction: ancient peptides with aldolase enzyme activity. *Chem. Commun.* **2005**, (39), 4946–4948.

(170) Krattiger, P.; Kovasy, R.; Revell, J. D.; Ivan, S.; Wennemers, H. Increased Structural Complexity Leads to Higher Activity: Peptides as Efficient and Versatile Catalysts for Asymmetric Aldol Reactions. *Org. Lett.* **2005**, *7* (6), 1101–1103.

(171) (a) Wiesner, M.; Revell, J. D.; Wennemers, H. Tripeptides as Efficient Asymmetric Catalysts for 1,4-Addition Reactions of Aldehydes to Nitroolefins–A Rational Approach. *Angew. Chem., Int. Ed.* **2008**, *47* (10), 1871–1874; (b) Wiesner, M.; Neuburger, M.; Wennemers, H. Tripeptides of the Type H-d-Pro-Pro-Xaa-NH_2 as Catalysts for Asymmetric 1,4-Addition Reactions: Structural Requirements for High Catalytic Efficiency. *Chem. – Eur. J.* **2009**, *15* (39), 10103–10109; (c) Lewandowski, B.; Wennemers, H. Asymmetric catalysis with short-chain peptides. *Curr. Opin. Chem. Biol.* **2014**, *22*, 40–46.

(172) Schnitzer, T.; Wennemers, H. Influence of the *Trans*/*Cis* Conformer Ratio on the Stereoselectivity of Peptidic Catalysts. *J. Am. Chem. Soc.* **2017**, *139* (43), 15356–15362.

(173) Juliá, S.; Masana, J.; Vega, J. C. "Synthetic Enzymes". Highly Stereoselective Epoxidation of Chalcone in a Triphasic Toluene-Water-Poly[(*S*)-alanine] System. *Angew. Chem. Int. Ed. Engl.* **1980**, *19* (11), 929–931.

(174) Juliá, S.; Guixer, J.; Masana, J.; Rocas, J.; Colonna, S.; Annuziata, R.; Molinari, H. Synthetic enzymes. Part 2. Catalytic asymmetric epoxidation by means of polyamino-acids in a triphase system. *J. Chem. Soc., Perkin Trans. 1* **1982**, 1317–1324.

(175) (a) Girvin, Z. C.; Gellman, S. H. Foldamer Catalysis. *J. Am. Chem. Soc.* **2020**, *142* (41), 17211–17223; (b) Akagawa, K.; Kudo, K. Development of Selective Peptide Catalysts with Secondary Structural Frameworks. *Acc. Chem. Res.* **2017**, *50* (10), 2429–2439.

(176) Akagawa, K.; Akabane, H.; Sakamoto, S.; Kudo, K. Organocatalytic Asymmetric Transfer Hydrogenation in Aqueous Media Using Resin-Supported Peptide Having a Polyleucine Tether. *Org. Lett.* **2008**, *10* (10), 2035–2037.

(177) Banfi, S.; Colonna, S.; Molinari, H.; Julia, S.; Guixer, J. Asymmetric epoxidation of electron-poor olefins-V: Influence on stereoselectivity of the structure of poly-α-aminoacids used as catalysts. *Tetrahedron* **1984**, *40* (24), 5207–5211.

(178) Bayer, E. Towards the Chemical Synthesis of Proteins. *Angew. Chem. Int. Ed. Engl.* **1991**, *30* (2), 113–129.

(179) Girvin, Z. C.; Gellman, S. H. Exploration of Diverse Reactive Diad Geometries for Bifunctional Catalysis via Foldamer Backbone Variation. *J. Am. Chem. Soc.* **2018**, *140* (39), 12476–12483.

(180) (a) Pauling, L.; Corey, R. B.; Branson, H. R. The structure of proteins: Two hydrogen-bonded helical configurations of the polypeptide chain. *PNAS* **1951**, *37* (4), 205–211; (b) Schmitt, M. A.; Choi, S. H.; Guzei, I. A.; Gellman, S. H. New Helical Foldamers: Heterogeneous Backbones with 1:2 and 2:1 α:β-Amino Acid Residue Patterns. *J. Am. Chem. Soc.* **2006**, *128* (14), 4538–4539.

(181) Kinghorn, M. J.; Valdivia-Berroeta, G. A.; Chantry, D. R.; Smith, M. S.; Ence, C. C.; Draper, S. R. E.; Duval, J. S.; Masino, B. M.; Cahoon, S. B.; Flansburg, R. R.; Conder, C. J.; Price, J. L.; Michaelis, D. J.

Proximity-Induced Reactivity and Product Selectivity with a Rationally Designed Bifunctional Peptide Catalyst. *ACS Catal.* **2017**, *7* (11), 7704–7708.

(182) (a) Pathak, T. P.; Miller, S. J. Site-Selective Bromination of Vancomycin. *J. Am. Chem. Soc.* **2012**, *134* (14), 6120–6123; (b) Barrett, K. T.; Miller, S. J. Enantioselective Synthesis of Atropisomeric Benzamides through Peptide-Catalyzed Bromination. *J. Am. Chem. Soc.* **2013**, *135* (8), 2963–2966; (c) Gustafson, J. L.; Lim, D.; Miller, S. J. Dynamic Kinetic Resolution of Biaryl Atropisomers via Peptide-Catalyzed Asymmetric Bromination. *Science* **2010**, *328* (5983), 1251–1255; (d) Diener, M. E.; Metrano, A. J.; Kusano, S.; Miller, S. J. Enantioselective Synthesis of 3-Arylquinazolin-4(3*H*)-ones via Peptide-Catalyzed Atroposelective Bromination. *J. Am. Chem. Soc.* **2015**, *137* (38), 12369–12377; (e) Hurtley, A. E.; Stone, E. A.; Metrano, A. J.; Miller, S. J. Desymmetrization of Diarylmethylamido Bis(phenols) through Peptide-Catalyzed Bromination: Enantiodivergence as a Consequence of a 2 amu Alteration at an Achiral Residue within the Catalyst. *J. Org. Chem.* **2017**, *82* (21), 11326–11336.

(183) Denmark, S. E.; Burk, M. T. Lewis base catalysis of bromo- and iodolactonization, and cycloetherification. *PNAS* **2010**, *107* (48), 20655–20660.

(184) Patra, S.; Mondal, H.; Dash, U.; Aziz, S. M.; Maji, M. S. Designing Peptide-Based Nucleophilic Catalysts Possessing Multiple Identical Active Sites for Late-Stage Chlorination of Peptides and Drugs. *Org. Lett.* **2025**, *27* (15), 3924–3929.

Chapter II

Synthesis, structure and fluoride binding of peptides

The experimental work described in Chapter II was carried out in collaboration with Jessica Sellar, Dr. Thomas Schlatzer and Dr. Francesco Ibba. Synthesis of catalysts was supported by Jessica Sellar (**2e**−**g**), Dr. Thomas Schlatzer (**2d**) and Dr. Francesco Ibba (**2c**). Dr. Francesco Ibba assisted with initial NMR titrations, while Jessica Sellar was involved in NMR titrations of **2f** and **2g**. The crystallographic results discussed within this chapter were obtained in collaboration with Jessica Sellar, Calum Patel and Dr. Agamemnon Crumpton. Further details are available in the Experimental section (Chapter V).

The results reported in this thesis are included within the publication *'Peptidic Catalysts Conformationally Tuned for Fluoride Binding and Delivery'* G. Poškaitė, T. Schlatzer, Z. Chen, M. V. Popescu, R. Paton, V. Gouverneur*, *J. Am. Chem. Soc.* **2026**, *148* (9), 9238–9243.

2.1. Introduction

2.1.1. Peptides for fluoride binding

Peptide binding to anion can be considered for a range of applications: anion transport, sensing, assembly, catalysis, therapeutics, and for understanding biological processes.[1] In case of fluoride binding, there are no reports of peptide-based receptors. Nevertheless, analytical studies on

(cyclo)peptide complexes with other halogens (Cl^-, Br^-, and I^-) have been performed to guide the construction of peptide-based hosts for anion binding. Previously studied peptide motifs include cyclic peptides consisting of L-α-amino[2] or D,L-α-aminoxy acids,[3] with a few examples of open-chain peptides.[4] The key examples, which provide insight on anion chelator design, are discussed below.

Theoretical studies suggest that peptides are excellent anionic and cationic ionophores. Later Section 3.1.1 discusses peptide-alkali metal chelation in more detail. Conversely, computational studies indicate that peptides can also bind fluoride with its NH groups.[5] The gas-phase calculations by Liu and Chen of cyclo$(Gly)_6$ complexation with F^- resulted in a hexacoordinated geometry with superior binding energy in comparison to corresponding Li^+, Na^+, and K^+ complexes (**Table 2.1.1**).[5c] Furthermore, optimisation of hexadentate cyclo$(Gly)_6$:X^- complexes (where X = F, Cl, Br) resulted in average calculated H-bond distances (**Table 2.1.1**) consistent with H-bonding ability of halides $F^- > Cl^- > Br^-$ based on their electronegativities (*v.* Section 1.1.2).[6] Such theoretical calculations should be taken with caution, considering their limitations for electron-dense species *i.e.* F^-, and the absence of solvation effects; nevertheless, they serve as proof of concept that peptides are promising fluoride receptor candidates.

Table 2.1.1. Calculated (gas-phase) binding energies (kJ mol^{-1}) for hexadentate complexes of cyclo$(Gly)_6$:X.[5c]

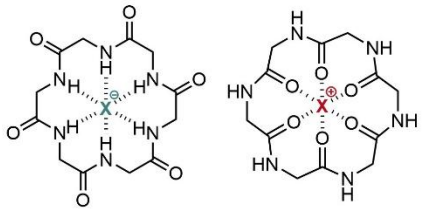

X =	F^-	Cl^-	Br^-	Li^+	Na^+	K^+
Binding energy (kJ mol^{-1})	541	219	276	491	400	242
d(NH—X^-/O—M^+) (Å)	2.88	3.41	3.46	2.21	2.36	2.67

Furthermore, it has been established that pre-organised and macrocyclic structures are superior for anion binding compared to unfolded linear peptides. Cyclopentaphenylalanine **2.1** has shown a 3-fold increase in Cl^- binding compared to its linear analogue **2.2** ($\log K_{a,\,TEACl}$) = 6.06 *versus* 2.79, in MeCN; **Figure 2.1.1**), even though in both cases pentadentate binding was achieved.[2c,4b]

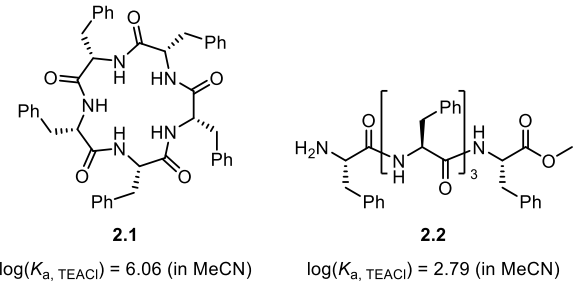

Figure 2.1.1. Linear and cyclic pentaphenylalanine analogues binding with chloride.[2c,4b]

And finally, the ionic radius of the anion should be taken into account in the design of fluoride receptors, since fluoride is the smallest halide ion. Size-dependent anion selectivity has been discussed previously in Section 1.3.1 describing *Fluc* family electrodiffusive channels that selectively excrete fluoride over chloride. In terms of small receptors, cyclic aminoxy hexapeptide **2.3** (**Figure 2.1.2a**) has been reported to selectively bind Cl^- ($\log K_{a(1:1,\ Ph_4PCl)} = 4.07$, in CD_2Cl_2) over F^- ($\log K_{a(1:1,\ TBAF)} = 1.48$, in $CDCl_3$) and Br^- (from Ph_4PBr; no binding) (**Figure 2.1.2b**).[3a] The selectivity was rationalised by the pore size of **2.3** (3.22 Å; based on computational calculations) being more compatible with the size of Cl^- (3.34 Å) compared to F^- (2.38 Å) or Br^- (3.64 Å).[7]

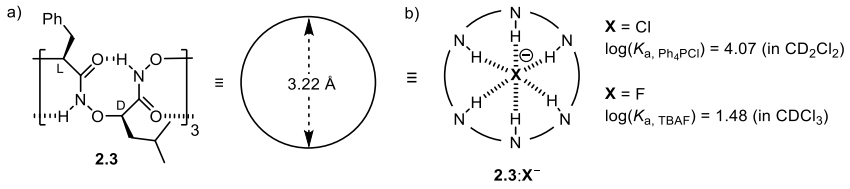

Figure 2.1.2. a) Structure and pore size of **2.3**, and b) anion binding selectivity of **2.3**.[3a]

In conclusion, the current field of peptide-based halide receptors directs to the aptitude of small cyclic peptides for F^- binding. Cyclic tetrapeptides are the smallest macrocycles that can adopt the all-*trans* prolyl conformation necessary for anion binding.[8] Experimentally their structural diversity is limited due to the lack of general synthetic methods for head-to-tail cyclisation of tetrapeptides.[4c,9] Cyclopenta- and cyclohexapeptides are more synthetically accessible and typically feature β- and γ-turn motifs (4→1 and 3→1 H-bonds, respectively) that can also rearrange for chelation to anions. However, understanding the sequence–structure relationship remains the most significant challenge in the design of cyclic peptides.[8b]

2.1.2. β-Turn peptides

β-Turns constitute the 3rd most common secondary structure, after α-helixes and β-sheets, found in approximately 25−30% of proteins.[10] The β-turn structural motif is defined by an NH(*i*−*2*)···O(*i*+*1*) intramolecular H-bond (4⟶1) or by an *i*−2 and *i*+*1* inter-residue distance of less than 7.0 Å (C^{α}(*i*−*2*)—C^{α}(*i*+*1*); **Figure 2.1.3**).[11] In addition to satisfying the distance criterion, the central residues (*i* and *i*−*1*) must not be helical or consisting of solely of β-strand residues. This non-regular secondary structure comprised of only four residues was first described by Venkatachalam in 1968, and the substructures were clustered into six different types: I, II, III and respective inverse conformations (I', II' and III').[12] Over the years, the initial classification of β-turns has been extended to thirteen well defined types (I, I', II, II', IV_{1-4}, IV_{misc}, VI_{a1-2}, VI_{b}, VIII) based on the dihedral angles φ,ψ of the central residues (*i* and *i*−*1*),[11-13] with types I and II the most commonly occurring (38% and 12%, respectively; **Figure 2.1.3**).[13a] In proteins, the most common β-turn-forming residues are Pro in position *i*, and Gly, Asn and Asp in position *i*−*1*.[10a,14]

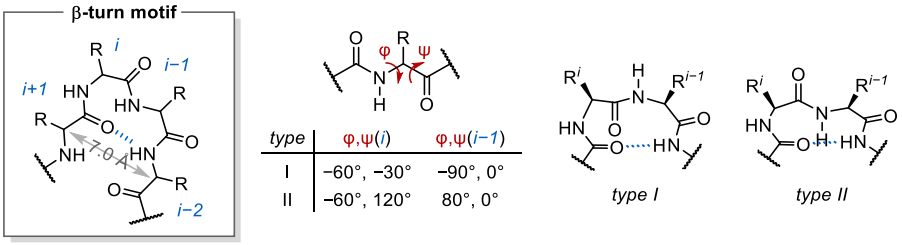

Figure 2.1.3. Distance criteria of a β-turn motif and characteristic angles φ,ψ of type I and II β-turns.[11-12]

Cyclic peptides were initially used as models to study isolated β-turns in solution due to their inherent rigidity.[15] Early studies have demonstrated that cyclohexapeptides can form double β-turns (**Figure 2.1.4a**).[8a,16] Incorporation of a proline residue has been shown to restrict conformational flexibility of cyclic peptides by preferentially positioning Pro within a loop region thus, limiting β-turn types to I/I' and II/II'. The L-Pro is the only naturally occurring tertiary amino acid featuring a narrow dihedral angle range φ (−55 to −80°) and the absence of NH resulting in its prevalence in turn regions of secondary structures. In addition, crystallographic studies of cyclic peptides have illustrated the formation of less common γ- and α-turns (3⟶1 and 5⟶1 H-bonds, respectively, **Figure 2.1.4b**).[17]

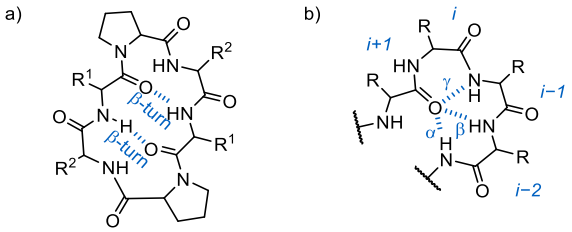

Figure 2.1.4. Turn motifs observed in cyclic peptides: a) double β-turn formation,[8a,16] and b) γ-, β- and α-turns as defined by H-bonding.[17]

In 1985, Dyson *et al.* have shown for the first time that a linear peptide, a *trans*-prolyl isomer of H-Tyr-Pro-Tyr-Asp-Val-Pro-Asp-Tyr-Ala-OH (**Scheme 2.1.1**), can form a type II β-turn in aqueous solution.[18] The systematic follow-up study of H-Tyr-Pro-X-Asp-Val-OH sequences (where X = any L-amino acid except Pro and Trp) have highlighted the conformational flexibility of linear peptides in water, in many cases hampering their conformational analysis via NMR.[19] Nevertheless, it was shown that sequences with X = Gly, Tyr or Phe residues provided stabilised β-turns, while X = hydrophilic residues significantly reduced β-turn stability in water.

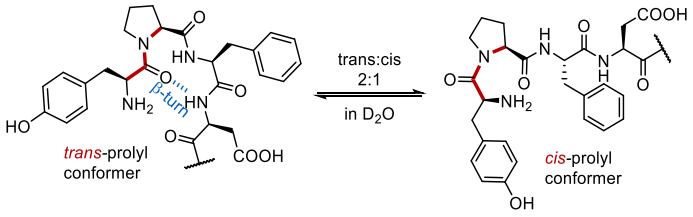

Scheme 2.1.1. *Cis-trans* prolyl isomerisation effect on β-turn formation.[18]

Since then, a range of noncanonical constrained amino acids were introduced to reduce the conformational flexibility of linear peptides.[20] In particular, the incorporation of achiral α,α-disubstituted amino acids into short peptides has shown success in promoting helical and turn type motifs.[21] For example, α-aminoisobutyric acid (Aib) tends to bias the 3_{10}- and α-helix conformations and to disfavour the formation of β-sheets.[22] Crystallographic studies of tetrapeptides containing a L/D-Pro-Xaa motif (where Xaa = α,α-disubstituted amino acid) in the loop region demonstrated that Aib residues nucleate type II/II' turns, while Acpc (1-aminocyclopropane-1-carboxylic acid) can adopt both, type II/II' and type I' β-turns (**Figure 2.1.5**).[23] The D-Pro-Gly motif has indicated a preference for type I/I' regimes, however, based on a limited data set (n = 2).

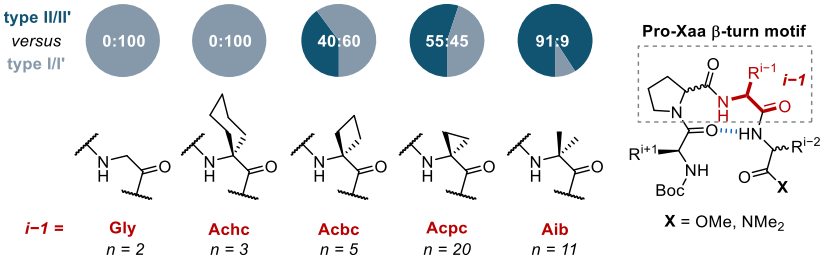

Figure 2.1.5. α,α-Dialkylation effect on occurrence of type II/II' and type I/I' turns.[23] *n* = number for data points.

These precedents demonstrate that β-turn-inducing motifs provide predictable conformational control in short peptides, making them attractive structural platforms for the development of preorganised anion-binding systems.

2.2. Results and discussion

2.2.1. Peptide β-turns for fluoride binding

2.2.1.1. Selection and synthesis of tetrapeptides

We hypothesised that the preorganisation and conformational rigidity of short peptides enforced by β-turn motifs could facilitate anion binding without the need for a macrocyclic scaffold. In order to investigate whether β-turns are suitable for fluoride recognition, we opted for tetrapeptides featuring Pro-Acpc as central motif: Boc-Leu-D-Pro-Acpc-Phe-NMe_2 and Boc-Leu-Pro-Acpc-Phe-NMe_2 (**2a** and **2b**, respectively, **Figure 2.2.1**). Both peptides represent a typical β-turn based on conformational analysis (*v.* Sections 2.2.1.2 and 2.2.1.3) and akin catalysts developed by the Miller group (*v.* Section 1.4.1).[23]

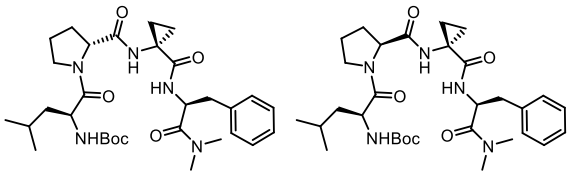

Figure 2.2.1. Structures of peptides **2a** and **2b** investigated in this study.

Peptides were synthesised from *C*- to *N*-terminus following the well-established EDC/HOBt (1-ethyl-3-(3-dimethylaminopropyl)carbodiimide and 1-hydroxybenzotriazole) peptide coupling protocol and the *tert*-butoxycarbonyl (Boc) *N*-protecting group strategy,[23] providing moderate overall yields of 46% and 71% respectively (7 steps each, **Scheme 2.2.1**). The final peptides were purified by flash column chromatography and their spectroscopic diastereomeric purity was assessed by NMR.

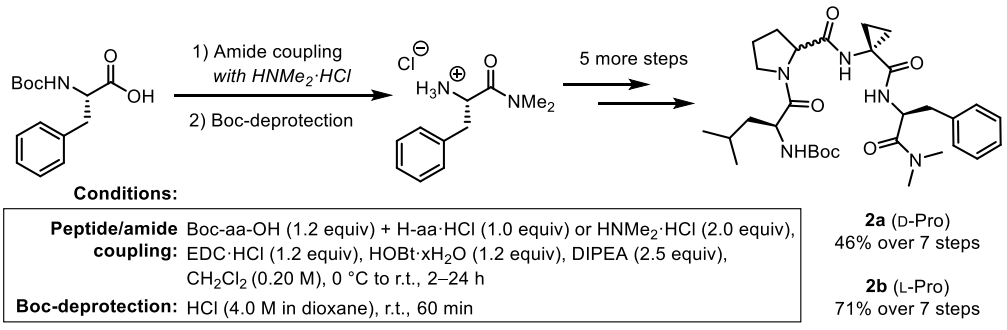

Scheme 2.2.1. General synthesis of peptides **2a** and **2b**. See Experimental, Section 5.2 for details.

2.2.1.2. Conformation in solution phase

At the onset of our investigation, we sought to gain insights into the ground-state conformation of peptides **2a** and **2b** in solution (via NMR spectroscopy) and solid state (via X-ray crystallography). NMR spectroscopic investigations were performed in CD_2Cl_2 in order to collect data comparable to our previous studies of HBD-TBAF complexes (*v.* Section 1.2.2.2). Also, CD_2Cl_2 is a non-coordinating solvent, and has an optimal chemical shift dispersion (^{1}H NMR: δ = 5.32 ppm) as well as a favourable temperature range (−97 °C melting point). Full assignments of ^{1}H and ^{13}C NMR spectra (298 K, CD_2Cl_2, 3.4 mM) of **2a** and **2b** peptides were accomplished via complementary 2D NMR experiments (^{1}H-^{1}H COSY, ^{1}H-^{13}C HSQC-DEPT, ^{1}H-^{13}C HMBC and ^{1}H-^{1}H NOESY; *v.* Experimental, Section 5.5.1). For both peptides, only one set of signals corresponding to a single averaged species was observed.

The following parameters were evaluated for NMR-based conformational analysis of peptides in solution: (1) the relative chemical shifts of the NH signals were compared to assign their H-bonding propensity;[24] (2) coupling constants of the H^{α} protons, in particular, $^3J_{NH-H\alpha}$ were extracted to calculate φ(*i+1*) and φ(*i−2*);[25] and (3) nuclear Overhauser effects (nOe) from two-dimensional ^{1}H–^{1}H-NOESY spectra were analysed to obtain through-space interactions.[24b,26]

NH chemical shifts. Measured NH shifts for **2a** and **2b** in CD_2Cl_2 are tabulated in **Table 2.2.1**. The NH protons of the Leu(*i+1*) residue for both, **2a** and **2b**, were more shielded when compared to other NHs due to the presence of a Boc protecting group (6.46 ppm and 5.80 ppm, respectively).

Table 2.2.1. Chemical shifts (δ) of amide protons (NH) of **2a** and **2b** (6−7 mM) in various NMR solvents.

Peptide	Solvent	$\delta_{NH(i+1)}$ /ppm	$\delta_{NH(i-1)}$ / ppm	$\delta_{NH(i-2)}$ / ppm
2a	CD_2Cl_2	6.46	7.00	7.75
	$CDCl_3$	6.43 (br)	7.09	7.72
	DMSO-d_6	7.14	8.63	7.92
2b	CD_2Cl_2	5.80	6.92	7.86
	$CDCl_3$	5.60	7.11	7.81
	DMSO-d_6	6.77	8.86	7.82

The H-bonding propensity of amide protons was evaluated by comparing NH chemical shifts (at 6 mM) in $CDCl_3$ and DMSO-d_6 (**Table 2.2.1**). DMSO-d_6 being a strong HBA solvent is expected

to disrupt intramolecular H-bonds among peptides and engage in solute–solvent interactions and *vice versa* for $CDCl_3$.[27] At the outset, for both peptides significant downfield shifting in DMSO-d_6 compared to $CDCl_3$ of NH(*i*+*1*) ($\Delta\delta$ = 0.71 and 1.17 ppm, for **2a** and **2b** respectively) and NH(*i*−*1*) ($\Delta\delta$ = 1.54 and 1.75 ppm, for **2a** and **2b** respectively) was observed, suggesting NH interacting with solvent. In contrast, NH(*i*−*2*) was minimally perturbed ($\Delta\delta$ = 0.2 and 0.01 ppm, for **2a** and **2b**, respectively), indicating a stable intramolecular H-bond.

The solute H-bond acidity values (A)[27-28] for the NH protons based on their chemical shift difference in $CDCl_3$ and DMSO-d_6 were calculated (**Table 2.2.2**). According to the A values, H-bonding interactions of NH hydrogens were then assigned as *strong* ($A \approx 0$), *weak* ($A \approx 0.1$), or *absent* ($A > 0.2$), following the classification by M. H. Abraham and R. J. Abraham.[24a]

Table 2.2.2. Calculated A values and assigned HB propensity of amide protons (NH) of **2a** and **2b**. H-bonding propensity assigned as *strong* ($A \approx 0$), *weak* ($A \approx 0.1$), or *absent* ($A > 0.2$).[24a]

$$A = 0.0065 + 0.133\,\Delta\delta \qquad \Delta\delta = \delta(\mathrm{DMSO}-d_6) - \delta(\mathrm{CDCl_3})$$

Peptide	$A_{NH(i+1)}$	$A_{NH(i-1)}$	$A_{NH(i-2)}$
2a	0.10	0.21	0.03
2b	0.16	0.24	0.01

The H-bonding interaction in $CDCl_3$ were proposed based on calculated A-values (**Figure 2.2.2**). $A_{NH(i-2)}$ values for both peptides were close to zero, supporting the formation of a β-turn (C=O(*i*+*1*)→NH(*i*−*2*)). Conversely, A values of NH(*i*−*1*) were > 0.2, which excluded the formation of a (bifurcate) γ-turn (C=O(*i*+*1*)→NH(*i*−*1*)). A weak intramolecular H-bond for **2a** involving NH(*i*+*1*) ($A_{NH(i+1)}$ = 0.10) suggested the formation of a β-hairpin (*i*−*2* → *i*+*1*), but not for **2b** ($A_{NH(i+1)}$ = 0.16).

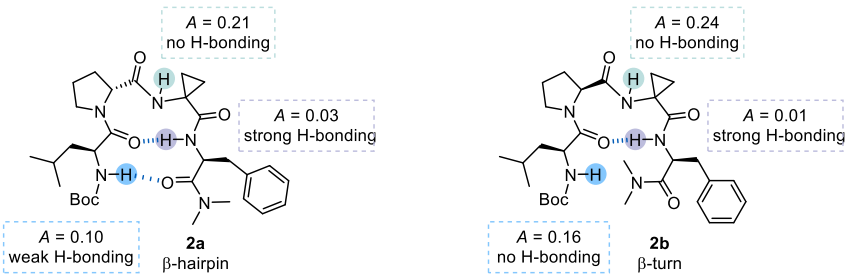

Figure 2.2.2. The proposed H-bonding pattern for **2a** and **2b** based on A-values of corresponding NHs.

φ(i) and φ(i+3). The chemical shifts of **2a** and **2b** were consistent with previous observations for analogous peptides reported by Miller *et al.*[23] The φ(*i+1*) and φ(*i−2*) backbone dihedral values were calculated from $^{3}J_{NH\text{-}H\alpha}$ coupling constants using Karplus equation[29] (**Table 2.2.3**) and compared with empirically derived cut-off values for type I/II β-turns and hairpins (**Figure 2.2.3**).[23] The resulting φ values suggested a type II β-turn (or hairpin) for **2b**, but did not allow assignment of a specific secondary structure for **2a**.

Table 2.2.3. Calculated φ(*i+1*) and φ(*i−2*) for **2a** and **2b** using $^{3}J_{NH\text{-}H\alpha}$ values (in CD_2Cl_2).

$$J = 6.98\,cos^2\left(\varphi - \frac{\pi}{3}\right) - 1.38\,cos\left(\varphi - \frac{\pi}{3}\right) + 1.72$$

Peptide	φ(*i+1*) (°)	φ(*i−2*) (°)
2a	-153 or -87	-147 or -93
2b	-101 or -139	-89 or -151

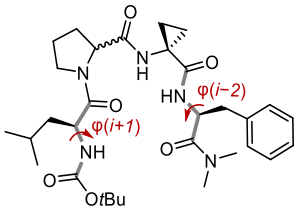

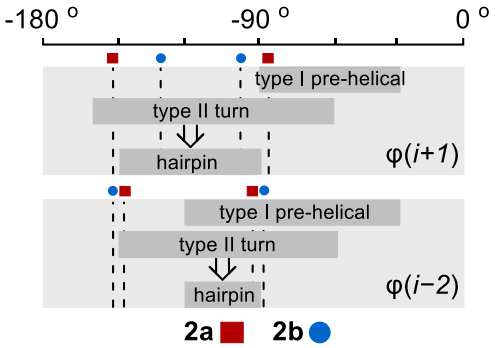

Figure 2.2.3. Typical ranges for φ(*i+1*) and φ(*i−2*) found in type I/II β-turns[23] compared to corresponding angles derived for peptides **2a** and **2b**.

NOESY NMR. As the formation of β-turns was established, NOE cross-peaks were used to determine the type of β-turn formed (**Figure 2.2.4**). First, a type II' turn was indicated for **2a** by nOes between Pro(H^{α})↔Acpc(NH) and Pro($H^{\delta(S)}$)↔Acpc(NH). A type II β-turn was suggested for **2b** due to strong correlation between Pro(H^{α})↔Acpc(NH). Additionally, for both peptides nOes between Leu(NH)↔NMe_2 and Leu(H^{β})↔Phe(H^{β}) perpetuated a β-hairpin structure, and excluded the presence of type I pre-helical conformation. These nOes, in conjunction with the proposed intramolecular H-bonds, point to a type II' β-hairpin structure for **2a**, and type II β-turn for **2b** in CD_2Cl_2 (**Figure 2.2.4**).

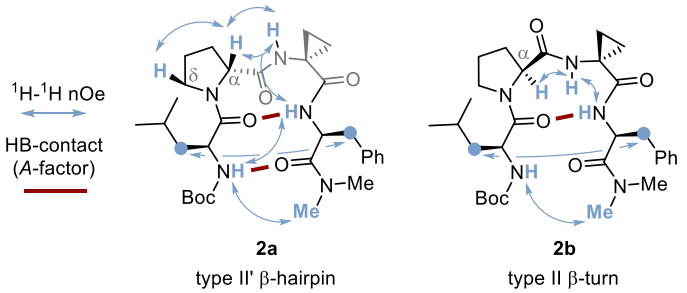

Figure 2.2.4. Proposed conformation of **2a** and **2b** in CD_2Cl_2 based on NMR studies.

2.2.1.3. Conformation in solid state

For solid-state conformational analysis of peptides **2a** and **2b**, crystals were grown via vapour diffusion method from EtOAc and pentane, and measured using Cu radiation (λ = 1.54 Å). The single crystal X-ray structures of **2a** and **2b** (**Figure 2.2.5**) slightly deviated from the solution state conformations discussed in the previous section (Section 2.2.1.2). In solid state, both peptides adopted type II'/II β-hairpins, according to φ,ψ(*i*) and φ,ψ(*i*−*1*) dihedrals and the presence of C=O(*i*+*1*)→NH(*i*−*2*) and C=O(*i*−*2*)→*NH*(*i*+*1*) intramolecular H-bonds (**Table 2.2.4**).[10b] The minor distortions of dihedral values from their canonical ones were within allowed ±30° limit[13a] and were in line with data collected by Mestrano *et al.* for a similar tetrapeptide library.[23]The most significant deviation from a typical type II β-turn was observed for **2b** with φ(*i*−*1*) and ψ(*i*−*1*) wider by 19° and 18°, respectively. Furthermore, the degree of twisting, as measured by the virtual dihedral angle (ϖ) defined by the four α-carbons (C^{α}), was consistent with planar structures attributed to type II/II' β-hairpins (ϖ = −0.6° and −11.7°, for **2a** and **2b** respectively).[30]

Baker and Hubbard defined H-bond geometry in proteins using distance criteria of 1.6–2.5 Å for NH···O and 2.5–3.5 Å for O···N (r), together with an NH···O angle (θ) of 130–170°, which only rarely falls below 120°.[31] H-bond contacts involved in β-hairpin formation (N(*i*+*3*)···O(*i*) and N(*i*)···O(*i*+*3*)) for peptides **2a** and **2b** satisfy typical constraints found in proteins (**Table 2.2.4**). Peptide **2b** displayed an extended C=O(*i*−*2*)→NH(*i*+*1*) contact of 3.096(1) Å in comparison to other H-bonds ($r \leq 2.9$ Å). In solution, **2b** did not form a hairpin structure (*v.* Section 2.2.1.2). Formation of a C=O(*i*+*1*)→NH(*i*−*1*) interaction corresponding to a γ-turn can be ruled out for both **2a** and **2b**, as the measured θ angles (~90°; **Table 2.2.4**) fall well below typical H-bond values.

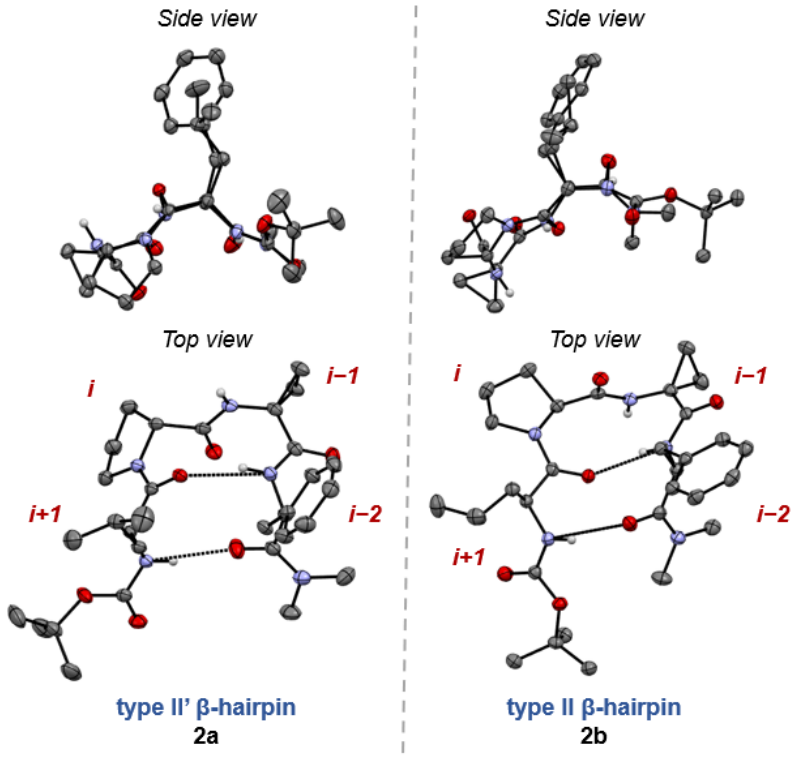

Figure 2.2.5. X-ray crystal structure of **2a** and **2b** with 50% thermal ellipsoids. Most of the H-atoms have been omitted for clarity, while some are depicted as circles. Dashed lines highlight H-bonding interactions.

Table 2.2.4. Relevant X-ray parameters obtained from single X-ray crystals of **2a** and **2b**.

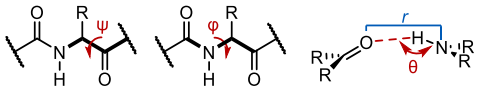

Peptide	φ,ψ(*i*)	φ,ψ(*i*−1)	*r*, θ (*i*+1 → *i*−2)	*r*, θ (*i*−2 → *i*+1)	*r*, θ (*i*+1 → *i*−1)
2a	64.8(1)°	−73.1(1)°	2.900(1) Å	2.896(1) Å	3.196(1) Å
	−125.28(9)°	−9.5(1)°	160(1)°	163(1)°	89.6(8)°
	(60°, −120°)[a]	(−80°, 0°)[a]			
2b	−58.6(1)°	61.0(1)°	2.838(1) Å	3.096(1) Å	3.114(1) Å
	127.5(1)°	17.8(1)°	163(1)°	164(1)°	84.3(9)°
	(-60°, 120°)[a]	(80°, 0°)[a]			

[a]Canonical values for type II/II' β-turns from ref[10b].

Residues *i+1* and *i−2* also display turn specific torsional angles φ(*i+1*) and φ(*i−2*) (*v.* **Figure 2.2.3**). These angles were measured in solid state and compared to the ones derived in solution from $^{3}J_{NH\text{-}H\alpha}$ coupling constants measured via NMR in CD_2Cl_2 (**Table 2.2.5**). For peptide **2a**, the solid-state φ(*i+1*) and φ(*i−2*) angles were consistent with those obtained in solution (**Table 2.2.5**). Meanwhile, **2b** displayed more pronounced deviations approximately 15° and 10°,

respectively, likely reflecting uncertainties in the $^3J_{NH\text{-}H\alpha}$ measurement due to resonance broadening. In both peptides, the side-chains at positions *i+1* and *i−2* exhibited negative χ_1 values, consistent with orientations that minimise steric interactions (**Table 2.2.6**). Despite this, the $C^\beta(i+1)$—$C^\beta(i-2)$ distances remained in close proximity (4.043 for **2a** and 5.151 Å for **2b**), which was also observed in solution through development of nOes.

Table 2.2.5. Calculated φ angles from $^3J_{NH\text{-}H\alpha}$ (in CD_2Cl_2) and measured from single crystal X-ray.

	Measured from X-ray		Calculated from $^3J_{NH\text{-}H\alpha}$	
Peptide	φ(*i+1*) (°)	φ(*i−2*) (°)	φ(*i+1*) (°)	φ(*i−2*) (°)
2a	−153.58(9)	−91.1(1)	−153 or −87	−147 or −93
2b	−116.3(1)	−161.8(1)	−101 or −139	−89 or −151

Table 2.2.6. Key parameters associated with *i+1* and *i−2* side chains from crystals of **2a** and **2b**.

Peptide	χ(*i+1*) (°)	χ(*i−2*) (°)	Cβ(*i+1*)—Cβ(*i−2*) (Å)
2a	−169.88(8)	−86.6(1)	4.043(1)
2b	−70.8(1)	−154.85(9)	5.151(2)

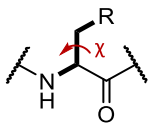

The data suggest that the conformations of **2a** and **2b** in solid state and in solution were similar, with only minor deviations. Previous reports have demonstrated that incorporation of D-Pro into an otherwise L-homochiral sequence is superior for nucleating β-hairpins in comparison to all-L homochiral sequences containing L-Pro.[23,30,32] In the case of peptides **2a** (D-Pro) and **2b** (L-Pro), however, we have observed the opposite trend. Peptide **2b** adopted a stable, canonical β-hairpin in both solution and the solid state, whereas **2a** formed a type II' β-turn in solution and a distorted hairpin in the solid state.

2.2.1.4. Complexation with TBAF(H_2O)$_3$: NMR titrations

Up to this date, β-turn conformational stability has not yet been explored with regard to anion binding. In order to establish whether β-turn peptides are suitable for fluoride binding and delivery, NMR titrations in the non-coordinating solvent CD_2Cl_2 with soluble fluoride source (TBAF(H_2O)$_3$) were conducted. The protocol chosen which reported by Ibba *et al.*[33] was previously used for titrations of BINAM *bis*-urea catalysts.

NMR titrations are well suited for the investigation of weak to medium binding (K_a up to 10^5 M^{-1}, depending on the experimental set up, *e.g.* magnetic field strength), and can provide insight not only into binding affinity, but also into the structure and conformation of such systems.[34] Proton chemical shifts are among the most sensitive indicators of H-bonding, where involvement in H-bonding leads to deshielding of the proton resonances.[35] Titrations of **2a** and **2b** were performed at millimolar concentration (3–4 mM) in CD_2Cl_2 to avoid aggregation. Upon addition of TBAF(H_2O)$_3$ (145–150 mM, in CD_2Cl_2) both peptides exhibited noticeable changes in ^{1}H chemical shifts. The chemical shifts remained variable throughout the titrations (up to 15–20 equivalents added) and did not reach limiting chemical shift values ($\Delta\delta_{NH}$), indicating weak complexation ($K_{a\ (1:1\ TBAF\text{-}3H2O)} < 10^3$ M^{-1}, in CD_2Cl_2).[34]

^{1}H NMR titrations in CD_2Cl_2 of **2a** (2.2 mM) with TBAF(H_2O)$_3$ (150 mM) are depicted in **Figure 2.2.6**. Over the course of the titrations, NH(*i−1)* has shifted downfield by +2.26 ppm at ~18 equiv. of fluoride added, while the NH chemical shifts of residues involved in β-hairpin formation, NH(*i−2*) and NH(*i+1*), have shifted by +0.20 and +0.50 ppm, respectively. Even though no $^{1h}J_{NH\text{-}F}$ through-bond coupling was observed due to weak and dynamic H-bonding, these results suggest tridentate binding to fluoride,[33] with a major contribution from the NH(*i−1)*, and mildly disrupted β-hairpin substructure based on chemical shift perturbation.

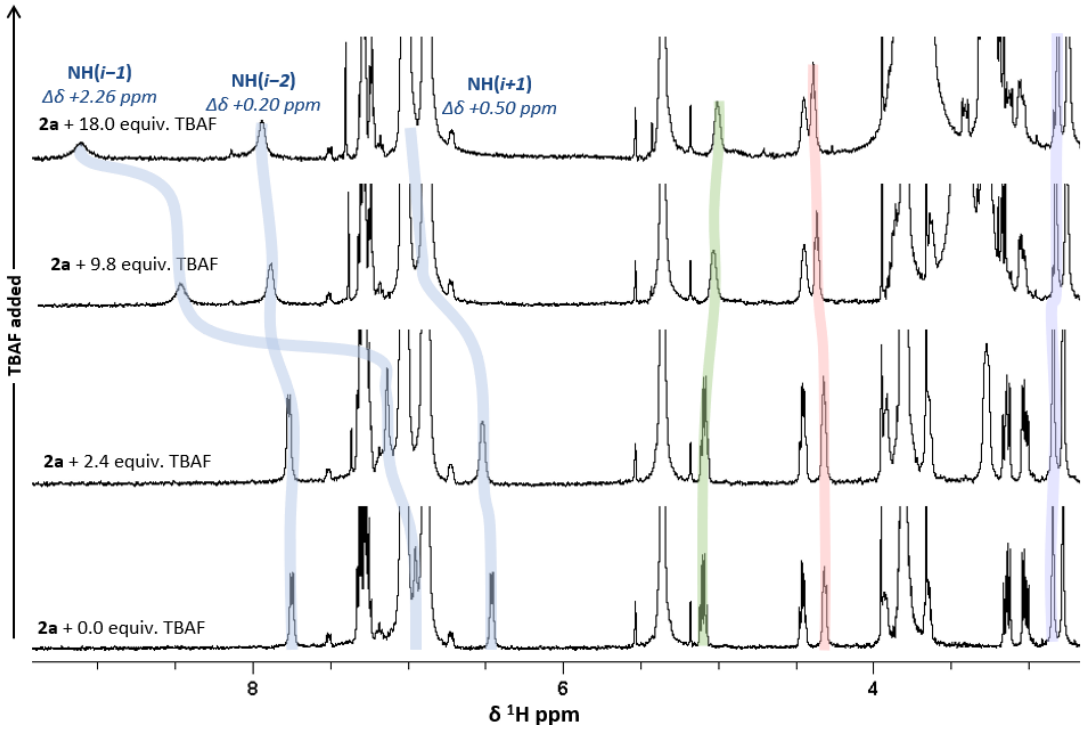

Figure 2.2.6. Stacked ^{1}H NMR spectra for the titration of **2a** (2.1 mM) with TBAF$(H_2O)_3$ (150 mM) in CD_2Cl_2 at 298 K.

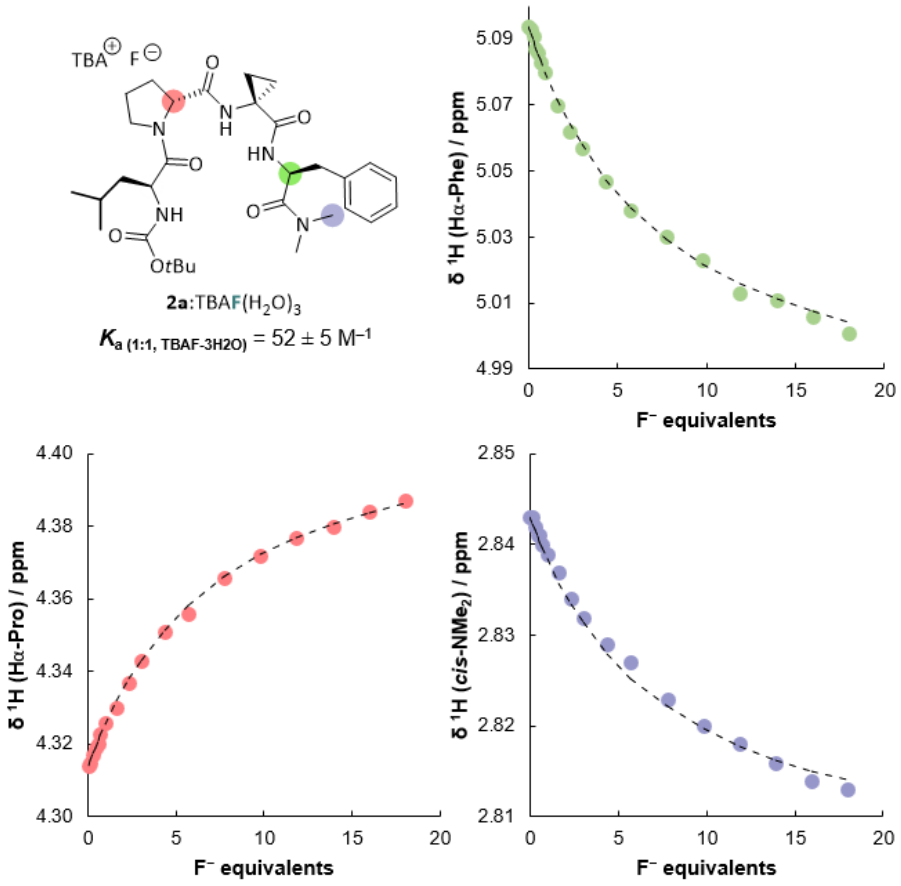

Figure 2.2.7. Titration profiles of selected protons between 0 and 18 equivalents of fluoride added, coloured spot indicates the experimental data while the black dashed line indicates the fitted model used to calculate $K_{a\ (1:1\ TBAF\text{-}3H2O)}$. See *Experimental* for details.

The change in chemical shifts for diagnostic resonances $H^{\alpha}(i)$, $H^{\alpha}(i-2)$ and *cis*-NMe_2 (highlighted in **Figure 2.2.7**) was plotted against the concentration of added fluoride, and the data was fitted via nonlinear least-squares regression using a dedicated software (DynaFit 4).[36] 1:1, 2:1 and 1:2 binding modes were considered, with 1:1 providing superior fitting results. The 2:1 and 1:2 models yielded physically unrealistic fitting parameters. Correspondingly, tetrapeptide **2a** showcased a modest 1:1 binding constant $K_{a\ (1:1\ TBAF\text{-}3H2O)} = 52 \pm 5\ M^{-1}$ (average of two experiments, in CD_2Cl_2), which complements its weak monodentate binding profile described above.

TBAF is commercially available as trihydrate ($TBAF(H_2O)_3$), and water can also engage in H-bonding with F^-. To assess the role of water, titrations of **2a** in CD_2Cl_2 were performed using (1) a nominally 'anhydrous' TBAF solution (150 mM), prepared by dilution of anhydrous 1 M TBAF in THF with CD_2Cl_2, and (2) TBAF with excess water (120 mM), prepared by addition of 7 equivalents of H_2O to the stock solution. Titrations with the 'anhydrous' TBAF solution provided reproducible titration profiles comparable to those obtained with $TBAF(H_2O)_3$ (as shown for NH($i-1$) in **Figure 2.2.8**), indicating that THF does not interfere with peptide–F^- binding. In contrast, titrations using $TBAF(H_2O)_7$ afforded markedly different titration curves, characterised by an initial linear regime followed by levelling off at a significantly reduced $\Delta\delta_{NH(i-1)}$ (~1.03 ppm), consistent with formation of a different species. These experiments demonstrate that, in the presence of excess water, the binding behaviour of **2a** becomes more complex and peptide is not preferentially binding fluoride. Similar investigations by Pfeifer *et al.*[37] showed that 1,3-diphenylurea **1.2.5** fully outcompetes water for fluoride binding due to its high affinity ($K_{a\ (1:1\ TBAF\text{-}3H2O)} = 19\ 500 \pm 500\ M^{-1}$ in MeCN).

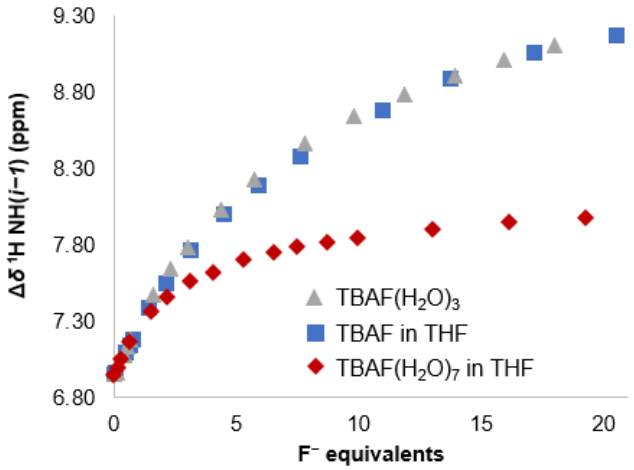

Figure 2.2.8. Titration profiles of NH(*i*−*1*) for **2a** using different TBAF$(H_2O)_n$ (where n = 0, 3 and 7) solutions in CD_2Cl_2/THF to investigate the effect of water. See text for further details.

Titrations of **2b** with TBAF$(H_2O)_3$ (*v.* Experimental, Section 5.5.2) also indicated weak overall binding to the fluoride ($K_{a\ (1:1\ TBAF\text{-}3H2O)}$ = 102 ± 1 M^{-1}, in CD_2Cl_2), however retaining the integrity of the β-turn; no fluoride binding to NH(*i*−*2*) was observed upon addition of 10 equiv. of TBAF$(H_2O)_3$ (**Table 2.2.7**). Consistent with the slightly higher binding constant of **2b,** addition of TBAF$(H_2O)_3$ resulted in a more pronounced downfield shift of NH(*i*−*1*) in **2b** than in **2a** ($\Delta\delta_{NH(i-1)}$ = 3.37 and 2.26 ppm, respectively).

Table 2.2.7. Difference in chemical shifts of NH protons between free and TBAF$(H_2O)_3$ bound **2a** and **2b** ($\Delta\delta_{NH}$)[a], and association constants (K_a)[b] for the formation of 1:1 complex.

Peptide	$K_{a\ (1:1\ TBAF\text{-}3H2O)}$ (M^{-1})	$\Delta\delta_{NH(i+1)}$ (ppm)	$\Delta\delta_{NH(i-1)}$ (ppm)	$\Delta\delta_{NH(i-2)}$ (ppm)
2a	52 ± 5	0.44	2.26[c]	0.16
2b	102 ± 1	0.19	3.37	0.02

[a]$\Delta\delta_{NH}$ = δ_{NH} (TBAF$(H_2O)_3$ 10 equiv.) − δ_{NH} (TBAF$(H_2O)_3$ 0 equiv.); [b]K_a are calculated by nonlinear regression using DynaFit 4 and expressed as the average of two experiments.[c]at 18 equiv. of TBAF$(H_2O)_3$ added.

Open chained peptides containing a turn motif (Pro-Gly) have been previously investigated by Pajewski *et al.*[38] for binding with Cl^-. NMR titrations of series of linear peptides $R^1(Gly)_nPro(Gly)_m\text{-}OCH_2C_6H_5$ **2.2.1** (where R^1 is a hydrophobic anchor) with TBACl in $CDCl_3$ have provided $K_{a,\ 1:1}$ ranging 10^1−10^3 M^{-1} depending on a peptide sequence length (**Figure 2.2.9**). It was proposed that elongated chains were superior in chloride binding due to increased denticity. In contrast to **2a** and **2b**, **2.2.1** receptors underwent conformation change upon binding with the

anion, which would be a result of a less stable secondary structure. In the study, significantly lower individual H-bonding contributions of NH protons were reported (up to $\Delta\delta_{NH}$ 1.67 ppm upon TBACl saturation) compared to tetrapeptides **2a** and **2b** binding to TBAF$(H_2O)_3$ ($\Delta\delta_{NH}$ = 2.26 and 3.37 ppm, for **2a** and **2b**, respectively), which is in line with the electronegativity of F > Cl.

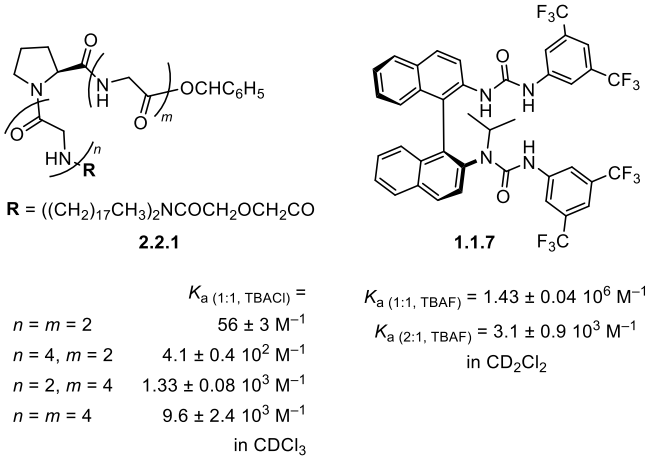

Figure 2.2.9. Binding constants of comparable fluoride and chloride receptors.[33,38]

In comparison, the BINAM-derived *bis*-urea catalyst **1.1.7** (*v.* Section 1.1.2.3) exhibited a 2:1 binding mode to TBAF$(H_2O)_3$ in CH_2Cl_2, with $K_{a\,(1:1\ TBAF\text{-}3H2O)} \approx 10^6\ M^{-1}$ (determined by UV-Vis titrations) and tridentate binding to fluoride (**Figure 2.2.9**).[33] NMR titrations of **1.1.7** with TBAF$(H_2O)_3$ in CD_2Cl_2 provided $\Delta\delta_{NH}$ values of 2.9, 5.3, and 5.7 ppm. The larger shifts ($\Delta\delta_{NH}$ > 5 ppm) can be attributed to the increased acidity of the urea protons, arising from the electron-withdrawing 1,3-*bis*(trifluoromethyl)phenyl substituent. The pK_a of diphenyl urea is 18.7, and the introduction of each CF_3 group decreases the pK_a by ~ 1.2 pK_a units, thereby giving Schreiner's urea (**1.2.5**; *N*,*N*'-bis(3,5-*bis*(trifluoromethyl)phenyl)urea) a pK_a of 13.8 in DMSO.[39] In contrast, the $\Delta\delta_{NH}$ values obtained in this study for NH(*i*−*1*) of **2a** and **2b** were lower (2.26 and 3.37 ppm, respectively), consistent with the lower acidity of the corresponding amide protons (pK_a of *N*-methylacetamide, a standard peptide model, is 25.5 in DMSO).[40] Tuning the acidity of peptide backbone NH protons is less straightforward. While inductive effects from side chains do propagate to peptide bonds, these effects are modest in magnitude (< 1 pKa unit).[41] Therefore, in peptide-based systems, enhanced fluoride binding affinity is more likely to be achieved through increased denticity rather than electronic tuning.

Based on our titration data, peptidic NH protons have been shown to be competent HBDs to fluoride anion. Meanwhile, the low binding constants are a result of a low denticity of peptides **2a** and **2b**, due to pre-organised β-hairpin motif limiting the availability of NH(*i+1*) and NH(*i−2*) for binding with fluoride. The L-Pro containing sequences were chosen for further binding optimisation due to a superior binding ability of **2b** compared to **2a**.

2.2.2. Urea-peptide hybrids for fluoride binding

2.2.2.1. Synthesis of ureido-peptide library

To further promote binding with fluoride, we designed sixteen tripeptides **2c–s** featuring proline analogues in position *i* and *N*-terminal urea cap (**Figure 2.2.10**). The urea moiety, which proved critical in BINAM *bis*-urea catalysts (*v.*Section 1.2.4),[42] was chosen to disrupt intramolecular H-bonding thus favouring multidentate binding to fluoride. We sought to investigate how rational modifications of the peptide sequence impact their conformation and their ability to complex with fluoride.

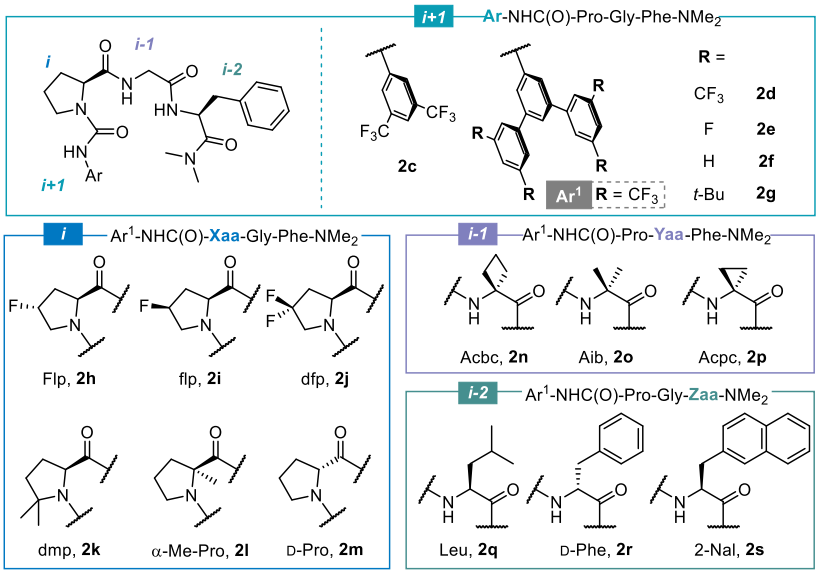

Figure 2.2.10. Structures of ureido-peptides investigated in this study.

The peptide library (**Figure 2.2.10**) included five analogues of Ar-NHC(O)-Pro-Gly-Phe-NMe_2 with varying aryl substituents of the urea *N*-cap (Ar = 3,5-$(CF_3)_2C_6H_3$ (**2c**), and Ar = 3,5-$[3,5\text{-R})_2C_6H_3]_2C_6H_3$, where R = CF_3 (**2d**), F (**2e**), H (**2f**), *t*-Bu (**2g**)). The central residues (*i* and *i–1*) involved in the loop formation were investigated to probe the β-turn conformational space through modification of Ar^1-NHC(O)-Xaa-Yaa-Phe-NMe_2 sequence (where Ar^1 = $3,5\text{-}[3,5\text{-}(CF3)_2C_6H_3]_2C_6H_3$). A systematic screening of Pro(*i*) modifications with Yaa = Gly included Xaa = Flp (**2h**), flp (**2i**), dfp (**2j**), (*S*)-5,5-dimethylproline (dmp, **2k**), (S)-2-methylproline (α-Me-Pro, **2l**), and D-Pro (**2m**). Three achiral analogues of Gly(*i–1*) with Xaa = Pro were chosen: 1-aminocyclobutane-1-carboxylic acid (Acbc, **2n**), Aib (**2o**), and Acpc (**2p**). Finally, Phe(*i–2*)

modifications included D-Phe (**2r**), (*S*)-2-naphthylalanine (2-Nal, **2s**) and a non-aromatic Leu (**2q**) to probe the NCIs with the aryl group of the *N*-cap.

Synthesis of peptides with *N*-cap, *i* and *i−1* modifications (**2c−p**) involved an assembly of corresponding tripeptides from *C*- to *N*-terminus following EDC/HOBt peptide coupling protocol and the Boc *N*-protecting group strategy (**Scheme 2.2.2a**).[23] The corresponding HCl·H-X-Y-Phe-NMe_2 salts were neutralised with NEt_3 and reacted with 3,5-bis(trifluoromethyl)phenyl isocyanate or 5'-isocyanato-3,3",5,5"-tetrakis(trifluoromethyl)-1,1':3',1"-terphenyl to afford **2c**, **2d** and **2h−p** (**Scheme 2.2.2b**, *method A*). Urea formation for **2e−g** was accomplished via one-pot-two-step protocol based on *in situ* formation of the isocyanate from the aniline precursor with triphosgene and triethylamine (**Scheme 2.2.2b**, *method B*). The corresponding aromatic anilines were prepared via Suzuki-Miyaura coupling[43] following published protocols (*v.* Experimental, Section 5.2.4.2).

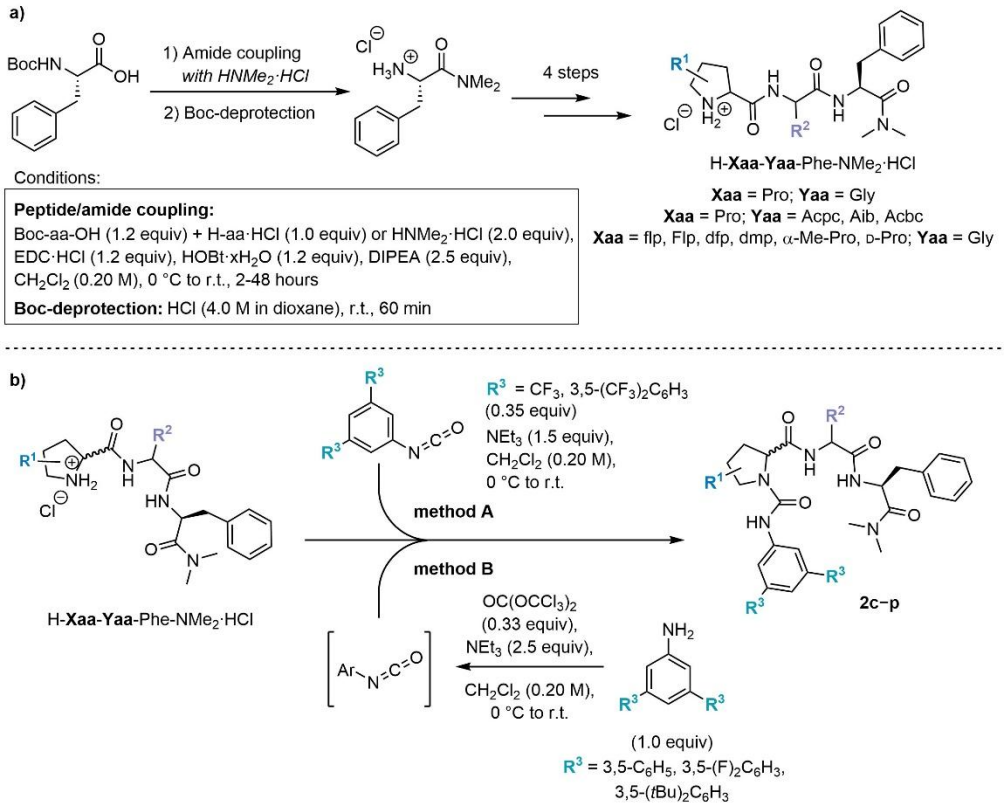

Scheme 2.2.2. Synthetic route for *N*-urea peptides **2c−p**. a) Preparation of tripeptide precursors H-X-Y-Phe-NMe_2·HCl; b) urea formation step via direct isocyanate coupling (method A) and *in situ* isocyanate formation from aniline (method B). See Experimental, Section 5.2 for details.

The synthesis route of Phe(*i*−*2*) analogues (**2q**−**s**) of Ar[1]-NHC(O)-Pro-Gly-Z-NMe_2 sequence was designed to allow late-stage peptide coupling with H-Z-NMe_2·HCl (**Scheme 2.2.3**, *bottom*). The coupling partner Ar[1]-NHC(O)-Pro-Gly-OH (**5.10**) was prepared in four steps consisting of peptide coupling, Boc- deprotection, urea formation and methyl ester hydrolysis (**Scheme 2.2.3**, *top*) with no observable signs of Pro epimerisation, which was assessed from crude NMR of the final compounds **2q**−**s**.

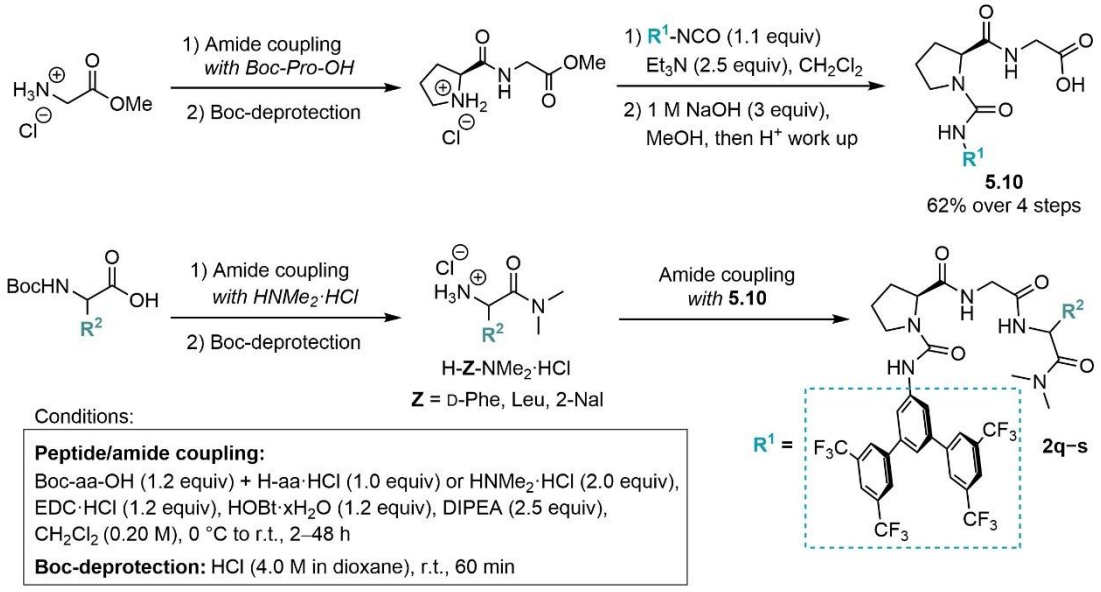

Scheme 2.2.3. Synthetic route for **2q**−**s**. See Experimental, Section 5.2 for details.

2.2.2.2. *Conformational properties in solution*

Prepared ureido-peptides **2c**−**r** were investigated in solution (via NMR spectroscopy) and **2c**, **2i**, and **2s** in solid state (via X-ray crystallography). Full assignment of ^{1}H and ^{13}C NMR spectra in CD_2Cl_2 for compounds **2c**−**r** were accomplished via complementary 2D NMR experiments (^{1}H-^{1}H COSY, ^{1}H-^{13}C HSQC-DEPT, ^{1}H-^{13}C HMBC and ^{1}H-^{1}H NOESY; *v.* Experimental, Section 5.5.1). The general structure of peptides **2c**−**r** was divided into two regions (**Figure 2.2.11**): *terminus* (*i+1* and *i*−*2*) and *loop* (*i* and *i+1* residues). *Terminus* region was investigated to establish the folding of peptides through NCIs such as intramolecular H-bonding and π-π stacking. The residues in the *loop* region affect backbone conformation through torsional constraints and NCIs *i.e.* backbone bond angle (τ, N−C^{α}−C), pyrrolidine ring puckering (*endo-exo*; defined by torsional angle γ, C^{α}−C^{β}−C^{γ}−C^{δ}), and prolyl *cis*−*trans* isomerisation (defined by torsional angle ω, N−C−N−C). Such conformational features would also have a pronounced effect on availability of NH(*i+1*) and NH(*i*−*1*) to engage in H-bonding affecting the conformation of the *terminus* region (*i.e.* peptide folding).

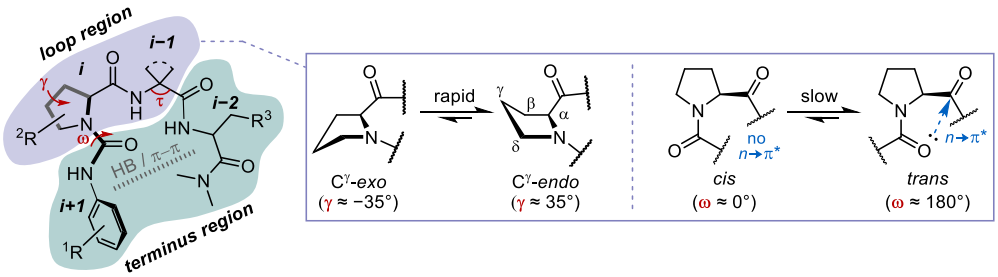

Figure 2.2.11. Conformational parameters evaluated in this study for ureido-peptides. Definitions of proline torsional angles taken from ref[44].

Conformation of proline analogues. The *cis-trans* and *endo-exo* isomerisation of proline and its analogues (**Figure 2.2.11**) are interrelated, complicating studies of structure-conformation relationship. The *exo*-pucker generally favours *trans* isomer responsible for $n_O(i+1)\rightarrow\pi_{C=O}^{*}(i)$ interaction commonly observed in α-helixes, collagen[45] and elastin-mimetic polypeptides.[46] Meanwhile, C^{γ}-*endo* ring puckering displays extended φ (≈ −80°) found in β-turns, as a result disfavouring $n_O(i+1)\rightarrow\pi_{C=O}^{*}(i)$ interaction and showcasing higher populations of *cis*- prolyl bond isomer.[14,47] Substituted prolines through steric and stereoelectronic factors can selectively probe one

equilibrium more drastically than the other,[48] which has been successfully utilised to induce or reduce stability of certain secondary structures.

Sequences 3,5-[3,5-$(CF_3)_2C_6H_3]_2C_6H_3$NHC(O)-Xaa-Gly-Phe-NMe_2 with proline analogues Xaa = Flp (**2h**), flp (**2i**), dfp (**2j**), Pro (**2d**), dmp (**2k**), and α-Me-Pro (**2l**) (**Figure 2.2.10**) were investigated to establish the relationship between proline conformation and peptide folding. Proline analogues flp (C^{γ}-*endo* preferred) and Flp (C^{γ}-*exo* preferred)[49] were chosen to study the effect of *endo-exo* equilibration probed by electronic effects (*v.* Section 1.1.2.2). The substitution of C^{α} and C^{δ} positions of Pro(*i*) are particularly receptive to steric repulsion with *i−1* and *i+1* residues, respectively, making such modifications valuable for controlling *cis*/*trans* equilibration.[48a] Accordingly, proline analogues dmp (*cis* preferred)[50] and α-Me-Pro (*trans* preferred)[51] were selected. Residue dfp has been reported to exhibit similar conformation to Pro,[52] and hence was chosen as a control for fluorine-substitution induced basicity and hydrophobicity.

Generally, the *cis*/*trans* ratio of proline derivatives can be obtained by integration of ^{1}H and ^{19}F NMR spectra, since rotamerisation rate is slow on the NMR timescale. The *trans*/*cis* distributions in $CDCl_3$ at 298 K for Ac-Xaa-OMe, a protected proline model which was introduced by Raines group,[49a,53] are provided in **Figure 2.2.12**. The *trans*/*cis* ratio (95:5) for Ac-α-Me-Pro-OMe in $CDCl_3$ was reported for the first time, while the corresponding values for other Ac-Xaa-OMe derivatives were in agreement with literature data.[52b,54] Within series, the α-Me-Pro and dmp amino acids represented the highest (95%) and the lowest (32%) %*trans* values within the series.

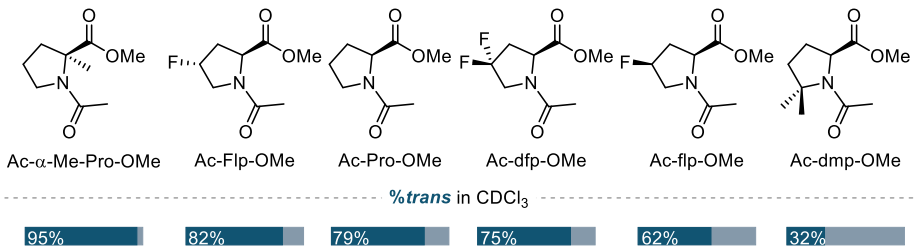

Figure 2.2.12. *Cis-trans* distributions of Ac-Xaa-OMe model prolines, expressed as %*trans*.[52b,54]

Peptides **2d**, **2h−i** did not display two sets of signals for *cis*/*trans* isomers in ^{1}H and ^{19}F NMR at room temperature spectra (in $CDCl_3$ or CD_2Cl_2) suggesting fast equilibration. At 298 K in CD_2Cl_2, **2h** and **2i** displayed only one resonance in ^{19}F spectra at −176.51 and −172.91 ppm, respectively,

which upon cooling (213 K and 233 K, respectively) revealed two broad signals suggesting dynamic exchange (**Figure 2.2.13**).

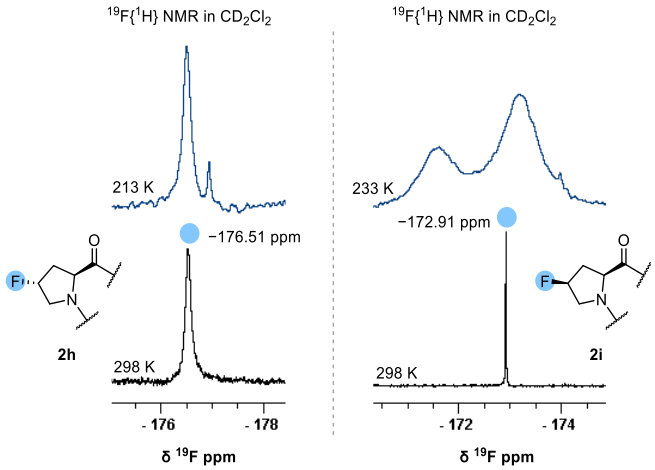

Figure 2.2.13. Expansion of $^{19}F\{^{1}H\}$ NMR (CD_2Cl_2, 471 MHz, with background suppression) spectra for **2h** and **2i**.

2D NOESY spectra in CD_2Cl_2 for **2d**, **2h**−**i** were used to confirm the presence of *cis-trans* isomerisation through cross-peaks with NH(*i*+*1*) (**Figure 2.2.14**, *bottom*). Through-space correlations of $H^{\delta(S)}(i)\leftrightarrow NH(i+1)$ and $H^{\delta(R)}(i)\leftrightarrow NH(i+1)$ were associated with *trans* isomer, while $H^{\alpha}(i)\leftrightarrow NH(i+1)$ with *cis*. All peptides apart from **2k** and **2l** displayed cross-peaks associated with both, *trans* and *cis*, conformers. Peptide **2h** showed only weak $H^{\alpha}(i)\leftrightarrow NH(i+1)$ NOE, suggesting a low population of the *cis* rotamer. Meanwhile **2k** and **2l** exhibited through-space correlations associated with only one isomer, *cis* for **2k** and *trans* for **2l**, which was expected based on *cis*/*trans* populations of their Ac-Xaa-OMe models. The %*trans* values obtained for Ac-Xaa-OMe were used to qualitatively rank the *cis-trans* propensities of **2d**, **2h**−**i** (**Figure 2.2.14**, *top*), as previous studies have shown that capped amino acid models provide a good representation of *cis-trans* ratios observed in peptide sequences.[55]

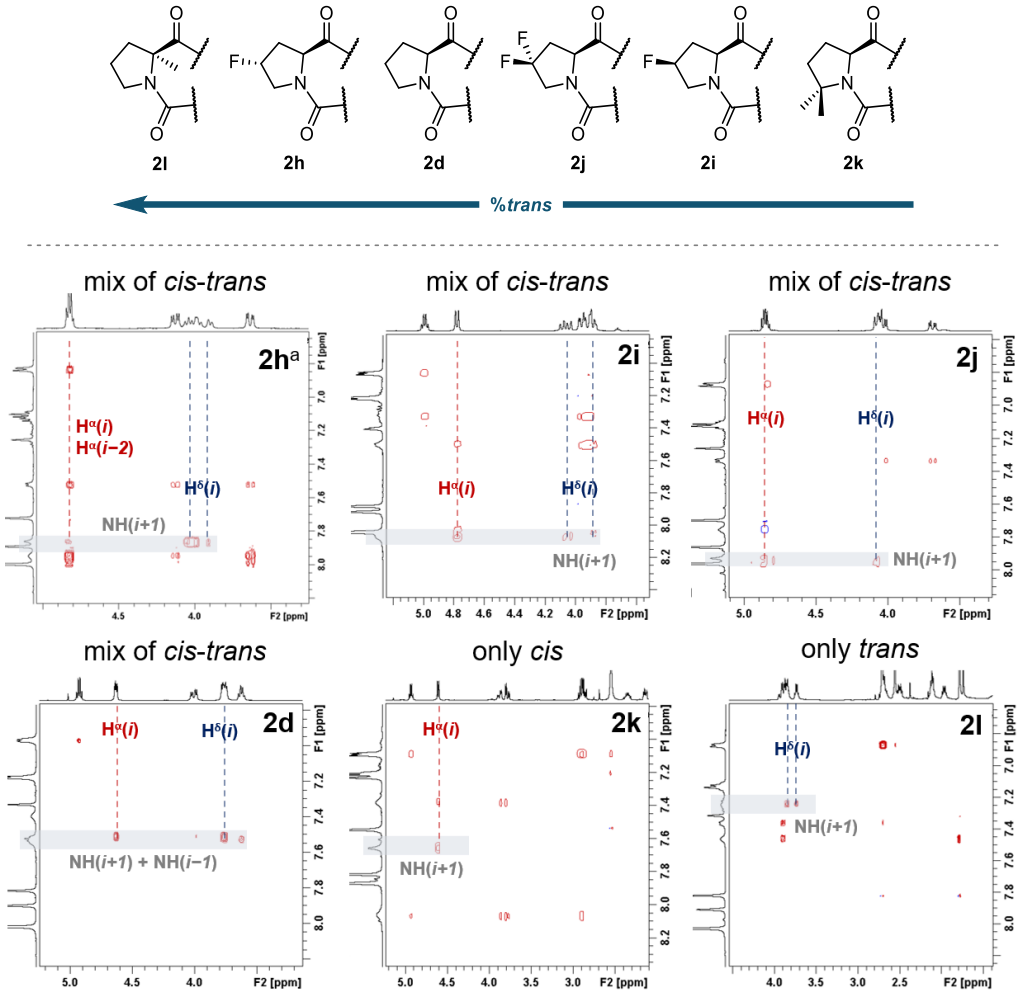

Figure 2.2.14. Top: *cis-trans* propensity for **2d**, **2h**−**j** based on NOESY NMR and Ac-Xaa-OMe data. Bottom: expansion of 2D NOESY (CD_2Cl_2, 500 MHz, 800 ms) spectra for **2d**, **2h**−**j**. [a]ROESY instead of NOESY.

The distinct *endo*/*exo* isoforms are known not to be observed in NMR due to fast exchange, and are rather determined through computational studies[52b,56] or mathematical modelling using experimentally obtained *J*-coupling constants[49b,57]. The *endo*/*exo* populations in $CDCl_3$ for Ac-Xaa-OMe (where Xaa = Pro and its fluorinated analogues) which were obtained from DFT calculation by Hofman *et al.*[52b] are depicted in **Figure 2.2.15** *top*, demonstrating Flp as *endo* and flp as *exo* stabilising residues. The calculated *endo*/*exo* distributions for α-Me-Pro have only been reported for Ac-Xaa-NHMe model.[58] The $^3J_{(H\alpha\text{-}H\beta)}$ coupling patterns in the ^{1}H NMR spectrum can also be used to qualitatively deduce *endo*/*exo* preference based on the Haasnoot–Altona equation with β-effect correction (**Figure 2.2.15**).[58-59] C$^\gamma$-*endo* conformation exhibits one large $^3J_{(H\alpha\text{-}H\beta(S))} > 7.1$ Hz and one small $^3J_{(H\alpha\text{-}H\beta(R))} < 2.9$ Hz coupling. In the case of Ac-flp-OMe in $CDCl_3$, H$^\alpha$ is observed as a doublet (J = 9.8 Hz for *trans* isomer), without measurable $^3J_{(H\alpha\text{-}H\beta(R))}$. Meanwhile, C$^\gamma$-*exo*

conformation displays two large *J*-couplings > 7.0 Hz. H^{α} of Ac-Flp-OMe was observed as a triplet (J = 8.5 Hz for *trans* isomer) indicating two very similar large coupling constants. In this study, the H^{α} of Ac-dmp-OMe model indicated similar coupling pattern to Ac-Pro-OMe (in $CDCl_3$), which is known to have a less defined pucker conformation (mixed *endo-exo*).

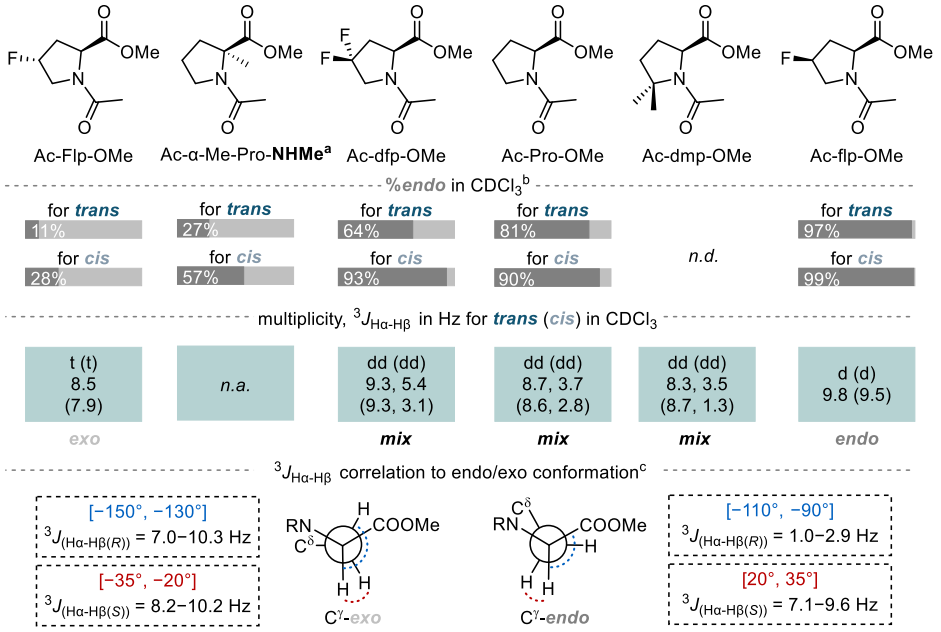

Figure 2.2.15. *Endo-exo* preference of Ac-Xaa-OMe model prolines based on DFT[52b] and NMR. From [a]ref[56b]; [b]ref[52b]; [c]ref[58]; n.d. = not determined; n.a.= not applicable; *mix* = mixture of two conformations.

Analogous NMR approach was used to assign *endo*/*exo* preference for peptides **2d**, **2h**−**k** (**Figure 2.2.16**). All sequences displayed expected pucker conformations, apart from **2j** (*i* = dfp), which has indicated *exo* pucker, rather than a mixture of two conformations that was observed for Ac-dfp-OMe. Peptide **2i** was the most (d, ^3J = 10.0 Hz), while **2h** and **2j** were the least (dd, ^3J = 8.6, 7.5, Hz, and t, ^3J = 7.9 Hz, respectively) C$^{\gamma}$-*endo* stabilising. The peptides were arranged based on their *endo* preference positioning **2l** (*i* = α-Me-Pro) in the *exo* region together with **2h** and **2j**, based on Ac-Xaa-OMe models and previous reports for α-Me-Pro to disfavour *endo* pucker due to all-eclipsed conformation.[48a,60] Notably, such NMR analysis does not consider the possibility of other envelope conformations, for example, C$^{\beta}$-*endo*/*exo* and *twisted* conformations have been reported for prolines in peptides and proteins.[61]

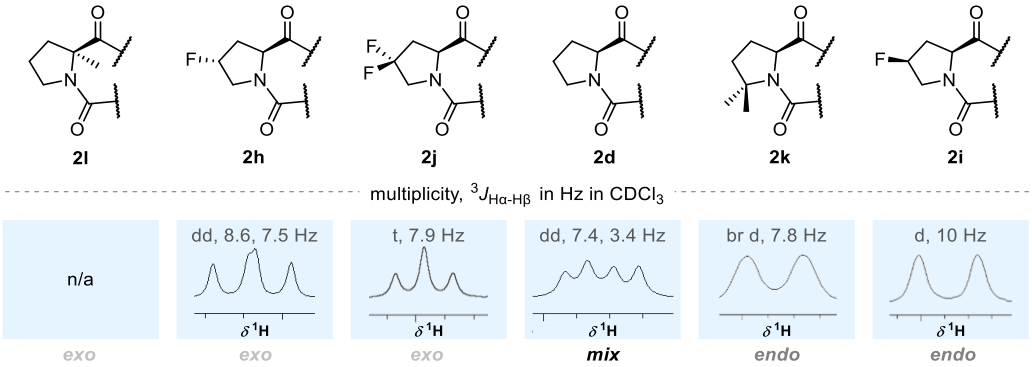

Figure 2.2.16. *Endo-exo* propensity for **2d**, **2h**–**j** based on $^3J_{(H\alpha-H\beta)}$ values.

Intramolecular H-bonding. We sought to investigate the intramolecular H-bonding network of the new peptide hybrids, since stable H-bonds were determined to be detrimental for availability of NHs to engage with fluoride. For this study peptides **2c** and **2d** were selected to investigate the effect of urea *N*-cap. The availability for H-bonding of NHs was established by measuring their chemical shifts in $CDCl_3$ and DMSO-d_6, which were used to derive the solute H-bonding acidity values (A), as described in Section 2.2.1.2. The introduction of Ar-urea *N*-terminal cap (Ar = 3,5-$(CF_3)_2C_6H_3$ (**2c**), 3,5-[3,5-$(CF_3)_2C_6H_3]_2C_6H_3$ (**2d**)) leads to disruption of the intramolecular H-bonding network as demonstrated by A values higher than 0.10 for all NHs (**Table 2.2.8**). Notably, NH(i+*1*) for **2c** and **2d** exhibited A = 0.18 indicating no H-bonding, even though this proton would be expected to be the most acidic due to electron-withdrawing aryl substituents (CF_3). Additionally, **2c** displayed elevated A-values for all NH protons, with the lowest A = 0.14 for NH(i−*1*). The extended aryl system of the *N*-terminal cap for **2d** resulted in slightly lower A-values for NH(i−*1*) and NH(i−*2*) (0.12 and 0.11, respectively), suggesting a more compact conformation compared to **2c**.

Table 2.2.8. Calculated A-values and assigned HB propensity of NH protons of **2c** and **2d**. H-bonding propensity assigned as *strong* ($A \approx 0$), *weak* ($A \approx 0.1$), or *absent* ($A > 0.2$).[24a]

$$A = 0.0065 + 0.133\,\Delta\delta \qquad \Delta\delta = \delta(\text{DMSO-}d_6) - \delta(CDCl_3)$$

Peptide	$A_{NH(i+1)}$	$A_{NH(i-1)}$	$A_{NH(i-2)}$
2c	0.18	0.14	0.15
2d	0.18	0.12	0.11

Solute H-bonding acidity has been investigated for various types of NH motifs (including peptides),[24a,27] with only one report of *A*-values for ureas in CD_3CN/ DMSO-d_6 system.[62] In this study, *A*-values obtained for BINAM-*bis* urea catalyst **1.1.7** were consistent with the H-bonding pattern proposed by Gouverneur group (**Figure 2.2.17**, *left*),[33] showcasing that *A*-value can be instrumental in describing H-bonding propensities of urea NH. The inherent flexibility of peptides investigated in this section resulted in multiple species averaged over NMR timescale, which hindered the identification of H-bond acceptors for the weak H-bonds involving NH(*i*−*1*) and NH(*i*−*2*). Based on the derived *A*-values for **2d**, it is unambiguous that NH(*i*+*1*) is predominantly solvent-exposed even though a minor population of *cis* prolyl conformer was observed via NOESY, suggesting that C=O(*i*+*1*) might be involved in β- or γ- turn formation (or both) (**Figure 2.2.17**, *right*).

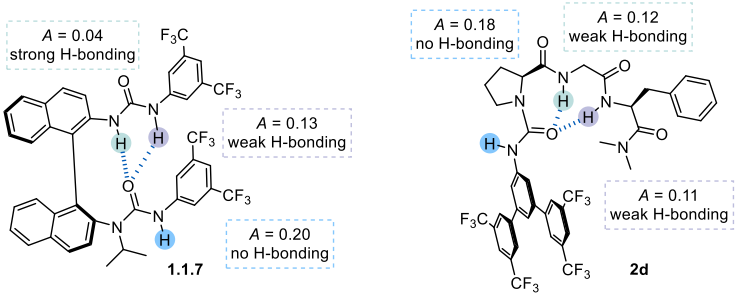

Figure 2.2.17. H-bonding pattern for **1.1.7**[33] and proposed model for **2d** based on *A*-values of corresponding NHs.

Table 2.2.9. Calculated *A*-values and assigned H-bonding propensity of NH protons of selected peptides. H-bonding propensity assigned as *strong* ($A \approx 0$), *weak* ($A \approx 0.1$), or *absent* ($A > 0.2$).[24a]

$$A = 0.0065 + 0.133\,\Delta\delta \qquad \Delta\delta = \delta(\mathrm{DMSO}-d_6) - \delta(\mathrm{CDCl_3})$$

Entry	Peptide	$A_{NH(i+1)}$	$A_{NH(i-1)}$	$A_{NH(i-2)}$
1	**2k**	0.06	0.12	0.09
2	**2i**	0.10	0.14	0.15
3	**2j**	0.16	0.12	0.10
4	**2d**	0.18	0.12	0.11
5	**2h**	0.19	0.15	0.10
6	**2l**	0.21	0.10	0.11

%*trans*

Bifurcate H-bonding was probed further by modifications of Pro(*i*). It was hypothesised that modulating *cis*-*trans* equilibrium would have a significant impact on H-bonding network. The *cis*

inducing *i* = dmp (**2k**) provided $A_{NH(i+1)}$ = 0.06, while *trans* inducing *i* = α-Me-Pro (**2l**) displayed $A_{NH(i+1)}$ = 0.21 (**Table 2.2.9**). These results propose that *A*-value can also be used to qualitatively assess the *cis-trans* population of Pro-containing peptides. Measured *A*-values of peptides consisting of various proline analogues (**2d**, **2h**−**l**) in **Table 2.2.9** were consistent with proposed order *trans*-prolyl bond population (*trans*%) in **Figure 2.2.14**.

The effect of α,α-dialkylation of *i*−*1* residue on H-bonding was also investigated through peptides **2n** (*i*−*1* = Acbc), **2o** (*i*−*1* = Aib) and **2p** (*i*−*1* = Acpc; **Table 2.2.10**). α,α-Dialkylation of amino acids has been shown to bias different secondary structures in Pro-Xaa containing sequences (where Xaa= α,α-dialkylated amino acid) through modulation of torsional angle (τ).[20,63] In our study we observed that increasing τ resulted in higher $A_{NH(i-1)}$ (**2p** (0.20) ≫ **2n** (0.14) > **2o** (0.12)), with other *A*-values unperturbed (**Table 2.2.10**). This indicates that dialkylation of *i*−*1* residue can control the conformation of NH(*i*−*1*) without affecting the remaining of the H-bonding network.

Table 2.2.10. Calculated *A*-values and assigned HB propensity of NH protons of **2n**, **2o** and **2p**. H-bonding propensity assigned as *strong* (*A* ≈ 0), *weak* (*A* ≈ 0.1), or *absent* (*A* > 0.2).[24a] τ taken from ref[23].

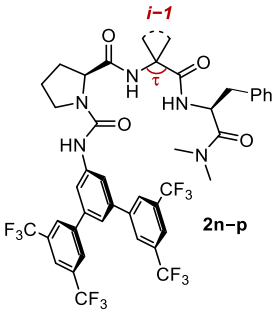

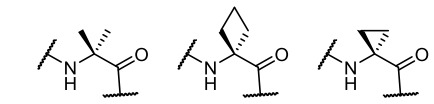

$A = 0.0065 + 0.133\,\Delta\delta$ $\qquad$ $\Delta\delta = \delta(\text{DMSO-}d_6) - \delta(\text{CDCl}_3)$

Peptide	$A_{NH(i+1)}$	$A_{NH(i-1)}$		$A_{NH(i-2)}$
2o	0.19	0.12		0.08
2n	0.20	0.14	τ (°)	0.04
2p	0.19	0.20		0.07

CH−*π stacking*. Finally, peptide folding was investigated via 2D NOESY NMR. For peptides (**2d**, **2f**−**r**) NOE cross-peaks between *i*+*1* and *i*−*2* residues indicate that the *C*- and *N*-termini of the catalysts are in close proximity and hence insinuate a loop structure. The observed NOE correlations between Phe(*i*−*2*) and Ar(*i*+*1*) strongly suggested π−π stacking (**Figure 2.2.18**). In

the case of **2q** (*i*−*2* = Leu), nOe correlation between C$^{\beta}$(*i*−*2*) and Ar(*i*+*1*) was observed instead. On the other hand, **2c**, **2f** and **2r** did not showcase any interactions between *i*+*1* and *i*−*2* residues. Peptides **2c** and **2f** feature modifications of the *i*+*1* aryl region (Ar = 3,5-$(CF_3)_2C_6H_3$ and 3,5-[3,5-C_6H_5]$_2C_6H_3$, respectively). In combination with previous results of H-bonding propensity of **2c**, it is apparent that extended aryl system (terphenyl) is necessary for stabilising peptide folding.

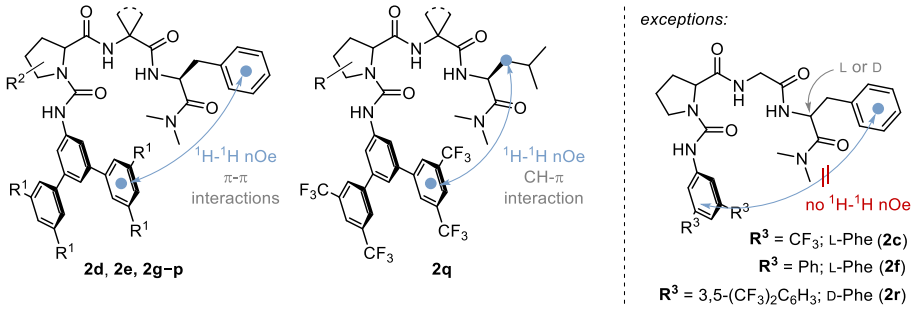

Figure 2.2.18. nOes (in CD_2Cl_2) indicating a loop structure for **2c**−**r**.

In conclusion, we have demonstrated that targeted modification of residues in the parent peptide **2d** enables modulation of peptide conformation and, most importantly, the H-bonding propensity of specific NH groups in solution (CD_2Cl_2).

1) The H-bonding ability of NH(*i*+*1*) can be probed by tuning *cis*-*trans* populations of the *i* residue. A *trans*-prolyl bond exposes NH(*i*+*1*) to the solvent, whereas the *cis* conformation favours intramolecular H-bonding involving NH(*i*+*1*).
2) The exposure of NH(*i*−*1*) to solvent can be altered through substitution of the *i*−*1* residue, with higher τ(*i*−*1*) angles correlating with greater NH(*i*−*1*) availability.
3) The H-bonding availability of NH(*i*−*2*) depends on the proximity of the *N*- and *C*-termini. π-π stacking between the *i*+*1* and *i*−*2* residues results in NH(*i*−*2*) being less exposed to solvent. Additional fine-tuning can be achieved by modulating φ(*i*) via pyrrolidine ring puckering, with C$^{\delta}$-*endo* providing extended φ conformations and *vice versa* for C$^{\delta}$-*exo*.

2.2.2.3. X-ray structures of ureido-peptides

Crystals of **2c**, **2s** and **2i** were grown via vapour diffusion method and single crystal X-ray data were collected following methods described in the Experimental section. Notably, many crystals of **2c−s** peptides were grown for crystallographic studies, however with limited success in acquiring good quality diffraction data due to air sensitivity (drying out), beam damage, poor high angle data or modulation. Single crystal of peptide **2i** was measured using synchrotron radiation at the Diamon Light Source which resulted in crystal decomposition from the beam after two runs. Moreover, solved crystal structures of **2s** and **2i** both contained solvent molecules within lattice structure (hexane and 1,2-dichloroethane, respectively), while **2c** co-crystalised with residual water (**Figure 2.2.19**).

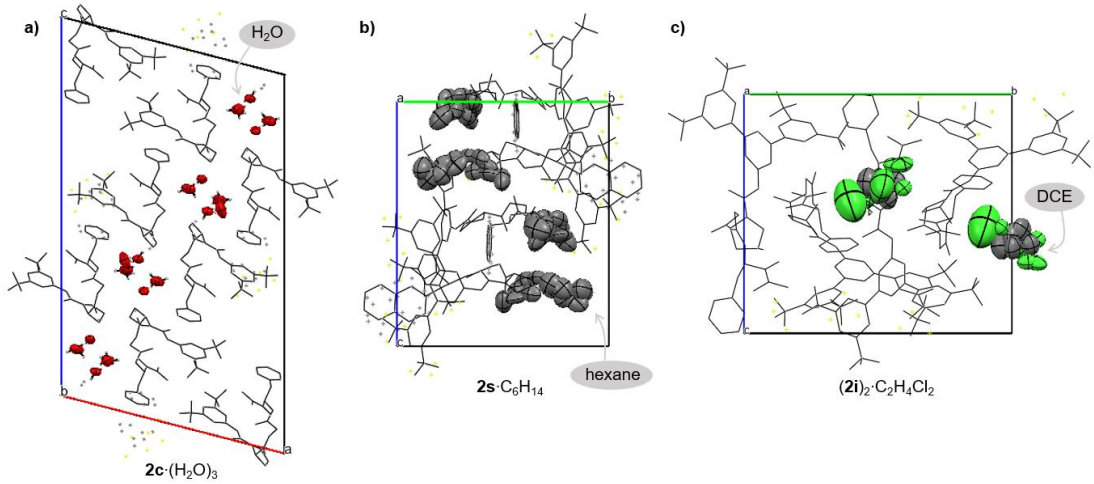

Figure 2.2.19. Packing of **2c**, **2s** and **2i** crystal structures showcasing co-crystalised solvent molecules: a) **2c**·$(H_2O)_3$; b) **2s**·C_6H_{14}, and c) (**2i**)$_2$·$C_2H_4Cl_2$.

Two conformers were identified within the same asymmetric unit for single crystals of **2i** (conformers **2i'** and **2i"**), and for **2c** (conformers **2c'** and **2c"**; RMSD = 0.33 Å). Peptide **2s** crystalised into a single conformer. At an outset, **2c'**, **2c"**, **2s** and **2i'** crystal structures insinuate formation of a *loop* region, while **2i"** appears unfolded (**Figure 2.2.20**). One characteristic of a β-turn is an inter-residue distance $d(C^{\alpha}(i-2)\text{—}C^{\alpha}(i+1)) < 7.0$ Å.[11] The urea N(*i*+*1*) was used instead of $C^{\alpha}(i+1)$ for structural analysis of urea *N*'-capped tripeptides. Measured N(*i*+*1*)—$C^{\alpha}(i-2)$ distances were above 7.0 Å for **2i"** (7.985(7) Å) and both **2c** conformers (7.621(5) and 7.566(6) Å for **2c'** and **2c"**, respectively). Meanwhile, **2s** and **2i'** had shorter N(*i*+*1*)—$C^{\alpha}(i-2)$ distances of 4.956(4) and 5.244(7) Å, respectively, which constitute a β-turn. Even though conformers of **2c**

featured H_2O which could disrupt the formation of a β-turn, the water molecules were observed in close proximity only to the C=O(*i*−*1*), which is not involved in a turn formation through H-bonding. The widened loop of **2c** was therefore associated with an absence of π-π interactions in the *terminus* region. Peptides **2s** and **2i'** displayed an offset π-π stacking and CH^{β}-π interactions between *i*−*2* and *i*+*1* residues. The shortest centroid distances between terphenyl (*i*+*1*) and phenylalanine (*i*−*2*) were 4.963 and 4.283 Å, for **2s** and **2i'**, respectively. Corresponding distances for **2c'** and **2c"** were only > 8 Å.

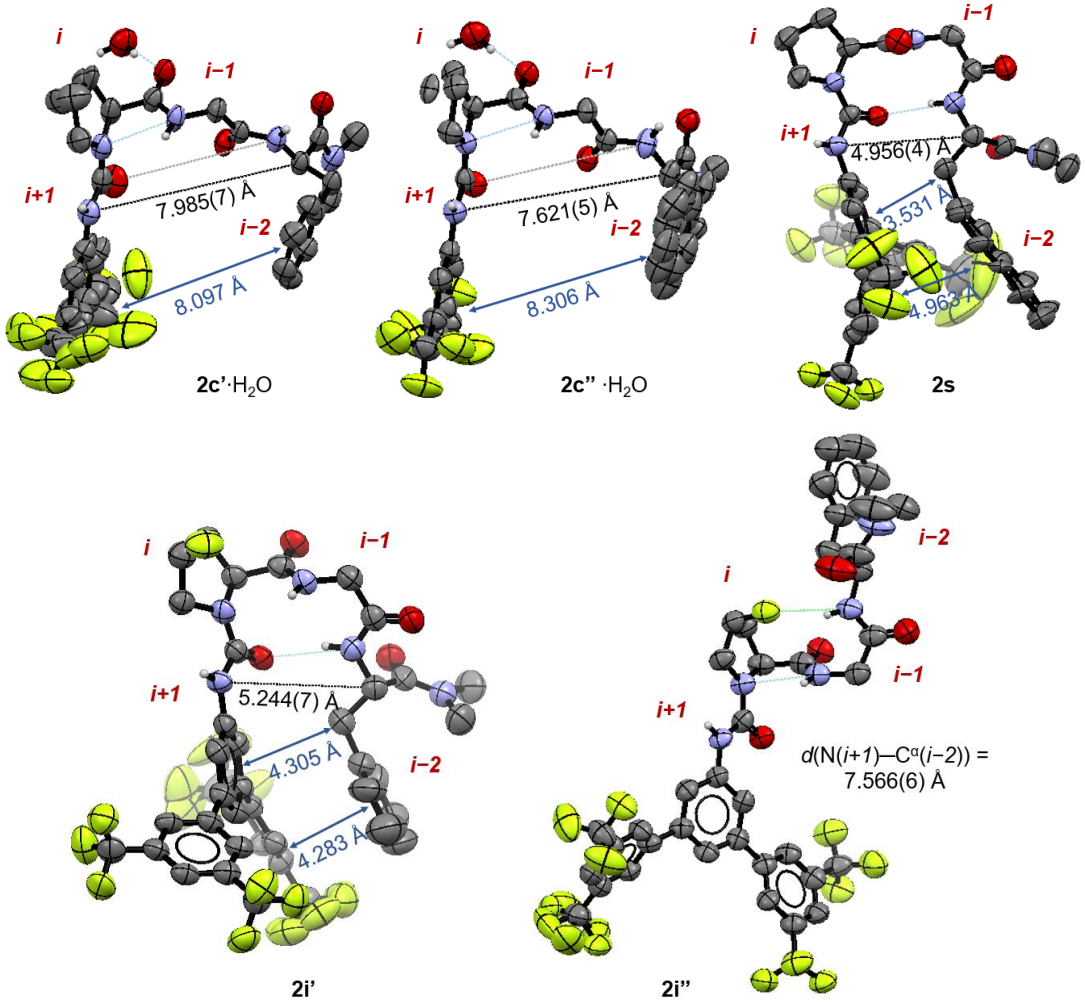

Figure 2.2.20. X-ray crystal structures of **2c** conformers, **2s**, and **2i** conformers with 50% thermal ellipsoids. Most of the H-atoms have been omitted for clarity. Solvent molecules were excluded for clarity, except for H_2O involved in H-bonding for **2c'** and **2c"**.

The backbone dihedral angles (φ,ψ) of the central residues in the β-turn containing peptides **2s** and **2i'** are summarised in **Table 2.2.11**. Canonical values[10b] indicated that **2s** adopts a type II, and **2i'** – a type I β-turns. The extended φ(*i*) for **2i'** was associated with the C$^{\gamma}$-*endo* pucker (γ =

−21.5(5)°). This pucker confirmation observed in solid state was consistent with solution state assignment in CD_2Cl_2, as determined from the $^3J_{(H\alpha\text{-}H\beta)}$ coupling pattern (**Figure 2.2.15**). Meanwhile, **2s** displayed a mixture of *endo-exo* conformers in solution, while Cγ-*exo* pucker (γ = 40.4(4)°) was observed in the solid state.

Table 2.2.11. Dihedral angles (φ,ψ) of the loop region obtained from single X-ray crystals of **2s** and **2i"**.

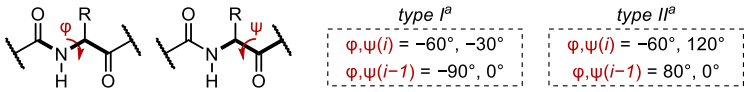

Peptide	φ,ψ(*i*)	φ,ψ(*i*−*1*)	turn type
2s	−59.9(4)°, 122.1(3)°	73.8(4)°, 7.3(5)°	II
2i'	−69(6)°, −14.3(7)°	−104.6(6)°, 14.6(7)°	I

[a]Canonical values for type II/II' β-turns from ref[10b].

The H-bonding interactions were identified using geometric (distance and angle) cut-off criteria defined by Baker and Hubbard[31] (see Section 2.2.1.3). The β-turn containing conformers **2s** and **2i'** displayed the characteristic C=O(*i*+*1*)→NH(*i*−*2*) H-bonds (**Table 2.2.12**). No additional canonical intramolecular C=O→NH were detected in conformers **2c'**, **2c"**, **2s**, **2i'** or **2i"**. Instead, a N(*i*)→NH(*i*−*1*) H-bonding motif[64] was observed for all structures except **2s** (**Table 2.2.12**), for which a ψ(*i*) angle of 122.1(3)° made such interaction inaccessible. Notably, the crystal structure of **2i"** revealed a multipolar CF→NH interaction, with donor-acceptor distance (r_d; F···N) of 3.105(5) Å and an angle (θ_d) of 160.4(1)°. This interaction, in conjunction with unconventional N(*i*)→NH(*i*−*1*) H-bond, likely contributes to stabilisation of the observed unfolded conformation. CF→NH dipole-dipole interaction involving backbone amide is well documented in ligand-protein complexes, typically exhibiting r_d = 3.1 Å and $\theta_d \geq 150°$ (*v.* Section 1.1.2.2).[65]

The ambiguous H-bonding patterns observed in solution by NMR prompted a direct comparison with solid-state X-ray structures. Peptide **2s** (*i*−*2* = 2-Nal) was considered as a proxy for **2d** (*i*−*2* = Phe) due to its analogous performance during catalytic optimisation (*v.* Section 3.2.2.1) and similar solution-phase conformation, as evidenced by NOESY correlations and calculated *A*-values (*v.* Experimental Section 5.5.1). In solution, *A*-values for peptide **2s** indicated a bifurcate-like C=O(*i*+*1*)→NH(*i*−*1*) and C=O(*i*+*1*)→NH(*i*−*2*) H-bonds with NH(*i*+*1*) solvent-exposed.

In the solid state, NH(*i*+*1*) and NH(*i*−*1*) did not engage in intramolecular H-bonding. This observation was consistent with NMR averaging in solution arising from dynamic equilibration between γ- and β-turn conformations and accounts for the observed *A*-values.

Table 2.2.12. X-ray parameters associated with H-bonding obtained from single X-ray crystals of **2a**, **2s** and **2i** (H-bonding bolded).

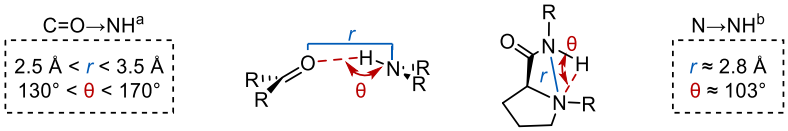

Peptide	*r*, θ C=O(*i*+*1*)→NH(*i*−*2*)	*r*, θ C=O(*i*+*1*)→NH(*i*−*1*)	*r*, θ N(*i*)→NH(*i*−*1*)
2c'	6.011(5) Å, 42.8(1)°	3.052(4) Å, 81.4(1)°	**2.763(5) Å, 107.3(1)°**
2c"	5.913(5) Å, 43.3(1)°	3.078(4) Å, 89.0(1)°	**2.742(4) Å, 108.1(1)°**
2s	**2.920(4) Å, 167.3(1)°**	3.260(5) Å, 96.0(1)°	3.459(4) Å, 73.5(1)°
2i'	**2.978(5) Å, 163.7(1)°**	3.078(4) Å, 89.0(1)°	**2.772(5) Å, 107.7(1)°**
2i"	5.928(5) Å, 122.1(1)°	3.260(5) Å, 96.0(1)°	**2.783(6) Å, 106.4(1)°**

[a]ref[31]; [b]ref[64].

Additional deviation between solution- and solid-state conformations were associated with the orientation of the NMe_2 *C*-cap. In the solid-state, for conformer **2i'** and **2s**, the NMe_2 groups were oriented away from the turn region, while in solution NOESY spectra displayed cross-peaks between the NMe_2 groups and the urea aryl moieties, indicating transient spatial proximity. In canonical tetrapeptide models, a *C*-cap can participate in β-hairpin formation, however, this interaction was not accessible here due to the absence of an *N*-terminal residue, contributing to dynamic conformations observed in solution.

In conclusion, solid-state conformers **2s** and **2i'** adopt type I and type II β-turns, respectively, while **2c** conformers were insufficiently compact to constitute β-turn motifs. Extension of the aryl system for substituted urea was key for nucleating folded β-turn conformations, while proline modifications modulated turn geometry in the solid state. Tetrapeptides **2a** and **2b** displayed good agreement between X-ray structures and solution-averaged conformations. Ureido-peptides exhibited pronounced deviations, suggesting substantial conformational plasticity. Such dynamic behaviour might be advantageous for anion binding but would pose challenges for achieving rigid, preorganised anion-binding sites required for enantioselective anion-binding catalysis.

2.2.2.4. *Complexation with TBAF(H_2O)$_3$*

After establishing that ureido-peptides **2c**–**s** display weaker intramolecular H-bonds, and consequently, more dynamic conformations, we next sought to investigate whether this enhanced flexibility increases denticity for fluoride binding. Fluoride binding to peptides **2c−r** was assessed via NMR titrations, in an analogous manner to **2a** and **2b** (*v.* Section 2.2.1.4), using TBAF(H_2O)$_3$ and millimolar peptide solutions (2−9 mM) in CD_2Cl_2.

Quantitative binding of **2c−r** during titrations was achieved upon addition of 1.2−3.0 equivalents of TBAF(H_2O)$_3$, indicating significantly stronger fluoride affinity than previously observed for tetrapeptides, which did not reach saturation even upon addition of 18 equivalents of TBAF(H_2O)$_3$. Moreover, all investigated ureido-peptides exhibited tridentate binding to F^-, as determined by significant ^{1}H downfield chemical shift perturbations of NH proton resonances during titrations; the corresponding $\Delta\delta_{NH}$ values are summarised in **Figure 2.2.21**. Representative stacked spectra from the titration of **2d** with TBAF(H_2O)$_3$ are shown in **Figure 2.2.22**. Upon saturation of **2d** with fluoride (1.9 equiv. of TBAF(H_2O)$_3$), NH(*i*+*1*) exhibited the largest downfield shift ($\Delta\delta_{NH} \approx +4.15$ ppm), followed by NH(*i*−*1*) and NH(*i*−*2*) ($\Delta\delta_{NH} \approx +2.95$ and +1.79 ppm, respectively). A similar trend was observed across most ureido-peptides, with $\Delta\delta_{NH(i+1)}$ (4.68–3.04 ppm) > $\Delta\delta_{NH(i-1)}$ (3.56–1.86 ppm) > $\Delta\delta_{NH(i-2)}$ (2.11–0.73 ppm). The only exception was observed for peptide **2g**, with $\Delta\delta_{NH(i+1)} \approx \Delta\delta_{NH(i-1)}$. This binding pattern can be rationalised by (i) higher acidity of NH(*i*+*1*) relative to NH(*i*−*1*) and NH(*i*−*2*), and (ii) conformational changes of the peptide scaffold, as discussed in Section 2.2.2.5. Interestingly, tetrapeptide **2b** in the previous section exhibited monodentate binding through NH(*i*−*1*) ($\Delta\delta_{NH}$ = 3.37 ppm at 10 equiv. TBAF(H_2O)$_3$). Among the ureido-peptides, only four (**2h**, **2j**, **2n** and **2o**) displayed peptidic $\Delta\delta_{NH}$ values exceeding this threshold, with the highest value measured for **2n** ($\Delta\delta_{NH(i-1)}$ = 3.56 ppm). This observation suggests that ~3.6 ppm represents an upper limit for peptidic $\Delta\delta_{NH}$ upon binding with F^-.

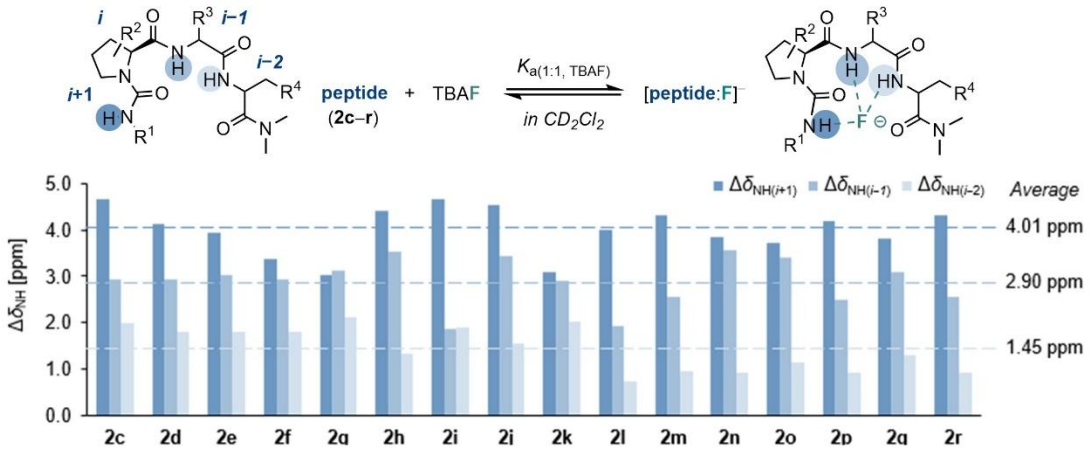

Figure 2.2.21. Chemical shift differences for NH contacts between unbound and TBAF$(H_2O)_3$-saturated peptides **2c**–**r** ($\Delta\delta_{NH}$) obtained from NMR titrations in CD_2Cl_2 at 298 K.

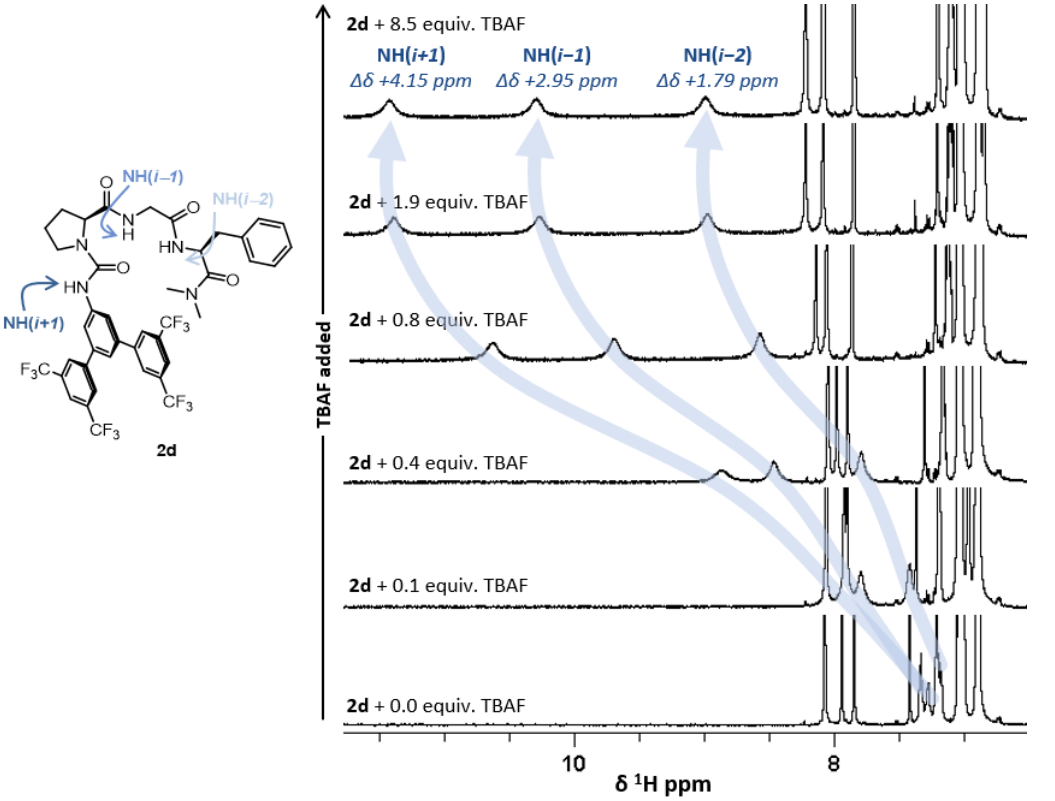

Figure 2.2.22. Selected NMR spectra of NH region for the titration of **2d** (5.8 mM) with TBAF$(H_2O)_3$ (69 mM) in CD_2Cl_2 at 298 K.

To probe the NH···F⁻ contacts in solution, the nOe developed between fluoride and NH was investigated by ^{19}F–^{1}H heteronuclear Overhauser effect spectroscopy (HOESY).[66] The HOESY spectrum of the 1:1 **2d**:TBAF$(H_2O)_3$ solution (3 mM in CD_2Cl_2) showcased three expected NH···F⁻ correlations and additional spatial correlations of the fluoride ion with the ureido *ortho*-aryl (*o*-ArH) and with $H^{\alpha}(i)$ protons (**Figure 2.2.23**). The latter confirms that upon fluoride

binding, the NH(*i*−*1*) and H$^{\alpha}$(*i*) are in close proximity, suggesting a type II β-turn conformation which was observed for **2i'** in the solid state, rather than a type I conformation which was observed for **2s** (*v.* Section 2.2.2.3).

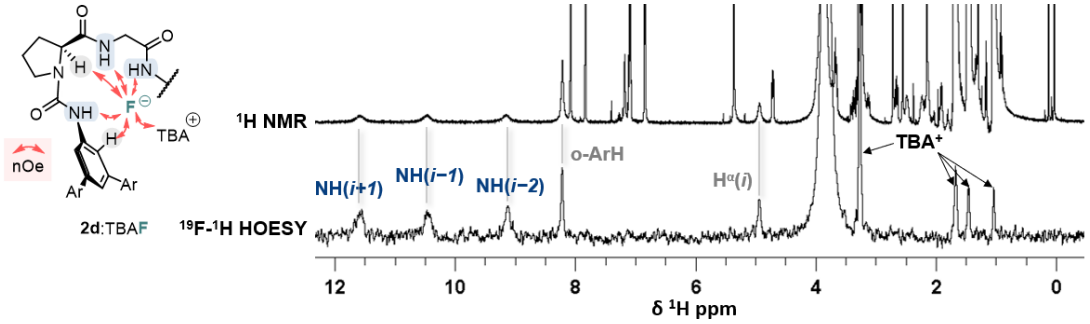

Figure 2.2.23. ^{1}H (*top*) and ^{19}F–^{1}H selective HOESY (δ ^{19}F at −114.79 ppm, *bottom*) NMR spectra of **2d**:TBAF(H$_2$O)$_3$ (6.4 mM **2d**, 1 equiv. of TBAF(H$_2$O)$_3$) in CD_2Cl_2 at 298 K.

To gain quantitative insight into peptide–fluoride interactions, the changes in chemical shifts of diagnostic resonances were plotted against the concentration of added fluoride (*v.* Section 5.5.2 for more detail). The resulting titration profiles were fitted to 1:1, 2:1 and 1:2 peptide–fluoride binding models via nonlinear least-square regression analysis implemented in DynaFit 4.[36] For peptides **2c**–**2r**, the titration data were the most consistent with 1:1 peptide:F$^-$ binding mode, with association constants $K_{a\,(1:1\ TBAF\text{-}3H2O)}$ ranging from 1.33 × 10^3 to 1.0 × 10^5 M^{-1} (in CD_2Cl_2, **Table 2.2.13**). In all cases, these values represent a significant improvement compared to the best-performing tetrapeptide **2b** ($K_{a\,(1:1\ TBAF\text{-}3H2O)}$ = 102 ± 1 M^{-1}, in CD_2Cl_2), which was attributed to the increased denticity of the peptide towards fluoride.

Table 2.2.13. Association Constants ($K_{a\,(1:1\ TBAF\text{-}3H2O)}$) and log($K_{a\,(1:1\ TBAF\text{-}3H2O)}$) for the formation of 1:1 peptide–TBAF complexes in CD_2Cl_2.[a]

peptide	$K_{a\,(1:1)}$ (M^{-1})	log($K_{a\,(1:1)}$)	peptide	$K_{a\,(1:1)}$ (M^{-1})	log($K_{a\,(1:1)}$)
2c	3.05 ± 0.95 × 10^4	4.5 ± 0.1	**2k**	4.3 ± 0.2 × 10^4	4.63 ± 0.02
2d	1.25 ± 0.04 × 10^4	4.10 ± 0.01	**2l**[b]	5.3 ± 0.8 × 10^3	3.72 ± 0.07
2e	8.5 ± 0.4 × 10^3	3.93 ± 0.02	**2m**	3.15 ± 0.65 × 10^4	4.49 ± 0.09
2f	4.8 ± 0.9 × 10^3	3.68 ± 0.08	**2n**	2.1 ± 0.3 × 10^3	3.31 ± 0.06
2g	1.33 ± 0.09 × 10^3	3.12 ± 0.02	**2o**	2.79 ± 0.09 × 10^3	3.44 ± 0.01
2h	1.15 ± 0.05 × 10^5	5.06 ± 0.02	**2p**	8.5 ± 0.6 × 10^3	3.93 ± 0.03
2i	1.45 ± 0.07 × 10^4	4.16 ± 0.02	**2q**	1.7 ± 0.1 × 10^4	4.23 ± 0.03
2j	6.3 ± 0.4 × 10^4	4.80 ± 0.03	**2r**	2.3 ± 0.2 × 10^4	4.36 ± 0.04

[a]K_a are calculated by nonlinear regression using DynaFit 4 and expressed as the average of two experiments; [b]n=1 and expressed with 1:1 model fitting error.

2.2.2.5. Residue specific binding

To enable the rational design of fluorination catalysts, we sought to establish whether fluoride binding to peptides can be systematically tuned through residue variation. As discussed in the previous section, single-residue modifications of peptide **2d** resulted in changes to both the overall fluoride binding affinity ($\log K_{a\ (1:1\ TBAF\text{-}3H2O)}$) and the localisation of fluoride within the H-bonding network, as reflected by the individual contributions of specific NH groups (*v.* **Table 2.2.13** and **Figure 2.2.21**, respectively). In 1966, Drago *et al.* demonstrated a linear relationship between the enthalpy of H-bond donor–acceptor complex formation (ΔH) and the maximum chemical shift change ($\Delta\delta_{max}$) of H-bonded protons for a range of phenol–base complexes.[67] More recently, F. Ibba *et al.* reported an inverse correlation between δ_{max} of fluoride-bound urea NH protons and H-bond length (*v.* Section 1.1.2.3).[33] Accordingly, this section discusses the effect of systematic modifications of the ureido-peptide scaffold on fluoride binding site through measured $\Delta\delta_{NH}$.

Initially, peptides **2c−g** bearing an *N*-terminal urea cap with different 3,5-disubstituted aryl groups were investigated (**Figure 2.2.24**, *left*). As previously reported for diarylurea−TBAF complexes (*v.* Section 1.2.2.2),[37] electron-withdrawing groups were expected to increase NH acidity and thereby strengthen H-bonding interactions with fluoride, and *vice versa* for electron-donating groups. Consistently, both $\Delta\delta_{NH(i+1)}$ and $\log K_{a\ (1:1\ TBAF\text{-}3H2O)}$ increased with enhanced NH(*i*+*1*) acidity induced through aryl substitution (**Figure 2.2.24**, *right*). Peptide **2c** (Ar = 3,5-$(CF_3)_2C_6H_3$) exhibited the largest $\Delta\delta_{NH(i+1)}$ (+4.68 ppm), while **2g** (Ar = 3,5-[3,5-(*t*-Bu)$_2C_6H_3$]$_2C_6H_3$) showed the smallest $\Delta\delta_{NH(i+1)}$ (+3.04 ppm), indicating a reduced interaction between NH(*i*+*1*) and fluoride. As the Δδ of NH(*i*−*1*) and NH(*i*−*2*) remained largely invariant across the **2c**–**g** series, the reduced binding of NH(*i*+*1*) also resulted in lower $\log K_{a\ (1:1\ TBAF\text{-}3H2O)}$ values.

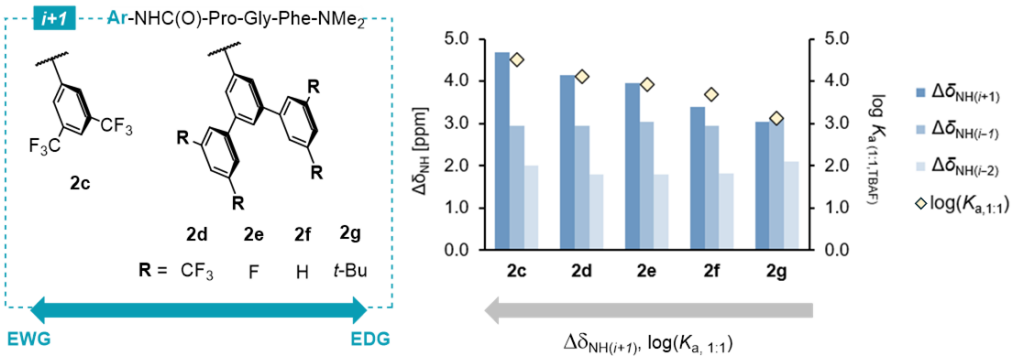

Figure 2.2.24. Effect of *N*-terminal aryl substitution on TBAF(H_2O)$_3$ binding affinity and NH chemical shift perturbations ($\Delta\delta_{NH}$) for peptides **2c**–**g**. EWG = electron-withdrawing group, EDG = electron-donating group.

For peptides **2d**, **2h**−**m**, β-turn conformational space was explored via systematic modification of the proline residue at position *i* (**Figure 2.2.25**). The L-Pro (**2d**) modification to its epimer D-Pro (**2m**) resulted in increased overall fluoride binding affinity ($\log K_{a\,(1:1\ TBAF\text{-}3H2O)}$ = 4.10 ± 0.01 *versus* 4.49 ± 0.09, in CD_2Cl_2), but reduced interaction with individual backbone peptidic NH protons, as reflected by lower Δδ values for NH(*i*−*1*) (2.95 *versus* 2.55 ppm) and NH(*i*−*2*) (1.79 *versus* 0.95 ppm). This pronounced change in global affinity and local NH engagement highlights the sensitivity of fluoride binding to subtle changes in turn geometry.

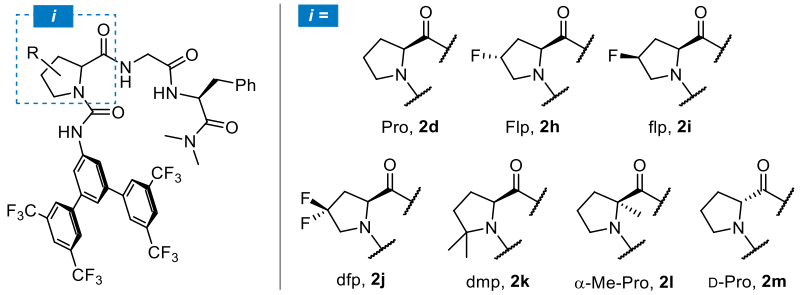

Figure 2.2.25. Residues explored in position *i*.

Accordingly, introduction of modified prolines in peptides **2h**–**l** proved particularly fruitful in diversifying the fluoride-binding profiles of the NH protons (**Figure 2.2.26**). The *cis*-inducing peptide **2k** exhibited substantially reduced binding by NH(*i*+*1*) relative to the parent peptide **2d** ($\Delta\delta_{NH(i+1)}$ = 3.11 *versus* 4.15 ppm). On the other hand, the *trans*-inducing peptide **2l** showcased diminished binding by the peptidic NH protons, with reduced Δδ values for NH(*i*−*1*) (2.95 *versus* 1.93 ppm) and NH(*i*−*2*) (1.79 *versus* 0.73 ppm), while maintaining NH(*i*+*1*) binding comparable to that of **2d**. In order for all three NHs to engage in 1:1 binding to TBAF(H_2O)$_3$, the peptide

must adopt a *cis*-prolyl conformation. Because all NH resonances are significantly perturbed upon fluoride addition, the observed binding behaviour is more likely governed by steric effects rather than by *cis*–*trans* populations. Notably, the HOESY spectrum of the **2d**:TBAF$(H_2O)_3$ complex revealed that F^- is in close proximity to the $H^{\alpha}(i)$ (Section 2.2.2.4), consequently, methyl substitution at this position could impose steric repulsion at the binding site. Consistently, fluorinated proline analogues, which introduce minimal steric perturbation, exhibited increased $\Delta\delta_{NH(i+1)}$ but showed no correlation between $\Delta\delta_{NH}$ and %*trans* (**Figure 2.2.26**).

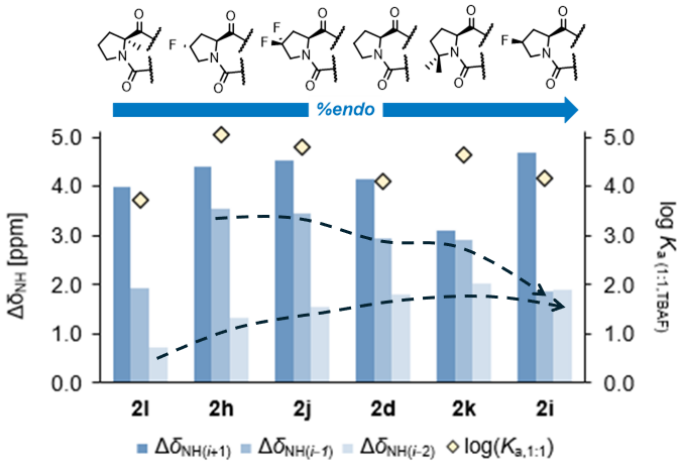

Figure 2.2.26. Impact of pyrrolidine ring puckering (*endo*/*exo*) on NH chemical shift perturbations ($\Delta\delta_{NH}$) upon TBAF$(H_2O)_3$ binding with peptides **2d** and **2h–l**.

The influence of pyrrolidine ring puckering on fluoride binding was investigated next. The *endo*-inducing residue flp (peptide **2i**) afforded the lowest $\Delta\delta_{NH(i-1)}$, while the *exo*-inducing Flp (**2j**) produced one of the highest $\Delta\delta_{NH(i-1)}$ across the entire library of 16 peptides. Furthermore, when peptides **2d**, **2h**−**l** were arranged based on relative *endo*-*exo* populations established in Section 2.2.2.2, $\Delta\delta_{NH(i-2)}$ correlated positively with %*endo*, while and $\Delta\delta_{NH(i-1)}$ correlated negatively, with the exception of **2l** (*i* = α-Me-Pro; **Figure 2.2.26**). *Endo* puckers are known to display extended φ (≈ −75°) compared to *exo* puckers (φ ≈ −60°) increasing the distance between *i+1* and *i−1* residues,[47,68] which results in a wider loop region and provides a structural basis for the observed variation in fluoride binding profiles. Notably, peptides **2h** and **2j** exhibited nearly identical NH binding profiles and comparable binding affinities toward TBAF$(H_2O)_3$, consistent with similar conformational features observed by NMR for the unbound peptides. These two peptides also

displayed the highest binding affinities within the library ($\log K_{a\,(1:1\ TBAF\text{-}3H2O)}$ = 5.06 ± 0.02 and 4.80 ± 0.03, respectively, in CD_2Cl_2).

Meanwhile, peptides **2d** and **2n–p** (*i–1* = Gly, Acbc, Aib and Acpc, respectively) were investigated to assess the role of increasing the torsional angle τ(*i–1*) in TBAF$(H_2O)_3$ binding (**Figure 2.2.27**). Residues with larger τ(*i–1*) angles are associated with more open binding sites and increased conformational flexibility.[23] The H-bonding acidity values (*A*) obtained in **Table 2.2.10** also indicated that higher τ(*i–1*) angles lead to increased solvent exposure of NH(*i–1*). Comparison of peptides **2n** (τ(*i–1*) ≈ 113°) and **2p** (τ(*i–1*) ≈ 117°) revealed a larger $\Delta\delta_{NH(i-1)}$ value (3.56 *versus* 2.48 ppm) and a smaller $\Delta\delta_{NH(i+1)}$ value (3.86 *versus* 4.19 ppm), indicating that a looser turn geometry shows preference for fluoride binding to NH(*i+1*) rather than to the solvent exposed NH(*i–1*). Consistently, across the **2d**, **2n–p** series, $\Delta\delta_{NH(i-1)}$ decreased and $\Delta\delta_{NH(i+1)}$ increased systematically with increasing τ(*i–1*) (**Figure 2.2.27**), resulting in increasing $\log K_{a\,(1:1\ TBAF\text{-}3H2O)}$ values. There is growing appreciation that peptide-based catalysts relying on non-covalent interactions benefit from conformational flexibility that enables reorganisation into optimal geometries for binding and catalysis.[69]

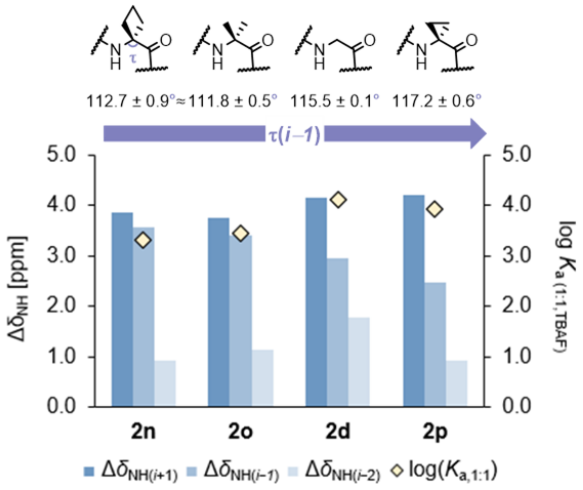

Figure 2.2.27. Effect of increasing τ(*i–1*) on TBAF$(H_2O)_3$ binding affinity and NH chemical shift perturbations ($\Delta\delta_{NH}$) for peptides **2d** and **2n–p**. τ(*i–1*) values taken from ref[23].

During ^1H and ^1H-^1H NOESY NMR analyses of the peptides, *π-π* stacking interactions between *i+1* and *i–2* residues was observed, promoting the formation of pseudo-cyclic conformations (*v.* Section 2.2.2.2). When the *i–2* residue was modified from Phe (**2d**) to Leu (**2q**), a decrease in

NH(*i+1*) and NH(*i−2*) binding to fluoride was observed, as reflected by reduced chemical shift perturbations ($\Delta\delta_{NH(i+1)}$ = 4.15 *versus* 3.83 ppm and $\Delta\delta_{NH(i-2)}$ = 1.79 *versus* 1.29 ppm, respectively). The *i−2* modification to D-Phe (**2r**) was also explored and resulted in a less favourable conformation for NH(*i−2*) interaction with fluoride compared to the L-Phe analogue (**2d**), with $\Delta\delta_{NH(i-2)}$ values of 0.93 and 1.79 ppm, respectively. Notably, despite these differences in local NH–fluoride interactions, the overall binding affinities for peptides **2d**, **2q**, and **2r** remained comparable, with $\log K_{a\ (1:1\ TBAF\text{-}3H2O)}$ values of 4.10 ± 0.01, 4.23 ± 0.03, and 4.36 ± 0.04, respectively (measured in CD_2Cl_2).

Collectively, these results demonstrate that fluoride binding to ureido-peptides can be systematically modulated through targeted residue variation, affecting both overall binding affinity and the localisation of fluoride within the H-bonding network. The effects of individual structural modifications on these parameters are summarised below.

1) Fluoride binding to NH(*i+1*) can be tuned by modifications of the *N*-terminal cap, *i* and *i-1* residues. Electron-withdrawing substituents at the *N*-terminal urea cap increased NH(*i+1*) acidity, resulting in larger $\Delta\delta_{NH(i+1)}$ values and higher binding affinities, while leaving other NH contributions largely unaffected. In addition, introduction of fluorinated proline derivatives in position *i* and increasing τ(*i−1*) enhanced NH(*i+1*) binding to $TBAF(H_2O)_3$.
2) Fluoride binding to NH(*i−1*) can be tuned through substitution at the *i−1* residue, with higher τ(*i−1*) angle correlating with lower $\Delta\delta_{NH(i-1)}$ values. Moreover, NH(*i−1*) binding can be increased by *exo*-inducing residues at position *i*.
3) Fluoride binding of NH(*i−2*) depends on the proximity of the *N*- and *C*-termini and secondary non-covalent interactions. *Endo*-inducing residues at position *i* increase φ(*i*), leading to larger $\Delta\delta_{NH(i-2)}$ values, while π–π stacking between the *i+1* and *i−2* residues promotes pseudo-cyclic conformations that further enhance binding of NH(*i−2*).

2.3. Conclusions

In this chapter, a detailed NMR spectroscopic investigation was undertaken to elucidate the structural, conformational, and fluoride-binding properties of proline-containing tetrapeptides (**2a** and **2b**) and ureido-tripeptides (**2c**−**s**), with the aim of identifying the key parameters that govern fluoride recognition through H-bonding.

Initial studies on tetrapeptides **2a** and **2b** established that well-defined type II and II' β-turn motifs persist both in solution (CD_2Cl_2) and in the solid state. NMR titrations with TBAF$(H_2O)_3$ demonstrated that peptidic NH protons are competent HBDs toward fluoride, exhibiting pronounced downfield chemical shift perturbations (Δδ values up to +3.37 ppm). However, the strong preorganisation imposed by the β-turn conformation restricted peptide binding to fluoride to a monodentate mode, with only the central NH(*i*−*1*) participating and the remaining NH groups engaged in intramolecular H-bonding. As a result, the overall binding affinities were relatively weak ($K_{a\ (1:1\ TBAF\text{-}3H2O)} \approx 10^1-10^2\ M^{-1}$, in CD_2Cl_2). These observations highlighted the trade-off between conformational rigidity and effective multidentate fluoride binding of peptides.

To overcome this limitation, a family of ureido-peptides (**2c**–**s**) were designed through the introduction of an *N*-terminal urea cap and systematic modifications of proline-based tripeptide residues. Structural investigations in solution and the solid state showed that incorporation of the urea motif disrupts intramolecular H-bonding, leading to more dynamic conformations while retaining partial organisation through β-turn geometry and secondary non-covalent interactions. This conformational plasticity enabled tridentate fluoride binding, as evidenced by significant Δδ of NH resonances during TBAF$(H_2O)_3$ titrations (+0.73 to +4.68 ppm) and substantially enhanced binding affinities to TBAF$(H_2O)_3$ ($K_{a\ (1:1\ TBAF\text{-}3H2O)} \approx 10^3-10^5\ M^{-1}$, in CD_2Cl_2).

Residue-specific analysis of $\Delta\delta_{NH}$ values enabled fluoride localisation within the H-bonding network to be characterised in detail. Electronic modulation of the *N*-terminal urea cap primarily controlled NH(*i+1*) binding, with electron-withdrawing aryl substituents producing increasing $\Delta\delta_{NH(i+1)}$ values (up to +4.68 ppm), while leaving other NH contributions largely unchanged. In contrast, modification of the proline residue at *i* position redistributed fluoride binding

contribution among backbone NH sites predominantly through control of pyrrolidine ring puckering. Substitution at the *i−1* position further demonstrated that increased torsional freedom selectively attenuates NH(*i+1*) and NH(*i−1*) binding affinities, whereas secondary non-covalent interactions, such as π–π stacking between *i+1* and *i−2* residues, promote pseudo-cyclic conformations that enhance binding of NH(*i−2*). Together, these observations show that local NH–fluoride interactions can be tuned independently of overall binding strength.

Taken together, these results demonstrate that peptide-based HBDs can engage fluoride in a controlled and tunable manner, with Δδ values providing a sensitive probe of binding-site localisation (**Figure 2.3.1**). From a fundamental perspective, this work advances the understanding of how pre-existing H-bonding networks and conformational flexibility govern fluoride binding in peptide systems. These insights establish key structure–binding principles for peptide-based fluoride recognition at the molecular level, that underpin the fluorination studies discussed in Chapter III.

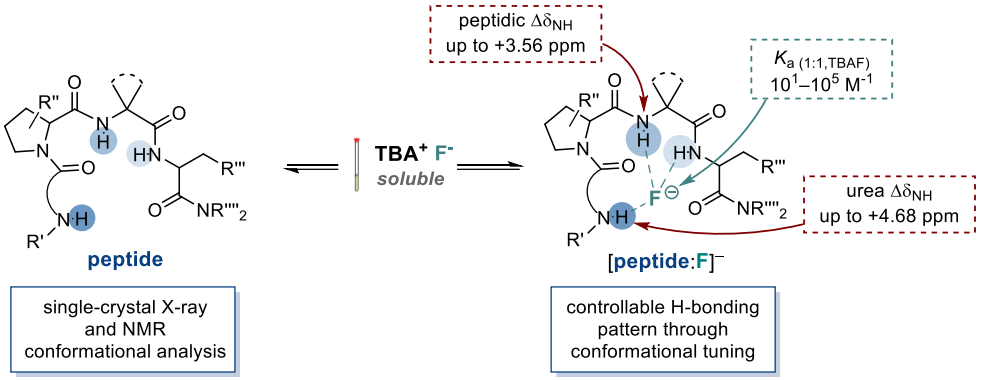

Figure 2.3.1. Spectroscopic investigation of fluoride binding by peptides **2a–s**.

2.4. References

(1) (a) Gale, P. A.; Davis, J. T.; Quesada, R. Anion transport and supramolecular medicinal chemistry. *Chem. Soc. Rev.* **2017**, *46* (9), 2497–2519; (b) Beer, P. D.; Gale, P. A. Anion Recognition and Sensing: The State of the Art and Future Perspectives. *Angew. Chem., Int. Ed.* **2001**, *40* (3), 486–516; (c) Sikora, K.; Jaśkiewicz, M.; Neubauer, D.; Migoń, D.; Kamysz, W. The Role of Counter-Ions in Peptides—An Overview. *Pharmaceuticals* **2020**, *13* (12), 442; (d) Gale, Philip A.; Howe, Ethan N. W.; Wu, X. Anion Receptor Chemistry. *Chem* **2016**, *1* (3), 351–422; (e) Macreadie, L. K.; Gilchrist, A. M.; McNaughton, D. A.; Ryder, W. G.; Fares, M.; Gale, P. A. Progress in anion receptor chemistry. *Chem* **2022**, *8* (1), 46–118; (f) Busschaert, N.; Caltagirone, C.; Van Rossom, W.; Gale, P. A. Applications of Supramolecular Anion Recognition. *Chem. Rev.* **2015**, *115* (15), 8038–8155.

(2) (a) Rinkovec, T.; Tarana, S.; Modrušan, M.; Vidović, N.; Tomić, A.; Cindro, N.; Speranza, G.; Tomišić, V.; Horvat, G. Anion complexes of small Boc-protected lysine cyclopeptides in solution. *J. Mol. Liq.* **2025**, *433*, 127837; (b) Horvat, G.; Tarana, S.; Vidović, N.; Cindro, N.; Speranza, G.; Tomišić, V. Thermodynamic and MD studies of anion complexation by cyclopentaleucine in acetonitrile and dimethyl sulfoxide. *J. Mol. Liq.* **2021**, *340*, 116848; (c) Petters, I.; Modrušan, M.; Vidović, N.; Crnolatac, I.; Cindro, N.; Piantanida, I.; Speranza, G.; Horvat, G.; Tomišić, V. Anion-Sensing Properties of Cyclopentaphenylalanine. *Molecules* **2022**, *27* (12), 3918; (d) Sergeant, G. E.; Jolliffe, K. A. Anion recognition using a simple cyclic peptide. *Supramol. Chem.* **2020**, *32* (3), 233–237.

(3) (a) Yang, D.; Qu, J.; Li, W.; Zhang, Y.-H.; Ren, Y.; Wang, D.-P.; Wu, Y.-D. Cyclic Hexapeptide of d,l-α-Aminoxy Acids as a Selective Receptor for Chloride Ion. *J. Am. Chem. Soc.* **2002**, *124* (42), 12410–12411; (b) Sharma, G. V. M.; Manohar, V.; Dutta, S. K.; Sridhar, B.; Ramesh, V.; Srinivas, R.; Kunwar, A. C. Self-Assembling Cyclic Tetrapeptide from Alternating C-Linked Carbo-β-amino Acid [(*S*)-β-Caa] and α-Aminoxy Acid [(*R*)-Ama]: A Selective Chloride Ion Receptor. *J. Org. Chem.* **2010**, *75* (4), 1087–1094; (c) Yang, D.; Li, X.; Sha, Y.; Wu, Y.-D. A Cyclic Hexapeptide Comprising Alternating α-Aminoxy and α-Amino Acids is a Selective Chloride Ion Receptor. *Chem. – Eur. J.* **2005**, *11* (10), 3005–3009; (d) Ishida, H.; Suga, M.; Donowaki, K.; Ohkubo, K. Highly Effective Binding of Phosphomonoester with Neutral Cyclic Peptides which Include a Non-natural Amino Acid. *J. Org. Chem.* **1995**, *60* (17), 5374–5375.

(4) (a) Gibb, C. L. D.; Tran, T. H.; Gibb, B. C. Assessing Weak Anion Binding to Small Peptides. *J. Phys. Chem. B* **2024**, *128* (15), 3605–3613; (b) Modrušan, M.; Glazer, L.; Otmačić, L.; Crnolatac, I.; Cindro, N.; Vidović, N.; Piantanida, I.; Speranza, G.; Horvat, G.; Tomišić, V. Anion-Binding Properties of Short Linear Homopeptides. *Int. J. Mol. Sci.* **2024**, *25* (10), 5235; (c) Vidović, N.; Horvat, G.; Riva, D.; Rinkovec, T.; Cindro, N.; Tomišić, V.; Speranza, G. Chloride-Assisted Peptide Macrocyclization. *Org. Lett.* **2020**, *22* (6), 2129–2134.

(5) (a) Suh, S. B.; Cui, C.; Son, H. S.; U, J. S.; Won, Y.; Kim, K. S. Novel Amphi-ionophore in Aqueous Solution: Cyclohexaalanyl. *J. Phys. Chem. B* **2002**, *106* (8), 2061–2064; (b) Kim, K. S.; Cui, C.; Cho, S. J. Novel Amphi-Ionophores. *J. Phys. Chem. B* **1998**, *102* (2), 461–463; (c) Liu, L.; Chen, S. Theoretical study on cyclopeptides as the nanocarriers for Li^+ , Na^+ , K^+ and F^- , Cl^- , Br^-. *J. Nanomater.* **2015**, *2015*, 4.

(6) Gilli, P.; Pretto, L.; Bertolasi, V.; Gilli, G. Predicting Hydrogen-Bond Strengths from Acid−Base Molecular Properties. The pK_a Slide Rule: Toward the Solution of a Long-Lasting Problem. *Acc. Chem. Res.* **2009**, *42* (1), 33–44.

(7) Cotton, F. A.; Wilkinson, G. *Advanced Inorganic Chemistry*; 5th ed., John Wiley & Son, 1988.

(8) (a) Ramakrishnan, C.; Paul, P. K. C.; Ramnarayan, K. Cyclic peptides — Small and big and their conformational aspects. *J. Biosci.* **1985**, *8* (1), 239–251; (b) Slough, D. P.; McHugh, S. M.; Lin, Y.-S. Understanding and designing head-to-tail cyclic peptides. *Biopolymers* **2018**, *109* (10), e23113.

(9) (a) Chen, H.; Zhang, Y.; Wen, Y.; Fan, X.; Sciolino, N.; Lin, Y.; Breindel, L.; Dai, Y.; Shekhtman, A.; Xue, X.-S.; Zhang, Q. Production of constrained L-cyclo-tetrapeptides by epimerization-resistant direct aminolysis. *Nat. Commun.* **2024**, *15* (1), 5372; (b) De Leon Rodriguez, L. M.; Weidkamp, A. J.; Brimble, M. A. An update on new methods to synthesize cyclotetrapeptides. *Org. Biomol. Chem.* **2015**, *13* (25), 6906–6921.

(10) (a) Guruprasad, K.; Rajkumar, S. *β*- and *γ*-turns in proteins revisited: A new set of amino acid turn-type dependent positional preferences and potentials. *J. Biosci.* **2000**, *25* (2), 143–156; (b) Rose, G. D.; Glerasch, L. M.; Smith, J. A. Turns in Peptides and Proteins. In *Adv. Protein Chem.*, Anfinsen, C. B., Edsall, J. T., Richards, F. M. Eds.; Vol. 37; Academic Press, 1985, 1–109.

(11) Richardson, J. S. The Anatomy and Taxonomy of Protein Structure. In *Adv. Protein Chem.*, Anfinsen, C. B., Edsall, J. T., Richards, F. M. Eds.; Vol. 34; Academic Press, 1981, 167–339.

(12) Venkatachalam, C. M. Stereochemical criteria for polypeptides and proteins. V. Conformation of a system of three linked peptide units. *Biopolymers* **1968**, *6* (10), 1425–1436.

(13) (a) de Brevern, A. G. Extension of the classical classification of β-turns. *Sci. Rep.* **2016**, *6* (1), 33191; (b) Hutchinson, E. G.; Thornton, J. M. PROMOTIF—A program to identify and analyze structural motifs in proteins. *Protein Sci.* **1996**, *5* (2), 212–220; (c) Chan, A. W. E.; Hutchinson, E. G.; Harris, D.; Thornton, J. M. Identification, classification, and analysis of beta-bulges in proteins. *Protein Sci.* **1993**, *2* (10), 1574–1590.

(14) Hutchinson, E. G.; Thornton, J. M. A revised set of potentials for β-turn formation in proteins. *Protein Sci.* **1994**, *3* (12), 2207–2216.

(15) (a) Rizo, J.; Gierasch, L. M. Constrained peptides: models of bioactive peptides and protein substructures. *Annu. Rev. Biochem* **1992**, *61*, 387–418; (b) Hill, T. A.; Shepherd, N. E.; Diness, F.; Fairlie, D. P. Constraining Cyclic Peptides To Mimic Protein Structure Motifs. *Angew. Chem., Int. Ed.* **2014**, *53* (48), 13020–13041.

(16) (a) Gierasch, L. M.; Deber, C. M.; Madison, V.; Niu, C.-H.; Blout, E. R. Conformations of (X-L-Pro-Y)$_2$ cyclic hexapeptides. Preferred β-turn conformers and implications for β turns in proteins. *Biochemistry* **1981**, *20* (16), 4730–4738; (b) Kopple, K. D.; Schamper, T. J.; Go, A. Conformation of cyclic peptides. VIII. Cyclic hexapeptides containing the L-pro-D-phe sequence. *J. Am. Chem. Soc.* **1974**, *96* (8), 2597–2605; (c) Torchia, D. A.; Di Corato, A.; Wong, S. C. K.; Deber, C. M.; Blout, E. R. Cyclic peptides. II. Solution conformations of cyclo(prolylserylglycylprolylserylglycyl) from nuclear magnetic resonance. *J. Am. Chem. Soc.* **1972**, *94* (2), 609–615; (d) Karle, I. L.; Karle, J. An application of a new phase determination procedure to the structure of cyclo(hexaglycyl)demihydrate. *Acta Crystallogr.* **1963**, *16* (10), 969–975.

(17) (a) Karle, I. L. Crystal structure and conformation of cyclo-(glycylprolylglycyl-D-alanylprolyl) containing 4 → 1 and 3 → 1 intramolecular hydrogen bonds. *J. Am. Chem. Soc.* **1978**, *100* (4), 1286–1289; (b) Karle, I. L.; Urry, D. W. Crystal structure of cyclic (APGVGV)$_2$, an analog of elastin, and a suggested mechanism for elongation/contraction of the molecule. *Biopolymers* **2005**, *77* (4), 198–204.

(18) Jane Dyson, H.; Cross, K. J.; Houghten, R. A.; Wilson, I. A.; Wright, P. E.; Lerner, R. A. The immunodominant site of a synthetic immunogen has a conformational preference in water for a type-II reverse turn. *Nature* **1985**, *318* (6045), 480–483.

(19) Dyson, H. J.; Rance, M.; Houghten, R. A.; Lerner, R. A.; Wright, P. E. Folding of immunogenic peptide fragments of proteins in water solution: I. Sequence requirements for the formation of a reverse turn. *J. Mol. Biol.* **1988**, *201* (1), 161–200.

(20) Hanessian, S.; McNaughton-Smith, G.; Lombart, H.-G.; Lubell, W. D. Design and synthesis of conformationally constrained amino acids as versatile scaffolds and peptide mimetics. *Tetrahedron* **1997**, *53* (38), 12789–12854.

(21) (a) Toniolo, C.; Crisma, M.; Formaggio, F.; Peggion, C. Control of peptide conformation by the Thorpe-Ingold effect (C^{α}-tetrasubstitution). *Pept. Sci.* **2001**, *60* (6), 396–419; (b) Peggion, C.; Moretto, A.; Formaggio, F.; Crisma, M.; Toniolo, C. Multiple, consecutive, fully-extended 2.0_5-helix peptide conformation. *Pept. Sci.* **2013**, *100* (6), 621–636.

(22) Moretto, V.; Crisma, M.; Bonora, G. M.; Toniolo, C.; Balaram, H.; Balaram, P. Comparison of the effect of five guest residues on the β-sheet conformation of host (L-val)$_n$ oligopeptides. *Macromolecules* **1989**, *22* (7), 2939–2944.

(23) Metrano, A. J.; Abascal, N. C.; Mercado, B. Q.; Paulson, E. K.; Hurtley, A. E.; Miller, S. J. Diversity of Secondary Structure in Catalytic Peptides with β-Turn-Biased Sequences. *J. Am. Chem. Soc.* **2017**, *139* (1), 492–516.

(24) (a) Abraham, M. H.; Abraham, R. J. A simple and facile NMR method for the determination of hydrogen bonding by amide N–H protons in protein models and other compounds. *New J. Chem.* **2017**, *41* (14), 6064–6066; (b) Awasthi, S. K.; Raghothama, S.; Balaram, P. A Designed β-Hairpin Peptide. *Biochem. Biophys. Res. Commun.* **1995**, *216* (1), 375–381.

(25) Wang, A. C.; Bax, A. Determination of the Backbone Dihedral Angles φ in Human Ubiquitin from Reparametrized Empirical Karplus Equations. *J. Am. Chem. Soc.* **1996**, *118* (10), 2483–2494.

(26) Jeener, J.; Meier, B. H.; Bachmann, P.; Ernst, R. R. Investigation of exchange processes by two-dimensional NMR spectroscopy. *J. Chem. Phys.* **1979**, *71* (11), 4546–4553.

(27) Abraham, M. H.; Abraham, R. J.; Byrne, J.; Griffiths, L. NMR Method for the Determination of Solute Hydrogen Bond Acidity. *J. Org. Chem.* **2006**, *71* (9), 3389–3394.

(28) Abraham, M. H.; Whiting, G. S.; Doherty, R. M.; Shuely, W. J. Hydrogen bonding: XVI. A new solute salvation parameter, π_2^H, from gas chromatographic data. *J. Chromatogr. A* **1991**, *587* (2), 213–228.

(29) (a) Karplus, M. Contact Electron-Spin Coupling of Nuclear Magnetic Moments. *J. Chem. Phys.* **1959**, *30* (1), 11–15; (b) Karplus, M. Vicinal Proton Coupling in Nuclear Magnetic Resonance. *J. Am. Chem. Soc.* **1963**, *85* (18), 2870–2871.

(30) Gunasekaran, K.; Ramakrishnan, C.; Balaram, P. β-hairpins in proteins revisited: lessons for *de novo* design. *Protein Eng.* **1997**, *10* (10), 1131–1141.

(31) Baker, E. N.; Hubbard, R. E. Hydrogen bonding in globular proteins. *Prog. Biophys. Mol. Biol.* **1984**, *44* (2), 97–179.

(32) Haque, T. S.; Little, J. C.; Gellman, S. H. Stereochemical Requirements for β-Hairpin Formation: Model Studies with Four-Residue Peptides and Depsipeptides. *J. Am. Chem. Soc.* **1996**, *118* (29), 6975–6985.

(33) Ibba, F.; Pupo, G.; Thompson, A. L.; Brown, J. M.; Claridge, T. D. W.; Gouverneur, V. Impact of Multiple Hydrogen Bonds with Fluoride on Catalysis: Insight from NMR Spectroscopy. *J. Am. Chem. Soc.* **2020**, *142* (46), 19731–19744.

(34) Fielding, L. Determination of Association Constants (K_a) from Solution NMR Data. *Tetrahedron* **2000**, *56* (34), 6151–6170.

(35) Dračínský, M. NMR spectroscopy studies of hydrogen bonding. *Coord. Chem. Rev.* **2026**, *549*, 217284.

(36) Kuzmič, P. Program DYNAFIT for the Analysis of Enzyme Kinetic Data: Application to HIV Proteinase. *Anal. Biochem.* **1996**, *237* (2), 260–273.

(37) Pfeifer, L.; Engle, K. M.; Pidgeon, G. W.; Sparkes, H. A.; Thompson, A. L.; Brown, J. M.; Gouverneur, V. Hydrogen-Bonded Homoleptic Fluoride–Diarylurea Complexes: Structure, Reactivity, and Coordinating Power. *J. Am. Chem. Soc.* **2016**, *138* (40), 13314–13325.

(38) Pajewski, R.; Ferdani, R.; Pajewska, J.; Li, R.; Gokel, G. W. Cation Dependence of Chloride Ion Complexation by Open-Chained Receptor Molecules in Chloroform Solution. *J. Am. Chem. Soc.* **2005**, *127* (51), 18281–18295.

(39) Jakab, G.; Tancon, C.; Zhang, Z.; Lippert, K. M.; Schreiner, P. R. (Thio)urea Organocatalyst Equilibrium Acidities in DMSO. *Org. Lett.* **2012**, *14* (7), 1724–1727.

(40) Bordwell, F. G.; Bartmess, J. E.; Hautala, J. A. Alkyl effects on equilibrium acidities of carbon acids in protic and dipolar aprotic media and the gas phase. *J. Org. Chem.* **1978**, *43* (16), 3095–3101.

(41) Lara-Popoca, J.; Thoke, H. S.; Stock, R. P.; Rudino-Pinera, E.; Bagatolli, L. A. Inductive effects in amino acids and peptides: Ionization constants and tryptophan fluorescence. *Biochemistry and Biophysics Reports* **2020**, *24*, 100802.

(42) (a) Pupo, G.; Ibba, F.; Ascough, D. M. H.; Vicini, A. C.; Ricci, P.; Christensen, K. E.; Pfeifer, L.; Morphy, J. R.; Brown, J. M.; Paton, R. S.; Gouverneur, V. Asymmetric nucleophilic fluorination under hydrogen bonding phase-transfer catalysis. *Science* **2018**, *360* (6389), 638–642; (b) Pupo, G.; Vicini, A. C.; Ascough, D. M. H.; Ibba, F.; Christensen, K. E.; Thompson, A. L.; Brown, J. M.; Paton, R. S.; Gouverneur, V. Hydrogen Bonding Phase-Transfer Catalysis with Potassium Fluoride: Enantioselective Synthesis of β-Fluoroamines. *J. Am. Chem. Soc.* **2019**, *141* (7), 2878–2883.

(43) Miyaura, N.; Suzuki, A. Stereoselective synthesis of arylated (*E*)-alkenes by the reaction of alk-1-enylboranes with aryl halides in the presence of palladium catalyst. *J. Chem. Soc., Chem. Commun.* **1979**, (19), 866–867.

(44) Ho, B. K.; Coutsias, E. A.; Seok, C.; Dill, K. A. The flexibility in the proline ring couples to the protein backbone. *Protein Sci.* **2005**, *14* (4), 1011–1018.

(45) Holmgren, S. K.; Taylor, K. M.; Bretscher, L. E.; Raines, R. T. Code for collagen's stability deciphered. *Nature* **1998**, *392* (6677), 666–667.

(46) (a) Kim, W.; McMillan, R. A.; Snyder, J. P.; Conticello, V. P. A Stereoelectronic Effect on Turn Formation Due to Proline Substitution in Elastin-Mimetic Polypeptides. *J. Am. Chem. Soc.* **2005**, *127* (51), 18121–18132; (b) Milner-White, E. J.; Bell, L. H.; Maccallum, P. H. Pyrrolidine ring puckering in cis and trans-proline residues in proteins and polypeptides: Different puckers are favoured in certain situations. *J. Mol. Biol.* **1992**, *228* (3), 725–734.

(47) Costantini, N. V.; Ganguly, H. K.; Martin, M. I.; Wenzell, N. A.; Yap, G. P. A.; Zondlo, N. J. The Distinct Conformational Landscapes of 4*S*-Substituted Prolines That Promote an *endo* Ring Pucker. *Chem. – Eur. J.* **2019**, *25* (48), 11356–11364.

(48) (a) Ganguly, H. K.; Basu, G. Conformational landscape of substituted prolines. *Biophys. Rev.* **2020**, *12* (1), 25–39; (b) Kubyshkin, V.; Rubini, M. Proline Analogues. *Chem. Rev.* **2024**, *124* (13), 8130–8232.

(49) (a) Panasik Jr., N.; Eberhardt, E. S.; Edison, A. S.; Powell, D. R.; Raines, R. T. Inductive effects on the structure of proline residues. *Int. J. Pept. Protein Res.* **1994**, *44* (3), 262–269; (b) DeRider, M. L.; Wilkens, S. J.; Waddell, M. J.; Bretscher, L. E.; Weinhold, F.; Raines, R. T.; Markley, J. L. Collagen Stability:

Insights from NMR Spectroscopic and Hybrid Density Functional Computational Investigations of the Effect of Electronegative Substituents on Prolyl Ring Conformations. *J. Am. Chem. Soc.* **2002**, *124* (11), 2497–2505.

(50) (a) An, S. S. A.; Lester, C. C.; Peng, J.-L.; Li, Y.-J.; Rothwarf, D. M.; Welker, E.; Thannhauser, T. W.; Zhang, L. S.; Tam, J. P.; Scheraga, H. A. Retention of the Cis Proline Conformation in Tripeptide Fragments of Bovine Pancreatic Ribonuclease A Containing a Non-natural Proline Analogue, 5,5-Dimethylproline. *J. Am. Chem. Soc.* **1999**, *121* (49), 11558–11566; (b) Magaard, V. W.; Sanchez, R. M.; Bean, J. W.; Moore, M. L. A Convenient synthesis of the, conformationally constrained amino acid 5,5-dimethylproline. *Tetrahedron Lett.* **1993**, *34* (3), 381–384.

(51) Delaney, N. G.; Madison, V. Novel conformational distributions of methylproline peptides. *J. Am. Chem. Soc.* **1982**, *104* (24), 6635–6641.

(52) (a) Shoulders, M. D.; Kamer, K. J.; Raines, R. T. Origin of the stability conferred upon collagen by fluorination. *Bioorg. Med. Chem. Lett.* **2009**, *19* (14), 3859–3862; (b) Hofman, G.-J.; Ottoy, E.; Light, M. E.; Kieffer, B.; Kuprov, I.; Martins, J. C.; Sinnaeve, D.; Linclau, B. Minimising conformational bias in fluoroprolines through vicinal difluorination. *Chem. Commun.* **2018**, *54* (40), 5118–5121.

(53) Bretscher, L. E.; Jenkins, C. L.; Taylor, K. M.; DeRider, M. L.; Raines, R. T. Conformational Stability of Collagen Relies on a Stereoelectronic Effect. *J. Am. Chem. Soc.* **2001**, *123* (4), 777–778.

(54) (a) Elaridi, J.; Jackson, W. R.; Robinson, A. J. A catalytic asymmetric synthesis of 5,5-dimethylproline. *Tetrahedron Asymm.* **2005**, *16* (11), 2025–2029; (b) Siebler, C.; Maryasin, B.; Kuemin, M.; Erdmann, R. S.; Rigling, C.; Grünenfelder, C.; Ochsenfeld, C.; Wennemers, H. Importance of dipole moments and ambient polarity for the conformation of Xaa–Pro moieties – a combined experimental and theoretical study. *Chem. Sci.* **2015**, *6* (12), 6725–6730.

(55) Wedemeyer, W. J.; Welker, E.; Scheraga, H. A. Proline Cis−Trans Isomerization and Protein Folding. *Biochemistry* **2002**, *41* (50), 14637–14644.

(56) (a) Testa, A.; Lucas, X.; Castro, G. V.; Chan, K.-H.; Wright, J. E.; Runcie, A. C.; Gadd, M. S.; Harrison, W. T. A.; Ko, E.-J.; Fletcher, D.; Ciulli, A. 3-Fluoro-4-hydroxyprolines: Synthesis, Conformational Analysis, and Stereoselective Recognition by the VHL E3 Ubiquitin Ligase for Targeted Protein Degradation. *J. Am. Chem. Soc.* **2018**, *140* (29), 9299–9313; (b) Park, H. S.; Kang, Y. K. Which DFT levels of theory are appropriate in predicting the prolyl *cis–trans* isomerization in solution? *New J. Chem.* **2019**, *43* (44), 17159–17173.

(57) (a) Džakula, Ž.; DeRider, M. L.; Markley, J. L. Conformational Analysis of Molecules with Five-Membered Rings through NMR Determination of the Continuous Probability Distribution (CUPID) for Pseudorotation. *J. Am. Chem. Soc.* **1996**, *118* (50), 12796–12803; (b) Terrien, A.; Rahgoshay, K.; Renaglia, E.; Lensen, N.; Jacquot, Y.; Marquant, R.; Brigaud, T.; Loison, C.; Chaume, G.; Miclet, E. Inviting C5-Trifluoromethylated Pseudoprolines into Collagen Mimetic Peptides. *Biomacromolecules* **2023**, *24* (4), 1555–1562.

(58) Cai, M.; Huang, Y.; Liu, J.; Krishnamoorthi, R. Solution conformations of proline rings in proteins studied by NMR spectroscopy. *J. Biomol. NMR* **1995**, *6* (2), 123–128.

(59) (a) Haasnoot, C. A. G.; de Leeuw, F. A. A. M.; Altona, C. The relationship between proton-proton NMR coupling constants and substituent electronegativities—I: An empirical generalization of the Karplus equation. *Tetrahedron* **1980**, *36* (19), 2783–2792; (b) Navarro-Vázquez, A.; Cobas, J. C.; Sardina, F. J.; Casanueva, J.; Díez, E. A Graphical Tool for the Prediction of Vicinal Proton−Proton $^{3}J_{HH}$ Coupling Constants. *J. Chem. Inf. Comput. Sci.* **2004**, *44* (5), 1680–1685.

(60) (a) Torbeev, V. Y.; Fumi, E.; Ebert, M.-O.; Schweizer, W. B.; Hilvert, D. *cis-trans* Peptide-Bond Isomerization in α-Methylproline Derivatives. *Helv. Chim. Acta* **2012**, *95* (12), 2411–2420; (b) Torbeev, V.; Ebert, M.-O.; Dolenc, J.; Hilvert, D. Substitution of Proline32 by α-Methylproline Preorganizes β2-Microglobulin for Oligomerization but Not for Aggregation into Amyloids. *J. Am. Chem. Soc.* **2015**, *137* (7), 2524–2535.

(61) (a) Ashida, T.; Kakudo, M. Conformations of Prolyl Residues in Oligopeptides. *Bull. Chem. Soc. Jpn.* **2006**, *47* (5), 1129–1133; (b) Saha, I.; Shamala, N. Investigating proline puckering states in diproline segments in proteins. *Biopolymers* **2013**, *99* (9), 605–610; (c) Verhoork, S. J. M.; Killoran, P. M.; Coxon, C. R. Fluorinated Prolines as Conformational Tools and Reporters for Peptide and Protein Chemistry. *Biochemistry* **2018**, *57* (43), 6132–6143.

(62) Gerken, J. B.; Ross, S. An NMR investigation of the existence of halide and carboxylate co-solute effects on the rotational barrier about the C□ N bonds in urea and thiourea. *J. Phys. Org. Chem.* **2010**, *23* (9), 806–809.

(63) Metrano, A. J.; Chinn, A. J.; Shugrue, C. R.; Stone, E. A.; Kim, B.; Miller, S. J. Asymmetric Catalysis Mediated by Synthetic Peptides, Version 2.0: Expansion of Scope and Mechanisms. *Chem. Rev.* **2020**, *120* (20), 11479–11615.

(64) Deepak, R. N. V. K.; Sankararamakrishnan, R. Unconventional N-H…N Hydrogen Bonds Involving Proline Backbone Nitrogen in Protein Structures. *Biophys. J.* **2016**, *110* (9), 1967–1979.

(65) Müller, K.; Faeh, C.; Diederich, F. Fluorine in Pharmaceuticals: Looking Beyond Intuition. *Science* **2007**, *317* (5846), 1881–1886.

(66) Yu, C.; Levy, G. C. Two-dimensional heteronuclear NOE (HOESY) experiments: investigation of dipolar interactions between heteronuclei and nearby protons. *J. Am. Chem. Soc.* **1984**, *106* (22), 6533–6537.

(67) Eyman, D. P.; Drago, R. S. Nuclear Magnetic Resonance Studies of Hydrogen Bonding. *J. Am. Chem. Soc.* **1966**, *88* (8), 1617–1620.

(68) (a) Vitagliano, L.; Berisio, R.; Mazzarella, L.; Zagari, A. Structural bases of collagen stabilization induced by proline hydroxylation. *Biopolymers* **2001**, *58* (5), 459–464; (b) Vitagliano, L.; Berisio, R.; Mastrangelo, A.; Mazzarella, L.; Zagari, A. Preferred proline puckerings in *cis* and *trans* peptide groups: Implications for collagen stability. *Protein Sci.* **2001**, *10* (12), 2627–2632.

(69) (a) Crawford, J. M.; Sigman, M. S. Conformational Dynamics in Asymmetric Catalysis: Is Catalyst Flexibility a Design Element? *Synthesis* **2019**, *51* (05), 1021–1036; (b) Stone, E. A.; Hosseinzadeh, P.; Craven, T. W.; Robertson, M. J.; Han, Y.; Hsieh, S.-Y.; Metrano, A. J.; Baker, D.; Miller, S. J. Isolating Conformers to Assess Dynamics of Peptidic Catalysts Using Computationally Designed Macrocyclic Peptides. *ACS Catal.* **2021**, *11* (8), 4395–4400.

Chapter III

Peptides as hydrogen bonding phase-transfer catalysts for fluorination

The experimental work described in Chapter III was carried out in collaboration with Dr. Thomas Schlatzer. Dr. Thomas Schlatzer prepared compound **2d**, was involved in preparation of **4.19** intermediate, and led catalyst **2c** degradation studies. Computational work discussed within Chapter III was performed by Dr. Mihai Popescu, Dr. Zijun Chen and Professor Robert Paton. Further details are available in the Experimental section (Chapter V).

3.1. Introduction

The binding studies described in Chapter II demonstrated that all peptides (**2a**−**r**) are capable of engaging in H-bonding with a soluble fluoride source containing a considerably weakly coordinating cation (TBA^+). In order for peptides to be successful catalyst for fluorination under HB-PTC conditions, the next requirements were the formation of a soluble HBD:MF complex, which was proposed as a reaction intermediate for BINAM *bis*-urea catalysts (Scheme 3.1.1), and the subsequent release of nucleophilic fluoride for fluorination.

A potential complication arises from numerous precedents describing peptides as alkali metal-binding species. Such interactions are known to perturb peptide H-bonding patterns, as discussed in Section 3.1.1. At present, however, there are no precedents describing how peptides interact

with alkali metal fluorides, rendering the behaviour of peptide–MF system under HB-PTC conditions uncertain. Furthermore, to evaluate the catalytic competence of these peptides in nucleophilic fluorination, an appropriate model reaction was required. We therefore selected the fluorination of cyclic β-haloamines as a benchmark transformation (Section 3.1.2).

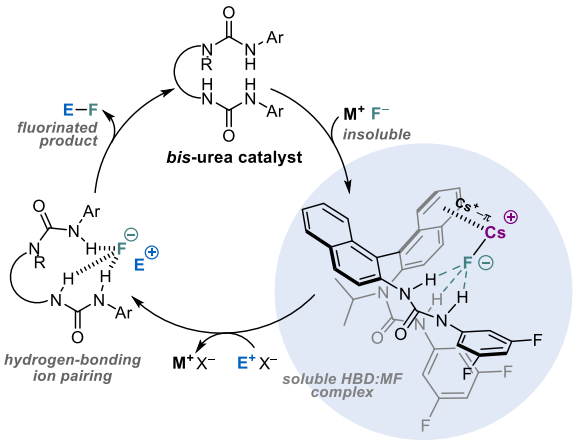

Scheme 3.1.1. Proposed mechanism for H-bonding phase-transfer catalysis (HB-PTC) with highlighted BINAM-derived *bis*-urea and CsF complex from single-crystal X-ray diffraction.[1]

3.1.1. Peptide-alkali metal interactions

Peptide–alkali metal (Li^+, Na^+, K^+, Rb^+, and Cs^+) interactions have been widely studied in the context of supramolecular assembly, ion transport and sensing.[2] Peptides coordinate alkali metals primarily through backbone carbonyl oxygen atoms and amide donors, with binding enhanced by side-chain interactions, particularly via aromatic residues (Phe, Tyr, Trp) through cation–π stabilisation (**Figure 3.1.1**).[3]

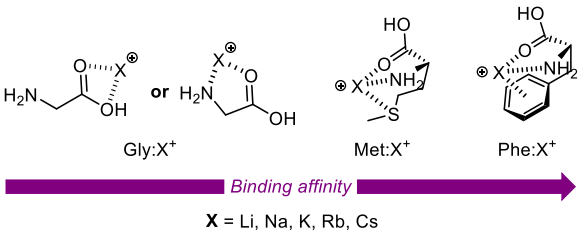

Figure 3.1.1. Binding modes of alkali-metal cations to Gly, Met and Phe amino acids.[3]

Cation size and charge density strongly influence coordination behaviour. As early as 1912, Paul Pfeiffer systematically investigated the crystallisation of amino acids (glycine, alanine, and sarcosine) in the presence of alkali metal salts and proposed that their affinity for peptides follows the order $Li^+ > Na^+ > K^+$, reflecting differences in cation charge density.[4] Smaller ions such as Li^+ and Na^+ exhibit higher charge density and stronger binding, typically preferring hard donor atoms such as carbonyl oxygens.[3c] Larger cations, including K^+, Rb^+, and Cs^+, display lower charge density and more diffuse coordination geometries, which generally result in weaker peptide binding.[3b,5]

Size-matched binding environments, however, can impart selectivity. The size selectivity of alkali metal cations underpins the well-known behaviour of biological ion channels (**Figure 3.1.2**).[2b] Valinomycin, a cyclic dodecadepsipeptide, remains one of the most selective K^+ ionophores ($\log K_{a,(1:1)}$) = 4.47 for KCl in MeOH).[6] Similarly, cyclic heptapeptide surfactin (**3.1.1**) exhibits selectivity for Cs^+ over Na^+ and K^+, attributed to its optimal coordination number (6) and cavity size (> 4 Å) matching the ionic diameter of Cs^+ (3.38 Å).[7]

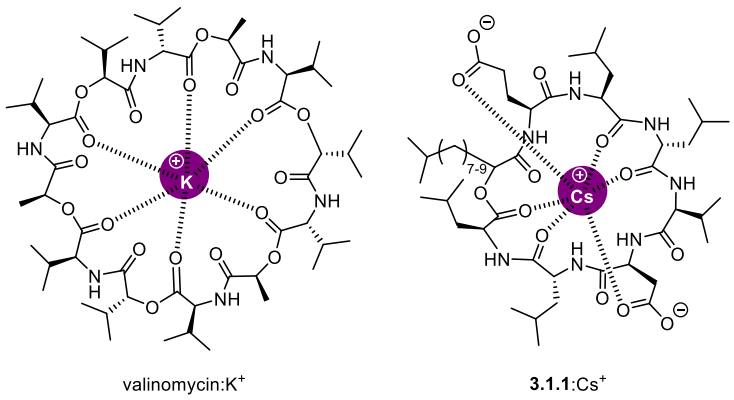

Figure 3.1.2. Examples of alkali metal selective binders: a) depsipeptide valinomycin for K^+,[6] and b) lipopeptide **3.1.1** for Cs^+.[7]

Alkali metal binding can also markedly perturb intramolecular H-bonding networks and induce conformational changes. For example, addition of Li^+ salts in biochemical assays of peptidyl prolyl *cis–trans* isomerases increases the proportion of *cis*-prolyl peptide bonds from 10% to 70%.[8] However, these effects are strongly cation-dependent. In the Ac-Ala-Ala-Pro-Ala-NHMe (**3.1.2**) peptide system, Li^+ and Na^+ induce distinct preferences for the central prolyl bond (**Figure 3.1.3a**).[9] The lowest free-energy conformer of **3.1.2**:Li^+ features the cation coordinated by three backbone carbonyl groups, with the prolyl bond shifting from *cis* to *trans*. In contrast, Na^+ binding leads to a more diverse conformational ensemble, and the lowest free-energy Na^+ adduct retains a *cis*-prolyl bond. This demonstrates that flexible peptide scaffolds adapt to varying ionic radii, resulting in cation-specific conformations.

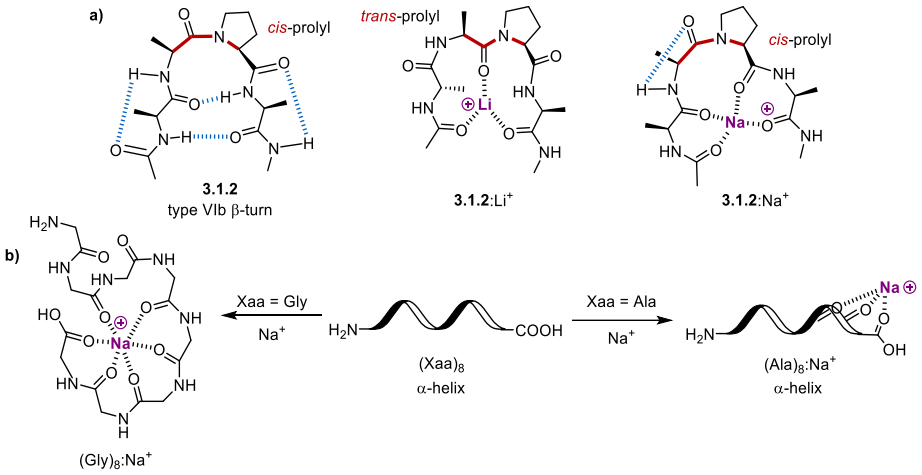

Figure 3.1.3. Conformational changes of peptides induced by alkali metal chelation.[9-10]

The consequences of metal coordination are also sequence-dependent (**Figure 3.1.3b**). The gas-phase spectroscopic and computational studies of the $(Gly)_8$:Na^+ complex resulted in loss of helical secondary structure due to suppression of intramolecular H-bonding by a hexacoordinated cation.[10a] Meanwhile, $(Ala)_8$:Na^+ retained its α-helical structure, with Na^+ bound at the *C*-terminus.[10b,c]

These observations highlight that alkali metal coordination may either stabilise or disrupt peptide conformations depending on geometric complementarity, side-chain functionality, and scaffold flexibility. Rigid binding pockets can enforce high selectivity, whereas more flexible systems adapt to different ionic radii with reduced selectivity.

3.1.2. Hydrogen-bonding phase-transfer catalysis for cyclic β-fluoroamines

To identify an appropriate model reaction for evaluating the reactivity of the designed peptide library under HB-PTC, we considered previously reported systems (*v.* Section 1.2.4). Early studies established that the TBA^+ cation can serve as a proxy for reactive onium intermediates (episulfonium, aziridinium, or azetidinium) ion-paired to hydrogen-bonded fluoride.[1,11] Building on TBAF-binding investigations of peptides **2a–r**, β-haloamines were selected as substrates, owing to their ability to ionise into *meso*-aziridinium ions (R_4N^+). The resulting ion pair, $[R_4N^+ \cdot HBD \cdot F^-]$, closely resembles the $[n Bu_4N^+ \cdot HBD \cdot F^-]$ complex derived from TBAF, making this substrate class mechanistically well-aligned with our catalyst platform.

Pupo *et al.* previously demonstrated the successful desymmetrisation of aziridinium ions formed *in situ* from β-haloamines under HB-PTC conditions using HBD catalyst **1.2.9** (*v.* Section 1.2.4).[12] While highly effective for stilbene-derived substrates, the method included only three cyclic examples (**3.1.3a–c**), which were obtained in moderate enantioselectivities (**Scheme 3.1.2a**). Among these, the synthesis of **3.1.3a** was investigated in a dedicated scale-up study (**Scheme 3.1.2b**),[13] underscoring its pharmaceutical relevance, as *trans*-2-fluorocyclohexan-1-amine structural motif appears in compounds under investigation for Alzheimer's disease.[14] Notably, an *e.r.* of 98:2 was ultimately achieved following chiral resolution by recrystallisation.

More broadly, chiral β-fluoroamines have found application across numerous therapeutic areas, including oncology, metabolic disorders, CNS pathologies, HIV, and antiviral research.[15] Structurally, these motifs are most commonly embedded within cycloalkyl or heterocyclic frameworks (**Figure 3.1.4**).

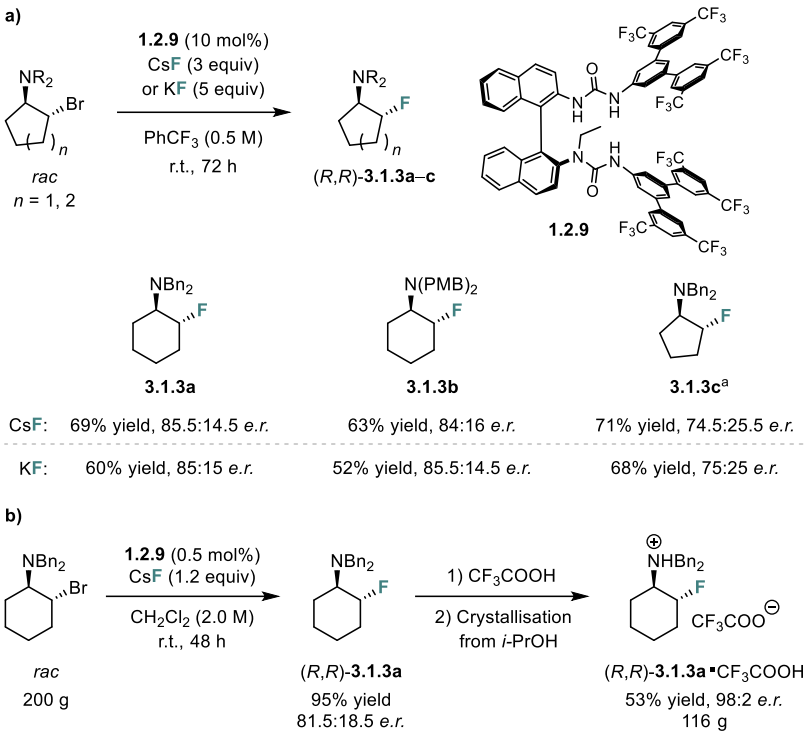

Scheme 3.1.2. HP-PTC for enantioselective synthesis of cyclic β-fluoroamines. [a]48 h; PMB = *para*-methoxybenzyl.

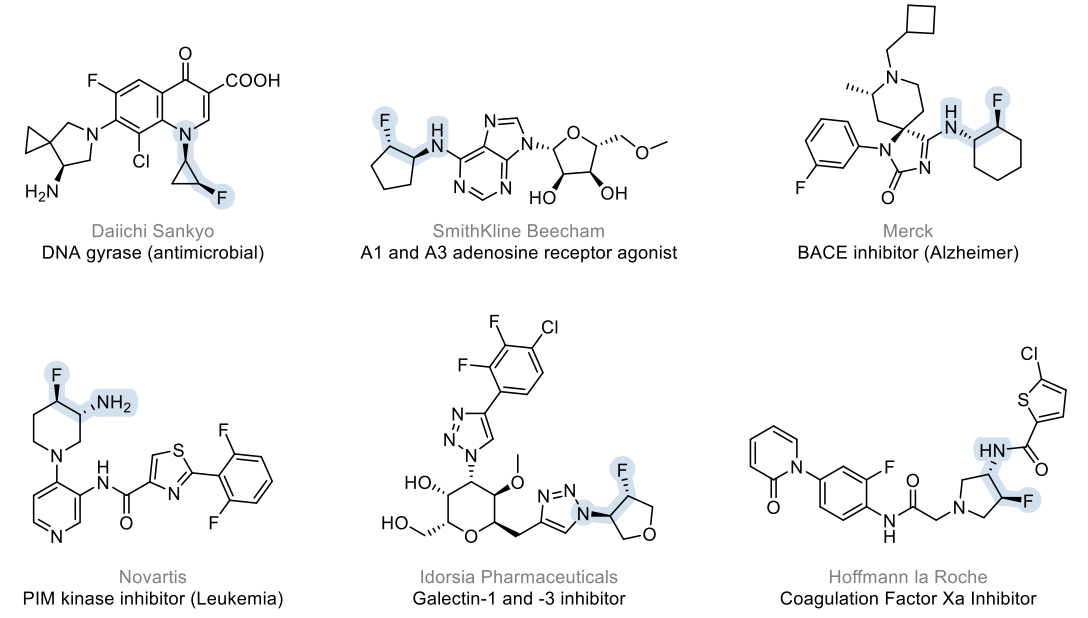

Figure 3.1.4. Representative cyclic β-fluoroamine scaffolds frequently encountered in medicinal chemistry: cycloalkyl (*top*)[14b,16] and heterocyclic (*bottom*)[17].

Therefore, cyclic β-haloamines were identified as a mechanistically relevant and synthetically valuable, yet challenging substrate class warranting further catalyst optimisation.

3.2. Results and discussion

3.2.1. Peptide complexation with CsF

Building on the established sensitivity of peptide H-bonding networks to alkali metal coordination, we examined how interaction with Cs^+ influences peptide structure and phase-transfer behaviour, focusing on the formation of soluble HBD:CsF complexes. CsF was chosen as the model alkali metal fluoride due to its comparatively low lattice energy. Peptides (in CD_2Cl_2) and CsF (30 equiv.) were sonicated for 1 hour, and the resulting complexes were investigated by NMR spectroscopy. Samples were prepared at 25 mM to reflect the concentrations used under HB-PTC conditions (*v.* Section 3.2.2).

*3.2.1.1. Tetrapeptide **2b** complexation with CsF*

We initially chose to study **2b**:CsF complexation. Peptide **2b** exhibited monodentate binding to $TBAF(H_2O)_3$ in CD_2Cl_2 with a low binding constant of $K_{a\ (1:1\ TBAF\text{-}3H2O)} = 102 \pm 1\ M^{-1}$ (*v.* Section 2.2.1.4). We sought to investigate if such low binding affinity to fluoride would allow for solubilisation of CsF. When peptide **2b** (25 mM) was saturated with CsF in CD_2Cl_2, the ^1H spectrum broadened, indicating solubilisation and complexation of CsF (**Figure 3.2.1**). The NH(*i*−2) was unperturbed while NH(*i*+1) shifted by −0.05 ppm, suggesting that H-bonding between C=O(*i+1*)→NH(*i*−2) was not disrupted for CsF chelation. Meanwhile, the resonance of NH(*i*−1) completely disappeared at 298 K, and was later observed only upon cooling to 188 K as a singlet at 6.91 ppm, indicating *i−1* as a key residue involved in binding.

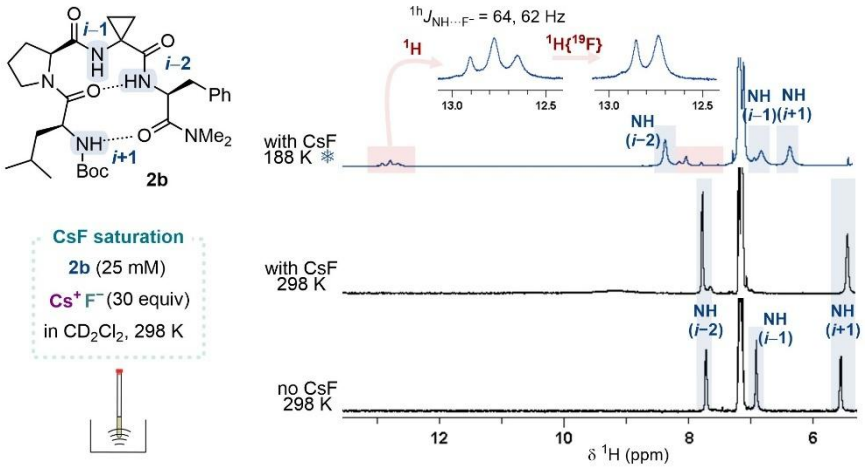

Figure 3.2.1. ^{1}H NMR of **2b** and **2b**:CsF at 298 K and 188 K; and ^{1}H{^{19}F} NMR 13.0–12.5 ppm expanded region of **2b**:CsF at 188 K. For decoupling, δ ^{19}F selected at −80 ppm.

At 188 K, additional low intensity peaks were observed in the ^{1}H spectrum (**Figure 3.2.1**), and ^{1}H−^{15}N HSQC experiments revealed two distinct **2b**:CsF complexes alongside unbound peptide (**Figure 3.2.2**). Both **2b**:CsF complexes featured chelation via single NH resonance at 12.84 ppm for the minor species ($^{1h}J_{NH\cdots F^-}$ = 62 Hz) and 12.72 ppm for the major species ($^{1h}J_{NH\cdots F^-}$ = 66 Hz). Through-bond scalar coupling was confirmed by ^{1}H{^{19}F} spectra (**Figure 3.2.1**). Since only NH(*i*−1) was perturbed upon addition of CsF, these data provide indirect evidence that NH(*i*−1) is the key HBD involved in fluoride complexation, consistent with the monodentate binding mode observed for TBAF(H_2O)$_3$ (*vide supra*). Three NH(*i+1*) resonances were identified based on their upfield ^{15}N chemical shift (~89 ppm)[18] in the ^{1}H−^{15}N HSQC spectrum: one at 6.43 ppm corresponding to the unbound peptide (NH(*i+1*)), and two at 5.16, 5.05 ppm corresponding to the peptide-CsF complexes (NH'(*i+1*)). The observed $\Delta\delta_{NH'(i+1)} \approx -1.30$ ppm for the **2b**:CsF complex indicated a substantial perturbation of the chemical environment, which is inconsistent with binding to F^- ($\Delta\delta > 0$) or a simple conformational change ($|\Delta\delta| < 0.5$ ppm),[19] but is rather consistent with disruption of an intramolecular H-bond and potential Cs^+ chelation.

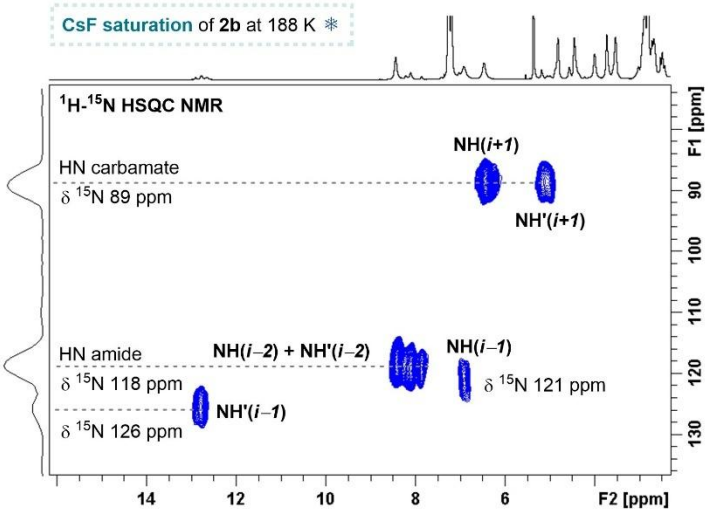

Figure 3.2.2. ^{1}H−^{15}N NMR spectrum of **2b** with CsF at 188 K. Adiabatic 180° on ^{15}N; NS = 800.

The ^{133}Cs NMR spectrum at 298 K exhibited a broad singlet at ~37 ppm, which at 188 K resolved into two doublets at 56.9 and 50.5 ppm ($^{1}J_{Cs–F}$ = 104 and 102 Hz, respectively), supporting the presence of two interconverting complexes in a ~2:1 ratio involving solubilised Cs^{+} (**Figure 3.2.3a**). The observed $^{1}J_{Cs–F}$ couplings, supported by ^{19}F, ^{19}F{^{133}Cs}, and ^{133}Cs{^{19}F} spectra, confirmed an intact Cs-F ion pair. Despite the quadrupolar nature of ^{133}Cs (I = 7/2), the relatively sharp peaks suggested that the Cs^{+} counterion resides in a locally ordered environment. The two closely spaced signals at −80.1 (major) and −80.6 (minor) ppm were observed in ^{19}F{^{133}Cs, ^{1}H} spectrum, indicating similar shielding environments for fluoride in both species. These observations suggested that the two **2b**:CsF complexes differ primarily by conformation rather than by distinct binding modes. The exact Cs^{+} chelation partners could not be identified due to the absence of direct spectroscopic evidence. However, since no chemical shift perturbation were observed for the aryl protons of the *i*−*2* residue (**Figure 3.2.1**), Cs^{+} is most likely coordinated by the *N*- and/or *C*-cap functional groups (carbamate and amide, respectively), which are also responsible for the observed upfield shifts of NH'(*i*−*2*). **Figure 3.2.3b** depicts **2b**:CsF binding model consistent with the experimental data, featuring F^{-}→NH(*i*−*1*) and C=O(*i*+*1*)→NH(*i*−*2*) H-bonds, retention of a Cs–F ion pair, and disruption of the intramolecular C=O(*i*−*2*)→NH(*i*+*1*).

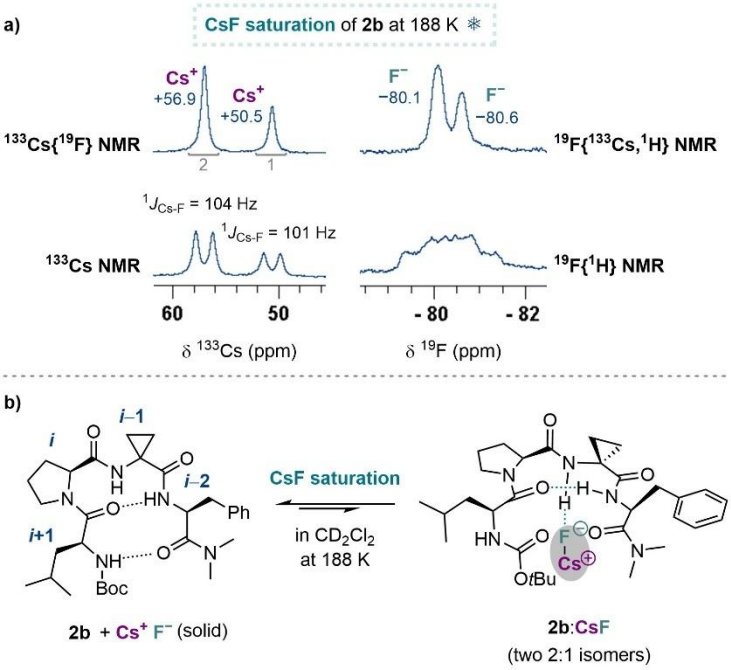

Figure 3.2.3. a) ^{19}F and ^{133}Cs NMR studies for peptide **2b** (25 mM, in CD_2Cl_2) with CsF at 188 K, and b) proposed binding model for **2b**:CsF complex (25 mM, in CD_2Cl_2) based in NMR studies.

Ultimately, these results showcased that even though **2b** displayed a poor chelating ability for fluoride due to low denticity, it can still act as a phase-transfer agent for CsF. The strong H-bond responsible for β-turn formation remained intact upon complexation with either $TBAF(H_2O)_3$ (*v.* Section 2.2.1.4) or CsF. In contrast, introduction of highly coordinating Cs^+ disrupted a H-bond associated with hairpin formation, however, without perturbing fluoride-binding denticity.

3.2.1.2. Ureido-peptides binding with CsF

Section 2.2.2.4 described the success of the introduction of a urea *N*-cap which exposed all of the NH protons to engage in H-bonding interactions with fluoride as indicated by titration experiments with TBAF(H_2O)$_3$. Similarly, upon saturation of **2c** and **2d** with CsF in CD_2Cl_2 (25 mM) all three NH resonances in the ^{1}H NMR spectra disappeared, indicating their proximity to the binding site of CsF (**Figure 3.2.4**, *top*). At 233 K corresponding CsF complexes displayed a broad peak each in ^{19}F NMR spectra at −72.4 ppm and −63.0 ppm, for **2c** and **2d** respectively, indicative of F^- solubilisation (**Figure 5.5.44**). Furthermore, in the ^{1}H spectra of CsF:**2c** and CsF:**2d** complexes at 233 K revealed three downfield resonances, with two of them at 13.3 and 11.5 ppm for CsF:**2d** appeared as doublets indicating stable H-bonds with fluoride ($^{1h}J_{H\cdots F^-}$ = 55 and 38 Hz; **Figure 3.2.4**, *bottom*). This showcased the advantage of using an extended *tetrakis*-trifluoromethylated *m*-terphenyl π-system compared to *bis*-trifluoromethylated phenyl as urea-cap in order to obtain more stable CsF complexes.

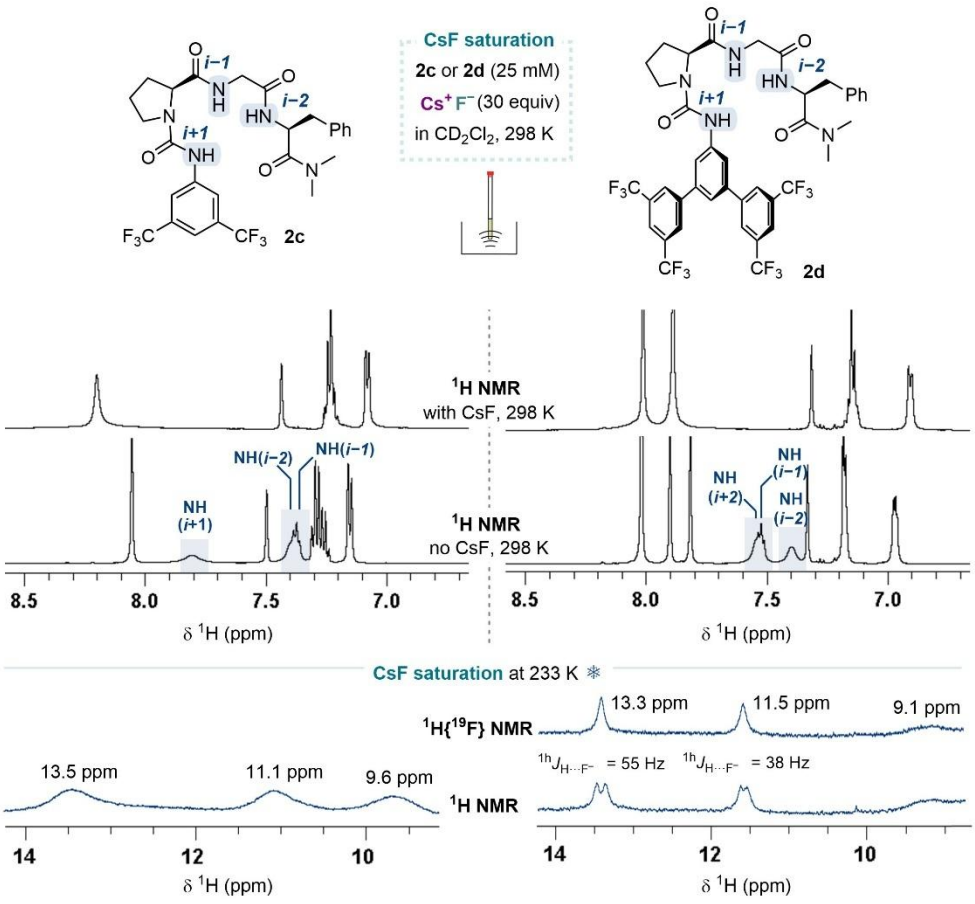

Figure 3.2.4. ^{1}H NMR spectra of **2c** and **2d** (25 mM, in CD_2Cl_2) with and without added CsF at 298 K (*top*). ^{1}H and ^{1}H{^{19}F} NMR spectra of **2c** and **2d** (25 mM, in CD_2Cl_2) with CsF at 233 K (*bottom*).

During NMR titrations with TBAF$(H_2O)_3$, **2c** and **2d** exhibited comparable fluoride binding affinities ($K_{a\ (1:1\ TBAF\text{-}3H2O)}$ = 3.05 ± 0.95 × 10^4 and 1.25 ± 0.04 × 10^4 M^{-1}, in CD_2Cl_2, respectively). More broadly, binding studies across the peptide series indicated that higher $K_{a\ (1:1\ TBAF\text{-}3H2O)}$ values do not directly translate into the formation of more stable CsF complexes. Consistent with this observation, the peptide showing the strongest fluoride binding in TBAF$(H_2O)_3$ titrations, **2h** (*i* = Flp; $K_{a\ (1:1\ TBAF\text{-}3H2O)}$ = 1.15 ± 0.05 × 10^5 M^{-1}, in CD_2Cl_2), displayed highly dynamic and complex binding behaviour with CsF, as evidenced by significantly broadened NMR resonances at 233 K (**Figure 3.2.5**). In contrast, peptides containing *cis*-prolyl and C*γ*-*endo* inducing proline analogues, **2k** (*i* = dmp; *cis* and *endo* preferred) and **2i** (*i* = flp; *endo* preferred), displayed bidentate binding profile similar to **2c** at 233 K (**Figure 3.2.5**). These spectra show a clear correlation between peptide conformation and CsF binding. In comparison, peptide **2l** (*i* = α-Me-Pro; *trans* and *exo* preferred) showed no detectable resonances in the 8−14 pm region at 233 K, suggesting poor or averaged binding to CsF , indicating weak, highly averaged, or transient interaction with CsF. Conversely, peptides that displayed a bidentate mode to CsF at 233 K were also found to engage in tridentate fluoride binding during TBAF$(H_2O)_3$ titrations. This observation highlights the active participation of Cs^+ in peptide–CsF complexation, a feature that is explored in greater detail in the case study of the **3.3j**:CsF complex, corresponding to the best-performing catalyst (Section 3.2.3.1).

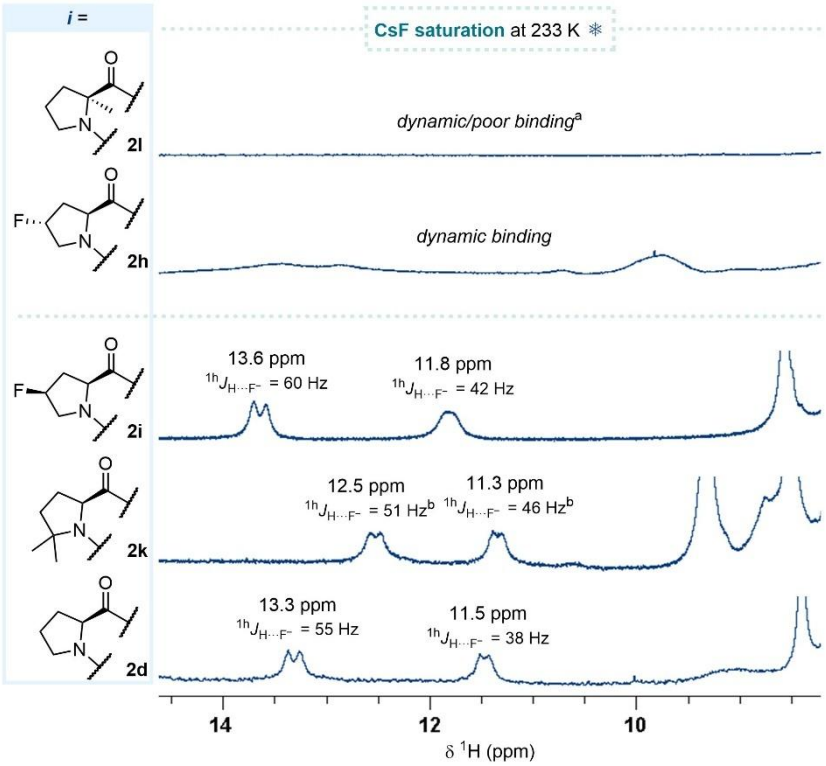

Figure 3.2.5. Expansion of ^{1}H NMR spectra of selected peptide:CsF complexes (25 mM, in CD_2Cl_2) at 233 K.[a]Acquired at 273 K, not soluble at 233 K; [b]measured at 226 K.

Taken together, these experiments demonstrate that conformational tuning of the peptide scaffold exerts a pronounced influence on CsF chelation, which is not captured solely by fluoride binding affinities measured using TBAF$(H_2O)_3$.

3.2.2. Peptide catalysts for nucleophilic fluorination via HB-PTC

*3.2.2.1. Screening of catalysts **2a–s***

Next, the ability of peptides **2a–s** to act as HBD catalysts for asymmetric fluorination was investigated. *trans-N,N*-dibenzyl-2-bromocyclohexan-1-amine (*rac*-**3.1a**) was selected as a model substrate for the initial evaluation of peptide catalytic performance. The starting material was synthesised following reported literature procedure in two steps from commercially available cyclohexene oxide, involving *meso*-epoxide ring opening with dibenzylamine followed by bromination of the intermediate alcohol via an aziridinium ion.[12] Substrate *rac*-**3.1a** was known to be reactive under HB-PTC conditions using BINAM *bis*-urea catalysts and CsF, however providing only moderate yield and enantioselectivity (69% and 85.5:14.5 *e.r.*; *v.* Section 3.1.2). In 1,2-dichloroethane (1,2-DCE, 0.25 M), using CsF (3 equiv.), the BINAM-urea catalyst **1.2.9** (10 mol%) furnished the fluorinated product **3.2a** in excellent NMR-yield (> 99%) and moderate 80:20 *e.r.* in favour of the (*R,R*)-**3.2a** enantiomer (**Scheme 3.2.1**). In the absence of an HBD catalyst, no fluorination was observed, reflecting the insolubility of CsF in 1,2-DCE.

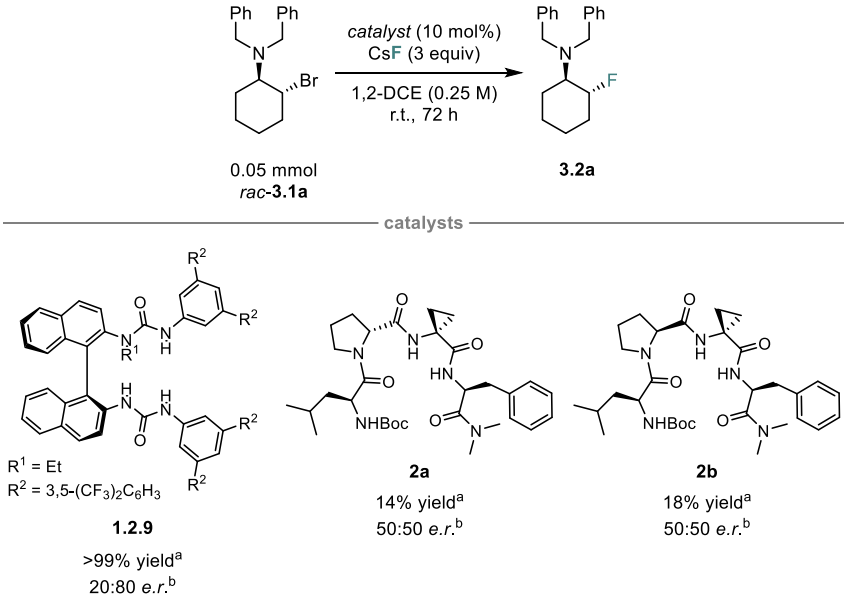

Scheme 3.2.1. Screening of model substrate with BINAM-urea catalyst **1.2.9** and tetrapeptides **2a** and **2b**. [a]Determined by ^{19}F NMR using 4-fluoroanisole, [b]*e.r.* (enantiomeric ratio (*S,S*):(*R,R*)) measured by HPLC using chiral stationary phase.

In contrast, the use of tetrapeptides **2a** and **2b** (10 mol%) afforded the fluorinated product **3.2a** in low NMR yields (14% and 18%, respectively), with no detectable enantiocontrol (50:50 *e.r.*;

Scheme 3.2.1). The low fluorination yields were consistent with weak, monodentate binding to fluoride previously established for tetrapeptides with TBAF$(H_2O)_3$ and CsF. Nevertheless, the observation of any fluorination is notable, given that peptide **2a** exhibits an incredibly low fluoride binding affinity ($K_{a\ (1:1\ TBAF\text{-}3H2O)}$ = 52 ± 5 M^{-1}, in CD_2Cl_2 via NMR), whereas BINAM *bis*-urea catalysts have been shown to bind fluoride much more strongly ($K_{a\ (1:1\ TBAF\text{-}3H2O)} \approx 10^6$ M^{-1}, in CH_2Cl_2 via UV-Vis).

Subsequently, the catalytic performance of tripeptides **2c–g**, featuring varied urea *N*-cap substitutions, was investigated. Screening revealed significantly improved fluorination yields (62–78%) together with enhanced enantioselectivity for (*S,S*)-**3.2a** in up to 70:30 *e.r.* (**Scheme 3.2.2**), indicating a fluoride embedded in a chiral H-bonding network. A modest increase in yield was observed for catalysts with higher TBAF$(H_2O)_3$ binding affinities ($K_{a\ (1:1\ TBAF\text{-}3H2O)}$), however, this trend was not linear. Notably, catalyst degradation (Cat. deg.) was detected and increased with the acidity of NH(*i*+*1*), with **2c** showing the highest degree of degradation (33%). Subsequent analysis (Section 3.2.2.2) identified alkylation at the *N*-cap as the primary degradation pathway, likely contributing to the absence of a clear correlation between fluorination yield and binding affinity. Overall, these results clearly demonstrate the benefit of urea *N*-cap modification in tripeptide catalysts, leading to marked improvements in both reactivity and enantioselectivity relative to the parent tetrapeptides. Within this series, peptide **2d** emerged as the most effective catalyst (78% yield, 70:30 *e.r.*), and was therefore selected as a benchmark for further catalyst evaluation.

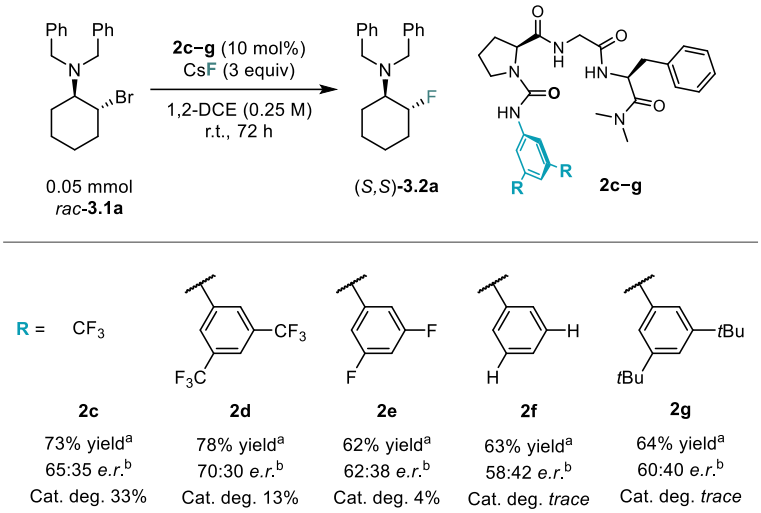

Scheme 3.2.2. Screening of model substrate with peptides **2c–g**. [a]Determined by ^{19}F NMR using 4-fluoroanisole. [b]*e.r.* (enantiomeric ratio (*S,S*):(*R,R*)) measured by HPLC using chiral stationary phase. Cat. deg. = catalyst degradation.

To probe stereochemical requirements for substrate recognition, the effect of inversion at the *i* and *i*−*1* positions was evaluated using epimers of **2d** (**Scheme 3.2.3**). In both cases, fluorination afforded near-racemic product **3.2a**, indicating that an L-Xaa-L configuration (where Xaa is achiral amino acid) is the most suited for efficient substrate discrimination.

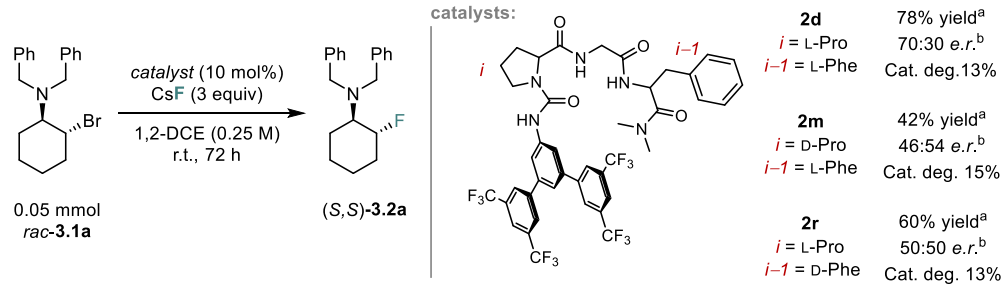

Scheme 3.2.3. Screening of epimeric peptides of **2d**. [a]Determined by ^{19}F NMR using 4-fluoroanisole. [b]*e.r.* (enantiomeric ratio (*S,S*):(*R,R*)) measured by HPLC using chiral stationary phase. Cat. deg. = catalyst degradation.

In a further set of experiments, variation of substituted prolines at position *i* revealed that *endo*/*exo* pyrrolidine puckering strongly influences catalytic performance. The C$^{\gamma}$-*endo*-locked fluoroproline flp (**2i**) delivered the best yield and enantioselectivity (80:20 *e.r.*, 86%) across the whole library **2c–s**, whereas the C$^{\gamma}$-*exo*-inducing Flp (**2h**) showed reduced enantiocontrol (59:41 *e.r.*). Overall, a clear trend emerged in which residues with stronger *endo* bias afforded higher enantiocontrol (**Scheme 3.2.4**). Notably, although dfp (**2j**) displayed a TBAF(H$_2$O)$_3$ binding profile resembling

Flp (**2h**), it exhibited distinct catalytic behaviour with improved enantioselectivity (65:35 *e.r.*), indicating that catalytic outcome is not solely dictated by TBAF$(H_2O)_3$ affinity.

These catalytic trends align with the CsF binding behaviour established by NMR spectroscopy (*v.* Section 3.2.1.2). Peptides **2d, 2k,** and **2i**, which afforded the best enantioselectivity, formed stable bidentate CsF complexes at 233 K, whereas less selective catalysts showed weak or averaged CsF binding. Importantly, the same peptides show tridentate fluoride coordination in TBAF$(H_2O)_3$ titrations with relatively significant binding of NH(*i*−*2*) and the lowest NH(*i*−*1*) involvement (*v.* Section 2.2.2.5). Taken together, the data point to NH(*i*−*2*) participation as a recurring feature of the better-performing catalysts, a correlation that suggests NH(*i*−*2*) positioning (and the conformational features that enable it) as a useful design handle.

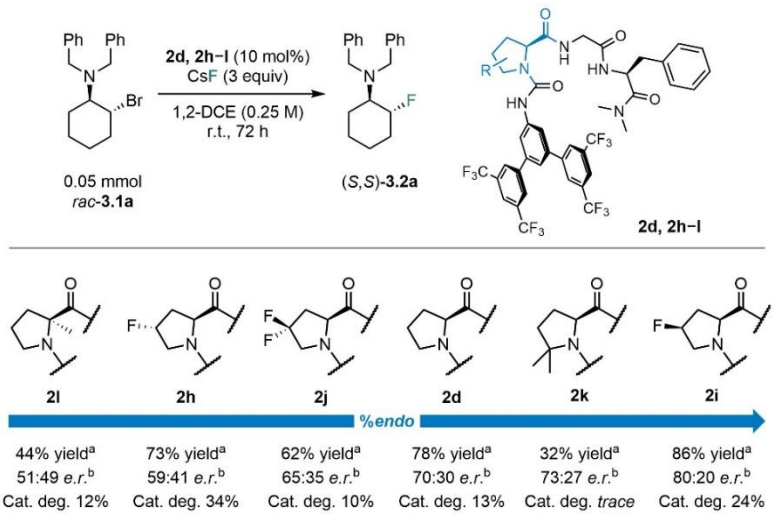

Scheme 3.2.4. Catalytic performance of catalysts featuring substituted prolines (**2h**−**l**) relative to parent peptide **2d**. [a]Determined by ^{19}F NMR using 4-fluoroanisole. [b]*e.r.* (enantiomeric ratio (*S,S*):(*R,R*)) measured by HPLC using chiral stationary phase. Cat. deg. = catalyst degradation.

To further assess the influence of the β-turn region on catalytic performance, peptides **2d**, **2n–p**, which display systematically varied τ(*i*−*1*) values, were evaluated. These catalysts, featuring α,α-dialkylated residues at the *i*−*1* position, exhibited a clear correlation between increasing τ(*i*−*1*) and improved enantioselectivity, rising from 53:47 *e.r.* for **2n** (*i*−*1* = Acbc), up to 71:29 *e.r.* for **2p** (*i*−*1* = Acpc; **Scheme 3.2.5**). Observed trend is consistent with enhanced conformational flexibility of the turn region facilitating more effective substrate binding and asymmetric induction. However, incorporation of α,α-dialkylated residues also led to poor catalyst solubility, which manifested in

poor fluorination yields (18−32%). Solubility was preliminarily assessed in CD_2Cl_2 to establish concentrations suitable for NMR titrations, revealing saturated catalyst concentrations of only 1.9–4.9 mM.

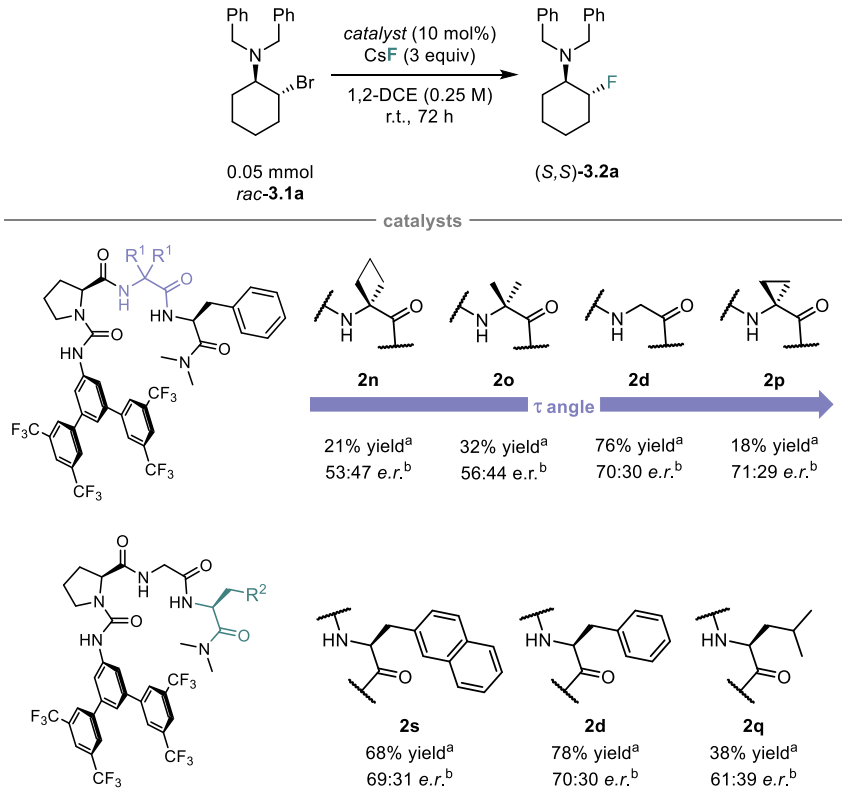

Scheme 3.2.5. Effect of residues *i*−*1* and *i*−*2* on catalytic fluorination of *rac*-**3.1a.** [a]Determined by ^{19}F NMR using 4-fluoroanisole. [b]*e.r.* (enantiomeric ratio (*S,S*):(*R,R*)) measured by HPLC using chiral stationary phase.

Finally, the role of π–π non-covalent interactions in catalysis was investigated through peptides **2d, 2q**, and **2s** (**Scheme 3.2.5**). Replacement of the aromatic Phe(*i*−*2*) residue with aliphatic Leu (**2q**) resulted in a pronounced decrease in both yield (38%) and enantioselectivity (61:39 *e.r.*). Conversely, extension of the π-system in **2s** (*i*−*2* = 2-Nal) led to fluorination outcomes nearly identical to those observed for **2d**, indicating that extension of the aromatic system does not confer additional benefit beyond that provided by the native phenylalanine residue.

On the basis of the results presented above, several conclusions can be drawn regarding fluoride delivery and asymmetric induction under HB-PTC conditions using peptide-based catalysts. Despite exhibiting significantly lower fluoride binding affinities toward TBAF$(H_2O)_3$ than benchmark BINAM *bis*-urea catalysts, the peptide HBD catalysts developed in this work proved

highly effective in promoting nucleophilic fluorination of the model substrate, delivering yields of up to 86%. Across a broad range of binding affinities ($K_{a\ (1:1\ TBAF\text{-}3H2O)} \approx 10^1$–$10^5\ M^{-1}$, in CD_2Cl_2), no direct correlation was observed between K_a and reactivity; instead, catalyst solubility exerted a pronounced effect on the fluorination outcome.

These findings highlight that fluoride binding strength alone is insufficient to rationalise catalytic performance in this complex system. Effective fluoride delivery requires not only CsF binding (phase-transfer), but also ion exchange between Cs^+ and the azetidinium intermediate, followed by fluoride dissociation to enable nucleophilic attack (*v.* **Scheme 3.1.1**). In this context, excessively strong fluoride binding may be counterproductive by attenuating fluoride nucleophilicity, whereas overly weak binding compromises phase-transfer efficiency. Most remarkably, in this study peptide **2a**, with only $K_{a\ (1:1\ TBAF\text{-}3H2O)} = 52 \pm 5\ M^{-1}$ (in CD_2Cl_2), was capable of mediating fluoride delivery under HB-PTC conditions, albeit with low conversion (14%). The most effective catalyst exhibited a moderate binding affinity ($K_{a\ (1:1\ TBAF\text{-}3H2O)} \approx 10^4\ M^{-1}$, in CD_2Cl_2) and afforded high fluorination yield (86%).

Beyond efficient fluoride delivery, this peptide platform also demonstrates clear potential for enantioselective fluorination. Analysis of the results presented in this section identifies a set of structural features that govern asymmetric induction in peptide-based catalysts (**Figure 3.2.6**). Together, these design elements form a coherent framework for rational peptide catalyst development and motivated the selection of **2i** for further optimisation, which is explored in the Section 3.2.3.1.

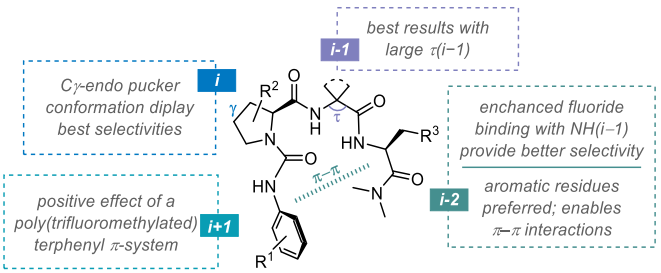

Figure 3.2.6. Effect of structural modifications of ureido-peptides on the enantioselectivity on the fluorination of *rac*-**3.1a**.

3.2.2.2. Catalyst degradation

To investigate the pathway of catalyst degradation, peptide **2c** was selected for in-depth study, as it exhibited the highest degree of degradation under catalytic conditions. Control experiments performed in the absence of either CsF or substrate showed no detectable degradation, confirming that decomposition occurs only under reaction conditions. Degradation was most pronounced in CH_2Cl_2, and this solvent was therefore chosen for further analysis. Accordingly, *rac*-**3.1a** (0.5 mmol) was subjected to fluorination under standard HB-PTC conditions in CH_2Cl_2 for 138 hours. After this time, two additional signals corresponding to degraded catalyst species (**3.2.1**) were observed in the ^{19}F NMR spectrum alongside the resonance of intact catalyst (**Figure 3.2.7**). Integration indicated that approximately 73% of the catalyst had undergone degradation.

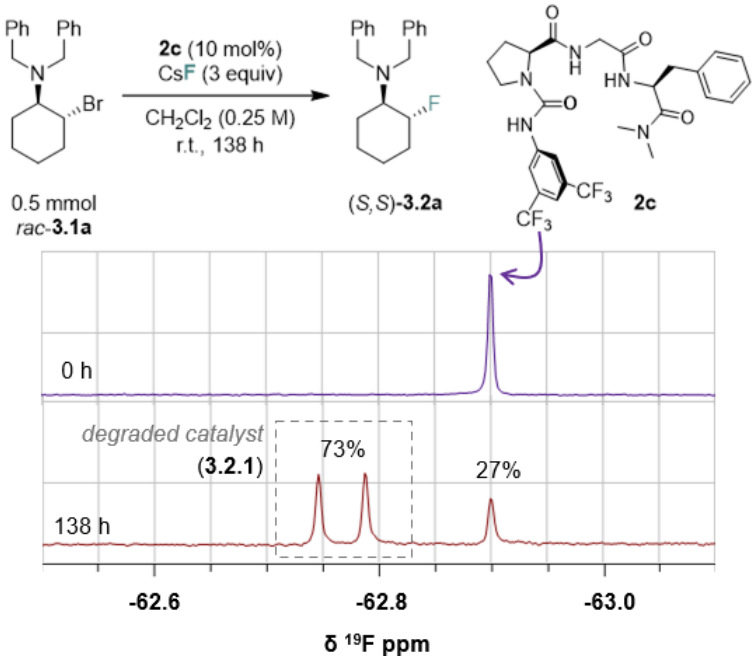

Figure 3.2.7. ^{19}F NMR spectra of catalyst **2c** and its degradation products **3.2.1** after 138 hours.

Following purification by column chromatography (0–5% (v/v) *i*-PrOH in toluene), the ratio of the two new resonances at −62.7 and −62.8 ppm shifted from 50:50 to 68:32, suggesting the presence of two distinct, non-interconverting species (**3.2.1-minor** and **3.2.1-major**). Since the two species could not be separated chromatographically, they were characterised as a mixture. Spectroscopic analysis using 2D NMR experiments (^1H-^1H COSY, ^1H-^{13}C HSQC, ^1H-^{15}N HSQC and ^1H-^{13}C HMBC) and ESI mass spectrometry established that the degraded species arise from

alkylation of catalyst **2c** by the aziridinium intermediate, with the two signals corresponding to diastereomers (**Figure 3.2.8**). The ^{1}H NMR spectrum displayed resonances consistent with both the cyclohexyl moiety and the catalyst backbone (**Figure 3.2.8c**). Based on ^{1}H–^{15}N HSQC correlations and characteristic coupling patterns of the NH(*i*+*1*), NH(*i*−*1*), and NH(*i*−*2*) protons (singlet, triplet, and doublet, respectively), alkylation was assigned to the most acidic site, namely the urea NH(*i*+*1*) (**Figure 3.2.8d**). While the obtained data did not allow unambiguous distinction between *N*- and *O*-alkylation, precedent from urea-based HB-PTC systems suggests that *O*-alkylation is the more likely pathway.[11,13,20]

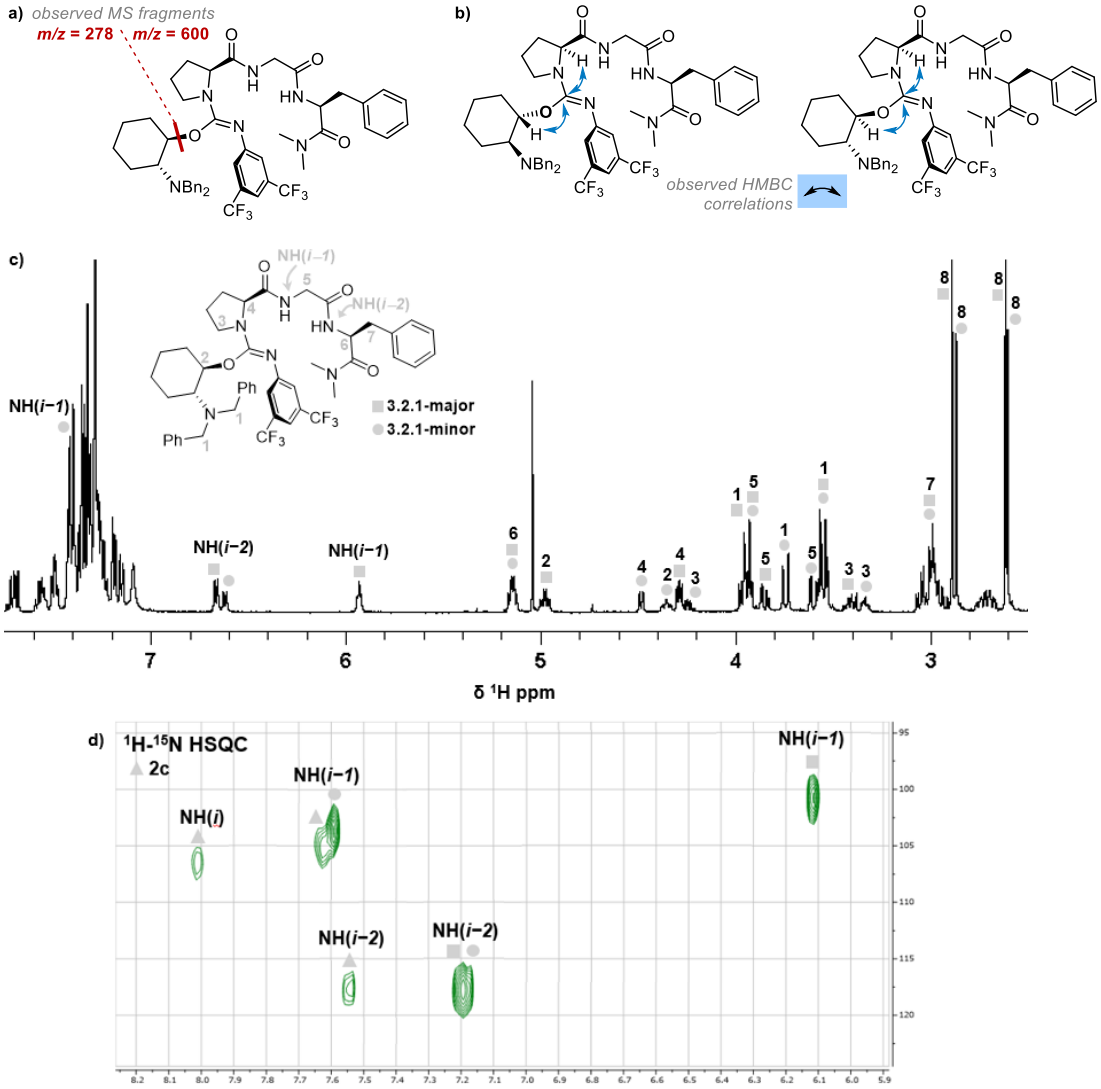

Figure 3.2.8. Characterisation of **3.2.1** by a) MS analysis, b) ^{1}H-^{13}C HMBC NMR, c) ^{1}H NMR and d) ^{1}H-^{15}N HSQC NMR of **2c** + **3.2.1** mixture (all in $CDCl_3$, 500 MHz). Note: *N*-alkylation at the urea motif cannot be excluded based on this data. MS = mass spectrometry.

Reaction monitoring showed that enantioselectivity remained unchanged despite catalyst degradation, indicating that alkylation results in deactivation rather than formation of a new active species. Pleasingly, optimised catalyst **3.3j** (Section 3.2.3.1) could be separated from its degraded analogue by a simple silica plug (CH_2Cl_2) filtration, then recovered by elution with acetone and reused with excellent reproducibility.

3.2.3. Optimisation for asymmetric fluorination with CsF

3.2.3.1. Catalyst optimisation

Building on the structure–enantioselectivity relationships identified in Section 3.2.2.1, catalyst optimisation initially focused on tuning the electronic effect of the *i*−*2* residue. The initial catalyst library screening indicated that natural Phe was optimal and that extending aromaticity did not enhance performance. To probe potential π–π and cation–π contributions, *para*-substituted Phe derivatives were synthesised: **3.3a** (*i*−*2* = Phe(*p*-NO_2); (*S*)-2-amino-3-(4-nitrophenyl)propanoic acid) and **3.3b** (*i*−*2* = Phe(*p*-NMe_2); (*S*)-2-amino-3-(4-(dimethylamino)phenyl)propanoic acid). Both afforded similar enantioselectivity (70:30 *e.r.*) to **2d** (71:29 *e.r.*), demonstrating tolerance to *para*-substitution but minimal electronic influence (**Scheme 3.2.6**). However, **3.3b** displayed reduced yield (54%), suggesting that factors other than the electronic nature of the *para*-substituent may influence reactivity, *e.g.* catalyst–CsF complex solubility.

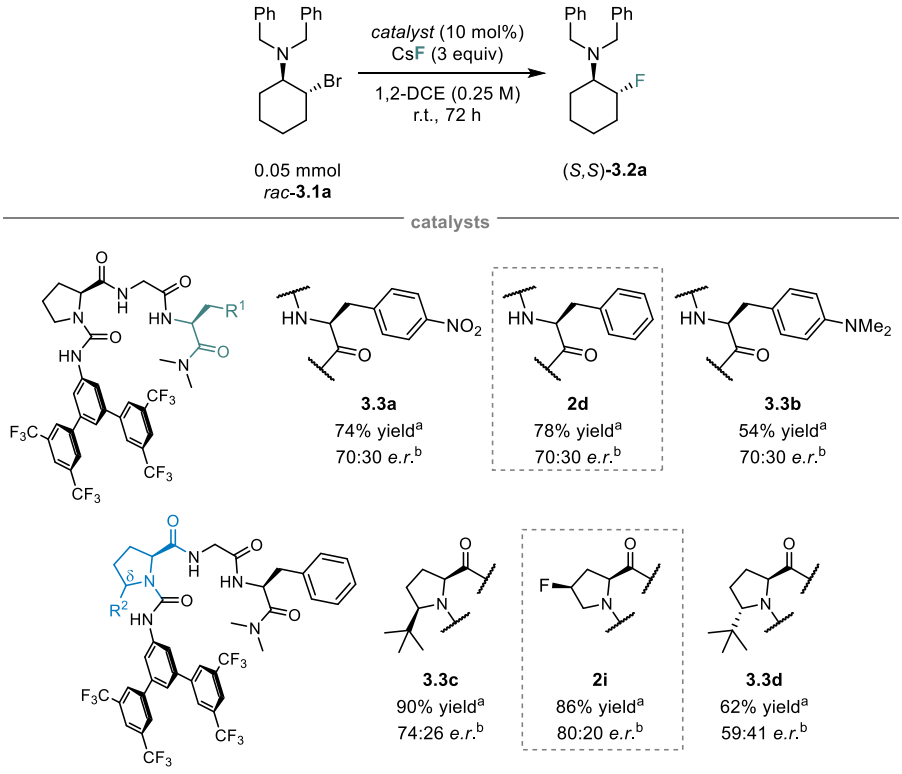

Scheme 3.2.6. Final optimisation of residues *i* and *i*−*2* on catalytic fluorination of *rac*-**3.1a.** [a]Determined by ^{19}F NMR using 4-fluoroanisole. [b]*e.r.* (enantiomeric ratio (*S*,*S*):(*R*,*R*)) measured by HPLC using chiral stationary phase.

Given the established correlation between proline C$^{\gamma}$-*endo* bias and enantioselectivity, optimisation next targeted strengthening this conformational preference. In search of proline analogues capable of exerting a stronger bias, the (5*R*)-*tert*-butyl proline derivative (*i* = Pro(5*R*-*t*Bu); **3.3c**) was prepared, which enforces *endo* puckering through steric hindrance with the C=O(*i*) group. Substitution at this position (C$^{\delta}$) is unique in that it avoids invoking an amide gauche effect; instead, pyrrolidine ring puckering is governed predominantly by steric repulsion. Additionally, C$^{\delta}$ substitution is known to increase the population of the *cis*-imide conformation. Although **3.3c** improved enantiocontrol relative to **2d** (74:26 *versus* 71:29 *e.r.*; **Scheme 3.2.6**), it remained inferior to the strongly *endo*-inducing **2i** (*i* = flp; 80:20 *e.r.*). The (5*S*)-Pro diastereomer **3.3d** (*i* = Pro(5*S*-*t*Bu)) mirrored the selectivity of **2h** (*i* = Flp; 59:41 *e.r.*), consistent with its *exo* preference. Notably, both C$^{\delta}$-substituted variants avoided catalyst degradation, but overall performance favoured continued use of the flp scaffold.

Attention was then directed toward the *C*-cap, whose influence on peptide conformation has been documented in the literature. D-Proline-containing tetrapeptides have been reported to favour type I' pre-helical β-turns when a methyl ester is used as the *C*-terminal protecting group, whereas *N*,*N*-dimethyl amides predominantly adopt type II' β-turns and hairpin conformations.[21] This observation has been ascribed to amides being better HBA than esters,[22] and such conformational differences have been reported to translate into significant variations in the enantioselectivity of catalytic systems. In this work, however, the *C*-cap is likely to influence catalytic performance not only by modulating the intramolecular H-bonding network of the peptide, but also by affecting potential Cs^+ chelation and organisation of the peptide–CsF complex. Accordingly, a range of peptides with varied *C*-caps (**3.3e–h**) were prepared (**Scheme 3.2.7**). Catalyst **3.3e** (R = OMe) showed lower enantioselectivity compared to **2i** (NMe_2; 68:32 versus 80:20 *e.r.*). Variation of the amide alkylation was also examined: the piperidine-based catalyst (**3.3f**) exhibited reduced *e.r.* (75:25), whereas extended alkyl chains revealed modest improvements (**3.3g**, NEt_2 = 82:28; **3.3h**, NBn_2 = 81:19 *e.r.*), albeit accompanied by reduced yields (76% and 68%, respectively).

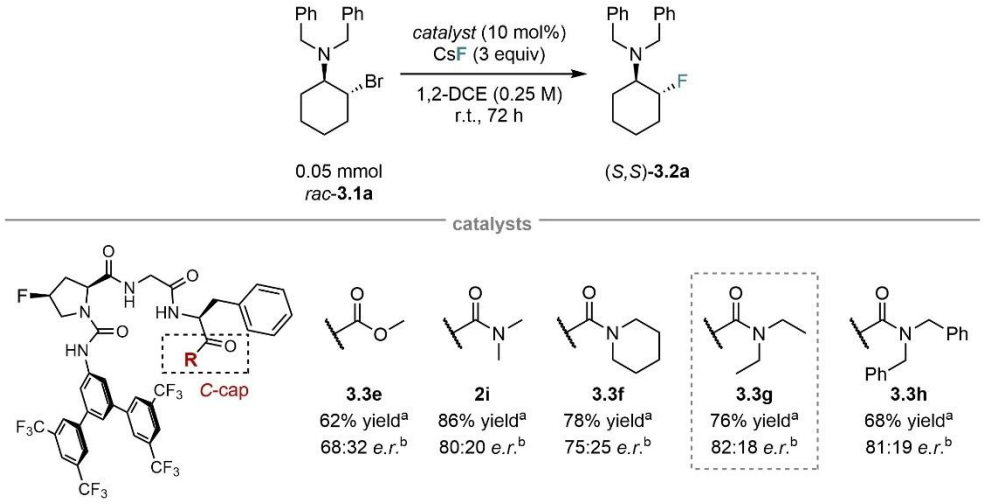

Scheme 3.2.7. Optimisation of the *C*-cap. [a]Determined by ^{19}F NMR using 4-fluoroanisole. [b]*e.r.* (enantiomeric ratio (*S,S*):(*R,R*)) measured by HPLC using chiral stationary phase.

The remaining residues (*i+1* and *i−1*) were examined in Section 3.2.2.1. Finally, independently optimised residues were combined in catalysts **3.3i** and **3.3j** to test additivity. Both exhibited enhanced enantioselectivity (87:13 and 88:12 *e.r.*, respectively) and high yields (86% and 82%, respectively), and **3.3j** selected for further optimisation of reaction conditions (**Scheme 3.2.8**).

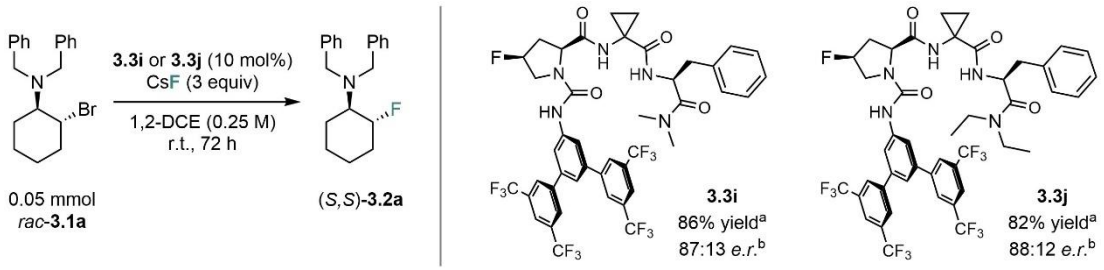

Scheme 3.2.8. Additive effect of optimised residues provides catalysts **3.3i** and **3.3j**. [a]Determined by ^{19}F NMR using 4-fluoroanisole. [b]*e.r.* (enantiomeric ratio (*S,S*):(*R,R*)) measured by HPLC using chiral stationary phase.

3.2.3.2. Optimisation of reaction conditions

Solvent effect. Catalyst **3.3j** was selected for further reaction optimisation, with initial efforts focused on the choice of reaction solvent, which can have a pronounced effect on reactivity. Typically, low polarity solvents (dielectric constant $\varepsilon_r < 3$) are employed in asymmetric ion-pairing catalysis to promote the formation of contact ion pairs.[23] Conversely, previous studies on HB-PTC systems (*v.* Section 1.2.4) have reported high fluorination yields and enantioselectivities in polar chlorinated solvents and polar fluorinated aromatics. This trend was attributed to the influence of solvent polarity on catalyst solubility and on the solid–liquid phase-transfer process, where increased polarity of the organic phase enhances the rate of phase-transfer.[24]

Among the solvents screened (**Table 3.2.1**), the highest enantioselectivities were obtained with 2-butanone and acetone (92:8 and 90:10 *e.r.*, respectively), albeit at relatively low fluorination yields (26% and 28%, respectively; **Table 3.2.1**, entries 2 and 4). In contrast, the best performing solvents in terms of reactivity were the polar chlorinated solvents $CHCl_3$ (99% yield, 51:49 *e.r.*), CH_2Cl_2 (98% yield, 81:19 *e.r.*), and 1,2-dichloroethane (1,2-DCE; 82% yield, 88:12 *e.r.*), the latter providing the most optimal balance between yield and enantioselectivity (**Table 3.2.1**, entries 6, 10 and 13). Polar aromatic solvents that had shown success in previous HB-PTC systems gave relatively low yields (24–34%), but comparable enantioselectivities to chlorinated aliphatic solvents (83:17 to 85:15 *e.r.*; **Table 3.2.1**, entries 5, 8 and 9). Screening of solvents with $\varepsilon_r < 8$ (**Table 3.2.1**, entries 11−15), such as toluene, EtOAc, and ethers, resulted in yields below 10%. The sole exception was $CHCl_3$, which afforded quantitative conversion despite prior filtration of the solvent through basic alumina or treatment with $NaHCO_3$ to neutralise residual HCl.

Notably, all solvents screened were used in anhydrous form, even though the reactions were not conducted under an inert atmosphere, as previous studies indicated that such conditions were unnecessary.[13] To assess future practicality, 'wet' 1,2-DCE was also evaluated. This solvent was prepared by adding water, followed by sonication and phase separation prior to use. The resulting 'wet' 1,2-DCE afforded yields and enantioselectivities comparable to those obtained with anhydrous 1,2-DCE (**Table 3.2.1**, entries 7 and 6, respectively).

Table 3.2.1. Solvent screening for fluorination of **3.1a** with catalyst **3.3j**.

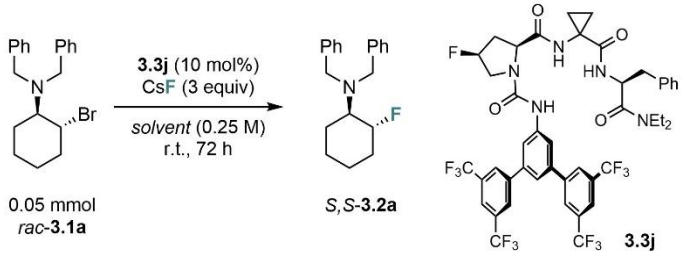

Entry	Solvent	NMR yield (%)[a]	Cat. deg. (%)	ε_r[b]	*e.r.*[c]
1	MeCN	42	13	37.5	87:13
2	acetone	28	0	20.7	90:10
3	*N*,*N*-dimethylformamide	15	0	19.9	n.d.
4	2-butanone	26	0	18.5	92:8
5	1,2-difluorobenzene	34	8	14.3	85:15
6	1,2-dichloroethane	82	20	10.4	88:12
7	1,2-dichloroethane[d]	78	24	10.4	87:13
8	1,2-dichlorobenzene	28	*trace*	9.9	85:15
9	α,α,α-trifluorotoluene	24	17	9.18	83:17
10	CH_2Cl_2	98	32	8.93	81:19
11	tetrahydrofuran	0	0	7.52	n.d.
12	EtOAc	8	0	6.1	n.d.
13	$CHCl_3$[e]	99	0	4.8	51:49
14	Et_2O	2	0	3.9	n.d.
15	toluene	4	0	2.38	n.d.

[a]Determined by ^{19}F NMR using 4-fluoroanisole. [b]dielectric constant. [c]*e.r.* (enantiomeric ratio (*S*,*S*):(*R*,*R*)) measured by HPLC using chiral stationary phase. [d]Saturated with water, see text for detail. [e]Dry $CHCl_3$, filtered over basic alumina. Cat. deg. = catalyst degradation, n.d. = not determined.

Catalyst solubility and concentration effects. During solvent optimisation studies, it was noted that catalyst **3.3j** was not fully soluble in CH_2Cl_2 (0.25 M), despite this solvent providing the best performance in terms of fluorination yield (**Figure 3.2.9**). ^{19}F qNMR experiment using 4-fluoroanisole as an internal standard revealed that the saturated concentration for **3.3j** in CD_2Cl_2 was only 7 mM. This corresponds to ~3 mol% of dissolved catalyst under the reaction conditions.

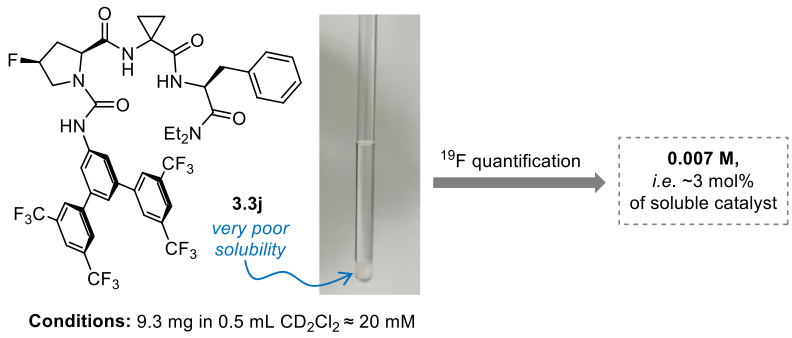

Figure 3.2.9. Poor catalyst **3.3j** solubility in CD_2Cl_2. Concertation was determined by qNMR using 4-fluoroanisole.

This observation prompted an investigation of catalyst loading in the optimised solvent 1,2-DCE, varying the catalyst amount from 2.5 mol% to 20 mol% (**Table 3.2.2**, entries 1−4). It was anticipated that reduced catalyst loadings would still afford high yields, as the concentration of solubilised catalyst was expected to remain largely unchanged. On the contrary, decreasing the amount of **3.3j** from 10 mol% led to diminished yields (70% and 56% at 5 mol% and 2.5 mol%, respectively), albeit with slightly improved enantioselectivities (up to 89:11 *e.r.* at 2.5 mol%). These results suggest that the catalytically active species involving the catalyst (*i.e.* catalyst-CsF complex) exhibits higher solubility under the reaction conditions. For example, the **3.3j**:CsF complex was significantly more soluble during NMR investigations in CD_2Cl_2 (*v.* Section 3.2.4.1) than the unbound catalyst, for which the ^{1}H NMR spectrum at 213 K could not be obtained due to its lack of solubility. Accordingly, the designed system appears to facilitate phase-transfer not only of CsF, but also of the catalyst itself. This observation was consistent with prior reports of a 100-fold increase in solubilisation of open-chain peptides in ether-type solvents upon addition of alkali-metal salts.[25]

Table 3.2.2. Effect of catalyst **3.3j** loading and concentration in 1,2-DCE.

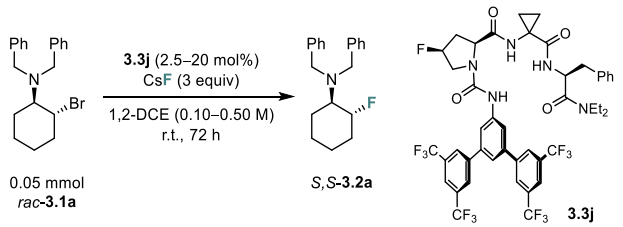

Entry	Catalyst loading (mol%)	Concentration (M)	NMR yield (%)[a]	Cat. deg. (%)	*e.r.*[b]
1	2.5	0.25	56	50	89:11
2	5	0.25	70	33	88.5:11.5
3	10	0.25	86	24	88:12
4	20	0.25	84	8	85:15
5	10	0.10	73	16	89:11
6	10	0.50	78	22	86:14

[a]Determined by ^{19}F NMR using 4-fluoroanisole. [b]*e.r.* (enantiomeric ratio (*S,S*):(*R,R*)) measured by HPLC using chiral stationary phase. Cat. deg. = catalyst degradation.

The catalyst concentration in solution was also adjusted by varying solvent volume (**Table 3.2.2**, entries 3, 5 and 6). This led to similar trends, whereby higher catalyst concentrations resulted in

decreased enantioselectivity. However, yield dropped slightly at 0.50 M, which may be attributed to inefficient stirring in the small reaction volume (100 μL).

Fluoride Source. Next the effect of different F^- sources for HB-PTC was investigated using catalyst **3.3j**. Previous studies with BINAM-*bis* urea catalyst **1.2.9** demonstrated that substrate *rac*-**3.1a** can be fluorinated using KF, affording yields comparable to those obtained with CsF (*v.* Section 3.1.2).[12] Unfortunately, no reactivity was observed when KF was employed using peptide-based catalyst **3.3j** (**Table 3.2.3**, entry 2), highlighting a pronounced counter-cation effect, which is discussed in more detail in Section 3.2.4. Use of the soluble fluoride source TBAF$(H_2O)_3$ in the absence of catalyst resulted in low fluorination yield (22%), accompanied together by copious formation of the undesired β-hydroxy amine (36%), arising from water acting as a competing nucleophile (**Table 3.2.3**, entry 3). Addition of catalyst **3.3j** did not improve the outcome (**Table 3.2.3**, entry 4), as expected, since soluble TBAF$(H_2O)_3$ does not require a phase-transfer agent, in contrast to insoluble CsF.

Table 3.2.3. Effect of fluoride source for fluorination of *rac*-**3.1a** using catalyst **3.3j**.

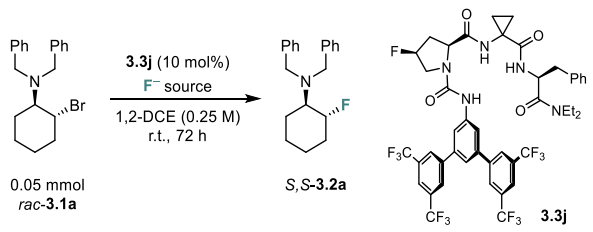

Entry	F^- source	Equiv.	NMR Yield (%)[a]	Cat. deg. (%)	*e.r.*[b]
1	CsF	3.0	82	24	88:12
2	KF	5.0	0	0	n.a.
3	TBAF$(H_2O)_3$	1.2	22 (36)[c]	0	50:50
4	TBAF$(H_2O)_3$ (without **3.3j**)	1.2	20 (34)[c]	0	50:50

[a]Determined by ^{19}F NMR using 4-fluoroanisole, yield. [b]*e.r.* (enantiomeric ratio (*S,S*):(*R,R*)) measured by HPLC using chiral stationary phase. [c]Yield of β-hydroxy amine indicated in parenthesis. Cat. deg. = catalyst degradation. n.a. = not applicable.

Temperature effect. The effect of reaction temperature on the fluorination was subsequently examined by analysing the reaction mixture after 72. Initially experiments at lower temperature were performed to assess whether lower temperatures would enhance enantioselectivity obtained at room temperature (88:12 *e.r.*; **Table 3.2.4**, entry 3). At 0 °C no product formation was observed (**Table 3.2.4**, entry 1), however, raising the temperature to 6 °C enabled product formation with higher stereocontrol (90:10 *e.r.*), but at a pronounced loss of reactivity (16% yield; **Table 3.2.4**, entry 2). On the other hand, at 40 °C, a significant decrease in enantioselectivity was observed (75:25 *e.r.*), accompanied by substantial background fluorination in the absence of catalyst (60% yield, 50:50 *e.r.*), indicating a solubilisation of CsF at elevated temperature (**Table 3.2.4**, entries 5 and 6).

Table 3.2.4. Temperature effect on fluorination of *rac*-**3.1a** using catalyst **3.3j**.

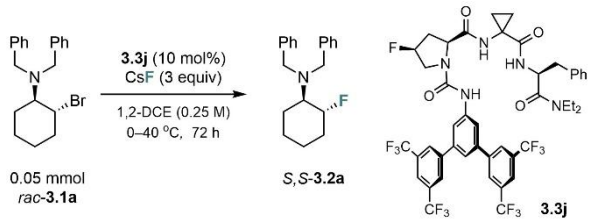

Entry	Temperature	NMR Yield (%)[a]	Cat. deg. (%)	*e.r.*[b]
1	0 °C	<1%	0	n.d.
2	6 °C	16	0	90:10
3	r.t.	88	24	88:12
4	r.t. (without catalyst)	<1%	n.a.	n.d.
5	40 °C	>99%	37	75:25
6	40 °C (without catalyst)	60	n.a.	50:50

[a]Determined by ^{19}F NMR using 4-fluoroanisole, yield. [b]*e.r.* (enantiomeric ratio (*S,S*):(*R,R*)) measured by HPLC using chiral stationary phase. Cat. deg. = catalyst degradation, n.a. = not applicable, n.d. = not determined.

Since no catalyst degradation was detected at 6 °C (**Table 3.2.4**, entry 2), reaction times were extended in order to obtain higher yields. Under these conditions, 34 days were required to reach quantitative conversion (97% yield), with the remaining 3% attributed to catalyst degradation (**Figure 3.2.10**). Time-course experiments indicated that catalyst degradation increased slowly over the course of the reaction; however, this did not lead to erosion of enantioselectivity, which

remained constant at 90:10 *e.r.* throughout. This observation suggests that the degraded catalyst species do not participate in the fluorination step.

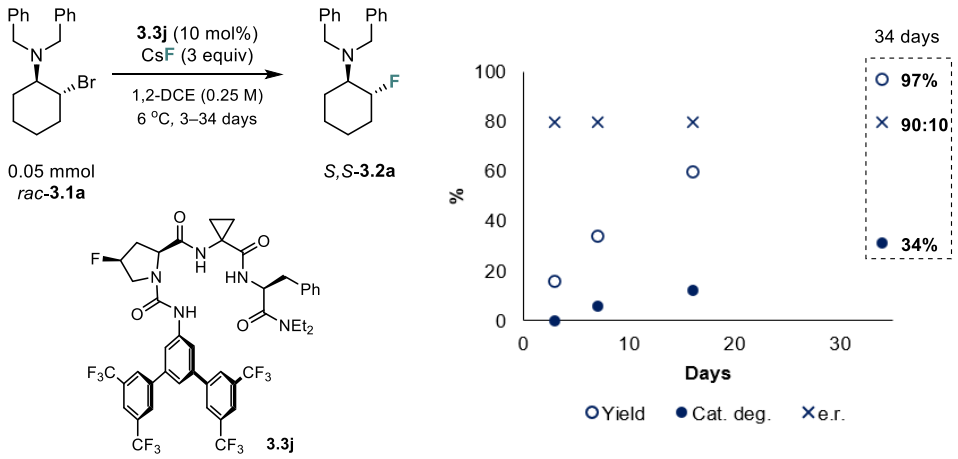

Figure 3.2.10. Time-course at 6°C for fluorination of *rac*-**3.1a** with **3.3j**.

Reaction scale-up. The final optimisation for the fluorination of *rac*-**3.1a** was carried out in 1,2-DCE (0.25 M) at room temperature. Screening of the CsF amount revealed that the reaction tolerates a broad range of fluoride equivalents (1.2–5 equiv.) affording comparable yields (77−82%; **Table 3.2.5**, entries 1−4). For future scalability, reducing the amount of catalyst was desirable as well, therefore, conditions employing 5 mol% of **3.3j** were examined. To achieve yields comparable to 10 mol% catalyst loading, the reaction time was extended from the standard 72 h to 120 h (**Table 3.2.5**, entries 5−7). These optimised conditions, using 1.2 equivalents of CsF and 5 mol% catalyst, were subsequently translated to a gram-scale reaction, affording the fluorinated product (*S*,*S*)-**3.2a** in 83% isolated yield and 89:11 *e.r.*

Table 3.2.5. Final optimization for *rac*-**3.1a** fluorination using **3.3j**.

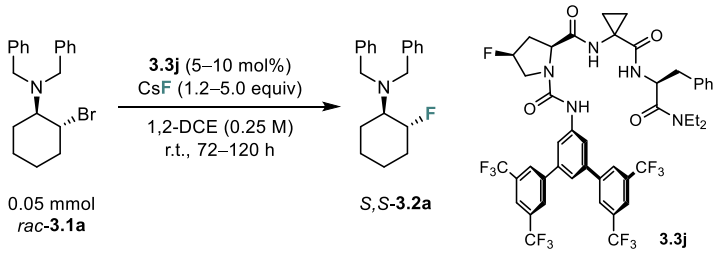

Entry	Catalyst loading (mol%)	CsF equiv.	Time	NMR yield (%)[a]	Cat. deg. (%)	*e.r.*[b]
1	10	1.2	72 h	77	21	88:12
2	10	2	72 h	79	23	88:12
3	10	3	72 h	82	24	88:12
4	10	5	72 h	78	26	88:12
5	5	3	72 h	70	33	88.5:11.5
6	5	3	96 h	76	37	88.5:11.5
7	5	1.2	120 h	88 (83)[c]	43	88.5:11.5 (89:11)[c]

[a]Determined by ^{19}F NMR using 4-fluoroanisole. [b]*e.r.* (enantiomeric ratio (*S*,*S*):(*R*,*R*)) measured by HPLC using chiral stationary phase. [c]isolated yield and enantioselectivity at 1 gram scale. Cat. deg. = catalyst degradation.

3.2.3.3. Reaction scope

Next, a range of cyclic β-bromoamines *rac*-**3.1a**−**f** were evaluated in the asymmetric fluorination with CsF in the presence of catalyst **3.3j** (**Scheme 3.2.9**). Substrates featuring five-, six-, and seven-membered rings (**3.1c**, **3.1a**, and **3.1b**, respectively) afforded the corresponding β-fluoroamines in high isolated yields (72–86%) and moderate enantioselectivities (89:11 *e.r.* for (*S*,*S*)-**3.2a**, and 81:19 *e.r.* for (*S*,*S*)-**3.2b** and (*S*,*S*)-**3.2c**). Substituted five-membered rings were also examined and displayed a broader range of enantioselectivities: the tetrahydrofuran derivative **3.1d** provided improved selectivity (85:15 *e.r.* for (3*S*,4*S*)-**3.2d**) relative to the unsubstituted analogue **3.1c** (81:19 *e.r.* for (*S*,*S*)-**3.2c**), whereas the *N*-Boc pyrrolidine derivative gave lower selectivity (76:24 *e.r.* for (*S*,*S*)-**3.2e**). Prior work has demonstrated that dibenzyl protecting group can be removed with retention of enantioselectivity. Deprotection of the corresponding fluorinated products can therefore afford precursors to medicinally relevant targets (**Scheme 3.2.9**).

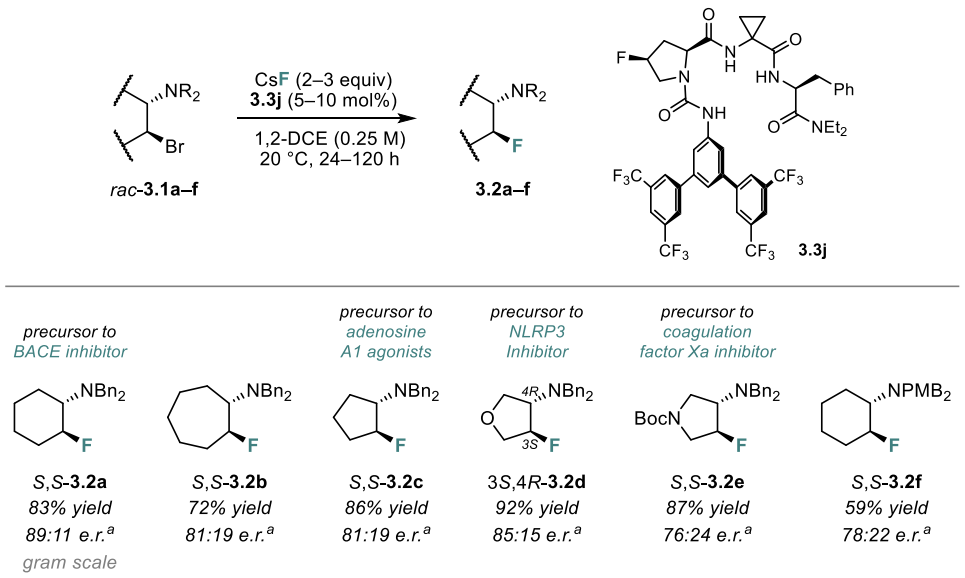

Scheme 3.2.9. Scope of the enantioselective fluorination of cyclic β-bromoamines with CsF under HB-PTC using peptide-based catalyst **3.3j**. [a]Enantiomeric ratio (*e.r.*) measured by HPLC using chiral stationary phase. PMB = *para*-methoxybenzyl.

The change of the *N*-protecting group revealed a pronounced effect on both yield and enantioselectivity. Introduction of an electron-donating *para*-methoxybenzyl (PMB) group led to a significant reduction in yield (83% for (*S*,*S*)-**3.2a** *versus* 59% for (*S*,*S*)-**3.2e**). Moreover, a marked decrease in enantioselectivity to 78:22 *e.r.* was observed, hinting at the importance of *N*-substituent for substrate recognition.

Given the moderate enantioselectivities obtained for cyclic β-fluoroamines, resolution of enantiomers by recrystallisation was explored. Previous studies reported successful enantioenrichment of (*R*,*R*)-**3.2a** (from 81.5:18.5 to 98:2 *e.r.* in 50% yield) as a trifluoroacetate (TFA) salt.[13] For this compound, recrystallisation as the free base was not feasible due to its low melting point (69–71 °C). In addition, the use of relatively strong acids (*i.e.* HCl, HBr, TFA, MsOH, TsOH) was required to achieve protonation to obtain corresponding salts, since the neighbouring fluorine substituent lowered the pK_a of the amine (*v.* Section 1.1.2.1).[26]

Based on these considerations, recrystallisation was investigated for (3*S*,4*R*)-**3.2d**, for which no alternative enantioselective synthesis is currently available. As both the free base and the corresponding TFA salt were obtained as oils, trichloroacetic acid (TCA) was employed. TCA has comparable acidity to (pK_a in water at 25 °C: 0.52 for TFA and 0.66 for TCA)[27] but significantly higher melting point (58 °C for TCA *versus* −15.4 °C for TFA). Formation of the (3S,4R)-**3.2d**·TCA salt afforded a crystalline solid (m.p. 107–108 °C), which was successfully recrystallised from hot *i*-PrOH to deliver the enantioenriched product in 98:2 *e.r.* and 60% yield (**Scheme 3.2.10**).

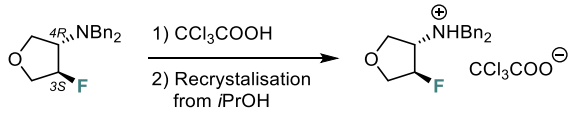

3*S*,4*R*-**3.2d**
85:15 e.r.[a]

3*S*,4*R*-**3.2d**·TCA
60% yield, 98:2 e.r.[a]

Scheme 3.2.10. Recrystallisation of (3*S*,4*R*)-**3.2d**. [a]Enantiomeric ratio (*e.r.*) measured by HPLC using chiral stationary phase.

Acyclic aliphatic substrates *rac*-**3.1g**−**l** were next evaluated using standard conditions with catalyst **3.3j** (**Scheme 3.2.11**). Stilbene-derived substrates were expected to display enhanced reactivity relative to aliphatic systems. Accordingly, all stilbene-based β-fluoroamines (*R,R*)-**3.2g**−**j** were obtained in excellent isolated yields (92−99%) from corresponding chlorides. However, enantioselectivity remained modest and was largely independent of *N*-substitution (74:26 to 76:24 *e.r.*). The products included enantioenriched fluorinated analogues of the *N*-methyl-D-aspartate receptor antagonists, lephetamine ((*R*,*R*)-**3.2j**; 92% yield, 74:26 *e.r.*) and diphenidine ((*R*,*R*)-**3.2i**; 99% yield, 75:25 *e.r.*), which have been investigated as analgesics.[28] In addition to stilbene

substrates, linear aliphatic β-bromoamines **3.2k** and **3.2l** were fluorinated in high yields (82% and 94%, respectively), but with poor enantioselectivities (67:33 and 50:50 *e.r.*, respectively).

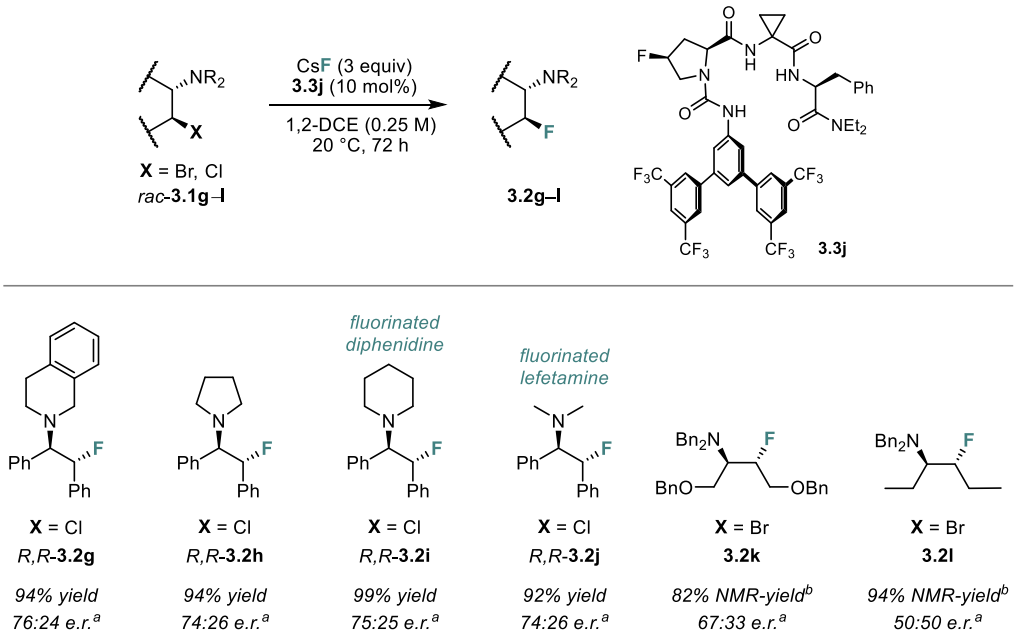

Scheme 3.2.11. Scope of the enantioselective fluorination of acyclic β-haloamines with CsF under HB-PTC using peptide-based catalyst **3.3j**. [a]Enantiomeric ratio (*e.r.*) measured by HPLC using chiral stationary phase. [b]Determined by ^{19}F NMR using 4-fluoroanisole as internal standard.

These results highlight the complementary selectivity profiles of peptide-based catalyst **3.3j** and BINAM *bis*-urea catalyst **1.2.9**. The BINAM catalyst displays a strong preference for stilbene-derived substrates, delivering excellent enantioselectivities (up to 96:4 *e.r.*), however, with more variable reactivity (*e.g.* 56% yield for **3.2i** and 92% for **3.2h**). On the other hand, catalyst **3.3j** affords cyclic substrates in superior enantioselectivities compared to **1.2.9** (up to 89:11 *e.r.* using **3.3j**), with the sole exception of the seven-membered substrate 3.2b, for which comparable selectivity was obtained (17:83 *e.r.* for **1.2.9** and 81:19 *e.r.* for **3.3j**). The most pronounced improvement with catalyst **3.3j** was observed for substrates derived from 5-membered rings.

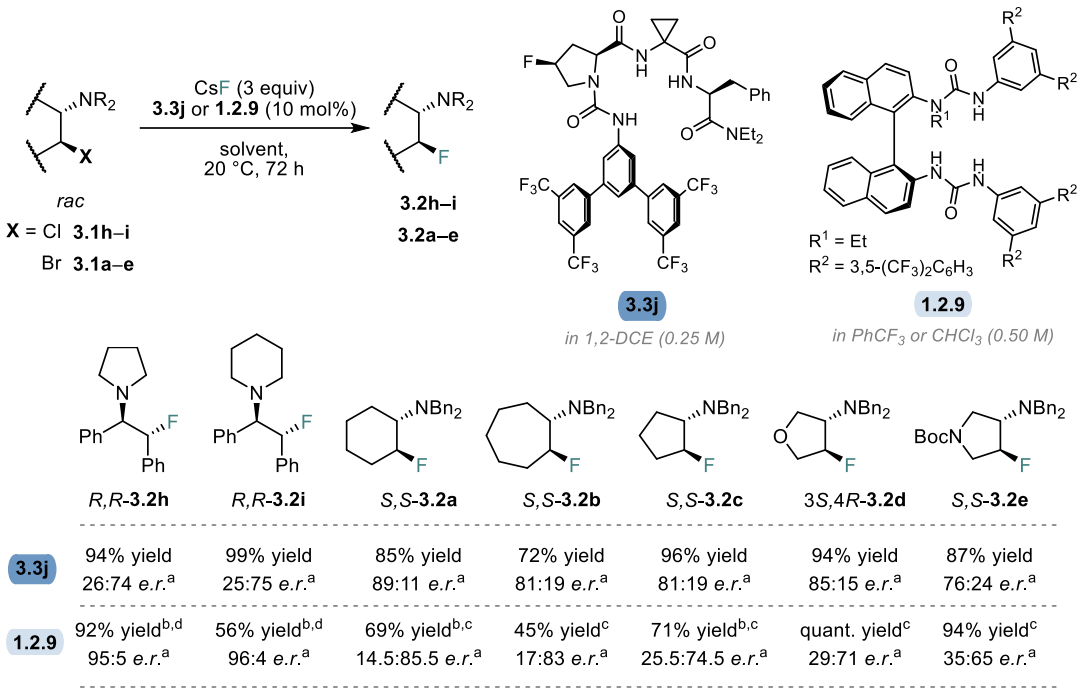

	R,R-**3.2h**	*R,R*-**3.2i**	*S,S*-**3.2a**	*S,S*-**3.2b**	*S,S*-**3.2c**	3*S*,4*R*-**3.2d**	*S,S*-**3.2e**
3.3j	94% yield 26:74 *e.r.*[a]	99% yield 25:75 *e.r.*[a]	85% yield 89:11 *e.r.*[a]	72% yield 81:19 *e.r.*[a]	96% yield 81:19 *e.r.*[a]	94% yield 85:15 *e.r.*[a]	87% yield 76:24 *e.r.*[a]
1.2.9	92% yield[b,d] 95:5 *e.r.*[a]	56% yield[b,d] 96:4 *e.r.*[a]	69% yield[b,c] 14.5:85.5 *e.r.*[a]	45% yield[c] 17:83 *e.r.*[a]	71% yield[b,c] 25.5:74.5 *e.r.*[a]	quant. yield[c] 29:71 *e.r.*[a]	94% yield[c] 35:65 *e.r.*[a]

Scheme 3.2.12. Catalytic performance of peptide **3.3j** *versus* BINAM *bis*-urea catalyst **1.2.9** for selected substrates. [a]enantiomeric ratios (*e.r.*; (*S,S*):(*R,R*)) measured by HPLC with chiral stationary phase; [b]from ref[12]; [c]in $PhCF_3$; [d]$CHCl_3$, at −10 or 0°C (see ref[12]).

3.2.4. Peptide catalyst **3.3j** binding with CsF

3.2.4.1. NMR studies

Lead peptide **3.3j** was discovered during catalyst optimisation for asymmetric nucleophilic fluorination, (*v.* Section 3.2.2), which prompted a study on its ability to bind CsF. Saturation of peptide **3.3j** with CsF in CD_2Cl_2 (25 mM) at 298 K caused NH(*i*−2) and NH(*i*+1) peaks to disappear, indicating fast equilibration of several species (**Figure 3.2.11**). Meanwhile the NH(*i*−1) resonance remained at the same chemical shift in the ^1H spectra acquired with and without CsF added, which suggested no binding to CsF. Using $^1H-^{13}C$ HSQC experiment an additional highly deshielded peak (8.54 ppm at 233 K) was characterised as a *o*-ArH.

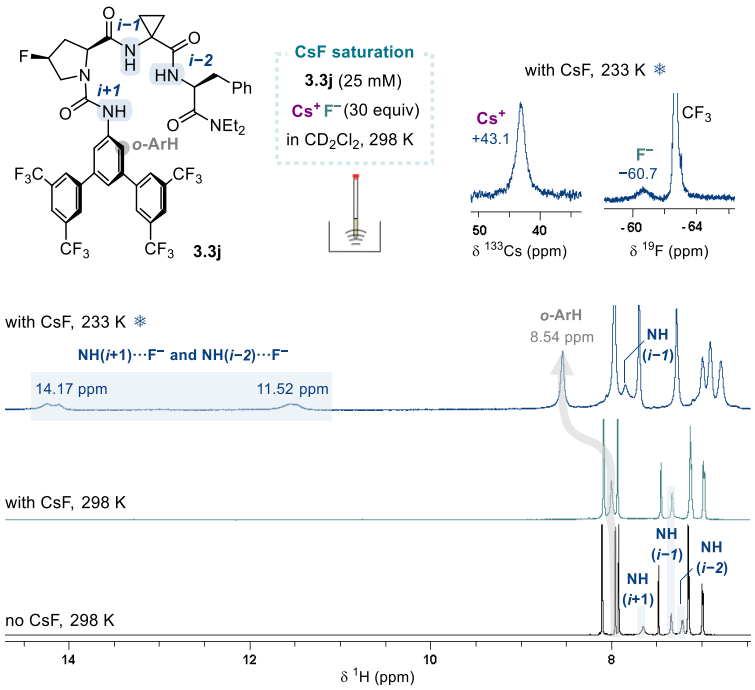

Figure 3.2.11. NMR studies for peptide **3.3j** (25 mM, in CD_2Cl_2) with CsF.

At 233 K, the ^1H NMR spectrum revealed two diagnostic doublets (at 14.17 and 11.52 ppm) indicating the presence of two stable H-bonds to fluoride, reminiscent of binding mode described for **2d** (*v.* Section 3.2.1.2). However, no 2D NMR techniques were successful in confirming the identity of NH resonances due to too short T_2 relaxation times caused by dynamic fluoride binding. The observation of a broad peak by both ^{19}F NMR (−60.7 ppm) and ^{133}Cs NMR (+43.1 ppm) at 233 K indicated the presence of one stable species observable by NMR, which was assigned as a 1:1 peptide-fluoride complex based on the chemical shift of F^-.[1]

The assignment of doublets in the ^{1}H NMR spectrum was established by the synthesis of ^{15}N-labelled variants **3.3j-^{15}NH(*i+1*)** and **3.3j-^{15}NH(*i−2*)** (**Figure 3.2.12a**). ^{15}N-labelled analogues were prepared following procedure described in **Scheme 2.2.2** using ^{15}N-labelled building blocks **5.19** and **5.12**. Isocyanate **5.19** was prepared in 8 steps adapting literature methods from commercially available $Na^{15}NO_3$ salt (details in Experimental section).

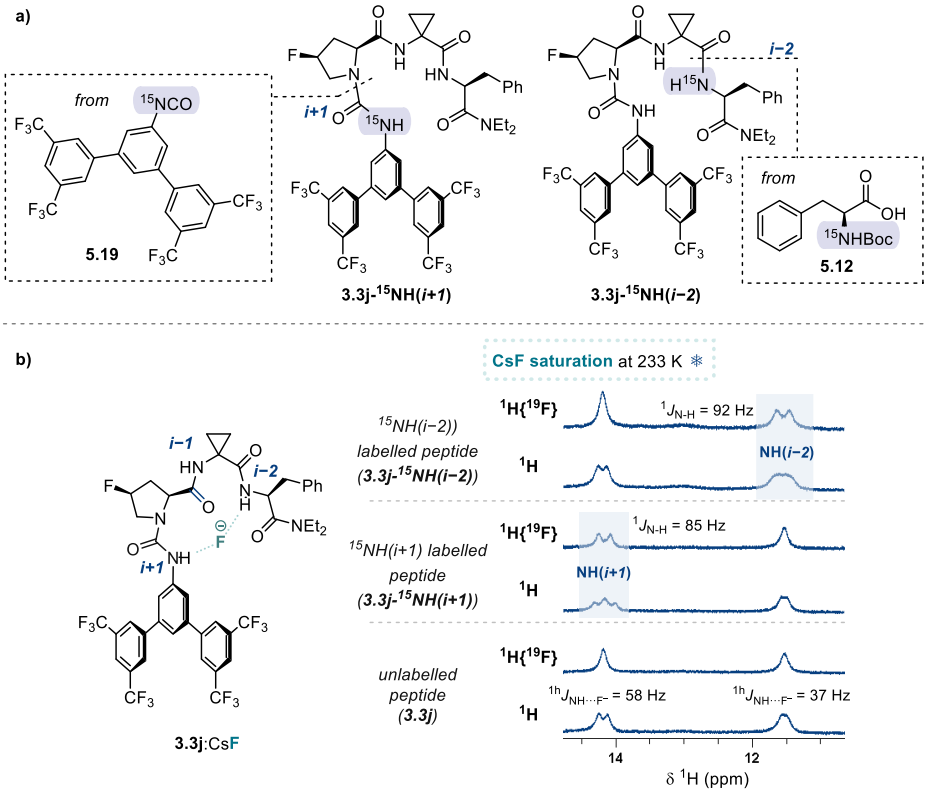

Figure 3.2.12. a) Structures of **3.3j-^{15}NH(*i+1*)** and **3.3j-^{15}NH(*i−2*)**. b) NMR studies for ^{15}N-labelled **3.3j** analogues with CsF and proposed binding mode of **3.3j**:CsF.

The ^{15}N-labelled analogues of **3.3j** were subjected to the same NMR experiment as described above to form peptide:CsF complexes (**Figure 3.2.12b**). ^{1}H{^{19}F} NMR experiments of the corresponding CsF complexes revealed $^{1}J_{H\text{-}N}$ heteronuclear couplings, which enabled unambiguous assignment of the resonances as NH(*i+1*) (14.17 ppm, $^{1h}J_{NH\cdots F^-}$ = 58 Hz, $^{1}J_{H\text{-}N}$ = 85 Hz) and NH(*i−2*) (11.52 ppm, $^{1h}J_{NH\cdots F^-}$ = 37 Hz, $^{1}J_{H\text{-}N}$ = 92 Hz). It has been previously shown that $^{1h}J_{NH\cdots F^-}$ values extracted for HBD:CsF complexes correlate with NH···F$^-$ internuclear distances measured from solid-state structures,[1] suggesting that the relative H-bonding distances for **3.3j** are NH(*i*+1)···F$^-$ < NH(*i−2*)···F$^-$, and no H-bonding interaction with NH(*i−1*).

3.2.4.2. Cesium chelation

Similarly to other ureido-peptides described in Section 3.2.1.2, bidentate fluoride binding within **3.3j**:CsF complex differs from the tridentate binding of TBAF$(H_2O)_3$, highlighting the impact of counter-cation (TBA^+ versus Cs^+) on peptide-fluoride binding (**Figure 3.2.13**).

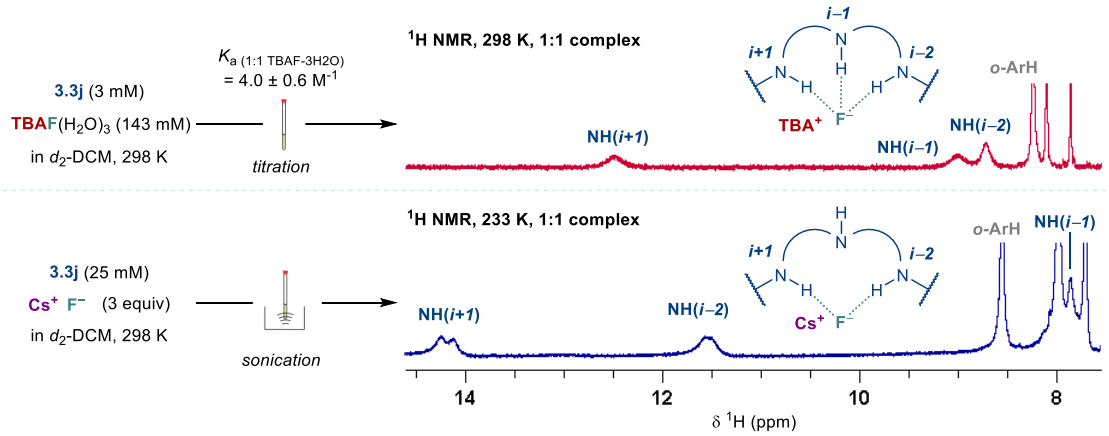

Figure 3.2.13. NH···F^- contacts for **3.3j**:TBAF$(H_2O)_3$ and **3.3j**:CsF complexes based on NMR studies.

This was in contrast to BINAM *bis*-ureas that exhibited tridentate binding to fluoride via X-ray single crystal crystallographic and computational studies, irrespective of the cation.[1,11-12] In previous investigation of BINAM *bis*-urea catalyst for HB-PTC, a HBD:CsF fluoride complex was successfully characterised via NMR spectroscopy (in CD_2Cl_2), DFT calculations and single X-ray crystallography.[1,11] Based on solid state (X-ray) and solution phase (qHOESY NMR) structural studies the change in cation (Cs^+ *versus* TBA^+) did not significantly alter the overall structure of the catalyst-F^- complex maintaining the tridentate binding mode to fluoride (**Figure 3.2.14**). Slightly deviated H-bonding distances by −5.7%, +1.1% and +9.0% were observed for NH(a−c)···F^- to accommodate for Cs^+—F^- ion pairing and Cs^+—π interaction.

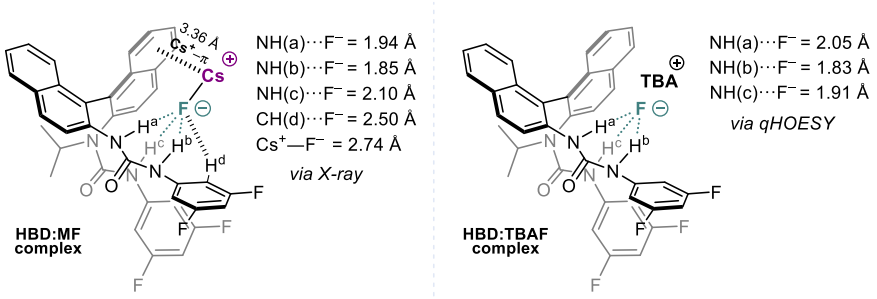

Figure 3.2.14. Comparison of F^- binding modes of corresponding BINAM *bis*-urea catalyst complexes with CsF and TBAF.[1,11-12]

The wide spectral dispersion of ^{133}Cs chemical shifts (~240 ppm)[29] offers ^{133}Cs NMR as a sensitive technique for the investigation of local environments of cesium ions, particularly for examining ion-pairing interactions. Since NMR investigations in this study are conducted in CD_2Cl_2, a non-coordinating solvent, cation–solvent interactions are expected to be minimal, implying that measured ^{133}Cs chemical shifts will be the most sensitive towards interactions with the peptide and counter anion. Generally, downfield chemical shifts of ^{133}Cs are attributed to increased electron density *i.e.* more coordinated Cs^+.[29a,30] The ^{133}Cs NMR spectrum of **3.3j**:CsF revealed a sharp peak at +25.9 ppm at room temperature (**Figure 3.2.15**). Previously only two cases of ^{133}Cs NMR in CD_2Cl_2 were reported; −14.1 ppm for BINAM-based *bis*-urea catalyst (**1.1.7**) and CsF complex,[1] and +17.3 ppm for $Cs^+[H_2NB_2(C_6F_5)_6]^-$,[31] both at 298 K. These data indicate that Cs^+ in **1.1.7**:CsF complex is the least shielded, which is consistent with the solid-state structure described previously (**Figure 3.2.14**). Meanwhile, **3.3j**:CsF showcased the most deshielded resonance indicating significant Cs^+ chelation to peptide. In comparison, even six-coordinate 18-crown-6:CsF complex at room temperature in CD_2Cl_2 displayed a sharp peak at slightly lower chemical shift compared to **3.3j**:CsF complex (25.9 *versus* 21.2 ppm). The 18-crown-6:CsF complex was prepared in an analogous manner to **3.3j**:CsF and was assigned as 1:1 complex due to excess of CsF used for sample preparation and prior precedence for CsCl.[32]

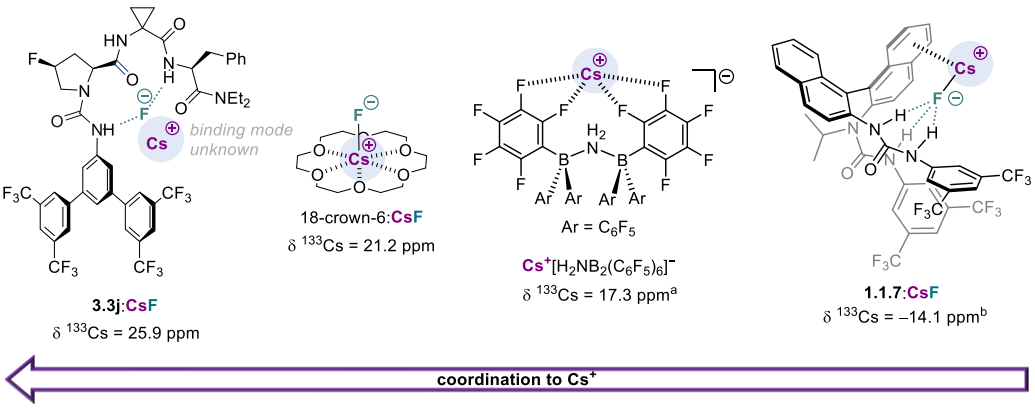

Figure 3.2.15. δ(^{133}Cs) of Cs^+ complexes in CD_2Cl_2 at 298 K. [a]ref[31]; [b]ref[1].

In order to probe Cs^+-binding further, insoluble $CsBAr^F_4$ (1.2 equiv.; BAr^F_4= *tetrakis*[3,5-*bis*(trifluoromethyl)phenyl]borate) with its weakly-coordinating anion was subjected to **3.3j** (25 mM in CD_2Cl_2). At room temperature, the ^{133}Cs NMR spectrum revealed two overlapping singlets

at 4.6 and 4.8 ppm, confirming that **3.3j** can specifically solubilise Cs^+ (**Figure 3.2.16**). The higher $\delta^{133}Cs$ for **3.3j**:CsF compared to **3.3j**:$CsBAr^F_4$ (25.9 *versus* ~4.7 ppm) was attributed to Cs^+—F^- ion pairing, and minimally perturbed binding site. In comparison, 18-crown-6:$CsBAr^F_4$ (−27.1 and −25.8 ppm) and 18-crown-6:CsF (+21.2 ppm) complexes displayed even more pronounced $\Delta\delta^{133}Cs$ due to stronger Cs^+—F^- interaction, since F^- only interacts with Cs^+. Of note, an opposite effect was observed for BINAM *bis*-urea catalyst **1.1.7** when comparing ^{133}Cs NMR chemical shifts of complexes with $CsBAr^F_4$ and CsF (+17.4 ppm *versus* −14.1 ppm, at 298 K in CD_2Cl_2; **Figure 3.2.16**), which indicates **1.1.7**:Cs^+ binding being outcompeted by ionic binding to F^- anion, consistent with the X-ray single crystal structure (**Figure 3.2.14**).

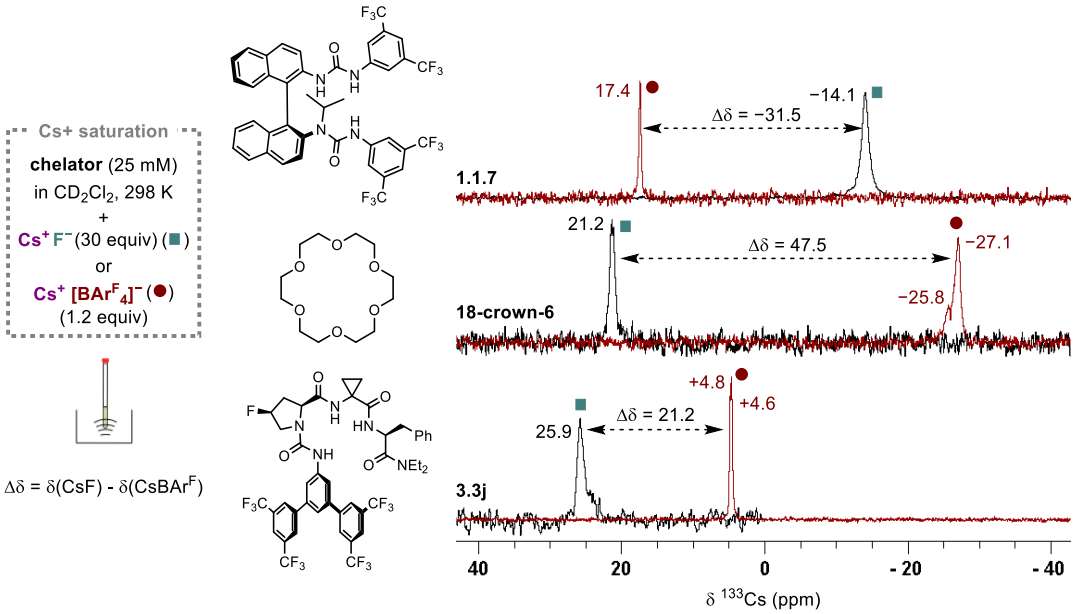

Figure 3.2.16. ^{133}C NMR spectrum of **3.3j**, **1.1.7** and 18-crown-6 complexed with CsF and $CsBAr^F_4$.

^1H NMR studies of **3.3j**:$CsBAr^F_4$ complex (**Figure 3.2.17**) showcased significant shifting upfield of resonances associated with 1,3-terphenyl ring, with H^1 and H^4 shifting the most ($\Delta\delta\ ^1H$ = −0.13 and −0.14 ppm, respectively). Also, significant shielding was observed for Phe(*i*−*2*) aromatic ring protons ($\Delta\delta$ H = −0.12 and −0.43 ppm), which was corroborated by slightly shifted C^β(*i*−*2*) ($\Delta\delta$ H = −0.16 and −0.20 ppm). This indicates disrupted CH−π stacking between aromatic rings and the formation of an aromatic cage around the cation, which has been well documented for Cs^+.[33] Also, calculations have shown that the Cs^+−π interaction with benzene are significantly more favourable than benzene dimer π−π interactions (ΔE = −9.6 kcal mol^{-1}, in the gas-phase).[34] For

3.3j:CsBAr$^{F}_{4}$ complex, upfield shifting of the NH(*i*+*1*) (Δδ H = −0.72 ppm) could be an indication of C=O(*i*+*1*) chelation, which is supported by slight shielding of H^{15} and H^{12} protons (Δδ ^{1}H = −0.14 and −0.09 ppm, respectively). Such backbone carbonyl and side-chain chelation has been calculated to be particularly favourable for aromatic residues (*v.* Section 3.1.1). Another potential C=O contact was proposed as C=O(*i*−*2*) due to the change of H^{23} by −0.34 ppm. Notably, similar shifting of the aromatic protons was not observed for the **3.3j**:CsF complex indicating a different binding mode, reliant only on C=O chelation. However, exact coordination of Cs^{+} in **3.3j**:CsF complex could not be determined. Full assignment of ^{1}H and ^{13}C NMR spectra of **3.3j**:CsBAr$^{F}_{4}$ complex is provided in the Experimental section.

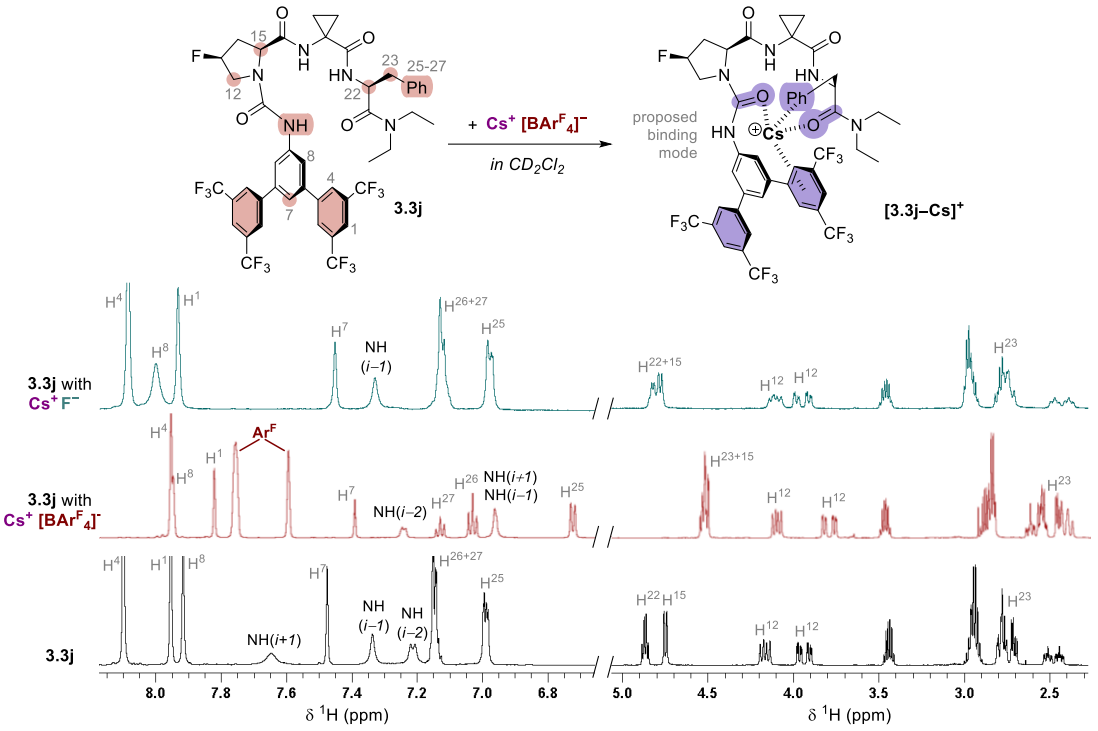

Figure 3.2.17. Proposed binding mode of **3.3j**:CsBAr$^{F}_{4}$ in CD_2Cl_2.

In conclusion, these results demonstrate that Cs^{+} plays an active role in the solubilisation of CsF by peptides. There is strong evidence that the Cs^{+} cation also coordinates to the **3.3j** peptide scaffold, inducing pronounced changes in the **3.3j**–F^{-} complex and altering its denticity toward fluoride. To gain further insight into the specific chelation sites and structural consequences of Cs^{+} coordination, we turned to computational studies.

3.2.4.3. Computational investigations

Further investigations of the Cs^+ binding mode involved computational studies of the solution-phase CsF-complex of **3.3i** (computationally less demanding analogue of **3.3j**). Experimentally, peptide **3.3i** displayed similar binding mode to TBAF (tridentate fluoride coordination) and CsF (bidentate binding to fluoride) compared to **3.3j** (*v.* Experimental section). Initial conformational search with Global Optimizer Algorithm (GOAT)[35] for **3.3i**:CsF resulted in conformers ranging from no chelation of fluoride to tridentate coordination. Conformers obtained from subsequent DFT calculations were further grouped into eight classes (**A**–**H**) based on the number of H-bonding contacts between **3.3i** and F^-, using an NH···F^- ≤ 2.0 Å criterion (**Figure 3.2.18**). **Class C** in which NH(*i*+*1*) and NH(*i*−2) bind to fluoride, was the most stable ensemble, followed by the other two bidentate binding modes (**Class D** and **Class B**). The tridentate mode (**Class A**) was ranked the fifth, whereas **Class H** without fluoride chelation was the least stable ensemble.

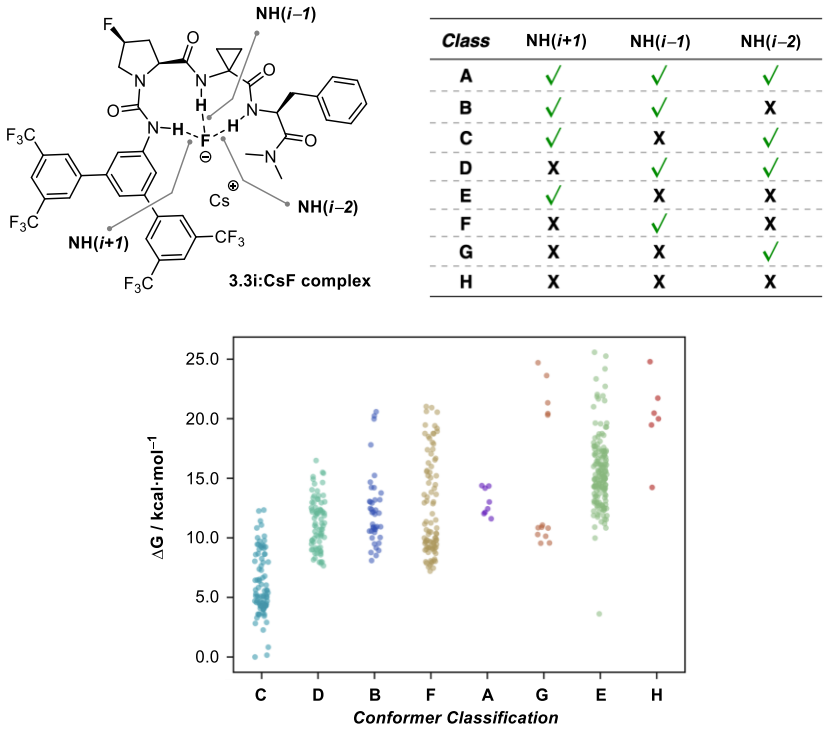

Figure 3.2.18. Conformer classification of **3.3i**:CsF complex.

The structure with the lowest global Gibbs free energy (conformer in **Class C**) featured bidentate H-bonding to fluoride with NH(*i*+*1*)···F^- (1.64 Å) < NH(*i*−*2*)···F^- (1.71 Å); **Figure 3.2.19**), in line with experimental NMR data. In addition, **3.3i**:CsF (**C**) complex featured bidentate chelation

to cesium via two carbonyls (2.98 and 3.01 Å) and a slightly elongated Cs^+—F^- ion pair (2.82 Å) compared to ionic CsF (2.69 Å).[36] An alternative conformation with tridentate binding to fluoride in **Class A** resulted in a complex that is 11.6 kcal mol^{-1} higher in energy, which could be attributed to a dissociated $Cs^+\cdots F^-$ pair (4.73 Å). These experiments showcase that the phase-transfer ability of peptide catalysts could be attributed to their ability to serve as chelators to F^- (via NH groups) and Cs^+ (via carbonyls), as evidenced by NMR spectroscopic studies and GOAT-DFT calculations.

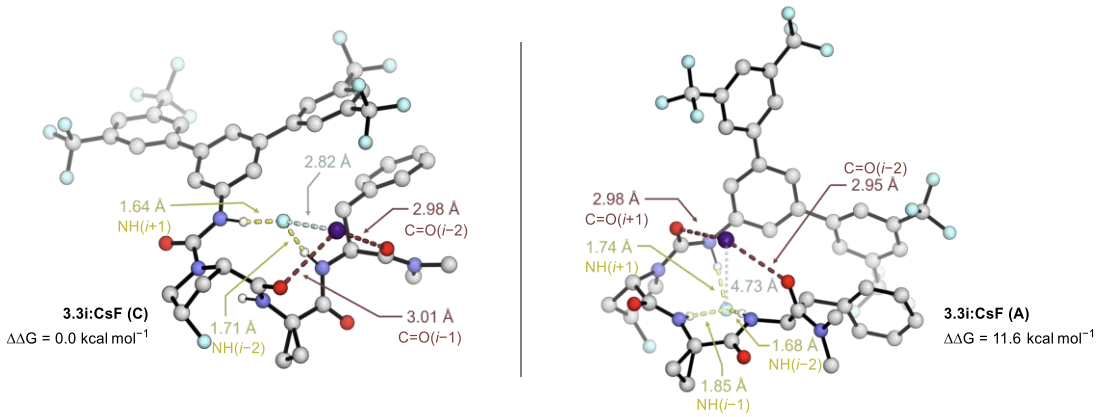

Figure 3.2.19. Structures of **3.3i**:CsF with the lowest Gibbs free energies in **Class C** and **A**.

The computed **3.3i**:CsF structure is consistent with comparative NMR experiments using CsF and $CsBArF_4$ salts, which indicated that Cs^+ in the **3.3j**:CsF complex does not engage in cation–π interactions with aromatic residues (*v.* Section 3.2.4.2). The identity of the coordinating carbonyl groups also rationalises trends observed during catalyst optimisation. For example, catalyst bearing a methyl ester *C*-cap compared to *N*,*N*-dimethylamide displayed lower enantioselectivity, consistent with weaker carbonyl coordination to Cs^+. Also, proline *endo*-pucker reduced NH(*i*−*1*) participation in fluoride binding resulted in higher selectivity, likely favouring interaction between C=O(*i*−*1*) and the cation. Although the catalytic cycle for HB-PTC indicates that the enantiodetermining step involves collapse of the catalyst–F^-/aziridinium ion pair, the data suggest that insights of Cs^+-induced organisation of the peptide could also be informative in rationalising the observed enantioselectivity.

3.3. Conclusion

In this chapter, NMR studies established that peptides **2a–s** are capable of solubilising CsF through dual chelation of F^- and Cs^+. Importantly, peptide–CsF complexation differs significantly from peptide–TBAF interactions. Whereas $TBAF(H_2O)_3$ titrations consistently revealed tridentate fluoride binding in ureido-peptides, CsF complexation frequently resulted in bidentate binding modes, reflecting the active structural role of Cs^+. Moreover, higher $K_{a\ (1:1\ TBAF\text{-}3H2O)}$ did not translate into more stable CsF–peptide complexes, as observed by low-temperature NMR experiments, underscoring the dominant influence of peptide conformation on complex stability.

Catalytic screening revealed that all investigated peptides were capable, to varying extents, of promoting nucleophilic fluorination under HB-PTC. Across a broad range of peptide–TBAF binding affinities ($K_{a\ (1:1\ TBAF\text{-}3H2O)}$ = 10^1–10^5 M^{-1}, in CD_2Cl_2), no direct correlation between binding strength and fluorination yield was observed. These findings highlight that fluoride binding strength alone is insufficient to rationalise catalytic performance in this complex system, which balances CsF solubilisation, catalyst solubility, ion-pair reorganisation, and controlled fluoride release. Excessively weak binding compromised phase-transfer efficiency, as demonstrated by tetrapeptide **2a** ($K_{a\ (1:1\ TBAF\text{-}3H2O)}$ = 52 ± 5 M^{-1}, in CD_2Cl_2), which afforded only 14% yield. In contrast, the most effective catalyst exhibited moderate affinity (**2i**, $K_{a\ (1:1\ TBAF\text{-}3H2O)}$ ≈ 10^4 M^{-1}, in CD_2Cl_2) and delivered fluorinated product in 86% yield, confirming that optimal reactivity requires a finely tuned binding environment rather than maximal affinity.

Guided by structural insights from Chapter II and screening of **2a–s**, iterative optimisation led to catalyst **3.3j**, which delivered 86% yield and 88:12 *e.r.* for the model substrate. Subjecting **3.3j** to a range of cyclic β-bromoamines and stilbene-based β-chloramines demonstrated clear complementarity with BINAM *bis*-urea catalyst **1.2.9**. Catalyst **3.3j** outperformed the BINAM system for most cyclic substrates, affording yields up to 92% and up to 89:11 *e.r.*

Finally, detailed NMR investigations of the **3.3j**:CsF complex in-depth insight into peptide–fluoride–cesium interactions. ^{15}N-labelling of **3.3j** confirmed bidentate H-bonding to fluoride via urea NH(*i*+*1*) (14.17 ppm, $^{1h}J_{NH\cdots F^-}$ = 58 Hz) and peptide backbone NH(*i*−*2*) (11.52 ppm, $^{1h}J_{NH\cdots F^-}$

= 37 Hz), while GOAT-DFT computations supported additional coordination of Cs^+ by peptide backbone C=O(*i*−*2*) and C=O(*i*−*1*). These studies demonstrate that Cs^+ induces pronounced conformational organisation of the peptide scaffold. Cesium chelation was observed even in the absence of fluoride, with proposed aromatic cage around Cs^+ formed by the *N*-cap and *i*−*2* residue. Evaluation of alternative alkali metal fluorides or mixed-cation systems in future work may further clarify how metal coordination geometry influences reactivity and selectivity.

Collectively, this chapter establishes that peptides can function as dual H-bonding and metal-chelating phase-transfer agents for CsF, enabling nucleophilic fluorination under HB-PTC (**Figure 3.3.1**). Through systematic conformational tuning and binding studies, it was shown that control over the fluoride microenvironment directly governs reactivity and selectivity. Beyond advancing the fundamental understanding of fluoride binding to peptidic scaffolds, this work defines a mechanistic and structural framework for the continued development of peptide-based anion-binding catalysis.

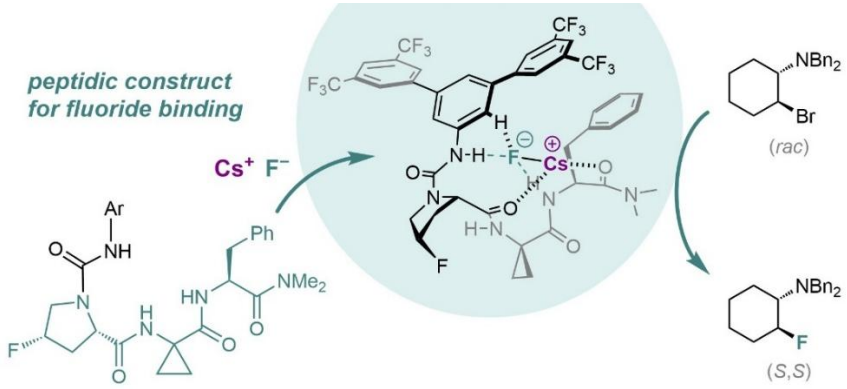

Figure 3.3.1. Peptide catalyst **3.3j** for HB-PTC-mediated asymmetric nucleophilic fluorination using CsF.

3.4. References

(1) Ibba, F.; Pupo, G.; Thompson, A. L.; Brown, J. M.; Claridge, T. D. W.; Gouverneur, V. Impact of Multiple Hydrogen Bonds with Fluoride on Catalysis: Insight from NMR Spectroscopy. *J. Am. Chem. Soc.* **2020**, *142* (46), 19731–19744.

(2) (a) Bassan, G. A.; Marchesan, S. Peptide-Based Materials That Exploit Metal Coordination. *Int. J. Mol. Sci.* **2023**, *24* (1), 456; (b) Ovchinnikov, Y. A. Ionophores and channels. *Int. J. Quantum Chem* **1981**, *20* (2), 461–478.

(3) (a) Ruan, C.; Rodgers, M. T. Cation−π Interactions: Structures and Energetics of Complexation of Na^+ and K^+ with the Aromatic Amino Acids, Phenylalanine, Tyrosine, and Tryptophan. *J. Am. Chem. Soc.* **2004**, *126* (44), 14600–14610; (b) Armentrout, P. B.; Yang, B.; Rodgers, M. T. Metal Cation Dependence of Interactions with Amino Acids: Bond Energies of Rb+ and Cs^+ to Met, Phe, Tyr, and Trp. *J. Phys. Chem. B* **2013**, *117* (14), 3771–3781; (c) Rodgers, M. T.; Armentrout, P. B. A Thermodynamic "Vocabulary" for Metal Ion Interactions in Biological Systems. *Acc. Chem. Res.* **2004**, *37* (12), 989–998.

(4) (a) Pfeiffer, P.; Modelski, J. Verhalten der Aminosäuren und Polypeptide gegen Neutralsalze. I. Mitteilung. *Biol. Chem.* **1912**, *81* (4), 329–354; (b) Pfeiffer, P. Neutralsalzverbindungen der Aminosäuren und Polypeptide. IV. Experimentell bearbeitet von Mathilde Klossmann und Olga Angern. *Biol. Chem.* **1924**, *133* (1-4), 22–61.

(5) Gal, J.-F.; Maria, P.-C.; Massi, L.; Mayeux, C.; Burk, P.; Tammiku-Taul, J. Cesium cation affinities and basicities. *Int. J. Mass Spectrom.* **2007**, *267* (1), 7–23.

(6) (a) Brockmann, H.; Schmidt-Kastner, G. Valinomycin I, XXVII. Mitteil. über Antibiotica aus Actinomyceten. *Chem. Ber.* **1955**, *88* (1), 57–61; (b) Andreoli, T. E.; Tieffenberg, M.; Tosteson, D. C. The Effect of Valinomycin on the Ionic Permeability of Thin Lipid Membranes. *J. Gen. Physiol.* **1967**, *50* (11), 2527–2545; (c) Rose, M. C.; Henkens, R. W. Stability of sodium and potassium complexes of valinomycin. *Biochim. Biophys. Acta, Gen. Subj.* **1974**, *372* (2), 426–435.

(7) (a) Taira, T.; Yanagisawa, S.; Nagano, T.; Zhu, Y.; Kuroiwa, T.; Koumura, N.; Kitamoto, D.; Imura, T. Selective encapsulation of cesium ions using the cyclic peptide moiety of surfactin: Highly efficient removal based on an aqueous giant micellar system. *Colloids Surf. B Biointerfaces* **2015**, *134*, 59–64; (b) Pichierri, F. DFT study of caesium ion complexation by cucurbit[*n*]urils (*n* = 5–7). *Dalton Trans.* **2013**, *42* (17), 6083–6091.

(8) Kofron, J. L.; Kuzmic, P.; Kishore, V.; Colon-Bonilla, E.; Rich, D. H. Determination of kinetic constants for peptidyl prolyl cis-trans isomerases by an improved spectrophotometric assay. *Biochemistry* **1991**, *30* (25), 6127–6134.

(9) Baldauf, C.; Pagel, K.; Warnke, S.; von Helden, G.; Koksch, B.; Blum, V.; Scheffler, M. How Cations Change Peptide Structure. *Chem. – Eur. J.* **2013**, *19* (34), 11224–11234.

(10) (a) Semrouni, D.; Balaj, O. P.; Calvo, F.; Correia, C. F.; Clavaguéra, C.; Ohanessian, G. Structure of sodiated octa-glycine: IRMPD spectroscopy and molecular modeling. *J. Am. Soc. Mass. Spectrom.* **2010**, *21* (5), 728–738; (b) Kohtani, M.; Kinnear, B. S.; Jarrold, M. F. Metal-Ion Enhanced Helicity in the Gas Phase. *J. Am. Chem. Soc.* **2000**, *122* (49), 12377–12378; (c) Martens, J. K.; Compagnon, I.; Nicol, E.; McMahon, T. B.; Clavaguéra, C.; Ohanessian, G. Globule to Helix Transition in Sodiated Polyalanines. *J. Phys. Chem. Lett.* **2012**, *3* (22), 3320–3324.

(11) Pupo, G.; Ibba, F.; Ascough, D. M. H.; Vicini, A. C.; Ricci, P.; Christensen, K. E.; Pfeifer, L.; Morphy, J. R.; Brown, J. M.; Paton, R. S.; Gouverneur, V. Asymmetric nucleophilic fluorination under hydrogen bonding phase-transfer catalysis. *Science* **2018**, *360* (6389), 638–642.

(12) Pupo, G.; Vicini, A. C.; Ascough, D. M. H.; Ibba, F.; Christensen, K. E.; Thompson, A. L.; Brown, J. M.; Paton, R. S.; Gouverneur, V. Hydrogen Bonding Phase-Transfer Catalysis with Potassium Fluoride: Enantioselective Synthesis of β-Fluoroamines. *J. Am. Chem. Soc.* **2019**, *141* (7), 2878–2883.

(13) Vicini, A. C.; Alozie, D.-M.; Courtes, P.; Roagna, G.; Aubert, C.; Certal, V.; El-Ahmad, Y.; Roy, S.; Gouverneur, V. Scalable Synthesis of (*R*,*R*)-*N*,*N*-Dibenzyl-2-fluorocyclohexan-1-amine with CsF under Hydrogen Bonding Phase-Transfer Catalysis. *Org. Process Res. Dev.* **2021**, *25* (12), 2730–2737.

(14) (a) Sakamoto, H.; Sugimoto, T. Preparation of Heterocyclic Compounds as Cholinergic Muscarinic M1 Receptor Positive Allosteric Modulators. WO2013129622, 2013; (b) Coburn, C. A.; Egbertson, M. S.; Graham, S. L.; Mcgaughey, G. B.; Stauffer, S. R.; Yang, W.; Lu, W.; Fahr, B. Spiropiperidine beta-secretase inhibitors for the treatment of alzheimer's disease WO2007011833, 2007.

(15) (a) Xie, Q.; Hu, J. Monofluoromethylation Reactions of Aliphatic Substrates and (Hetero)Arenes. In *Emerging Fluorinated Motifs*, 2020, 119–133; (b) Grygorenko, O. O.; Melnykov, K. P.; Holovach, S.;

Demchuk, O. Fluorinated Cycloalkyl Building Blocks for Drug Discovery. *ChemMedChem* **2022**, *17* (21), e202200365.

(16) (a) Sato, K.; Hoshino, K.; Tanaka, M.; Hayakawa, I.; Osada, Y. Antimicrobial activity of DU-6859, a new potent fluoroquinolone, against clinical isolates. *Antimicrob. Agents Chemother.* **1992**, *36* (7), 1491–1498; (b) David, E. C.; Kenneth, P. A. M. Chemical compounds. US2003158146A1, 2003.

(17) (a) Burger, M. L., J.; Lindvall, M.; Nishiguchi, G.; Tetalman, M. PIM Kinase Inhibitors and Methods of Their Use. WO2009109576A1, 2009; (b) Bolli, M.; Gatfield, J.; Grisostomi, C.; Remen, L.; Sager, C.; Zumbrunn, C. Triazolyl-methyl substituted alpha-d-galactopyranoside derivatives. WO2022184755A1, 2022; (c) Groebke-Zbinden, K.; Haap, W.; Hilpert, H.; Panday, N.; Ricklin, F.; Wirz, B. Novel cyclic amines WO2006114401A2, 2006.

(18) (a) Lichter, R. L. Nitrogen Nuclear Magnetic Resonance Spectroscopy. In *The Multinuclear Approach to NMR Spectroscopy*, Lambert, J. B., Riddell, F. G. Eds.; Springer Netherlands, 1983, 207–244; (b) Hoch, J. C.; Baskaran, K.; Burr, H.; Chin, J.; Eghbalnia, Hamid R.; Fujiwara, T.; Gryk, Michael R.; Iwata, T.; Kojima, C.; Kurisu, G.; Maziuk, D.; Miyanoiri, Y.; Wedell, Jonathan R.; Wilburn, C.; Yao, H.; Yokochi, M. Biological Magnetic Resonance Data Bank. *Nucleic Acids Res.* **2022**, *51* (D1), D368–D376.

(19) Williamson, M. P. Using chemical shift perturbation to characterise ligand binding. *Prog. Nucl. Magn. Reson. Spectrosc.* **2013**, *73*, 1–16.

(20) Wang, B.; Fan, S.; Zhang, C.; Sun, J. Catalytic Enantioselective α-Fluorination of Ketones with CsF. *J. Am. Chem. Soc.* **2025**, *147* (12), 10059–10065.

(21) Metrano, A. J.; Abascal, N. C.; Mercado, B. Q.; Paulson, E. K.; Hurtley, A. E.; Miller, S. J. Diversity of Secondary Structure in Catalytic Peptides with β-Turn-Biased Sequences. *J. Am. Chem. Soc.* **2017**, *139* (1), 492–516.

(22) Gilli, P.; Pretto, L.; Bertolasi, V.; Gilli, G. Predicting Hydrogen-Bond Strengths from Acid−Base Molecular Properties. The pK_a Slide Rule: Toward the Solution of a Long-Lasting Problem. *Acc. Chem. Res.* **2009**, *42* (1), 33–44.

(23) (a) Brak, K.; Jacobsen, E. N. Asymmetric Ion-Pairing Catalysis. *Angew. Chem., Int. Ed.* **2013**, *52* (2), 534–561; (b) Ovian, J. M.; Vojáčková, P.; Jacobsen, E. N. Enantioselective transition-metal catalysis via an anion-binding approach. *Nature* **2023**, *616* (7955), 84–89; (c) Dooley, C.; Ibba, F.; Botlik, B. B.; Palladino, C.; Goult, C. A.; Gao, Y.; Lister, A.; Paton, R. S.; Lloyd-Jones, G. C.; Gouverneur, V. Enantioconvergent nucleophilic substitution via synergistic phase-transfer catalysis. *Nat. Catal.* **2025**, *8* (2), 107–115.

(24) Starks, C. M.; Liotta, C. L.; Halpern, M. E. *Phase-Transfer Catalysis: Fundamentals, Applications, and Industrial Perspectives*; Chapman and Hall Publications, 1994.

(25) Seebach, D.; Thaler, A.; Beck, A. K. Solubilization of Peptides in Non-polar Organic Solvents by the Addition of Inorganic Salts: Facts and Implications. *Helv. Chim. Acta* **1989**, *72* (5), 857–867.

(26) Vicini, A. Hydrogen bonding phase-transfer catalysis with alkali metal fluorides: enantioselective synthesis of β-fluoroamines from reaction development to scale-up. University of Oxford, 2020.

(27) Haynes, W. M. *CRC Handbook of Chemistry and Physics*; 84th ed., CRC Press, 2004.

(28) (a) Luethi, D.; Hoener, M. C.; Liechti, M. E. Effects of the new psychoactive substances diclofensine, diphenidine, and methoxphenidine on monoaminergic systems. *Eur. J. Pharmacol.* **2018**, *819*, 242–247; (b) Janiri, L.; Persico, A. M.; Tempesta, E. Dual effects of lephetamine on spontaneous and evoked neuronal firing in the somatosensory cortex of the rat. *Neuropharmacology* **1989**, *28* (12), 1405–1410.

(29) (a) Dijkstra, G.; Kruizinga, W. H.; Kellogg, R. M. An assessment of the causes of the "cesium effect". *J. Org. Chem.* **1987**, *52* (19), 4230–4234; (b) Hayashi, S.; Hayamizu, K. Accurate Determination of NMR Chemical Shifts in Alkali Halides and Their Correlation with Structural Factors. *Bull. Chem. Soc. Jpn.* **1990**, *63* (3), 913–919.

(30) (a) Popov, A. I. Multinuclear NMR studies of alkali ions in nonaqueous solvents. *Pure Appl. Chem.* **1979**, *51* (1), 101–110; (b) DeWitte, W. J.; Liu, L.; Mei, E.; Dye, J. L.; Popov, A. I. Spectroscopic studies of ionic solvation. XX. Cesium-133 NMR study of cesium salts in different solvents. *J. Solution Chem.* **1977**, *6* (5), 337–348; (c) Khazaeli, S.; Dye, J. L.; Popov, A. I. Cesium-133 nuclear magnetic resonance study of the complexation of cesium salts by 18-crown-6 in methylamine and liquid ammonia. 2. 2:1 Complex formation. *J. Phys. Chem.* **1983**, *87* (10), 1830–1833.

(31) Pollak, D.; Goddard, R.; Pörschke, K.-R. Cs[$H_2NB_2(C_6F_5)_6$] Featuring an Unequivocal 16-Coordinate Cation. *J. Am. Chem. Soc.* **2016**, *138* (30), 9444–9451.

(32) Jing, Z.; Zhou, Y.; Zhang, W.; Yamaguchi, T.; Yoshida, K.; Wang, G.; Han, L. Structures of 18-crown-6/Cs^+ complexes in aqueous solutions by wide angle X-ray scattering and density functional theory. *J. Mol. Liq.* **2022**, *360*, 119477.

(33) (a) Kennedy, C. R.; Guidera, J. A.; Jacobsen, E. N. Synergistic Ion-Binding Catalysis Demonstrated via an Enantioselective, Catalytic [2,3]-Wittig Rearrangement. *ACS Cent. Sci.* **2016**, *2* (6), 416–423; (b) Yamada, S. Cation−π Interactions in Organic Synthesis. *Chem. Rev.* **2018**, *118* (23), 11353–11432.

(34) (a) Tsuzuki, S.; Yoshida, M.; Uchimaru, T.; Mikami, M. The Origin of the Cation/π Interaction: The Significant Importance of the Induction in Li^+ and Na^+ Complexes. *J. Phys. Chem. A* **2001**, *105* (4), 769–773; (b) Tsuzuki, S.; Mikami, M.; Yamada, S. Origin of Attraction, Magnitude, and Directionality of Interactions in Benzene Complexes with Pyridinium Cations. *J. Am. Chem. Soc.* **2007**, *129* (27), 8656–8662.

(35) de Souza, B. GOAT: A Global Optimization Algorithm for Molecules and Atomic Clusters. *Angew. Chem., Int. Ed.* **2025**, *64* (18), e202500393.

(36) Zhu, Q.; Oganov, A. R.; Zeng, Q. Formation of Stoichiometric CsF_n Compounds. *Sci. Rep.* **2015**, *5* (1), 7875.

Chapter IV

Summary and outlook

4.1. Summary

In search of new catalysts to expand the scope of nucleophilic fluorination via hydrogen bonding phase-transfer catalysis (HB-PTC), this work focuses on peptide-based scaffolds as structurally versatile alternatives to traditional urea and squaramide hydrogen bond donors (HBDs). Conceptually, such a system can be viewed as a minimalistic analogue of the fluorinase enzyme; however, its implementation is highly challenging. Achieving successful HB-PTC requires precise control over the balance between fluoride binding, solubilisation, and reactivity. This challenge is compounded by the limited understanding of peptide–fluoride interactions and the absence of established design strategies. Accordingly, this work explores peptides as a new platform for fluoride binding and delivery from first principles.

A central outcome of this study is the demonstration that peptide backbones can function as effective HBDs toward fluoride. Chapter II showed that fluoride binding in peptides is governed not simply by intrinsic NH acidity, but by a subtle interplay between conformational preorganisation, intramolecular H-bonding, and backbone flexibility. Rigid β-turn tetrapeptides were shown to enforce well-defined conformations but restrict fluoride binding to monodentate interactions due to internal hydrogen bonding (H-bonding) networks (binding affinity, $K_{a\ (1:1\ TBAF\text{-}3H2O)} \approx 10^1 - 10^2\ M^{-1}$, in CD_2Cl_2). In contrast, incorporation of a urea motif introduced

conformational plasticity, enabling tridentate fluoride binding and significantly enhanced binding affinities ($K_{a\ (1:1\ TBAF\text{-}3H2O)} \approx 10^3-10^5\ M^{-1}$, in CD_2Cl_2). These results demonstrate that strategic destabilisation of internal hydrogen-bonding networks is a critical design principle for enabling anion binding in peptide scaffolds.

Furthermore, this work demonstrates that fluoride binding in peptide systems can be tuned in a site-specific and modular manner. Through systematic variation of urea substituents and peptide residues, individual NH contributions to fluoride binding were independently modulated without necessarily altering overall affinity. This represents a departure from classical small-molecule HBDs, where acidity and binding strength are often intrinsically coupled, and highlights the unique advantage of peptides as conformationally tunable HBD scaffolds.

Building on these insights, translation into catalysis (Chapter III) revealed that peptide–fluoride interactions are inherently more complex under HB-PTC conditions than suggested by prior binding studies. In particular, the behaviour of CsF differs fundamentally from that of $TBAF(H_2O)_3$ (TBA^+ = tetra-*n*-butylammonium), with Cs^+ playing an active structural role in organising peptide conformation and modulating binding modes. The lack of direct correlation between $TBAF(H_2O)_3$ binding affinity and catalytic performance underscores that optimal catalysis arises from a balance of binding strength, ion-pair organisation, solubility, and controlled fluoride release, rather than maximal affinity alone.

In this context, this work reports the first example of peptide-mediated enantioselective nucleophilic fluorination using alkali metal fluorides. The optimised catalyst **3.3j** delivers cyclic β-fluoroamines in high yields (up to 99%) and moderate enantioselectivities (up to 89:11 *e.r.*) and shows clear complementarity to established C_2-symmetric BINAM-derived (BINAM = 1,1'-binaphthyl-2,2'-diamine) *bis*-urea catalysts. These results demonstrate that peptides can function as dual H-bonding and metal-chelating phase-transfer catalysts, capable of activating fluoride and controlling stereochemical outcome.

4.2. Future work

Building on the findings of this work, several opportunities for further development of peptide-based anion chemistry can be identified, spanning catalyst design, reactivity, and broader applications (**Figure 4.2.1**).

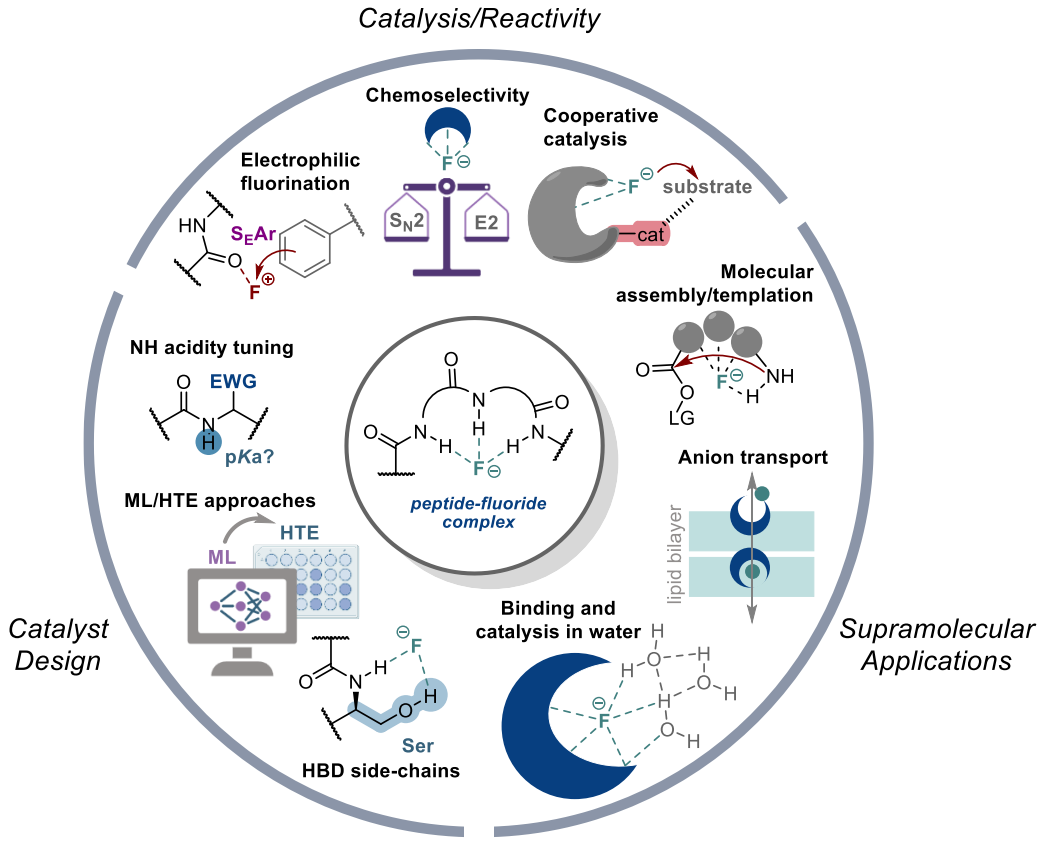

Figure 4.2.1. Overview of future directions in peptide–fluoride chemistry.

One of the challenges identified in this work was the limited practical strategies available to modulate the acid dissociation constant (p*K*a) of peptide backbone NH groups. While inductive effects from amino acid side chains are known to influence local electronic environments,[1] their impact on peptide backbone NH acidity has not been systematically quantified. Future studies on the systematic incorporation of electron-withdrawing amino acid side chains, such as fluorinated residues (*e.g.* β,β,β-trifluoroleucine), and the quantification of how inductive effects propagate to the backbone would therefore be highly insightful and provide a quantitative framework for rational catalyst design. In addition, as a natural progression of this work, exploration of functionalised amino acids capable of directly engaging fluoride or the associated alkali metal cation may offer complementary design strategies. For example, alcohol-containing side chains

(*e.g.* Ser or Thr), reminiscent of the fluorinase active site, may contribute to fluoride binding, while residues such as Met could potentially participate in alkali metal coordination. However, the increased conformational flexibility associated with such functionalities is likely to present a significant challenge for maintaining well-defined binding geometries.

Beyond tuning binding strength, such modifications are expected to influence the intrinsic reactivity of the bound fluoride species, including its basicity and nucleophilicity. Investigations into the chemoselectivity of fluoride species generated upon binding to HB-PTC catalysts remain underexplored. Prior work on TBAF complexes with urea and alcohol HBDs has shown a correlation between the interplay of fluoride basicity and nucleophilicity, with lower nucleophilicity resulting in improved selectivity (bimolecular nucleophilic substitution (S_N2) *versus* bimolecular elimination (E2)).[2] Related studies in H-bonding catalysis have shown that ion-pairing and non-covalent interactions strongly influence anion reactivity.[3] Similarly, Dooley *et al.* reported that the use of a BINAM-catalyst with alkali metal fluorides (CsF or KF) and an onium co-catalyst provides improved selectivity over TBAF–catalyst systems while maintaining comparable fluorination yields,[4] indicating that ion-pair structure under HB-PTC conditions also affects fluoride reactivity. Importantly, the present work demonstrates that binding affinity measured with $TBAF(H_2O)_3$ does not directly correlate with catalytic performance using CsF, highlighting the critical role of the alkali metal cation. Future work should therefore systematically investigate how cation identity, coordination geometry, and ion-pair dynamics influence fluoride reactivity.

The controlled modulation of fluoride binding and reactivity in peptide scaffolds may enable catalytic strategies that extend beyond traditional HB-PTC paradigms. The incorporation of (non-)canonical functionalised amino acids may enable cooperative activation of both the nucleophile (F^-) and electrophile, provided that the introduced functionalities are compatible with the fluoride species. For example, integration of transition metal centres within peptide scaffolds could further enable synergistic catalytic systems, combining peptide-controlled fluoride binding with metal-mediated substrate activation. The feasibility of such approaches is supported by recent work by Wang *et al.*,[5] demonstrating compatibility between HB-PTC and Rh-catalysed allylic fluorination, as well as by studies from Miller and co-workers on peptide–transition metal

(*e.g.* Cu[6] and Rh[7]) cooperative catalysis. In addition, the principles developed in this work may be extended to electrophilic fluorination. Developments in peptide-catalysed electrophilic halogenation reactions, *i.e.* S_EAr (electrophilic aromatic substitution) bromination and chlorination,[8] suggest that analogous strategies could be applied to F^+ reagents.

Achieving higher levels of stereocontrol will require advances in peptide architecture and structural preorganisation. Exploration of alternative secondary structures, including helices, turn–helix motifs, and cyclic peptides, may provide more rigid and well-defined chiral environments while maintaining multidentate binding capability. However, the vast structural diversity accessible to peptide catalysts presents a significant challenge for rational optimisation. Given this high-dimensional design space associated with peptides, high-throughput experimentation (HTE) offers a powerful approach for the rapid generation of structure–activity relationships. Work by Wennemers and co-workers has demonstrated the effectiveness of modular peptide libraries and combinatorial screening in identifying highly active catalysts.[9] More recently, the emergence of data-driven approaches has enabled the prediction of peptide catalyst performance from molecular descriptors and experimental datasets.[10] In this context, integration of HTE with machine-learning (ML) guided analysis could enable efficient navigation of peptide chemical space and identification of optimal sequences and non-intuitive structure–reactivity relationships.

A particularly challenging yet highly rewarding direction is the development of peptide-mediated fluorination in aqueous or biphasic systems. Given the strong hydration of fluoride, achieving effective binding and reactivity in the presence of water represents a significant challenge. Direct competition with water through peptide binding alone is unlikely to be sufficient and may instead lead to inert fluoride species. In fluorinase, partial dehydration is achieved via substrate docking within a well-defined binding pocket, where the reactive fluoride species is stabilised by only three hydrogen bonds (H-bonds).[11] Amphiphilic peptide designs may enable the formation of micellar or vesicular assemblies that encapsulate fluoride, while fluorous or hydrophobic domains could create water-excluding environments that stabilise reactive species. In such confined environments, reorganisation of the ion-pair may also become relevant, allowing cooperative

interactions between fluoride and its counter-cation to influence reactivity. Related work on peptide-based self-assembly and supramolecular ion transport demonstrates that amphiphilic peptides can form well-defined nanostructures capable of modulating ion behaviour.[12] Notably, diphenyl urea has been shown to maintain comparable binding affinity toward TBAF even in the presence of excess water (10 equivalents), suggesting that H-bonding receptors can tolerate a degree of hydration.[2b] In this context, systematic water titration studies would be valuable to assess whether the most effective peptide catalysts identified in this work can similarly retain fluoride binding under partially hydrated conditions. Furthermore, the effect of hydration on CsF–catalyst ion pairs remains largely unexplored and represents an important direction for future investigation.

Beyond catalysis, the fluoride-binding properties developed in this work open opportunities in anion transport and molecular organisation. For example, incorporation of amphiphilic features into peptide scaffolds may enable fluoride transport across membranes, drawing inspiration from both synthetic anion transporters and biological fluoride channels.[12a,13] Similarly, fluoride binding could be exploited to template peptide assembly, including head-to-tail cyclisation processes analogous to those reported for chloride-templated systems,[14] with the smaller size and higher charge density of fluoride potentially enabling tighter and more selective cyclic architectures.

Taken together, these directions highlight the potential of peptides as a modular platform for controlling fluoride binding and reactivity, with applications extending beyond catalysis.

4.3. References

(1) (a) Dwyer, D. S. Electronic properties of amino acid side chains: quantum mechanics calculation of substituent effects. *BMC Chemical Biology* **2005**, *5* (1), 2; (b) Lara-Popoca, J.; Thoke, H. S.; Stock, R. P.; Rudino-Pinera, E.; Bagatolli, L. A. Inductive effects in amino acids and peptides: Ionization constants and tryptophan fluorescence. *Biochemistry and Biophysics Reports* **2020**, *24*, 100802; (c) Salwiczek, M.; Nyakatura, E. K.; Gerling, U. I. M.; Ye, S.; Koksch, B. Fluorinated amino acids: compatibility with native protein structures and effects on protein–protein interactions. *Chem. Soc. Rev.* **2012**, *41* (6), 2135–2171.

(2) (a) Engle, K. M.; Pfeifer, L.; Pidgeon, G. W.; Giuffredi, G. T.; Thompson, A. L.; Paton, R. S.; Brown, J. M.; Gouverneur, V. Coordination diversity in hydrogen-bonded homoleptic fluoride–alcohol complexes modulates reactivity. *Chem. Sci.* **2015**, *6* (9), 5293–5302; (b) Pfeifer, L.; Engle, K. M.; Pidgeon, G. W.; Sparkes, H. A.; Thompson, A. L.; Brown, J. M.; Gouverneur, V. Hydrogen-Bonded Homoleptic Fluoride–Diarylurea Complexes: Structure, Reactivity, and Coordinating Power. *J. Am. Chem. Soc.* **2016**, *138* (40), 13314–13325.

(3) (a) Doyle, A. G.; Jacobsen, E. N. Small-Molecule H-Bond Donors in Asymmetric Catalysis. *Chem. Rev.* **2007**, *107* (12), 5713–5743; (b) Zhang, Z.; Schreiner, P. R. (Thio)urea organocatalysis—What can be learnt from anion recognition? *Chem. Soc. Rev.* **2009**, *38* (4), 1187–1198.

(4) Dooley, C.; Ibba, F.; Botlik, B. B.; Palladino, C.; Goult, C. A.; Gao, Y.; Lister, A.; Paton, R. S.; Lloyd-Jones, G. C.; Gouverneur, V. Enantioconvergent nucleophilic substitution via synergistic phase-transfer catalysis. *Nat. Catal.* **2025**, *8* (2), 107–115.

(5) Wang, Z.; Dooley, C.; Chen, Z.; Poškaitė, G.; Paton, R. S.; Lloyd-Jones, G. C.; Gouverneur, V. Synergistic Transition Metal and Hydrogen Bonding Phase-Transfer Catalysis Enables Enantioconvergent Allylic Fluorination with KF. *J. Am. Chem. Soc.* **2026**, *148* (13), 14213–14222.

(6) Um, H.-S.; Miller, S. J. Asymmetric Desymmetrizing Sulfonylation of Diarylmethanes via Peptidyl-Cu(I)-Catalysis with Remote Stereocontrol. *J. Am. Chem. Soc.* **2026**, *148* (2), 2810–2819.

(7) van den Heuvel, N.; Mason, S. M.; Mercado, B. Q.; Miller, S. J. Aspartyl β-Turn-Based Dirhodium(II) Metallopeptides for Benzylic C(sp^3)–H Amination: Enantioselectivity and X-ray Structural Analysis. *J. Am. Chem. Soc.* **2023**, *145* (22), 12377–12385.

(8) (a) Barrett, K. T.; Miller, S. J. Enantioselective Synthesis of Atropisomeric Benzamides through Peptide-Catalyzed Bromination. *J. Am. Chem. Soc.* **2013**, *135* (8), 2963–2966; (b) Gustafson, J. L.; Lim, D.; Miller, S. J. Dynamic Kinetic Resolution of Biaryl Atropisomers via Peptide-Catalyzed Asymmetric Bromination. *Science* **2010**, *328* (5983), 1251–1255; (c) Patra, S.; Mondal, H.; Dash, U.; Aziz, S. M.; Maji, M. S. Designing Peptide-Based Nucleophilic Catalysts Possessing Multiple Identical Active Sites for Late-Stage Chlorination of Peptides and Drugs. *Org. Lett.* **2025**, *27* (15), 3924–3929.

(9) Kastl, R.; Wennemers, H. Peptide-Catalyzed Stereoselective Conjugate Addition Reactions Generating All-Carbon Quaternary Stereogenic Centers. *Angew. Chem., Int. Ed.* **2013**, *52* (28), 7228–7232.

(10) (a) Schnitzer, T.; Schnurr, M.; Zahrt, A. F.; Sakhaee, N.; Denmark, S. E.; Wennemers, H. Machine Learning to Develop Peptide Catalysts─Successes, Limitations, and Opportunities. *ACS Cent. Sci.* **2024**, *10* (2), 367–373; (b) Crawford, J. M.; Stone, E. A.; Metrano, A. J.; Miller, S. J.; Sigman, M. S. Parameterization and Analysis of Peptide-Based Catalysts for the Atroposelective Bromination of 3-Arylquinazolin-4(3*H*)-ones. *J. Am. Chem. Soc.* **2018**, *140* (3), 868–871.

(11) (a) O'Hagan, D.; Schaffrath, C.; Cobb, S. L.; Hamilton, J. T. G.; Murphy, C. D. Biosynthesis of an organofluorine molecule. *Nature* **2002**, *416* (6878), 279–279; (b) Dong, C.; Huang, F.; Deng, H.; Schaffrath, C.; Spencer, J. B.; O'Hagan, D.; Naismith, J. H. Crystal structure and mechanism of a bacterial fluorinating enzyme. *Nature* **2004**, *427* (6974), 561–565.

(12) (a) Busschaert, N.; Gale, P. A. Small-Molecule Lipid-Bilayer Anion Transporters for Biological Applications. *Angew. Chem., Int. Ed.* **2013**, *52* (5), 1374–1382; (b) Matile, S.; Vargas Jentzsch, A.; Montenegro, J.; Fin, A. Recent synthetic transport systems. *Chem. Soc. Rev.* **2011**, *40* (5), 2453–2474.

(13) Stockbridge, R. B.; Kolmakova-Partensky, L.; Shane, T.; Koide, A.; Koide, S.; Miller, C.; Newstead, S. Crystal structures of a double-barrelled fluoride ion channel. *Nature* **2015**, *525* (7570), 548–551.

(14) (a) Duvnjak, M.; Vidović, N.; Užarević, K.; Horvat, G.; Tomišić, V.; Speranza, G.; Cindro, N. Rapid and Green Anion-Assisted Mechanochemical Peptide Cyclization. *ACS Sustainable Chem. Eng.* **2025**, *13* (1), 30–35; (b) Vidović, N.; Horvat, G.; Riva, D.; Rinkovec, T.; Cindro, N.; Tomišić, V.; Speranza, G. Chloride-Assisted Peptide Macrocyclization. *Org. Lett.* **2020**, *22* (6), 2129–2134.

Chapter V

Experimental

5.1. General information

Unless otherwise stated, all reagents were purchased from commercial suppliers and used without further purification. Unless otherwise stated, solvents were used without prior drying/degassing. Reactions requiring anhydrous conditions are clearly stated and were conducted after flame-drying of the round-bottom two-neck flasks and under an inert atmosphere of nitrogen. CsF (99.9 % trace metal basis from Sigma-Aldrich) was ground prior to reactions and used without pre-drying. Reactions were monitored by thin layer chromatography (TLC) on silica gel pre-coated aluminium sheets (Merck Kieselgel 60 F_{254} plates). Visualisation was accomplished by irradiation with UV light at 254 nm, and/or ninhydrin stain, and/or permanganate stain. Column chromatography was performed on Merck silica gel (60, particle size 0.040-0.062 mm). Optical rotations were measured on an Autopol L 2000 (Schmidt-Haensh) at 589 nm, 25 °C. Data are reported as $[\alpha]_D^T$, concentration (c in g/100 mL) and solvent. High resolution mass spectra (HRMS, m/z) were recorded on an ACQUITY I-Class PLUS UPLC System (Waters, Milford, MA, USA) coupled to an ACQUITY RDa mass spectrometer (Waters, Milford, MA, USA) equipped with an ESI probe, in positive or negative ion mode. Infrared spectra were recorded as the neat compound or in solution using a Bruker Tensor 27 FT-IR spectrometer; wavenumbers (ν) are reported in cm^{-1}. Melting points (m.p.) of solids were measured on a Griffin apparatus and are uncorrected. The

enantiomeric ratios (*e.r.*) were determined by HPLC analysis on a Shimadzu *i*-Prominence LC-2030 (PDA detector) using a chiral stationary phase column as specified for each substrate.

All NMR spectra were recorded on Bruker AVIIIHD 400, AVIIIHD 500 or AVII 500. The spectra were acquired at 298 K or at low temperature (stated where applicable) using an liquid N_2 exchanger assembled on AVIIIHD 500. CD_2Cl_2 was stored at 4 °C over 3 Å molecular sieves, under nitrogen atmosphere. $CDCl_3$ was stored at room temperature. CD_3OD was stored at room temperature under nitrogen environment. DMSO-d_6 was stored at room temperature in ampules, which were immediately consumed upon opening. Spectra were processed with Topspin 4.0.7, spectral data are reported as follows: chemical shift, multiplicity (singlet (s), doublet (d), triplet (t), quartet (q), quintet (quint), sextet (sx), septet (sept), broad (br), multiplet (m), or combination of those), coupling constant (Hz) and relative integration. Coupling constants, *J*, are reported in Hz. ^{1}H and ^{13}C NMR spectral data are reported as chemical shifts (δ) in parts per million (ppm) relative to the solvent peak. ^{19}F and ^{133}Cs NMR spectra are referenced relative to $CFCl_3$ and 0.1 M $CsNO_2$ in D_2O, respectively, using the Bruker internal referencing procedure (*edlock*). Non-standard pulse sequences and acquisition parameters are clearly stated in the text according to the following naming convention: NS = number of scans, DS = number of dummy scans, TD = time domain points [pt], SI = spectrum data size, SW = spectral window [ppm], o1p = spectrum offset, center of spectrum [ppm], o2p = selection of second nuclei [ppm], d = delay [s].

5.2. Catalyst synthesis and characterisation

Catalyst **1.2.9** was prepared following published procedure.[1] The solution phase peptide synthesis of catalysts **2a–2s** and **3.3a–3.3j** was accomplished using the Boc group strategy.[2] Once synthesised, peptides were stored at 0 °C to prevent epimerisation and other adverse side-reactivity. Yields were not optimised. Herein synthesis for catalyst **3.3j** is provided, which represents a synthetic route for catalysts **2a–2p**, **3.3c**, **3.3d**, **3.3i** and **3.3j** (*v.* Section 2.2.2.1 and Section 3.2.3.1). Peptides **2q–2s**, **3.3a**, **3.3b** and **3.3e–3.3h** were prepared following a route analogous to the synthesis of catalyst **2r**.

Remaining of this section includes full characterisation data of catalysts **2a–2s** and **3.3a–3.3j**, preparation of not commercially available amino acid (**5.12−5.16**) and aniline intermediates (**5.17–5.19**).

5.2.1. General procedures for catalyst assembly

General Procedure I: peptide coupling

H-peptide-NR_2·HCl (1.0 mmol), Boc-peptide-OH (1.2 mmol) and HOBt·xH_2O (1.2 mmol) were dissolved in CH_2Cl_2 (5.0 mL) at 0 °C and allowed to stir for 5 min, followed by addition of EDC·HCl (1.2 mmol) and a drop-wise addition of DIPEA (2.5 mmol). The reaction mixture was allowed to stir for 2–24 h at room temperature (monitored via TLC or LC-MS). The solution was diluted with CH_2Cl_2 (10 mL) and the organic layer was washed sequentially with distilled water (15 mL x 3), 1 M HCl (15 mL x 2), sat. aq. $NaHCO_3$ (15 mL x 2), and brine (15 mL). The organic layer was dried with Na_2SO_4, filtered and concentrated *in vacuo*, which was carried forward without further purification, unless otherwise stated.

General Procedure II: Boc-deprotection

Boc-peptide-NR_2 (1.0 mmol) was dissolved in 4 M HCl in dioxane (3.0 mL) and stirred vigorously for 1 h at r.t. Then the solvent was removed *in vacuo*, followed by co-evaporation with CH_2Cl_2 (3 x 10 mL). The resulting crude product was thoroughly dried under reduced pressure and carried forward without further purification.

General Procedure IIIa (method A): urea formation from isocyanates

H-peptide-NR_2 (1.0 mmol) was dissolved in anhydrous CH_2Cl_2 (5.0 mL) followed by the addition of NEt_3 (1.5 mmol) under an atmosphere of N_2. The mixture was cooled to 0 °C and Ar-NCO (1.2 mmol) was added dropwise. The reaction mixture was stirred at 0 °C until complete consumption of the starting material as indicated by TLC. Excess isocyanate was quenched by the addition of MeOH (0.5 mL) before the reaction mixture was allowed to warm to r.t. Solvents were removed under reduced pressure and the crude mixture was purified by column chromatography.

General Procedure IIIb: urea formation from isocyanates

H-peptide-NR_2 (1.0 mmol) was dissolved in a mixture of anhydrous THF and pyridine (10 mL, v/v 25:3) under an atmosphere of N_2. The mixture was cooled to 0 °C followed by addition of Ar-NCO (1.1 mmol). The reaction mixture was stirred at 0 °C until complete consumption of the starting material as indicated by TLC. Excess isocyanate was quenched by the addition of MeOH (0.5 mL) before the reaction mixture was allowed to warm to r.t. Solvents were removed under reduced pressure and the crude mixture was purified by column chromatography.

General Procedure IV (method B): *urea formation from anilines*

Triphosgene (0.33 mmol) was dissolved in anhydrous CH_2Cl_2 (0.95 M) under an atmosphere of N_2. In a separate flame-dried Schlenk tube under N_2 atmosphere, a solution of aniline (1.5 mmol) in anhydrous CH_2Cl_2 (0.20 M) was prepared and transferred to the triphosgene solution at 0 °C. Anhydrous NEt_3 (2.5 mmol) was then added dropwise, the mixture was allowed to warm to r.t. and stirred for 2 h. H-Pro-Gly-Phe-NMe_2·HCl (1.0 mmol) was added and allowed to stir for 16 h. The reaction was quenched with H_2O (1.0 mL) and the aqueous phase was extracted with CH_2Cl_2 (3 x 10 mL) and washed with brine (15 mL). The organic layer was dried with Na_2SO_4, filtered and concentrated *in vacuo*, and the crude mixture was purified by column chromatography.

5.2.2. Exemplary synthesis I: **3.3j**

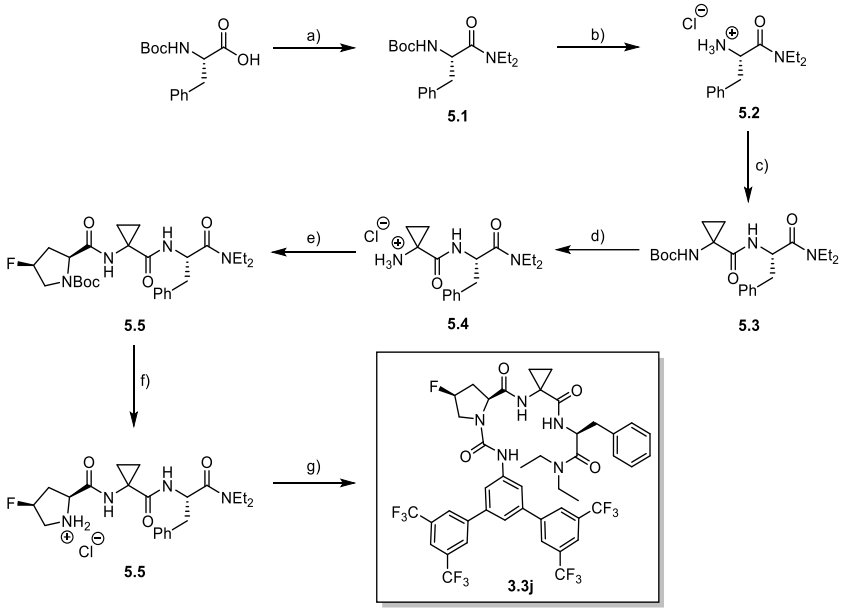

Scheme 5.2.1. Representative synthesis for the preparation of lead catalyst 3,5-[3,5-$(CF_3)_2C_6H_3]_2C_6H_3$NHC(O)-flp-Acpc-Phe-NEt_2 (**3.3j**). a) $HNEt_2$ (2.0 equiv.), EDC·HCl (1.2 equiv.), HOBt·H_2O (1.2 equiv.), DIPEA (2.5 equiv.), CH_2Cl_2 (0.2 M), 2 h; b) HCl (4.0 M in dioxane), 1 h; c) Boc-Acpc-OH (1.2 equiv.), EDC·HCl (1.2 equiv.), HOBt·H_2O (1.2 equiv.), DIPEA (2.5 equiv.), CH_2Cl_2 (0.2 M), 2 h; d) HCl (4.0 M in dioxane), 1 h; e) Boc-flp-OH (1.2 equiv.), EDC·HCl (1.2 equiv.), HOBt·H_2O (1.2 equiv.), DIPEA (2.5 equiv.), CH_2Cl_2 (0.2 M), 24 h; f) HCl (4.0 M in dioxane), 1 h; g) 3,5-[3,5-$(CF_3)_2C_6H_3]_2C_6H_3$NCO (1.2 equiv.), THF/pyridine 25:3 (0.1 M), 0 °C, overnight.

Boc-Phe-NEt_2 (5.1)

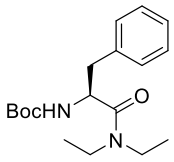

Title compound was prepared following *General Procedure I* using commercially available Boc-Phe-OH (5.32 g, 20.0 mmol) and diethylamine (4.1 mL, 40.0 mmol). The title compound was obtained as a yellow oil (6.40 g, quantitative yield). **^{1}H NMR** (400 MHz, $CDCl_3$): δ 7.27–7.19 (m, 5H), 5.36 (d, J = 8.6 Hz, 1H), 4.74 (q, J = 8.3 Hz, 1H), 3.52 (sx, J = 6.9 Hz, 1H), 3.08 (sx, J = 7.1 Hz, 1H), 3.04–2.90 (m, 4H), 1.41 (s, 9H), 1.04 (t, J = 7.1 Hz, 3H), 0.97 (t, J = 6.9 Hz, 3H) ppm; **^{13}C NMR** (101 MHz, $CDCl_3$): δ 170.9, 155.0, 136.6, 129.6, 128.4, 126.8, 79.6, 51.4, 41.6, 40.5, 40.4, 28.3, 14.2, 12.8 ppm; **IR** (thin layer film): ν 3291, 2978, 2936, 1708, 1635, 1526, 1494, 1454, 1391, 1366, 1221, 1173, 1081, 1051, 1020, 978, 914, 888, 867, 800, 783, 752, 737, 701, 662, 649, 625 cm^{-1}; $[\alpha]_D^{20°C}$ = +7.5 (*c* 0.9, $CHCl_3$); **HRMS** (ESI+) = *m/z* calculated for $C_{18}H_{28}N_2O_3Na^+$ $[M+Na]^+$ 343.1992, found 343.1991. Spectroscopic data were in agreement with the literature values.[3] *Note:* Some low intensity broad peaks were observed in ^{1}H NMR indicating the presence of Boc-rotamers (5.08, 4.56, 1.37 ppm); 100:1 ratio.

H-Phe-NEt$_2$·HCl (5.2)

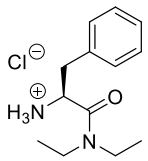

The title compound was prepared following *General Procedure II* from **5.1** (6.37 g, 19.9 mmol) using 4 M HCl in dioxane (40 mL). Compound **5.2** was obtained as a white solid (5.10 g, quantitative yield). **^{1}H NMR** (400 MHz, $CDCl_3$): δ 8.74 (s, 3H), 7.33–7.23 (m, 5H), 4.68 (br quint, *J* = 4.7 Hz, 1H), 3.64–3.55 (m, 2H), 3.24 (dd, *J* = 12.6, 10.3 Hz, 1H), 2.99 (sx, *J* = 6.8 Hz, 1H), 2.89 (sx, *J* = 7.1 Hz, 1H), 2.69 (sx, *J* = 7.1 Hz, 1H), 1.04 (t, *J* = 7.1 Hz, 3H), 0.95 (t, *J* = 7.0 Hz, 3H) ppm; **^{13}C NMR** (101 MHz, $CDCl_3$): δ 167.4, 134.4, 130.0, 128.6, 127.5, 51.3, 41.5, 40.6, 38.1, 13.7, 12.6 ppm; **IR** (thin layer film): ν 3505, 3460, 2976, 2935, 2877, 1646, 1496, 1457, 1383, 1362, 1304, 1268, 1215, 1150, 1100, 912, 762, 732, 701, 646 cm^{-1}. $[\alpha]_D^{20°C}$ = +68.6 (*c* 0.9, $CHCl_3$); **HRMS** (ESI+) = *m*/*z* calculated for $C_{13}H_{21}N_2O^+$ $[M+H]^+$ 221.1648, found 221.1654. *Note:* Highly hydroscopic solid.

Boc-Acpc-Phe-NEt$_2$ (5.3)

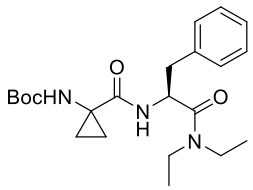

The title compound was prepared following *General Procedure I* using **5.2** (4.40 g, 17.1 mmol) and Boc-Acpc-OH (4.13 g, 20.5 mmol). The reaction yielded **5.3** as a white gum (6.74 g, 98%). **^{1}H NMR** (400 MHz, $CDCl_3$): δ 7.28–7.19 (m, 6H), 5.17 (s, 1H), 5.03 (q, *J* = 8.2 Hz, 1H), 3.50 (sx, *J* = 7.2 Hz, 1H), 3.07 (sx, *J* = 7.2 Hz, 1H), 3.06–2.87 (m, 4H), 1.61–1.55 (m, 1H), 1.53–1.46 (m, 1H) 1.46 (s, 9H), 1.07–0.97 (m, 2H), 1.03 (t, *J* = 7.2 Hz, 3H), 0.92 (t, *J* = 6.9 Hz, 3H) ppm; **^{13}C NMR** (101 MHz, $CDCl_3$): δ 171.2 (br), 170.4, 155.3 (br), 136.4, 129.6, 128.4, 126.9, 80.6 (br), 50.6, 41.6, 40.4, 40.2 (br), 35.4 (br), 28.3, 18.3 (br), 17.7 (br), 14.1, 12.8 ppm; **IR** (thin layer film): ν 3414, 3301, 2979, 2934, 1719, 1635, 1sx 509, 1456, 1413, 1366, 1315, 1250, 1218, 1168, 1073, 1033, 1010, 956, 914, 784, 737, 702, 669, 647, 632 cm^{-1}; $[\alpha]_D^{20°C}$ = –6.2 (*c* 0.9, $CHCl_3$); **HRMS** (ESI+) = *m*/*z* calculated for $C_{22}H_{34}N_3O_4^+$ $[M+H]^+$ 404.2544, found 404.2553. *Note:* Resonances in ^{13}C NMR spectrum corresponding to Acpc residue appear broad due to presence of Boc-rotamers.

H-Acpc-Phe-NEt2·HCl (5.4)

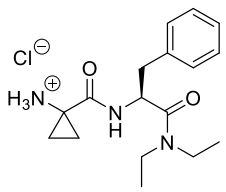

The title compound was prepared following *General Procedure II* from **5.3** (6.68 g, 16.5 mmol). H-Acpc-Phe-NEt_2·HCl was obtained as a white powder (5.53 g, 99%). **^{1}H NMR** (400 MHz, D_2O): δ 7.40–7.32 (m, 3H), 7.29–7.27 (m, 2H), 5.03 (t, *J* = 7.6 Hz, 1H), 3.45 (sx, *J* = 7.1 Hz, 1H), 3.26 (sx, *J* = 7.2 Hz, 1H), 3.16 (sx, *J* = 7.1 Hz, 2H), 3.06 (dd, *J* = 13.8, 7.7 Hz, 1H), 2.99 (dd, *J* = 13.8, 7.6 Hz, 1H), 1.61–1.57 (m, 1H), 1.48–1.43 (m, 3H), 1.05 (t, *J* = 7.1 Hz, 3H), 1.03 (t, *J* = 7.2 Hz, 3H) ppm; **^{13}C NMR** (101 MHz, D_2O): δ 171.4, 170.1, 136.0, 129.4, 128.8, 127.3, 51.4, 42.4, 41.1, 37.4, 35.0, 13.0, 12.8, 12.7, 11.9 ppm; **m.p.** 233 °C; $[\alpha]_D^{20°C}$ = 16.0 (*c* 0.5, H_2O); **HRMS** (ESI+) = *m/z* calculated for $C_{17}H_{26}N_3O_2^+$ $[M+H]^+$ 304.2020, found 304.2014; **IR** (neat): ν 3460, 2693, 2648, 1438, 1376, 1308, 1283, 1261, 1094, 971, 748, 701, 634 cm^{-1}.

Boc-flp-Acpc-Phe-NEt_2 (5.5)

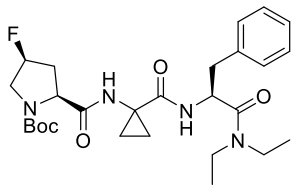

The title compound was prepared following *General Procedure I* using **5.4** (5.50 g, 16.2 mmol) and Boc-flp-OH (4.52 g, 19.4 mmol). The crude product was purified via flash column chromatography (98:2 then 90:10, *i*-PrOH in CH_2Cl_2) to yield **5.5** as a white foam (5.72 g, 68 %). **^{1}H NMR** (500 MHz, $CDCl_3$, **at 333 K**): δ 7.28–7.19 (m, 5H), 7.03 (br s, 1H), 6.86 (br s, 1H), 5.31 (br d, $^2J_{HF}$ = 52.4 Hz, 1H), 5.02 (appt q, *J* = 8.6 Hz, 1H), 4.41 (d, *J* = 10.1 Hz, 1H), 3.90 (ddd, $^3J_{HF}$ = 22.7 Hz, J_{HH} = 13.4, 1.3 Hz, 1H), 3.62 (ddd, $^3J_{HF}$ = 39.3 Hz, J_{HH} = 13.4, 2.7 Hz, 1H), 3.49 (sx, *J* = 7.1 Hz, 1H), 3.11 (sx, *J* = 7.1 Hz, 1H), 3.08–3.00 (m, 3H), 2.92 (dd, *J* = 13.0, 5.5 Hz, 1H), 2.64 (br t, $^3J_{HF}$ = 15.9 Hz, J_{HH} = 14.9 Hz, 1H), 3.08 (br dt, $^3J_{HF}$ = 44.2 Hz, J_{HH} = 11.8 Hz, 1H), 1.71 (br s, 1H), 1.49 (s, 9H), 1.49–1.45 (m, 1H), 1.13 (ddd, *J* = 10.0, 8.1, 4.9 Hz, 1H), 1.04 (t, *J* = 7.1 Hz, 3H), 0.93 (t, *J* = 7.1 Hz, 3H), 0.89 (ddd, *J* = 10.0, 8.0, 4.5 Hz, 1H) ppm; **^{13}C NMR** (126 MHz, $CDCl_3$, **at 333 K**): δ 172.3 (br s), 170.6, 170.4, 154.6 (br s), 136.8, 129.6, 128.3, 126.7, 92.7 (d, $^1J_{CF}$ = 174 Hz), 81.5 (br), 59.9, 53.9 (d, $^2J_{CF}$ = 23 Hz), 50.6, 41.6, 40.4, 39.7, 36.7 (br), 34.5, 28.3, 17.6, 17.2, 13.9, 12.7 ppm; **^{19}F{^{1}H} NMR** (377 MHz, $CDCl_3$, at 298 K, 1.0:0.8 ratio of rotamers by integration): δ –171.35 (s, major), –172.96 (s, minor) ppm; $[\alpha]_D^{20°C}$ = –43.3 (*c* 0.9, $CHCl_3$); **HRMS** (ESI+) = *m/z*

calculated for $C_{27}H_{40}FN_4O_5^+$ [M+H]$^+$ 519.2977, found 519.2992; **IR** (thin layer film): ν 3488, 3294, 2979, 2936, 1688, 1640, 1520, 1496, 1455, 1393, 1367, 1317, 1258, 1217, 1169, 1122, 1073, 758 cm^{-1}. *Note:* NMR spectra appeared broad due to the presence of rotamers. Hence, spectra were collected at 333 K.

H-flp-Acpc-Phe-NEt$_2$·HCl (5.6)

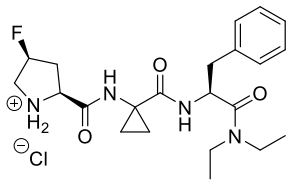

The title compound was prepared following *General Procedure II* from **5.5** (5.90 g, 11.4 mmol). **5.6** was obtained a white powder (2.27 g, 99% yield). **^{1}H NMR** (500 MHz, $CDCl_3$): δ 10.59 (br s, 1H), 9.42 (s, 1H), 8.91 (br s, 1H), 7.59 (br s, 1H), 7.17–7.16 (m, 3H), 6.94 (br s, 2H), 5.31 (d, $^2J_{HF}$ = 52.0 Hz, 1H), 5.30 (br s, 1H), 4.80–4.75 (m, 1H), 3.90–3.75 (m, 2H), 3.41 (sx, *J* = 7.2 Hz, 1H), 3.08 (br t, *J* = 11.5 Hz, 1H), 2.99 (sx, *J* = 7.2 Hz, 1H), 2.92–2.75 (m, 3H), 2.77 (dd, *J* = 12.7, 4.7 Hz, 1H), 2.64 (br t, $^3J_{HF}$ = 18.6 Hz, J_{HH} = 15.0 Hz, 1H), 1.60–1.56 (m, 1H), 1.41–1.38 (m, 1H), 1.18–1.14 (m, 1H), 1.03–0.99 (m, 1H), 0.98 (t, *J* = 7.2 Hz, 3H), 0.79 (t, *J* = 7.2 Hz, 3H) ppm; **^{13}C NMR** (126 MHz, $CDCl_3$): δ 171.5, 170.9, 170.0, 136.3, 129.7, 128.4, 126.9, 91.5 (*d*, $^1J_{CF}$ = 179 Hz), 59.9, 52.5 (*d*, $^2J_{CF}$ = 24 Hz), 51.4, 41.9, 40.9, 39.3, 37.8 (*d*, $^2J_{CF}$ = 22 Hz), 34.9, 17.4, 17.1, 13.4, 12.6 ppm; **^{19}F{^{1}H} NMR** (471 MHz, $CDCl_3$): δ –172.74 (s) ppm; $[\alpha]_D^{20°C}$ = 3.5 (*c* 0.9, $CHCl_3$); **HRMS** (ESI+) = *m/z* calculated for $C_{22}H_{32}FN_4O_3^+$ [M+H]$^+$ 419.2453, found 419.2451; **IR** (thin layer film): ν 3445, 3013, 2936, 1696, 1633, 1519, 1454, 1413, 1383, 1358, 1315, 1217, 1074, 1034, 758 cm^{-1}.

3,5-[3,5-(CF$_3$)$_2$C$_6$H$_3$]$_2$C$_6$H$_3$NHC(O)-flp-Acpc-Phe-NEt$_2$ (3.3j)

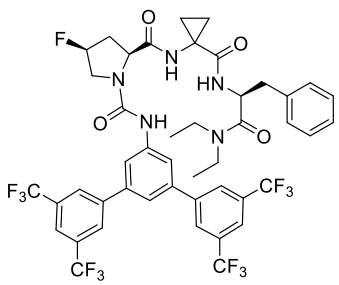

The title compound was prepared following *General Procedure IIIb* from **5.6** (455 mg, 1.00 mmol, 1 equiv.). The crude product was purified via flash column chromatography (10–40% (v/v) acetone in toluene) to give the title compound as a white solid (809 mg, 84%). **^{1}H NMR** (500 MHz, CD_2Cl_2): δ 8.10 (s, 4H), 7.95 (s, 2H), 7.92 (s, 2H), 7.65 (br s, 1H), 7.48 (s, 1H), 7.32 (s, 1H), 7.20 (d, *J* = 8.2 Hz, 1H), 7.15–7.14 (m, 3H), 7.00–6.98 (m, 2H), 5.46 (dt, *J* = 52.4, 3.5 Hz, 1H), 4.87 (q, *J* = 7.9 Hz, 1H), 4.75 (d, *J* = 9.6 Hz,

1H), 4.16 (dd, *J* = 22.4, 11.6 Hz, 1H), 3.93 (ddd, *J* = 35.2, 11.8, 3.7 Hz, 1H), 3.44 (sx, *J* = 7.0 Hz, 1H), 3.00–2.91 (m, 3H), 2.82–2.76 (m, 2H), 2.71 (dd, *J* = 13.3, 6.5 Hz, 1H), 2.47 (dddd, *J* = 41.0, 14.7, 10.0, 3.8 Hz, 1H), 1.49–1.40 (m, 2H), 1.09 (ddd, *J* = 10.2, 7.2, 4.1 Hz, 1H), 0.98 (ddd, *J* = 10.2, 6.5, 3.2 Hz, 1H), 0.91 (appt q, *J* = 7.3 Hz, 6H) ppm; **^{13}C NMR** (151 MHz, CD_2Cl_2): δ 172.3, 170.6, 170.3, 155.2, 142.6, 140.6, 139.9, 136.5, 132.0 (q, J_{CF} = 33 Hz), 129.3, 128.1, 127.5 (br d, J_{CF} = 3 Hz), 126.6, 122.3 (q, J_{CF} = 273 Hz), 121.5 (br t, J_{CF} = 4 Hz), 121.1, 119.6, 92.4 (d, J_{CF} = 173 Hz), 59.9, 53.9, 50.6, 41.5, 40.3, 39.6, 35.6 (br d, J_{CF}= 2 Hz), 34.6, 16.5, 16.3, 13.6, 12.3 ppm; **^{19}F{^{1}H} NMR** (471 MHz, CD_2Cl_2): δ –63.07 (12F), –173.39 (1F) ppm; **HRMS** (ESI+) = *m*/*z* calculated for $C_{45}H_{40}F_{13}N_5O_4Na^+$ $[M+Na]^+$ 984.2765, found 984.2743; $[\alpha]_D^{20°C}$ = –31.2 (*c* 0.9, acetone); **IR** (thin layer film): ν 3290, 2926, 2855, 1717, 1649, 1631, 1542, 1468, 1432, 1371, 1280, 1178, 1139, 844, 683 cm^{-1}; **m.p.** 151−152 °C.

5.2.3. Exemplary synthesis II: **2r**

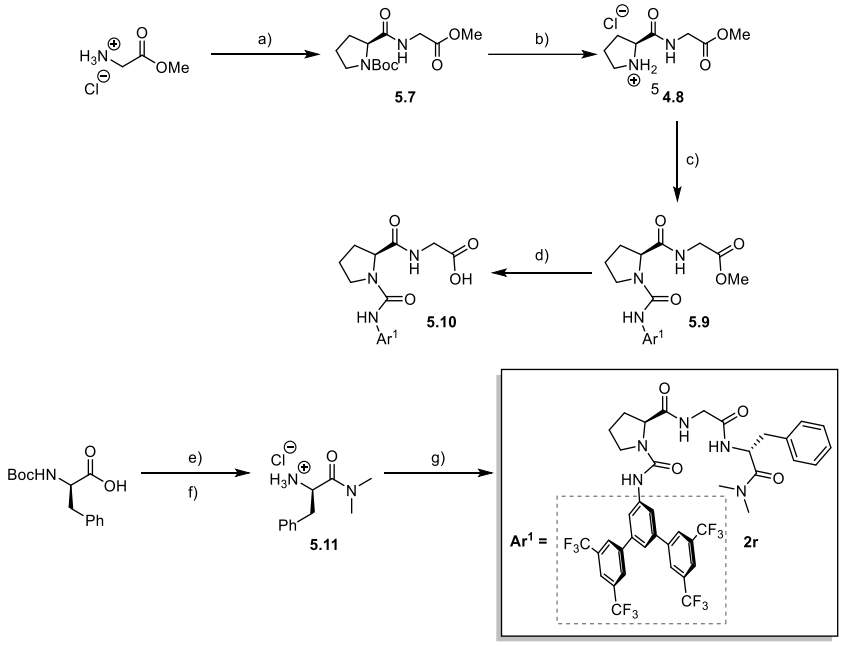

Scheme 5.2.2. Representative synthesis for the preparation of catalyst 3,5-[3,5-$(CF_3)_2C_6H_3]_2C_6H_3$NHC(O)-Pro-Gly-D-Phe-NMe_2 (**2r**). a) Boc-Pro-OH (1.2 equiv.), EDC·HCl (1.2 equiv.), HOBt·H_2O (1.2 equiv.), DIPEA (2.5 equiv.), CH_2Cl_2 (0.2 M), 24 h; b) HCl (4.0 M in dioxane), 1 h; c) 3,5-[3,5-$(CF_3)_2C_6H_3]_2C_6H_3$NCO (1.2 equiv.), Et_3N (1.5 equiv.), CH_2Cl_2 (0.2 M), 0 °C to r.t., overnight; d) 2 M NaOH in MeOH (v/v 4:1, 0.1 M), 0 °C, 3 h, then pH < 3; e) $HNMe_2$·HCl (2.0 equiv.), EDC·HCl (1.2 equiv.), HOBt·H_2O (1.2 equiv.), DIPEA (2.5 equiv.), CH_2Cl_2 (0.2 M), 2 h; f) HCl (4.0 M in dioxane), 1 h; g) **5.10** (1 equiv.), EDC·HCl (1.2 equiv.), HOBt·H_2O (1.2 equiv.), DIPEA (2.5 equiv.), CH_2Cl_2 (0.2 M), overnight.

Boc-Gly-Phe-OMe (5.7)

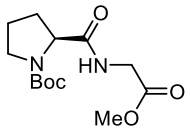

Boc-Gly-Phe-OMe was prepared following *General Procedure I* using Boc-Pro-OH (1.29 g, 6.00 mmol) and H-Gly-OMe·HCl (0.90 g, 7.20 mmol). Compound was obtained as a colourless oil (1.64 g, 5.70 mmol, 95% yield). **^{1}H NMR** (400 MHz, $CDCl_3$, 0.65:0.35 *mixture of rotamers*): δ 7.28 (br s, 0.65H), 6.54 (br s, 0.35H), 4.38–4.17 (br m, 1H), 4.12–3.95 (m, 2H), 3.72 (s, 3H), 3.44 (br s, 1H), 3.34 (br s, 1H), 2.32 (br s, 0.65H), 2.13 (br s, 0.35H), 1.96–1.84 (m, 3H), 1.45 (br s, 9H) ppm; **^{13}C NMR** (126 MHz, $CDCl_3$, *mixture of rotamers*): δ 173.0 (minor), 172.4 (major), 170.1 (br s), 155.9 (major), 154.7 (minor), 80.6 (br s), 61.1 (minor), 59.9 (major), 52.3, 47.1, 41.2 (br s), 30.9 (major), 28.4 (minor), 28.4, 24.5 (major), 23.7 (minor) ppm; $[\alpha]_D^{20°C} = -17.6$ (*c* 1.0, CH_2Cl_2); **HRMS** (ESI+) = *m/z* calculated for $C_{13}H_{23}N_2O_5^+$ $[M+H]^+$ 287.1601, found 287.1605. Spectroscopic data was consistent with literature reported data.[4]

H-Gly-Phe-OMe·HCl (5.8)

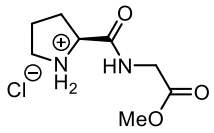

H-Gly-Phe-OMe·HCl was prepared following *General Procedure II* using Boc-Gly-Phe-OMe (1.72 g, 6.00 mmol) yielding as a colourless oil (1.33 g, quantitative yield). **^{1}H NMR** (400 MHz, CD_3OD): δ 4.37−4.32 (m, 1H), 4.07 (d, *J* =17.7 Hz, 1H), 3.99 (d, *J* =17.7 Hz, 1H), 3.74 (s, 3H), 3.44−3.32 (m, 2H), 2.51−2.42 (m, 1H), 2.16−2.03 (m, 3H) ppm; **^{13}C NMR** (126 MHz, CD_3OD): δ 170.0, 168.9, 59.7, 51.4, 46.0, 40.6, 29.5, 23.6 ppm; **HRMS** (ESI+) = *m*/*z* calculated for $C_8H_{15}N_2O_3^+$ $[M+H]^+$ 187.1077, found 187.1085; $[\alpha]_D^{20^\circ C}$ = −77.6 (*c* 1.0, CH_2Cl_2). Spectroscopic data was consistent with literature reported data.[4]

3,5-[3,5-$(CF_3)_2C_6H_3]_2C_6H_3$NHC(O)-Pro-Gly-OMe (5.9)

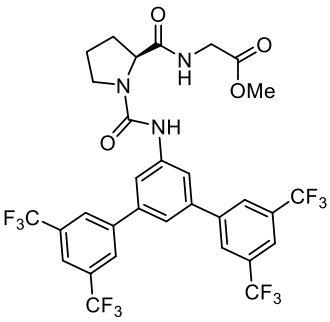

The title compound was prepared following *General Procedure IIIa* using H-Gly-Phe-OMe·HCl (1.00 g, 4.50 mmol) and 5'-isocyanato-3,3",5,5"-tetrakis(trifluoromethyl)-1,1':3',1"-terphenyl[1,5] (3.00 g, 5.40 mmol). The crude product was purified by column chromatography (0:100 to 5:95 = IPA:toluene, followed by 5:95 to 10:90 = acetone:toluene) to afford **5.9** as a white solid (2.22 g, 67 %). **^{1}H NMR** (400 MHz, $CDCl_3$): δ 7.92 (s, 4H), 7.78 (s, 2H), 7.71 (d, *J* = 1.5 Hz, 1H), 7.23–7.22 (m, 2H), 4.52 (dd, *J* = 7.7, 2.6 Hz, 1H), 4.05 (dd, *J* = 18.2, 6.1 Hz, 1H), 3.88 (dd, *J* = 18.2, 5.6 Hz, 1H), 3.65 (s, 3H), 3.64–3.59 (m, 1H), 3.88 (q, *J* = 8.2 Hz, 1H), 2.31–2.23 (m, 1H), 2.16–1.97 (m, 4H) ppm; **^{19}F NMR** (377 MHz, $CDCl_3$): *δ* −62.80 (s, 12F) ppm; **^{13}C NMR** (101 MHz, $CDCl_3$): δ 172.7, 170.6, 155.1, 142.5, 140.7, 139.8, 132.1 (q, J_{CF} = 33 Hz), 127.3 (br s), 123.3 (q, J_{CF} = 273 Hz), 121.4 (br s), 120.4, 118.9, 60.8, 47.2, 41.2, 29.7, 29.4 (br s), 24.8 ppm; **HRMS** (ESI+) = *m*/*z* calculated for $C_{31}H_{24}F_{12}N_3O_4^+$ $[M+H]^+$ 730.1570, found 730.1565; **m.p.** 181 °C; $[\alpha]_D^{20^\circ C}$ = −93.2 (*c* 1.0, CH_2Cl_2); **IR** (thin layer film): ν 3054, 2954, 1753, 1673, 1556, 1371, 1281, 1182, 1133, 901, 845, 706, 683 cm^{-1}.

3,5-[3,5-$(CF_3)_2C_6H_3]_2C_6H_3NHC(O)$-Pro-Gly-OH (5.10)

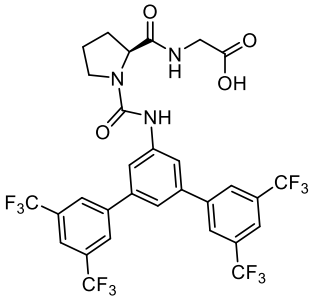

Into solution of **5.9** (395 mg, 0.54 mmol) in MeOH (5.5 mL, 0.10 M) at 0 °C, 1.0 M aq. NaOH (1.5 mL) was added. The reaction mixture was gradually warmed to r.t., resulting in white precipitation. The slurry was left to stir until completion (monitored via TLC). MeOH was evaporated under reduced pressure, the remaining aqueous phase was diluted with H_2O (10 mL) and was washed with EtOAc (3 x 10 mL). The aqueous phase was then then acidified with 1 N aq. HCl at 0 °C to pH < 3, and extracted with EtOAc (3 x 10 mL). The organic layer was collected, washed with brine (10 mL), dried over Na_2SO_4, filtered, concentrated *in vacuo.* and thoroughly dried under reduced pressure. Compound **5.10** was obtained as a white powder (365 mg, quantitative yield). **^{1}H NMR** (400 MHz, DMSO-d_6): δ 12.50 (s, 1H), 8.55 (s, 1H), 8.39 (s, 4H), 8.21 (t, J = 5.8 Hz, 1H), 8.17 (br s, 2H), 8.09 (d, J = 1.4 Hz, 2H), 7.86 (t, J = 1.6 Hz, 1H), 4.43 (br dd, J = 9.0, 2.5 Hz, 1H), 3.75 (d, J = 5.8 Hz, 2H), 3.72–3.66 (m, 1H), 3.54–3.48 (m, 1H), 3.33 (s, 3H), 2.13–2.05 (m, 1H), 2.01–1.91 (m, 4H) ppm; **^{13}C NMR** (101 MHz, DMSO-d_6): δ 173.1, 171.7, 154.3, 143.2, 142.5, 138.7, 131.4 (q, J_{CF} = 33 Hz), 128.1, 123.8 (q, J_{CF} = 274 Hz), 121.7 (br s), 120.3, 118.9, 60.3, 47.0, 41.1, 30.4, 24.5 ppm; **^{19}F NMR** (377 MHz, DMSO-d_6): δ −61.02 (s, 12F) ppm; **HRMS** (ESI−) = m/z calculated for $C_{30}H_{20}F_{12}N_3O_4^-$ $[M+H]^-$ 714.1268, found 714.1269; **m.p.** 226 °C; $[\alpha]_D^{20°C}$ = −49.2 (*c* 0.33, acetone); **IR** (thin layer film): ν 3016, 2926, 2854, 1728, 1669, 1556, 1372, 1284, 1187, 1136, 901, 845, 706, 684, 640 cm^{-1}.

H-D-Phe-NMe_2·HCl (5.11)

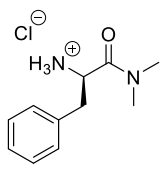

Boc-D-Phe-NMe_2 was prepared following *General Procedure I* using commercially available Boc-D-Phe-OH (531 mg, 2.00 mmol). and $NHMe_2$·HCl (330 mg, 4.00 mmol). Boc-D-Phe-NMe_2 was obtained as an off-white foam (495 mg, 85 %). Title compound was prepared following *General Procedure I* from Boc-D-Phe-NMe_2 (495 mg, 1.69 mmol). Compound **5.11** was obtained as a white powder (386 mg, quantitative yield). **^{1}H NMR** (500 MHz, CD_3OD): δ 7.30–7.20 (m, 3H), 7.18–7.15 (m, 2H), 4.50 (t, J = 7.4 Hz, 1H), 3.01–2.99

(m, 2H), 2.80 (s, 3H), 2.55 (s, 3H) ppm; **^{13}C NMR** (126 MHz, CD_3OD): δ 168.1, 134.0, 129.2, 128.7, 127.6, 51.2, 37.1, 35.7, 34.6 ppm; $[\alpha]_D^{25°C}$ = −73.1 (*c* 1.0, MeOH); **HRMS** (ESI+) = *m*/*z* calculated for $C_{11}H_{17}N_2O^+$ [M-Cl]$^+$ 193.1335, found 193.1341. Spectroscopic data were in agreement with the literature values.[6] *Note:* Highly hydroscopic solid.

3,5-[3,5-$(CF_3)_2C_6H_3]_2C_6H_3$NHC(O)-Pro-Gly-D-Phe-NMe_2 (2r)

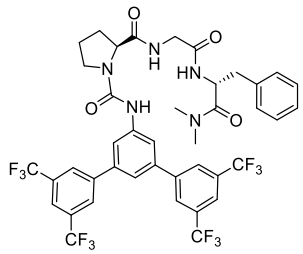

The title compound was prepared following *General Procedure I* using **5.10** (215 mg, 0.3 mmol, 1 equiv.) and **5.11** (103 mg, 0.45 mmol, 1.5 equiv.). The residue was purified via flash column chromatography (10% (v/v) *i*-PrOH in toluene), giving compound **2r** as a white powder (261 mg, 98%). **^{1}H NMR** (400 MHz, $CDCl_3$): δ 7.88 (s, 4H), 7.73 (s, 4H), 7.53 (t, *J* = 4.8 Hz, 1H), 7.40 (s, 1H), 7.24 (d, *J* = 4.3 Hz, 1H), 7.19 (s, 1H), 7.05–7.00 (m, 3H), 6.86–6.84 (br d, *J* = 7.5 Hz, 2H), 4.77 (br q, *J* = 6.9 Hz, 1H), 4.57 (dd, *J* = 6.9, 3.2 Hz, 1H), 3.91–3.72 (m, 3H), 3.54 (br q, *J* = 7.9 Hz, 1H), 2.77 (dd, *J* = 13.0, 5.6 Hz, 1H), 2.60 (dd, *J* = 13.0, 9.4 Hz, 1H), 2.59 (s, 3H), 2.31 (s, 3H), 2.28–2.01 (m, 4H) ppm; **^{19}F NMR** (377 MHz, $CDCl_3$): δ −62.76 ppm; **^{13}C NMR** (101 MHz, $CDCl_3$): δ 172.4, 171.0, 168.3, 155.4, 142.5, 140.8, 139.8, 135.9, 132.2 (q, J_{CF} = 33 Hz), 129.1, 128.2, 127.3 (br s), 126.9, 123.2 (q, J_{CF} = 272 Hz), 121.3 (br s), 120.6, 118.5, 61.6, 50.7, 47.0, 42.5, 39.2, 36.6, 35.4, 29.0, 25.1 ppm; **HRMS** (ESI+) = *m*/*z* calculated for $C_{41}H_{36}F_{12}N_5O_4^+$ [M+H]$^+$ 890.2570, found 890.2557; $[\alpha]_D^{20°C}$ = −66.4 (*c* 0.9, $CHCl_3$); **IR** (thin layer film): v 3301, 2932, 1655, 1556, 1372, 1281, 1179, 1137, 900, 845, 759, 683 cm^{-1}; **m.p.** 132−133 °C.

5.2.4. Synthesis of novel building blocks

5.2.4.1. Amino acid derivatives

Unless otherwise stated, all amino acid derivatives were purchased from commercial suppliers. 1-(*tert*-Butyl) 2-methyl (2*S*)-5-(*tert*-butyl)pyrrolidine-1,2-dicarboxylate (*d.r.* 1:1)[7] was prepared following reported procedures.

Boc-[^{15}N]Phe-OH (5.12)

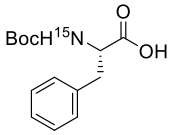

Title compound was prepared adapting published procedure.[8] H-[^{15}N]Phe-OH (0.50 g, 3.0 mmol) was dissolved in 1,4-dioxane (4.6 mL) and water (2.3 mL), and NaOH (0.12 g, 3.0 mmol) was added. The solution was cooled to 0 °C, followed by a portion-wise addition of Boc_2O (0.72 g, 3.3 mmol). The solution was allowed to warm to r.t. and stirred for 1 h (monitored via TLC). The volatiles were evaporated *in vacuo* and the resulting residue was dissolved in water (15 mL), washed with EtOAc (2 x 10 mL). Aqueous phase was then carefully acidified over ice using 6 M HCl to pH 1–2 and extracted with EtOAc (3 x 10 mL). The organic fraction was dried over $MgSO_4$, filtered and evaporated under reduced pressure to give **5.11** as colourless crystals (0.79 g, 99%). **^{1}H NMR** (400 MHz, $CDCl_3$): δ 7.22–7.11 (m, 5H), 5.35 (dd, $^1J_{HN}$ = 91.7 Hz, J_{HH} = 8.7 Hz, 1H), 4.75 (br q, J = 7.8 Hz, 1H), 2.93–2.83 (m, 2H), 2.78 (s, 3H), 2.54 (s, 3H), 1.35 (s, 9H) ppm; **^{13}C NMR** (101 MHz, $CDCl_3$): δ 171.6, 155.1 (d, $^1J_{CN}$ = 26 Hz), 136.5, 129.4, 128.4, 126.9, 79.6, 51.4 (d, $^1J_{CN}$ = 13 Hz), 40.3, 36.8, 35.5, 28.4 ppm; $[\alpha]_D^{20°C}$ = +49.5 (*c* 0.9, $CHCl_3$); **^{15}N NMR** (51 MHz, $CDCl_3$): δ 85.0 (d, $^1J_{NH}$ = 92 Hz) ppm; **HRMS** (ESI+) = *m/z* calculated for $C_{14}H_{19}[^{15}N]O_4Na^+$ $[M+Na]^+$ 289.1177, found 289.1184. Spectroscopic data consistent with literature reported data for unlabelled analogue.[9]

Boc-Phe(*p*-NO_2)-NMe_2 (5.13)

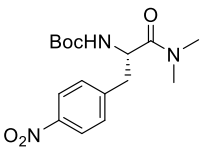

Boc-Phe(*p*-NO_2)-NMe_2 (**5.12**) was prepared from commercially available Boc-Phe(*p*-NO_2)-OH (0.93 g, 3.0 mmol) following *General Procedure I*. Compound **5.12** was obtained as a white foam (0.97 g, 96%). **^{1}H NMR** (400 MHz, $CDCl_3$): δ 8.08 (d, J = 8.7 Hz, 2H), 7.29 (d, J = 8.7 Hz, 2H), 5.34 (br d, J = 8.5 Hz, 1H), 4.81 (appt q, J = 7.1 Hz, 1H), 3.05 (dd, J = 13.1, 7.3 Hz, 1H), 2.94 (dd, J = 13.1, 6.5 Hz, 1H), 2.84

(s, 3H), 2.78 (s, 3H), 1.32 (s, 9H) ppm; **^{13}C NMR** (101 MHz, $CDCl_3$): δ 170.7, 155.0, 147.0, 144.4, 130.4, 123.6, 80.0, 50.9, 39.5, 37.1, 35.7, 28.3 ppm; $[\alpha]_D^{20°C}$ = 9.4 (*c* 1.0, $CHCl_3$); **IR** (thin layer film): ν 3306, 2978, 2934, 1709, 1644, 1605, 1520, 1347, 1251, 1169, 1052, 755 cm^{-1}; **HRMS** (ESI+) = *m*/*z* calculated for $C_{16}H_{24}N_3O_5^+$ $[M+H]^+$ 338.1710, found 338.1711; **m.p.** 98−99 °C.

Boc-Phe(*p*-NH_2)-NMe_2 (5.14)

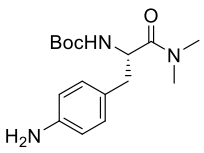

Title compound was prepared adapting published procedure.[10] In two-neck round bottom flask, Pd/C (10% on activated charcoal, 80 mg, 0.08 mmol) was added to **5.12** (0.67 g, 2.0 mmol) in MeOH (20 mL), and was allowed to stir in H_2 environment until full conversion (monitored via TLC, 10% (v/v) *i*-PrOH in toluene). The reaction mixture was filtered through Celite under N_2 environment, and solvent was evaporated under reduced pressure to afford **5.13** as a white solid (0.59 g, 95%). **^{1}H NMR** (400 MHz, $CDCl_3$): δ 6.69 (d, *J* = 8.3 Hz, 2H), 6.53 (d, *J* = 8.3 Hz, 2H), 5.36 (br d, *J* = 8.6 Hz, 1H), 4.67 (appt td, *J* = 8.8, 5.8 Hz, 1H), 3.56 (br s, 2H), 2.80 (dd, *J* = 13.1, 5.8 Hz, 1H), 2.78 (s, 3H), 2.74 (dd, *J* = 13.1, 8.9 Hz, 1H), 2.55 (s, 3H), 1.35 (s, 9H) ppm; **^{13}C NMR** (101 MHz, $CDCl_3$): δ 171.9, 155.1, 145.2, 130.2, 126.3, 115.1, 79.5, 51.6, 39.6, 36.9, 35.5, 28.4 ppm; $[\alpha]_D^{20°C}$ = 55.6 (*c* 1.5, $CHCl_3$); **IR** (thin layer film): ν 3431, 3356, 2977, 2932, 1702, 1638, 1514, 1368, 1290, 1252, 1172, 1054, 758 cm^{-1}; **HRMS** (ESI+) = *m*/*z* calculated for $C_{16}H_{26}N_3O_3^+$ $[M+H]^+$ 308.1969, found 308.1977.

Boc-Phe(*p*-NMe_2)-NMe_2 (5.15)

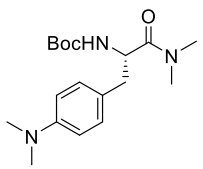

Title compound was prepared adapting published procedure.[11] **5.13** (0.56 g, 1.8 mmol) was dissolved in CH_2Cl_2 (18 mL), followed by addition of anhydrous Na_2SO_4 (2.5 g, 18 mmol) and aq. formaldehyde solution (35%, 0.6 mL, 5.7 mmol). The suspension was stirred for 10 min, and $NaBH(OAc)_3$ (1.2 g, 5.7 mmol) was added portion-wise. After gas evolution subsided, reaction mixture was capped and left to stir for 5 h. The suspension was washed with sat. aq. $NaHCO_3$ (20 mL), 1 M HCl (20 mL), brine (20 mL), dried with anhydrous Na_2SO_4, filtered and evaporated under reduced pressure to give **5.14** as a white solid (0.55 g, 90%). **^{1}H NMR** (400 MHz, $CDCl_3$): δ 6.69 (d, *J* = 8.3 Hz, 2H), 6.53 (d, *J* =

8.3 Hz, 2H), 5.36 (br d, *J* = 8.6 Hz, 1H), 4.67 (appt td, *J* = 8.8, 5.8 Hz, 1H), 3.56 (br s, 2H), 2.80 (dd, *J* = 13.1, 5.8 Hz, 1H), 2.78 (s, 3H), 2.74 (dd, *J* = 13.1, 8.9 Hz, 1H), 2.55 (s, 3H), 1.35 (s, 9H) ppm; **^{13}C NMR** (101 MHz, $CDCl_3$): δ 171.9, 155.1, 145.2, 130.2, 126.3, 115.1, 79.5, 51.6, 39.6, 36.9, 35.5, 28.4 ppm; $[\alpha]_D^{20°C}$ = 51.4 (*c* 1.4, $CHCl_3$); **IR** (thin layer film): ν 3307, 2977, 2931, 1708, 1643, 1521, 1366, 1250, 1169, 1054, 813 cm^{-1}; **HRMS** (ESI+) = *m*/*z* calculated for $C_{18}H_{29}N_3O_3Na^+$ $[M+Na]^+$ 358.2101, found 358.2101.

(2*S*)-1-(*tert*-Butoxycarbonyl)-5-(*tert*-butyl)pyrrolidine-2-carboxylic acid (5.16)

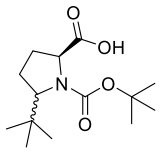

1-(*tert*-Butyl) 2-methyl (2*S*)-5-(*tert*-butyl)pyrrolidine-1,2-dicarboxylate (*d.r.* 1:1)[7] (320 mg, 1.12 mmol) was dissolved in MeOH (5.6 mL, 0.20 M), followed by addition of NaOH (4.0 mL, aq. 1 M) at 0 °C. The reaction mixture was warmed to r.t. and left to stir for 1 week. MeOH was evaporated under reduced pressure, the remaining aqueous phase was extracted with CH_2Cl_2 (3 x 5 mL). Collected organic phase was washed with brine (10 mL), dried over Na_2SO_4, filtered and concentrated *in vacuo* to afford remaining starting material (84 mg, 0.31 mmol). The aqueous phase was then acidified with aq. 1 M HCl to pH < 3, and extracted with EtOAc (3 x 5 mL). The organic layer was collected, washed with brine (10 mL), dried over Na_2SO_4, filtered and concentrated *in vacuo* to give **5.16** as a white powder (220 mg, 0.81 mmol, 72%, *d.r.* 1.0:0.6 (5*S*)/(5*R*) based on NMR). **^{1}H NMR** (400 MHz, $CDCl_3$, two diastereomers (1.0:0.6 5*S*/5*R*): δ 4.32 (t, *J* = 9.2 Hz, 1H, 5*S*), 4.21 (d, *J* = 9.6 Hz, 1H, 5*R*), 3.92 (t, *J* = 8.8 Hz, 1H, 5*R*), 3.78 (dd, *J* = 8.5, 0.7 Hz, 1H, 5*S*), 2.37−2.18 (m, 2H, 5*S* and 5*R*), 2.12−2.05 (m, 1H, 5*S*), 2.03−1.75 (m, 5H, 5*S* and 5*R*), 1.43 (s, 9H, 5*S*), 1.34 (s, 9H, 5*R*), 0.83 (s, 9H, 5*R*), 0.81 (s, 9H, 5*S*) ppm; **^{13}C NMR** (101 MHz, $CDCl_3$, two diastereomers (5*S* and 5*R*)): δ 180.2 (5*S*), 179.3 (5*R*), 156.4 (5*R*), 155.3 (5*S*), 80.6 (5*R*), 80.2 (5*S*), 67.3 (5*R*), 66.2 (5*S*), 61.6 (5*S*), 61.1 (5*R*), 30.1 (5*S*), 29.7 (5*S*), 29.1 (5*R*), 28.3 (5*S*), 28.2 (5*S*), 28.1 (5*R*), 27.7 (5*R*), 27.5 (5*R*), 27.3 (5*S*), 26.0 (5*R*), 26.1 (5*R*), 25.1 (5*S*) ppm; **HRMS** (ESI−) = *m*/*z* calculated for $C_{14}H_{24}NO_4^-$ $[M-H]^-$ 270.1711, found 270.1715. Spectroscopic data consistent with literature reported data.[12]

5.2.4.2. Isocyanates and anilines

Intermediate 3,5-bis(trifluoromethyl)phenyl isocyanate was purchased from a commercial supplier, while [1,1':3',1''-terphenyl]-5'-amine and 5'-isocyanato-3,3'',5,5''-tetrakis(trifluoromethyl)-1,1':3',1''-terphenyl were prepared according to literature procedures and their spectroscopic data were consistent with literature.[1,5,13]

General Procedure V: Suzuki coupling

The aniline derivative (1.0 mmol), boronic acid derivative (3.5 mmol), *S*-Phos (0.10 mmol) and K_2CO_3 (5.0 mmol) were dissolved in N_2-spurged THF and H_2O (4:1 v/v, 13 mL), followed by addition of $Pd(OAc)_2$ (50 μmol). The mixture was refluxed for 16 h and then cooled to r.t. THF was evaporated under reduced pressure and the remaining slurry was diluted with H_2O (10 mL) and the aqueous layer was extracted with CH_2Cl_2 (10 mL x 3). The organic layer was collected and washed with brine (10 mL), dried over $MgSO_4$, filtered and concentrated *in vacuo*. The crude mixture was purified by column chromatography.

3,3'',5,5''-Tetrafluoro-[1,1':3',1''-terphenyl]-5'-amine (5.17)

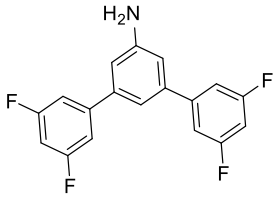

Synthesised by Jessica B. Sellar

Title compound was prepared according to *General procedure V* using 3,5-dibromoaniline (453 mg, 1.80 mmol) and 3,5-difluorophenyl boronic acid (996 mg, 6.30 mmol). The crude product was purified via flash column chromatography (70:30 pentane:CH_2Cl_2), giving **5.17** as a white solid (300 mg, 52%). **^{1}H NMR** (400 MHz, $CDCl_3$): δ 7.15–7.07 (m, 4H), 7.06 (t, J = 1.6 Hz, 1H), 6.86 (d, J = 1.6 Hz, 2H), 6.80 (tt, J = 8.9, 2.3 Hz, 2H), 3.90 (s, 2H) ppm; **^{19}F{^{1}H} NMR** (377 MHz, $CDCl_3$): δ −109.6 ppm; **^{13}C NMR** (101 MHz, $CDCl_3$): δ 163.2 (dd, J_{CF} = 248, 13 Hz), 147.5, 144.3 (t, J_{CF} = 10 Hz), 141.0 (t, J_{CF} = 2 Hz), 116.3, 113.5, 110.9–109.4 (m), 102.8 (t, J_{CF} = 25 Hz) ppm; **HRMS** (ESI+) = m/z calculated for $C_{18}H_{12}F_4N^+$ $[M+H]^+$ 318.0900, found 318.0907; **IR** (thin layer film): ν 3450, 2361, 2342, 1628, 1592, 1406, 1323, 1273, 1116, 912, 839, 739, 679, 656 cm^{-1}; **m.p.** 188−189 °C.

3,3'',5,5''-Tetra-*tert*-butyl-[1,1':3',1''-terphenyl]-5'-amine (5.18)

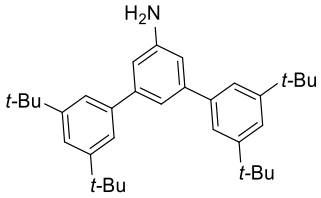

Synthesised by Jessica B. Sellar

Title compound was prepared according to *General procedure V* using 3,5-dibromoaniline (251 mg, 1.00 mmol) and 3,5-di-*tert*-butylphenyl boronic acid (820 mg, 3.40 mmol). The crude product was purified via flash column chromatography (70:30 pentane:CH_2Cl_2), giving **5.18** as a white solid (301 mg, 64%). **^{1}H NMR** (400 MHz, $CDCl_3$): δ 7.65 (t, *J* = 6.1 Hz, 1H), 7.56 (d, *J* = 1.6 Hz, 2H), 7.45 (q, *J* = 1.8 Hz, 3H), 7.41 (d, *J* = 1.8 Hz, 4H), 7.29–7.12 (m, 4H), 7.10–7.04 (m, 2H), 6.99 (d, *J* = 7.8 Hz, 1H), 6.79 (s, 1H), 5.01 (td, *J* = 8.1, 5.4 Hz, 1H), 4.74–4.64 (m, 1H), 4.12 (dd, *J* = 17.0, 6.8 Hz, 1H), 3.80–3.65 (m, 2H), 3.56–3.44 (m, 1H), 3.00–2.81 (m, 2H), 2.72 (s, 3H), 2.51 (s, 4H), 2.19–1.93 (m, 3H) 1.37 (s, 36H) ppm; **^{13}C NMR** (101 MHz, $CDCl_3$): δ 151.0, 146.8, 144.3, 141.1, 121.9, 121.5, 117.9, 113.2, 35.0, 31.6 ppm. Spectroscopic data was consistent with literature.[14]

[^{15}*N*]-5'-(Isocyanato)-3,3'',5,5''-tetrakis(trifluoromethyl)-1,1':3',1''-terphenyl (5.19)

5.19 was prepared following the route depicted below; compounds **5.19a**-**5.19** were prepared following literature procedures for non-labelled analogues.[5,15]

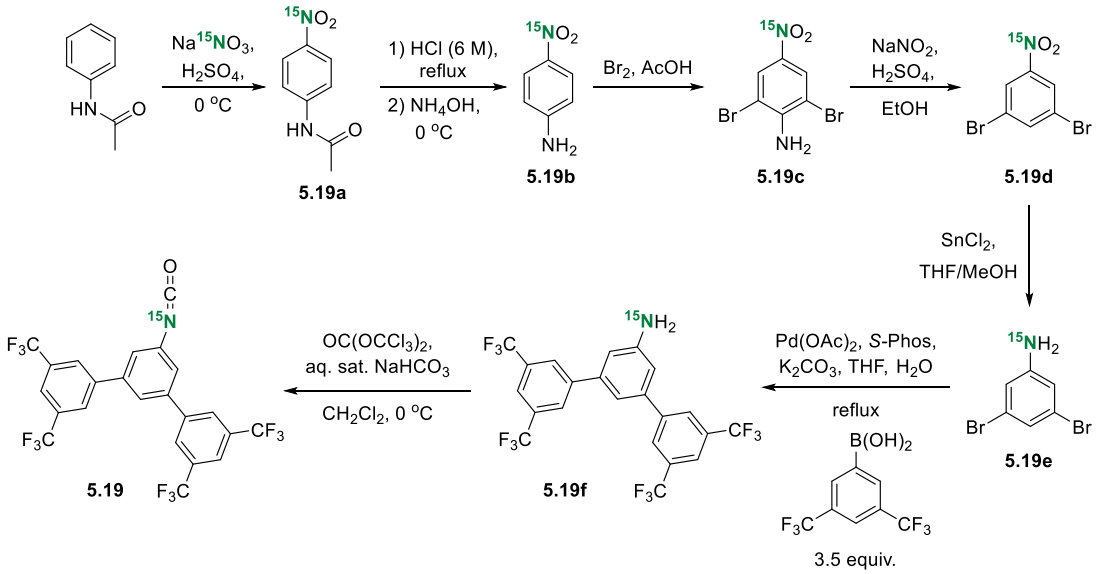

Scheme 5.2.3. Multi-step synthesis of **5.19**.

_N_-(4-(Nitro-^{15}N)phenyl)acetamide (5.19a)

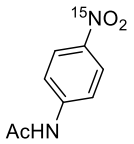

Synthesised by Dr. Thomas Schlatzer

In a 150 mL round-bottom flask, acetanilide (3.00 g, 22.2 mmol) was dissolved in conc. H_2SO_4 (35 mL) and cooled to 0 °C, followed by addition of a solution of $Na^{15}NO_3$ (1.91 g, 22.2 mmol) in conc. H_2SO_4 (25 mL) over 20 min. The reaction mixture was stirred at 0 °C for 3 h (reaction monitoring via GC-MS and TLC) and quenched onto ice (200 mL). The resulting precipitate was collected by filtration, washed with ice-cold H_2O (2 x 50 mL) and dried under a stream of N_2. **5.19a** was obtained as a colourless solid (3.87 g, 96%) and was used without further purification. **^{1}H NMR** (400 MHz, DMSO-d_6): δ 10.55 (s, 1H), 8.25–8.16 (m, 2H), 7.86–7.77 (m, 2H), 2.12 (s, 3H) ppm; **^{13}C NMR** (101 MHz, DMSO-d_6): δ 169.4, 145.5, 142.0 (d, J_{CN} = 15 Hz), 125.0 (d, J_{CN} = 2 Hz), 118.5 (d, J_{CN} = 2 Hz), 24.2 ppm; **HRMS** (ESI$^-$) = *m/z* calculated for $C_8H_7N[^{15}N]O_3$ $[M-H]^-$ 180.0433, found 180.0417. Spectroscopic data consistent with literature reported data for unlabelled analogue.[16]

4-(Nitro-^{15}N)aniline (5.19b)

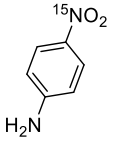

Synthesised by Dr. Thomas Schlatzer

In a 250 mL round-bottom flask, **5.19a** (3.80 g, 21.0 mmol) was suspended in 6 M HCl (135 mL) and heated under reflux for 62 h (reaction monitoring via GC-MS and TLC). The solution was allowed to cool to r.t. and the pH was adjusted to 10 by addition of conc. NH_4OH (80 mL). The resulting precipitate was collected by filtration, washed with ice-cold H_2O (3 x 20 mL) and dried *in vacuo*. **5.19b** was obtained as a yellow solid (2.50 g, 86%) and was used without further purification. **^{1}H NMR** (400 MHz, DMSO-d_6): δ 7.94 (dd, J = 9.1, 1.7 Hz, 2H), 6.71 (s, 2H), 6.59 (d, J = 9.1 Hz, 2H) ppm; **^{13}C NMR** (101 MHz, DMSO-d_6): δ 155.7, 135.6 (d, J_{CN} = 16 Hz), 126.4 (d, J_{CN} = 2 Hz), 112.4 (d, J_{CN} = 3 Hz) ppm; **HRMS** (ESI$^+$) = *m/z* calculated for $C_6H_7N[^{15}N]O_2^+$ $[M+H]^+$ 140.0472, found 140.0471. Spectroscopic data consistent with literature reported data for unlabelled analogue.[17]

2,6-Dibromo-4-(nitro-^{15}N)aniline (5.19c)

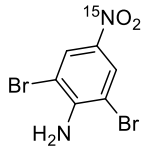

Synthesised by Dr. Thomas Schlatzer

In a 150 mL round-bottom flask, **5.19b** (2.41 g, 17.3 mmol) was suspended in AcOH (30 mL) and heated to 65 °C before a solution of Br_2 (1.95 mL, 38.0) in AcOH (15 mL) was added over 30 min. After 24 h (reaction monitoring via GC-MS), the reaction mixture was quenched onto ice (150 mL) and the resulting precipitate was collected by filtration, washed with ice-cold H_2O (3 x 25 mL) and dried *in vacuo*. **5.19c** was obtained as a yellow solid (4.87 g, 95%) and was used without further purification. **^{1}H NMR** (400 MHz, DMSO-d_6): δ 8.28 (d, J = 1.8 Hz, 2H), 6.79 (s, 2H) ppm; **^{13}C NMR** (101 MHz, DMSO-d_6): δ 149.2, 136.4 (d, J_{CN} = 17 Hz), 128.0 (d, J_{CN} = 2 Hz), 105.3 (d, J_{CN} = 3 Hz) ppm; **HRMS** (ESI$^+$) = m/z calculated for $C_6H_4Br_2N[^{15}N]O_2Na^+$ $[M+Na]^+$ 317.8502, found 317.9446. Spectroscopic data consistent with literature reported data for unlabelled analogue.[18]

1,3-Dibromo-5-(nitro-^{15}N)benzene (5.19d)

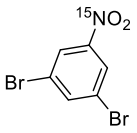

Synthesised by Dr. Thomas Schlatzer

In a 150 mL round-bottom flask, **5.19c** (4.76 g, 16.0 mmol) was suspended in a mixture of EtOH (50 mL) and conc. H_2SO_4 (6 mL). The yellow suspension was heated to 80 °C before $NaNO_2$ (3.32 g, 48.1 mmol) was added in portions. After 17 h (reaction monitoring via GC-MS), the reaction mixture was quenched onto ice (150 mL) and the resulting precipitate was collected by filtration, washed with ice-cold H_2O (3 x 25 mL) and dried *in vacuo*. The crude material was recrystallised from hot EtOH and **5.19d** was obtained as a tan crystalline solid (2.92 g, 65%). **^{1}H NMR** (400 MHz, $CDCl_3$): δ 8.32 (t, J = 1.8 Hz, 2H), 8.00 (t, J = 1.7 Hz, 1H) ppm; **^{13}C NMR** (101 MHz, $CDCl_3$): δ 149.2 (d, J_{CN} = 16 Hz), 140.2, 125.7 (d, J_{CN} = 2 Hz), 123.6 (d, J_{CN} = 3 Hz) ppm; **HRMS** (ESI+) = m/z calculated for $C_6H_5Br_2[^{15}N]O_2^+$ $[M+H]^+$ 280.8574, found 280.8900. Spectroscopic data consistent with literature reported data for unlabelled analogue.[19]

3,5-Dibromoaniline-^{15}N (5.19e)

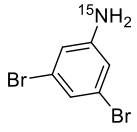

Synthesised by Dr. Thomas Schlatzer

In a 250 mL round-bottom flask, **5.19d** (2.84 g, 10.1 mmol) and $SnCl_2{\cdot}2H_2O$ (11.38 g, 50.5 mmol) were suspended in a mixture of MeOH (35 mL) and THF (10 mL) and heated to 60 °C for 20 h (reaction monitoring via GC-MS). The reaction mixture was concentrated under reduced pressure, followed by the addition of NaOH (9.83 g) dissolved in H_2O (120 mL). The resulting suspension was stirred at r.t. for 2 h, extracted with CH_2Cl_2 (3 x 50 mL) and the combined organic layers were dried over Na_2SO_4, filtered and concentrated under reduced pressure. **5.19e** was obtained as a beige solid (2.49 g, 98%) and was used without further purification. **^{1}H NMR** (400 MHz, CD_3CN): δ 6.92 (t, J = 1.7 Hz, 1H), 6.77 (t, J = 1.8 Hz, 2H), 4.49 (d, J_{HN} = 85.0 Hz, 2H) ppm; **^{13}C NMR** (101 MHz, CD_3CN): δ 151.8 (d, J_{CN} = 13 Hz), 123.8 (d, J_{CN} = 2 Hz), 122.4, 116.6 (d, J_{CN} = 3 Hz); **HRMS** (ESI+) = *m/z* calculated for $C_6H_5Br_2[^{15}N]^+$ $[M+H]^+$ 250.8832, found 250.8828. Spectroscopic data consistent with literature reported data for unlabelled analogue.[20]

3,3'',5,5''-Tetrakis(trifluoromethyl)-[1,1':3',1''-terphenyl]-5'-amine-^{15}N (5.19f)

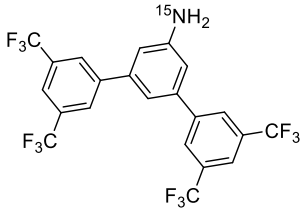

Title compound was prepared according to *General procedure V* using **5.19e** (501 mg, 1.98 mmol) and 3,5-bis(trifluoromethyl)phenylboronic acid (1.79 g, 6.95 mmol) allowing reaction to reflux for 21 hours. The crude product was purified via flash column chromatography (0% to 10% (v/v) EtOAc in pentane) to give **5.19f** as an off-white solid (864 mg, 84%). **^{1}H NMR** (400 MHz, CD_3CN): δ 8.29–8.23 (m, 3H), 8.00 (tt, J = 1.7, 0.9 Hz, 2H), 7.33 (t, J = 1.7 Hz, 1H), 7.09 (t, J = 1.7 Hz, 2H), 4.51 (d, J_{HN} = 82.8 Hz, 2H) ppm; **^{19}F NMR** (377 Hz, CD_3CN): δ −63.23 ppm; **^{13}C NMR** (101 MHz, CD_3CN): δ 150.6 (d, J_{CN} = 13 Hz), 144.3, 140.7, 132.5 (q, J_{CF} = 33 Hz), 128.6 (d, J_{CN} = 4 Hz), 124.7 (q, J_{CF} = 272 Hz), 122.1 (sept, J_{CF} = 4 Hz), 116.2, 114.6 (d, J_{CN} = 3 Hz) ppm; **HRMS** (ESI+) = *m/z* calculated for $C_{22}H_{11}F_{12}[^{15}N]K^+$ $[M+K]^+$ 608.3419, found 608.3428. Spectroscopic data consistent with literature reported data for unlabelled analogue.[1]

5'-(Isocyanato-^{15}N)-3,3'',5,5''-tetrakis(trifluoromethyl)-1,1':3',1''-terphenyl (5.19)

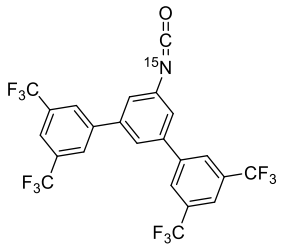

Compound **5.19** was prepared following procedure for unlabelled analogue.[5] In a Schlenk flask, aniline **5.19f** (122 mg, 0.24 mmol) was dissolved in anhydrous CH_2Cl_2 (1.5 mL) under an atmosphere of N_2. The solution was cooled to 0 °C, followed by addition of triphosgene (24 mg, 0.08 mmol), and dropwise addition of sat. aq. $NaHCO_3$ (1.5 mL), which resulted in the formation of a slurry. The reaction mixture was allowed vigorously stirred for 15 min. The organic phase was separated and extracted with CH_2Cl_2 (2 x 5 mL), washed with brine (5 mL), dried over $MgSO_4$, filtered over Celite and concentrated *in vacuo*. **5.19** was obtained as an off-white solid (127 mg, 99%) and was used without further purification. **^{1}H NMR** (400 MHz, $CDCl_3$): δ 7.95 (s, 4H), 7.85 (s, 2H), 7.50 (s, 1H), 7.32 (s, 2H) ppm; **^{13}C NMR** (126 MHz, $CDCl_3$): δ 141.5, 141.2 (d, J_{CN} = 2 Hz), 135.5 (d, J_{CN} = 18 Hz), 132.6 (q, J_{CF} = 34 Hz), 127.5–127.4 (m), 125.3 (d, J_{CN} = 46 Hz), 123.2 (q, J_{CF} = 273 Hz), 123.9 (d, J_{CN} = 3 Hz), 123.6, 122.1–122.0 (m) ppm; **^{15}N NMR** (51 MHz, $CDCl_3$): δ 48.4 (s) ppm; **^{19}F NMR** (377 MHz, $CDCl_3$): δ −62.82 (s) ppm. Spectroscopic data consistent with literature reported data for unlabelled analogue.[5]

5.2.5. Catalyst characterisation

5.2.5.1. Peptides described in chapter II

Peptide **2r** synthesis and characterisation is described in Section 5.2.3.

Boc-Leu-D-Pro-Acpc-Phe-NMe$_2$ (2a)

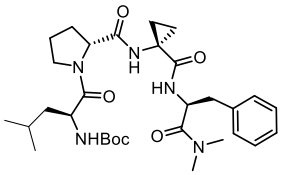

The title compound was prepared following *General Procedure I*, allowing reaction to stir for 16 h. Crude product (158 mg), was purified via flash column chromatography (5% then 10% (v/v) *i*-PrOH in CH_2Cl_2), giving **2a** as white powder (112 mg, 64%). **^{1}H NMR** (500 MHz, CD_2Cl_2): δ 7.74 (d, *J* = 8.7 Hz, 1H), 7.32–7.23 (m, 5H), 7.00 (s, 1H), 6.46 (d, *J* = 7.7 Hz), 5.08 (td, *J* = 8.5, 6.7 Hz, 1H), 4.45 (br q, *J* = 7.9 Hz, 1H), 4.43–4.30 (m, 1H), 3.94–3.91 (m, 1H), 3.64 (dt, *J* = 10.0, 6.7 Hz, 1H), 3.13 (dd, *J* = 13.1, 8.4 Hz, 1H), 3.02 (dd, *J* = 13.1, 6.5 Hz, 1H), 2.84 (s, 3H), 2.77 (s, 3H), 2.16–2.08 (m, 3H), 2.02–1.96 (m, 1H), 1.76–1.62 (m, 3H), 1.45 (s, 9H), 1.43–1.41 (m, 2H), 1.01 (d, *J* = 4.6 Hz, 3H), 1.00 (d, *J* = 4.8 Hz, 3H), 0.98–0.96 (m, 2H) ppm; **^{13}C NMR** (126 MHz, CD_2Cl_2): δ 172.7, 172.5, 171.1, 170.6, 156.4, 137.4, 129.4, 128.2, 126.5, 79.3, 61.3, 50.7, 50.4, 47.4, 40.9, 38.9, 36.8, 35.4, 34.3, 28.7, 28.1, 25.1, 24.7, 22.9, 22.1, 16.9, 16.7 ppm; $[\alpha]_D^{20°C}$ = −28.8 (*c* 0.9, $CHCl_3$); **HRMS** (ESI+) = *m/z* calculated for $C_{31}H_{48}N_5O_6^+$ $[M+H]^+$ 586.3599, found 586.3626; **IR** (thin layer film): ν 3295, 3012, 2958, 2872, 1694, 1638, 1528, 1446, 1219, 1170, 1045, 759 cm^{-1}; **m.p.** 181−182 °C.

Boc-Leu-Pro-Acpc-Phe-NMe$_2$ (2b)

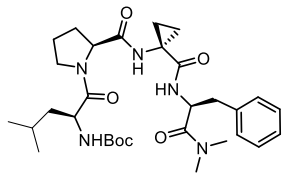

The title compound was prepared following *General Procedure I*, allowing reaction to stir for 24 h. The crude product was purified via flash column chromatography (5% then 10% (v/v) *i*-PrOH in CH_2Cl_2), giving **2b** as a white powder (127 mg, 72%). **^{1}H NMR** (500 MHz, CD_2Cl_2): δ 7.87 (d, *J* = 7.8 Hz, 1H), 7.30–7.21 (m, 5H), 6.92 (s, 1H), 5.80 (d, *J* = 9.0 Hz, 1H), 4.97 (td, *J* = 8.4, 5.3 Hz, 1H), 4.45 (br td, *J* = 10.3, 2.3 Hz, 1H), 4.22 (t, *J* = 7.1 Hz, 1H), 3.90–3.76 (m, 1H), 3.62 (dt, *J* = 9.6, 7.1 Hz), 3.05 (dd, *J* = 13.2, 8.7 Hz, 1H), 2.90 (s, 3H), 2.89 (dd, *J* = 13.2, 5.5 Hz, 1H), 2.79 (s, 3H), 2.20–2.12 (m, 1H), 2.11 (q, *J* = 6.1 Hz, 2H), 2.03–1.96 (m, 1H), 1.86–1.78 (m, 1H), 1.63 (ddd, *J* = 13.4, 11.4, 3.9 Hz, 1H), 1.52 (ddd, *J* = 10.2, 7.7, 4.4 Hz, 1H), 1.49–1.46 (m, 1H), 1.44 (s), 1.42 (ddd, *J*

= 10.2, 7.5, 4.1 Hz, 1H), 1.04 (ddd, *J* = 11.5, 7.5, 4.4 Hz, 1H), 1.02 (d, *J* = 6.5 Hz, 3H), 0.97 (d, *J* = 6.6 Hz, 3H), 0.93 (ddd, *J* = 11.5, 7.7, 4.1 Hz, 1H) ppm; **^{13}C NMR** (126 MHz, CD_2Cl_2): δ 173.3, 172.8, 170.6, 155.8, 137.8, 129.5, 128.1, 126.4, 79.0, 61.4, 51.5, 50.8, 47.4, 41.1, 38.7, 36.7, 35.5, 34.5, 28.2, 28.1, 25.6, 24.7, 23.2, 22.1, 17.3, 16.3 ppm; $[\alpha]_D^{20°C}$ = −38.5 (*c* 0.9, $CHCl_3$); **HRMS** (ESI+) = *m*/*z* calculated for $C_{31}H_{47}N_5O_6Na^+$ $[M+Na]^+$ 608.3419, found 608.3428; **IR** (thin layer film): ν 3305, 3296, 3013, 2962, 1702, 1638, 1525, 1453, 1392, 1367, 1046, 1027, 760, 702 cm^{-1}; **m.p.** 98 °C.

3,5-$(CF_3)_2C_6H_3$NHC(O)-Pro-Gly-Phe-NMe_2 (2c)

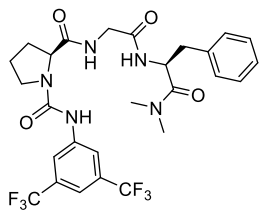

The title compound was prepared following *General Procedure IIIa*. The crude product was purified via flash column chromatography (0−5% (v/v) *i*-PrOH in CH_2Cl_2, followed by 0−20% (v/v) *i*-PrOH in toluene), giving **2c** as a white solid (452 mg, 69%). **^{1}H NMR** (500 MHz, CD_2Cl_2): δ 8.05 (s, 2H), 7.80 (br s, 1H), 7.50 (s, 1H), 7.40 (br s, 1H), 7.37 (t, *J* = 6.4 Hz, 1H), 7.31–7.24 (m, 3H), 7.15 (d, *J* = Hz, 2H), 5.07 (q, *J* = 7.1 Hz, 1H), 4.54 (dd, *J* = 8.3, 2.3 Hz, 1H), 3.91 (br s, 2H), 3.65–3.25 (m, 2H), 2.98 (dd, *J* = 13.5, 7.0 Hz, 1H), 2.98 (dd, *J* = 13.5, 6.4 Hz, 1H), 2.85 (s, 3H), 2.76 (s, 3H), 2.34–2.29 (m, 1H), 2.21–2.13 (m, 1H), 2.09–2.00 (m, 2H) ppm; **^{19}F NMR** (377 MHz, $CDCl_3$): δ −62.94 ppm; **^{13}C NMR** (126 MHz, $CDCl_3$): δ 172.9, 171.03, 168.1, 155.4, 140.8, 137.9, 135.8, 131.7 (q, J_{CF} = 34 Hz), 129.4, 129.1, 128.5, 128.2, 127.1, 125.3, 123.3 (q, J_{CF} = 272 Hz), 119.9 (br s), 60.8, 50.7, 47.3, 42.6, 39.3, 36.8, 35.5, 29.7, 29.4, 24.4, 21.5 ppm; **HRMS** (ESI+) = *m*/*z* calculated for $C_{27}H_{30}F_6N_5O_4^+$ $[M+H]^+$ 602.2196, found 602.2205; **IR** (thin layer film): ν 3293, 2928, 1654, 1557, 1444, 1362, 1280, 1180, 1134, 883, 759 cm^{-1}; **m.p.** 115−116 °C; $[\alpha]_D^{20°C}$ = −24.4 (*c* 0.8, $CHCl_3$).

3,5-[3,5-$(CF_3)_2C_6H_3]_2C_6H_3$NHC(O)-Pro-Gly-Phe-NMe_2 (2d)

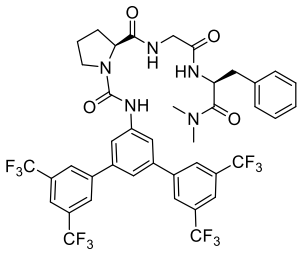

Synthesised by Dr. Thomas Schlatzer

The title compound was prepared following *General Procedure IIIa*. The crude product was purified via flash column chromatography (15−85% (v/v) acetone in toluene), giving **2d** as a white solid

(459 mg, 79%). **^{1}H NMR** (400 MHz, $CDCl_3$): δ 7.93 (s, 4H), 7.84 (s, 2H), 7.72 (d, *J* = 1.6 Hz, 2H), 7.51 (t, *J* = 6.1 Hz, 1H), 7.45–7.34 (m, 1H), 7.30 (d, *J* = 7.4 Hz, 1H), 7.25 (t, *J* = 1.6 Hz, 1H), 7.20–7.10 (m, 3H), 6.99–6.88 (m, 2H), 4.92 (td, *J* = 7.9, 5.8 Hz, 1H), 4.67–4.59 (m, 1H), 4.09 (dd, *J* = 17.0, 6.8 Hz, 1H), 3.79–3.68 (m, 2H), 3.59 (q, *J* = 7.8 Hz, 1H), 2.88–2.73 (m, 2H), 2.70 (s, 3H), 2.50 (s, 3H), 2.43–2.31 (m, 1H), 2.22–2.01 (m, 3H) ppm; **^{13}C NMR** (126 MHz, $CDCl_3$): δ 173.1, 171.3, 168.3, 155.5, 142.6, 140.9, 139.9, 136.0, 132.3 (q, J_{CF} = 33 Hz), 129.4, 128.5, 127.5–127.3 (m), 127.2, 123.4 (q, J_{CF} = 273 Hz), 121.7–121.5 (m), 120.8, 119.7, 60.7, 50.7, 47.2, 42.9, 39.2, 36.8, 35.6, 29.0, 25.1 ppm; **^{19}F NMR** (377 MHz, $CDCl_3$): δ –62.72 ppm; **m.p.** 126–128 °C; **HRMS** (ESI+) = *m*/*z* calculated for $C_{41}H_{35}F_{12}N_5O_4Na^+$ $[M+Na]^+$ 912.2390, found 912.2410; $[\alpha]_D^{20°C}$ = –24.8 (*c* 0.9, $CHCl_3$); **IR** (thin layer film): ν 3291, 2932, 1727, 1642, 1605, 1535, 1374, 1283, 1178, 1141, 924, 684, 665 cm^{-1}.

3,5-[3,5-(F)$_2$C$_6$H$_3$]$_2$C$_6$H$_3$NHC(O)-Pro-Gly-Phe-NMe$_2$ (2e)

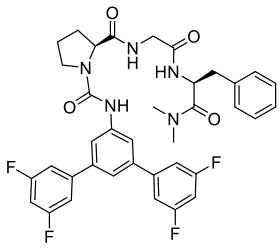

Synthesised by Jessica B. Sellar

The title compound was prepared following *General Procedure IIIc*. The crude product was purified via flash column chromatography (10−50% (v/v) acetone in toluene), giving **2e** as a white solid (214 mg, 62%). **^{1}H NMR** (400 MHz, $CDCl_3$): δ 7.63 (d, *J* = 1.6 Hz, 2H), 7.59 (t, *J* = 6.2 Hz, 1H), 7.48 (d, *J* = 7.4 Hz, 1H), 7.35 (s, 1H), 7.23 (t, *J* = 1.7 Hz, 1H), 7.20–7.13 (m, 3H), 7.10–7.00 (m, 4H), 6.97 (dd, *J* = 6.5, 2.9 Hz, 2H), 6.75 (tt, *J* = 8.8, 2.3 Hz, 2H), 4.96 (td, *J* = 7.8, 6.1 Hz, 1H), 4.60 (dd, *J* = 7.6, 3.4 Hz, 1H), 4.04 (dd, *J* = 17.0, 6.5 Hz, 1H), 3.78 (dd, *J* = 17.0, 5.5 Hz, 1H), 3.77–3.67 (m, 1H), 3.64–3.52 (m, 1H), 2.87 (dd, *J* = 13.3, 6.2 Hz, 1H), 2.83 (dd, *J* = 13.3, 8.0 Hz, 1H), 2.71 (s, 3H), 2.50 (s, 3H), 2.37–2.30 (m, 1H), 2.17–2.00 (m, 3H) ppm; **^{19}F{^{1}H} NMR** (377 MHz, $CDCl_3$): δ −109.43 ppm; **^{13}C NMR** (101 MHz, $CDCl_3$): δ 173.2, 171.3, 168.3, 163.2 (dd, J_{CF} = 248, 13 Hz), 155.5, 143.8 (t, J_{CF} = 9 Hz), 140.3, 140.0 (br s), 135.9, 129.3, 128.3, 127.0, 120.3, 119.1, 110.1 (d, J_{CF} = 26 Hz), 102.8 (t, J_{CF} = 26 Hz), 60.8, 50.6, 47.1, 42.8, 39.0, 36.7, 35.5, 29.3, 24.8 ppm; $[\alpha]_D^{25°C}$ = −11.4 (*c* 1.0, MeOH); **HRMS** (ESI+) = *m*/*z* calculated for $C_{37}H_{36}F_4N_5O_4^+$ $[M+H]^+$ 690.2698,

found 690.2687; **IR** (thin layer film): ν 3289, 2931, 1641, 1591, 1548, 1422, 1320, 1119, 989, 852, 761 cm^{-1}; **m.p.** 191–192 °C.

3,5-$(C_6H_5)_2C_6H_3$NHC(O)-Pro-Gly-Phe-NMe_2 (2f)

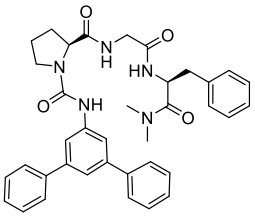

Synthesised by Jessica B. Sellar

The title compound was prepared following *General Procedure IIIc*. The crude product was purified via flash column chromatography (20−70% (v/v) acetone in toluene), giving **2f** as a white solid (160 mg, 48%). **^{1}H NMR** (400 MHz, $CDCl_3$): δ 7.57 (d, *J* = 1.4 Hz, 2H), 7.52–7.51 (m, 5H), 7.37–7.31 (m, 5H), 7.28–7.24 (m, 2H), 7.15–7.09 (m, 4H), 6.95–6.92 (m, 2H), 6.90 (br s, 1H), 4.91 (td, *J* = 8.0, 6.0 Hz, 1H), 4.59–4.57 (m, 1H), 4.04 (dd, *J* = 16.9, 6.8 Hz, 1H), 3.69 (dd, *J* = 16.9, 5.6 Hz, 1H), 3.64–3.59 (m, 1H), 3.49–3.43 (m, 1H), 2.83 (dd, *J* = 13.1, 5.4 Hz, 1H), 2.77 (dd, *J* = 13.1, 8.5 Hz, 1H), 2.65 (s, 3H), 2.41 (s, 3H), 2.37–2.34 (m, 1H), 2.10–1.95 (m, 3H) ppm; **^{13}C NMR** (101 MHz, $CDCl_3$): δ 173.1, 171.1, 168.3, 155.7, 142.3, 140.9, 139.6, 136.1, 129.4, 128.7, 128.3, 127.4, 127.2, 126.9, 121.2, 118.2, 60.6, 50.4, 46.9, 42.8, 39.1, 36.7, 35.5, 28.8, 24.9 ppm; $[\alpha]_D^{25^\circ C}$ = −16.1 (*c* 1.0, MeOH); **HRMS** (ESI+) = *m*/*z* calculated for $C_{37}H_{40}N_5O_4^+$ $[M+H]^+$ 618.3075, found 618.3081; **IR** (thin layer film): ν 3312, 3008, 2358, 1642, 1599, 1546, 1497, 1452, 1429, 1340, 1217, 1159, 1044, 873, 761, 701, 669, 647, 634 cm^{-1}; **m.p.** 114–115 °C.

3,5-[3,5-(*t*Bu)$_2$$C_6H_3$]$_2$$C_6H_3$NHC(O)-Pro-Gly-Phe-$NMe_2$ (2g)

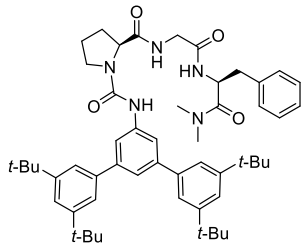

Synthesised by Jessica B. Sellar

The title compound was prepared following *General Procedure IIIc*. The crude product was purified via flash column chromatography (10−70% (v/v) acetone in toluene), giving **2g** as a white solid (214 mg, 51%). **^{1}H NMR** (400 MHz, $CDCl_3$): δ 7.65 (t, *J* = 6.1 Hz, 1H), 7.56 (d, *J* = 1.6 Hz, 2H), 7.45 (q, *J* = 1.8 Hz, 3H), 7.41 (d, *J* = 1.8 Hz, 4H), 7.30–7.14 (m, 3H), 7.10–7.03 (m, 2H), 6.99 (d, *J* = 7.8 Hz, 1H), 6.79 (s, 1H), 5.01 (td, *J* = 8.1, 5.4 Hz, 1H), 4.74–4.64 (m, 1H), 4.12 (dd, *J* = 17.0, 6.8 Hz, 1H), 3.81–3.64 (m, 2H), 3.56–3.42 (m, 1H), 3.00–2.78 (m, 2H), 2.72 (s, 3H), 2.51 (s, 4H), 2.15–1.93 (m, 3H), 1.37 (s, 36H) ppm; **^{13}C NMR** (101 MHz, $CDCl_3$): δ 172.7, 170.7, 168.2, 155.8,

151.1, 143.8, 140.7, 139.0, 136.01, 129.5, 129.1, 128.4, 128.2, 126.9, 125.3, 122.50, 121.9, 121.6, 118.3, 60.2, 50.3, 46.9, 42.9, 39.4, 36.7, 35.5, 35.0, 31.6, 27.8, 25.2 ppm; $[\alpha]_D^{25℃}$ = −23.5 (*c* 1.0, MeOH); **HRMS** (ESI+) = *m*/*z* calculated for $C_{53}H_{72}N_5O_4^+$ $[M+H]^+$ 842.5579, found 842.5611; **IR** (thin layer film): ν 3296, 2962, 1644, 1592, 1546, 1456, 1417, 1363, 1248, 1207, 863, 759, 714, 657, 621 cm^{-1}; **m.p**. 141−142 °C.

3,5-[3,5-$(CF_3)_2C_6H_3$]$_2C_6H_3$NHC(O)-Flp-Gly-Phe-NMe_2 (2h)

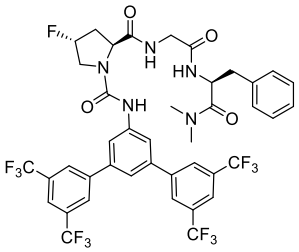

The title compound was prepared following *General Procedure IIIa*. The crude product was purified via flash column chromatography (5−10% *i*-PrOH in toluene), giving **2h** as a white solid (241 mg, 90%). **^{1}H NMR** (500 MHz, $CDCl_3$): δ 7.99 (s, 5H), 7.89 (s, 2H), 7.83 (br s, 1H), 7.71 (s, 2H), 7.53 (d, *J* = 6.1 Hz, 1H), 7.25 (s, 1H), 7.15–7.08 (m, 3H), 6.82 (d, *J* = 7.1 Hz, 2H), 5.37 (br d, J_{HF} = 52.5 Hz, 1H), 4.84–4.79 (m, 2H), 4.14 (dd, *J* = 17.6, 6.8 Hz, 1H), 4.04 (dd, J_{HF} = 21.1 Hz, J_{HH} = 11.6 Hz, 1H), 3.94 (br dd, J_{HF} = 35.1 Hz, J_{HH} = 11.3 Hz, 1H), 3.62 (dd, *J* = 17.6, 5.0 Hz, 1H), 2.73 (dd, *J* = 13.2, 5.8 Hz, 1H), 2.68 (dd, *J* = 13.2, 8.7 Hz, 1H), 2.65 (s, 3H), 2.50 (s, 3H), 2.62–2.43 (m, 2H) ppm; **^{13}C NMR** (126 MHz, CD_2Cl_2): δ 172.8, 171.2, 168.1, 155.2, 142.4, 140.7, 139.4, 136.1, 131.9 (q, J_{CF} = 33 Hz), 129.1, 128.0, 127.3 (br s), 126.8, 123.4 (q, J_{CF} = 273 Hz), 121.3 (br s), 120.5, 119.9, 92.4 (d, J_{CF} = 178 Hz), 59.1, 53.7, 50.9, 43.1, 38.3, 36.4, 35.7, 35.2 ppm; **^{19}F NMR** (470 MHz, CD_2Cl_2): δ −62.68 (s, 12F), −176.94 (br s, 1F) ppm; **HRMS** (ESI+) = *m*/*z* calculated for $C_{41}H_{34}F_{13}N_5O_4Na^+$ $[M+Na]^+$ 930.2295, found 930.2265; $[\alpha]_D^{20℃}$ = −15.8 (*c* 0.9, $CHCl_3$); **m.p**. 133 °C; **IR** (thin layer film): ν 3271, 3081, 2934, 1641, 1608, 1546, 1430, 1367, 1279, 1176, 1134, 901, 870, 844, 704, 683 cm^{-1}.

3,5-[3,5-$(CF_3)_2C_6H_3$]$_2C_6H_3$NHC(O)-flp-Gly-Phe-NMe_2 (2i)

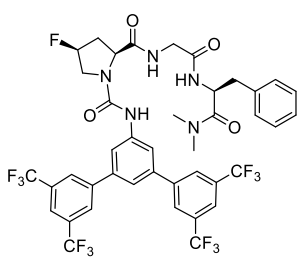

The title compound was prepared following *General Procedure IIIa*. The crude product was purified via flash column chromatography (20−60% (v/v) acetone in toluene), giving **2i** as a white solid (799 mg, 89%). **^{1}H NMR** (500 MHz, CD_2Cl_2): δ 8.05 (s, 4H), 8.03 (s, 1H), 7.92 (s, 2H), 7.72 (d, *J* = 1.5 Hz, 2H), 7.46 (t, *J* = 5.5 Hz, 1H), 7.41 (t, *J* = 1.5 Hz, 1H),

7.27 (d, J = 7.9 Hz, 1H), 7.24–7.20 (m, 3H), 7.07–7.05 (m, 2H), 5.42 (dt, J_{HF} = 51.8 Hz, J_{HH} = 3.2 Hz, 1H), 4.99 (q, J = 7.6 Hz, 1H), 4.77 (d, J = 10.0 Hz, 1H), 4.06 (br dd, J_{HF} = 23.1 Hz, J_{HH} = 12.4 Hz, 1H), 3.98–3.86 (m, 3H), 2.91 (dd, J = 13.4, 7.6 Hz, 1H), 2.83 (dd, J = 13.4, 6.4 Hz, 1H), 2.77 (br t, J_{HF} = 16.0 Hz, J_{HH} = 16.0 Hz, 1H), 2.75 (s, 3H), 2.60 (s, 3H), 2.53 (dddd, J_{HF} = 42.9 Hz, J_{HH} = 14.8, 10.3, 3.7 Hz, 1H) ppm; **^{13}C NMR** (126 MHz, CD_2Cl_2): δ 172.2, 170.9, 167.9, 155.4, 142.5, 140.9, 139.6, 136.1, 132.0 (q, J_{CF} = 33 Hz), 129.3, 128.2, 127.3 (br s), 127.9, 123.4 (q, J_{CF} = 273 Hz), 121.4 (br s), 120.5, 119.5, 92.4 (d, J_{CF} = 118 Hz), 60.2, 50.4, 47.6, 38.7, 36.6, 36.5, 35.2, 29.7 ppm; **^{19}F NMR** (470 MHz, CD_2Cl_2): δ −63.11 (12F), −172.93 (1F) ppm; **HRMS** (ESI+) = *m/z* calculated for $C_{41}H_{34}F_{13}N_5O_4Na^+$ $[M+Na]^+$ 930.2295, found 930.2339; **IR** (thin layer film): ν 3315, 2928, 1656, 1561, 1371, 1232, 1178, 1137, 757, 870, 845, 683 cm^{-1}; **m.p.** 152 °C; $[\alpha]_D^{20°C}$ = −23.7 (*c* 0.9, $CHCl_3$).

3,5-[3,5-$(CF_3)_2C_6H_3$]$_2C_6H_3$NHC(O)-Pro[4,4-F_2]-Gly-Phe-NMe_2 (2j)

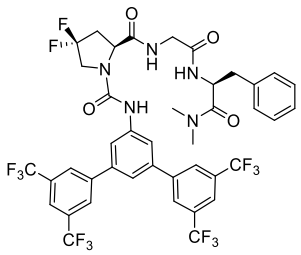

The title compound was prepared following *General Procedure IIIa.* The crude product was purified via flash column chromatography (10−20% (v/v) *i*-PrOH in CH_2Cl_2 followed by 40% acetone in toluene), giving **2j** as a white solid (278 mg, 77%). **^{1}H NMR** (500 MHz, CD_2Cl_2): δ 7.96 (s, 4H), 7.93 (br s, 1H), 7.86 (br s, 2H), 7.75 (br t, J = 4.9 Hz, 1H), 7.70 (d, J = 1.1, 2H), 7.33 (d, J = 7.10 Hz, 1H), 7.26 (br t, J = 1.3 Hz, 1H), 7.14–7.09 (m, 3H), 6.88–6.86 (m, 2H), 4.88–4.83 (m, 2H), 4.09–4.05 (m, 2H), 4.03 (dd, J = 16.7, 6.5 Hz, 1H), 3.69 (dd, J = 16.7, 5.6 Hz, 1H), 2.87–2.69 (m, 4H), 2.66 (s, 3H), 2.50 (s, 3H) ppm; **^{19}F NMR** (377 MHz, $CDCl_3$): δ −62.71 (s, 12F), −97.85 (br d, J_{FF} = 233.9 Hz, 1F), −103.19 (br d, J_{FF} = 233.9 Hz, 1F) ppm; **^{13}C NMR** (126 MHz, CD_2Cl_2): δ 171.8, 171.5, 168.3, 155.6, 142.7, 140.9, 139.9, 136.3, 132.3 (q, J_{CF} = 33 Hz), 129.6, 128.6, 127.7 (br s), 127.3, 126.9 (t, J_{CF} = 250 Hz), 123.8 (q, J_{CF} = 273 Hz), 121.8 (br s), 121.1, 120.1, 58.9, 54.0, 51.3, 43.4, 38.9, 37.2 (t, J_{CF} = 25 Hz), 36.9, 35.7 ppm; **HRMS** (ESI+) = *m/z* calculated for $C_{41}H_{33}F_{14}N_5O_4Na^+$ $[M+Na]^+$ 948.2201, found 948.2208; $[\alpha]_D^{20°C}$ = −19.3 (*c* 0.9, $CHCl_3$). **IR** (thin layer film): ν 3290, 2927, 1664, 1640, 1556, 1371, 1280, 1176, 1137, 901, 760, 706 cm^{-1}; **m.p**. 146−148 °C.

3,5-[3,5-$(CF_3)_2C_6H_3]_2C_6H_3$NHC(O)-Pro[5,5-Me_2]-Gly-Phe-NMe_2 (2k)

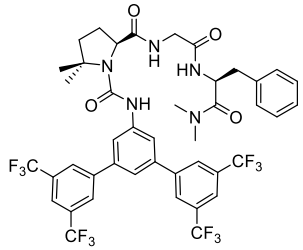

The title compound was prepared following *General Procedure IIIa.* The crude product was purified via flash column chromatography (0−5% (v/v) *i*-PrOH in CH_2Cl_2), giving **2k** as a white solid (271 mg, 81%). **^{1}H NMR** (500 MHz, CD_2Cl_2): δ 8.05 (br s, 1H), 7.87 (s, 4H), 7.81(s, 2H), 7.65 (br s, 1H), 7.54 (s, 2H), 7.38 (br s, 1H), 7.23–7.20 (m, 4H), 7.10–7.08 (m, 2H), 4.93 (q, *J* = 7.4 Hz, 1H), 4.60 (d, *J* = 8.9 Hz, 1H), 3.88 (dd, *J* = 16.9, 6.2 Hz, 1H), 3.78 (dd, *J* = 16.9, 6.4 Hz, 1H), 2.92 (d, *J* = 13.3, 7.7 Hz, 1H), 2.86 (d, *J* = 13.3, 7.0 Hz, 1H), 2.54 (s, 6H), 2.39–2.31 (m, 1H), 2.13 (ddt, *J* = 12.7, 6.5, 1.2 Hz, 1H), 2.05 (td, *J* = 12.4, 6.7 Hz, 1H), 1.84 (ddd, *J* = 12.1, 6.7, 1.2 Hz, 1H), 1.74 (s, 3H), 1.51 (s, 3H) ppm; **^{19}F NMR** (470 MHz, CD_2Cl_2): δ −63.18 ppm; **^{13}C NMR** (126 MHz, CD_2Cl_2): δ 173.8, 171.7, 168.2, 155.5, 142.1, 141.2, 138.8, 136.3, 131.9 (q, J_{CF} = 34 Hz), 129.4, 128.3, 126.9, 126.9 (br s), 123.3 (q, J_{CF} = 272 Hz), 122.1 (br s), 121.3 (sept, J_{CF} = 4 Hz), 120.4 (br s), 63.7, 63.4, 50.8, 42.4, 40.2, 38.6, 36.5, 35.0, 28.2, 27.8, 24.5 ppm; **HRMS** (ESI+) = *m*/*z* calculated for $C_{43}H_{39}F_{12}N_5O_4Na^+$ $[M+Na]^+$ 940.2703, found 940.2722; **IR** (thin layer film): ν 3440, 3277, 3077, 2970, 1673, 1634, 1605, 1534, 1369, 1281, 1181, 1108, 918, 845, 761, 706, 669 cm^{-1}; **m.p**. 143 °C; $[\alpha]_D^{20℃}$ = −15.2 (*c* 0.9, $CHCl_3$).

3,5-[3,5-$(CF_3)_2C_6H_3]_2C_6H_3$NHC(O)-α-Me-Pro-Gly-Phe-NMe_2 (2l)

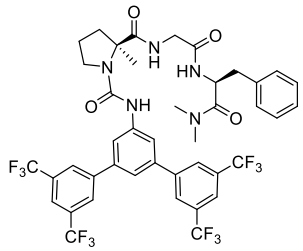

The title compound was prepared following *General Procedure IIIa.* The crude product was purified via flash column chromatography (50% (v/v) acetone in toluene), giving **2l** as a white solid (606 mg, 82%). **^{1}H NMR** (500 MHz, CD_2Cl_2): δ 8.02 (s, 4H), 7.90 (s, 2H), 7.81 (s, 2H), 7.46 (br t, *J* = 5.1 Hz), 7.36 (d, *J* = 6.7 Hz, 1H), 7.31 (s, 1H), 7.24 (br s), 7.16–7.12 (m, 3H), 6.87 (d, *J* = 6.7 Hz, 2H), 4.84 (q, *J* = 7.5 Hz, 1H), 3.93 (dd, *J* = 17.2, 6.0 Hz), 3.88–3.83 (m, 2H), 3.73 (q, *J* = 7.1 Hz, 1H), 2.74–2.64 (m, 2H), 2.71 (s, 3H), 2.56 (s, 3H), 2.50 (dt, *J* = 12.5, 7.3, 1H), 2.16–2.09 (m, 2H), 1.97 (dt, *J* = 12.5, 6.7 Hz, 1H), 1.79 (s, 3H) ppm; **^{19}F NMR** (377 MHz, $CDCl_3$): δ −62.66 ppm; **^{13}C NMR** (126 MHz, CD_2Cl_2): δ 175.1, 171.1, 168.5, 154.4, 142.5, 140.6, 139.9, 136.0, 132.1 (q, J_{CF} = 33 Hz), 129.1, 128.2, 127.4 (br s), 126.9, 123.0 (q, J_{CF} = 273

Hz), 121.4 (br s), 121.0, 119.8, 67.5, 50.7, 48.1, 43.2, 39.3, 38.8, 36.6, 35.4, 23.4, 22.4 ppm; $[\alpha]_D^{25°C}$ = −24.5 (*c* 1.0, acetone); **m.p.** 157−159 °C; **IR** (thin layer film): ν 3295, 2928, 1644, 1541, 1468, 1426, 1371, 1279, 1178, 1136, 899, 844, 706, 683 cm^{-1}; **HRMS** (ESI+) = *m*/*z* calculated for $C_{42}H_{38}F_{12}N_5O_4^+$ [M+H]$^+$ 904.2727, found 904.2653.

3,5-[3,5-(CF$_3$)$_2$C$_6$H$_3$]$_2$C$_6$H$_3$NHC(O)-D-Pro-Gly-Phe-NMe$_2$ (2m)

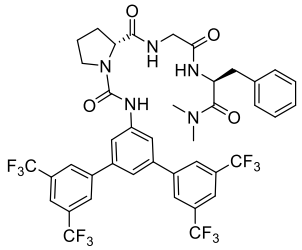

The title compound was prepared following *General Procedure IIIa*. The crude product was purified via flash column chromatography (40−60% (v/v) acetone in toluene), giving **2m** as a white solid (532 mg, 78%). **^{1}H NMR** (400 MHz, $CDCl_3$): δ 7.95 (s, 4H), 7.80 (br s, 4H), 7.64 (br t, *J* = 5.1 Hz. 1H), 7.51 (s, 1H), 7.37 (d, *J* = 6.7 Hz, 1H), 7.25 (t, *J* = 1.5 Hz, 1H), 7.13–7.07 (m, 3H), 6.92 (dd, *J* = 7.3, 1.4 Hz, 2H), 4.83 (ddd, *J* = 9.2, 6.9, 5.6 Hz, 1H), 4.63 (dd, *J* = 7.1, 3.6 Hz, 1H), 3.97–3.91 (m, 2H), 3.88–3.81 (m, 1H), 3.73 (q, *J* = 7.8 Hz, 1H), 2.85 (dd, *J* = 13.0, 5.6 Hz, 1H), 2.68 (dd, *J* = 13.0, 9.2 Hz, 1H), 2.65 (s, 3H), 2.37 (s, 3H), 2.33–2.06 (m, 4H) ppm; **^{19}F NMR** (470 MHz, $CDCl_3$): δ –62.75 ppm; **^{13}C NMR** (101 MHz, $CDCl_3$): δ 172.5, 171.0, 168.3, 155.4, 142.5, 140.8, 139.8, 135.9, 132.1 (q, J_{CF} = 33 Hz), 129.1, 128.2, 127.3 (br s), 126.9, 123.0 (q, J_{CF} = 273 Hz), 121.4 (br s), 120.6, 118.5, 61.2, 50.7, 47.0, 42.5, 39.2, 36.6, 35.4, 29.1, 25.1 ppm; $[\alpha]_D^{25°C}$ = 93.7 (*c* 1.0, MeOH); **m.p.** 143–145 °C; **IR** (thin layer film): ν 3307, 1646, 1547, 1475, 1443, 1359, 1279, 1177, 1130, 883, 702, 682, 628 cm^{-1}; **HRMS** (ESI+) = *m*/*z* calculated for $C_{41}H_{36}F_{12}N_5O_4^+$ [M+H]$^+$ 890.2570, found 890.2488.

3,5-[3,5-(CF$_3$)$_2$C$_6$H$_3$]$_2$C$_6$H$_3$NHC(O)-Pro-Acbc-Phe-NMe$_2$ (2n)

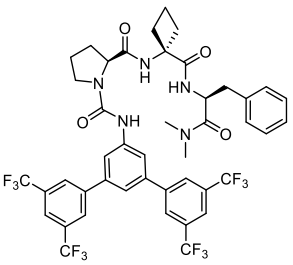

Synthsised by Jessica B. Sellar

The title compound was prepared following *General Procedure IIIa*. The residue was purified via flash column chromatography (10−50% (v/v) acetone in toluene) to give compound **2n** as a white powder (350 mg, 75%). **^{1}H NMR** (400 MHz, CD_3OD): δ 8.09 (d, *J* = 1.7 Hz, 4H), 7.93 (d, *J* = 1.9 Hz, 2H), 7.86 (d, *J* = 1.7 Hz, 2H), 7.40 (t, *J* = 1.7 Hz, 1H), 7.09–6.92 (m, 3H), 6.69–6.60 (m, 2H), 4.60 (dd, *J* = 10.4, 5.2 Hz, 1H), 4.47 (dd, *J* = 7.5, 6.0 Hz, 1H), 3.76 (dt, *J* = 9.2, 7.0 Hz, 1H), 3.66 (ddd,

J = 9.1, 6.9, 4.8 Hz, 1H), 2.86–2.66 (m, 2H), 2.62 (s, 3H), 2.54 (dd, J = 13.0, 10.4 Hz, 1H), 2.40 (s, 4H), 2.33–2.17 (m, 3H), 2.19–1.90 (m, 6H) ppm; **^{19}F NMR** (377 MHz, CD_2Cl_2): δ −63.06 ppm; **^{13}C NMR** (101 MHz, CD_3OD): δ 174.3, 173.7, 172.1, 155.1, 142.9, 141.3, 139.2, 136.4, 131.8 (q, J_{CF} = 33 Hz), 128.7, 127.6, 127.3, 126.3, 123.5 (q, J_{CF} = 271 Hz), 120.7, 120.2, 120.1, 60.5, 58.9, 51.4, 46.5, 38.0, 35.8, 34.4, 30.9, 30.6, 29.2, 25.0, 15.1 ppm; $[\alpha]_D^{25°C}$ = −50.5 (c 1.0, MeOH); **HRMS** (ESI+) = m/z calculated for $C_{44}H_{40}F_{12}N_5O_4^+$ $[M+H]^+$ 930.2883, found 930.2903; **IR** (thin layer film): ν 3260**,** 2947, 2361, 1641, 1430, 1373, 1281, 1216, 1180, 1138, 1106, 844, 762, 706, 683 cm^{-1}; **m.p**. 181 °C.

3,5-[3,5-(CF$_3$)$_2$C$_6$H$_3$]$_2$C$_6$H$_3$NHC(O)-Pro-Aib-Phe-NMe$_2$ (2o)

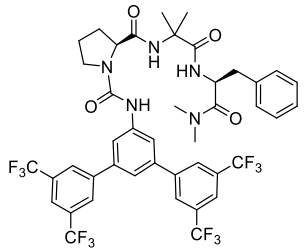

The title compound was prepared following *General Procedure IIIa.* The residue was purified via flash column chromatography (10−50% (v/v) acetone in toluene) to give compound **2o** as a white powder (156 mg, 85%). **^{1}H NMR** (500 MHz, DMSO-d_6): δ 8.61 (s, 1H), 8.37 (s, 1H), 8.29 (s, 4H), 8.11 (s, 2H), 8.03 (d, J = 1.3 Hz, 2H), 7.73 (br t, J = 1.3 Hz, 1H), 7.50 (d, J = 8.0 Hz, 1H), 7.02–6.96 (m, 3H), 6.71 (dd, J = 7.2, 1.0 Hz, 2H), 4.67 (td, J = 8.4, 5.9 Hz, 1H), 4.39 (br t, J = 5.6 Hz, 1H), 3.67–3.63 (m, 1H), 3.57–3.53 (m, 1H), 2.64 (dd, J = 13.3, 9.0 Hz, 1H), 2.56 (dd, J = 13.3, 5.9 Hz, 1H), 2.52 (s, 3H), 2.47 (s, 3H), 2.13–2.05 (m, 2H), 1.95–1.86 (m, 2H), 1.35 (s, 3H), 1.26 (s, 3H) ppm; **^{19}F NMR** (377 MHz, CD_2Cl_2): δ −63.07 ppm; **^{13}C NMR** (126 MHz, DMSO-d_6): δ 173.7, 172.6 (br s), 170.7, 154.4, 143.2, 142.2, 138.8, 137.7, 131.3 (q, J_{CF} = 33 Hz), 129.3, 128.2 (br s), 128.0, 126.5, 123.9 (q, J_{CF} = 272 Hz), 121.6 (br s), 120.5, 119.4, 60.3, 56.3, 50.4, 47.1, 38.3, 36.5, 35.1, 29.8 (br s), 26.8, 25.1 (br s), 24.3 ppm; **IR** (thin layer film): ν 3284, 2928, 2856, 1642, 1606, 1543, 1429, 1373, 1281, 1181, 1139, 1106, 900, 798, 683, 659 cm^{-1}; **HRMS** (ESI+) = m/z calculated for $C_{43}H_{40}F_{12}N_5O_4^+$ $[M+H]^+$ 918.2883, found 918.2886; $[\alpha]_D^{20°C}$ = −17.1 (c 0.9, acetone); **m.p.** 155−158 °C.

3,5-[3,5-$(CF_3)_2C_6H_3$]$_2C_6H_3$NHC(O)-Pro-Acpc-Phe-NMe_2 (2p)

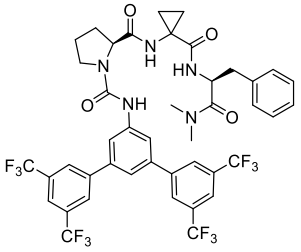

The title compound was prepared following *General Procedure IIIa.* The crude product was purified via flash column chromatography (10−50% (v/v) acetone in toluene), giving **2p** as a white solid (180 mg, 99%). **^{1}H NMR** (500 MHz, DMSO-d_6): δ 8.97 (s, 1H), 8.67 (s, 1H), 8.26 (s, 4H), 8.09 (s, 2H), 8.05 (d, J = 1.3 Hz, 2H), 7.90 (d, J = 7.4 Hz, 1H), 7.69 (t, J = 1.5 Hz, 1H), 7.00 (tt, J = 7.2, 1.2 Hz, 1H), 6.94 (br t, J = 7.3 Hz, 2H), 6.61 (br d, J = 7.1 Hz, 2H), 4.58 (ddd, J = 9.1, 7.5, 6.0 Hz, 1H), 4.27 (br t, J = 6.7 Hz, 1H), 3.68 (td, J = 9.2, 6.6 Hz, 1H), 3.59–3.54 (m, 1H), 2.53 (dd, J = 12.9, 9.2 Hz, 1H), 2.49 (s, 3H), 2.42 (s, 3H), 2.53 (dd, J = 12.9, 6.0 Hz, 1H), 2.12–2.05 (m, 2H), 1.95–1.89 (m, 1H), 1.85–1.78 (m, 1H), 1.09 (ddd, J = 9.8, 7.2, 3.4 Hz, 1H), 1.28 (ddd, J = 10.0, 7.2, 3.8 Hz, 1H), 0.86 (ddd, J = 10.0, 6.9, 3.4 Hz, 1H), 0.80 (ddd, J = 9.8, 6.9, 3.8 Hz, 1H) ppm; **^{19}F NMR** (470 MHz, DMSO-d_6): δ −61.00 ppm; **^{13}C NMR** (151 MHz, DMSO-d_6): δ 173.7, 170.5, 170.2, 154.2, 142.6, 141.6, 138.3, 137.0, 130.8 (q, J_{CF} = 33 Hz), 128.6, 127.7 (br), 127.5, 126.0, 123.4 (q, J_{CF} = 273 Hz), 121.1 (t, J_{CF} = 3 Hz), 120.3, 119.2, 60.3, 50.5, 46.6, 37.7, 36.0, 34.6, 33.5, 29.1 (br), 24.7 (br), 16.1, 15.6 ppm; **HRMS** (ESI+) = m/z calculated for $C_{43}H_{37}F_{12}N_5O_4Na^+$ $[M+Na]^+$ 938.2546, found 938.2524; $[\alpha]_D^{20°C}$ = –45.9 (*c* 0.9, acetone); **m.p.** 241−243 °C; **IR** (thin layer film): ν 3272, 2926, 2856, 1719, 1663, 1641, 1536, 1372, 1281, 1180, 1139, 900, 846, 706 cm^{-1}.

3,5-[3,5-$(CF_3)_2C_6H_3$]$_2C_6H_3$NHC(O)-Pro-Gly-Leu-NMe_2 (2q)

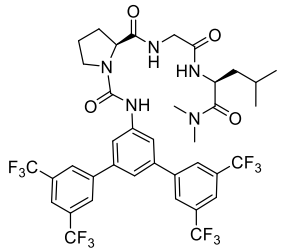

The title compound was prepared following *General Procedure I* using **5.10** (215 mg, 0.3 mmol, 1 equiv.) and H-Leu-NMe_2·HCl (88 mg, 0.45 mmol, 1.5 equiv.). The residue was purified via flash column chromatography (10% (v/v) *i*-PrOH in toluene), giving compound **2q** as a white powder (205 mg, 80%). **^{1}H NMR** (400 MHz, $CDCl_3$): δ 7.98 (s, 4H), 7.87 (s, 2H), 7.77 (d, J = 1.7 Hz, 2H), 7.42 (br s, 1H), 7.41 (br t, J = 6.0 Hz, 1H), 7.32 (t, J = 1.7 Hz, 1H), 7.02 (br d, J = 8.5 Hz, 1H), 4.89 (ddd, J = 9.9, 8.5, 3.7 Hz, 1H), 4.65–4.62 (m, 1H), 4.05 (dd, J = 17.2, 6.5 Hz, 1H), 3.82 (dd, J = 17.2, 5.5 Hz, 1H), 3.78–3.73 (m, 1H), 3.62–3.56 (m, 1H), 2.96 (s, 3H), 2.82

(s, 3H), 2.41–2.35 (m, 1H), 2.19–2.07 (m, 3H), 1.59–1.49 (m, 1H), 1.41 (ddd, J = 14.3, 10.2, 4.4 Hz, 1H), 1.33–1.23 (m, 1H), 0.84 (d, J = 6.5 Hz, 3H), 0.75 (d, J = 6.7 Hz, 3H) ppm; **^{19}F NMR** (377 MHz, $CDCl_3$): δ −63.73 ppm; **^{13}C NMR** (101 MHz, $CDCl_3$): δ 172.9, 172.4, 168.4, 155.5, 142.7, 141.0, 140.1, 132.3 (q, J_{CF} = 33 Hz), 127.5 (br), 123.4 (q, J_{CF} = 271 Hz), 121.5 (br), 120.8, 119.4, 60.8, 47.6, 47.3, 42.9, 42.1, 37.0, 35.7, 29.1, 24.9, 24.6, 23.3, 21.8 ppm; **HRMS** (ESI+) = m/z calculated for $C_{38}H_{37}F_{12}N_5O_4Na^+$ $[M+Na]^+$ 878.2546, found 878.2529; $[\alpha]_D^{20°C}$ = −42.2 (c 0.9, $CHCl_3$); **m.p.** 139 °C; **IR** (thin layer film): ν 3078, 2956, 2872, 1643, 1606, 1555, 1371, 1281, 1181, 1134, 925, 845, 761, 708, 683 cm^{-1}.

3,5-[3,5-$(CF_3)_2C_6H_3$]$_2C_6H_3$NHC(O)-Pro-Gly-2-Nal-NMe_2 (2s)

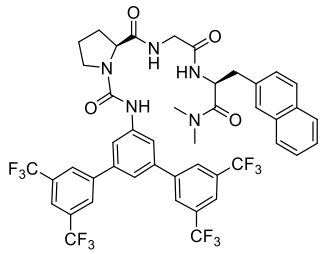

The title compound was prepared following *General Procedure I* using **5.10** (215 mg, 0.3 mmol, 1 equiv.) and H-2-Nal-NMe_2·HCl (125 mg, 0.45 mmol, 1.5 equiv.). The residue was purified via flash column chromatography (10−20% (v/v) *i*-PrOH in toluene), giving compound **2s** as a white powder (277 mg, 98%). **^{1}H NMR** (600 MHz, CD_2Cl_2): δ 7.97 (s, 4H), 7.85 (br s, 2H), 7.77 (d, J = 1.7 Hz, 2H), 7.74–7.72 (m, 1H), 7.66–7.65 (m, 1H), 7.63 (d, J = 8.4 Hz, 1H), 7.44–7.37 (m, 6H), 7.37 (br s, 1H), 7.29 (t, J = 1.7 Hz, 1H), 7.08 (dd, J = 8.4, 1.5 Hz, 1H), 5.01 (q, J = 7.1 Hz, 1H), 4.59 (dd, J = 7.9, 3.4 Hz, 1H), 3.99 (dd, J = 17.5, 6.9 Hz, 1H), 3.73 (dd, J = 17.5, 5.1 Hz, 1H), 3.66 (td, J = 8.3, 4.6 Hz, 1H), 3.55 (q, J = 8.3 Hz, 1H), 2.96 (dd, J = 13.6, 7.3 Hz, 1H), 2.93 (dd, J = 13.6, 6.4 Hz, 1H), 2.70 (s, 3H), 2.60 (s, 3H), 2.30–2.25 (m, 1H), 2.15–1.96 (m, 3H) ppm; **^{19}F NMR** (377 MHz, $CDCl_3$): δ −62.72 ppm; **^{13}C NMR** (151 MHz, CD_2Cl_2): δ 173.3, 171.3, 168.5, 155.6, 142.8, 141.3, 139.9, 134.1, 133.6, 132.6, 132.2 (q, J_{CF} = 33 Hz), 128.3, 128.0, 127.83, 127.82, 127.81, 127.7 (br), 126.3, 126.0, 123.8 (q, J_{CF} = 273 Hz), 121.7 (sept, J_{CF} = 3.7 Hz), 120.6, 119.8, 61.1, 50.9, 47.4, 43.1, 39.0, 37.0, 35.6, 29.4, 25.2 ppm; **HRMS** (ESI+) = m/z calculated for $C_{45}H_{38}F_{12}N_5O_4^+$ $[M+H]^+$ 940.2727, found 940.2723; $[\alpha]_D^{20°C}$ = −36.6 (c 1.0, $CHCl_3$); **m.p.** 145 °C; **IR** (thin layer film): ν 3272, 3068, 2931, 2856, 1642, 1605, 1546, 1372, 1281, 1179, 1136, 900, 844, 707 cm^{-1}.

5.2.5.2. Peptides described in chapter III

Peptide **3.3j** synthesis and characterisation is described in Section 5.2.2.

3,5-[3,5-$(CF_3)_2C_6H_3]_2C_6H_3$NHC(O)-Pro-Gly-Phe(*p*-NO_2)-NMe_2 (3.3a)

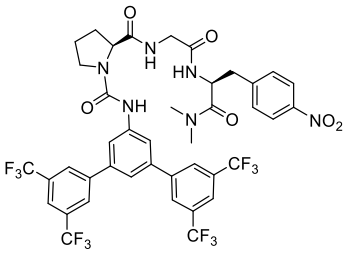

The title compound was prepared following *General Procedure I* using **5.10** (215 mg, 0.3 mmol, 1 equiv.) and H-Phe(*p*-NO_2)-NMe_2·HCl (123 mg, 0.45 mmol, 1.5 equiv.). The residue was purified via flash column chromatography (10% (v/v) *i*-PrOH in toluene) giving compound **3.3a** as a white powder (262 mg, 93%). **^{1}H NMR** (500 MHz, $CDCl_3$): δ 8.04 (dt, *J* = 8.7, 2.4 Hz, 2H), 7.96 (br s, 4H), 7.86 (br s, 2H), 7.71 (d, *J* = 1.4 Hz, 2H), 7.46 (br t, *J* = 6.2 Hz, 1H), 7.32 (t, *J* = 1.4 Hz, 1H), 7.30 (br s, 1H), 7.21 (br s), 7.17 (dt, *J* = 8.7, 2.3 Hz, 2H), 5.02 (q**,** *J* = 6.8 Hz, 1H), 4.63–4.60 (m, 1H), 4.06 (d, *J* = 16.9, 6.7 Hz, 1H), 3.75 (d, *J* = 16.9, 5.3 Hz, 1H), 3.70–3.65 (m, 1H), 3.60–3.54 (m, 1H), 3.03 (d, *J* = 13.4, 6.9 Hz, 1H), 3.03 (d, *J* = 13.4, 6.0 Hz, 1H), 2.80 (s, 3H), 2.78 (s, 3H), 2.40–2.21 (m, 1H), 2.18–2.04 (m, 3H) ppm; **^{19}F NMR** (377 MHz, $CDCl_3$): δ -62.72 ppm; **^{13}C NMR** (101 MHz, $CDCl_3$): δ 172.8, 170.1, 168.3, 155.3, 147.0, 143.6, 142.4, 140.6, 140.0, 13.2, (q, J_{CF} = 33 Hz), 130.3, 127.3 (br s), 123.1 (q, J_{CF} = 273 Hz), 123.5, 121.5 (br s), 120.8, 119.3, 60.6, 49.9, 47.0, 42.8, 38.1, 37.0, 35.6, 28.7, 25.0 ppm; **HRMS** (ESI+) = *m*/*z* calculated for $C_{41}H_{34}F_{12}N_6O_6K^+$ $[M+K]^+$ 973.1980, found 973.1988; $[\alpha]_D^{20℃}$ = −43.0 (*c* 1.0, $CHCl_3$); **m.p.** 232 °C; **IR** (thin layer film): ν 3291, 2928, 1644, 1606, 1524, 1371, 1349, 1279, 1176, 1133, 900, 806, 706, 683 cm^{-1}.

3,5-[3,5-$(CF_3)_2C_6H_3]_2C_6H_3$NHC(O)-Pro-Gly-Phe(*p*-NMe_2)-NMe_2 (3.3b)

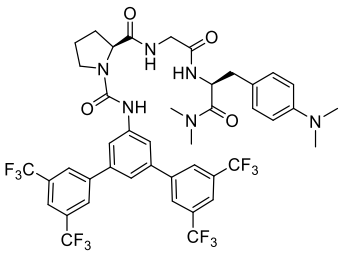

The title compound was prepared following *General Procedure I* using **5.10** (215 mg, 0.3 mmol, 1 equiv.) and H-Phe(*p*-NMe_2)-NMe_2·HCl (122 mg, 0.45 mmol, 1.5 equiv.). The residue was purified via flash column chromatography (10% (v/v) *i*-PrOH in toluene), giving compound **3.3b** as a white powder (260 mg, 93%). **^{1}H NMR** (400 MHz, $CDCl_3$): δ 7.89 (s, 4H), 7.78 (br s, 2H), 7.67 (br d, *J* = 1.2 Hz, 2H), 7.20 (br s, 1H), 7.12 (br d, *J* = 7.3 Hz, 1H), 6.71 (d, *J* = 8.4 Hz, 2H), 6.45 (d, *J* = 8.4 Hz, 2H), 4.80 (ddd**,** *J* = 7.8, 7.3, 5.5 Hz, 1H), 4.58

(dd, J = 7.2, 2.7 Hz), 4.04 (dd, J = 17.2, 6.8 Hz), 3.71–3.65 (m, 2H), 3.51 (q, J = 8.0 Hz, 1H), 2.80 (s, 6H), 2.70–2.57 (m, 2H), 2.66 (s, 3H), 2.46 (s, 3H), 2.33–2.29 (m, 1H), 2.11–1.96 (m, 3H) ppm; **^{19}F NMR** (377 MHz, $CDCl_3$): δ -62.69 ppm; **^{13}C NMR** (101 MHz, $CDCl_3$): δ 172.9, 171.4, 168.1, 155.5, 142.5, 140.8, 139.8, 132.2 (q, J_{CF} = 33 Hz), 129.9, 127.3 (br s), 123.2 (q, J_{CF} = 273 Hz), 121.4 (br s), 120.7, 119.6, 112.4, 60.6, 50.8, 47.1, 42.8, 40.5, 38.1, 36.8, 35.5, 28.8, 24.8 ppm; **HRMS** (ESI+) = m/z calculated for $C_{43}H_{40}F_{12}N_6O_4^+$ $[M+Na]^+$ 955.2812, found 955.2839; $[\alpha]_D^{20°C}$ = −26.2 (c 1.0, $CHCl_3$); **m.p.** 148 °C; **IR** (thin layer film): ν 3289, 3079, 2932, 1644, 1551, 1523, 1372, 1281, 1180, 1137, 899, 811, 707, 683 cm^{-1}.

3,5-[3,5-$(CF_3)_2C_6H_3$]$_2C_6H_3$NHC(O)-Pro(5*R*-*t*-Bu)-Gly-Phe-NMe_2 (3.3c) and

3,5-[3,5-$(CF_3)_2C_6H_3$]$_2C_6H_3$NHC(O)-Pro(5*S*-*t*-Bu)-Gly-Phe-NMe_2 (3.3d)

The title compounds were prepared following *General Procedure IIIa* from H-Pro(5-*t*-Bu)-Gly-Phe-NMe_2.HCl (200 mg, 0.59 mmol, *d.r.* 1.0:0.6 (5*S*)/(5*R*)). Crude mixture was purified via flash column chromatography (15 to 50% (v/v) acetone in toluene, followed by 5% (v/v) *i*-PrOH in CH_2Cl_2) affording **3.3c** (180 mg, 32%) and **3.3d** (347 mg, 62%).

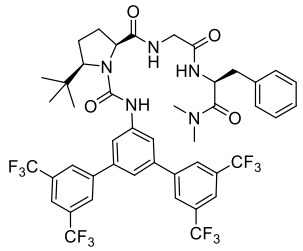

Compound **3.3c** was obtained as white powder. **^{1}H NMR** (400 MHz, $CDCl_3$): δ 7.84 (s, 4H), 7.80 (s, 2H), 7.73 (br s, 1H), 7.64 (s, 1H), 7.41 (br s, 2H), 7.14–7.05 (m, 3H), 6.99 (br s, 1H), 6.77 (br d, J = 7.0 Hz, 2H), 4.75 (br s, 1H), 4.61 (d, J = 9.1 Hz, 1H), 4.32 (br d, J = 7.7 Hz, 1H), 4.00–3.94 (m, 1H), 3.72–3.63 (m, 1H), 2.69–2.55 (m, 2H), 2.64 (s, 3H), 2.46–2.32 (m, 2H), 2.38 (s, 3H), 2.06–1.96 (m, 2H), 0.98 (s, 9H) ppm; **^{19}F NMR** (377 MHz, $CDCl_3$): δ −62.67 ppm; **^{13}C NMR** (151 MHz, $CDCl_3$): δ 174.7, 171.6, 168.4, 156.0, 142.5, 140.8, 139.6, 136.1, 132.0 (q, J_{CF} = 32 Hz), 129.0, 128.1, 127.3 (br s), 126.9, 123.3 (q, J_{CF} = 273 Hz), 121.3 (br s), 120.3 (br s), 119.0 (br s), 66.5, 62.9, 50.9, 43.0, 38.5, 37.2, 36.6, 35.4, 29.2, 27.6, 27.0 ppm; $[\alpha]_D^{20°C}$ = −33.2 (c 1.0, $CHCl_3$); **m.p.** 219−220 °C; **IR** (thin layer film): ν 3306, 2957, 1668, 1638, 1546, 1368, 1280, 1177, 1136, 899, 844, 705, 683 cm^{-1}; **HRMS** (ESI+) = m/z calculated for $C_{45}H_{44}F_{12}N_5O_4^+$ $[M+H]^+$ 946.3196, found 946.3200.

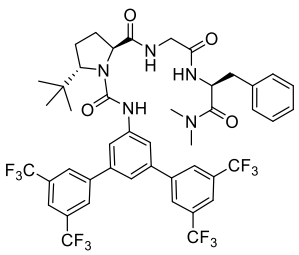

Compound **3.3d** was obtained as white powder. **^{1}H NMR** (400 MHz, $CDCl_3$): δ 8.50 (s, 1H), 8.03 (s, 4H), 7.87 (s, 2H), 7.77 (d, *J* = 1.2 Hz, 2H), 7.34 (t, *J* = 1.2 Hz, 1H), 7.23–7.19 (m, 3H), 7.06–7.02 (m, 3H), 6.91 (d, *J* = 7.3 Hz, 1H), 5.04 (q, *J* = 7.5 Hz, 1H), 4.58 (t, *J* = 8.5 Hz, 1H), 4.31 (dd, *J* = 7.7, 4.0 Hz, 1H), 4.12 (dd, *J* = 16.7, 5.7 Hz, 1H), 3.93 (dd, *J* = 16.7, 4.5 Hz, 1H), 2.94 (d, *J* = 7.3 Hz, 2H), 2.82 (s, 3H), 2.52 (s, 3H), 2.43–2.35 (m, 1H), 2.26 (dq, *J* = 13.0, 8.5 Hz, 1H), 2.09–1.99 (m, 2H), 0.97 (s, 9H) ppm; **^{19}F NMR** (377 MHz, $CDCl_3$): δ −62.64 ppm; **^{13}C NMR** (151 MHz, $CDCl_3$): δ 173.4, 170.6, 167.5, 158.5, 142.9, 141.2, 140.6, 135.6, 132.2 (q, J_{CF} = 33 Hz), 129.3, 128.5, 127.6 (br s), 127.2, 123.3 (q, J_{CF} = 273 Hz), 121.4 (sept, J_{CF} =3.6 Hz), 120.8, 119.3, 67.1, 64.2, 50.5, 42.7, 39.4, 36.6, 35.9, 35.6, 29.3, 27.4, 26.1 ppm; **m.p.** 128 °C; **IR** (thin layer film): ν 3302, 2957, 2874, 1642, 1603, 1425, 1281, 1181, 1138, 900, 845, 735, 706 cm^{-1}; $[\alpha]_D^{20°C}$ = 2.4 (*c* 1.0, acetone); **HRMS** (ESI+) = *m/z* calculated for $C_{45}H_{44}F_{12}N_5O_4^+$ $[M+H]^+$ 946.3196, found 946.3229.

3,5-[3,5-$(CF_3)_2C_6H_3]_2C_6H_3$NHC(O)-flp-Gly-Phe-OMe (3.3e)

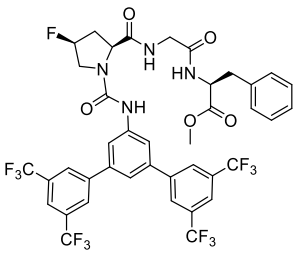

The title compound was prepared following *General Procedure I* from 3,5-[3,5-$(CF_3)_2C_6H_3]_2C_6H_3$NHC(O)-flp-Gly-OH (147 mg, 0.20 mmol). The residue was purified via flash column chromatography (2−5% (v/v) *i*-PrOH in CH_2Cl_2, followed by 10−40% (v/v) acetone in toluene), giving compound **3.3e** as a white powder (89 mg, 50%). **^{1}H NMR** (400 MHz, $CDCl_3$): δ 8.05 (s, 4H), 7.95 (br s, 1H), 7.90 (s, 4H), 7.41 (t, *J* = 1.7 Hz, 1H), 7.28–7.20 (m, 3H), 7.15 (br t, *J* = 5.8 Hz, 1H), 7.06 (dd, *J* = 7.8, 1.0 Hz, 2H), 6.17 (d, *J* = 7.7 Hz, 1H), 5.32 (dt, J_{HF} = 52.3 Hz, J_{HH} = 3.1 Hz, 1H), 4.81 (q, *J* = 5.0 Hz, 1H), 4.63 (d, *J* = 10.3 Hz, 1H), 4.15 (dd, *J* = 16.8, 4.8 Hz, 1H), 3.96–3.82 (m, 3H), 3.64 (s, 3H), 3.12 (dd, *J* = 13.8, 5.7 Hz, 1H), 3.04 (dd, *J* = 13.8, 5.6 Hz, 1H), 2.75 (br t, J_{HF} = J_{HH} = 15.8 Hz, 1H), 2.75 (dddd, J_{HF} = 43.2 Hz, J_{HH} = 15.3, 10.3, 3.7 Hz, 1H) ppm; **^{19}F{^{1}H} NMR** (377 MHz, $CDCl_3$): δ −62.69 (12F), −173.25 (1F) ppm; **^{13}C NMR** (126 MHz, $CDCl_3$): δ 172.3, 171.6, 168.2, 155.6, 142.7, 140.8, 140.0, 135.2, 132.3 (q, J_{CF} = 33 Hz), 129.2, 128.7, 127.4 (br s), 127.3, 123.3 (q, J_{CF} = 273 Hz), 121.5 (br s), 120.9, 119.1, 91.9 (d, J_{CF} = 176 Hz),

60.5, 54.2 (d, J_{CF} = 23 Hz), 53.3, 52.3, 42.8, 37.5, 36.9 (d, J_{CF} = 21 Hz) ppm; **HRMS** (ESI+) = *m*/*z* calculated for $C_{40}H_{31}F_{13}N_5O_5K^+$ $[M+K]^+$ 933.1718, found 933.1720; $[\alpha]_D^{20°C}$ = −29.8 (*c* 1.0, acetone); **m.p.** 245 °C; **IR** (thin layer film): ν 3316, 2927, 2855, 1746, 1657, 1555, 1370, 1280, 1178, 1135, 901, 845, 736, 683 cm^{-1}.

3,5-[3,5-$(CF_3)_2C_6H_3]_2C_6H_3$NHC(O)-flp-Gly-Phe-NCp (3.3f)

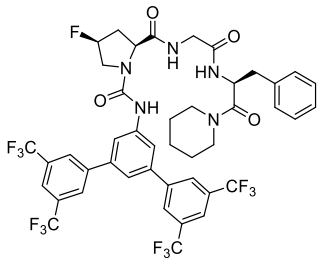

The title compound was prepared following *General Procedure I* from 3,5-[3,5-$(CF_3)_2C_6H_3]_2C_6H_3$NHC(O)-flp-Gly-OH (110 mg, 0.15 mmol). The residue was purified via flash column chromatography (2−5% (v/v) *i*-PrOH in CH_2Cl_2), giving compound **3.3f** as a white powder (74 mg, 52%). **^{1}H NMR** (400 MHz, $CDCl_3$): δ 8.03 (br s, 1H), 8.01 (s, 4H), 7.88 (s, 2H), 7.85 (d, *J* = 1.1 Hz, 2H), 7.36 (t, *J* = 1.1 Hz, 1H), 7.31 (br t, *J* = 5.2 Hz, 1H), 7.22–7.15 (m, 3H), 7.05–7.03 (m, 2H), 6.95 (d, *J* = 8.0 Hz, 1H), 5.41 (dt, J_{HF} = 52.2 Hz, J_{HH} = 3.0 Hz, 1H), 5.07–5.01 (m, 1H), 4.75 (d, *J* = 9.9 Hz, 1H), 4.07 (dd, J_{HF} = 22.6 Hz, J_{HF} = 12.8 Hz, 1H), 3.97 (s, 2H), 3.90 (ddd, J_{HF} = 38.1 Hz, J_{HF} = 12.8, 3.6 Hz, 1H), 3.48–3.45 (m, 1H), 3.34–3.29 (m, 1H), 3.07 (ddd, *J* =13.2, 7.8, 3.4 Hz, 1H), 3.05–2.80 (m, 4H), 2.48 (dddd, J_{HF} = 43.1 Hz, J_{HH} = 15.1, 10.4, 3.6 Hz, 1H), 1.50–1.26 (m, 6H) ppm; **^{19}F{^{1}H} NMR** (377 MHz, $CDCl_3$): δ −62.69 (12F), −172.41 (1F) ppm; **^{13}C NMR** (126 MHz, $CDCl_3$): δ 172.1, 169.1, 167.7, 155.5, 142.6, 140.8, 140.1, 135.7, 132.2 (q, J_{CF} = 33 Hz), 129.4, 128.5, 127.4 (br s), 127.1, 123.2 (q, J_{CF} = 273 Hz), 121.5 (br s), 120.9, 119.3, 92.1 (d, J_{CF} = 175 Hz), 60.2, 54.2 (d, J_{CF} = 23 Hz), 49.9, 46.5, 43.1, 42.8, 39.3, 36.6 (d, J_{CF} = 22 Hz), 25.7, 25.2, 24.1 ppm; **HRMS** (ESI+) = *m*/*z* calculated for $C_{44}H_{39}F_{13}N_5O_4^+$ $[M+H]^+$ 948.2789, found 948.2788; $[\alpha]_D^{20°C}$ = −25.6 (*c* 1.0, acetone); **m.p.** 154−156 °C; **IR** (thin layer film): ν 3307, 2943, 2861, 1651, 1556, 1370, 1279, 1178, 1134, 900, 845, 706, 683 cm^{-1}.

3,5-[3,5-$(CF_3)_2C_6H_3]_2C_6H_3$NHC(O)-flp-Gly-Phe-NEt_2 (3.3g)

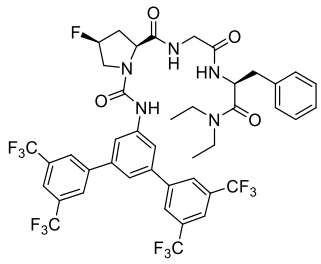

The title compound was prepared following *General Procedure I* from 3,5-[3,5-$(CF_3)_2C_6H_3]_2C_6H_3$NHC(O)-flp-Gly-OH (147 mg, 0.20 mmol). The title compound was prepared following *General Procedure IIIa.* The residue was purified via flash column chromatography (0−5% (v/v) *i*-PrOH in CH_2Cl_2), giving compound **3.3g** as a white powder (107 mg, 57%). **^{1}H NMR** (400 MHz, $CDCl_3$): δ 8.12 (br s, 1H), 7.99 (s, 4H), 7.87 (s, 2H), 7.82 (d, J = 1.2 Hz, 2H), 7.36 (br s, 1H), 7.35 (t, J = 1.2 Hz, 1H), 7.18–7.17 (m, 3H), 7.07 (d, J = 6.1 Hz, 1H), 7.06–7.03 (m, 2H), 5.41 (dt, J_{HF} = 52.6 Hz, J_{HH} = 3.6 Hz, 1H), 4.94 (q, J = 7.3 Hz, 1H), 4.75 (d, J = 9.8 Hz, 1H), 4.07 (dd, J_{HF} = 22.9 Hz, J_{HF} = 12.8 Hz, 1H), 3.96 (s, 2H), 3.90 (ddd, J_{HF} = 38.6 Hz, J_{HF} = 12.8, 3.6 Hz, 1H), 3.46 (sx, J =6.6 Hz, 1H), 3.00–2.79 (m, 6H), 2.49 (dddd, J_{HF} = 43.1 Hz, J_{HH} = 14.7, 10.1, 3.4 Hz, 1H), 0.96 (t, J =7.1 Hz, 1H), 0.85 (t, J =7.1 Hz, 1H) ppm; **^{19}F{^{1}H} NMR** (377 MHz, $CDCl_3$): δ −62.72 (12F), −172.26 (1F) ppm; **^{13}C NMR** (126 MHz, $CDCl_3$): δ 172.3, 170.5, 167.9, 155.7, 142.6, 140.9, 140.1, 135.9, 132.4 (q, J_{CF} = 33 Hz), 129.5, 128.5, 127.4 (br s), 127.2, 123.4 (q, J_{CF} = 273 Hz), 121.6 (br s), 121.1, 119.8, 92.2 (d, J_{CF} = 177 Hz), 60.3, 54.4 (d, J_{CF} = 21 Hz), 50.4, 42.9, 41.7, 40.7, 39.7, 36.8 (d, J_{CF} = 21 Hz), 13.9, 12.7 ppm; **HRMS** (ESI+) = m/z calculated for $C_{43}H_{39}F_{13}N_5O_4^+$ $[M+H]^+$ 936.2789, found 936.2792; **IR** (thin layer film): ν 3316, 2936, 1653, 1556, 1370, 1280, 1179, 1135, 900, 845, 772, 705, 683 cm^{-1}; **m.p.** 211−214 °C; $[\alpha]_D^{20℃}$ = −49.6 (*c* 1.0, $CHCl_3$).

3,5-[3,5-$(CF_3)_2C_6H_3]_2C_6H_3$NHC(O)-flp-Gly-Phe-NBn_2 (3.3h)

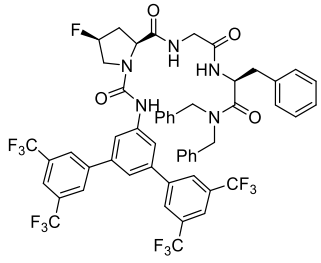

The title compound was prepared following *General Procedure I* from 3,5-[3,5-$(CF_3)_2C_6H_3]_2C_6H_3$NHC(O)-flp-Gly-OH (147 mg, 0.20 mmol). The residue was purified via flash column chromatography (0−5% (v/v) *i*-PrOH in CH_2Cl_2), giving compound **3.3h** as a white powder (74 mg, 50%). **^{1}H NMR** (600 MHz, $CDCl_3$): δ 8.05 (br s, 1H), 7.94 (s, 4H), 7.85 (s, 2H), 7.83 (d, J = 1.2 Hz, 2H), 7.39 (t, J = 1.2 Hz, 1H), 7.29–7.24 (m, 4H), 7.19–7.14 (m, 4H), 7.12 (d, J = 7.5 Hz, 1H), 7.09 (t, J = 7.9 Hz, 2H), 7.05–7.03 (m, 2H), 6.95–

6.93 (m, 4H), 5.42 (dt, J_{HF} = 52.4 Hz, J_{HH} = 3.3 Hz, 1H), 5.15 (q, J = 7.3 Hz, 1H), 4.77 (d, J = 10.1 Hz, 1H), 4.73 (d, J = 14.7 Hz, 1H), 4.24 (d, J = 16.5 Hz, 1H), 4.09 (dd, J_{HF} = 22.9 Hz, J_{HF} = 12.6 Hz, 1H), 4.05–3.94 (m, 4H), 3.92 (ddd, J_{HF} = 38.1 Hz, J_{HF} = 12.6, 3.5 Hz, 1H), 2.96 (dd, J = 13.2, 7.5 Hz, 1H), 2.89 (dd, J = 13.2, 6.6 Hz, 1H), 2.83 (br t, J_{HF} = J_{HH} = 15.7 Hz, 1H), 2.50 (dddd, J_{HF} = 42.9 Hz, J_{HH} = 15.0, 10.1, 3.6 Hz, 1H) ppm; **^{19}F{^{1}H} NMR** (377 MHz, $CDCl_3$): δ −62.67 (12F), −172.33 (1F) ppm; **^{13}C NMR** (151 MHz, $CDCl_3$): δ 172.3, 172.0, 168.1, 155.7, 142.5, 140.8, 140.0, 136.2, 135.7, 135.5, 132.3 (q, J_{CF} = 33 Hz), 129.4, 128.9, 128.7, 128.6, 128.4, 127.9, 127.7, 127.4 (br s), 127.2, 127.1, 123.3 (q, J_{CF} = 273 Hz), 121.6 (br s), 121.1, 119.6, 92.3 (d, J_{CF} = 176 Hz), 60.4, 54.3 (d, J_{CF} = 23 Hz), 50.9, 49.8, 48.3, 42.8, 39.3, 36.8 (d, J_{CF} = 22 Hz) ppm; **HRMS** (ESI+) = m/z calculated for $C_{53}H_{42}F_{13}N_5O_4Na^+$ $[M+Na]^+$ 1082.2921, found 1082.2908; $[\alpha]_D^{20°C}$ = −61.0 (*c* 1.0, $CHCl_3$); **m.p.** 133−134 °C; **IR** (thin layer film): ν 3305, 3066, 3033, 2931, 1652, 1555, 1454, 1370, 1280, 1230, 900, 845, 683, 664 cm^{-1}.

3,5-[3,5-$(CF_3)_2C_6H_3$]$_2C_6H_3$NHC(O)-flp-Acpc-Phe-NMe_2 (3.3i)

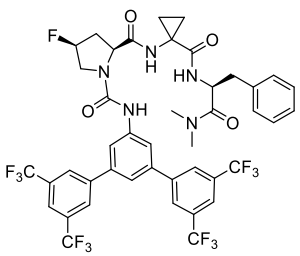

The title compound was prepared following *General Procedure IIIb*. The crude product was purified via flash column chromatography (20−50% (v/v) acetone in toluene), giving **1c** as a white solid (98 mg, 65%). **^{1}H NMR** (600 MHz, DMSO-d_6): δ 8.77 (s, 1H), 8.72 (s, 1H), 8.29 (s, 4H), 8.10 (d, J = 1.6 Hz, 2H), 8.08 (s, 2H), 7.76 (t, J = 1.1 Hz, 1H), 7.71 (d, J = 7.7 Hz, 1H), 7.04–6.97 (m, 3H), 6.73 (br d, J = 7.1 Hz, 2H), 5.42 (br dt, $^{2}J_{HF}$ = 53.8 Hz, J = 3.9 Hz, 1H), 4.63 (dt, J = 8.1, 6.5 Hz, 1H), 4.49 (br d, J = 7.9 Hz, 1H), 3.95 (br dd, $^{3}J_{H–F}$ = 24.1 Hz, J = 12.1 Hz, 1H), 3.84 (ddd, $^{3}J_{HF}$ = 32.5 Hz, J = 12.1, 4.1 Hz, 1H), 2.62 (dd, J = 13.1, 8.8 Hz, 1H), 2.63–2.54 (m, 1H), 2.59 (s, 3H), 2.54 (s, 3H), 2.45 (dd, J = 13.1, 6.4 Hz, 1H), 2.20 (br t, $^{3}J_{HF}$ = 18.0 Hz, 1H), 1.22 (ddd, J = 10.1, 7.4, 3.9 Hz, 1H), 1.14 (ddd, J = 10.1, 7.5, 3.9 Hz, 1H), 0.87 (ddd, J = 9.8, 7.5, 3.9 Hz, 1H), 0.79 (ddd, J = 9.8, 7.5, 3.9 Hz, 1H) ppm; **^{19}F NMR** (377 MHz, $CDCl_3$): δ –62.70 (s, 12F), –172.96 (br s, 1F) ppm; **^{13}C NMR** (151 MHz, DMSO-d_6): δ 173.0, 171.2, 170.7, 154.8, 143.1, 142.2, 138.8, 137.4, 131.3 (q, $^{2}J_{CF}$ = 33 Hz), 129.2, 128.1, 126.5, 123.8 (q, $^{1}J_{CF}$ = 271 Hz), 121.7 (br), 120.8, 119.4, 92.8 (d, $^{1}J_{CF}$ = 175 Hz), 59.6, 53.3 (d, $^{2}J_{CF}$ = 24 Hz), 51.0, 38.3, 36.6 (*two*

peaks overlapping; based on HSQC), 35.3, 34.1, 16.6, 16.5 ppm; **HRMS** (ESI+) = *m*/*z* calculated for $C_{43}H_{37}F_{13}N_5O_4^+$[M+H]$^+$ 934.2632, found 934.2674; $[\alpha]_D^{20°C}$ = –32.3 (*c* 0.9, acetone); **m.p.** 241 °C; **IR** (thin layer film): ν 3269, 3065, 2938, 1715, 1642, 1608, 1430, 1180, 1137, 900, 845, 706, 683 cm^{-1}.

3,5-[3,5-(CF$_3$)$_2$C$_6$H$_3$]$_2$C$_6$H$_3$^{15}NHC(O)-flp-Acpc-Phe-NEt$_2$ (3.3j-^{15}NH(*i+1*))

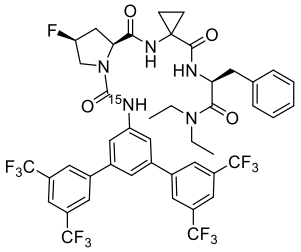

The title compound was prepared following *General Procedure IIIb*. The crude product was purified via flash column chromatography (10−40% (v/v) acetone in toluene, followed by 2−5% (v/v) *i*-PrOH in CH_2Cl_2), giving **3.3j-^{15}NH(*i+1*)** as a white solid (122 mg, 62%). **^{1}H NMR** (500 MHz, CD_2Cl_2): δ 8.10 (s, 4H), 7.95 (s, 2H), 7.92 (s, 2H), 7.65 (br d, J_{NH} = 88.5 Hz, 1H), 7.48 (s, 1H), 7.32 (s, 1H), 7.20 (d, *J* = 8.2 Hz, 1H), 7.15–7.14 (m, 3H), 7.00–6.98 (m, 2H), 5.46 (dt, J_{HF} = 52.4 Hz, J_{HH} = 3.5 Hz, 1H), 4.87 (q, *J* = 7.9 Hz, 1H), 4.75 (d, *J* = 9.6 Hz, 1H), 4.16 (dd, J_{HF} = 22.4 Hz, J_{HH} = 11.6 Hz, 1H), 3.93 (ddd, J_{HF} = 35.2 Hz, J_{HH} = 11.8, 3.7 Hz, 1H), 3.44 (sx, *J* = 7.0 Hz, 1H), 3.00–2.91 (m, 3H), 2.82–2.76 (m, 2H), 2.71 (dd, *J* = 13.3, 6.5 Hz, 1H), 2.47 (dddd, J_{HF} = 41.0 Hz, J_{HH} = 14.7, 10.0, 3.8 Hz, 1H), 1.49–1.40 (m, 2H), 1.09 (ddd, *J* = 10.2, 7.2, 4.1 Hz, 1H), 0.98 (ddd, *J* = 10.2, 6.5, 3.2 Hz, 1H), 0.91 (q, *J* = 7.3 Hz, 6H) ppm; **^{13}C NMR** (151 MHz, CD_2Cl_2): δ 172.3, 170.6, 170.3, 155.2, 142.6 (d, J_{CN} = 21 Hz), 140.6 (d, J_{CN} = 17 Hz), 139.9, 136.5, 132.0 (q, J_{CF} = 33 Hz), 129.3, 128.1, 127.5 (br d, J_{CF} = 3 Hz), 126.6, 122.3 (q, J_{CF} = 273 Hz), 121.5 (br t, J_{CF} = 4 Hz), 121.1, 119.6, 92.4 (d, J_{CF} = 173 Hz), 59.9, 53.9 (*overlapping with solvent peak*), 50.6, 41.5, 40.3, 39.6, 35.6 (br d, J_{CF} = 2 Hz), 34.6, 16.5, 16.3, 13.6, 12.3 ppm; **^{19}F{^{1}H} NMR** (470 MHz, $CDCl_3$): δ –62.69 (12F), –172.74 (1F) ppm; **^{15}N NMR** (120 MHz, CD_2Cl_2): δ 105.5 (d, J_{NH} = 89 Hz) ppm; **HRMS** (ESI+) = *m*/*z* calculated for $C_{45}H_{40}F_{13}N_4[^{15}N]O_4Na^+$ [M+Na]$^+$ 985.2735, found 985.2737; $[\alpha]_D^{20°C}$ = –32.1 (*c* 0.9, acetone); **IR** (powder): ν 3290, 2926, 2855, 1662, 1636, 1540, 1462, 1432, 1367, 1280, 1177, 1135, 843, 703, 634 cm^{-1}; **m.p.** 152 °C.

3,5-[3,5-$(CF_3)_2C_6H_3]_2C_6H_3$NHC(O)-flp-Acpc-[^{15}N]Phe-NEt_2 (3.3j-^{15}NH(*i*−*2*))

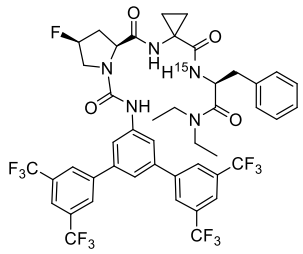

The title compound was prepared following *General Procedure IIIb*. The crude product was purified via flash column chromatography (10−40% (v/v) acetone in toluene), giving **3.3j-^{15}NH(*i*−*2*)** as a white solid (253 mg, 60%). **^{1}H NMR** (500 MHz, CD_2Cl_2): δ 8.10 (s, 4H), 7.95 (s, 2H), 7.92 (s, 2H), 7.65 (br s, 1H), 7.48 (s, 1H), 7.32 (s, 1H), 7.20 (dd, $^1J_{NH}$ = 92.8 Hz, $^1J_{HH}$ = 8.2 Hz, 1H), 7.15–7.14 (m, 3H), 7.00–6.98 (m, 2H), 5.46 (dt, *J* = 52.4, 3.5 Hz, 1H), 4.87 (q, *J* = 7.9 Hz, 1H), 4.75 (d, *J* = 9.6 Hz, 1H), 4.16 (dd, *J* = 22.4, 11.6 Hz, 1H), 3.93 (ddd, *J* = 35.2, 11.8, 3.7 Hz, 1H), 3.44 (sx, *J* = 7.0 Hz, 1H), 3.00–2.91 (m, 3H), 2.82–2.76 (m, 2H), 2.71 (dd, *J* = 13.3, 6.5 Hz, 1H), 2.47 (dddd, *J* = 41.0, 14.7, 10.0, 3.8 Hz, 1H), 1.49–1.40 (m, 2H), 1.09 (ddd, *J* = 10.2, 7.2, 4.1 Hz, 1H), 0.98 (ddd, *J* = 10.2, 6.5, 3.2 Hz, 1H), 0.91 (appt q, *J* = 7.3 Hz, 6H) ppm; **^{13}C NMR** (151 MHz, CD_2Cl_2): δ 172.3, 170.6, 170.3 (d, J_{CN} = 17 Hz,), 155.2, 142.6, 140.6, 139.9, 136.5, 132.0 (q, J_{CF} = 33 Hz), 129.3, 128.1 127.5 (br d, J_{CF} = 3 Hz), 126.6, 122.3 (q, J_{CF} = 273 Hz), 121.5 (br t, J_{CF} = 4 Hz), 121.1, 119.6, 92.4 (d, J_{CF} = 173 Hz), 59.9, 53.9 (*overlapping with solvent peak*), 50.6 (d, J_{CN} = 12 Hz), 41.5, 40.3, 39.6, 35.6 (br d, J_{CF} = 2 Hz), 34.6 (d, J_{CN} = 9 Hz), 16.5, 16.3, 13.6, 12.3 ppm; **^{19}F{^{1}H} NMR** (470 MHz, $CDCl_3$): δ –62.70 (12F), –172.74 (1F) ppm; **^{15}N NMR** (120 MHz, CD_2Cl_2): δ 115.9 (d, J_{NH} = 92 Hz) ppm; **HRMS** (ESI+) = *m*/*z* calculated for $C_{45}H_{40}F_{13}N_4[^{15}N]O_4Na^+$ $[M+Na]^+$ 985.2735, found 985.2722; $[\alpha]_D^{20°C}$ = –31.6 (*c* 0.9, acetone); **IR** (powder): ν 3243, 3062, 2973, 2937, 1658, 1639, 1546, 1511, 1464, 1432, 1366, 1280, 1177, 1135, 870, 704, 683 cm^{-1}; **m.p.** 154 °C.

5.3. Substrate synthesis and characterisation

β-Bromoamines *trans*-*N*,*N*-dibenzyl-2-bromocyclohexan-1-amine (*rac*-**3.1a**), *trans*-*N*,*N*-dibenzyl-2-bromocyclopentan-1-amine (*rac*-**3.1b**), *trans*-2-bromo-*N*,*N*-*bis*(4-methoxybenzyl)cyclohexan-1-amine (*rac*-**3.1f**), 2-(*trans*-2-bromo-1,2-diphenylethyl)-1,2,3,4-tetrahydroisoquinoline (*rac*-**3.1g**), 1-(*trans*-2-bromo-1,2-diphenylethyl)pyrrolidine (*rac*-**3.1h**), 1-(*trans*-2-bromo-1,2-diphenylethyl)piperidine (*rac*-**3.1i**) *trans*-2-bromo-*N*,*N*-dimethyl-1,2-diphenylethan-1-amine (*rac*-**3.1j**) were prepared and characterised in the group previously.[1] Substrates *trans*-*N*,*N*-dibenzyl-1,4-*bis*(benzyloxy)-3-bromobutan-2-amine (*rac*-**3.1k**) and *trans*-*N*,*N*-dibenzyl-4-bromohexan-3-amine (*rac*-**3.1l**) were available in the group.

5.3.1. β-Aminoalcohols

General Procedure VI: Synthesis of β-Aminoalcohols:

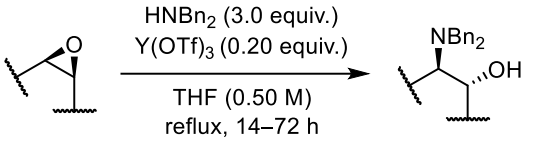

rac *rac*-**5.20–5.22**

cis-Epoxide (1.0 mmol), the corresponding amine (3.0 mmol) and $Y(OTf)_3$ (0.20 mmol) were refluxed in anhydrous THF (2.0 mL) under N_2 atmosphere until complete conversion of the epoxide (14–72 h, monitored by TLC) or for 48 hours if epoxide is not visible on TLC (relevant to epoxides *cis*-3,6-dioxabicyclo[3.1.0]hexane and *cis*-8-oxabicyclo[5.1.0]octane). The reaction mixture was then cooled to r.t. and the solvent was evaporated *in vacuo*. The crude product was purified by flash column chromatography over silica gel.

trans-2-(Dibenzylamino)cycloheptan-1-ol (_rac_-5.20)

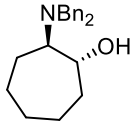

Alcohol *rac*-**5.20** was prepared following *General Procedure VI* from *cis*-8-oxabicyclo[5.1.0]octane[21] (560 mg, 5.00 mmol, 1 equiv.). Purification by flash column chromatography (80:20 (v/v) pentane/EtOAc) afforded white clear crystals (0.80 g, 52% yield). **^{1}H NMR** (400 MHz, $CDCl_3$): δ 7.35–7.23 (m, 10H), 4.08 (s, 1H), 3.84 (d, *J* = 13.1 Hz, 2H), 3.49 (ddd, *J* = 13.3, 8.6, 3.9 Hz, 1H), 3.33 (d, *J* = 13.1 Hz, 2H), 2.42 (td, *J* = 9.4, 2.7 Hz, 1H),

1.97–1.90 (m, 2H), 1.82–1.75 (m, 1H), 1.61–1.49 (m, 3H), 1.41–1.27 (m, 4H) ppm; **^{13}C NMR** (101 MHz, $CDCl_3$): δ 139.3, 129.2, 128.6, 127.4, 71.7, 65.6, 53.7, 33.1, 27.4, 24.9, 21.9, 21.6 ppm; **HRMS** (ESI+) = *m*/*z* calculated for $C_{21}H_{28}NO^+$ $[M+H]^+$ 310.2165, found 310.2163; **IR** (thin layer film): ν 3458, 2930, 2859, 1494, 1454, 748, 699 cm^{-1}.

trans-4-(Dibenzylamino)tetrahydrofuran-3-ol (*rac*-5.21)

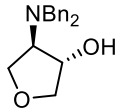

Alcohol *rac*-**5.21** was prepared following *General Procedure VI* from *cis*-3,6-dioxabicyclo[3.1.0]hexane[22] (0.86 g, 10 mmol). Purification by flash column chromatography (100:0 to 90:10 (v/v) pentane/EtOAc + 1% NEt_3, then 3:2 (v/v) pentane/EtOAc) afforded the title compound as a colourless oil (2.19 g, 77% yield). **^{1}H NMR** (400 MHz, $CDCl_3$): δ 7.40–7.25 (m, 10H), 4.53–4.50 (m, 1H), 4.03 (dd, *J* = 9.6, 6.0 Hz, 1H), 4.01 (dd, *J* = 10.0, 7.4 Hz, 1H), 3.83 (dd, *J* = 9.6, 5.3 Hz, 1H), 3.75 (d, *J* = 14.1 Hz, 2H), 3.67 (d, *J* = 14.1 Hz, 2H), 3.63 (dd, *J* = 10.0, 4.2 Hz, 1H), 1.77 (br s, 1H) ppm; **^{13}C NMR** (101 MHz, $CDCl_3$): δ 139.3, 128.6, 128.4, 127.1, 75.0, 73.8, 69.8, 69.4, 55.5 ppm; **HRMS** (ESI+) = *m*/*z* calculated for $C_{18}H_{22}NO_2^+$ $[M+H]^+$ 284.1645, found 284.1634; **IR** (thin layer film): ν 3413, 3028, 2917, 2842, 1493, 1452, 1076, 1028, 980, 917, 741, 698 cm^{-1}.

tert-Butyl *trans*-3-(dibenzylamino)-4-hydroxypyrrolidine-1-carboxylate (*rac*-5.22)

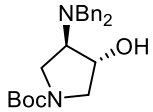

Alcohol *rac*-**5.22** was prepared following *General Procedure VI* from *tert*-butyl *cis*-6-oxa-3-azabicyclo[3.1.0]hexane-3-carboxylate[23] (1.00 g, 5.4 mmol, 1 equiv.). Purification by flash column chromatography (80:20 (v/v) pentane/EtOAc) afforded title compound as colourless clear crystals (2.03 g, 97% yield). **^{1}H NMR** (400 MHz, $CDCl_3$): δ 7.37–7.23 (m, 10H), 4.33–4.28 (m, 1H), 3.82–3.49 (m, 7H), 3.37–3.23 (m, 2H), 3.09–3.00 (m, 1H), 1.45 (s, 9H) ppm; **^{13}C NMR** (101 MHz, $CDCl_3$, *mixture of rotamers*): δ 154.6 (major), 154.4 (minor), 139.4, 128.52 (major), 128.50 (br), 128.4 (minor), 127.3 (major), 127.2 (minor), 79.6, 70.9 (major), 70.3 (minor), 66.1 (minor), 65.4 (major), 55.1, 52.8 (minor), 51.0 (major), 44.6 (minor), 43.2 (major), 28.5 ppm; **HRMS** (ESI+) = *m*/*z* calculated for $C_{23}H_{31}N_2O_3^+$ $[M+H]^+$ 383.2329, found 383.2328. Spectroscopic data consistent with literature reported data.[24]

5.3.2. β-Bromoamines

β-Bromoamines were unstable on silica gel leading to hydrolysis and proved to be unstable for MS analysis with a variety of ionisation methods (HRMS of the molecular ion was therefore not recorded). Hence, the crude products were purified with a short silica plug, and bromides were always stored in the freezer to prevent any decomposition.

***trans*-*N,N*-Dibenzyl-2-bromocycloheptan-1-amine (*rac*-3.1b)**

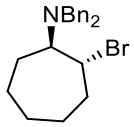

Alcohol **5.20** (226 mg, 0.73 mmol, 1 equiv.), CBr_4 (1.39 g, 0.77 mmol) and PPh_3 (202 mg, 0.77 mmol) were stirred in anhydrous CH_3CN (3.5 mL) at r.t. for 18 h. Following, Et_2O (5 mL) was added causing the precipitation of a white solid. The mixture was filtered, washed with Et_2O (2 x 3 mL), and the filtrate was concentrated *in vacuo*. The crude product was then purified with a short silica plug (95:5 (v/v) pentane/EtOAc) affording a white waxy solid (128 mg, 47%). Note: Product was unstable on silica. **^{1}H NMR** (400 MHz, $CDCl_3$): δ 7.37 (br d, *J* = 7.5 Hz, 4H), 7.23 (br t, *J* = 7.6 Hz, 4H), 7.16 (br t, *J* = 7.3 Hz, 2H), 4.37 (dt, *J* = 8.7, 4.5 1H), 3.71 (d, *J* = 14.1 Hz, 2H), 3.31 (d, *J* = 14.1 Hz, 2H), 2.92 (td, *J* = 8.7, 1.6 Hz, 1H), 2.19–2.12 (m, 1H), 2.04–1.96 (m, 1H), 1.87–1.78 (m, 2H), 1.66–1.60 (m, 1H), 1.52–1.49 (m, 1H), 1.36–1.11 (m, 4H) ppm; **^{13}C NMR** (126 MHz, $CDCl_3$): δ 139.7, 129.3, 128.2, 127.0, 68.1, 59.9, 54.5, 37.2, 29.3, 27.6, 24.8, 23.7 ppm; **IR** (thin layer film): ν 3061, 3027, 2908, 2855, 2800, 1494, 1454, 1148, 744, 698 cm^{-1}.

***trans*-*N,N*-Dibenzyl-4-bromotetrahydrofuran-3-amine (*rac*-3.1d)**

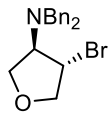

Alcohol **5.21** (280 mg, 1.0 mmol). under N_2 atmosphere was dissolved in anhydrous CH_2Cl_2 (5.0 mL). The solution was cooled to 0 °C and NEt_3 (0.20 mL, 1.5 mmol) was added at once, followed by a dropwise addition of MsBr (0.15 mL, 1.5 mmol). The reaction mixture was allowed to warm to r.t. and stirred for 3 h. Then reaction mixture was washed with sat. aq. $NaHCO_3$ (10 mL) and with brine (10 mL). The organic layer was dried over $MgSO_4$, filtered and concentrated *in vacuo*. The crude product was purified with a short silica plug (9:1 (v/v) pentane/Et_2O) affording *rac*-**3.1d** as a colourless oil (212 mg, 61%). **^{1}H NMR** (400 MHz, $CDCl_3$): *δ* 7.31–7.16 (m, 10H), 4.40–4.36 (m, 1H), 4.25 (dd, *J* = 10.3, 6.8 Hz, 1H), 3.89 (dd, *J* =

9.4, 7.5 Hz, 1H), 3.80–3.76 (m, 3H), 3.73 (d, *J* = 13.8 Hz, 2H), 3.58 (d, *J* = 13.8 Hz, 2H) ppm; **^{13}C NMR** (101 MHz, $CDCl_3$): *δ* 138.8, 128.7, 128.4, 127.3, 76.1, 69.9, 69.2, 54.7, 44.8 ppm; **HRMS** (ESI$^+$) = *m*/*z* calculated for $C_{18}H_{21}[^{79}Br]NO^+$ $[M+H]^+$ 346.0801, found 346.0800; **IR** (thin layer film): *ν* 3028, 2862, 1493, 1453, 1136, 1087, 1026, 922, 746, 697 cm^{-1}.

***tert*-Butyl *trans*-3-bromo-4-(dibenzylamino)pyrrolidine-1-carboxylate (*rac*-3.1e)**

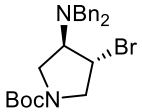

Alcohol **5.22** (380 mg, 1.0 mmol). under N_2 atmosphere was dissolved in anhydrous CH_2Cl_2 (5.0 mL). The solution was cooled to 0 °C and NEt_3 (0.20 mL, 1.5 mmol) was added at once, followed by a dropwise addition of MsBr (0.15 mL, 1.5 mmol). The reaction mixture was allowed to warm to r.t. and stirred for 3 h. Then reaction mixture was washed with sat. aq. $NaHCO_3$ (10 mL) and with brine (10 mL). The organic layer was dried over $MgSO_4$, filtered and concentrated *in vacuo*. The crude product was purified with a short silica plug (7:3 (v/v) pentane/Et_2O) affording *rac*-**3.1e** as a light-yellow solid (330 mg, 73%). **^{1}H NMR** (500 MHz, $CDCl_3$, *mixture of rotamers*): *δ* 7.40 (br d, *J* = 7.2 Hz, 4H), 7.33 (br t, *J* = 6.8 Hz, 4H), 7.27–7.24 (br m, 2H), 4.38 (br s, 1H), 3.99 (br t, J = 8.6 Hz, 0.4H, minor), 3.91 (br t, *J* = 8.6 Hz, 0.6H, major), 3.84–3.80 (m, 2H), 3.72–3.42 (m, 5H), 3.34 (br s, 1H), 1.44 (br s, 9H) ppm; **^{13}C NMR** (101 MHz, $CDCl_3$, *mixture of rotamers*): *δ* 154.0, 139.0, 128.8, 128.5, 127.4, 80.1, 66.7 (minor), 65.7 (major), 54.4, 53.5, 46.0 (major), 44.6 (major), 44.6 (minor), 44.2 (major), 28.6 ppm; **IR** (thin layer film): *ν* 3028, 2976, 2886, 1696, 1454, 1403, 1366, 1166, 1136, 1115, 767, 698 cm^{-1}. *Note*: ^{1}H NMR spectrum appeared broad due to mixture of rotamers.

5.4. Fluorination under HB-PTC

5.4.1. General procedures

General Procedure VII: reaction screenings

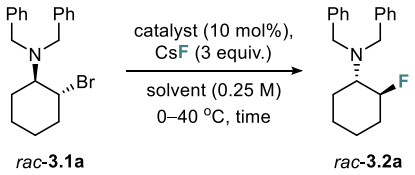

rac-**3.1a** *rac*-**3.2a**

A 1.75 mL screw-cap glass vial equipped with a stirring bar was charged with *rac*-*N*,*N*-dibenzyl-2-bromocyclohexan-1-amine (*rac*-**3.1a**) (1.0 equiv., 0.050 mmol), catalyst (2.5–20 mol%), CsF (1.2–5 equiv.) and solvent (0.10–0.50 M). The reaction mixture was stirred at 1200 rpm for 3−34 days at 0−40 °C. The crude mixture was filtered through a small plug of Celite, which was washed with CH_2Cl_2. The filtrate was evaporated to dryness, dissolved in $CDCl_3$ (0.7 mL) and analysed by ^{1}H and ^{19}F NMR (400 MHz and 377 MHz respectively) using 4-fluoroanisole as internal standard (5 μL, 0.044 mmol) to determine the yield. ^{19}F qNMR parameters were set-up as o1p = –150 ppm, d_1 = 35 s. To determine the *e.r.* an aliquot of the reaction mixture was purified by preparative TLC (500 micron; 99.8:0.2 hexane:Et_2O x 4 times) and analysed by chiral analytical HPLC: DAICEL CHIRALPAK® IB-3, heptane:*i*-PrOH = 99.5:0.5, 1 mL/min; t_1 = 3.52 min (major), t_2 = 4.69 min (minor).

General Procedure VIII: asymmetric nucleophilic fluorination using CsF

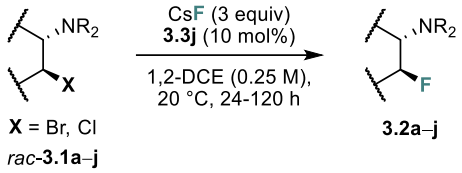

To an RBF with a magnetic stirring bar were sequentially the appropriate substrate (0.15–2.79 mmol, 1 equiv.), catalyst **3.3j** (10 mol% or 5 mol%), CsF (2.0 or 3.0 equiv.) and dry 1,2-DCE (0.25 M). The reaction mixture was stirred at 900 rpm at r.t. for 24−120 hours. The crude mixture was then filtered through a plug of silica and eluted with CH_2Cl_2, and the filtrate was evaporated to dryness under reduced pressure followed by purification of the crude material by flash column chromatography if necessary. The silica was further eluted with acetone to recover the catalyst.

Note: Although crude reaction mixtures of (*S*,*S*)-**3.2b**, (*S*,*S*)-**3.2c**, and (3*S*,4*S*)-**3.2d** showed quantitative conversion by NMR analysis, the isolated yields were consistently lower, suggesting partial decomposition upon chromatographic purification.

Racemate synthesis: The racemic reference products for HPLC analysis were obtained from β-amino-alcohols using DAST (2 equiv.) in CH_2Cl_2 (0.2 M) over 24 h at r.t., or from β-bromo-amines using AgF (0.12 equiv.) in MeCN (0.1 M) over 2 h at 60 °C.[1]

5.4.2. Characterisation of products

(*S*,*S*)-*N*,*N*-Dibenzyl-2-fluorocyclohexan-1-amine (*S*,*S*-3.1a)



S,*S*-**3.2a** was prepared from *rac*-**3.1a** (1.00 g, 2.79 mmol, 1.0 equiv.) according to *General Procedure VIII* using catalyst **3.3j** (134 mg, 0.14 mmol, 5 mol%) and CsF (840 mg, 5.58 mmol, 2.0 equiv.). The reaction was stirred at r.t. for 120 h. Purification by flash column chromatography (100:0 to 99.6:0.4, gradient, hexane/Et_2O) afforded colourless solid (0.99 g, 83% yield, *e.r.* = 89:11). **^{1}H NMR** (400 MHz, $CDCl_3$): δ 7.42–7.07 (m, 10H), 4.55 (dddd, *J* = 50.7, 10.4, 10.4, 4.8 Hz, 1H), 3.75 (d, *J* = 13.9 Hz, 2H), 3.67 (d, *J* = 14.0 Hz, 2H), 2.68–2.54 (m, 1H), 2.12–1.97 (m, 1H), 1.91–1.76 (m, 1H), 1.67–1.52 (m, 2H), 1.35–1.17 (m, 2H), 1.15–0.93 (m, 2H); **^{19}F NMR** (377 MHz, $CDCl_3$): δ −174.71 (d, *J* = 50.6 Hz); **^{13}C NMR** (101 MHz, $CDCl_3$): δ 140.7, 128.6, 128.1, 126.6, 93.3 (d, J_{CF} = 178 Hz), 61.2 (d, J_{CF} = 15 Hz), 54.4, 32.6 (d, J_{CF} = 18 Hz), 27.7 (d, J_{CF} = 9 Hz), 24.9 (d, J_{CF} = 2 Hz), 24.0 (d, J_{CF} = 11 Hz); **HRMS** (ESI+) = *m*/*z* calculated for $C_{20}H_{25}FN^+$ $[M+H]^+$ 298.1966, found 298.1969; **HPLC separation**: DAICEL CHIRALPAK® IB-3, heptane:*i*-PrOH = 99.5:0.5, 1 mL/min; t_1 = 3.52 min (major), t_2 = 4.69 min (minor). Spectroscopic data were in agreement with the ones previously reported in literature.[1]

The value for optical rotation of (*R*,*R*)-*N*,*N*-dibenzyl-2-fluorocyclohexan-1-amine ((*R*,*R*)-**3.2a**) was previously reported as $[\alpha]_D^{25°C}$ = –9.0 (*c* 0.2, $CHCl_3$, *e.r.* = 85.5:14.5.[1] The optical rotation of the obtained product above was $[\alpha]_D^{20°C}$ = +11.2 (*c* 1.0, $CHCl_3$, *e.r.* = 88.8:11.2) indicating (*S*,*S*) configuration. The configuration of the other cyclic products was assigned by analogy.

(1*S*,2*S*)-*N*,*N*-Dibenzyl-2-fluorocycloheptan-1-amine (*S*,*S*-3.2b)

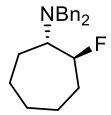

S,*S*-**3.2b** was prepared from *rac*-**3.1b** (69 mg, 0.18 mmol, 1 equiv.) according to *General Procedure VIII* catalyst **3.3j** (16 mg, 0.018 mmol, 10 mol%). The reaction was stirred at r.t. for 72 h. Purification by flash column chromatography (99.5:0.5 (v/v) hexane/Et_2O) afforded white waxy solid (40 mg, 72% yield, *e.r.* = 81:19). **^{1}H NMR** (400 MHz, $CDCl_3$): δ 7.42 (br d, *J* = 7.2 Hz, 4H), 7.30 (t, *J* = 7.2 Hz, 4H), 7.22 (br t, *J* = 7.2 Hz, 2H), 4.88 (dddd, *J* = 48.3, 7.7, 5.4, 3.9 1H), 3.78 (d, *J* = 14.0 Hz, 2H), 3.58 (d, *J* = 14.0 Hz, 2H), 2.89 (dddd, *J* = 20.8, 10.3, 7.7, 2.0 Hz, 1H), 2.00–1.61 (m, 5H), 1.50–1.21 (m, 5H) ppm; **^{19}F NMR** (377 MHz, $CDCl_3$): δ –

167.64 (dddd, J = 48.3, 20.8, 15.5, 2.9 Hz) ppm; **^{13}C NMR** (101 MHz, $CDCl_3$): δ 140.1, 128.7, 128.3, 126.9, 95.3 (d, $^1J_{CF}$ = 169 Hz), 64.0 (d, $^2J_{CF}$ = 20 Hz), 54.4, 33.4 (d, $^2J_{CF}$ = 22 Hz), 29.5, 27.5, 26.1 (d, $^3J_{CF}$ = 10 Hz), 21.7 (d, $^3J_{CF}$ = 4 Hz) ppm; **HRMS** (ESI+) = *m/z* calculated for $C_{21}H_{27}FN^+$ $[M+H]^+$ 312.2122, found 312.2115; **IR** (thin layer film): ν 3061, 3028, 2930, 2856, 2800, 1494, 1454, 1369, 1120, 1023, 973, 741, 698 cm^{-1}; $[\alpha]_D^{20℃}$ = 6.0 (*c* 1.0, $CHCl_3$, *e.r.* = 82:18); **HPLC separation**: DAICEL CHIRALPAK® IC-3, heptane:*i*-PrOH = 99.5:0.5, 1 mL/min; t_1 = 3.37 min (major), t_2 = 3.76 min (minor).

(*S*,*S*)-*N*,*N*-Dibenzyl-2-fluorocyclopentan-1-amine (*S*,*S*-3.2c)

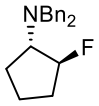

S,*S*-**3.2c** was prepared from *rac*-**3.1c** (344 mg, 1.00 mmol, 1 equiv.) according to *General Procedure VIII* using catalyst **3.3j** (48 mg, 0.05 mmol, 5 mol%). The reaction was stirred at r.t. for 96 h. Residue was purified via flash column chromatography (100:0 to 99.6:0.4 (v/v) hexane:Et_2O) giving title product as a white solid (244 mg, 86%, *e.r.* = 81:19). **^{1}H NMR** (400 MHz, $CDCl_3$): δ 7.41–7.36 (m, 4H), 7.34–7.28 (m, 4H), 7.27–7.19 (m, 2H), 5.15 (ddt, J = 54.0, 6.9, 3.6 Hz, 1H), 3.70 (d, J = 14.1 Hz, 2H), 3.63 (d, J = 14.1 Hz, 2H), 3.37 (dtd, J = 28.5, 8.5, 3.9 Hz, 1H), 2.01–1.72 (m, 3H), 1.72–1.48 (m, 3H); **^{19}F NMR** (377 MHz, $CDCl_3$): δ -172.99 (dtd, J = 53.5, 28.3, 23.5 Hz) ppm; **^{13}C NMR** (101 MHz, $CDCl_3$): δ 139.9, 128.8, 128.3, 127.0, 97.1 (d, J_{CF} = 177 Hz), 68.1 (d, J_{CF} = 22 Hz), 55.5, 32.8 (d, J_{CF} = 23 Hz), 27.4 (d, J_{CF} = 6 Hz), 22.0 (d, J_{CF} = 2 Hz) ppm; **HRMS** (ESI+) = *m/z* calculated for $C_{19}H_{22}FNK^+$ $[M+K]^+$ 322.1368, found 322.1375; $[\alpha]_D^{20℃}$ = +9.4 (*c* 1.0, $CHCl_3$, *e.r.* = 82:18) [lit.[1] $[\alpha]_D^{25℃}$ = –10.0 (*c* 0.5, $CHCl_3$, *e.r.* = 74.5:25.5, for (*R*,*R*) configuration)]; **HPLC separation**: DAICEL CHIRALPAK® OJ-H, heptane:EtOH = 98:2, 1 mL/min; t_1 = 8.09 min (major), t_2 = 10.13 min (minor). Spectroscopic data were in agreement with the ones previously reported in literature.[1]

(3*S*,4*R*)-*N*,*N*-Dibenzyl-4-fluorotetrahydrofuran-3-amine (3*S*,4*R*-3.2d)

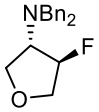

3*S*,4*R*-**3.2d** was prepared from *rac*-**3.1d** (345 mg, 1.00 mmol, 1 equiv.) according to *General Procedure VIII* using catalyst **3.3j** (48 mg, 0.05 mmol, 5 mol%). The reaction was stirred at r.t. for 96 h. Residue was purified via flash column chromatography (95:5 (v/v) hexane:Et_2O) giving the title product as a colourless oil (263 mg, 92%, *e.r.* = 85:15). **^{1}H NMR**

(400 MHz, $CDCl_3$): δ 7.25–7.16 (m, 10H), 5.22 (br d, J = 55.0 Hz, 1H), 3.94–3.84 (m, 3H), 3.70–3.47 (m, 6H) ppm; **^{19}F NMR** (377 MHz, $CDCl_3$): δ –177.43 (sx, J = 27.5 Hz) ppm; **^{13}C NMR** (101 MHz, $CDCl_3$): δ 138.8, 128.7, 128.4, 127.3, 94.8 (d, $^1J_{CF}$ = 182 Hz), 73.3 (d, $^2J_{CF}$ = 26 Hz), 70.0 (d, $^3J_{CF}$ = 3 Hz), 67.5 (d, $^2J_{CF}$ = 24 Hz), 55.6 ppm; **IR** (thin layer film): ν 3064, 2805, 1494, 1454, 1368, 1255, 1209, 1093, 1028, 976, 925, 751. 699, 650 cm^{-1}; **HRMS** (ESI+) = m/z calculated for $C_{18}H_{21}FNO^+$ $[M+H]^+$ 286.1602, found 286.1604; $[\alpha]_D^{20°C}$ = –4.2 (*c* 1.0, $CHCl_3$, *e.r.* = 85:15); **HPLC separation**: DAICEL CHIRALPAK® IB-3, heptane:*i*-PrOH = 99.5:0.5, 1 mL/min; t_1 = 13.07 min (major), t_2 = 17.90 min (minor).

Crystallisation: 3*S*,4*R*-**3.2d** (290 mg, 85:15 *e.r.*, 1 equiv.) and trichloroacetic acid (TCA, 150 mg, 1 equiv.) were dissolved in EtOH (2.0 mL) at 60 °C and volatiles were removed in vacuo giving 3*S*,4*R*-**3.2d**·TCA as a white solid (442 mg, quantitative yield). **^{1}H NMR** (600 MHz, $CDCl_3$): δ 9.21 (br s, 1H), 7.47–7.42 (m, 10H), 5.93 (ddt, $^1J_{HF}$ = 53.8 Hz, J_{HH} = 5.2, 2.3 Hz 1H), 4.26 (d, J = 13.9 Hz, 2H), 4.19–4.02 (m, 6H), 3.86 (dtd, $^3J_{HF}$ = 25.8 Hz, J_{HH} = 7.4, 2.2 Hz, 1H) ppm; **^{19}F NMR** (565 MHz, $CDCl_3$): δ −176.62 (ddt, 53.8, 30.0, 24.9 Hz, 1F) ppm; **^{13}C NMR** (151 MHz, $CDCl_3$): δ 165.4, 130.7, 130.0 (br s), 129.9, 129.5, 94.9, 93.8 (d, $^1J_{CF}$ = 184 Hz), 73.2 (d, $^2J_{CF}$ = 26 Hz), 69.1 (d, $^2J_{CF}$ = 26 Hz), 68.4 (d, $^3J_{CF}$ = 3 Hz), 55.8 ppm; **m.p.** 107−108 °C.

3*S*,4*R*-**3.2d**·TCA (442 mg) and *i*-PrOH (0.5 ml) were heated to 65 °C until complete dissolution of the solid. The solution was allowed to cool down step-wise to 35 °C over 4 h, and further crystallisation for 3 h at 35 °C. The mother liquor was removed at 35 °C and the obtained crystals were washed with cold *i*-PrOH (0.1 mL x 2), affording colourless crystals of near-racemic material (145 mg, 33%, *e.r.* 60:40) as well as enantioenriched product after evaporation of the mother liquor (264 mg, 60%, *e.r.* 98:2). All the *e.r.* were determined of the free amine base by neutralising **3.2d**·TCA samples with 1.0 M aq. NaOH and extracting with Et_2O. The solvent was evaporated *in vacuo* and *e.r.* was measured by chiral HPLC.

***tert*-Butyl (3*S*,4*S*)-3-(dibenzylamino)-4-fluoropyrrolidine-1-carboxylate (*S*,*S*-3.2e)**

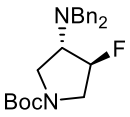

S,*S*-**3.2e** was prepared from *rac*-**3.1e** (89 mg, 0.20 mmol, 1 equiv.) according to *General Procedure VIII* using catalyst **3.3j** (19 mg, 0.02 mmol, 10 mol%). The reaction was stirred at r.t. for 72 h. Purification by flash column chromatography (90:10 (v/v), hexane/Et_2O) afforded white solid (67 mg, 87% yield, *e.r.* = 76:24). **^{1}H NMR** (400 MHz, $CDCl_3$): δ 7.36–7.24 (m, 10H), 5.23 (br d, J = 52.2 Hz, 1H), 3.72–3.40 (m, 9H), 1.45 (s, 9H) ppm; **^{19}F NMR** (377 MHz, $CDCl_3$, two conformers): δ –179.31 to −179.63 (m), –179.68 to −180.00 (m) ppm; **^{13}C NMR** (101 MHz, $CDCl_3$, two conformers): δ 154.3, 139.0, 128.7, 128.5, 127.4, 93.1 (d, $^1J_{CF}$ = 182 Hz), 92.0 (d, $^1J_{CF}$ = 182 Hz), 80.0, 64.7 (d, $^2J_{CF}$ = 24 Hz), 63.9 (d, $^2J_{CF}$ = 24 Hz), 55.1, 50.9 (t, $^2J_{CF}$ = 27 Hz), 47.1, 46.2, 28.6 ppm; **HRMS** (ESI+) = *m*/*z* calculated for $C_{23}H_{30}FN_2O_2^+$ $[M+H]^+$ 385.2286, found 385.2277; **IR** (thin layer film): ν 3029, 2975, 2885, 1698, 1454, 1403, 1366, 1171, 1142, 1118, 882, 745, 698 cm^{-1}; $[\alpha]_D^{20^\circ C}$ = 11.2 (*c* 1.0, $CHCl_3$, *e.r.* = 76:24); **HPLC separation**: DAICEL CHIRALPAK® IB-3, heptane:*i*-PrOH = 99.0:1.0, 1 mL/min; t_1 = 7.60 min (major), t_2 = 11.42 min (minor).

(1S,2S)-2-fluoro-N,N-bis(4-methoxybenzyl)cyclohexan-1-amine (*S*,*S*-3.2f)

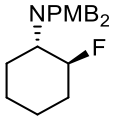

S,*S*-**3.2f** was prepared from *rac*-**3.1f** (84 mg, 0.20 mmol, 1 equiv.) according to *General Procedure VIII* using catalyst **3.3j** (19 mg, 0.02 mmol, 10 mol%). The reaction was stirred at r.t. for 72 h. Purification by flash column chromatography (50% to 65% (v/v) toluene in hexane) afforded white solid (42 mg, 59% yield, *e.r.* = 78:22). **^{1}H NMR** (400 MHz, $CDCl_3$): δ 7.22 (d, J = 8.5 Hz, 4H), 6.75 (d, J = 8.5 Hz, 4H), 4.52 (dtd, J_{HF} = 50.6 Hz, J_{HH} = 10.3, 4.9 Hz, 1H), 3.70 (s, 6H), 3.66 (d, J = 13.5 Hz, 2H), 3.56 (d, J = 13.5 Hz, 2H), 2.63–2.54 (m, 1H), 2.07–2.00 (m, 1H), 1.81–1.74 (m, 1H), 1.61–1.54 (m, 2H), 1.30–1.18 (m, 2H), 1.11–0.94 (m, 2H) ppm; **^{19}F NMR** (377 MHz, $CDCl_3$): δ –174.73 (br d, J_{HF} = 50.6 Hz, 1F) ppm; **HRMS** (ESI+) = *m*/*z* calculated for $C_{22}H_{29}FNO_2^+$ $[M+H]^+$ 358.2177, found 358.2182; **HPLC separation**: DAICEL CHIRALPAK® IJ-3, heptane:*i*-PrOH = 98.5:1.5, 1 mL/min; t_1 = 8.00 min (major), t_2 = 10.32 min (minor). Spectroscopic data were in agreement with the ones previously reported in literature.[1]

2-((1*R*,2*R*)-2-Fluoro-1,2-diphenylethyl)-1,2,3,4-tetrahydroisoquinoline (*R*,*R*-3.2g)

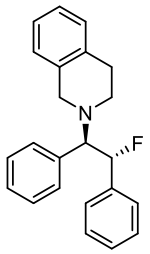

R,*R*-**3.2g** was prepared from *rac*-**3.1g** (52 mg, 0.15 mmol, 1 equiv.) according to *General Procedure VIII* using catalyst **3.3j** (14 mg, 0.015 mmol, 10 mol%). The reaction was stirred at r.t. for 72 h. Residue was purified via silica plug filtration with CH_2Cl_2 giving product as a colourless oil (47 mg, 94%, *e.r.* 24:76). **^{1}H NMR** (400 MHz, $CDCl_3$): δ 7.19–7.10 (m, 13H), 7.01 (br d, *J* = 6.1 Hz, 1H), 6.04 (br dd, *J* = 47.5, 7.0 Hz, 1H), 4.16 (dd, *J* = 14.3, 8.3 Hz, 1H), 3.99–3.89 (m, 2H), 3.16 (br s, 1H), 3.01–2.85 (m, 3H) ppm; **^{19}F{^{1}H} NMR** (377 MHz, $CDCl_3$): δ −172.25 (s, 1F) ppm; **^{13}C NMR** (101 MHz, $CDCl_3$): δ 138.0 (d, J_{CF} = 21 Hz), 136.4 (d, J_{CF} = 6 Hz), 135.3, 134.7, 129.5, 128.7, 128.2 (d, J_{CF} = 2 Hz), 128.1, 128.0, 127.7, 126.9 (d, J_{CF} = 6 Hz), 126.8, 126.2, 125.6, 94.8 (d, J_{CF} = 179 Hz), 73.5 (d, J_{CF} = 22 Hz), 53.7 (d, J_{CF} = 3 Hz), 48.3 (br s), 29.1 ppm; **HRMS** (ESI+) = *m*/*z* calculated for $C_{23}H_{23}FN^+$ $[M+H]^+$ 332.1809, found 332.1799; **HPLC separation**: DAICEL CHIRALPAK® IF-3, heptane:*i*-PrOH = 99:1, 1 mL/min; t_1 = 4.97 min (minor), t_2 = 6.09 min (major). Spectroscopic data were in agreement with the ones previously reported in literature.[1]

The (*R*,*R*) configuration was assigned based on HPLC conditions reported previously for (*S*,*S*) product (*e.r.* 96:4).[1] **HPLC separation**: DAICEL CHIRALPAK® IF-3, heptane:*i*-PrOH = 99:1, 1 mL/min; t_1 = 4.77 min (major), t_2 = 5.83 min (minor). The configuration of the other stilbene-based products was assigned by analogy.

(1*R*,2*R*)-(2-fluoro-1,2-diphenylethyl)pyrrolidine (*R*,*R*-3.2h)

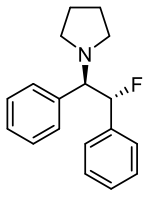

R,*R*-**3.2h** was prepared from *rac*-**3.1h** (43 mg, 0.15 mmol, 1 equiv.) according to *General Procedure VIII* using catalyst **3.3j** (14 mg, 0.015 mmol, 10 mol%). The reaction was stirred at r.t. for 72 h. Residue was purified via silica plug with Et_2O giving product as a white solid (38 mg, 94%, *e.r.* 26:74). **^{1}H NMR** (400 MHz, $CDCl_3$): δ 7.16–7.13 (m, 6H), 7.06–7.01 (m, 4H), 5.80 (dd, *J* = 46.8, 7.7 Hz, 1H), 3.74 (dd, *J* = 13.0, 7.7 Hz, 1H), 2.80–2.78 (m, 2H), 2.65–2.60 (m, 2H), 1.84–1.77 (m, 4H) ppm; **^{19}F{^{1}H} NMR** (377 MHz, $CDCl_3$): δ −170.61 (s, 1F) ppm; **^{13}C NMR** (101 MHz, $CDCl_3$): δ 138.0 (d, J_{CF} = 8 Hz), 137.9 (d, J_{CF} = 21 Hz), 129.2, 128.0 (d, J_{CF} = 2 Hz), 127.9, 127.7, 127.4, 126.7 (d, J_{CF} = 7 Hz), 97.0 (d, J_{CF} = 178 Hz),

74.8 (d, J_{CF} = 23 Hz), 53.4 (d, J_{CF} = 4 Hz), 23.2 ppm; **HRMS** (ESI+) = *m/z* calculated for $C_{18}H_{21}FN^+$ $[M+H]^+$ 270.1653, found 270.1662; **HPLC separation**: DAICEL CHIRALPAK® OJ-3, heptane:*i*-PrOH = 97.5:1.5, 0.6 mL/min; t_1 = 5.37 min (minor), t_2 = 6.12 min (major). Spectroscopic data were in agreement with the ones previously reported in literature.[1]

1-((1*R*,2*R*)-2-Fluoro-1,2-diphenylethyl)piperidine (*R,R*-3.2i)

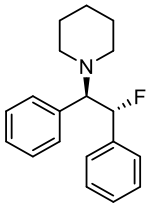

R,R-**3.2i** was prepared from *rac*-**3.1i** (45 mg, 0.15 mmol) according to *General Procedure VIII* using catalyst **3.3j** (14 mg, 0.015 mmol, 10 mol%). The reaction was stirred at r.t. for 24 h. Residue was purified via silica plug filtration with CH_2Cl_2 giving product as a white solid (44 mg, 99%, *e.r.* 24:76). **^{1}H NMR** (400 MHz, $CDCl_3$): δ 7.21–7.18 (m, 8H), 7.09 (br d, *J* = 6.6 Hz, 2H), 5.93 (dd, *J* = 47.4, 8.6 Hz, 1H), 3.97 (dd, *J* = 13.3, 8.5 Hz, 1H), 2.67–2.52 (m, 4H), 1.73–1.58 (m, 4H), 1.45–1.39 (m, 2H) ppm; **^{19}F{^{1}H} NMR** (377 MHz, $CDCl_3$): δ −174.18 (s, 1F) ppm; **^{13}C NMR** (101 MHz, $CDCl_3$): δ 138.4 (d, J_{CF} = 20 Hz), 135.7 (d, J_{CF} = 6 Hz), 129.6, 128.1 (d, J_{CF} = 2 Hz), 127.9, 127.8, 127.3, 127.0 (d, J_{CF} = 6 Hz), 93.7 (d, J_{CF} = 178 Hz), 74.6 (d, J_{CF} = 22 Hz), 51.5, 26.4, 24.6 ppm; **HRMS** (ESI+) = *m/z* calculated for $C_{19}H_{23}FN^+$ $[M+H]^+$ 284.1809, found 284.1810. **HPLC separation**: DAICEL CHIRALPAK® IC-3, heptane:EtOH = 99:1, 1 mL/min; t_1 = 6.18 min (major), t_2 = 6.70 min (minor). Spectroscopic data were in agreement with the ones previously reported in literature.[1]

(1*R*,2*R*)-2-Fluoro-*N,N*-dimethyl-1,2-diphenylethan-1-amine (*R,R*-3.2j)

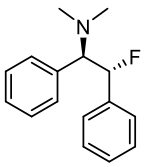

R,R-**3.2j** was prepared from *rac*-**3.1j** (39 mg, 0.15 mmol, 1 equiv.) according to *General Procedure VIII* using catalyst **3.3j** (14 mg, 0.015 mmol, 10 mol%). The reaction was stirred at r.t. for 72 h. Residue was purified via silica plug filtration with Et_2O giving product as a colourless oil (33 mg, 92%, *e.r.* 26:74). **^{1}H NMR** (400 MHz, $CDCl_3$): δ 7.21–7.15 (m, 8H), 7.08–7.06 (m, 2H), 5.89 (dd, *J* = 47.2, 8.8 Hz, 1H), 3.93 (dd, *J* = 12.2, 8.8 Hz, 1H), 2.42 (s, 6H) ppm; **^{19}F{^{1}H} NMR** (377 MHz, $CDCl_3$): δ −172.48 (s, 1F) ppm; **^{13}C NMR** (101 MHz, $CDCl_3$): δ 137.0 (d, J_{CF} = 20 Hz), 134.8 (d, J_{CF} = 7 Hz), 129.5, 128.3 (d, J_{CF} = 2 Hz), 128.0, 127.9, 127.6, 127.0 (d, J_{CF} = 6 Hz), 94.1 (d, J_{CF} = 178 Hz), 74.3 (d, J_{CF} = 22 Hz), 42.7 (d, J_{CF} = 2 Hz) ppm; **HRMS** (ESI+) = *m/z* calculated for $C_{16}H_{19}FN^+$ $[M+H]^+$ 244.1496, found

244.1504; **HPLC separation**: DAICEL CHIRALPAK® IC-3, heptane:*i*-PrOH = 99:1, 1 mL/min; t_1 = 5.43 min (minor), t_2 = 10.44 min (major). Spectroscopic data were in agreement with the ones previously reported in literature.[1]

N,N-Dibenzyl-1,4-*bis*(benzyloxy)-3-fluorobutan-2-amine (3.2k)

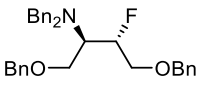

3.2k was prepared from *rac*-**3.1k** (24 mg, 0.05 mmol, 1 equiv.) according to *General Procedure VII* using catalyst **3.3j** (4.8 mg, 0.005 mmol, 10 mol%). NMR yield 82%, *e.r.* 67:33 (TLC: 10% (v/v) Et_2O in hexane). **^{1}H NMR** (400 MHz, $CDCl_3$): δ 7.30–7.09 (m, 20H), 5.89 (dddd, J_{HF} = 49.6 Hz, J_{HH} = 7.0, 4.4, 2.5 Hz, 1H), 4.45 (d, J = 12.1 Hz, 1H), 4.41 (d, J = 12.1 Hz, 1H), 4.41 (s, 2H), 3.88–3.77 (m, 2H), 3.87 (d, J = 13.4 Hz, 2H), 3.72 (d, J = 13.4 Hz, 2H), 3.68 (dd, J = 9.6, 6.7 Hz, 1H), 3.32 (ddd, J_{HF} = 32.1 Hz, J_{HH} = 11.7, 2.5 Hz, 1H), 3.32 (dq, J_{HF} = 26.8 Hz, J_{HH} = 5.1 Hz, 1H) ppm; **^{19}F{^{1}H} NMR** (377 MHz, $CDCl_3$): δ −196.69 (s, 1F) ppm; **^{13}C NMR** (101 MHz, $CDCl_3$): δ 140.1, 138.2, 138.0, 129.0, 128.5, 128.43, 128.37, 128.2, 127.9, 127.7, 127.6, 126.9, 94.3 (d, J_{CF} = 178 Hz), 73.4, 71.2 (d, J_{CF} = 22 Hz), 66.9 (d, J_{CF} = 4 Hz), 57.3 (d, J_{CF} = 17 Hz), 55.7, 55.6 ppm; **HPLC separation**: DAICEL CHIRALPAK® IB-3, heptane:*i*-PrOH = 99.5:0.5, 1 mL/min; t_1 = 8.91 min (major), t_2 = 9.79 min (minor).

N,N-Dibenzyl-4-fluorohexan-3-amine (3.2l)

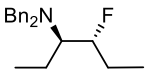

3.2l was prepared from *rac*-**3.1l** (15 mg, 0.05 mmol, 1 equiv.) according to *General Procedure VII* using catalyst **3.3j** (4.8 mg, 0.005 mmol, 10 mol%). NMR yield 94%, *e.r.* 50:50 (TLC: 0.5% (v/v) Et_2O in hexane). **^{1}H NMR** (400 MHz, $CDCl_3$): δ 7.31–7.12 (m, 10H), 4.42 (dddd, J_{HF} = 48.7 Hz, J_{HH} = 8.6, 5.0, 4.1 Hz, 1H), 3.81 (d, J = 13.6 Hz, 1H), 3.50 (d, J = 13.6 Hz, 1H), 4.42 (dddd, J_{HF} = 24.5 Hz, J_{HH} = 7.8, 6.1, 5.0 Hz, 1H), 1.87–1.70 (m, 1H), 1.66–1.40 (m, 3H), 0.86 (t, J = 7.9 Hz, 3H), 0.77 (t, J = 7.9 Hz, 3H) ppm; **^{19}F NMR** (377 MHz, $CDCl_3$): δ −190.53 (dddd, J = 48.7, 33.5, 24.5, 16.5 Hz, 1F) ppm; **^{13}C NMR** (101 MHz, $CDCl_3$): δ 140.6, 129.1, 128.1, 126.7, 97.6 (d, J_{CF} = 167 Hz), 60.6 (d, J_{CF} = 17 Hz), 55.0 (d, J_{CF} = 4 Hz), 25.7 (d, J_{CF} = 22 Hz), 17.7 (d, J_{CF} = 6 Hz), 11.8, 9.8 (d, J_{CF} = 6 Hz) ppm; **HPLC separation**: DAICEL CHIRALPAK® IB-3, heptane, 1 mL/min; t_1 = 3.24 min, t_2 = 4.12 min.

5.5. NMR studies

5.5.1. ^{1}H and ^{13}C NMR spectra assignments and NOESY correlations

Additional 2D NMR experiments that were used for spectral assignment are given in parenthesis. Copies of 2D NOESY spectra used for conformational analysis are provided below. The samples were prepared at 25 mM concentration in CD_2Cl_2, unless otherwise stated.

Boc-Leu-D-Pro-Acpc-Phe-NMe$_2$ (2a)

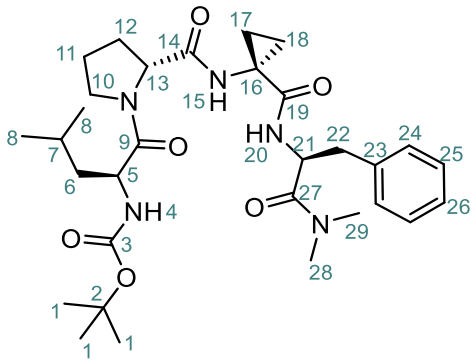

Scheme 5.5.1. Structure and numbering of **2a**.

^{1}H (^{1}H-^{1}H COSY, ^{1}H-^{13}C multiplicity-edited HSQC, ^{1}H-^{1}H NOESY) NMR (500 MHz, CD_2Cl_2): δ 7.74 (d, J_{HH} = 8.7 Hz, 1H, H^{20}), 7.32–7.23 (m, 5H, H^{24}+H^{25}+H^{26}), 7.00 (s, 1H, H^{15}), 6.46 (d, J_{HH} = 7.7 Hz, 1H, H^{4}), 5.08 (td, J_{HH} = 8.5, 6.7 Hz, 1H, H^{21}), 4.45 (br q, J_{HH} = 7.9 Hz, 1H, H^{5}), 4.43–4.30 (m, 1H, H^{13}), 3.94–3.91 (m, 1H, H^{10a}), 3.64 (dt, J_{HH} = 10.0, 6.7 Hz, 1H, H^{10b}), 3.13 (dd, J_{HH} = 13.1, 8.4 Hz, 1H, H^{22a}), 3.02 (dd, J_{HH} = 13.1, 6.5 Hz, 1H, H^{22b}), 2.84 (s, 3H, H^{29}), 2.77 (s, 3H, H^{28}), 2.16–2.08 (m, 3H, H^{11a}+H^{12}), 2.02–1.96 (m, 1H, H^{11b}), 1.76–1.62 (m, 3H, H^{6}+H^{7}), 1.45 (s, 9H, H^{1}), 1.43–1.41 (m, 2H, H^{17}), 1.01 (d, J_{HH} = 4.6 Hz, 3H, H^{8a}), 1.00 (d, J = 4.8 Hz, 3H, H^{8b}), 0.98–0.96 (m, 2H, H^{18}) ppm.

^{13}C (^{1}H-^{13}C multiplicity-edited HSQC, ^{1}H-^{13}C HMBC) NMR (126 MHz, CD_2Cl_2): δ 172.7 (C^{9}), 172.5 (C^{14}), 171.1 (C^{27}), 170.6 (C^{19}), 156.4 (C^{3}), 137.4 (C^{23}), 129.4 (C$^{24/25}$), 128.2 (C$^{24/25}$), 126.5 (C^{26}), 79.3 (C^{2}), 61.3 (C^{13}), 50.7 (C^{5}), 50.4 (C^{21}), 47.4 (C^{10}), 40.9 (C^{6}), 38.9 (C^{22}), 36.8 (C^{29}), 35.4 (C^{28}), 34.3 (C^{16}), 28.7 (C^{12}), 28.1 (C^{1}), 25.1 (C^{11}), 24.7 (C^{7}), 22.9 (C^{8}), 22.1 (C^{8}), 16.9 (C^{17}), 16.7 (C^{18}) ppm.

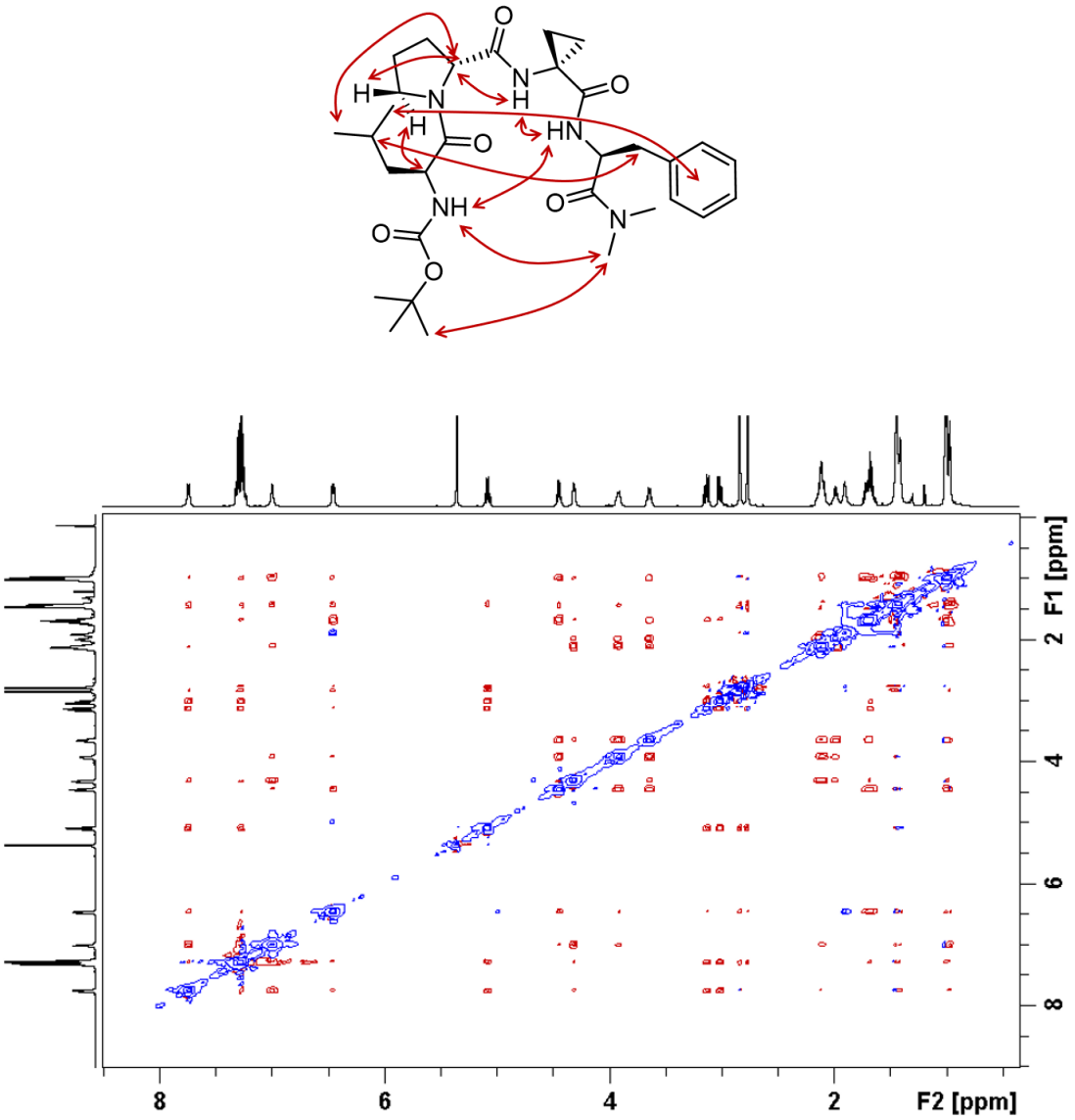

Figure 5.5.1. $^{1}H-^{1}H$ NOESY NMR spectrum of **2a** (500 MHz, CD_2Cl_2, 25 mM, d_8 = 800 ms) with inter-residue correlations displayed as arrows.

Boc-Leu-Pro-Acpc-Phe-NMe$_2$ (2b)

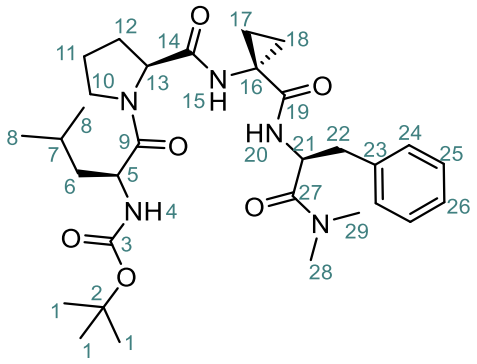

Scheme 5.5.2. Structure and numbering of **2b**.

^{1}H NMR (^{1}H-^{1}H COSY, ^{1}H-^{13}C multiplicity-edited HSQC, ^{1}H-^{1}H NOESY) (500 MHz, CD_2Cl_2): δ 7.87 (d, J_{HH} = 7.8 Hz, 1H, H^{20}), 7.30–7.21 (m, 5H, H^{24}+H^{25}+H^{26}), 6.92 (s, 1H, H^{15}), 5.80 (d, J_{HH} = 9.0 Hz, 1H, H^4), 4.97 (td, J_{HH} = 8.4, 5.3 Hz, 1H, H^{21}), 4.45 (br td, J_{HH} = 10.3, 2.3 Hz, 1H, H^5), 4.22 (t, J_{HH} = 7.1 Hz, 1H, H^{13}), 3.90–3.76 (m, 1H, H^{10a}), 3.62 (dt, J_{HH} = 9.6, 7.1 Hz, 1H, H^{10b}), 3.05 (dd, J_{HH} = 13.2, 8.7 Hz, 1H, H^{22a}), 2.90 (s, 3H, H^{29}), 2.89 (dd, J_{HH} = 13.2, 5.5 Hz, 1H, H^{22b}), 2.79 (s, 3H, H^{28}), 2.20–2.12 (m, 1H, H^{11a}), 2.11 (q, J_{HH} = 6.1 Hz, 2H, H^{12}), 2.03–1.96 (m, 1H, H^{11a}), 1.86–1.78 (m, 1H, H^7), 1.63 (ddd, J_{HH} = 13.4, 11.4, 3.9 Hz, 1H, H^{6a}), 1.52 (ddd, J_{HH} = 10.2, 7.7, 4.4 Hz, 1H, H^{17a}), 1.49–1.46 (m, 1H, H^{6b}), 1.44 (s, 9H, H^1), 1.42 (ddd, J_{HH} = 10.2, 7.5, 4.1 Hz, 1H, H^{17b}), 1.04 (ddd, J_{HH} = 11.5, 7.5, 4.4 Hz, 1H, H^{18a}), 1.02 (d, J_{HH} = 6.5 Hz, 3H, H^{8a}), 0.97 (d, J_{HH} = 6.6 Hz, 3H, H^{8b}), 0.93 (ddd, J_{HH} = 11.5, 7.7, 4.1 Hz, 1H, H^{18b}) ppm.

^{13}C (^{1}H-^{13}C multiplicity-edited HSQC, ^{1}H-^{13}C HMBC) NMR (126 MHz, CD_2Cl_2): δ 173.3 (C^9), 172.8 (C^{14}), 170.6 (C^{19}+C^{27}), 155.8 (C^3), 137.8 (C^{23}), 129.5 (C$^{24/25}$), 128.1 (C$^{24/25}$), 126.4 (C^{26}), 79.0 (C^2), 61.4 (C^{13}), 51.5 (C^5), 50.8 (C^{21}), 47.4 (C^{10}), 41.1 (C^6), 38.7 (C^{22}), 36.7 (C^{29}), 35.5 (C^{28}), 34.5 (C^{16}), 28.2 (C^{12}), 28.1 (C^1), 25.6 (C^{11}), 24.7 (C^7), 23.2 (C^{8a}), 22.1 (C^{8b}), 17.3 (C^{17}), 16.3 (C^{18}) ppm.

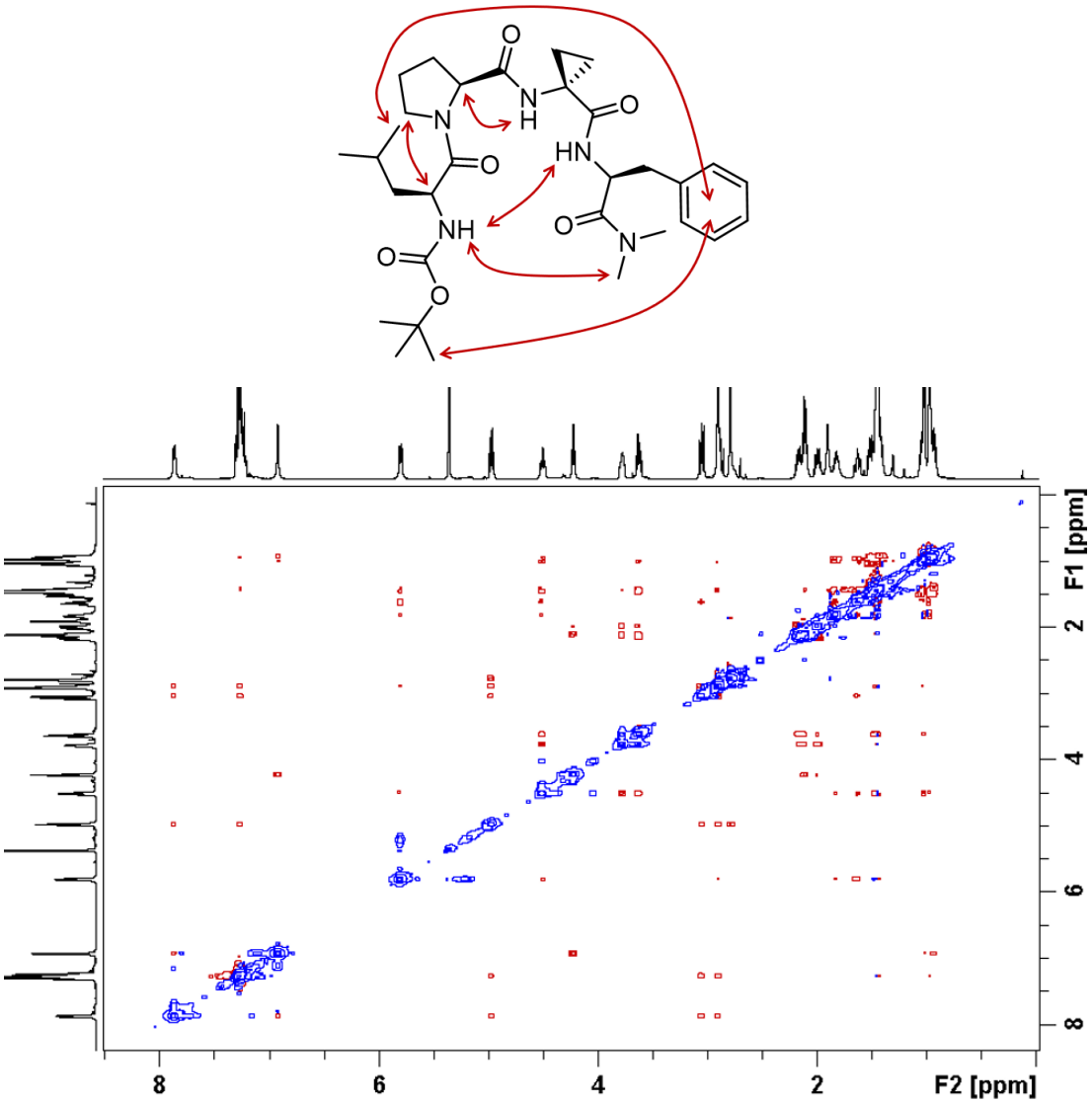

Figure 5.5.2. $^{1}H-^{1}H$ NOESY NMR spectrum of **2b** (500 MHz, CD_2Cl_2, 25 mM, d_8 = 800 ms) with inter-residue correlations displayed as arrows.

3,5-$(CF_3)_2C_6H_3NHC(O)$-Pro-Gly-Phe-NMe_2 (2c)

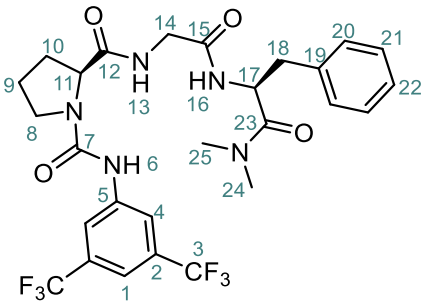

Scheme 5.5.3. Structure and numbering of **2c**.

^{1}H NMR (^{1}H-^{1}H COSY, ^{1}H-^{13}C multiplicity-edited HSQC, ^{1}H-^{1}H NOESY) (500 MHz, CD_2Cl_2): δ 8.05 (s, 2H, H^4), 7.80 (br s, 1H, H^6), 7.50 (s, 1H, H^1), 7.40 (br s, 1H, H^{16}), 7.37 (t, J_{HH} = 6.4 Hz, 1H, H^{13}), 7.31–7.24 (m, 3H, H^{22}+H^{21}), 7.15 (d, J_{HH} = 6.9 Hz, 2H, H^{20}), 5.07 (q, J_{HH} = 7.1 Hz, 1H, H^{17}), 4.54 (dd, J_{HH} = 8.3, 2.3 Hz, 1H, H^{11}), 3.91 (br s, 2H, H^{14}), 3.65–3.25 (m, 2H, H^8), 2.98 (dd, J_{HH} = 13.5, 7.0 Hz, 1H, H^{18a}), 2.98 (dd, J_{HH} = 13.5, 6.4 Hz, 1H, H^{18b}), 2.85 (s, 3H, H^{25}), 2.76 (s, 3H, H^{24}), 2.34–2.29 (m, 1H, H^{10a}), 2.21–2.13 (m, 1H, H^{10b}), 2.09–2.00 (m, 2H, H^9) ppm.

^{13}C (^{1}H-^{13}C multiplicity-edited HSQC, ^{1}H-^{13}C HMBC) NMR (126 MHz, CD_2Cl_2): δ 172.8 (C^{11}), 170.8 (C^{23}), 168.1 (C^{15}), 155.1 (C^7), 141.2 (C^5), 136.2 (C^{19}), 131.5 (q, J_{CF} = 34 Hz, C^2), 129.4 (C^{20}), 128.3 ($C^{22/21}$), 126.9($C^{22/21}$), 123. (q, J_{CF} = 272 Hz, C^3), 119.7 (br s, C^4), 115.7 (br s, C^1), 60.9 (C^{11}), 50.6 (C^{17}), 47.2 (C^8), 42.6 (C^{14}), 38.8 (C^{18}), 36.6 (C^{24}), 35.3 (C^{25}), 29.7 (br s, C^{10}), 24.3 (C^9) ppm.

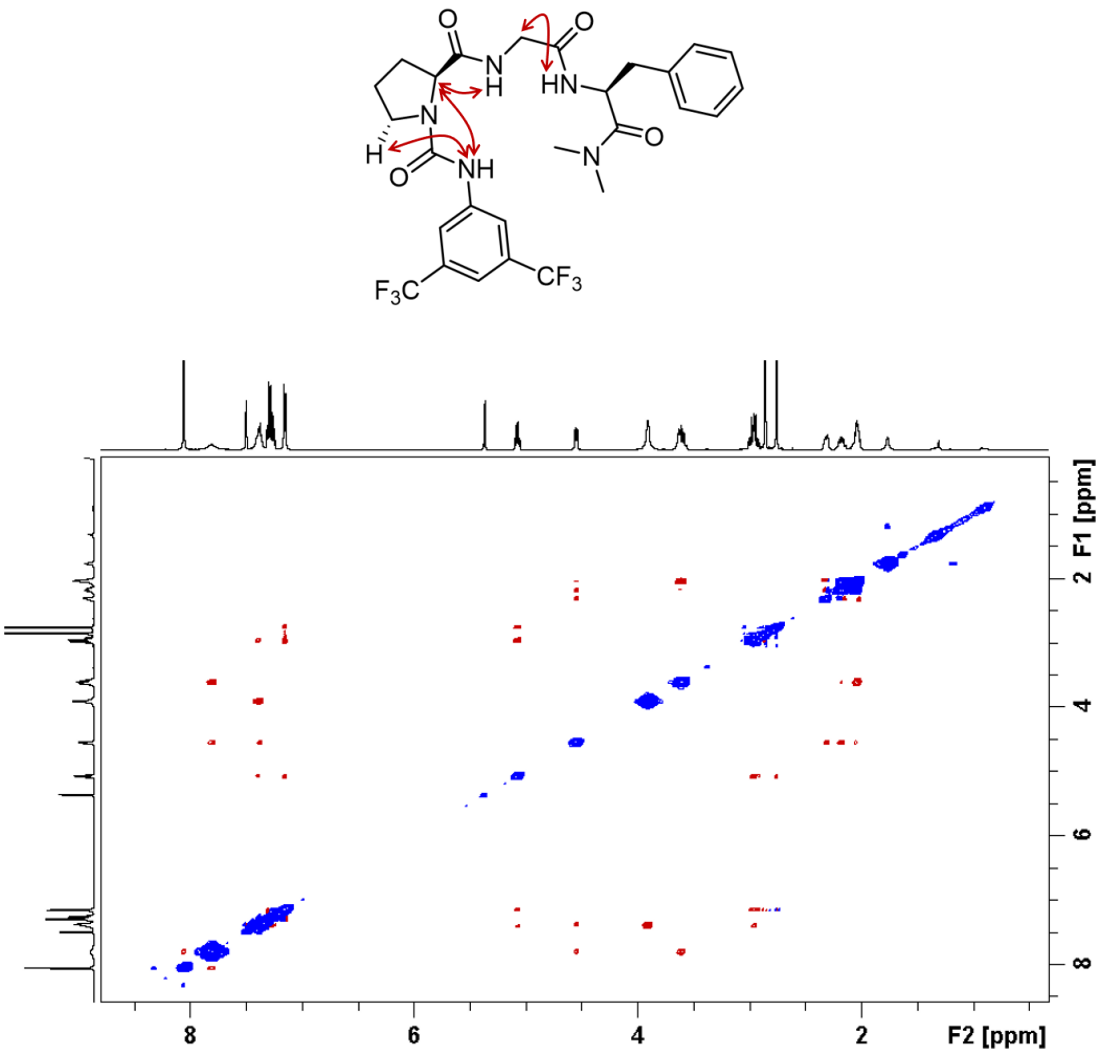

Figure 5.5.3. $^{1}H-^{1}H$ NOESY NMR spectrum of **2c** (500 MHz, CD_2Cl_2, 25 mM, d_8 = 800 ms) with inter-residue correlations displayed as arrows.

3,5-[3,5-$(CF_3)_2C_6H_3]_2C_6H_3NHC(O)$-Pro-Gly-Phe-$NMe_2$ (2d)

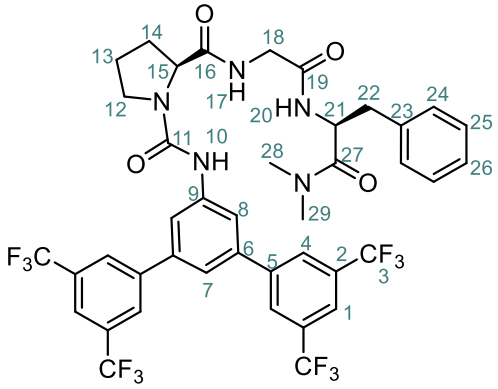

Scheme 5.5.4. Structure and numbering of **2d**.

^{1}H NMR (^{1}H-^{1}H COSY, ^{1}H-^{13}C multiplicity-edited HSQC, ^{1}H-^{1}H NOESY) (500 MHz, CD_2Cl_2): δ 8.02 (s, 4H, H^4), 7.90 (s, 2H, H^1), 7.81 (d, J_{HH} = 1.5 Hz, 2H, H^8), 7.54 (br s, H^{10}), 7.51 (t, J_{HH} = 6.1 Hz, H^{17}), 7.38 (br d, J_{HH} = 5.3 Hz, 1H, H^{20}), 7.33 (t, J_{HH} = 1.5 Hz, 1H, H^7), 7.19–7.17 (m, 3H, H^{26}+H^{25}), 6.98–6.96 (m, 2H, H^{24}), 4.93 (q, J_{HH} = 7.0 Hz, 1H, H^{21}), 4.63 (br dd, J_{HH} = 7.3, 3.5 Hz, 1H, H^{15}), 4.01 (dd, J_{HH} = 17.1, 6.7 Hz, 1H, H^{18a}), 3.78–3.74 (m, 2H, H^{18b}+ H^{12a}), 3.62 (q, J_{HH} = 7.8 Hz, 1H, H^{12b}), 2.82–2.81 (m, 2H, H^{22}), 2.71 (s, 3H, H^{28}), 2.59 (s, 3H, H^{29}), 2.36–2.29 (m, 1H, H^{14a}), 2.22–2.14 (m, 2H, H^{14b}+H^{13a}), 2.12–2.05 (m, 1H, H^{13b}) ppm.

^{13}C (^{1}H-^{13}C multiplicity-edited HSQC, ^{1}H-^{13}C HMBC) NMR (126 MHz, CD_2Cl_2): δ 173.0 (C^{16}), 170.9 (C^{27}), 168.1 (C^{19}), 155.2 (C^{11}), 142.5 (C^5), 141.0 (C^9), 139.4 (C^6), 136.2 (C^{23}), 131.9 (q, J_{CF} = 33 Hz, C^2), 129.2 (C^{24}), 128.1 (C^{25}), 127.3 (br s, C^4), 126.8 (C^{26}), 123.4 (q, J_{CF} = 273 Hz, C^3), 121.3 (br s, C^1), 120.2 (C^8), 119.5 (C^7), 60.8 (C^{15}), 50.6 (C^{21}), 47.1 (C^{12}), 42.7 (C^{18}), 38.6 (C^{22}), 36.5 (C^{29}), 35.2 (C^{28}), 29.2 (C^{13}), 24.9 (C^{14}) ppm.

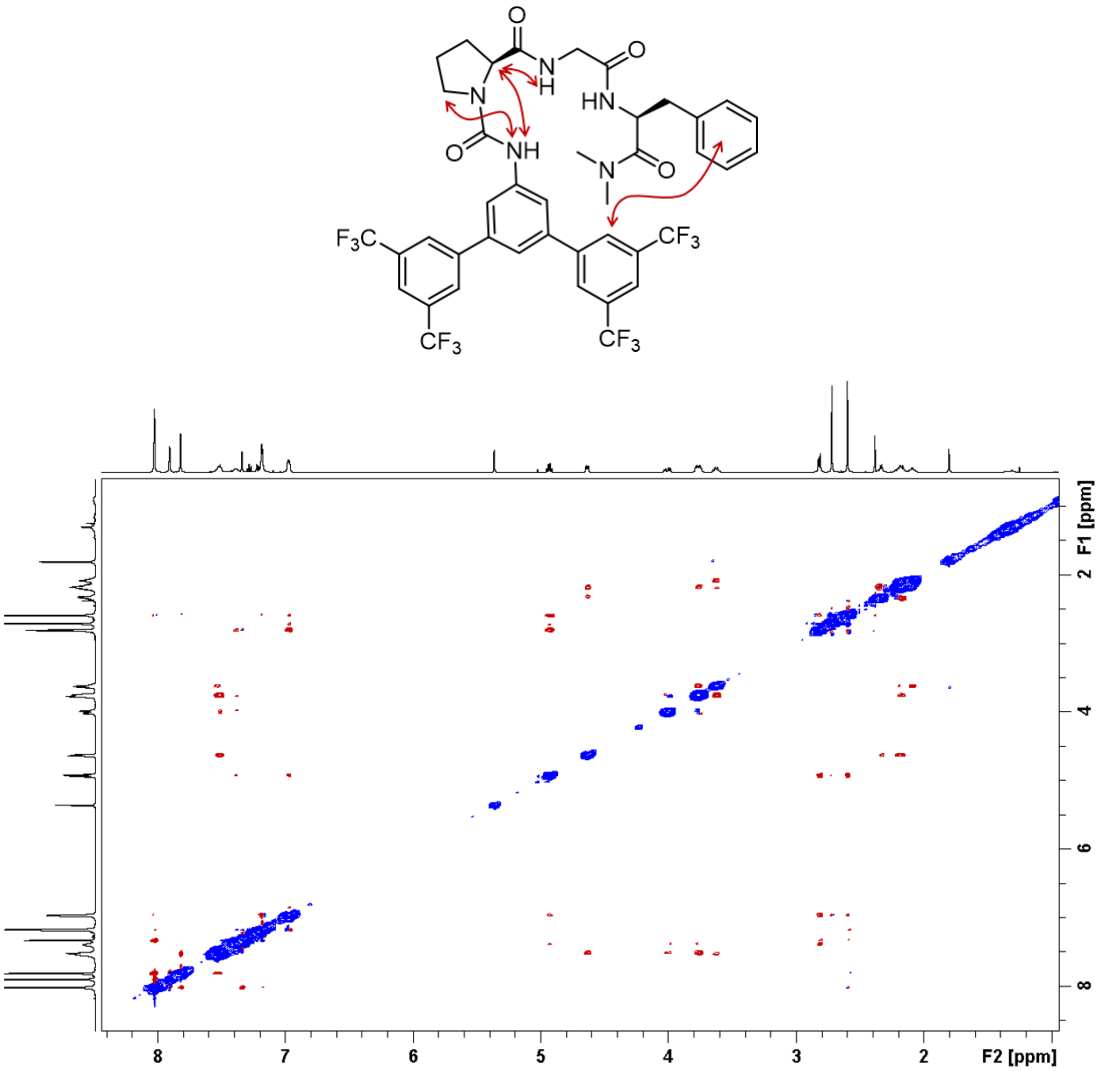

Figure 5.5.4. $^{1}H-^{1}H$ NOESY NMR spectrum of **2d** (500 MHz, CD_2Cl_2, 25 mM, d_8 = 800 ms) with inter-residue correlations displayed as arrows.

3,5-$(C_6H_5)_2C_6H_3NHC(O)$-Pro-Gly-Phe-NMe_2 (2f)

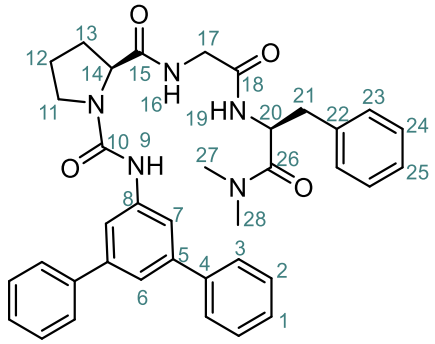

Scheme 5.5.5. Structure and numbering of **2f**.

^{1}H NMR (^{1}H-^{1}H COSY, ^{1}H-^{13}C multiplicity-edited HSQC, ^{1}H-^{1}H NOESY) (500 MHz, CD_2Cl_2): δ 7.69 (d, J_{HH} = 1.4 Hz, 2H, H^7), 7.60 (br d, J_{HH} = 7.5 Hz, 4H, H^3), 7.48 (br t, J_{HH} = 5.6 Hz, 1H, H^{16}), 7.46 (t, J_{HH} = 1.3 Hz, 1H, H^6), 7.41 (br t, J_{HH} = 7.5 Hz, 4H, H^2), 7.33 (br t, J_{HH} = 7.4 Hz, 2H, H^1), 7.26 (br d, J_{HH} = 6.8 Hz, 1H, H^{19}), 7.21–7.15 (m, 3H, H^{24}+H^{25}), 7.08 (br s, 1H, H^9), 7.01 (dd, J_{HH} = 7.7, 2.0 Hz, 2H, H^{23}), 4.96 (q, J_{HH} = 7.0 Hz, 1H, H^{20}), 4.55 (dd, J_{HH} = 7.8, 3.0 Hz, 1H, H^{14}), 3.94 (dd, J_{HH} = 16.9, 6.5 Hz, 1H, H^{17a}), 3.76 (dd, J_{HH} = 16.9, 5.7 Hz, 1H, H^{17b}), 3.66–3.61 (m, 1H, H^{11a}), 3.53 (q, J_{HH} = 8.4 Hz, 1H, H^{11b}), 2.83 (d, J_{HH} = 7.0 Hz, 2H, H^{21}), 2.73 (s, 3H, H^{27}), 2.58 (s, 3H, H^{28}), 2.32–2.27 (m, 1H, H^{12a}), 2.10–1.98 (m, 3H, H^{12b}+H^{13}) ppm.

^{13}C (^{1}H-^{13}C multiplicity-edited HSQC, ^{1}H-^{13}C HMBC) NMR (126 MHz, CD_2Cl_2): δ 172.9 (C^{15}), 170.9 (C^{26}), 168.2 (C^{18}), 155.4 (C^{10}), 142.1 (C^4), 140.8 (C^5), 139.9 (C^8), 136.5 (C^{22}), 129.4 (C^{23}), 128.7 (C^2), 128.2 (C^{24}), 127.5 (C^1), 127.1 (C^3), 126.7 (C^{25}), 120.8 (C^6), 118.0 (C^7), 60.8 (C^{14}), 50.4 (C^{20}), 47.0 (C^{11}), 42.8 (C^{17}), 38.7 (C^{21}), 36.6 (C^{28}), 35.3 (C^{27}), 29.0 (br s, C^{12}), 24.8 (C^{14}) ppm.

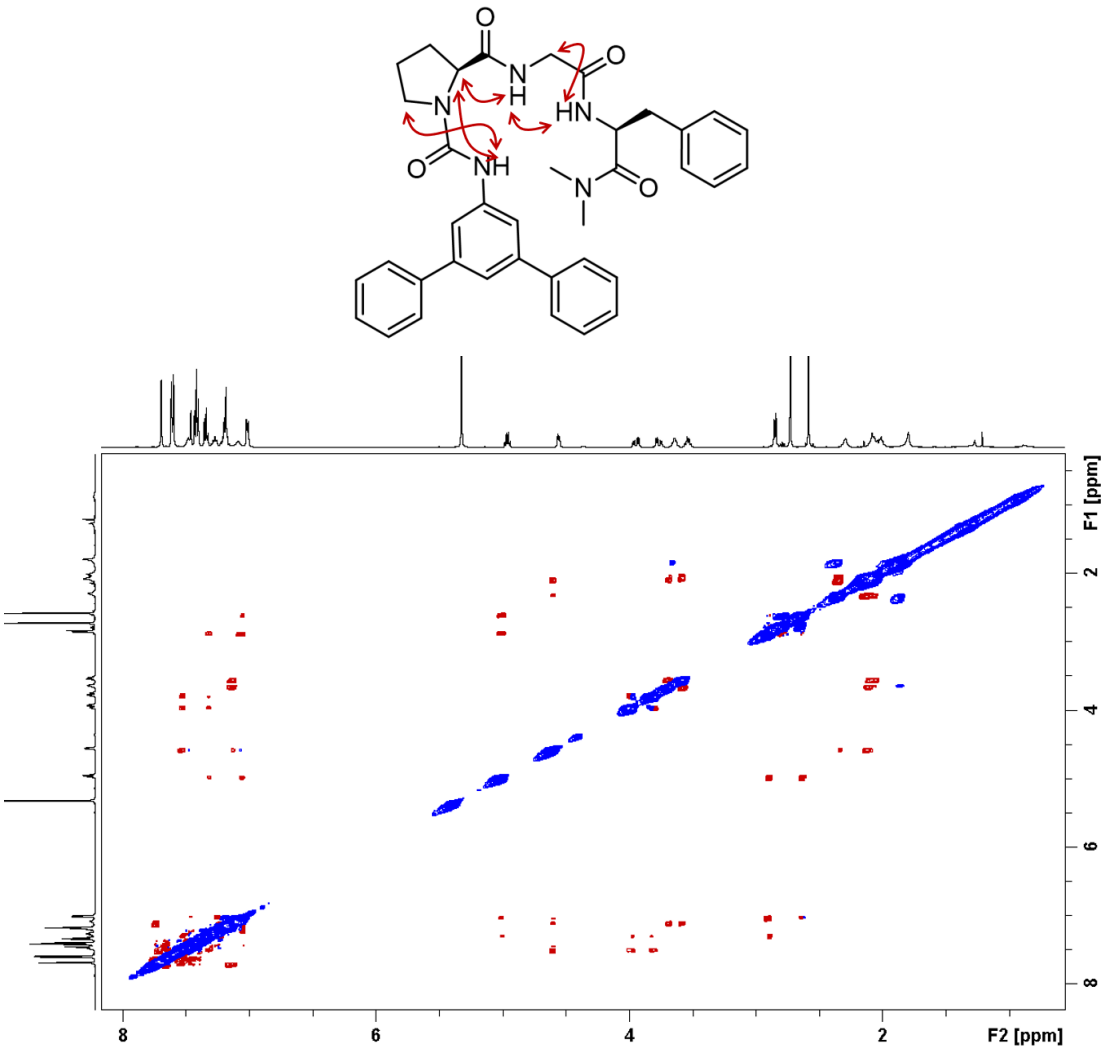

Figure 5.5.5. $^{1}H-^{1}H$ NOESY NMR spectrum of **2f** (500 MHz, CD_2Cl_2, 25 mM, d_8 = 800 ms) with inter-residue correlations displayed as arrows.

3,5-[3,5-(F)$_2$C$_6$H$_3$]$_2$C$_6$H$_3$NHC(O)-Pro-Gly-Phe-NMe$_2$ (2e)

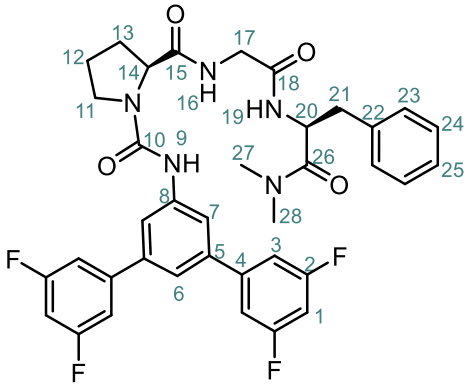

Scheme 5.5.6. Structure and numbering of **2e**.

^{1}H NMR (^{1}H-^{1}H COSY, ^{1}H-^{13}C multiplicity-edited HSQC, ^{1}H-^{1}H NOESY) (600 MHz, CD_2Cl_2): δ 7.69 (d, J_{HH} = 1.7 Hz, 2H, H^7), 7.45 (br t, J_{HH} = 6.3 Hz, 1H, H^{16}), 7.34 (br d, J_{HH} = 7.2 Hz, 1H, H^{19}), 7.30 (t, J_{HH} = 1.5 Hz, 1H, H^6), 7.25 (br s, 1H, H^9), 7.20–7.16 (m, 3H, H^{24}+H^{25}), 7.13–7.08 (m, 4H, H^4), 6.98 (dd, J = 6.5, 2.9 Hz, 2H, H^{23}), 6.80 (tt, J_{HF} = 8.9 Hz, J_{HH} = 2.2 Hz, 2H, H^1), 4.95 (q, J_{HH} = 7.5 Hz, 1H, H^{20}), 4.54 (dd, J_{HH} = 8.0, 3.6 Hz, 1H, H^{14}), 3.95 (dd, J_{HH} = 16.8, 6.5 Hz, 1H, H^{17a}), 3.76 (dd, J_{HH} = 16.8, 5.3 Hz, 1H, H^{17b}), 3.67 (ddd, J_{HH} = 8.9, 7.8, 4.2 Hz, 1H, H^{11a}), 3.60–3.55 (m, 1H, H^{11b}), 2.84 (dd, J_{HH} = 13.2, 7.7 Hz, 1H, H^{21a}), 2.80 (dd, J_{HH}= 13.2, 6.1 Hz, 1H, H^{21b}), 2.72 (s, 3H, H^{27}), 2.60 (s, 3H, H^{28}), 2.30–2.26 (m, 1H, H^{12a}), 2.17–1.99 (m, 3H, H^{12b}+H^{13}) ppm.

^{13}C (^{1}H-^{13}C multiplicity-edited HSQC, ^{1}H-^{13}C HMBC) NMR (151 MHz, CD_2Cl_2): δ 173.0 (C^{15}), 171.0 (C^{26}), 168.2 (C^{18}), 163.3 (dd, J_{CF} = 248, 13 Hz, C^2), 155.3 (C^{10}), 143.9 (t, J_{CF} = 9 Hz, C^4), 140.5, 139.9 (br s, C^5), 136.3, 129.3 (C^{23}), 128.2 (C^{24}), 126.7 (C^{25}), 120.1 (C^6), 118.9 (C^7), 110.0 (dd, J_{CF} = 21, 5 Hz, C^3), 102.7 (t, J_{CF} = 26 Hz, C^1), 60.9 (C^{14}), 50.5 (C^{20}), 47.1 (C^{11}), 42.7 (C^{17}), 38.6 (C^{21}), 36.5 (C^{28}), 35.2 (C^{27}), 29.4 (br s, C^{12}), 24.8 (C^{14}) ppm.

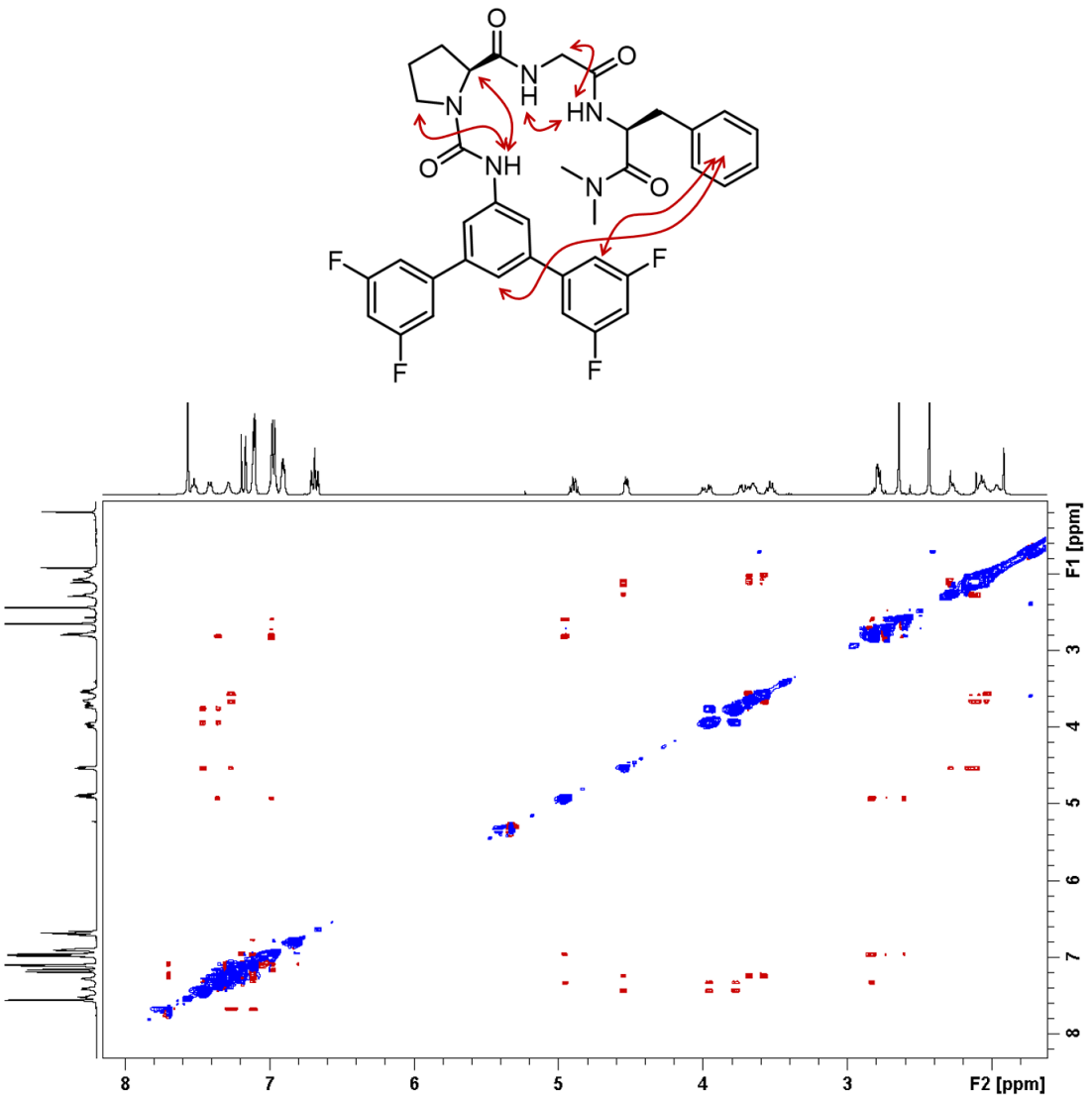

Figure 5.5.6. $^{1}H-^{1}H$ NOESY NMR spectrum of **2e** (600 MHz, CD_2Cl_2, 25 mM, d_8 = 800 ms) with inter-residue correlations displayed as arrows.

3,5-[3,5-(*t*-Bu)$_2$C$_6$H$_3$]$_2$C$_6$H$_3$NHC(O)-Pro-Gly-Phe-NMe$_2$ (2g)

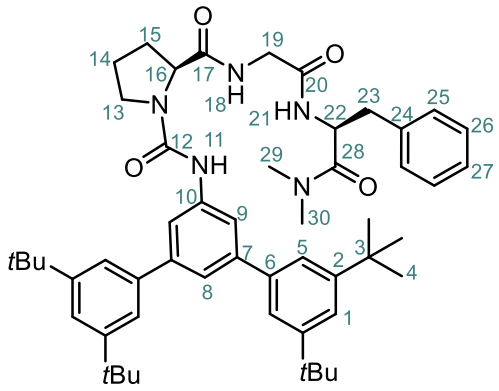

Scheme 5.5.7. Structure and numbering of **2g**.

^{1}H NMR (^{1}H-^{1}H COSY, ^{1}H-^{13}C multiplicity-edited HSQC, ^{1}H-^{1}H NOESY) (600 MHz, CD_2Cl_2): δ 7.60 (d, J_{HH} = 1.6 Hz, 2H, H^9), 7.51 (t, J_{HH} = 5.8 Hz, 1H, H^{18}), 7.46 (t, J_{HH} = 1.7 Hz, 2H, H^1), 7.44–7.43 (m, 5H, H^8+H^5), 7.21–7.15 (m, 3H, H^{26}+H^{27}), 7.04–7.03 (m, 2H, H^{25}), 6.98 (d, J_{HH} = 7.8 Hz, 1H, H^{21}), 6.83 (s, 1H, H^{11}), 4.97 (dt, J_{HH} = 7.7, 6.7 Hz, 1H, H^{22}), 4.62 (dd, J_{HH} = 8.0, 2.6 Hz, 1H, H^{16}), 3.98 (dd, J_{HH} = 16.9, 6.6 Hz, 1H, H^{19a}), 3.74 (dd, J_{HH} = 16.9, 5.5 Hz, 1H, H^{19b}), 3.66–3.62 (m, 1H, H^{13a}), 3.53–3.49 (m, 1H, H^{13b}), 2.86 (d, J_{HH} = 6.7 Hz, 2H, H^{23}), 2.62 (s, 3H, H^{30}), 2.72 (s, 3H, H^{29}), 2.39–2.37 (m, 1H, H^{14a}), 2.10–2.01 (m, 3H, H^{14b}+H^{15}), 1.37 (s, 36H, H^4) ppm.

^{13}C (^{1}H-^{13}C multiplicity-edited HSQC, ^{1}H-^{13}C HMBC) NMR (151 MHz, CD_2Cl_2): δ 172.6 (C^{17}), 170.5 (C^{28}), 168.0 (C^{20}), 155.5 (C^{12}), 151.3 (C^2), 143.6 (C^6), 140.5 (C^7), 139.5 (C^{10}), 136.4 (C^{24}), 129.4 (C^{25}), 128.2 (C^{26}), 126.7 (C^{27}), 121.9 (br s, C^8), 121.7 (C^5), 121.7 (C^1), 118.1 (C^9), 60.4 (C^{16}), 50.3 (C^{22}), 46.9 (C^{13}), 42.9 (C^{19}), 38.8 (C^{23}), 36.5 (C^{29}), 35.2 (C^{30}), 34.9 (C^3), 31.3 (C^4), 28.3 (br s, C^{14}), 25.0 (C^{15}) ppm.

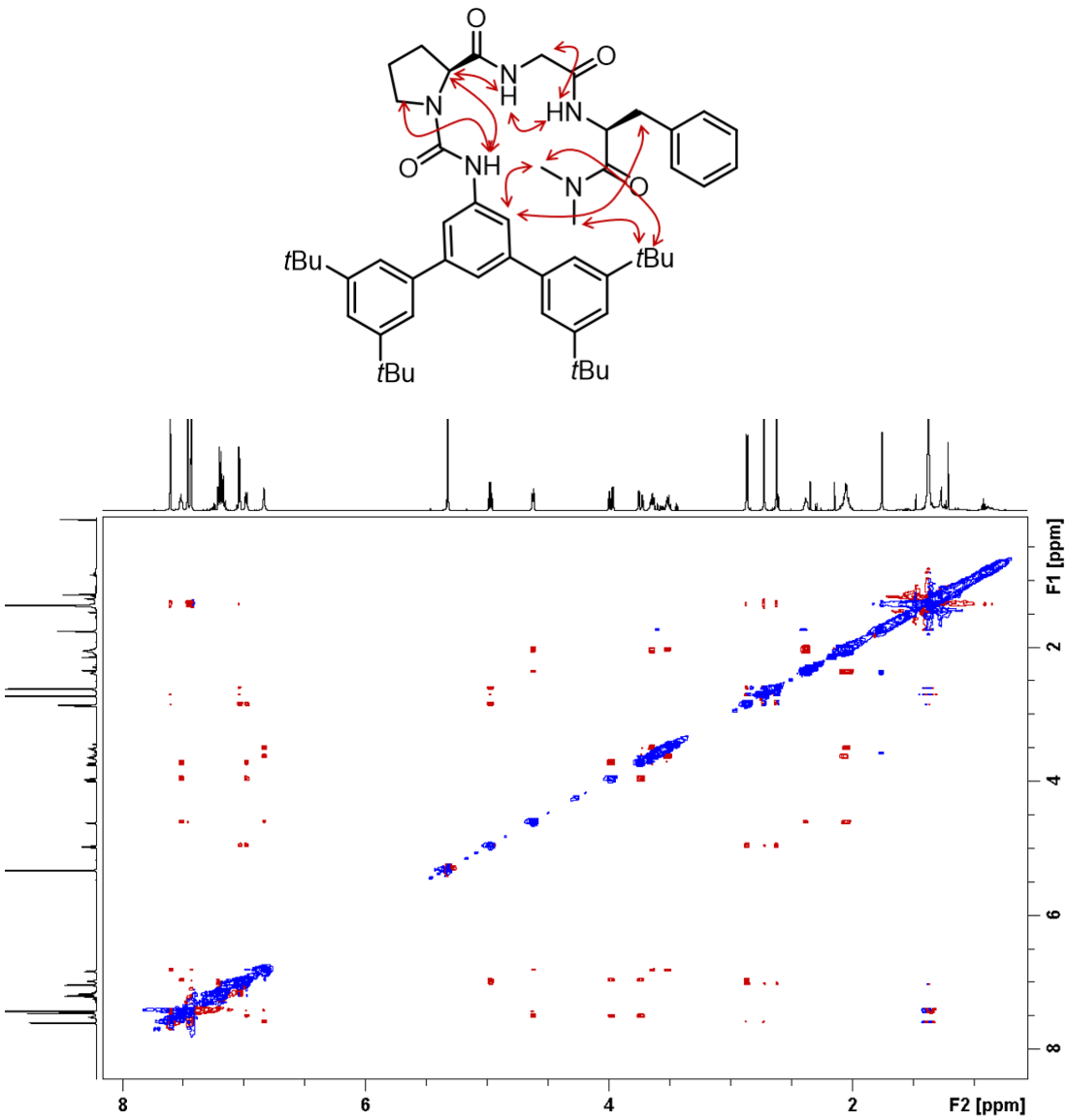

Figure 5.5.7. $^{1}H-^{1}H$ NOESY NMR spectrum of **2g** (600 MHz, CD_2Cl_2, 25 mM, d_8 = 800 ms) with inter-residue correlations displayed as arrows.

3,5-[3,5-$(CF_3)_2C_6H_3]_2C_6H_3NHC(O)$-Flp-Gly-Phe-$NMe_2$ (2h)

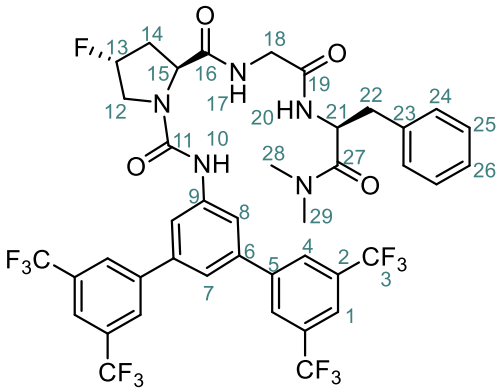

Scheme 5.5.8. Structure and numbering of **2h**.

^{1}H NMR (^{1}H-^{1}H COSY, ^{1}H-^{13}C multiplicity-edited HSQC, ^{1}H-^{1}H NOESY) (500 MHz, CD_2Cl_2): δ 7.96 (s, 4H, H^4), 7.91 (br t, J_{HH} = 6.1 Hz, 1H, H^{17}), 7.85 (s, 2H, H^1), 7.82 (br s, 1H, H^{10}), 7.68 (d, J_{HH} = 1.0 Hz, 1H, H^8), 7.48 (d, J_{HH} = 6.1 Hz, 1H, H^{20}), 7.21 (br s, 1H, H^7), 7.10–7.04 (m, 3H, H^{25}+H^{26}), 6.79 (d, J_{HH} = 7.1 Hz, 2H, H^{24}), 5.32 (br dt, J_{HF} = 52.9 Hz, J_{HH} = 2.2 Hz, 1H, H^{13}), 4.80–4.76 (m, 2H, H^{15}+H^{21}), 4.09 (dd, J_{HH} = 17.3, 6.8 Hz, 1H, H^{18a}), 3.99 (dd, J_{HF} = 22.1 Hz, J_{HH} = 11.6 Hz, 1H, H^{12a}), 3.90 (br ddd, J_{HF} = 36.2 Hz, J_{HH} = 11.6, 2.2 Hz, 1H, H^{12b}), 3.60 (dd, J_{HH} = 17.3, 5.0 Hz, 1H, H^{18b}), 2.71 (dd, J_{HH} = 13.4, 5.9 Hz, 1H, H^{22a}), 2.66 (dd, J_{HH} = 13.4, 8.6 Hz, 1H, H^{22b}), 2.61 (s, 3H, H^{28}), 2.46 (s, 3H, H^{29}), 2.61–2.46 (m, 2H, H^{14}) ppm.

^{13}C (^{1}H-^{13}C multiplicity-edited HSQC, ^{1}H-^{13}C HMBC) NMR (126 MHz, CD_2Cl_2): δ 172.8 (C^{16}), 171.2 (C^{27}), 168.1 (C^{19}), 155.2 (C^{11}), 142.4 (C^5), 140.7 (C^6), 139.4 (C^9), 136.1 (C^{23}), 131.9 (q, J_{CF} = 33 Hz, C^3), 129.1 (C^{24}), 128.0 (C^{25}), 127.3 (br s, C^4), 126.8 (C^{26}), 123.4 (q, J_{CF} = 273 Hz, C^2), 121.3 (br s, C^1), 120.5 (C^8), 119.9 (C^7), 92.4 (d, J_{CF} = 178 Hz, C^{13}), 59.1 (C^{15}), 53.7 (C^{12}), 50.9 (C^{21}), 43.1 (C^{18}), 38.3 (C^{22}), 36.4 (br s, C^{14}), 35.7 (C^{29}), 35.2 (C^{28}) ppm.

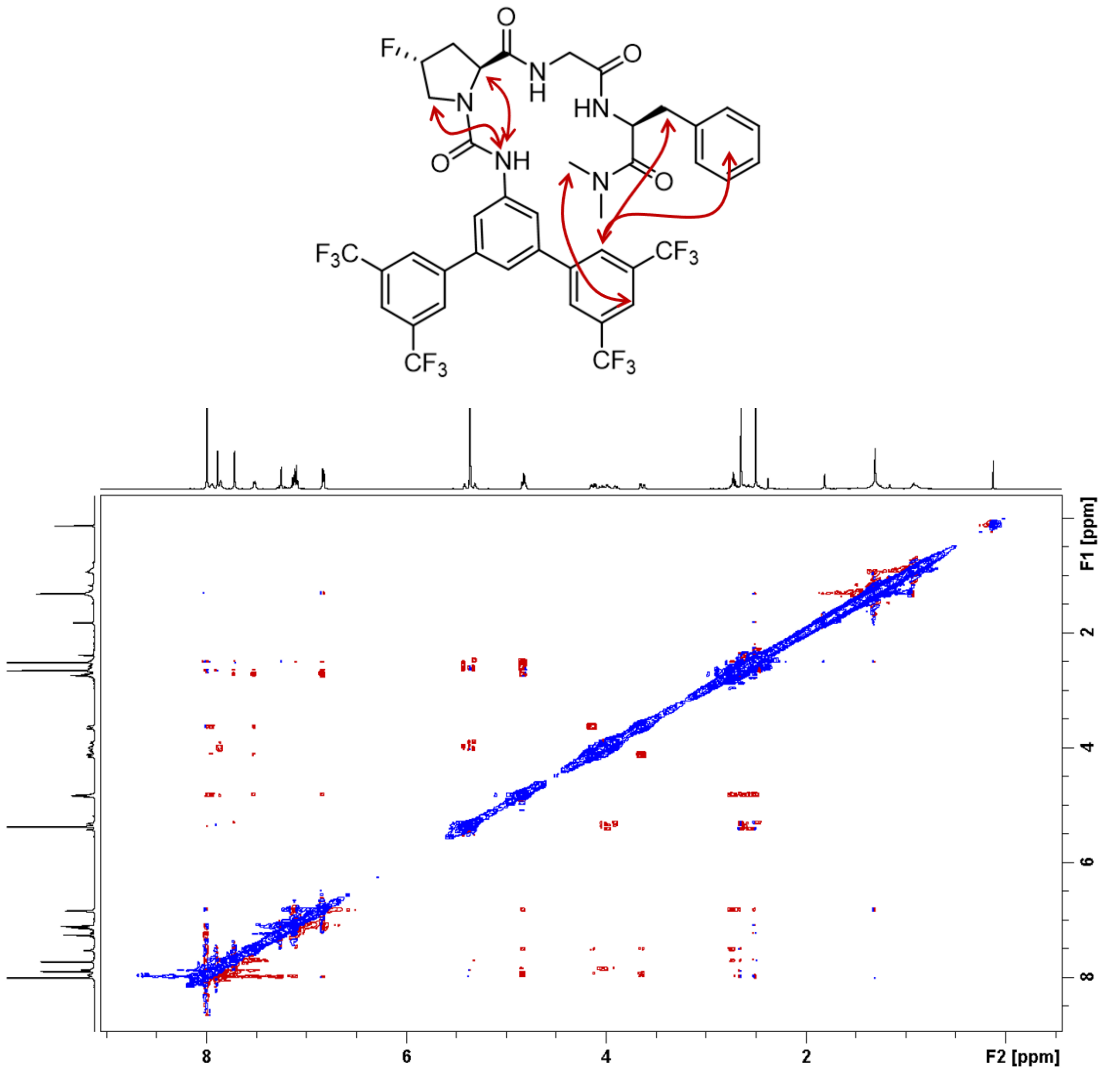

Figure 5.5.8. $^{1}H-^{1}H$ ROESY NMR spectrum of **2h** (600 MHz, CD_2Cl_2, 25 mM) with inter-residue correlations displayed as arrows.

Note: the NOESY has resulted in zero NOE intensity, hence ROESY was acquired instead.

3,5-[3,5-$(CF_3)_2C_6H_3]_2C_6H_3NHC(O)$-flp-Gly-Phe-$NMe_2$ (2i)

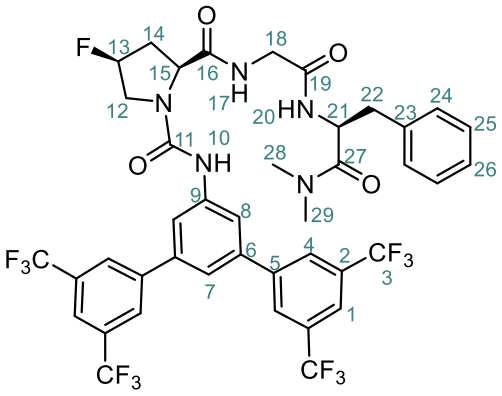

Scheme 5.5.9. Structure and numbering of **2i**.

^{1}H (^{1}H-^{1}H COSY, ^{1}H-^{13}C multiplicity-edited HSQC, ^{1}H-^{1}H NOESY) NMR (500 MHz, CD_2Cl_2): δ 8.05 (s, 4H, H^4), 8.03 (s, 1H, H^{10}), 7.92 (s, 2H, H^1), 7.72 (d, J_{HH} = 1.5 Hz, 2H, H^8), 7.46 (t, J_{HH} = 5.5 Hz, 1H, H^{17}), 7.41 (t, J_{HH} = 1.5 Hz, 1H, H^7), 7.27 (d, J_{HH} = 7.9 Hz, 1H, H^{20}), 7.24–7.20 (m, 3H, H^{25}+H^{26}), 7.07–7.05 (m, 2H, H^{24}), 5.42 (dt, J_{HF} = 51.8 Hz, J_{HH} = 3.2 Hz, 1H, H^{13}), 4.99 (q, J_{HH} = 7.6 Hz, 1H, H^{21}), 4.77 (d, J_{HH} = 10.0 Hz, 1H, H^{15}), 4.06 (br dd, J_{HF} = 23.1 Hz, J_{HH} = 12.4 Hz, 1H, H^{12a}), 3.98–3.86 (m, 3H, H^{12b}+H^{18}), 2.91 (dd, J_{HH} = 13.4, 7.6 Hz, 1H, H^{22a}), 2.83 (dd, J_{HH} = 13.4, 6.4 Hz, 1H, H^{22b}), 2.77 (br t, J_{HF} = 16.0 Hz, J_{HH} = 16.0 Hz, 1H, H^{14a}), 2.75 (s, 3H, H^{28}), 2.60 (s, 3H, H^{29}), 2.53 (dddd, J_{HF} = 42.9 Hz, J_{HH} = 14.8, 10.3, 3.7 Hz, 1H, H^{14b}) ppm.

^{13}C (^{1}H-^{13}C multiplicity-edited HSQC, ^{1}H-^{13}C HMBC) NMR (126 MHz, CD_2Cl_2): δ 172.2 (C^{16}), 170.9 (C^{27}), 167.9 (C^{19}), 155.4 (C^{11}), 142.5 (C^5), 140.9 (C^6), 139.6 (C^9), 136.1 (C^{23}), 132.0 (q, J_{CF} = 33 Hz, C^3), 129.3 (C^{24}), 128.2 (C^{25}), 127.3 (br s, C^4), 127.9 (C^{26}), 123.4 (q, J_{CF} = 273 Hz, C^2), 121.4 (br s, C^1), 120.5 (C^8), 119.5 (C^7), 92.4 (d, J_{CF} = 118 Hz, C^{13}), 60.2 (C^{15}), 54.1 (C^{12}, *overlapping with solvent peak*), 50.4 (C^{21}), 42.6 (C^{18}), 38.7 (C^{22}), 36.6 (br, C^{14}), 36.5 (C^{29}), 35.2 (C^{28}) ppm.

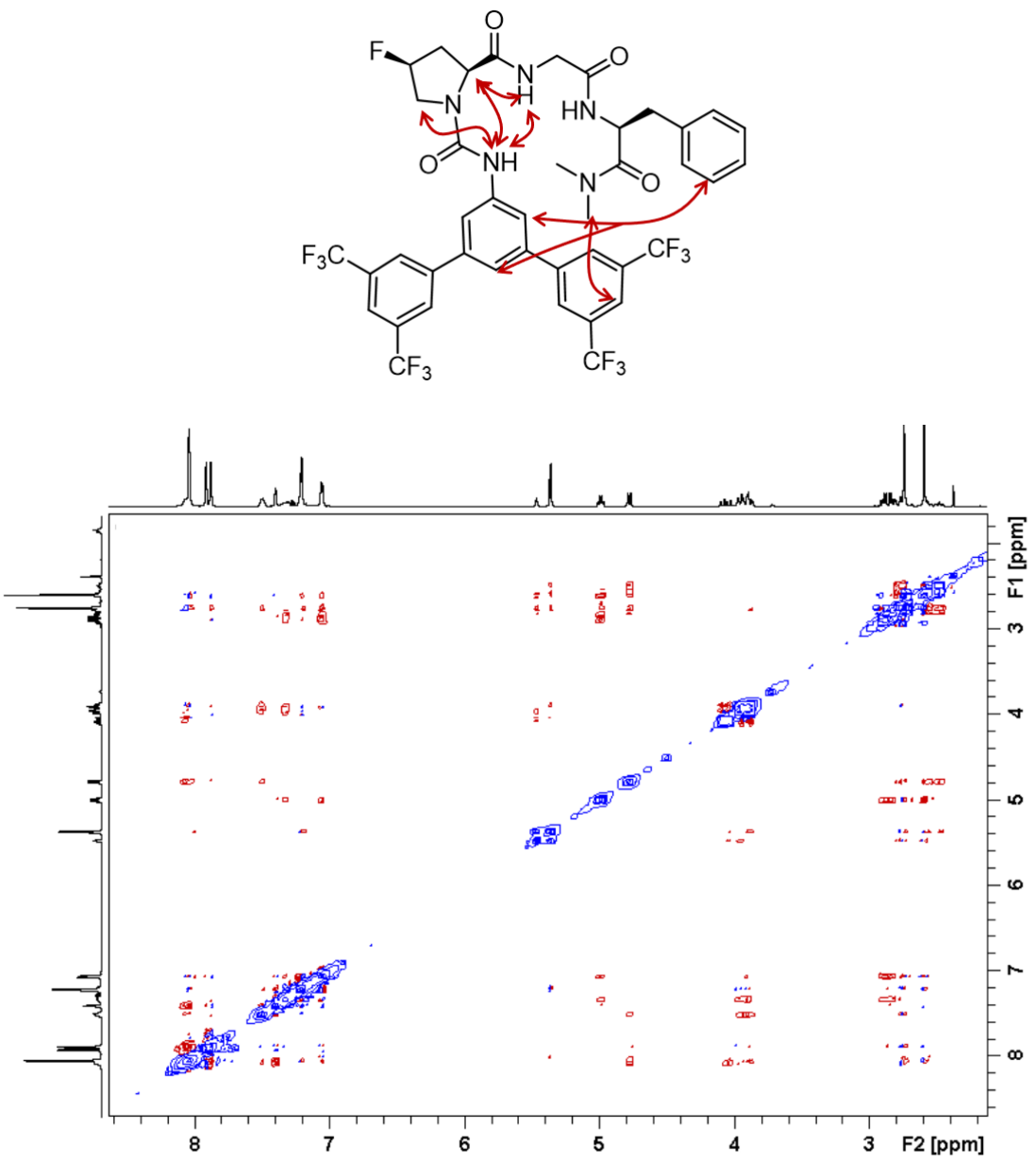

Figure 5.5.9. $^{1}H-^{1}H$ NOESY NMR spectrum of **2i** (500 MHz, CD_2Cl_2, 25 mM, d_8 = 800 ms) with inter-residue correlations displayed as arrows.

3,5-[3,5-$(CF_3)_2C_6H_3]_2C_6H_3NHC(O)$-Pro[4,4-$F_2$]-Gly-Phe-$NMe_2$ (2j)

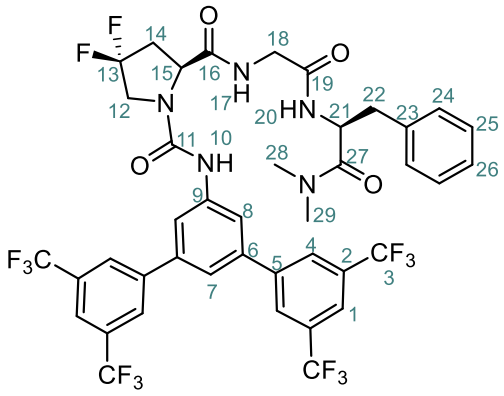

Scheme 5.5.10. Structure and numbering of **2j**.

^{1}H (^{1}H-^{1}H COSY, ^{1}H-^{13}C multiplicity-edited HSQC, ^{1}H-^{1}H NOESY) NMR (500 MHz, CD_2Cl_2): δ 7.96 (s, 4H, H^4), 7.93 (br s, 1H, H^{10}), 7.86 (br s, 2H, H^1), 7.75 (br t, J_{HH} = 4.9 Hz, 1H, H^{17}), 7.70 (d, J_{HH} = 1.1, 2H, H^8), 7.33 (d, J_{HH} = 7.10 Hz, 1H, H^{20}), 7.26 (br t, J_{HH} = 1.3 Hz, 1H, H^7), 7.14–7.09 (m, 3H, H^{26}+H^{25}), 6.88–6.86 (m, 2H, H^{24}), 4.88–4.83 (m, 2H, H^{21}+H^{15}), 4.09–4.05 (m, 2H, H^{12}), 4.03 (dd, J_{HH} = 16.7, 6.5 Hz, 1H, H^{18a}), 3.69 (dd, J_{HH} = 16.7, 5.6 Hz, 1H, H^{18b}), 2.87–2.69 (m, 4H, H^{22}+H^{14}), 2.66 (s, 3H, H^{28}), 2.50 (s, 3H, H^{29}) ppm.

^{13}C (^{1}H-^{13}C multiplicity-edited HSQC, ^{1}H-^{13}C HMBC) NMR (126 MHz, CD_2Cl_2): δ 171.8 (C^{16}), 171.5 (C^{27}), 168.3 (C^{19}), 155.6 (C^{11}), 142.7 (C^6), 140.9 (C^9), 139.9 (C^5), 136.3 (C^{23}), 132.3 (q, J_{CF} = 33 Hz, C^3), 129.6 (C^{24}), 128.6 (C^{25}), 127.7 (br s, C^4), 127.3 (C^{26}), 126.9 (t, J_{CF} = 250 Hz, C^{13}), 123.8 (q, J_{CF} = 273 Hz, C^2), 121.8 (br s, C^1), 121.1 (C^7), 120.1 (C^8), 58.9 (C^{15}), 54.0 (C^{12}), 51.3 (C^{21}), 43.4 (C^{18}), 38.9 (C^{22}), 37.2 (t, J_{CF} = 25 Hz, C^{14}), 36.9 (C^{29}), 35.7 (C^{28}) ppm.

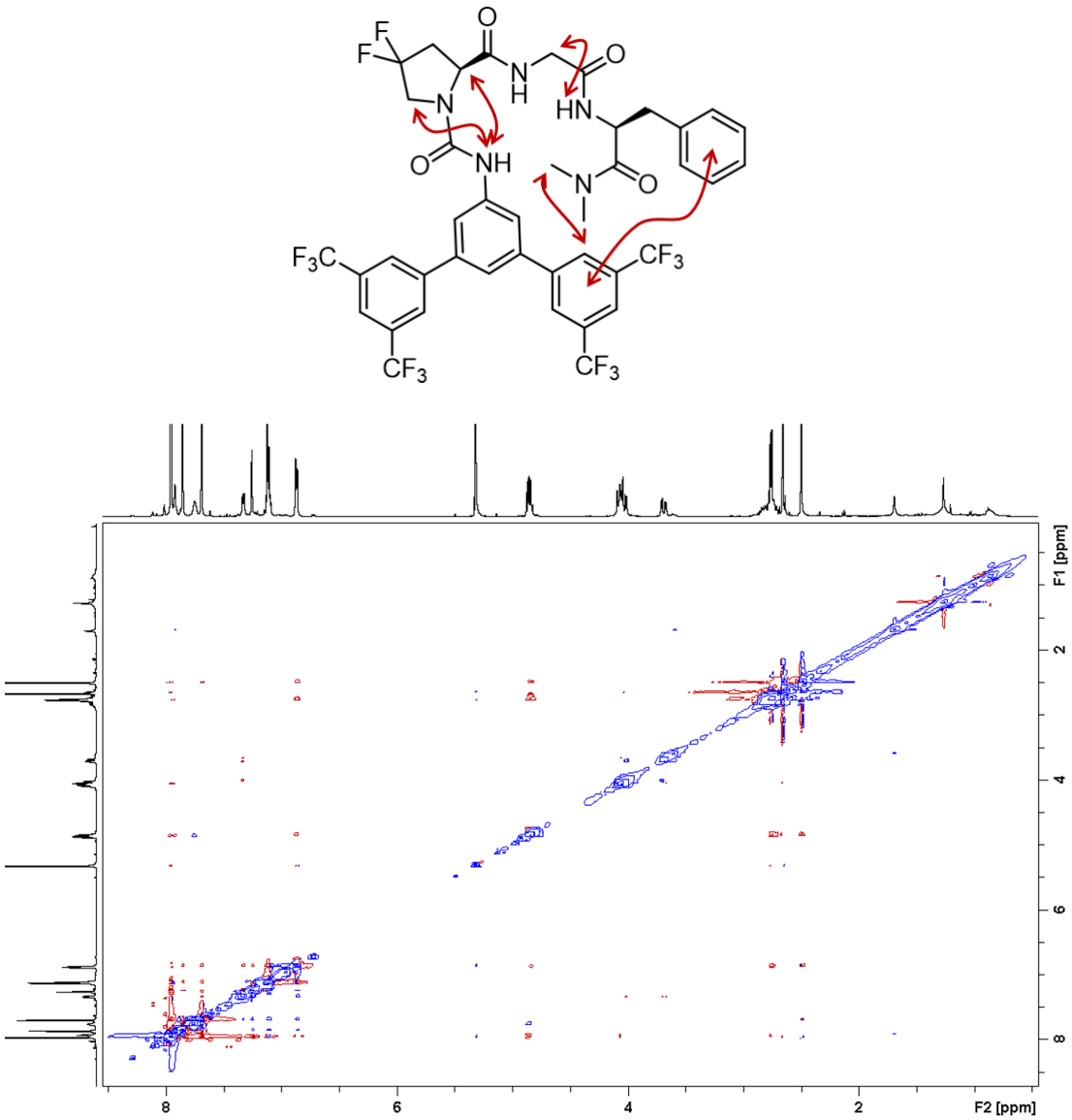

Figure 5.5.10. $^{1}H-^{1}H$ NOESY NMR spectrum of **2j** (500 MHz, CD_2Cl_2, 25 mM, d_8 = 800 ms) with inter-residue correlations displayed as arrows.

3,5-[3,5-$(CF_3)_2C_6H_3]_2C_6H_3NHC(O)$-Pro[5,5-$Me_2$]-Gly-Phe-$NMe_2$ (2k)

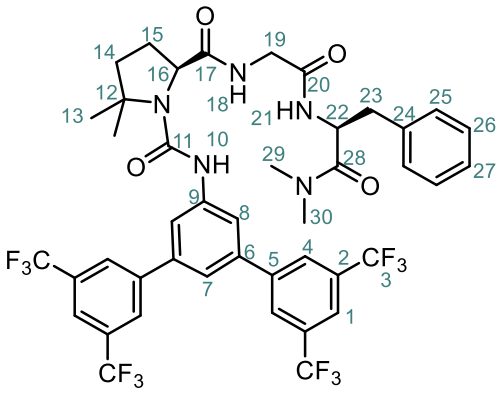

Scheme 5.5.11. Structure and numbering of **2k**.

^{1}H (^{1}H-^{1}H COSY, ^{1}H-^{13}C multiplicity-edited HSQC, ^{1}H-^{1}H NOESY) NMR (500 MHz, CD_2Cl_2): δ 8.05 (br s, 1H, H^{21}), 7.87 (s, 4H, H^4), 7.81(s, 2H, H^1), 7.65 (br s, 1H, H^{10}), 7.54 (s, 2H, H^8), 7.38 (br s, 1H, H^{18}), 7.23–7.20 (m, 4H, H^{26}+H^{27}+H^7), 7.10–7.08 (m, 2H, H^{25}), 4.93 (q, J_{HH} = 7.4 Hz, 1H, H^{22}), 4.60 (d, J_{HH} = 8.9 Hz, 1H, H^{16}), 3.88 (dd, J_{HH} = 16.9, 6.2 Hz, 1H, H^{19a}), 3.78 (dd, J_{HH} = 16.9, 6.4 Hz, 1H, H^{19b}), 2.92 (d, J_{HH} = 13.3, 7.7 Hz, 1H, H^{23a}), 2.86 (d, J_{HH} = 13.3, 7.0 Hz, 1H, H^{23b}), 2.54 (s, 6H, H^{13}), 2.39–2.31 (m, 1H, H^{15a}), 2.13 (ddt, J_{HH} = 12.7, 6.5, 1.2 Hz, 1H, H^{15b}), 2.05 (td, J_{HH} = 12.1, 6.7 Hz, 1H, H^{14a}), 1.84 (ddd, J_{HH} = 12.1, 6.5, 1.2 Hz, 1H, H^{14b}), 1.74 (s, 3H, H^{29}), 1.51 (s, 3H, H^{30}) ppm;

^{13}C (^{1}H-^{13}C multiplicity-edited HSQC, ^{1}H-^{13}C HMBC) NMR (126 MHz, CD_2Cl_2): δ 173.8 (C^{17}), 171.7 (C^{28}), 168.2 (C^{20}), 155.5 (C^{11}), 142.1 (C^6), 141.2 (C^9), 138.8 (C^5), 136.3 (C^{24}), 131.9 (q, J_{CF} = 34 Hz, C^3), 129.4 (C^{25}), 128.3 (C^{26}), 126.9 (C^{27}), 126.9 (br s, C^4), 123.3 (q, J = 272 Hz, C^2), 122.1 (br s, C^1), 121.3 (sept, J = 4 Hz, C^7), 120.4 (br s, C^8), 63.7 (C^{12}), 63.4 (C^{16}), 50.8 (C^{22}), 42.4 (C^{19}), 40.2 (C^{14}), 38.6 (C^{23}), 36.5 (C^{13a}), 35.0 (C^{13}), 28.2 (C^{29}), 27.8 (C^{15}), 24.5 (C^{30}) ppm.

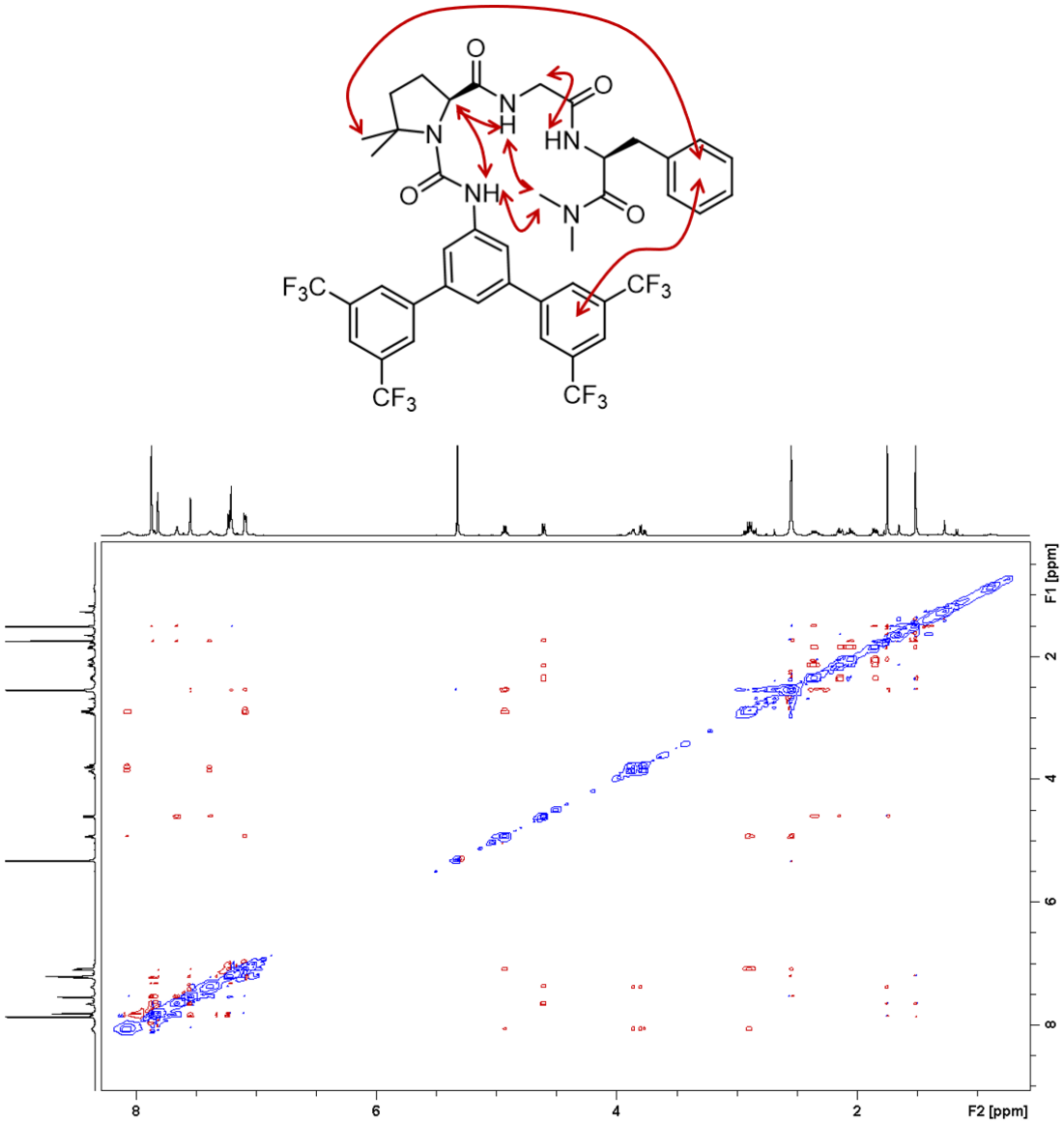

Figure 5.5.11. $^{1}H-^{1}H$ NOESY NMR spectrum of **2k** (500 MHz, CD_2Cl_2, 25 mM d_8 = 800 ms) with inter-residue correlations displayed as arrows.

3,5-[3,5-$(CF_3)_2C_6H_3]_2C_6H_3NHC(O)$-α-Me-Pro-Gly-Phe-$NMe_2$ (2l)

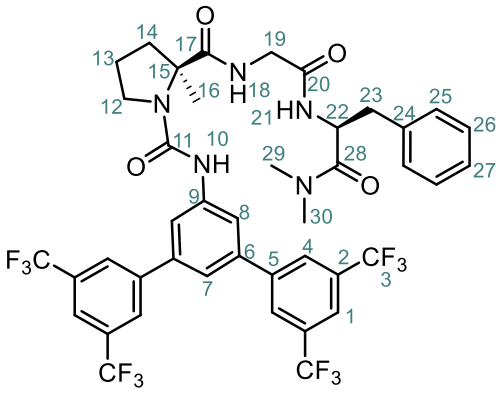

Scheme 5.5.12. Structure and numbering of **2l**.

^{1}H (^{1}H-^{1}H COSY, ^{1}H-^{13}C multiplicity-edited HSQC, ^{1}H-^{1}H NOESY) NMR (500 MHz, CD_2Cl_2): δ 8.02 (s, 4H, H^4), 7.90 (s, 2H, H^1), 7.81 (s, 2H, H^8), 7.46 (br t, J_{HH} = 5.1 Hz, H^{18}), 7.36 (d, J_{HH} = 6.7 Hz, 1H, H^{21}), 7.31 (s, 1H, H^7), 7.24 (br s, H^{10}), 7.16–7.12 (m, 3H, H^{26}+H^{27}), 6.87 (d, J_{HH} = 6.7 Hz, 2H, H^{25}), 4.84 (q, J_{HH} = 7.5 Hz, 1H, H^{22}), 3.93 (dd, J_{HH} = 17.2, 6.0 Hz, H^{19a}), 3.88–3.83 (m, 2H, H^{19a}+H^{12a}), 3.73 (q, J_{HH} = 7.1 Hz, 1H, H^{12b}), 2.74–2.64 (m, 2H, H^{23}), 2.71 (s, 3H, H^{29}), 2.56 (s, 3H, H^{30}), 2.50 (dt, J_{HH} = 12.5, 7.3, 1H, H^{14a}), 2.16–2.09 (m, 2H, H^{13}), 1.97 (dt, J_{HH} = 12.5, 6.7 Hz, 1H, H^{14b}), 1.79 (s, 3H, H^{16}) ppm.

^{13}C (^{1}H-^{13}C multiplicity-edited HSQC, ^{1}H-^{13}C HMBC) NMR (126 MHz, CD_2Cl_2): δ 175.0 (C^{17}), 170.8 (C^{28}), 168.4 (C^{20}), 154.2 (C^{11}), 142.5 (C^6), 140.8 (C^9), 139.6 (C^5), 136.4 (C^{24}), 131.8 (q, J_{CF} = 33 Hz, C^3), 129.1 (C^{25}), 128.0 (C^{26}), 127.4 (br s, C^4), 126.6 (C^{27}), 123.4 (q, J_{CF} = 273 Hz, C^2), 121.4 (br s, C^1), 120.7 (C^7), 119.6 (C^8), 67.4 (C^{15}), 50.7 (C^{22}), 47.8 (C^{12}), 43.1 (C^{19}), 39.2 (C^{14}), 38.4 (C^{23}), 36.4 (C^{30}), 35.2 (C^{29}), 23.4 (C^{13}), 21.7 (C^{16}) ppm.

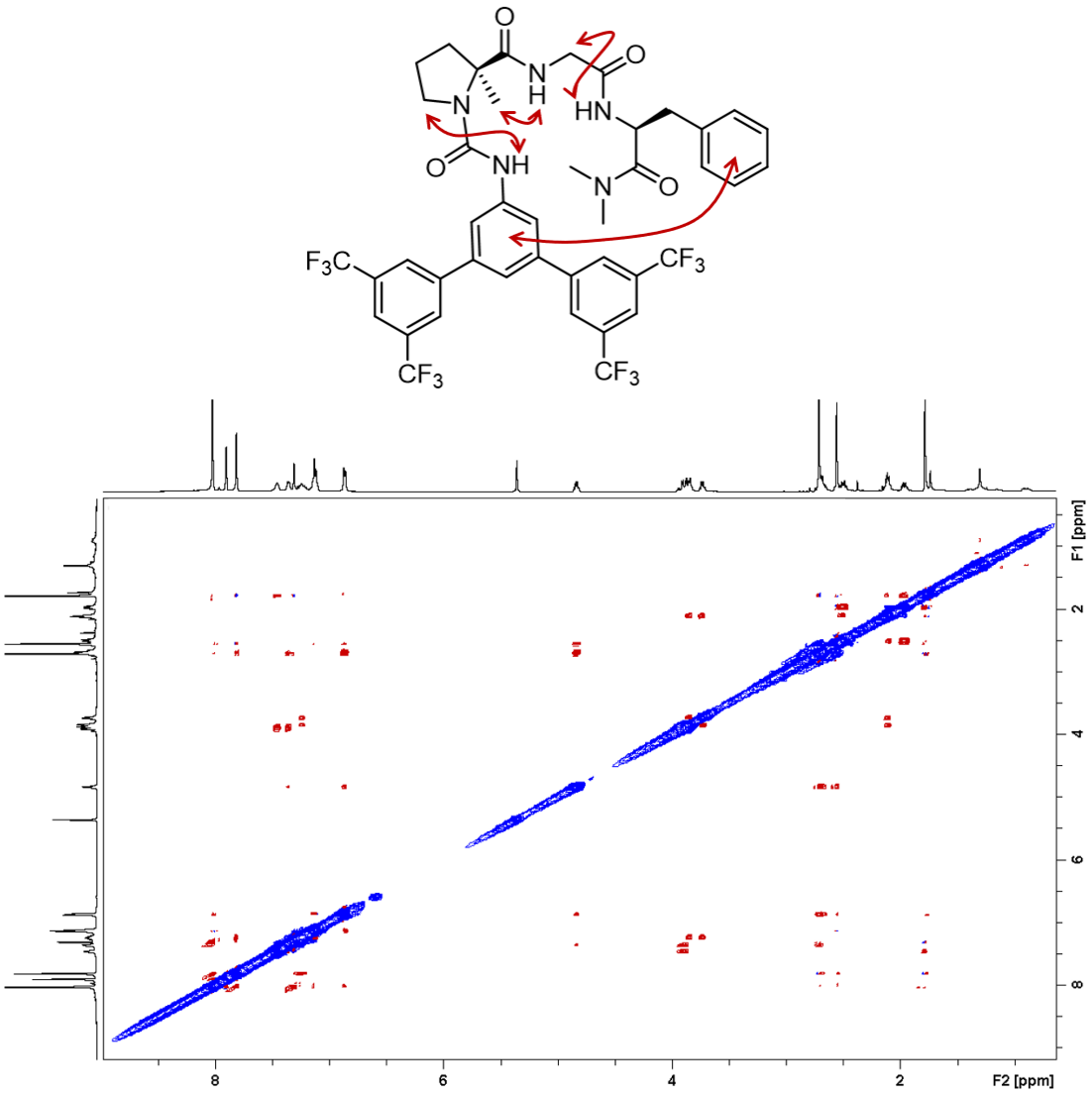

Figure 5.5.12. $^{1}H-^{1}H$ NOESY NMR spectrum of **2l** (500 MHz, CD_2Cl_2, 25 mM, d_8 = 800 ms) with inter-residue correlations displayed as arrows.

3,5-[3,5-$(CF_3)_2C_6H_3]_2C_6H_3$NHC(O)-D-Pro-Gly-Phe-NMe_2 (2m)

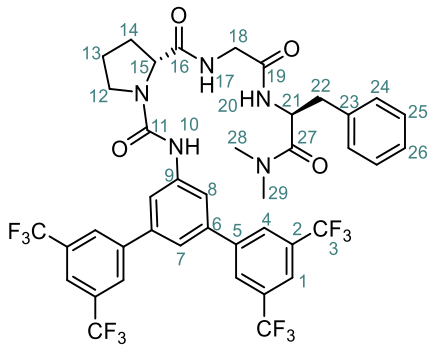

Scheme 5.5.13. Structure and numbering of **2m**.

^{1}H (^{1}H-^{1}H COSY, ^{1}H-^{13}C multiplicity-edited HSQC, ^{1}H-^{1}H NOESY) NMR (500 MHz, CD_2Cl_2): δ 8.03 (s, 4H, H^4), 7.90 (d, J_{HH} = 1.4 Hz, 2H, H^8), 7.85 (s, 2H, H^1), 7.68 (br t, J_{HH} = 4.9 Hz, 1H, H^{17}), 7.55 (s, 1H, H^{10}), 7.46 (d, J_{HH} = 6.7 Hz, 1H, H^{20}), 7.33 (t, J_{HH} = 1.4 Hz, 1H, H^7), 7.16–7.12 (m, 3H, H^{25}+H^{26}), 7.01–6.98 (m, 2H, H^{24}), 4.84 (q, J_{HH} = 7.2 Hz, 1H, H^{21}), 4.60 (t, J_{HH} = 6.2 Hz, 1H, H^{15}), 3.92–3.84 (m, 3H, H^{12a}+H^{18}), 3.64 (q, J_{HH} = 7.8 Hz, 1H, H^{12b}), 2.86 (dd, J_{HH} = 13.2, 6.1 Hz, H^{22a}), 2.75 (dd, J_{HH} = 13.2, 7.7 Hz, H^{22b}), 2.66 (s, 3H, H^{28}), 2.47 (s, 3H, H^{29}), 2.28–2.24 (m, 2H, H^{14}), 2.22–2.08 (m, 2H, H^{13}) ppm.

^{13}C (^{1}H-^{13}C multiplicity-edited HSQC, ^{1}H-^{13}C HMBC) NMR (126 MHz, CD_2Cl_2): δ 172.5 (C^{16}), 170.9 (C^{27}), 168.3 (C^{19}), 155.2, (C^{11}), 142.5 (C^6), 141.0 (C^9), 139.5 (C^5), 136.3 (C^{24}), 131.8 (q, J_{CF} = 33 Hz, C^3), 129.1 (C^{25}), 128.1 (C^{26}), 127.3 (br s, C^4), 126.7 (C^{27}), 123.4 (q, J_{CF} = 273 Hz, C^2), 121.3 (br s, C^1), 120.2 (C^7), 118.2 (C^8), 61.5 (C^{15}), 50.7 (C^{21}), 47.1 (C^{12}), 42.4 (C^{18}), 38.7 (C^{22}), 36.4 (C^{29}), 35.1 (C^{28}), 29.4 (C^{14}), 25.1 (C^{13}) ppm.

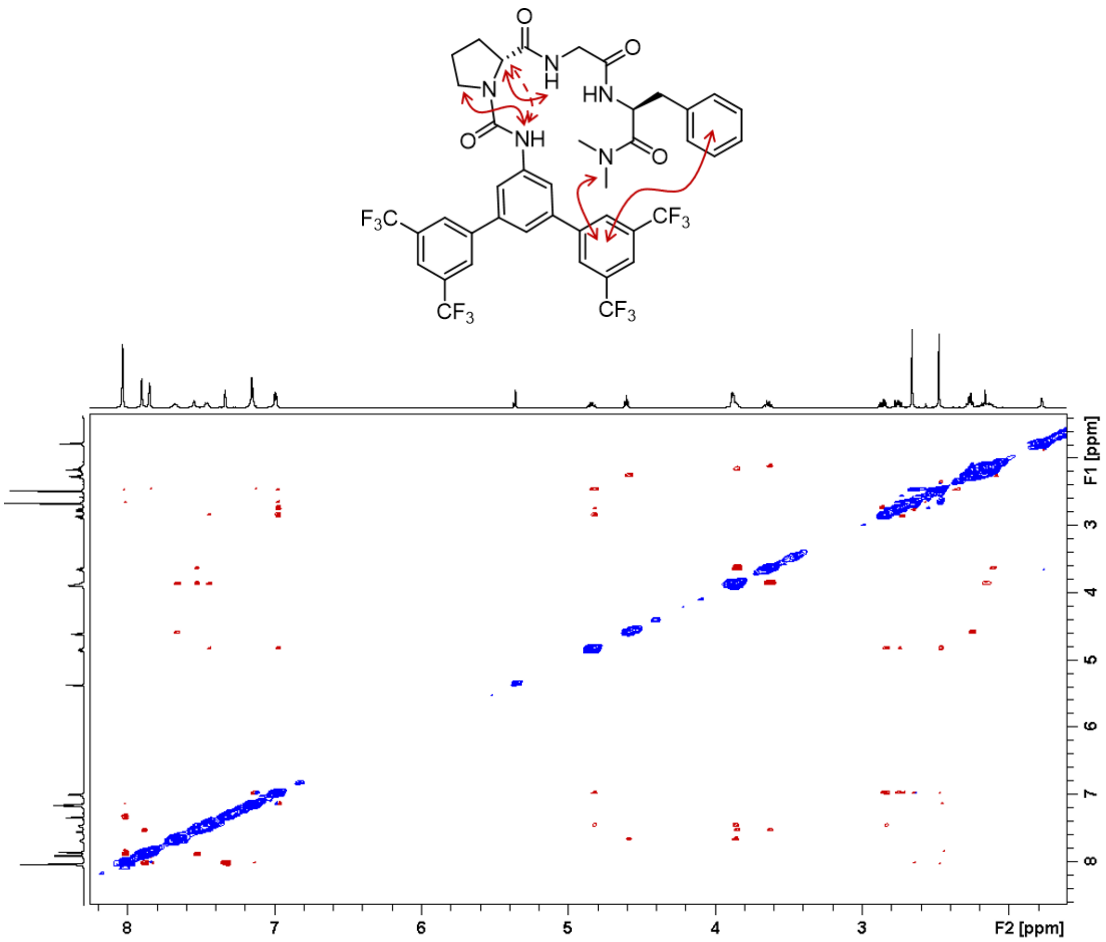

Figure 5.5.13. $^{1}H-^{1}H$ NOESY NMR spectrum of **2m** (500 MHz, CD_2Cl_2, 25 mM, d_8 = 800 ms) with inter-residue correlations displayed as arrows. Dashed arrow indicate very weak correlation.

3,5-[3,5-$(CF_3)_2C_6H_3]_2C_6H_3NHC(O)$-Pro-Acbc-Phe-$NMe_2$ (2n)

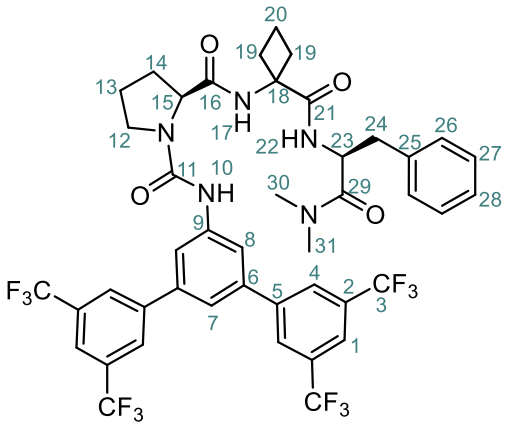

Scheme 5.5.14. Structure and numbering of **2n**.

Note: Concentrated solution in CD_2Cl_2 were characterised instead of 25 mM, due to very poor solubility. Solubility was measured to be ~1.9 mM by ^{19}F qNMR using 4-fluoroanisole as internal standard (for NMR method see Section 5.5.2).

^1H NMR (^1H-^1H COSY, ^1H-^{13}C multiplicity-edited HSQC, ^1H-^1H NOESY) (600 MHz, CD_2Cl_2): δ 8.05 (s, 4H, H^4), 7.91 (s, 2H, H^1), 7.81 (s, 2H, H^8), 7.40 (t, J_{HH} = 1.2 Hz, H^7), 7.39 (br s, 1H, H^{17}), 7.25 (br s, 1H, H^{10}), 7.14–7.12 (m, 3H, H^{27}+H^{28}), 7.11 (d, J_{HH} = 4.9 Hz, 1H, H^{22}), 6.94–6.92 (m, 2H, H^{26}), 4.86 (td, J_{HH} = 7.7, 6.1 Hz, 1H, H^{23}), 4.56 (br dd, J_{HH} = 7.1, 2.6 Hz, 1H, H^{15}), 3.75 (td, J_{HH} = 8.9, 4.1 Hz, 1H, H^{12a}), 3.59−3.54 (m, 1H, H^{12b}), 2.75 (dd, J_{HH} = 13.1, 5.6 Hz, 1H, H^{24a}), 2.69 (dd, J_{HH} = 13.1, 7.7 Hz, 1H, H^{24b}), 2.69 (s, 3H, H^{30}), 2.53 (s, 3H, H^{31}), 2.53–2.49 (m, 1H, H^{14a}), 2.35–2.33 (m, 1H, H^{14b}), 2.21–2.14 (m, 2H, H^{13}), 2.12–2.00 (m, 4H, H^{19}), 1.99–1.92 (m, 2H, H^{20}) ppm.

^{13}C (^1H-^{13}C multiplicity-edited HSQC, ^1H-^{13}C HMBC) NMR (151 MHz, CD_2Cl_2): δ 172.7 (C^{16}), 172.2 (C^{29}), 171.6 (C^{21}), 155.7 (C^{11}), 143.0 (C^5), 141.2 (C^9), 140.2 (C^6), 136.9 (C^{25}), 132.1 (q, J_{CF} = 33 Hz, C^2), 129.6 (C^{26}), 128.4 (C^{27}), 127.9 (br s, C^4), 127.0 (C^{28}), 123.8 (q, J_{CF} = 273 Hz, C^3), 121.8 (br, C^1), 121.1 (C^8), 119.8 (C^7), 60.8 (C^{15}), 59.7 (C^{18}), 51.0 (C^{23}), 47.4 (C^{12}), 39.4 (C^{24}), 36.9 (C^{30}), 35.5 (C^{31}), 2.1 (br s, C^{14}), 31.4 (C^{13}), 28.3 (C^{19a}), 25.0 (C^{19b}), 16.2 (C^{20}) ppm.

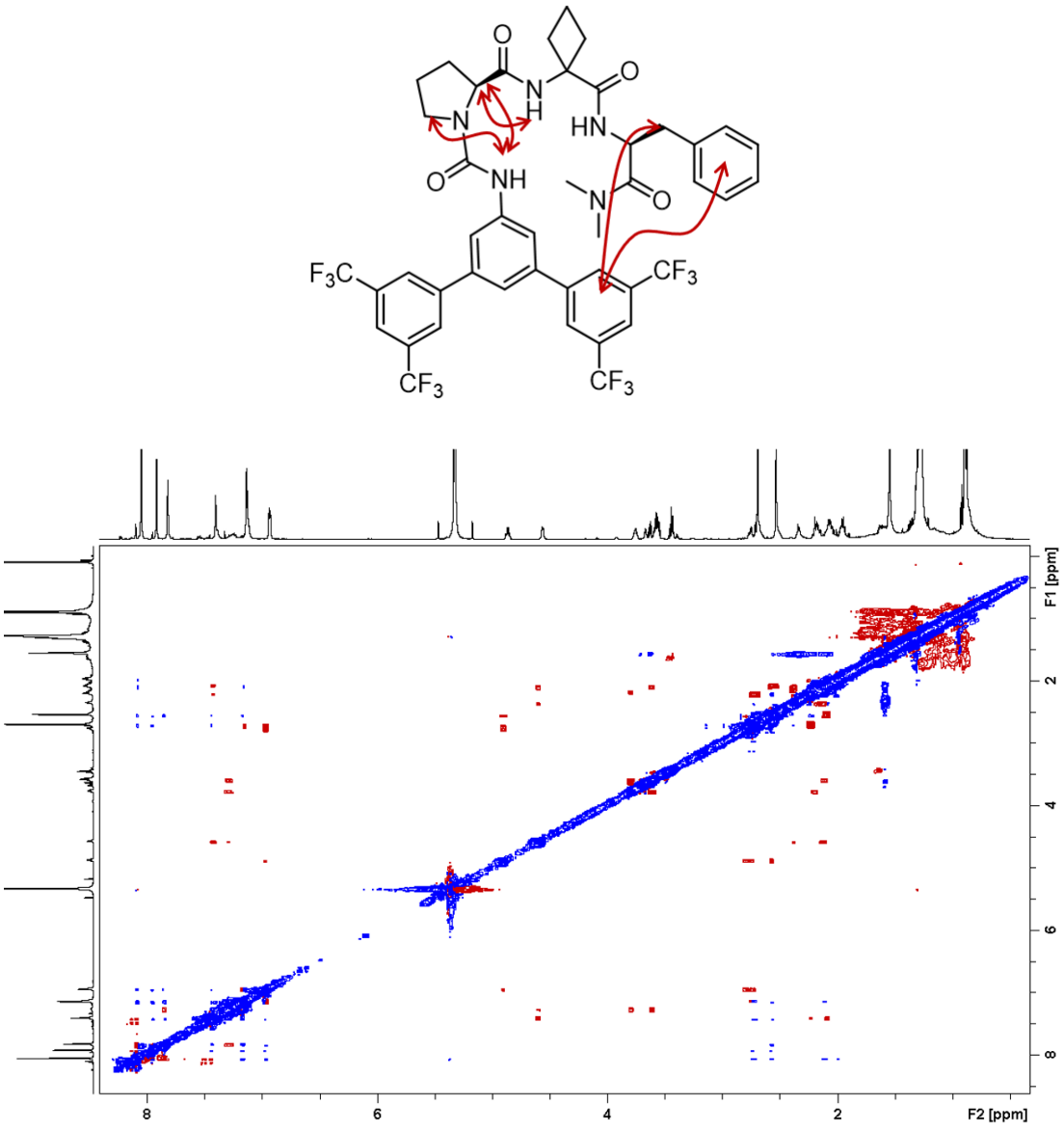

Figure 5.5.14. $^{1}H-^{1}H$ NOESY NMR spectrum of **2n** (600 MHz, CD_2Cl_2, 2 mM, d_8 = 800 ms) with inter-residue correlations displayed as arrows.

3,5-[3,5-$(CF_3)_2C_6H_3]_2C_6H_3NHC(O)$-Pro-Aib-Phe-$NMe_2$ (2o)

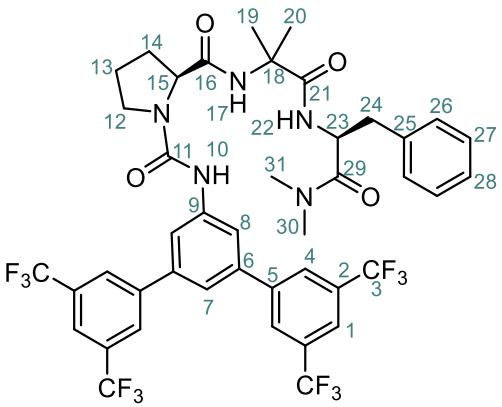

Scheme 5.5.15. Structure and numbering of **2o**.

Note: Concentrated solution in CD_2Cl_2 were characterised instead of 25 mM, due to very poor solubility. Solubility was measured to be ~5.0 mM by ^{19}F qNMR using 4-fluoroanisole as internal standard (for NMR method see Section 5.5.2).

^1H (^1H-^1H COSY, ^1H-^{13}C multiplicity-edited HSQC, ^1H-^1H NOESY) NMR (500 MHz, CD_2Cl_2): δ 8.09 (s, 4H, H^4), 7.94 (s, 2H, H^1), 7.88 (s, 2H, H^8), 7.50 (br s, 1H, H^{17}), 7.43 (br s, 1H, H^7), 7.17–7.14 (m, 4H, H^{27}+H^{28}+H^{10}), 7.03 (d, J_{HH} = 7.8 Hz, 1H, H^{22}), 7.00–6.98 (m, 2H, H^{26}), 4.91 (dt, J_{HH} = 7.8, 6.4 Hz, 1H, H^{23}), 4.53 (dd, J_{HH} = 7.4, 2.8 Hz, 1H, H^{15}), 3.79–3.76 (m, 1H, H^{12a}), 3.62 (q, J_{HH} = 7.3 Hz, 1H, H^{12b}), 2.82 (dd, J_{HH} = 13.3, 5.8 Hz, 1H, H^{24a}), 2.76 (dd, J_{HH} = 13.3, 8.5 Hz, 1H, H^{24b}), 2.76 (s, 3H, H^{31}), 2.58 (s, 3H, H^{30}), 2.33–2.31 (m, 1H, H^{14a}), 2.18–2.06 (m, 3H, H^{13a}+ H^{13b}+H^{14b}), 1.51 (s, 3H, H^{19}), 1.41(s, 3H, H^{20}) ppm.

^{13}C (^1H-^{13}C multiplicity-edited HSQC, ^1H-^{13}C HMBC) NMR (126 MHz, CD_2Cl_2): δ 173.4 (C^{16}), 171.5 (C^{29}), 171.0 (C^{21}), 155.3 (C^{11}), 142.7 (C^5), 141.1 (C^9), 139.7 (C^6), 136.5 (C^{25}), 131.9 (q, J_{CF} = 33 Hz, C^2), 129.3 (C^{26}), 128.1 (C^{27}), 127.5 (br, C^4), 126.7 (C^{28}), 123.4 (q, J_{CF} = 273 Hz, C^3), 121.4 (br, C^1), 120.4 (C^8), 119.4 (C^7), 60.8 (C^{15}), 57.0 (C^{18}), 50.6 (C^{23}), 47.1 (C^{12}), 39.1 (C^{24}), 36.5 (C^{31}), 35.1 (C^{30}), 28.5 (br s, C^{14}), 25.7 (C^{20}), 25.1 (C^{13}), 24.6 (C^{19}) ppm.

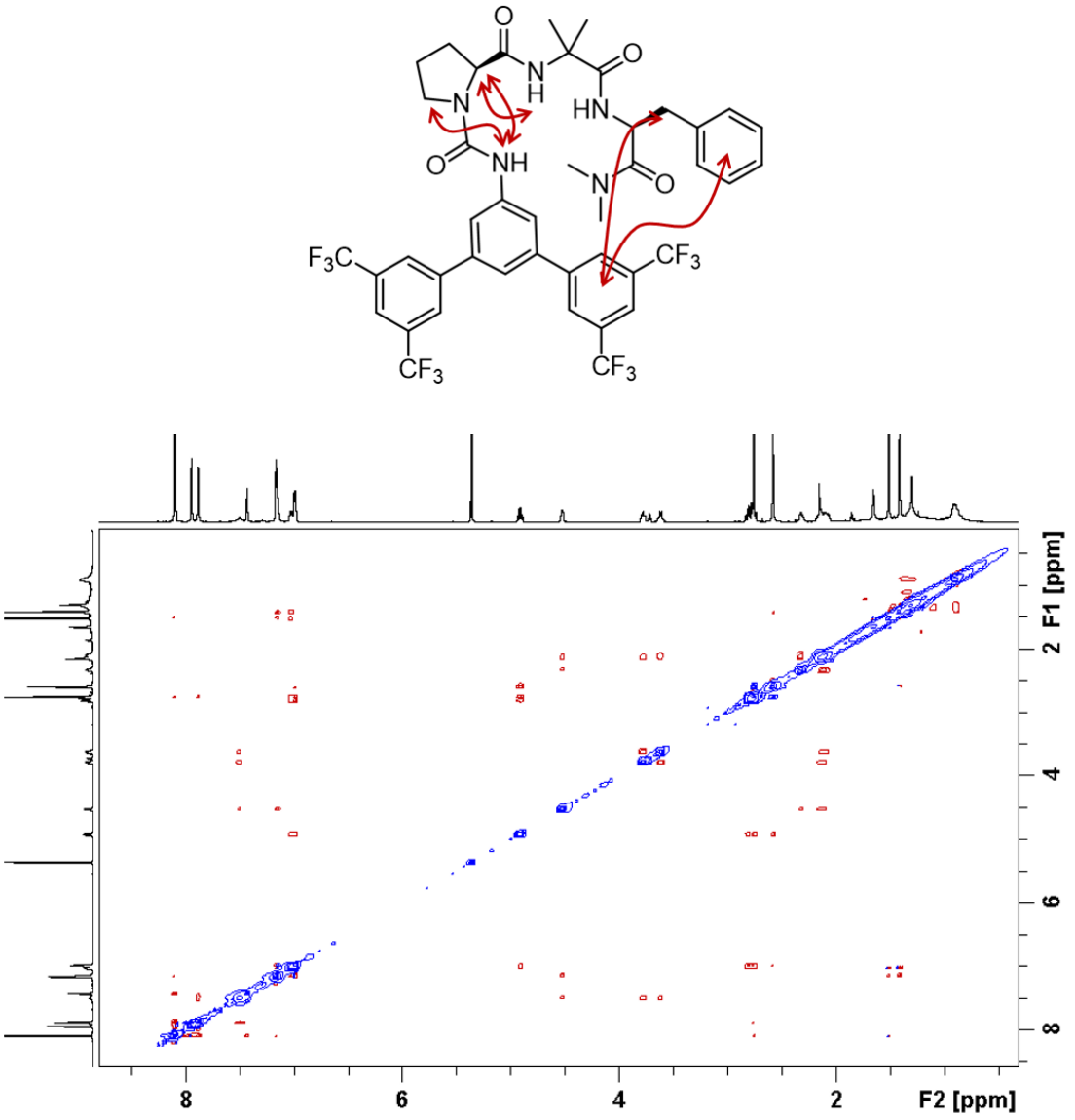

Figure 5.5.15. $^{1}H-^{1}H$ NOESY NMR spectrum of **2o** (500 MHz, CD_2Cl_2, 5 mM, d_8 = 800 ms) with inter-residue correlations displayed as arrows.

3,5-[3,5-$(CF_3)_2C_6H_3]_2C_6H_3NHC(O)$-Pro-Acpc-Phe-$NMe_2$ (2p)

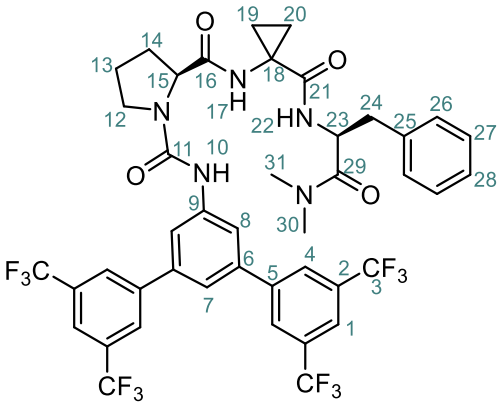

Scheme 5.5.16. Structure and numbering of **2p**.

Note: Concentrated solution in CD_2Cl_2 were characterised instead of 25 mM, due to very poor solubility. Solubility was measured to be ~1.9 mM by ^{19}F qNMR using 4-fluoroanisole as internal standard (for NMR method see Section 5.5.2).

^1H (^1H-^1H COSY, ^1H-^{13}C multiplicity-edited HSQC, ^1H-^1H NOESY) NMR (600 MHz, CD_2Cl_2): δ 8.05 (s, 4H, H^4), 7.94 (s, 2H, H^1), 7.78 (d, J_{HH} = 1.2 Hz, 2H, H^8), 7.64 (br s, 1H, H^{17}), 7.60 (d, J_{HH} = 7.4 Hz, 1H, H^{22}), 7.36 (t, J_{HH} = 1.6 Hz, 1H, H^7), 7.26 (s, 1H, H^{10}), 7.16–7.11 (m, 3H, H^{27}+H^{28}), 6.85–6.83 (m, 2H, H^{26}), 4.82 (br q, J_{HH} = 7.0 Hz, 1H, H^{23}), 4.53 (dd, J_{HH} = 7.7, 4.6 Hz, 1H, H^{15}), 3.80 (td, J_{HH} = 8.2, 5.5 Hz, 1H, H^{12a}), 3.62 (q, J_{HH} = 7.4 Hz, 1H, H^{12b}), 2.72 (dd, J_{HH} = 13.2, 5.8 Hz, 1H, H^{24a}), 2.69 (dd, J_{HH} = 13.2, 8.4 Hz, 1H, H^{24b}), 2.64 (s, 3H, H^{31}), 2.51 (s, 3H, H^{30}), 2.34–2.28 (m, 1H, H^{14a}), 2.25–2.21 (m, 1H, H^{13a}), 2.16–2.06 (m, 2H, H^{13b}+H^{14b}), 1.58 (ddd, J_{HH} = 10.0, 7.8, 4.4 Hz, 1H, H^{19a}), 1.32 (ddd, J_{HH} = 10.0, 7.8, 4.2 Hz, 1H, H^{20a}), 1.10 (ddd, J_{HH} = 9.9, 7.8, 4.5 Hz, 1H, H^{19b}), 0.96 (ddd, J_{HH} = 10.1, 7.7, 4.2 Hz, 1H, H^{20b}) ppm.

^{13}C (^1H-^{13}C multiplicity-edited HSQC, ^1H-^{13}C HMBC) NMR (151 MHz, CD_2Cl_2): δ 173.4 (C^{16}), 171.4 (C^{29}), 170.7 (C^{21}), 155.4 (C^{11}), 142.5 (C^5), 140.7 (C^9), 139.8 (C^6), 136.4 (C^{25}), 131.9 (q, J_{CF} = 33 Hz, C^2), 129.2 (C^{26}), 128.0 (C^{27}), 127.5 (br d, J_{CF} = 3 Hz, C^4), 126.6 (C^{28}), 123.4 (q, J_{CF} = 273 Hz, C^3), 121.4 (br quint, J_{CF} = 3 Hz, C^1), 120.9 (C^8), 119.9 (C^7), 60.6 (C^{15}), 51.1 (C^{23}), 46.9 (C^{12}), 38.7 (C^{24}), 36.5 (C^{30}), 35.1 (C^{31}), 34.4 (C^{18}), 28.1 (br s, C^{14}), 25.4 (C^{13}), 16.9 (C^{19}), 16.3 (C^{20}) ppm.

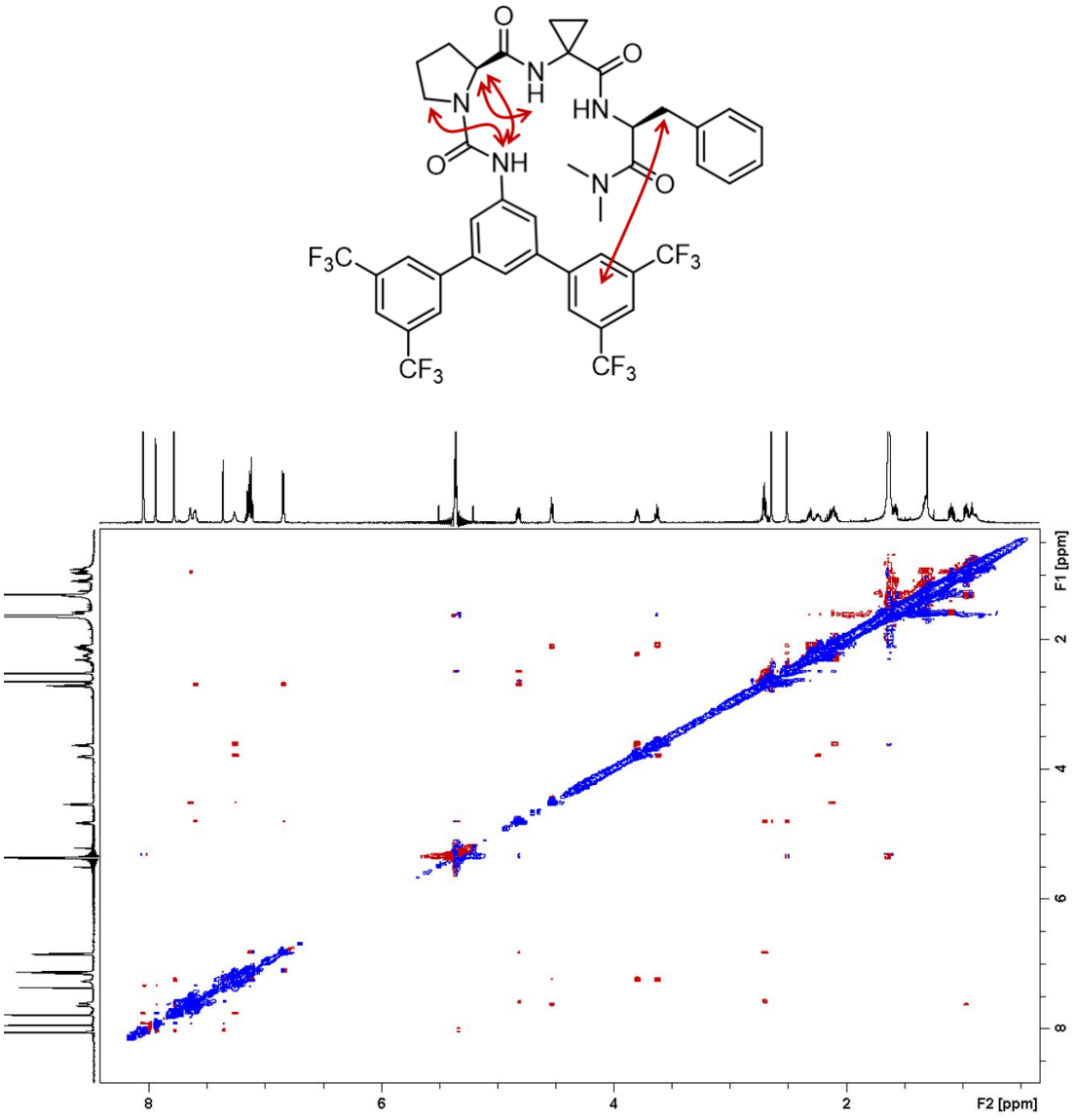

Figure 5.5.16. $^{1}H-^{1}H$ NOESY NMR spectrum of **2p** (600 MHz, CD_2Cl_2, 2 mM, d_8 = 800 ms) with inter-residue correlations displayed as arrows.

3,5-[3,5-$(CF_3)_2C_6H_3]_2C_6H_3NHC(O)$-Pro-Gly-Leu-$NMe_2$ (2q)

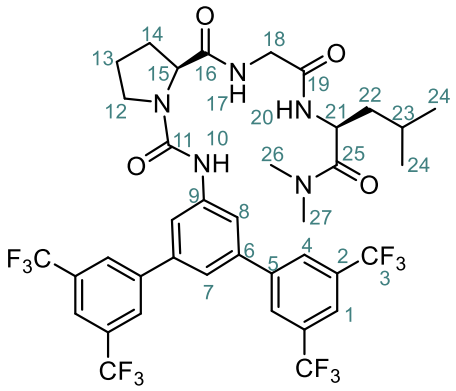

Scheme 5.5.17. Structure and numbering of **2q**.

^{1}H NMR (^{1}H-^{1}H COSY, ^{1}H-^{13}C multiplicity-edited HSQC, ^{1}H-^{1}H NOESY) (600 MHz, CD_2Cl_2): δ 8.05 (s, 4H, H^4), 7.91 (s, 2H, H^1), 7.86 (d, J_{HH} = 1.5 Hz, 2H, H^8), 7.59 (br s, H^{10}), 7.51 (t, J_{HH} = 5.9 Hz, H^{17}), 7.38 (t, J_{HH} = 1.5 Hz, 1H, H^7), 7.14 (br s, 1H, H^{20}), 4.87 (ddd, J_{HH} = 10.0, 8.5, 3.8 Hz, 1H, H^{21}), 4.64 (dd, J_{HH} = 7.6, 2.8 Hz, 1H, H^{15}), 3.97 (dd, J_{HH} = 17.1, 6.3 Hz, 1H, H^{18a}), 3.84 (dd, J_{HH} = 17.1, 5.5 Hz, 1H, H^{18b}), 3.78 (ddd, J_{HH} = 9.1, 7.5, 3.6 Hz, 1H, H^{12a}), 3.60 (q, J_{HH} = 8.6 Hz, 1H, H^{12b}), 2.95 (s, 3H, H^{26}), 2.81 (s, 3H, H^{27}), 2.38–2.33 (m, 1H, H^{14a}), 2.22–2.05 (m, 3H, H^{14b}+H^{13}), 1.57–1.50 (m, 1H, H^{23}), 1.41 (ddd, J_{HH} = 14.2, 10.0, 4.4 Hz, 1H, H^{22a}), 1.29 (ddd, J_{HH} = 14.2, 9.3, 3.8 Hz, 1H, H^{22b}), 1.29 (d, J_{HH} = 6.6 Hz, 3H, H^{24a}), 1.29 (d, J_{HH} = 6.7 Hz, 3H, H^{24b}) ppm.

^{13}C (^{1}H-^{13}C multiplicity-edited HSQC, ^{1}H-^{13}C HMBC) NMR (151 MHz, CD_2Cl_2): δ 173.1 (C^{16}), 172.5 (C^{25}), 168.6 (C^{19}), 155.6 (C^{11}), 143.0 (C^5), 141.5 (C^9), 139.8 (C^6), 132.3 (q, J_{CF} = 33 Hz, C^2), 127.7 (br s, C^4), 123.7 (q, J_{CF} = 273 Hz, C^3), 121.7 (sept, J_{CF} = 3 Hz, C^1), 120.4 (C^8), 119.5 (C^7), 61.1 (C^{15}), 47.8 (C^{21}), 47.5 (C^{12}), 43.0 (C^{18}), 42.2 (C^{22}), 37.0 (C^{27}), 35.6 (C^{26}), 29.6 (C^{14}), 25.2 (C^{13}), 24.9 (C^{23}), 23.3 (C^{24b}), 21.6 (C^{24a}) ppm.

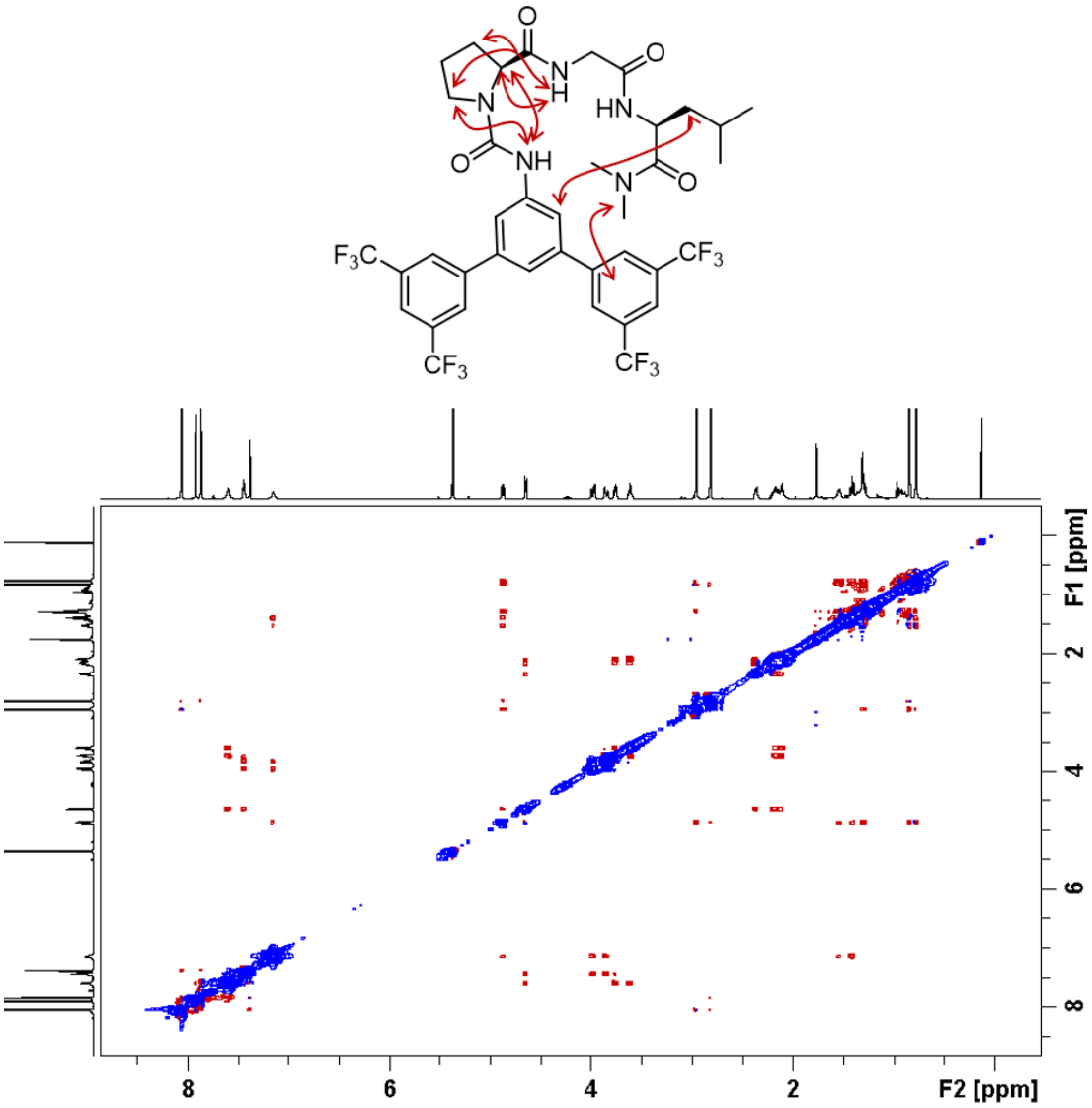

Figure 5.5.17. $^{1}H-^{1}H$ NOESY NMR spectrum of **2q** (600 MHz, CD_2Cl_2, 25 mM, d_8 = 800 ms) with inter-residue correlations displayed as arrows.

3,5-[3,5-$(CF_3)_2C_6H_3]_2C_6H_3$NHC(O)-Pro-Gly-D-Phe-NMe_2 (2r)

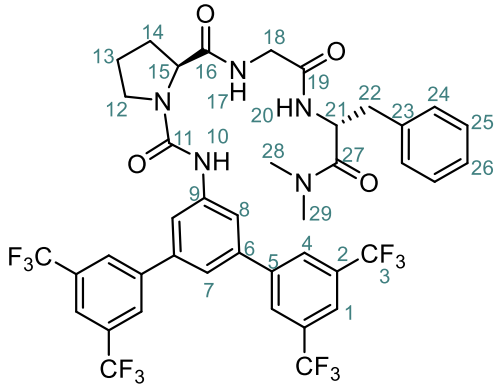

Scheme 5.5.18. Structure and numbering of **2r**.

^{1}H NMR (^{1}H-^{1}H COSY, ^{1}H-^{13}C multiplicity-edited HSQC, ^{1}H-^{1}H NOESY) (600 MHz, CD_2Cl_2): δ 8.00 (s, 4H, H^4), 7.86 (d, J_{HH} = 1.3 Hz, 2H, H^8), 7.82 (s, 2H, H^1), 7.62 (br t, J_{HH} = 5.1 Hz, H^{17}), 7.49 (s, H^{10}), 7.39 (d, J_{HH} = 6.9 Hz, 1H, H^{20}), 7.30 (t, J_{HH} = 1.3 Hz, 1H, H^7), 7.12–7.09 (m, 3H, H^{26}+H^{25}), 6.96–6.94 (m, 2H, H^{24}), 4.81 (q, J_{HH} = 7.1 Hz, 1H, H^{21}), 4.56 (dd, J_{HH} = 7.3, 4.8 Hz, 1H, H^{15}), 3.85–3.84 (m, 2H, H^{18}), 3.82 (td, J_{HH} = 8.2, 4.2 Hz, 1H, H^{12a}), 3.60 (q, J_{HH} = 7.6 Hz, 1H, H^{12b}), 2.82 (dd, J_{HH} = 13.1, 6.1 Hz, 1H, H^{22a}), 2.71 (dd, J_{HH} = 13.1, 8.4 Hz, 1H, H^{22b}), 2.63 (s, 3H, H^{28}), 2.45 (s, 3H, H^{29}), 2.27–2.19 (m, 2H, H^{14}), 2.17–2.05 (m, 2H, H^{13}) ppm.

^{13}C (^{1}H-^{13}C multiplicity-edited HSQC, ^{1}H-^{13}C HMBC) NMR (151 MHz, CD_2Cl_2): δ 172.8 (C^{16}), 171.2 (C^{27}), 168.6 (C^{19}), 155.6 (C^{11}), 142.9 (C^5), 141.4 (C^9), 140.0 (C^6), 136.7 (C^{23}), 132.2 (q, J_{CF} = 33 Hz, C^2), 129.5 (C^{24}), 128.5 (C^{25}), 127.7 (br s, C^4), 127.1 (C^{26}), 123.8 (q, J_{CF} = 273 Hz, C^3), 121.7 (sept, J_{CF} = 3 Hz, C^1), 120.6 (C^8), 118.7 (C^7), 61.8 (C^{15}), 51.1 (C^{21}), 47.4 (C^{12}), 42.8 (C^{18}), 39.1 (C^{22}), 36.8 (C^{29}), 35.5 (C^{28}), 30.1 (C^{13}), 25.5 (C^{14}) ppm.

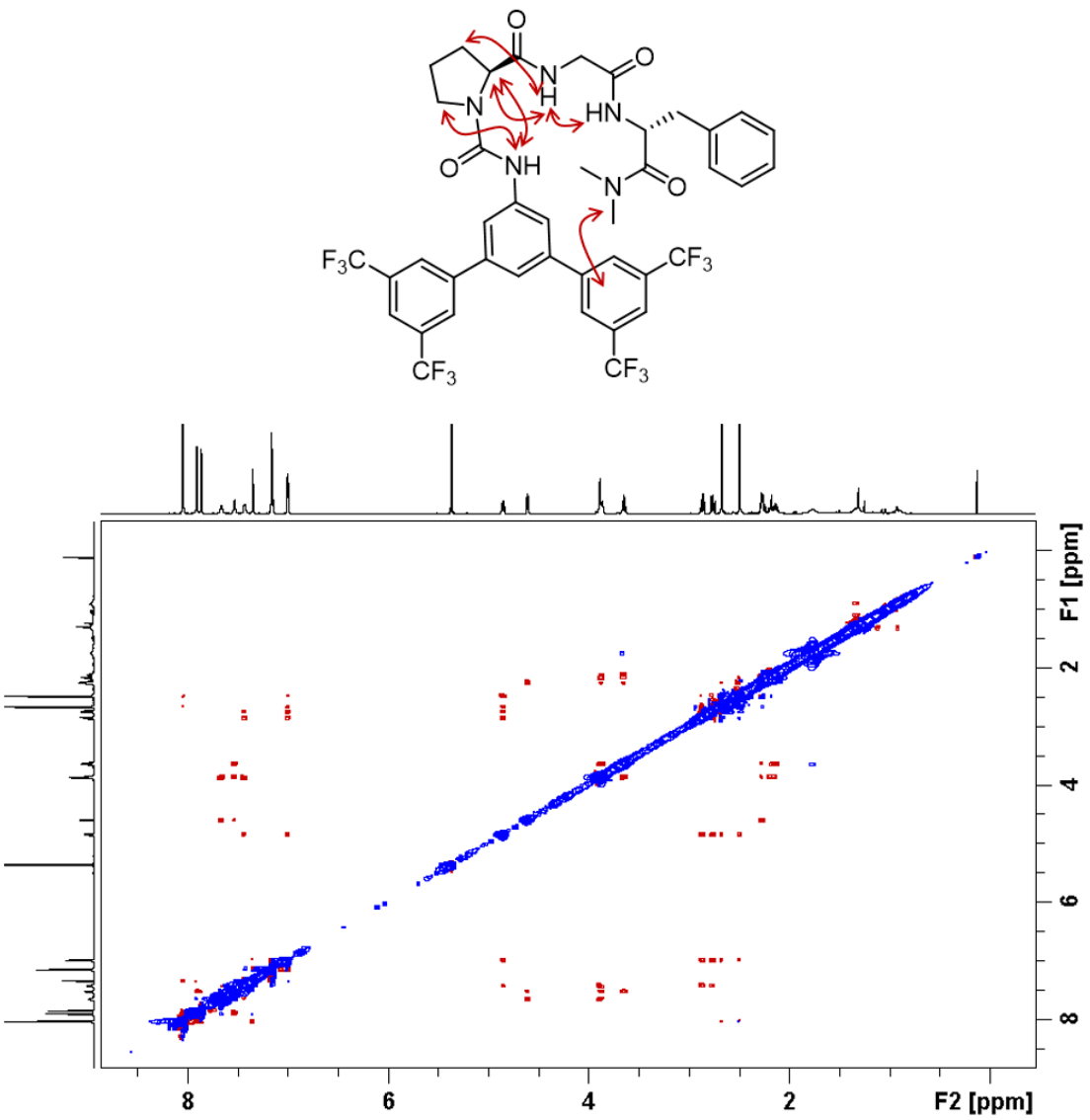

Figure 5.5.18. $^{1}H-^{1}H$ NOESY NMR spectrum of **2r** (600 MHz, CD_2Cl_2, 25 mM, d_8 = 800 ms) with inter-residue correlations displayed as arrows.

3,5-[3,5-$(CF_3)_2C_6H_3]_2C_6H_3$NHC(O)-Pro-Gly-D-Phe-NMe_2 (2s)

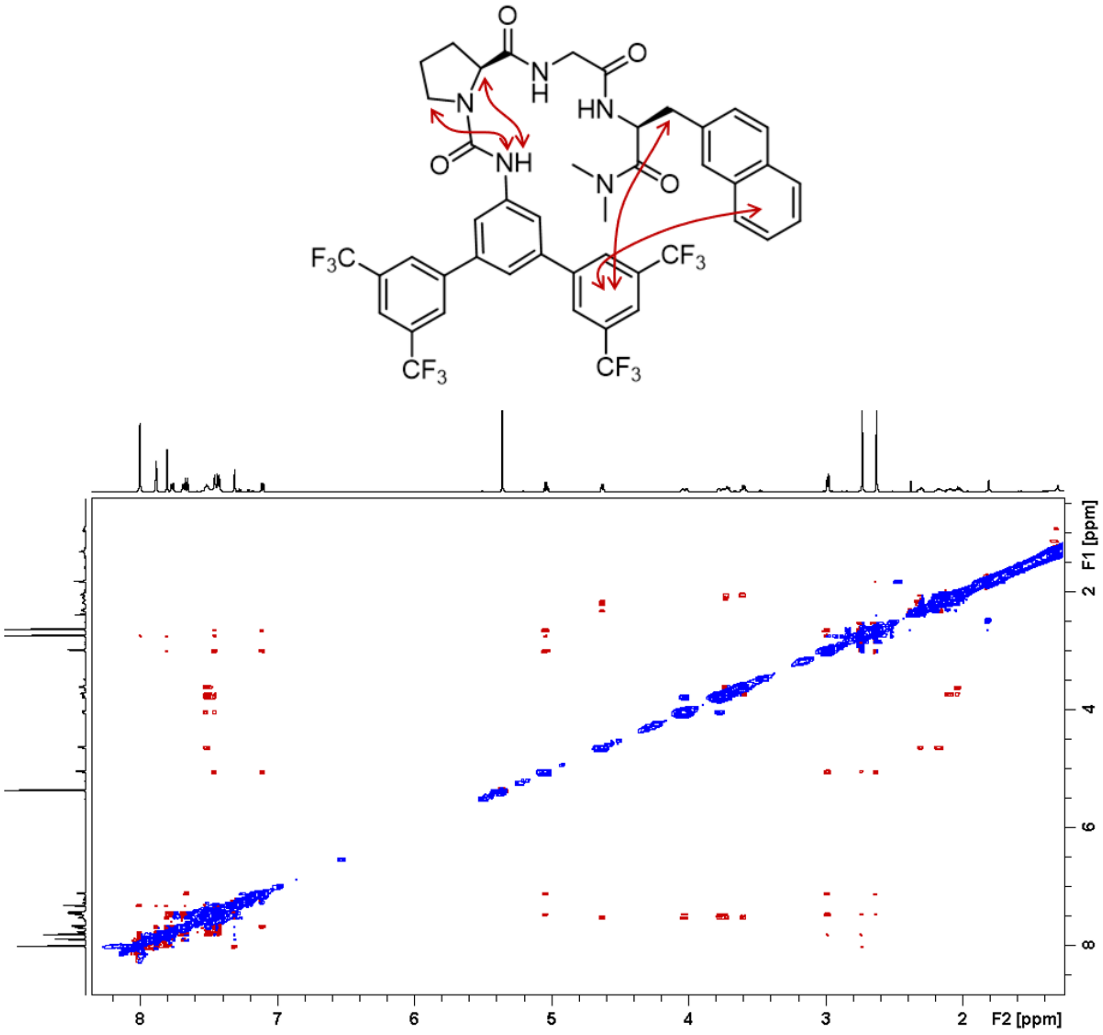

Figure 5.5.19. $^1H-^1H$ NOESY NMR spectrum of **2s** (600 MHz, CD_2Cl_2, 25 mM, d_8 = 800 ms) with inter-residue correlations displayed as arrows.

Table 5.5.1. Comparison of *A*-values for NH protons of **2d** and **2s**.

Peptide	$A_{NH(i+1)}$	$A_{NH(i-1)}$	$A_{NH(i-2)}$
2s	0.20	0.12	0.11
2d	0.18	0.12	0.11

3,5-[3,5-$(CF_3)_2C_6H_3]_2C_6H_3NHC(O)$-flp-Acpc-Phe-$NEt_2$ (3.3j)

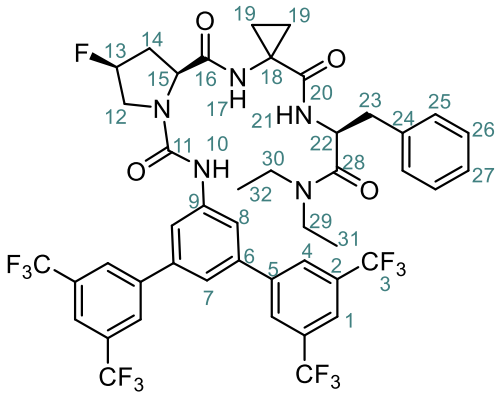

Scheme 5.5.19. Structure and numbering of **3.3j**.

^{1}H (^{1}H-^{1}H COSY, ^{1}H-^{13}C multiplicity-edited HSQC, ^{1}H-^{1}H NOESY) NMR (500 MHz, CD_2Cl_2): δ 8.10 (s, 4H, H^4), 7.95 (s, 2H, H^1), 7.92 (s, 2H, H^8), 7.65 (br s, 1H, H^{10}), 7.48 (s, 1H, H^7), 7.32 (s, 1H, H^{17}), 7.20 (d, J_{HH} = 8.2 Hz, 1H, H^{21}), 7.15–7.14 (m, 3H, H^{26}+H^{27}), 7.00–6.98 (m, 2H, H^{25}), 5.46 (dt, J_{HF} = 52.4 Hz, J_{HH} = 3.5 Hz, 1H, H^{13}), 4.87 (q, J_{HH} = 7.9 Hz, 1H, H^{22}), 4.75 (d, J_{HH} = 9.6 Hz, 1H, H^{15}), 4.16 (dd, J_{HF} = 22.4 Hz, J_{HH} = 11.8 Hz, 1H, H^{12a}), 3.93 (ddd, J_{HF} = 35.2 Hz, J_{HH} = 11.8, 3.7 Hz, 1H, H^{12b}), 3.44 (sx, J_{HH} = 7.0 Hz, 1H, H^{30a}), 3.00–2.91 (m, 3H, H^{30b}+H^{29}), 2.82–2.76 (m, 2H, H^{14a}+H^{23a}), 2.71 (dd, J_{HH} = 13.3, 6.5 Hz, 1H, H^{23b}), 2.47 (dddd, J_{HF} = 41.0 Hz, J_{HH} = 14.7, 10.0, 3.8 Hz, 1H, H^{14b}), 1.49–1.40 (m, 2H, H^{19a}), 1.09 (ddd, J_{HH} = 10.2, 7.2, 4.1 Hz, 1H, H^{19b}), 0.98 (ddd, J_{HH} = 10.2, 6.5, 3.2 Hz, 1H, H^{19b}), 0.91 (appt q, J_{HH} = 7.3 Hz, 6H, H^{32}+H^{31}) ppm.

^{13}C (^{1}H-^{13}C multiplicity-edited HSQC, ^{1}H-^{13}C HMBC) NMR (151 MHz, CD_2Cl_2): δ 172.3 (C^{16}), 170.6 (C^{20}), 170.3 (C^{28}), 155.2 (C^{11}), 142.6 (C^5), 140.6 (C^6), 139.9 (C^9), 136.5 (C^{24}), 132.0 (q, J_{CF} = 33 Hz, C^2), 129.3 (C^{25}), 128.1 (C^{26}), 127.5 (br, C^4), 126.6 (C^{27}), 122.3 (q, J_{CF} = 273 Hz, C^3), 121.5 (sept, J_{CF} = 4 Hz, C^1), 121.1 (C^8), 119.6 (C^7), 92.4 (d, J_{CF} = 173 Hz, C^{13}), 59.9 (C^{15}), 53.9 (C^{12}, *overlapping with solvent peak*), 50.6 (C^{22}), 41.5 (C^{30}), 40.3 (C^{29}), 39.6 (C^{23}), 35.6 (br d, J_{CF} = 2 Hz, C^{14}), 34.6 (C^{18}), 16.5 (C^{19b}), 16.3 (C^{19a}), 13.6 (C^{32}), 12.3 (C^{31}) ppm.

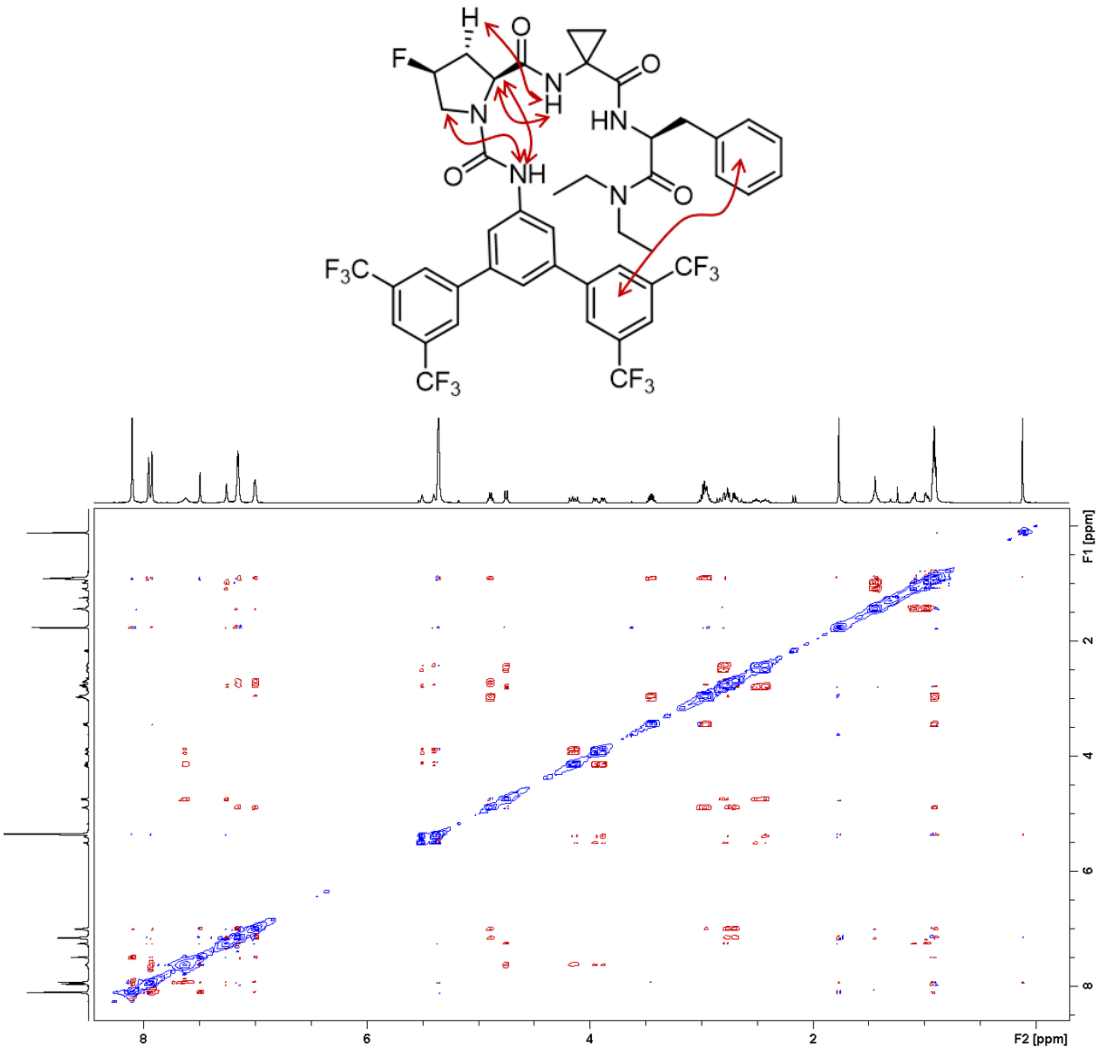

Figure 5.5.20. $^{1}H-^{1}H$ NOESY NMR spectrum of **3.3j** (500 MHz, CD_2Cl_2, 25 mM, d_8 = 800 ms) with inter-residue correlations displayed as arrows.

5.5.2. Method for *A*-value determination

^{1}H NMR spectra in $CDCl_3$ and DMSO-d_6 were all recorded at 298 K using 400 MHz spectrometer (Bruker AVIIIHD 400). All samples were set to 6−7 mM concentration, except for **2n−p**, for which 2 mM concentration was used to ensure solubility in $CDCl_3$. Samples were prepared in a glass vial using 0.6 mL of deuterated solvent and an appropriate amount of weighted peptide. Solutions were then sonicated until full dissolution and transferred to the NMR tube. ^{1}H chemical shifts (δ, ppm) are measured relative to an internal reference (tetramethylsilane). Generally, NH protons could be assigned by the splitting pattern of the resonances in the ^{1}H spectra: s, d and t, for NH(*i*+*1*), NH(*i*−*2*) and NH(*i*−*1*), respectively. 2D COSY, HSQC and HMBC spectra were acquired in addition for selected samples to aid in NH shift assignment – in case of overlapping peaks or dialkylated residues in the *i*−*1* position. The solute H-bond acidity values (*A*)[25] for the NH protons were calculated based on their chemical shift difference in $CDCl_3$ and DMSO-d_6 using equation derived by Abraham *et al.*[26] for amide protons (**Equation 1**).

Equation 1: $\boldsymbol{A = 0.0065 + 0.133\,\Delta\delta}$, where $\boldsymbol{\Delta\delta = \delta(DMSO\text{-}d_6) - \delta(CDCl_3)}$

5.5.3. NMR titrations of peptides **2a−r** and **3.3j**

The titration experiments were obtained in collaboration with Jessica Sellar (JS) and Dr. Francesco Ibba (FI). Peptide **2c** was titrated in collaboration with FI, while titrations of **2f** and **2g** were performed in collaboration with JS.

5.5.3.1. Methodology

Titration were performed following procedure by Ibba *et al.*[27] A known amount of peptide (~ 3.0 mmol) was weighted in an NMR tube and dissolved in 0.5 mL of CD_2Cl_2 and 5.0 μL 4-fluoroanisole solution. A TBAF$(H_2O)_3$ stock solution was prepared dissolving ~50 mg of TBAF$(H_2O)_3$ (Merck, Tetrabutylammonium fluoride hydrate 98%) and 5.0 μL of 4-fluoranisole in 1.0 mL of CD_2Cl_2 measured in a volumetric flask.

The exact concentrations of fluoride and peptides were determined by ^{19}F qNMR, integrating the F^- peak (−118.9 ppm for TBAF$(H_2O)_3$), CF_3 peak (around −63 ppm for peptides **2c**, **2d**, **2h−r**) or F peak (−110.2 ppm for peptide **2e**), and 4-fluoroanisole peak (−125.3 ppm, 0.044 M). Peptides **2a**, **2b**, **2f**, **2g** were quantified via ^{1}H qNMR, integrating the 4-fluoroanisole peak (6.89 ppm, 2H, 0.088 M) and all resolved H^α (averaged). The data were collected on an AVIII HD 500 at 298 K using parameters in **Table 5.5.2**, and concentrations used for each titration are provided in **Table 5.5.3**.

Table 5.5.2. Parameters for quantitative ^{1}H and ^{19}F NMR spectra acquisition for quantification of peptide and TBAF$(H_2O)_3$ solutions in CD_2Cl_2 used for NMR titrations.

^{19}F qNMR:	
Parameter	Value
TD (SI)	131072 (262144) pt
SW	20 or 100 ppm
o1p	−122 and −94 ppm
NS (DS)	16 (2)
relaxation delay d_1	35 s

^{1}H qNMR:	
Parameter	Value
TD (SI)	131072 (262144) pt
SW	20 ppm
o1p	5.0 ppm
NS (DS)	16 (4)
relaxation delay d_1	75 s

The TBAF$(H_2O)_3$ solution was added in aliquots and after each addition ^{1}H NMR spectra were acquired. The chemical shifts of selected proton signals were plotted against the amount of added TBAF$(H_2O)_3$. The association constants ($K_{a\ (1:1\ TBAF\text{-}3H2O)}$) were determined from the titration data points by non-linear least squares regression using DynaFit 4.08.161.

The following shows a typical input file for the determination of $K_{a\ (1:1\ TBAF\text{-}3H2O)}$:

```
[task]
  task = fit
  data = equilibria

[mechanism]
  U + F <==> UF : Ka equilibrium

[constants]
Ka = 1000 ?

[responses]
intensive

[data]
variable F, U
plot titration

set NMR.a | resp U = 4.9007, UF = 4.7206 ?
set NMR.b | resp U = 4.7560, UF = 5.0680 ?
set NMR.c | resp U = 7.1660, UF = 8.640 ?

[set:NMR.a]
0.000000000     0.006811111     4.9007
0.000292018     0.006796009     4.8924
0.000872185     0.006766004     4.8663
0.002017287     0.006706783     4.8188
0.002582353     0.006677560     4.8000
0.003142516     0.006648590     4.7844
0.003973707     0.006605603     4.7637
0.004794218     0.006563169     4.7500
0.005604255     0.006521277     4.7380
0.006668354     0.006466245     4.7311
0.007714644     0.006412134     4.7271
0.008743568     0.006358921     4.7260
0.009755556     0.006306584     4.7257
0.010751020     0.006255102     4.7253
0.013170000     0.006130000     4.7235
0.015494118     0.006009804     4.7239
0.017728846     0.005894231     4.7224
0.019879245     0.005783019     4.7221
0.023945455     0.005572727     4.7206
0.027726316     0.005377193     4.7206

[set:NMR.b]
0       0.006811111     4.7560
0.000292018     0.006796009     4.7642
0.000872185     0.006766004     4.7994
0.002017287     0.006706783     4.8669
0.002582353     0.006677560     4.9002
0.003142516     0.00664859      4.9325
0.003973707     0.006605603     4.9774
0.004794218     0.006563169     5.0131
0.005604255     0.006521277     5.0367
0.006668354     0.006466245     5.0575
0.007714644     0.006412134     5.0570
0.008743568     0.006358921     5.0594
0.009755556     0.006306584     5.0640
0.010751020     0.006255102     5.0650
0.013170000     0.006130000     5.0640
0.015494118     0.006009804     5.0650
0.017728846     0.005894231     5.0631
0.019879245     0.005783019     5.0660
0.023945455     0.005572727     5.0660
0.027726316     0.005377193     5.0680

[set:NMR.c]
0       0.006811111     7.1660
0.000292018     0.006796009     7.2000
0.000872185     0.006766004     7.3290
0.001447253     0.006736264     7.4610
0.002017287     0.006706783     7.6040
0.002582353     0.00667756      7.7430
0.003142516     0.00664859      7.8920
0.003973707     0.006605603     8.1270
0.004794218     0.006563169     8.3260
0.005604255     0.006521277     8.4860
0.006668354     0.006466245     8.6230
0.007714644     0.006412134     8.6860
0.008743568     0.006358921     8.7040
0.009755556     0.006306584     8.7110
0.01075102      0.006255102     8.7150
0.01317  0.00613  8.7040
0.015494118     0.006009804     8.7000
0.017728846     0.005894231     8.6840
0.019879245     0.005783019     8.6790
0.023945455     0.005572727     8.6630
0.027726316     0.005377193     8.6400

[output]
  directory ./output
[end]
```

Table 5.5.3. Concentrations and TBAF equivalents in CD_2Cl_2 used for NMR titrations.

Titration	[peptide] (mM)	[TBAF] (mM)	Equiv. added
2a (exp 1)	4.6	141	17.0
2a (exp 2)	2.2	150	18.0
2b (exp 1)	1.8	141	15.8
2b (exp 2)	4.0	145	19.5
2c (exp 1)	9.0	60	3.5
2c (exp 2)	6.5	70	12.0
2d (exp 1)	5.8	69	10.8
2d (exp 2)	6.4	78	12.9
2e (exp 1)	6.5	116	3.9
2e (exp 2)	4.8	156	5.5
2f (exp 1)	5.4	128	5.0
2f (exp 2)	6.8	148	4.4
2g (exp 1)	3.6	177	9.8
2g (exp 2)	5.3	153	5.8
2h (exp 1)	4.8	145	3.6
2h (exp 2)	3.8	135	4.3
2i (exp 1)	4.6	72	2.4
2i (exp 2)	5.1	139	4.6
2j (exp 1)	3.5	141	2.1
2j (exp 2)	3.0	148	3.9
2k (exp 1)	4.2	153	2.4
2k (exp 2)	3.4	120	3.9
2l (exp 1)	4.0	141	4.7
2m (exp 1)	3.9	169	5.0
2m (exp 2)	3.8	138	5.1
2n (exp 1)	1.7	130	7.2
2n (exp 2)	1.6	141	10.1
2o (exp 1)	4.9	118	6.2
2o (exp 2)	1.8	143	4.9
2p (exp 1)	1.8	151	2.9
2p (exp 2)	1.6	108	3.1
2q (exp 1)	4.1	151	2.5
2q (exp 2)	6.7	153	4.0
2r (exp 1)	5.5	138	3.0
2r (exp 2)	4.6	127	3.5
3.3j (exp 1)	6.0	143	5.0
3.3j (exp 2)	5.9	154	4.9

Table 5.5.4. Association constants ($K_{a\ (1:1,\ TBAF)}$) for the formation of 1:1 catalyst-TBA**F**$(H_2O)_3$ complexes in CD_2Cl_2.

	$\Delta\delta_{NH(i+1)}$ (ppm)	$\Delta\delta_{NH(i-1)}$ (ppm)	$\Delta\delta_{NH(i-2)}$ (ppm)	$K_{a\ (1:1\ TBAF)}$ (M^{-1})	$\log K_{a\ (1:1\ TBAF)}$	MSD[a]
2a (exp 1)	0.56[b]	2.29[c]	0.20[b]	48	1.68	7.2×10^{-7}
2a (exp 2)	0.57[b]	2.16[c]	0.19[b]	55	1.74	1.9×10^{-6}
2a (average)	0.57	2.22	0.20	52 ± 5	1.72 ± 0.04	
2b (exp 1)	0.20[b]	3.51[b]	0.03[b]	103	2.013	5.8×10^{-6}
2b (exp 2)	0.17[b]	3.22[b]	0.01[b]	101	2.003	1.9×10^{-6}
2b (average)	0.19	3.37	0.02	102 ± 1	2.008 ± 0.005	
2c (exp 1)	4.66	2.95	1.97	40 000	4.6	4.1×10^{-4}
2c (exp 2)	4.74	2.96	2.02	21 000	4.3	9.5×10^{-4}
2c (average)	4.68	2.95	2.00	$3.05 \pm 0.95 \times 10^4$	4.5 ± 0.1	
2d (exp 1)	4.20	3.01	1.86	12 200	4.09	1.7×10^{-3}
2d (exp 2)	4.10	2.89	1.72	12 700	4.10	1.1×10^{-4}
2d (average)	4.15	2.95	1.79	$1.25 \pm 0.04 \times 10^4$	4.10 ± 0.01	
2e (exp 1)	4.02	3.10	1.84	8 200	3.91	1.9×10^{-5}
2e (exp 2)	3.87	2.98	1.74	8 800	3.94	2.4×10^{-5}
2e (average)	3.95	3.04	1.79	$8.5 \pm 0.4 \times 10^3$	3.93 ± 0.02	
2f (exp 1)	3.41	2.98	1.84	5 600	3.75	2.2×10^{-5}
2f (exp 2)	3.37	2.92	1.78	3 900	3.59	8.2×10^{-3}
2f (average)	3.39	2.95	1.81	$4.8 \pm 0.9 \times 10^3$	3.68 ± 0.08	
2g (exp 1)	3.10	3.13	2.07	1 260	3.10	3.74×10^{-6}
2g (exp 2)	2.98	3.12	2.15	1 390	3.14	4.41×10^{-6}
2g (average)	3.04	3.13	2.11	$1.33 \pm 0.09 \times 10^3$	3.12 ± 0.02	
2h (exp 1)	4.40	3.47	1.35	110 000	5.04	6.5×10^{-4}
2h (exp 2)	4.41	3.61	1.33	120 000	5.08	3.1×10^{-3}
2h (average)	4.41	3.54	1.32	$1.15 \pm 0.05 \times 10^5$	5.06 ± 0.02	
2i (exp 1)	4.73	1.86	1.93	15 000	4.18	5.6×10^{-5}
2i (exp 2)	4.63	1.86	1.85	14 000	4.15	3.0×10^{-4}
2i (average)	4.68	1.86	1.89	$1.45 \pm 0.07 \times 10^4$	4.16 ± 0.02	
2j (exp 1)	4.55	3.47	1.54	59 000	4.77	8.6×10^{-4}
2j (exp 2)	4.52	3.41	1.56	67 000	4.83	5.2×10^{-3}
2j (average)	4.54	3.44	1.55	$6.3 \pm 0.4 \times 10^4$	4.80 ± 0.03	
2k (exp 1)	3.21	2.92	1.94	45 000	4.65	9.4×10^{-4}
2k (exp 2)	3.00	2.88	2.07	41 000	4.61	4.7×10^{-4}
2k (average)	3.11	2.90	2.01	$4.3 \pm 0.2 \times 10^4$	4.63 ± 0.02	
2l (exp 1)[d]	4.00	1.93	0.73	$5.3 \pm 0.8 \times 10^3$	3.72 ± 0.07	8.2×10^{-4}
2m (exp 1)	4.34	2.55	0.90	38 000	4.58	3.9×10^{-4}
2m (exp 2)	4.30	2.55	1.00	25 000	4.40	3.9×10^{-4}
2m (average)	4.32	2.55	0.95	$3.15 \pm 0.65 \times 10^4$	4.49 ± 0.09	
2n (exp 1)	3.88	3.60	0.89	1 800	3.25	6.4×10^{-4}
2n (exp 2)	3.83	3.52	0.95	2 400	3.37	1.1×10^{-3}
2n (average)	3.86	3.56	0.92	$2.1 \pm 0.3 \times 10^3$	3.31 ± 0.06	

[a]MSD = mean square deviation. [b]$\Delta\delta_{NH} = \delta_{NH}$ (TBAF$(H_2O)_3$ 10 equiv.) − δ_{NH} (TBAF$(H_2O)_3$ 0 equiv.); [c]TBAF$(H_2O)_3$ (18 equiv.); [d]n=1, expressed with error of data fit.

Table 4.5.4. (continued) Association constants ($K_{a\ (1:1,\ TBAF)}$) for the formation of 1:1 catalyst-TBA**F**$(H_2O)_3$ complexes in CD_2Cl_2.

	$\Delta\delta_{NH(i+1)}$ (ppm)	$\Delta\delta_{NH(i-1)}$ (ppm)	$\Delta\delta_{NH(i-2)}$ (ppm)	$K_{a\ (1:1,\ TBAF)}$ (M^{-1})	log $K_{a\ (1:1,\ TBAF)}$	MSD[a]
2o (exp 1)	3.68	3.40	1.10	2 870	3.46	8.8×10^{-6}
2o (exp 2)	3.79	3.41	1.17	2 700	3.43	5.3×10^{-5}
2o (average)	3.74	3.41	1.14	$2.79 \pm 0.09 \times 10^3$	3.44 ± 0.01	
2p (exp 1)	4.26	2.47	0.89	7 900	3.90	1.2×10^{-4}
2p (exp 2)	4.19	2.49	0.95	9 100	3.96	3.1×10^{-5}
2p (average)	4.19	2.48	0.92	$8.5 \pm 0.6 \times 10^3$	3.93 ± 0.03	
2q (exp 1)	3.88	3.17	1.25	18 000	4.26	2.4×10^{-5}
2q (exp 2)	3.78	3.00	1.33	16 000	4.20	8.5×10^{-6}
2q (average)	3.83	3.09	1.29	$1.7 \pm 0.1 \times 10^4$	4.23 ± 0.03	
2r (exp 1)	4.31	2.54	0.95	21 000	4.32	2.3×10^{-4}
2r (exp 2)	4.33	2.59	0.91	25 000	4.40	2.2×10^{-4}
2r (average)	4.32	2.57	0.93	$2.3 \pm 0.2 \times 10^4$	4.36 ± 0.04	
3.3j (exp 1)	4.62	1.42	1.83	47 000	4.66	2.6×10^{-4}
3.3j (exp 2)	4.70	1.45	1.78	34 100	4.53	2.8×10^{-4}
3.3j (average)	4.66	1.44	1.81	$4.0 \pm 0.6 \times 10^4$	4.60 ± 0.07	

[a]MSD = mean square deviation.

5.5.3.2. Titration profiles

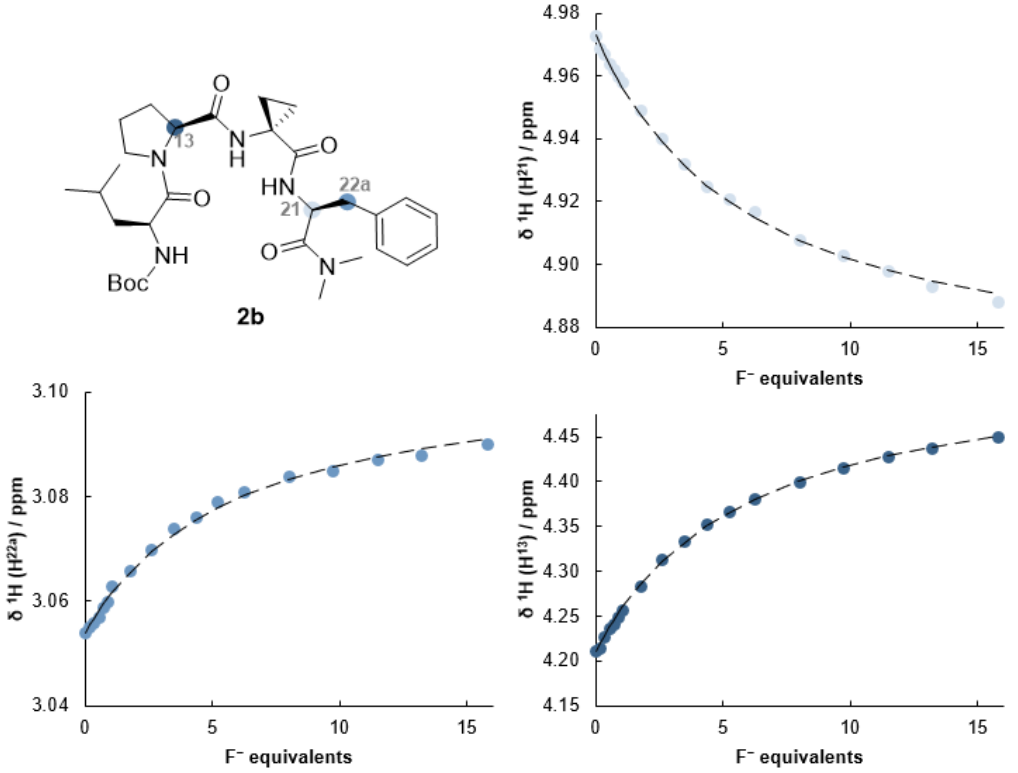

Figure 5.5.21. Titration profiles for selected protons of **2b**; experimental points (colored circles) and fitted function (dashed lines).

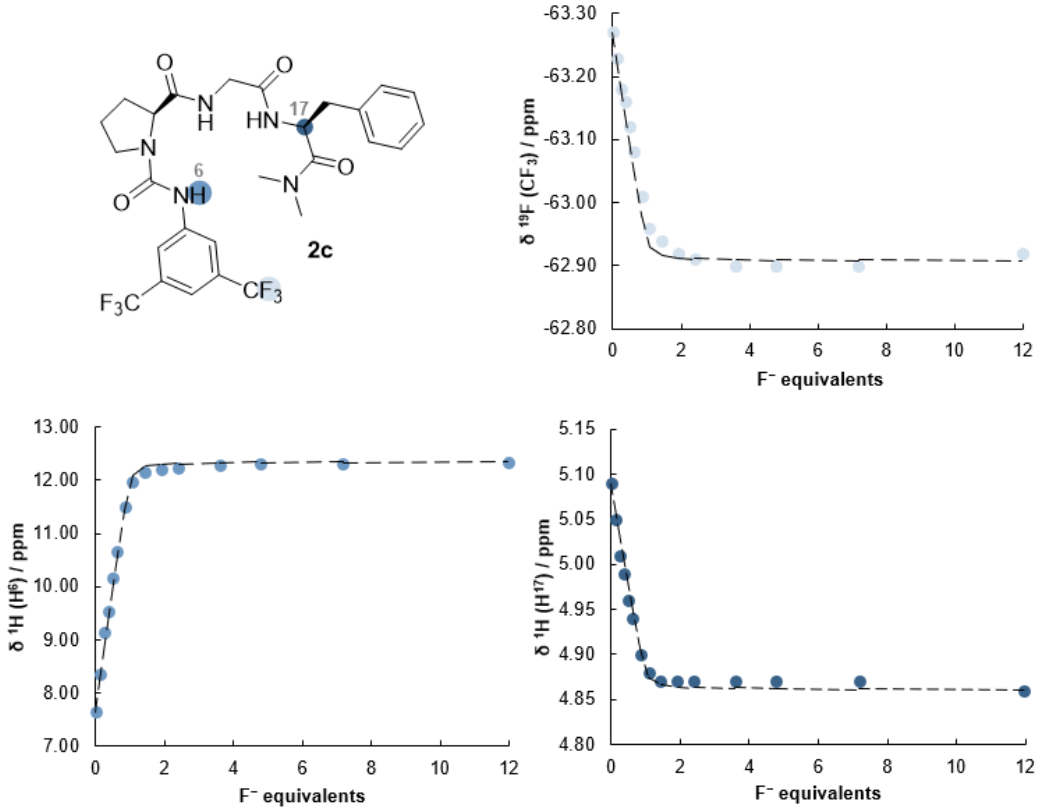

Figure 5.5.22. Titration profiles for selected protons of **2c**; experimental points (colored circles) and fitted function (dashed lines).

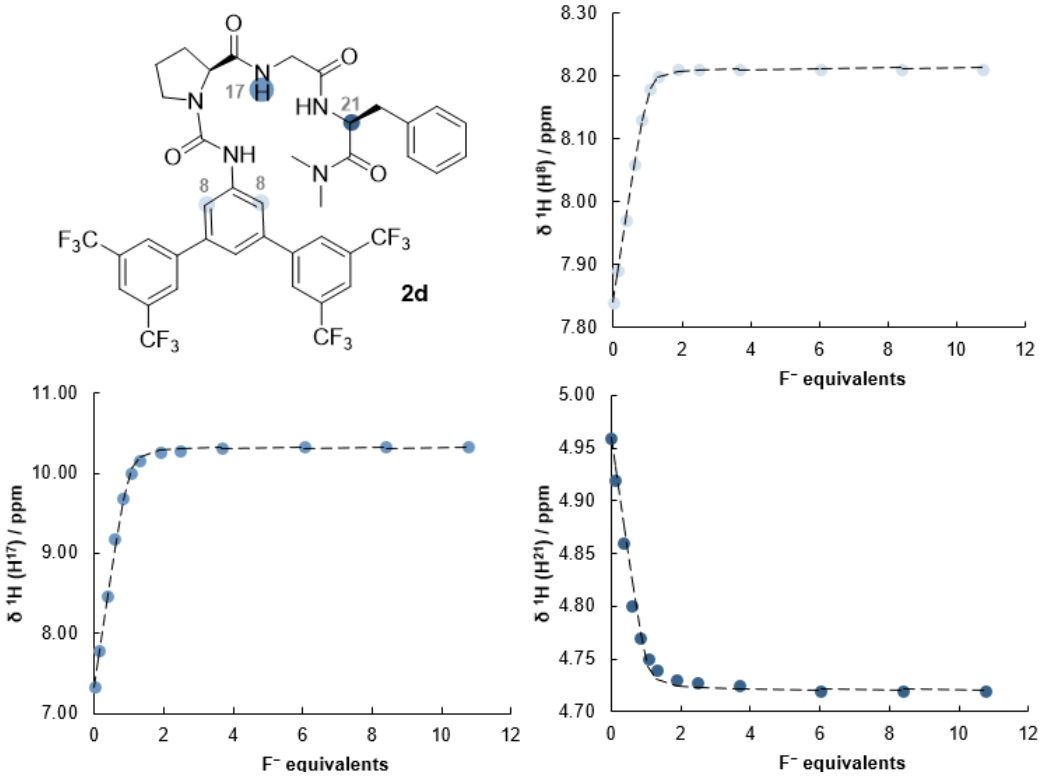

Figure 5.5.23. Titration profiles for selected protons of **2d**; experimental points (colored circles) and fitted function (dashed lines).

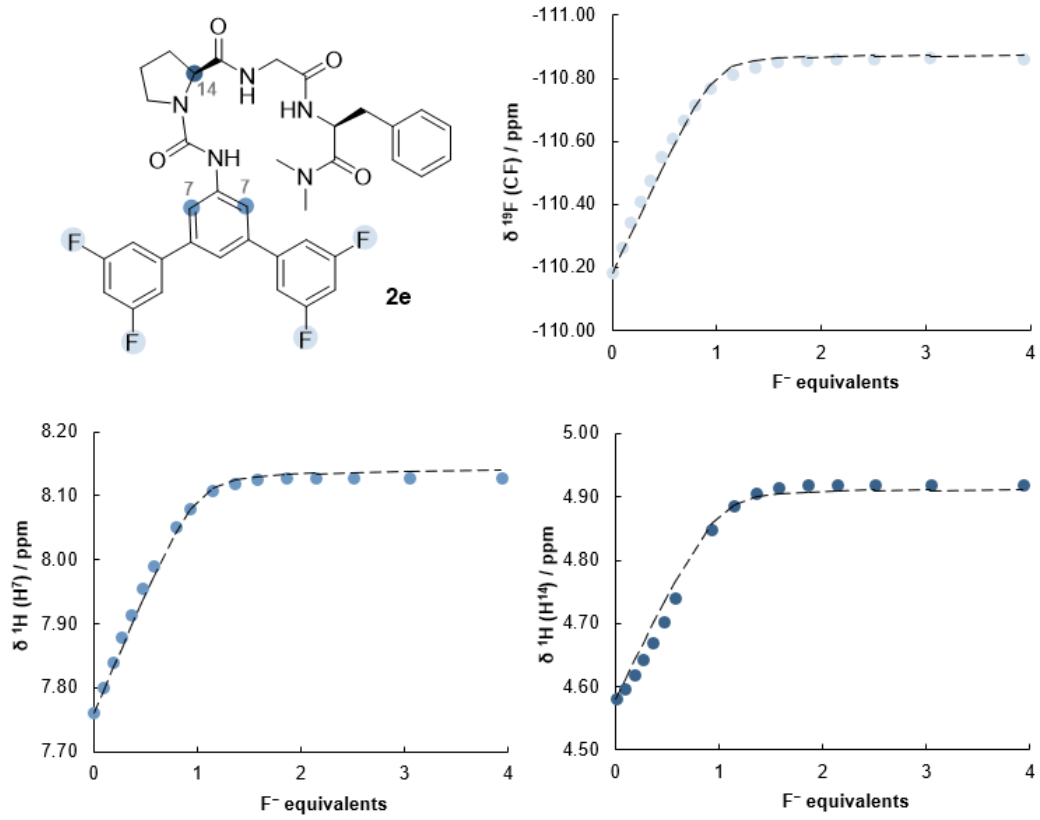

Figure 5.5.24. Titration profiles for selected protons of **2e**; experimental points (colored circles) and fitted function (dashed lines).

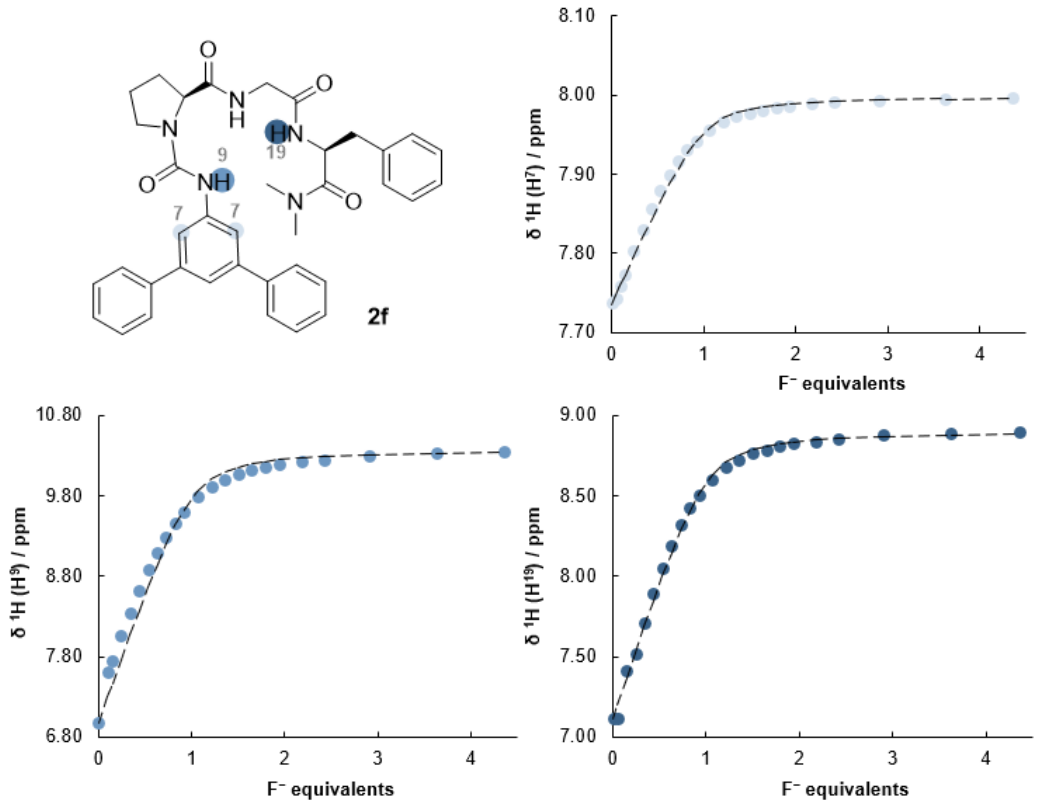

Figure 5.5.25. Titration profiles for selected protons of **2f**; experimental points (colored circles) and fitted function (dashed lines).

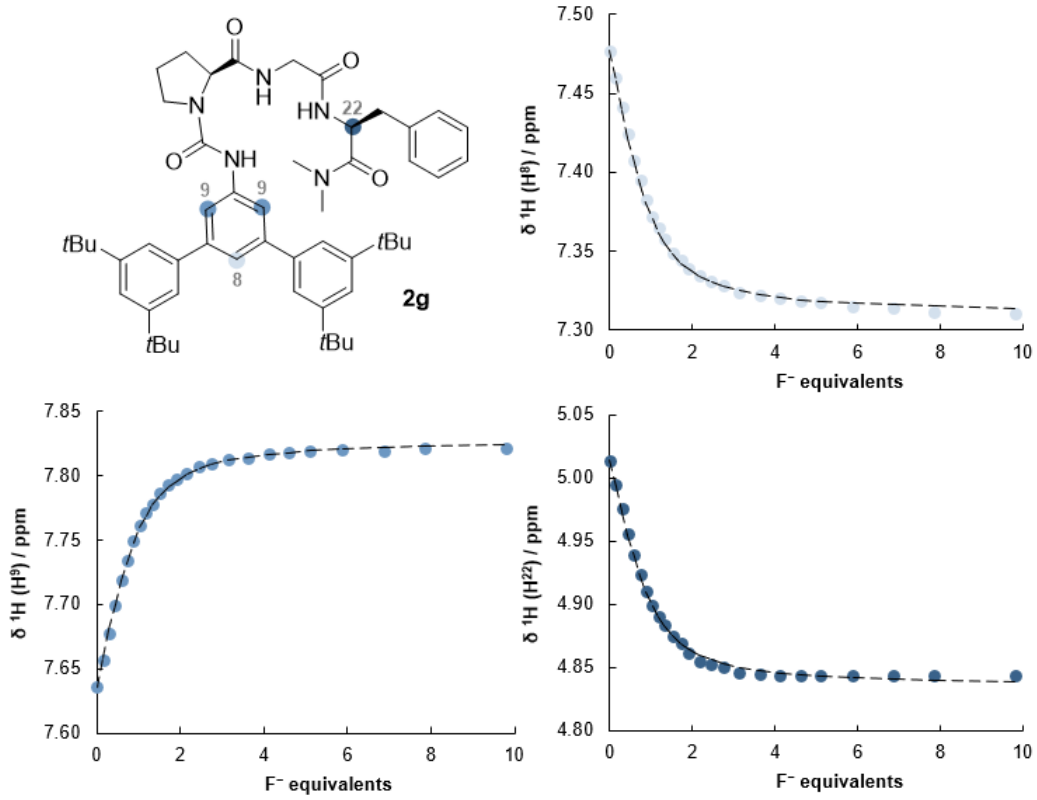

Figure 5.5.26. Titration profiles for selected protons of **2g**; experimental points (colored circles) and fitted function (dashed lines).

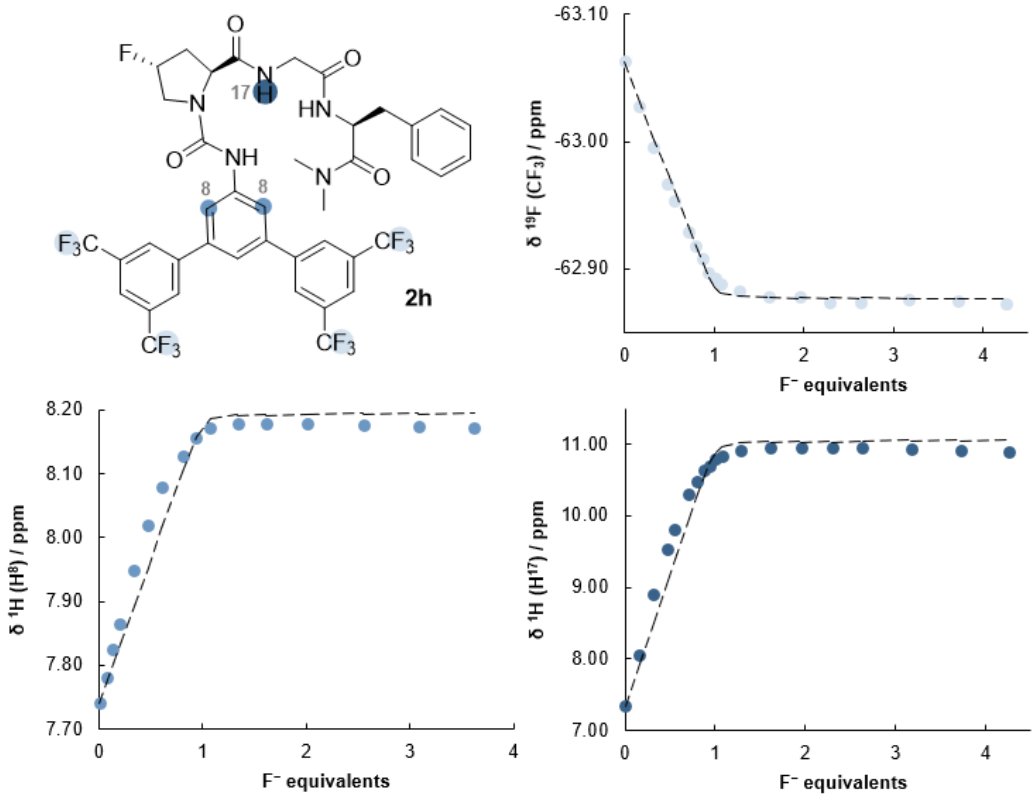

Figure 5.5.27. Titration profiles for selected protons of **2h**; experimental points (colored circles) and fitted function (dashed lines).

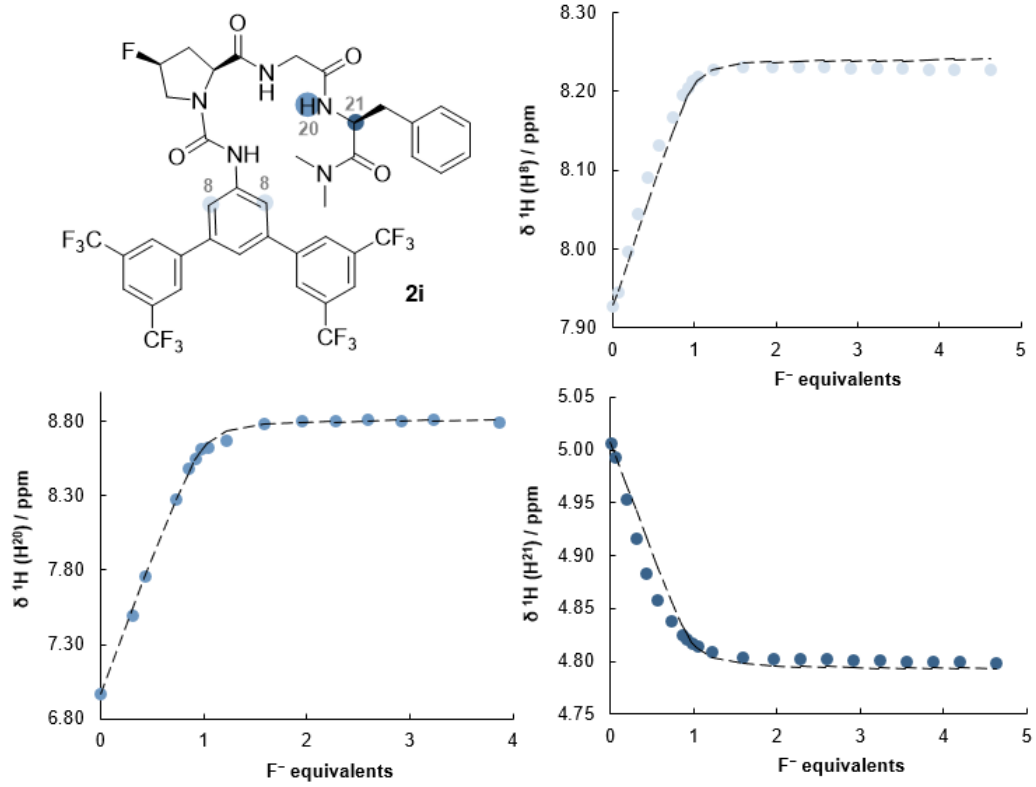

Figure 5.5.28. Titration profiles for selected protons of **2i**; experimental points (colored circles) and fitted function (dashed lines).

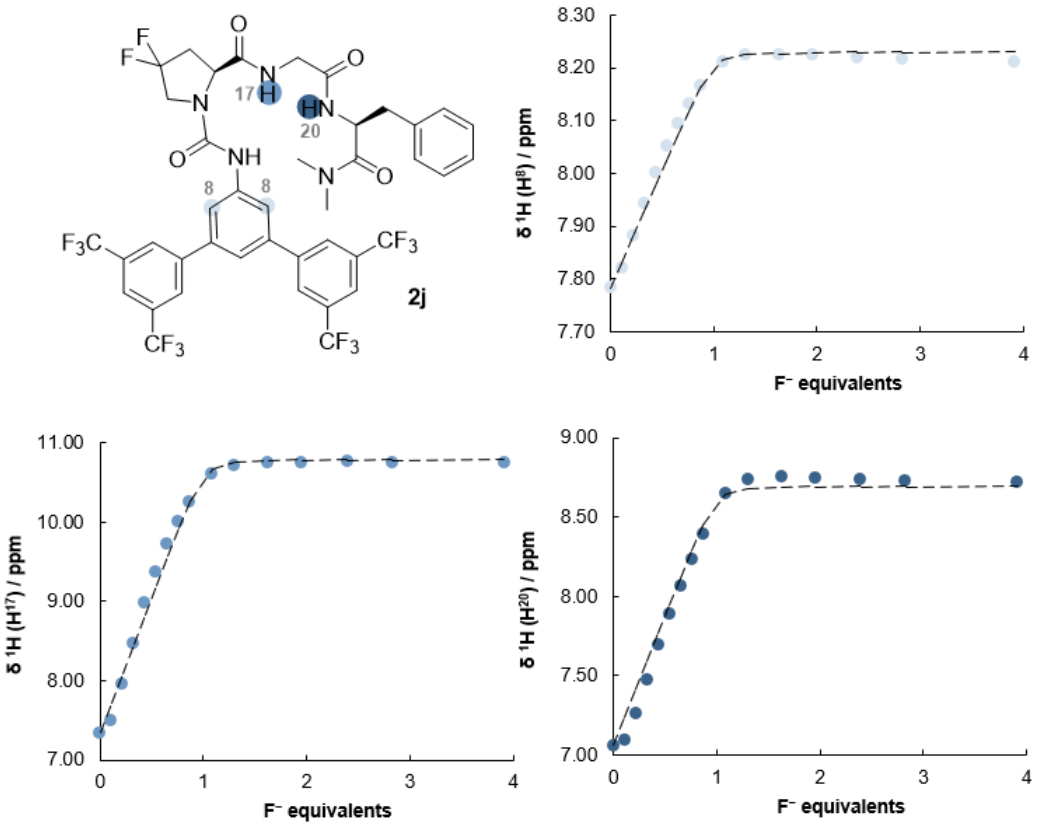

Figure 5.5.29. Titration profiles for selected protons of **2j**; experimental points (colored circles) and fitted function (dashed lines).

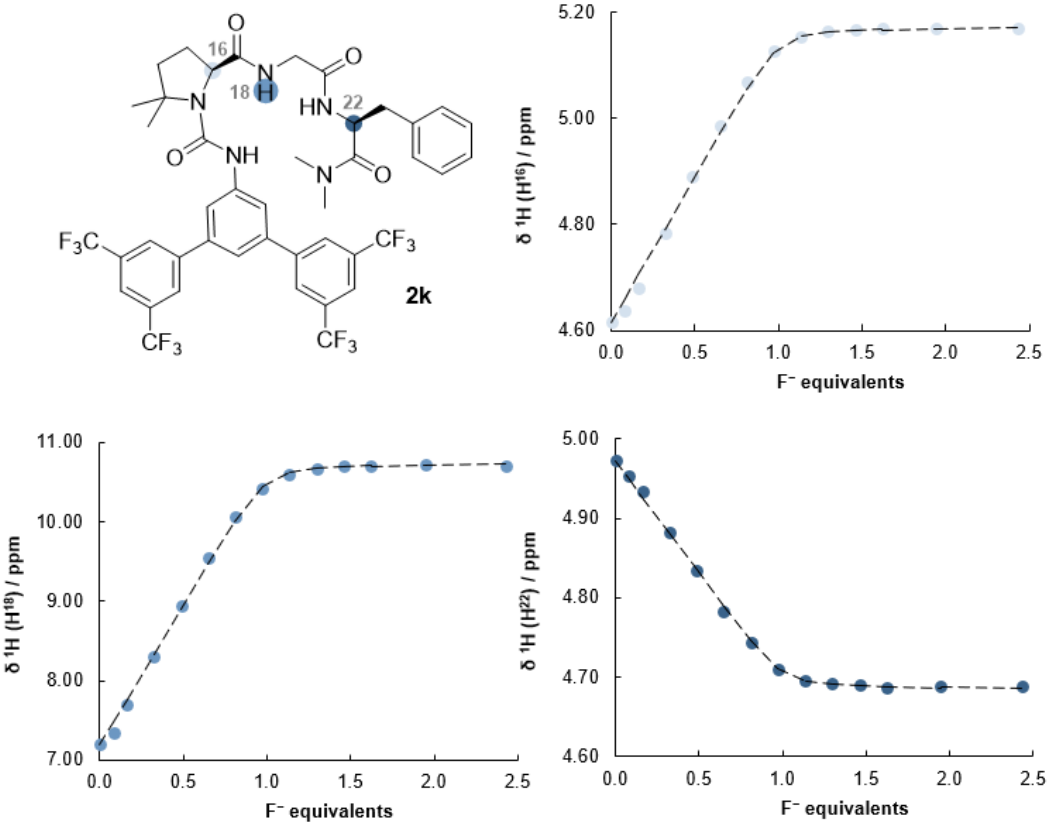

Figure 5.5.30. Titration profiles for selected protons of **2k**; experimental points (colored circles) and fitted function (dashed lines).

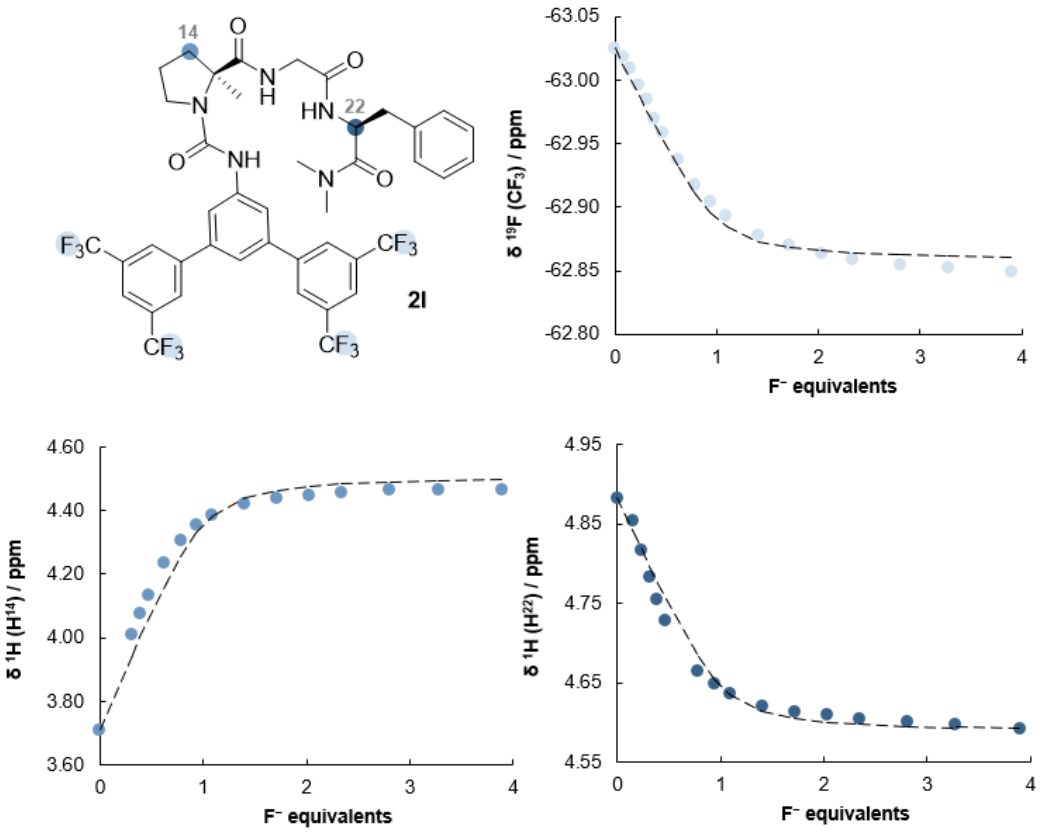

Figure 5.5.31. Titration profiles for selected protons of **2l**; experimental points (colored circles) and fitted function (dashed lines).

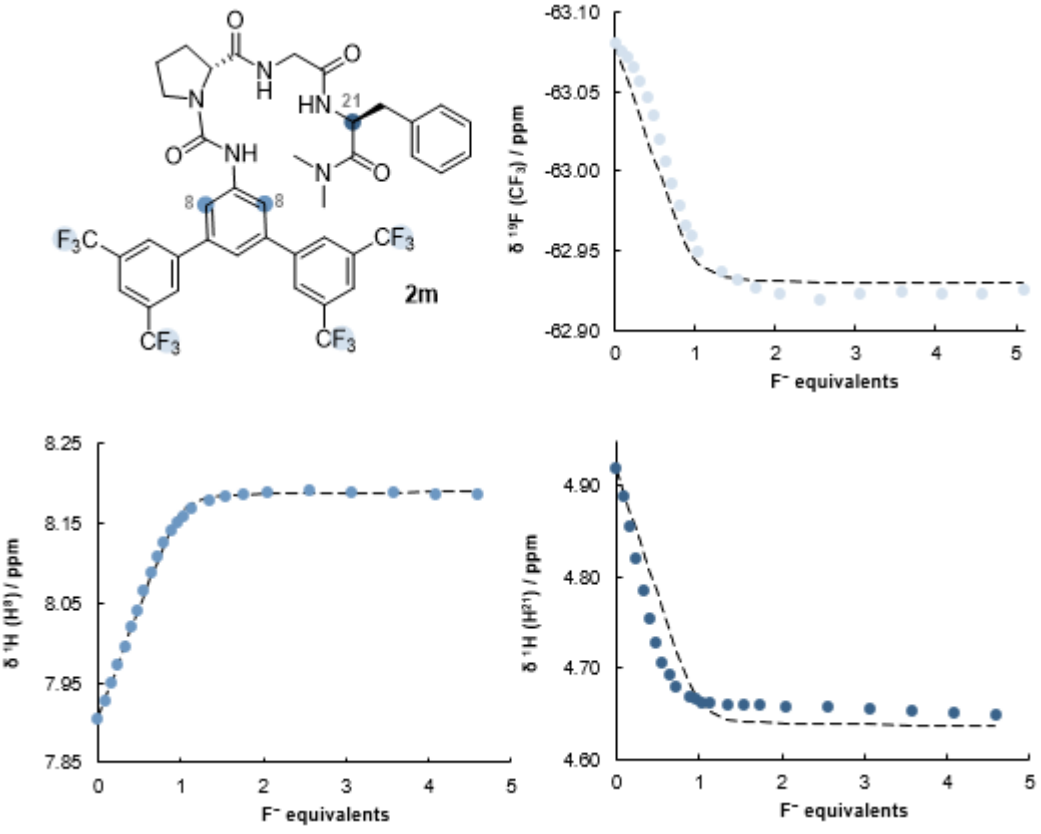

Figure 5.5.32. Titration profiles for selected protons of **2m**; experimental points (colored circles) and fitted function (dashed lines).

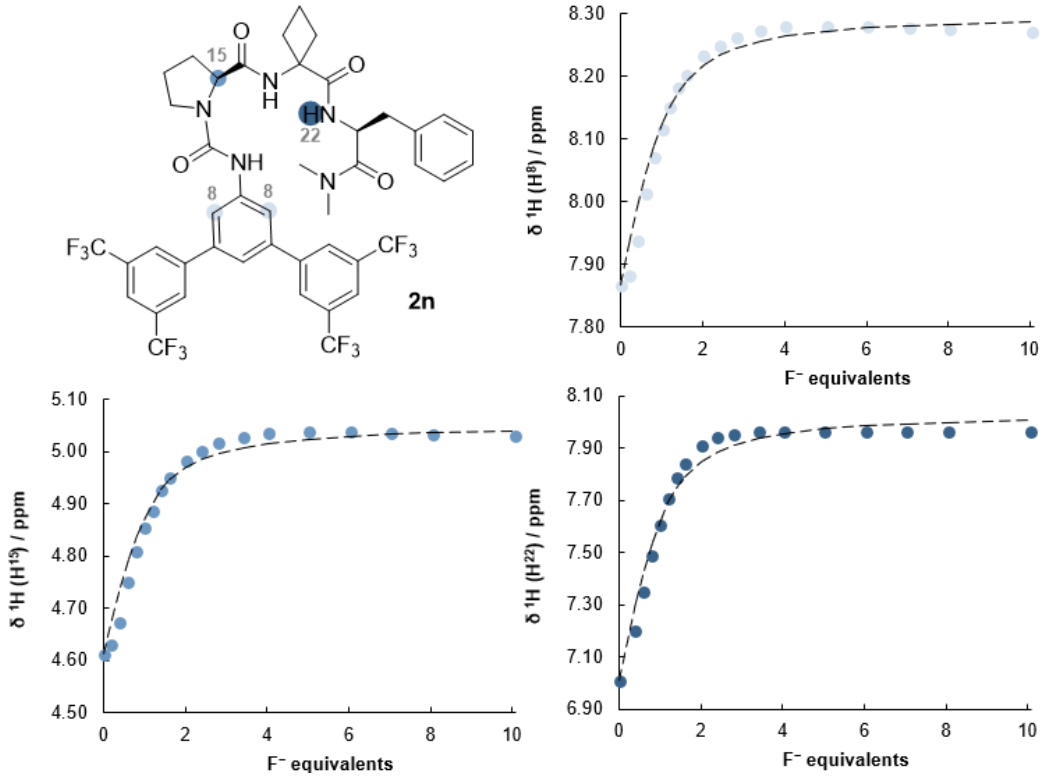

Figure 5.5.33. Titration profiles for selected protons of **2n**; experimental points (colored circles) and fitted function (dashed lines).

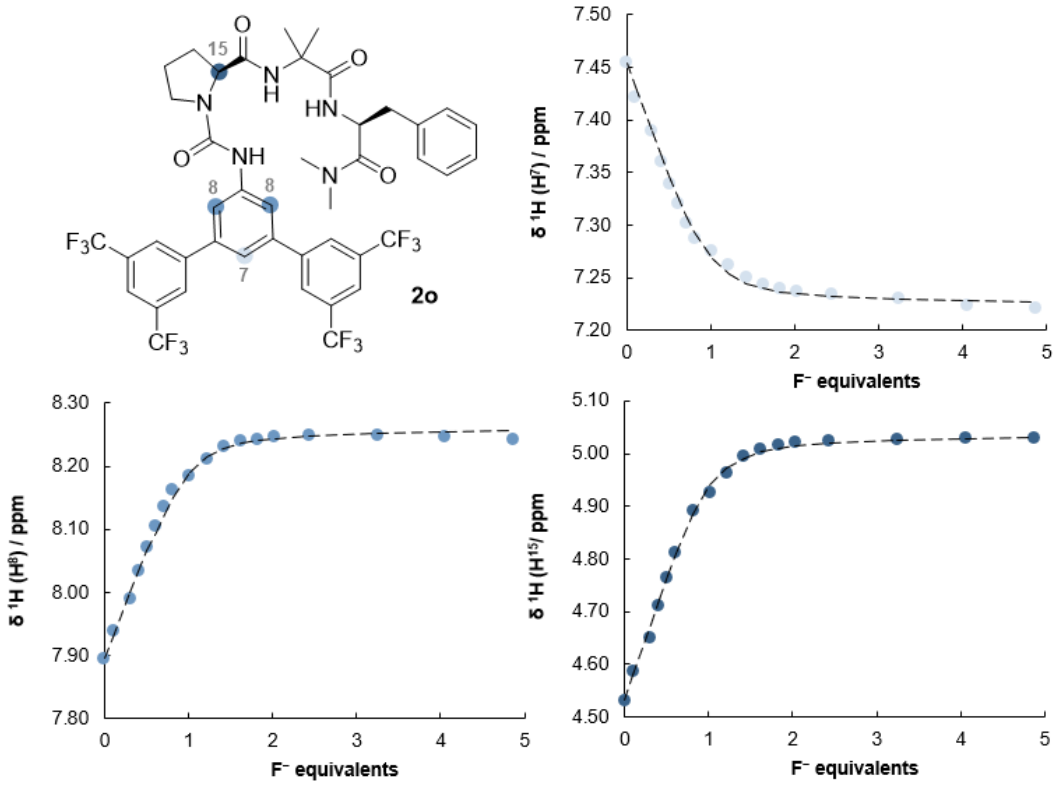

Figure 5.5.34. Titration profiles for selected protons of **2o**; experimental points (colored circles) and fitted function (dashed lines).

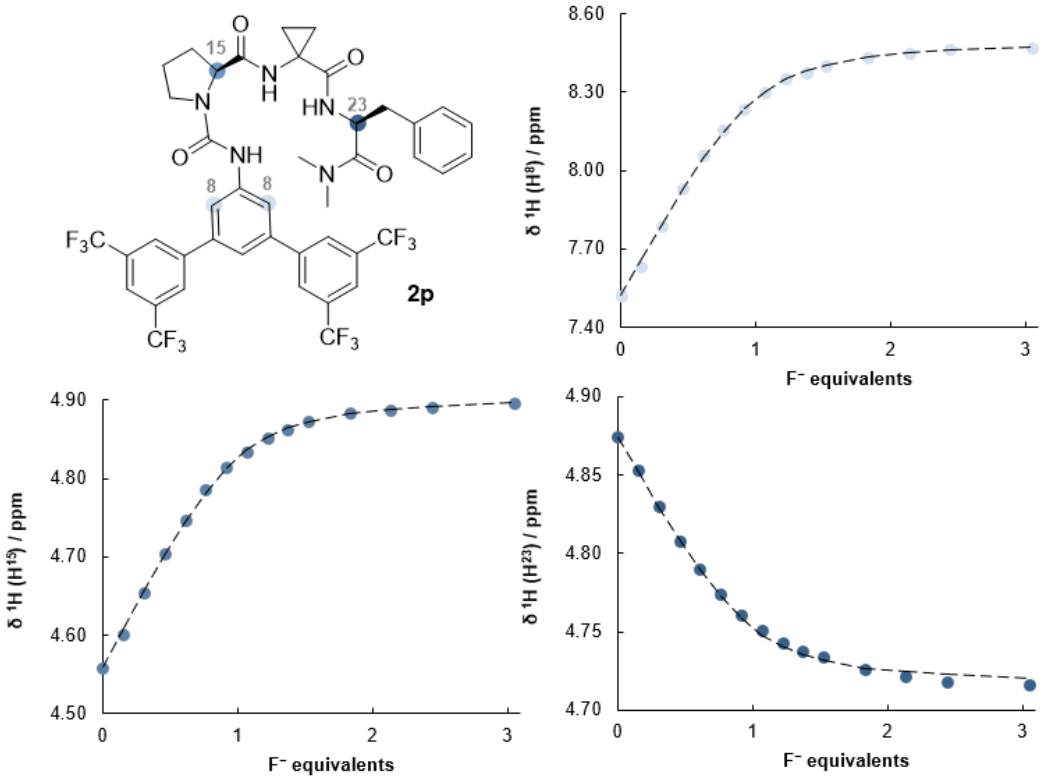

Figure 5.5.35. Titration profiles for selected protons of **2p**; experimental points (colored circles) and fitted function (dashed lines).

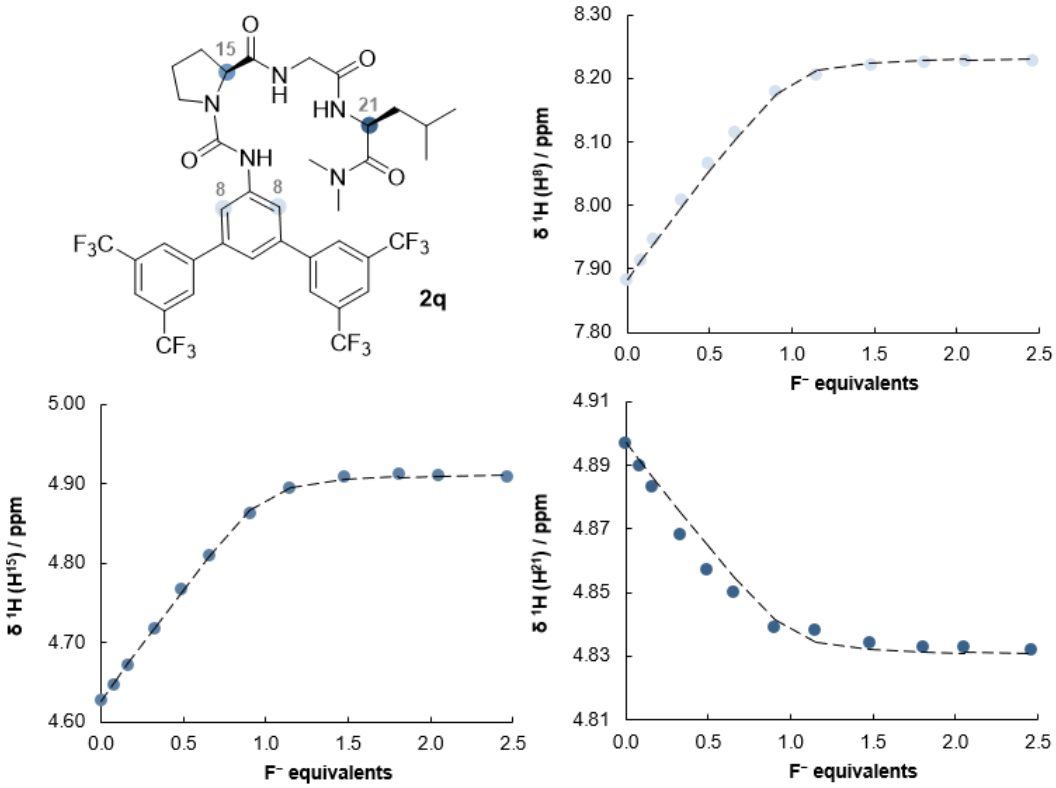

Figure 5.5.36. Titration profiles for selected protons of **2q**; experimental points (colored circles) and fitted function (dashed lines).

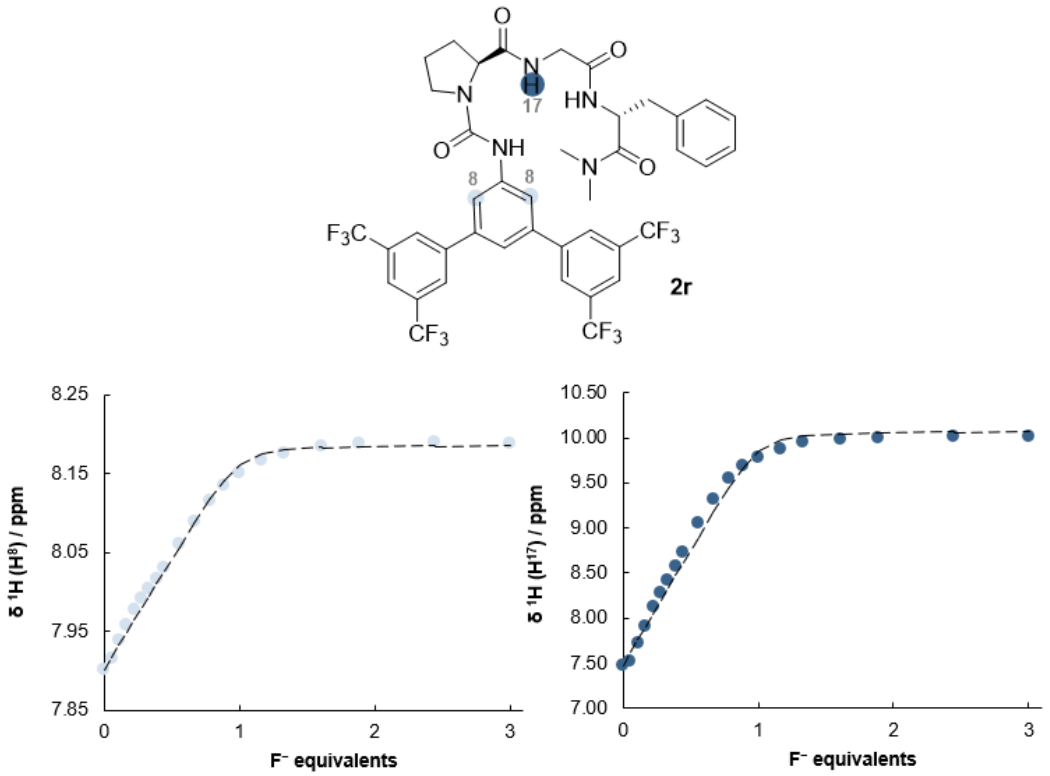

Figure 5.5.37. Titration profiles for selected protons of **2r**; experimental points (colored circles) and fitted function (dashed lines).

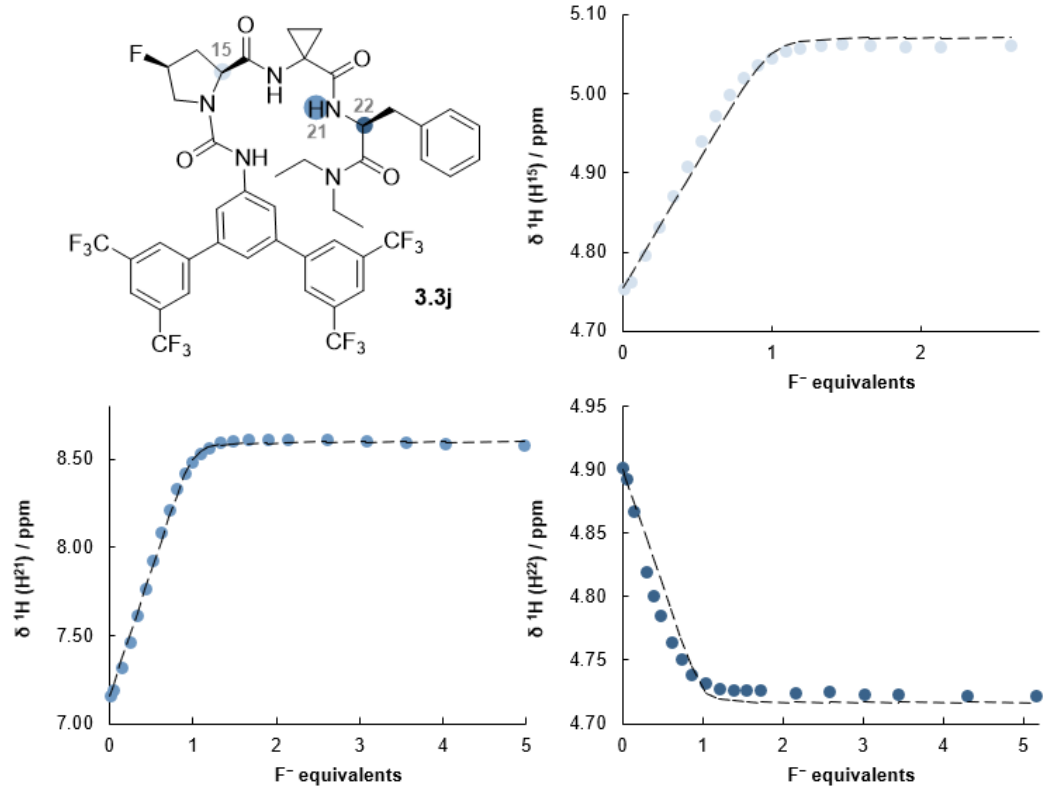

Figure 5.5.38. Titration profiles for selected protons of **3.3j**; experimental points (colored circles) and fitted function (dashed lines).

5.5.4. ^{19}F–^{1}H HOESY NMR for **2d**:TBAF$(H_2O)_3$ and **3.3j**:TBAF$(H_2O)_3$

1D heteronuclear ^{19}F–^{1}H nOe experiments, utilising ^{19}F inversion and ^{1}H detection, were acquired on AVIIHD 500 using a previously developed sequence (*hoesyfhgb1d*)[15] and the parameters reported below (**Table 5.5.5**).

Table 5.5.5. Parameters used to acquire ^{1}H-^{19}F HOESY spectra for **2d**:TBAF$(H_2O)_3$ and **3.3j**:TBAF$(H_2O)_3$.

Parameter	**2d**:TBAF$(H_2O)_3$ complex	**3.3j**:TBAF$(H_2O)_3$ complex
TD	32768 pt	32768 pt
SW	20 ppm	20 ppm
o2p	−114.79 ppm	−110.85 ppm
NS (DS)	54 (4)	1280 (16)
relaxation delay d_1	3 s	3 s
mixing time d_8	800 ms	600 ms

The ^{19}F – ^{1}H HOESY NMR experiment was acquired for **2d**:TBAF$(H_2O)_3$ and **3.3j**:TBAF$(H_2O)_3$ complex prepared using the titration sample preparation procedure, in absence of 4-fluoroanisole. Peak assignment was achieved during NMR titrations described above, by tracking chemical shifts. ^{1}H−^{19}F HOESY spectrum of **2d**:TBAF$(H_2O)_3$ can be found in Section 2.2.2.4.

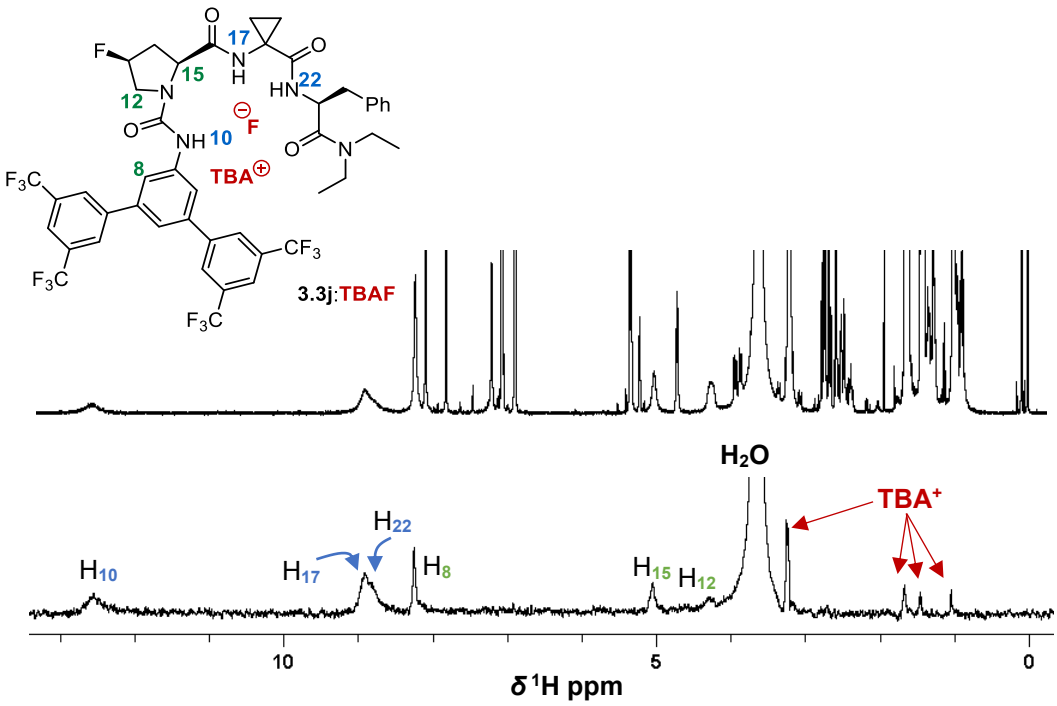

Figure 5.5.39. ^{1}H (*top*) and ^{19}F–^{1}H selective HOESY (δ ^{19}F at −110.85 ppm, τ_m = 600 ms; *bottom*) NMR spectra of **3.3j**:TBAF$(H_2O)_3$ (3.0 mM **3.3j**, 1 equiv. of TBAF$(H_2O)_3$) in CD_2Cl_2 at 298 K.

5.5.5. Peptide-CsF complexes: low temperature NMR

Catalyst (0.0125 mmol), CsF (100 mg/0.66 mmol) and were suspended in 0.5 mL of CD_2Cl_2 (25 mM) inside a sealed NMR tube. The sample was sonicated for 1 hour, after which it was directly taken to the NMR spectrometer. All the NMR spectra were recorded on an AVIII HD 500 MHz equipped with liquid nitrogen heat exchanger allowing for variable temperature studies. The samples can be stored at room temperature without any signs of degradation.

*5.5.5.1. **2b**–CsF complex*

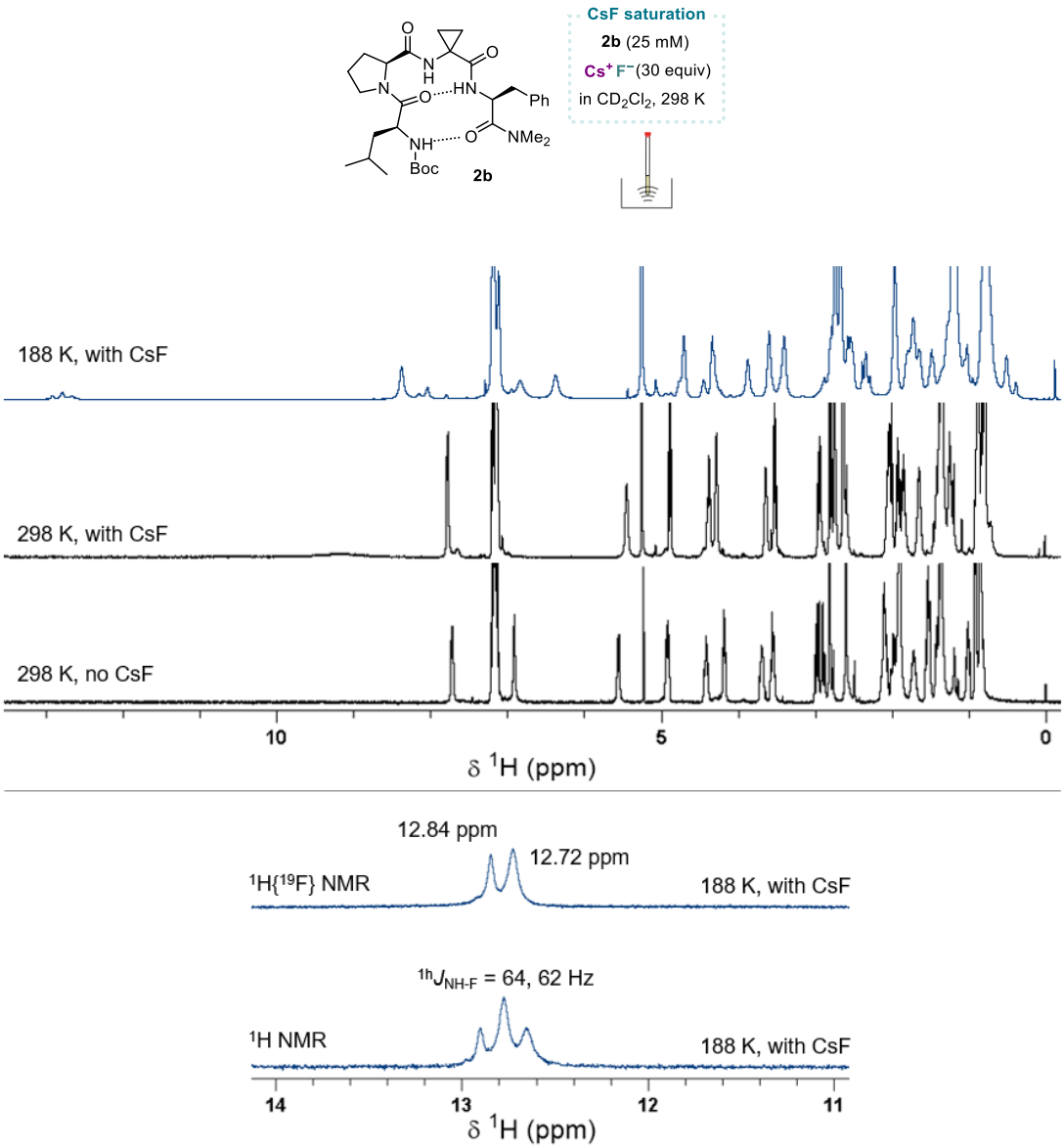

Figure 5.5.40. ^{1}H NMR of **2b** and **2b**:CsF at 298 K and 188 K (*top*), and ^{1}H{^{19}F} NMR 14–12 ppm expanded region of **2b**:CsF at 188 K (*bottom*). For decoupling, δ ^{19}F (o2p) selected at −80 ppm.

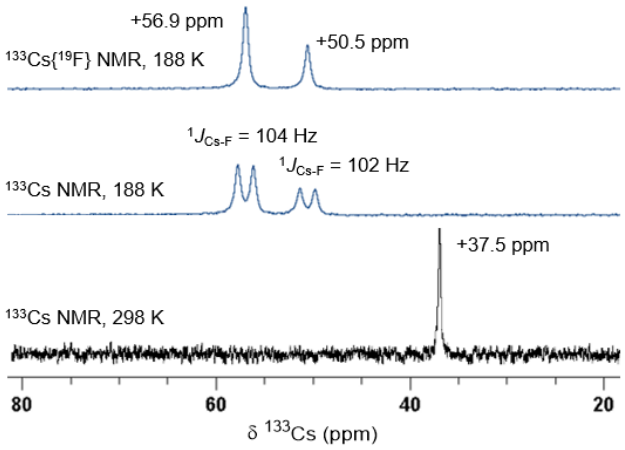

Figure 5.5.41. ^{133}Cs and ^{133}Cs{^{19}F} NMR of **2b**:CsF at 188 K and 298 K. ^{133}C{^{19}F} was achieved using GARP decoupling[28], δ ^{19}F (o2p) selected at −80 ppm.

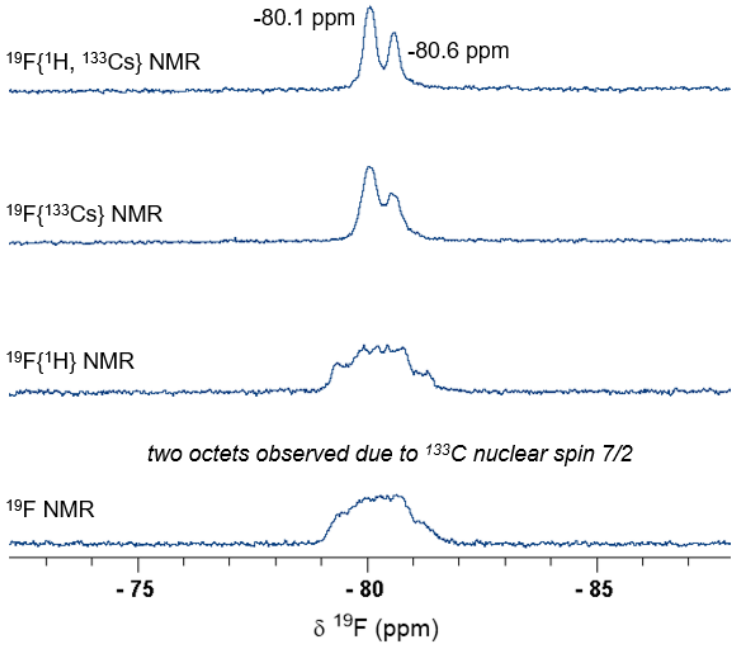

Figure 5.5.42. ^{19}F NMR with and without ^{1}H/^{133}Cs decoupling of **2b**:CsF (188 K). For ^{133}Cs (o2p = 53.6 ppm) - continuous-wave decoupling, for ^{1}H (o2p/o3p = 6.175 ppm) - circularly polarised decoupling.

5.5.5.2. *2c–CsF and 2d–CsF complexes*

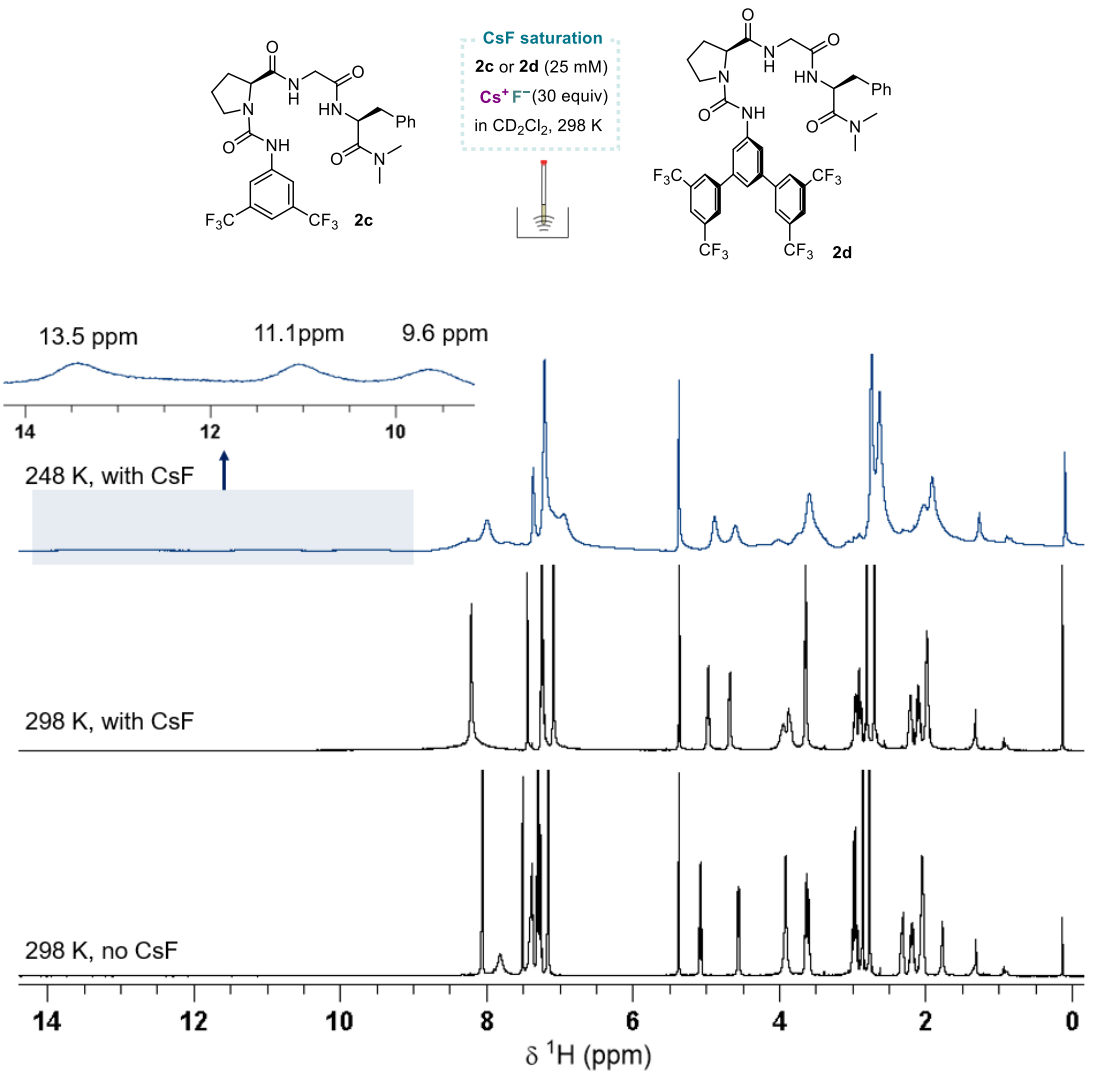

Figure 5.5.43. ^{1}H NMR of **2c** and **2c**:CsF at 298 K and 248 K.

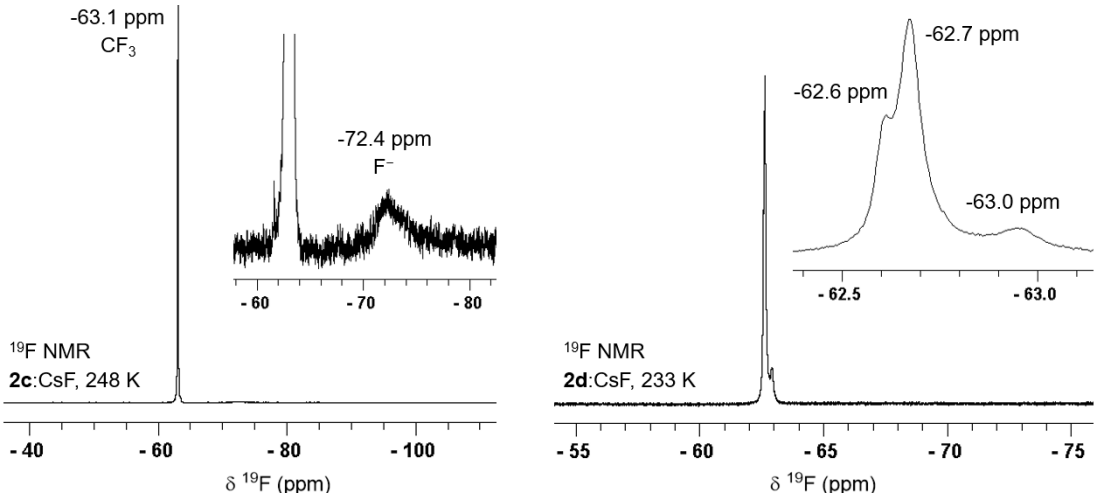

Figure 5.5.44. ^{19}F NMR spectra of **2c**:CsF at 248 K and **2d**:CsF at 233 K.

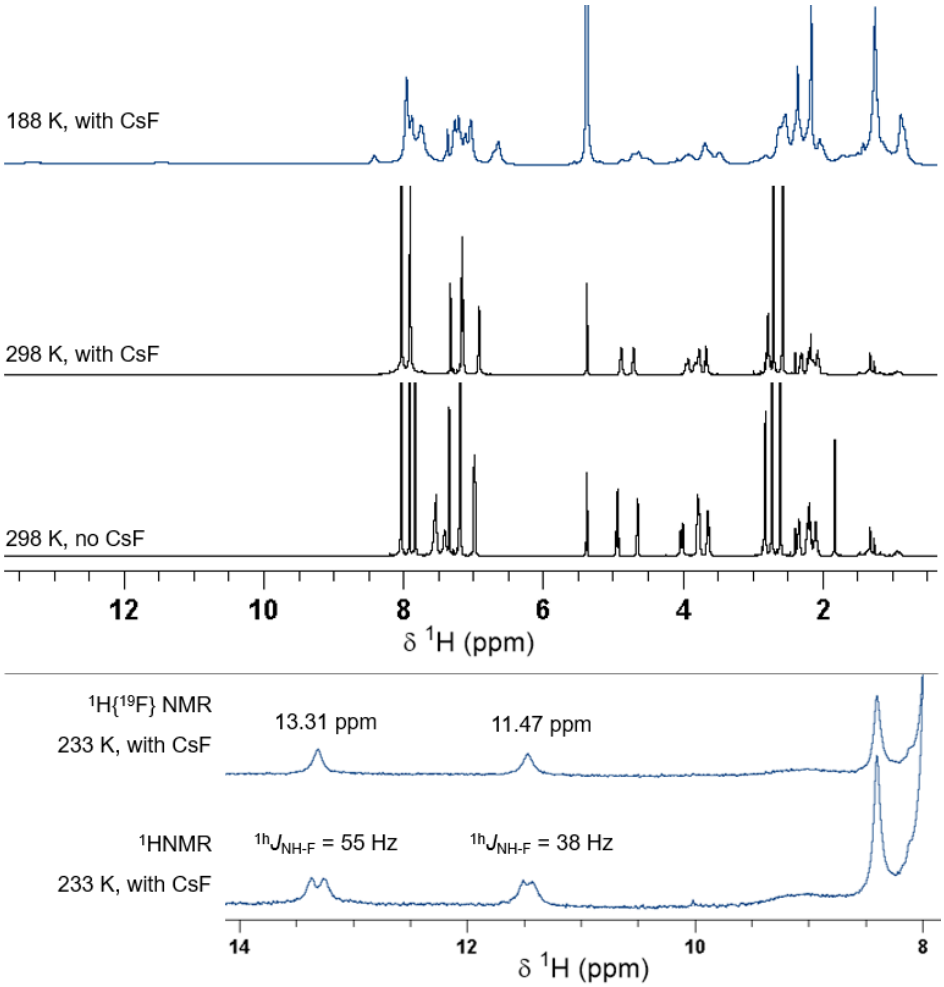

Figure 5.5.45. ^{1}H NMR spectra of **2d** and **2d**:CsF at 298 K and 233 K (*top*), and ^{1}H{^{19}F} NMR 14–8 ppm expanded region of **2d**:CsF at 233 K (*bottom*). For decoupling, δ ^{19}F (o2p) selected at −65 ppm.

5.5.5.3. *2k, 2l, 2i and 2h complexation with CsF*

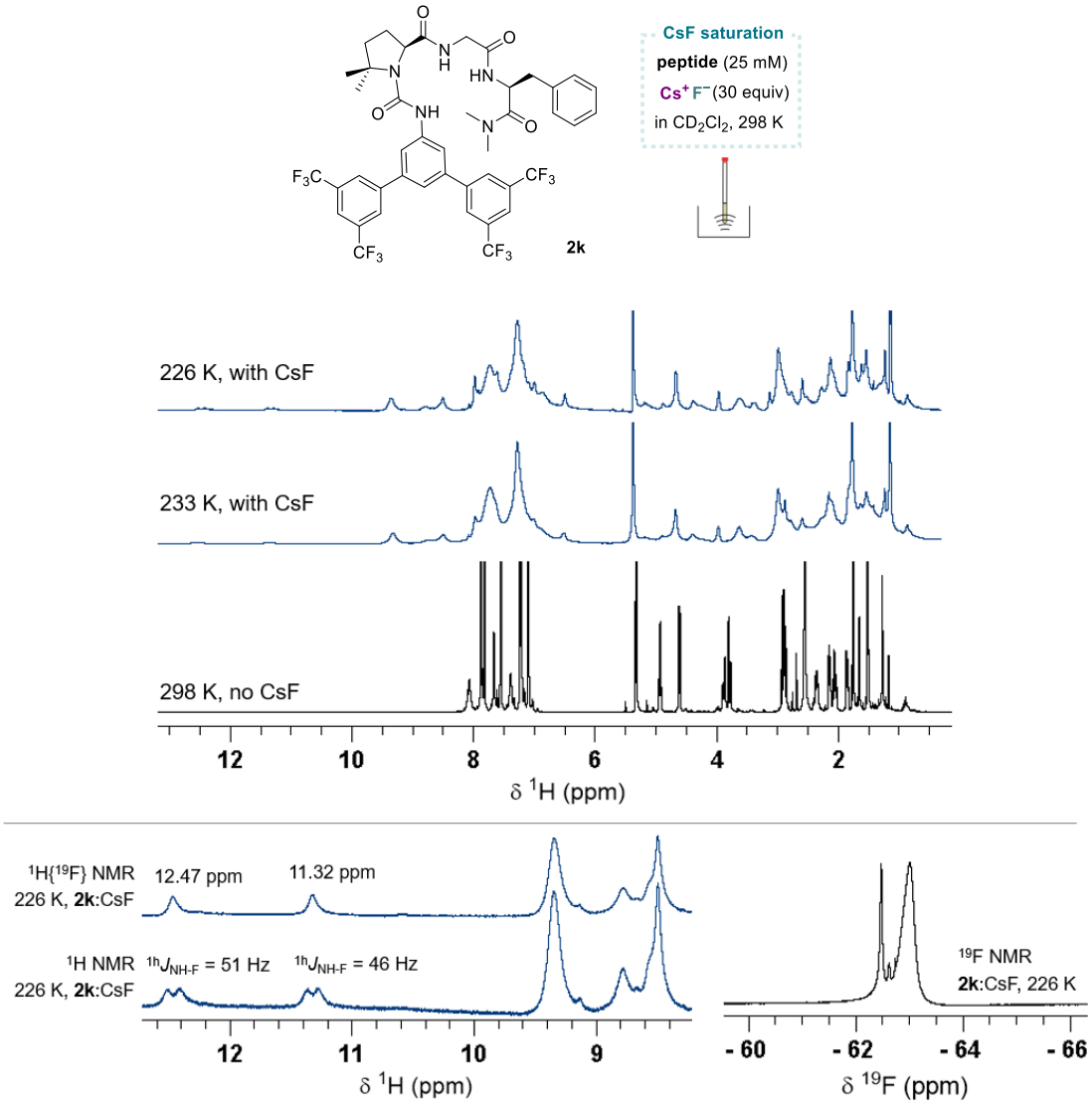

Figure 5.5.46. ^{1}H NMR spectra of **2k** and **2k**:CsF at varying temperatures (*top*).^{19}F NMR spectra of CsF:**2k** and ^{1}H{^{19}F}, ^{1}H NMR 13–8 ppm expanded region of **2k**:CsF spectra at 226 K (*bottom*). For decoupling, δ ^{19}F (o2p) selected at −60 ppm.

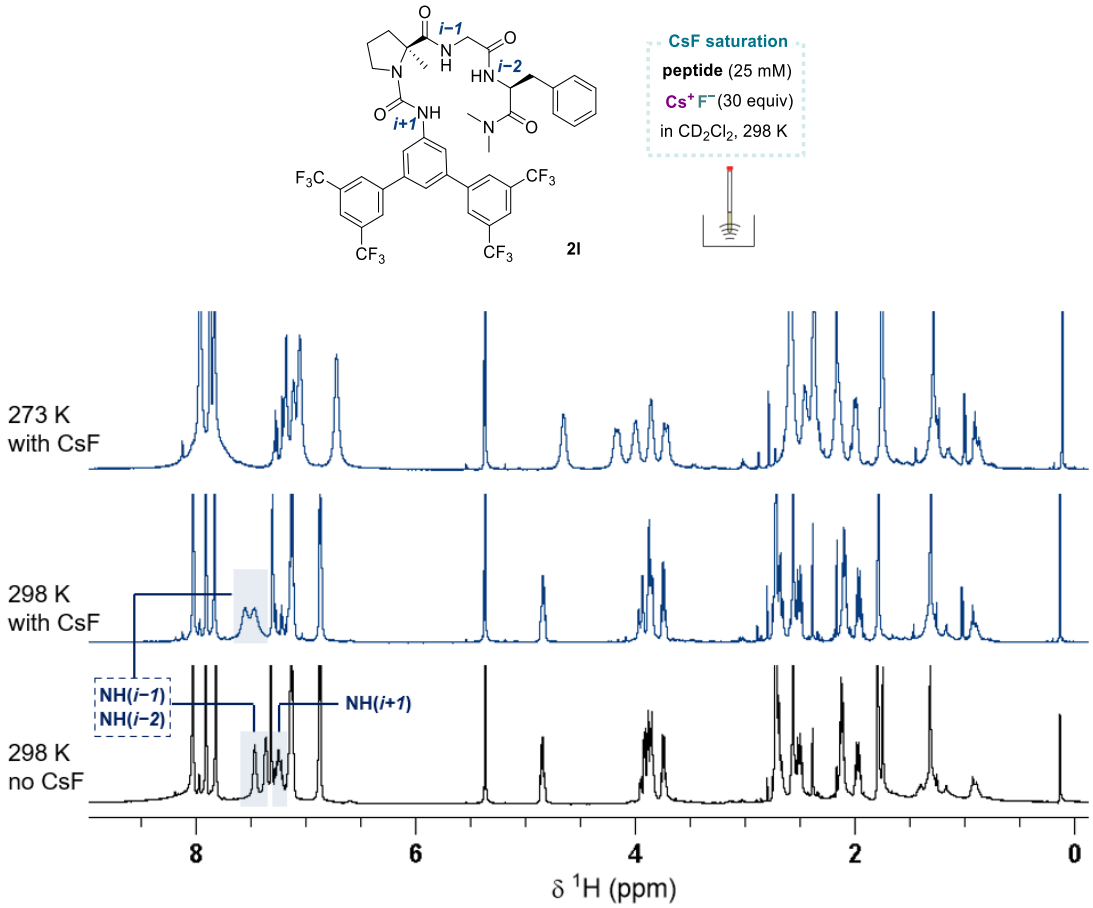

Figure 5.5.47. ^{1}H NMR spectra of **2l** and **2l**:CsF at 298 K and 273 K.

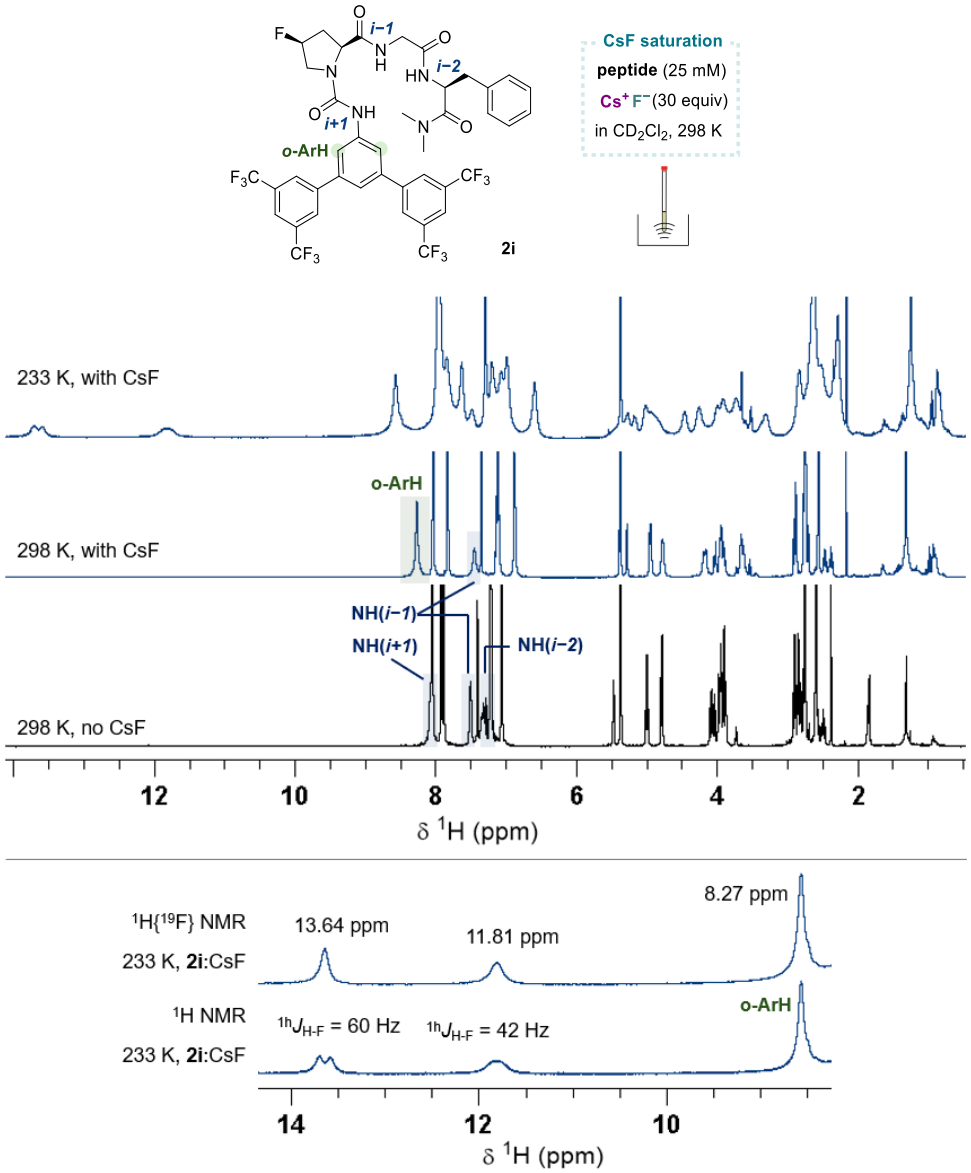

Figure 5.5.48. ^{1}H NMR spectra of **2i** and **2i**:CsF at varying temperatures (*top*). ^{1}H{^{19}F}, ^{1}H NMR 14–8 ppm expanded region of **2i**:CsF at 233 K (*bottom*). For decoupling, δ ^{19}F (o2p) selected at −63 ppm.

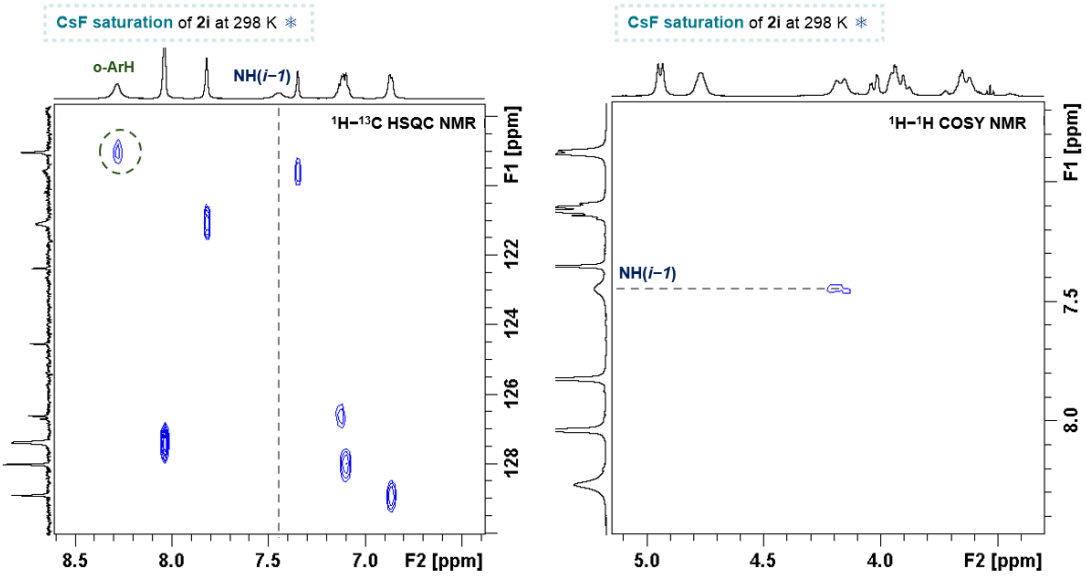

Figure 5.5.49. Expansion of relevant region for 2D ^{1}H-^{13}C HSQC and ^{1}H-^{1}H COSY spectra of **2i**:CsF complex at 298 K in CD_2Cl_2 (25 mM).

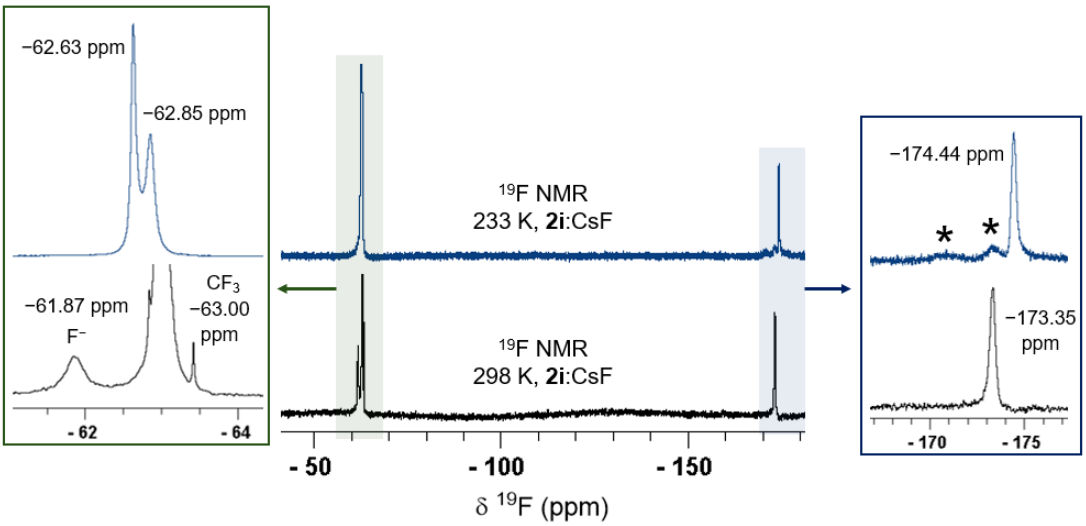

Figure 5.5.50. ^{19}F NMR spectra of **2i**:CsF at 233 K and 298 K.

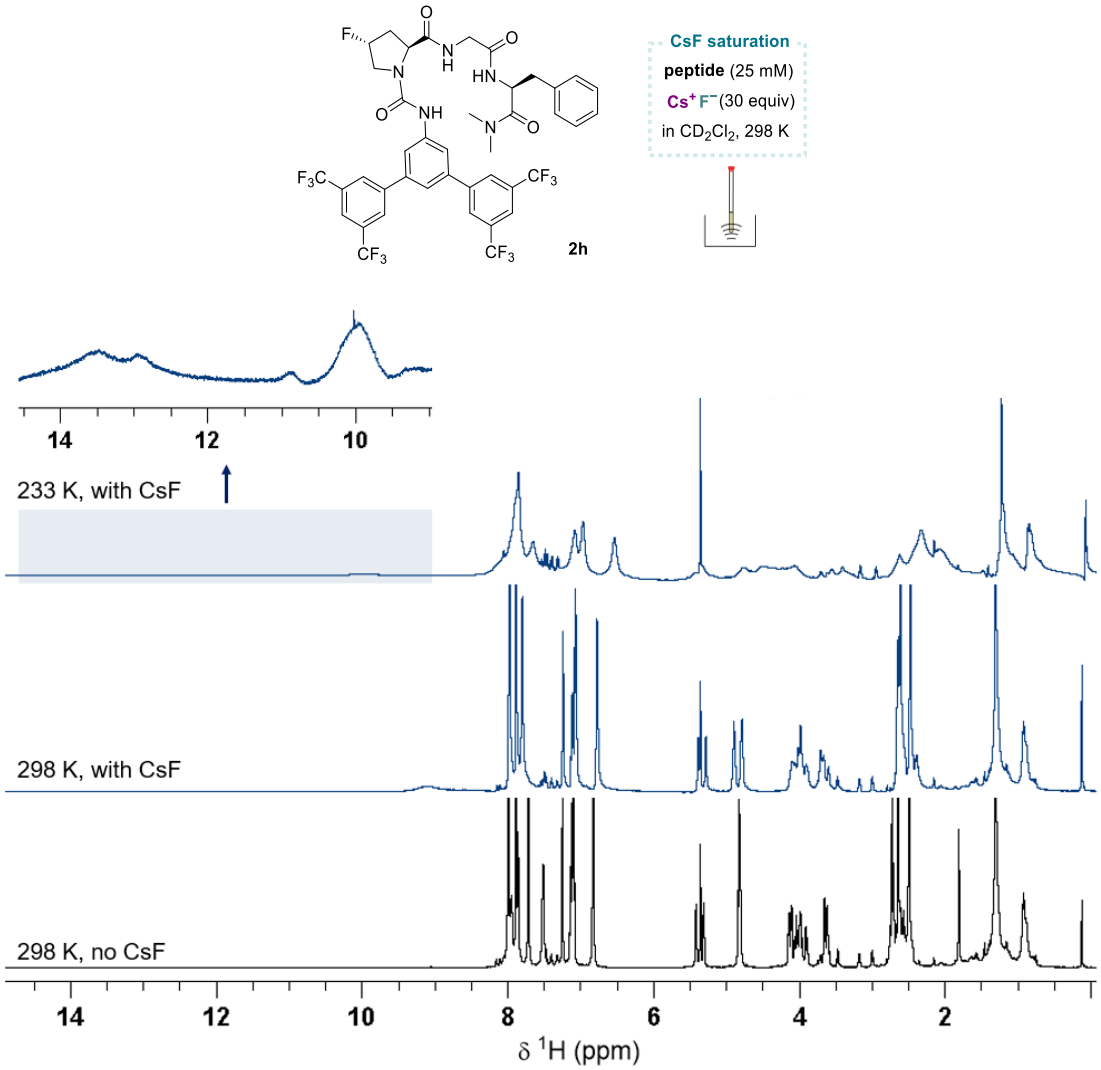

Figure 5.5.51. ^{1}H NMR of **2h** and **2h**:CsF at 298 K and 233 K.

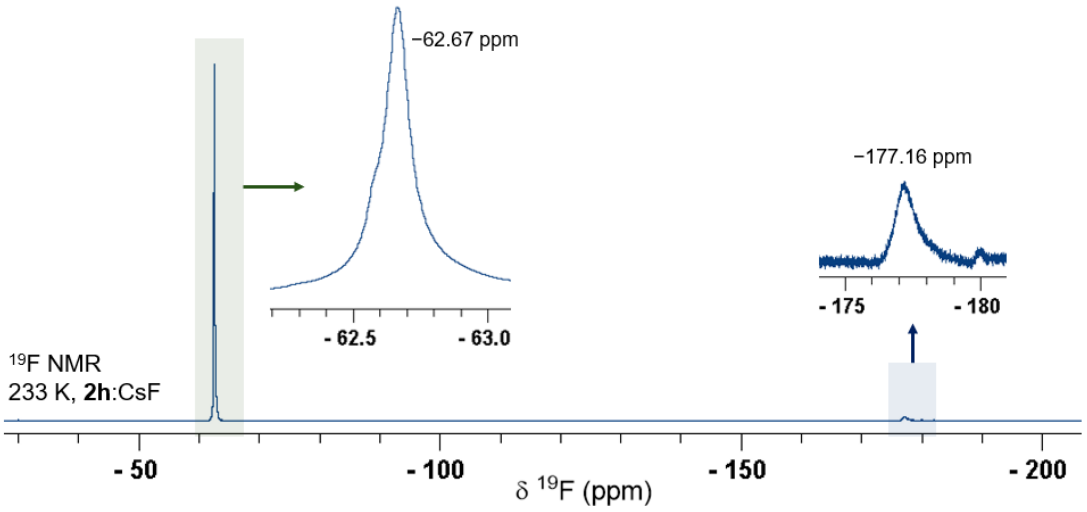

Figure 5.5.52. ^{19}F NMR spectra of **2h**:CsF at 233 K.

5.5.5.4. ***3.3j***–*CsF complex*

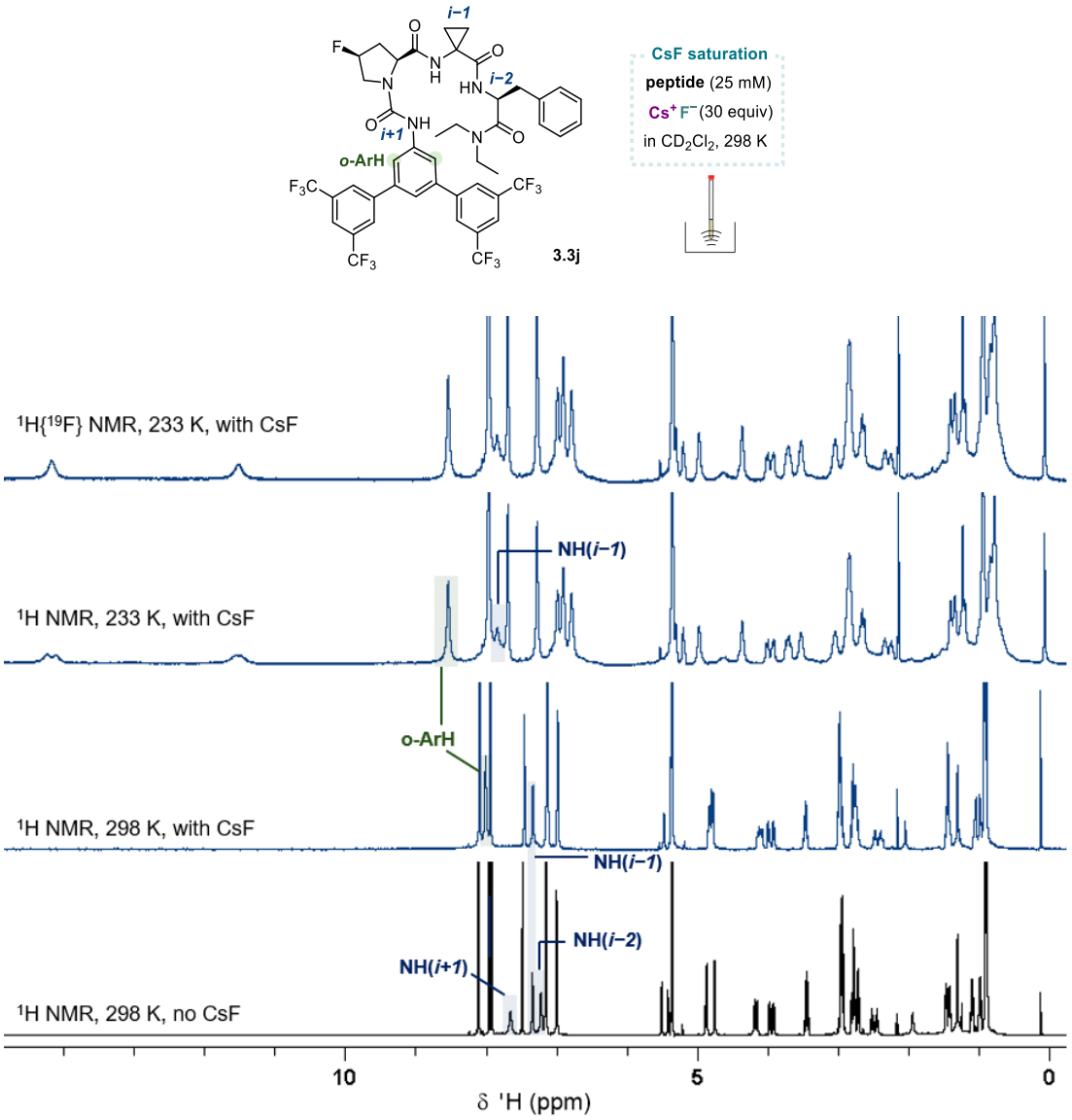

Figure 5.5.53. ^{1}H and $^{1}H\{^{19}F\}$NMR spectra of **3.3j** and **3.3j**:CsF at 298 K and 233 K. For decoupling, δ ^{19}F (o2p) selected at −63 ppm.

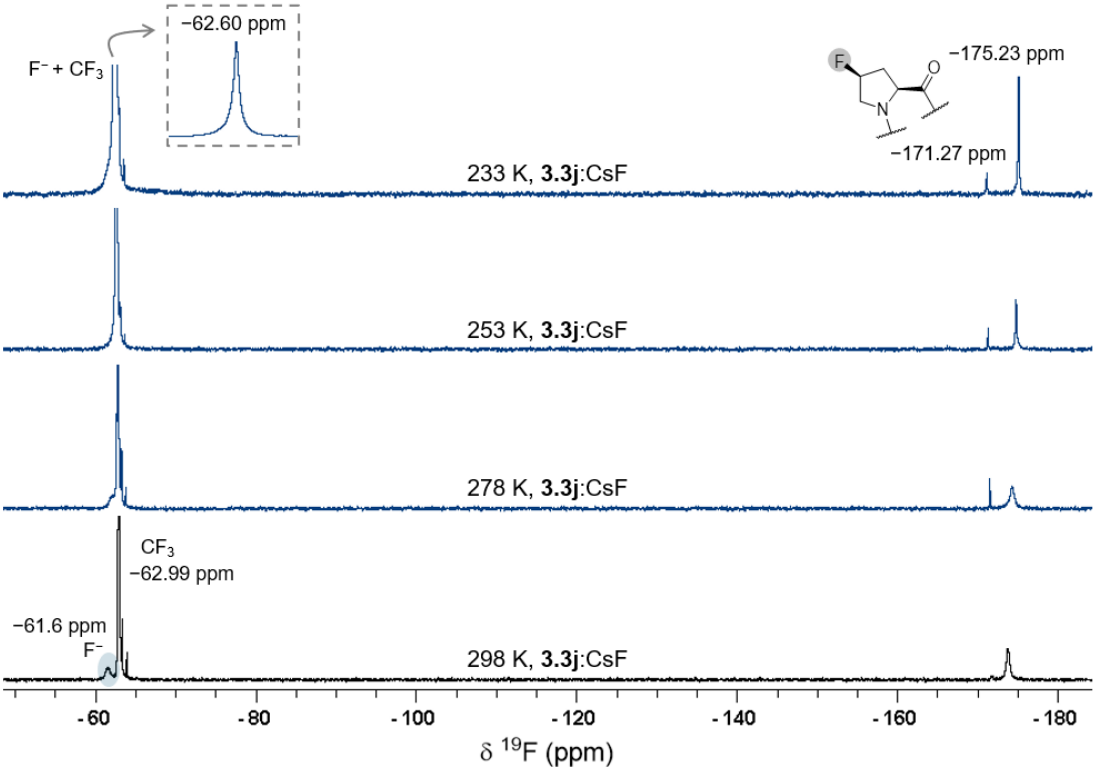

Figure 5.5.54. $^{19}F\{^{1}H\}$ NMR of **3.3j**:CsF at 298–233 K.

For ^{133}Cs NMR experiments parameters were set according to **Table 5.5.6** in the section below.

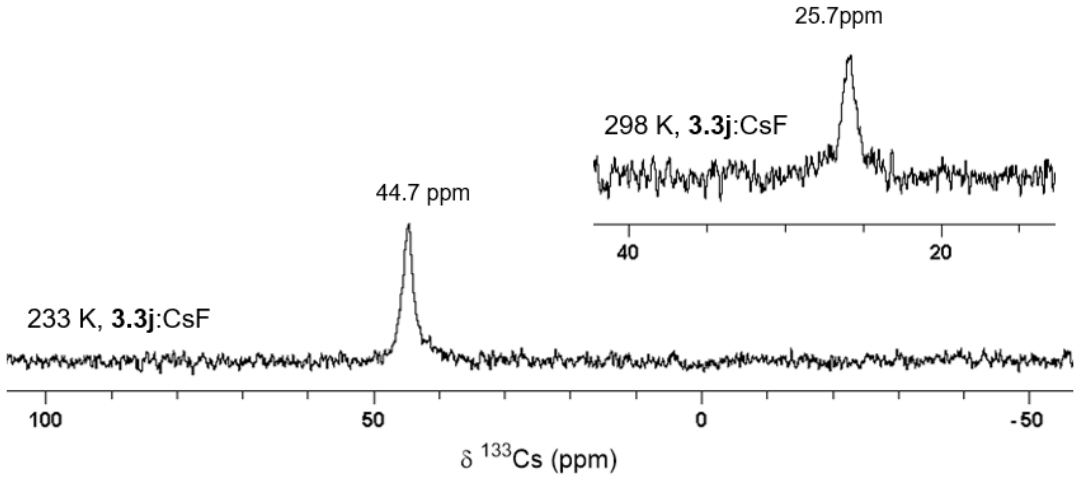

Figure 5.5.55. ^{133}Cs NMR of **3.3j**:CsF at 298 and 233 K.

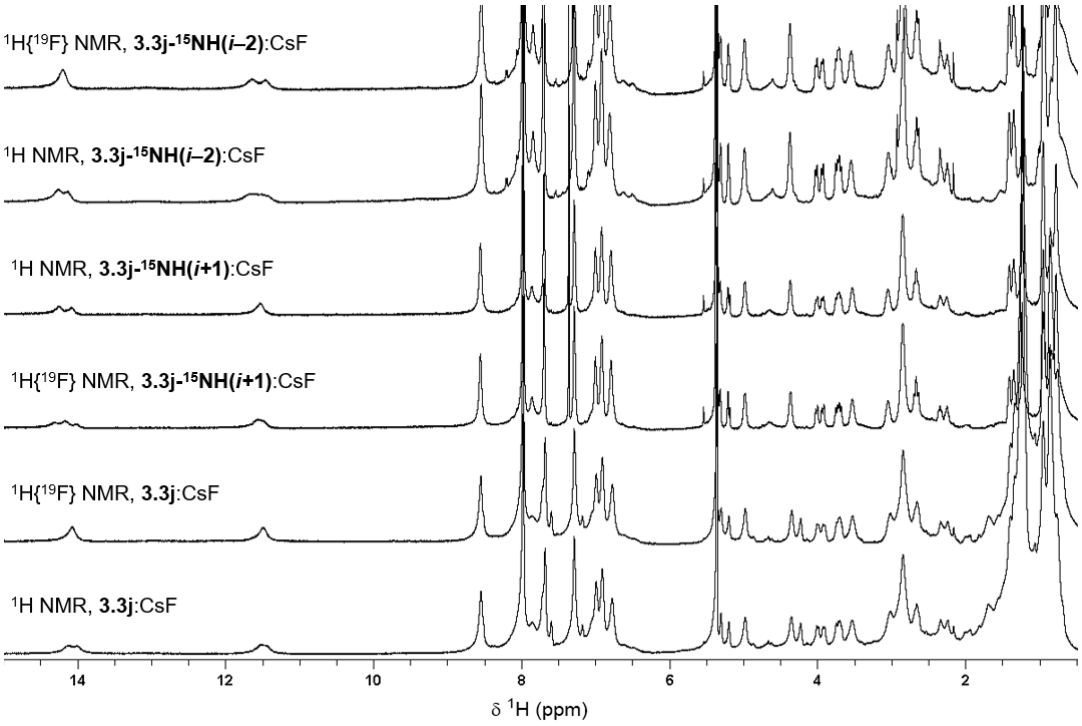

Figure 5.5.56. ^{1}H and ^{1}H{^{19}F} NMR of **3.3j**, **3.3j-^{15}NH(*i*–2)**, **3.3j-^{15}NH(*i*+1)**:CsF at 233 K. For decoupling, δ ^{19}F (o2p) selected at −60 ppm.

5.5.6. $CsBAr^{F}_{4}$ complexation

5.5.6.1. Preparation of cesium tetrakis[3,5-bis(trifluoromethyl)phenyl]borate

The $CsBAr^{F}_{4}$ salt was prepared by Dr. Christopher Goult modifying published procedure by Vidal-Ferran et al.[29] To a hot (90 °C), aqueous solution of $NaBAr^{F}_{4}$ (300 mg, 0.34 mmol, 1.0 equiv.) in H_2O (7 mL), CsCl (362 mg, 2.03 mmol, 6.0 equiv.) was added. A white precipitate was immediately formed. The suspension was heated and rapidly stirred for 1 h before being allowed to cool to room temperature. Crude $CsBAr^{F}_{4}$ was obtained by vacuum filtration before being washed with H_2O (3 x 10 mL) and being allowed to dry. $CsBAr^{F}_{4}$ was recrystallised from a minimum amount of hot THF. Title compound was obtained as a white powder (275 mg, 82%).

^{1}H NMR (400 MHz, CD_3CN): δ 7.70−7.67 (m, 12H) ppm; **^{19}F NMR** (377 MHz, CD_3CN): δ −63.26 ppm; **^{13}C NMR** (126 MHz, CD_3CN): δ 162.6 (q, $^{1}J_{BC}$ = 50 Hz), 134.7 (br q, $^{2}J_{BC}$ = 2 Hz), 129.9 (qq, $^{3}J_{BC}$ = 3 Hz, $^{2}J_{FC}$ = 32 Hz), 125.5 (q, $^{1}J_{FC}$ = 271 Hz), 118.7 (sept (or qq), $^{3}J_{FC}$ = 4 Hz) ppm. ^{13}C spectrum *J*-coupling corroborated via $^{13}C\{^{1}H, ^{19}F\}$ (o1p = −63.26) spectrum. Spectroscopic data consistent with literature reported data.[29]

5.5.6.2. NMR investigations

The NMR samples were prepared as described in Section 5.5.5, but with $CsBAr^{F}_{4}$ (5 equiv., 50 mg, 0.06 mmol), instead of CsF. The data were collected on an AVIII HD 500 at 233 K using the following parameters in **Table 5.5.6**.

Table 5.5.6. Parameters for ^{133}Cs NMR spectra acquisition in CD_2Cl_2.

Parameter	Value
TD	65536 pt
SW	300 ppm
o1p	50 ppm
NS (DS)	64 (4)
relaxation delay d_1	2 s

At 233 K (**Figure 5.5.57**, *top*) or at 298 K $CsBAr^{F}_{4}$ was not soluble in CD_2Cl_2. The addition of catalyst 3.3j showcased a phase-transfer of Cs^+ as indicated by ^{133}C NMR (**Figure 5.5.57**, *bottom*).

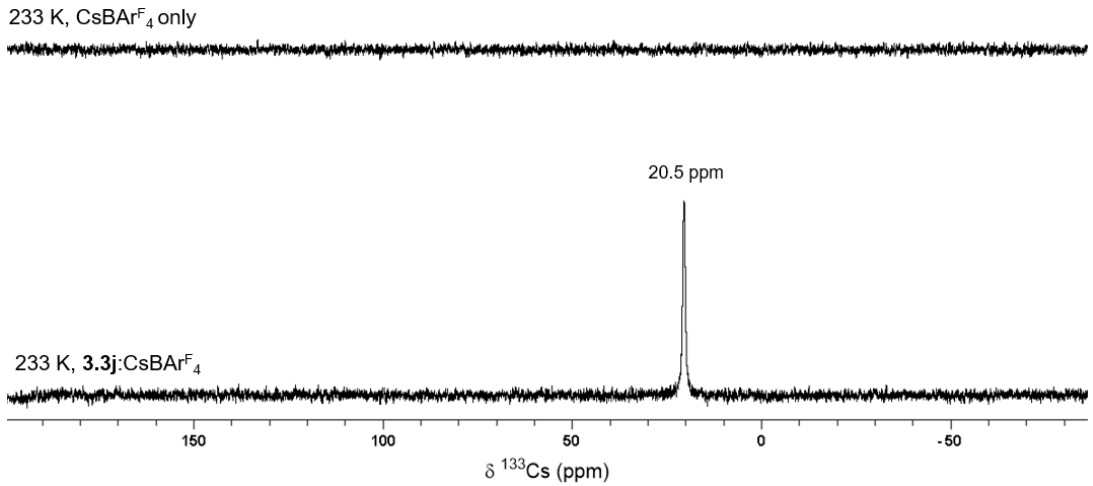

Figure 5.5.57. ^{133}Cs NMR of $CsBAr^{F}_{4}$ (*top*) and **3.3j:**$CsBAr^{F}_{4}$ (*bottom*); both in CD_2Cl_2 at 233 K.

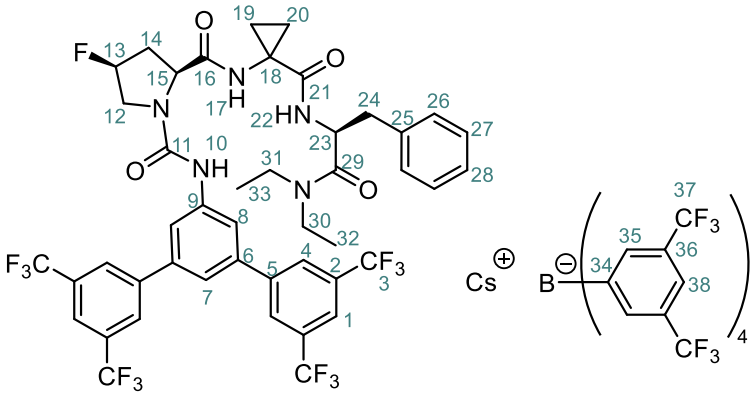

Scheme 5.5.20. Structure and numbering of **3.3j**:CsBAr$^{F}_{4}$ complex.

^{1}H (^{1}H-^{1}H COSY, ^{1}H-^{13}C multiplicity-edited HSQC, ^{1}H-^{1}H NOESY) NMR (600 MHz, 298 K, CD_2Cl_2): δ 7.96 (br s, 4H, H^{4}), 7.95 (br s, 2H, H^{1}), 7.83 (d, J_{HH} = 1.5 Hz, 2H, H^{8}), 7.78 (br s, 8H, H^{35}), 7.60 (br s, 4H, H^{38}), 7.40 (t, J_{HH} = 1.5 Hz, 1H, H^{7}), 7.25 (br d, J_{HH} = 6.3 Hz, 1H, H^{22}), 7.13 (t, J_{HH} = 7.5 Hz, 1H, H^{28}), 7.03 (t, J_{HH} = 7.7 Hz, 2H, H^{27}), 6.97 (br s, 2H, H^{17}+H^{10}), 6.72 (d, J_{HH} = 7.4 Hz, 2H, H^{26}), 5.46 (br d, J_{HF} = 51.9 Hz, 1H, H^{13}), 4.55 (dt, J_{HH} = 8.5, 6.3 Hz, 1H, H^{23}), 4.75 (dd, J_{HH} = 10.9, 1.9 Hz, 1H, H^{15}), 4.12 (ddd, J_{HF} = 19.9 Hz, J_{HH} = 10.8, 1.4 Hz, 1H, H^{12a}), 3.82 (ddd, J_{HF} = 35.9 Hz, J_{HH} = 10.8, 2.7 Hz, 1H, H^{12b}), 3.49 (sx, J_{HH} = 7.1 Hz, 1H, H^{31a}), 2.93–2.85 (m, 3H, H^{31b}+H^{30}), 2.61 (dddd, J_{HF} = 43.8 Hz, J_{HH} = 16.1, 10.9, 3.8 Hz, 1H, H^{14b}), 2.58 (dd, J_{HH} = 13.3, 8.8 Hz, 1H, H^{24a}), 2.48 (dd, J_{HH} = 13.3, 5.8 Hz, 1H, H^{24b}), 2.43 (br t, J_{HF} = J_{HH} = 16.9 Hz, 1H, H^{14a}), 1.59 (ddd, J_{HH} = 10.4, 7.9, 4.3 Hz, 1H, H^{19a}), 1.43 (ddd, J_{HH} = 10.2, 7.9, 4.8 Hz, 1H, H^{20a}), 1.12 (ddd, J_{HH} = 10.4, 8.3, 4.8 Hz, 1H, H^{19b}), 0.96 (ddd, J_{HH} = 10.2, 8.3, 4.3 Hz, 1H, H^{20b}), 0.93 (t, J_{HH} = 7.1 Hz, 3H, H^{33}), 0.88 (t, J_{HH} = 7.3 Hz, 3H, H^{32}) ppm.

^{13}C (^{1}H-^{13}C multiplicity-edited HSQC, ^{1}H-^{13}C HMBC) NMR (151 MHz, 298 K, CD_2Cl_2): δ 173.6 (C^{21}), 171.2 (C^{29}), 170.7 (C^{16}), 161.7 (q, $^{1}J_{BC}$ = 50 Hz, C^{34}), 155.2 (C^{11}), 141.9 (C^{5}), 140.2 (C^{6}), 138.9 (C^{9}), 135.8 (C^{25}), 134.8 (C^{35}), 132.1 (q, J_{CF} = 33 Hz, C^{2}), 128.8 (qq, $^{2}J_{FC}$ = 31 Hz, $^{3}J_{BC}$ = 2 Hz, C^{36}), 128.9 (C^{26}), 128.2 (C^{27}), 127.3 (br, C^{4}), 127.1 (C^{28}), 124.5 (q, J_{CF} = 273 Hz, C^{37}), 123.3 (q, J_{CF} = 273 Hz, C^{3}), 122.6 (C^{7}), 121.58 (sept, J_{CF} = 4 Hz, C^{1}), 120.4 (C^{8}), 117.6 (sept, J_{CF} = 4 Hz, C^{38}), 93.1 (d, J_{CF} = 177 Hz, C^{13}), 61.7 (C^{15}), 53.1 (C^{12}, *overlapping with solvent peak*), 51.8 (C^{23}), 41.6 (C^{31}), 40.6 (C^{30}), 38.5 (C^{24}), 35.3 (d, J_{CF} = 21 Hz, C^{14}), 34.0 (C^{18}), 17.3 (C^{20}), 17.0 (C^{19}), 12.9 (C^{33}), 12.3 (C^{32}) ppm.

5.6. Computational methods

Computational studies were conducted by Dr. Zijun Chen, Dr. Mihai Popescu, and Professor Robert Paton.

Geometry optimisation and vibrational frequency calculations were performed using *Gaussian 16, revision C.01* at the M06-L-D3/def2-SVP;def2-TZVPPD[Cs^+, F^-] level of theory, where the double-zeta def2-SVP basis set was used for all atoms, except for Cs^+ and F^- where the triple-zeta def2-TZVPPD basis set was used.[30] Solvation in dichloromethane was modelled using the universal solvation model (SMD).[31] Ground state geometries were identified by the absence of imaginary frequency vibrational modes. Single-point energy calculations were performed using *ORCA 6.0.0* software package at the M06-2X-D3/def2-TZVP; def2-TZVPPD[Cs^+, F^-] level of theory, where the triple-zeta def2-TZVP basis set was used for all atoms except for Cs^+ and F^- where the triple-zeta def2-TZVPPD was applied.[32] All bond lengths are reported in Angstroms (Å). Thermochemistry was evaluated at 298.15 K and a concentration of 0.25 $mol \cdot L^{-1}$ using Paton's *GoodVibes* script.[33] The entropic contribution of low vibrational modes was corrected using a frequency cutoff value of 100 cm^{-1}.[34]

Conformational sampling was performed prior to geometry optimisation of key structures using a Global Optimizer Algorithm (GOAT) featured in *ORCA 6.0.0*, based on the GFN2-XTB method.[35] Conformational sampling was performed in dichloromethane using the extended conductor-like polarisable continuum model (CPCM-X).[36] A 6 $kcal \cdot mol^{-1}$ energy window was applied during sampling.

A total of 487 unique conformers of the **3.3i**:CsF complex were identified after optimisation, ranging from tridentate H-bonding mode to no chelation of fluoride. Analysis of the NH···F⁻ bond distance revealed a large fraction of geometries with NH···F⁻ ≤ 2.0 Å, consistent with effective H-bonding interactions (**Figure 5.6.1**).

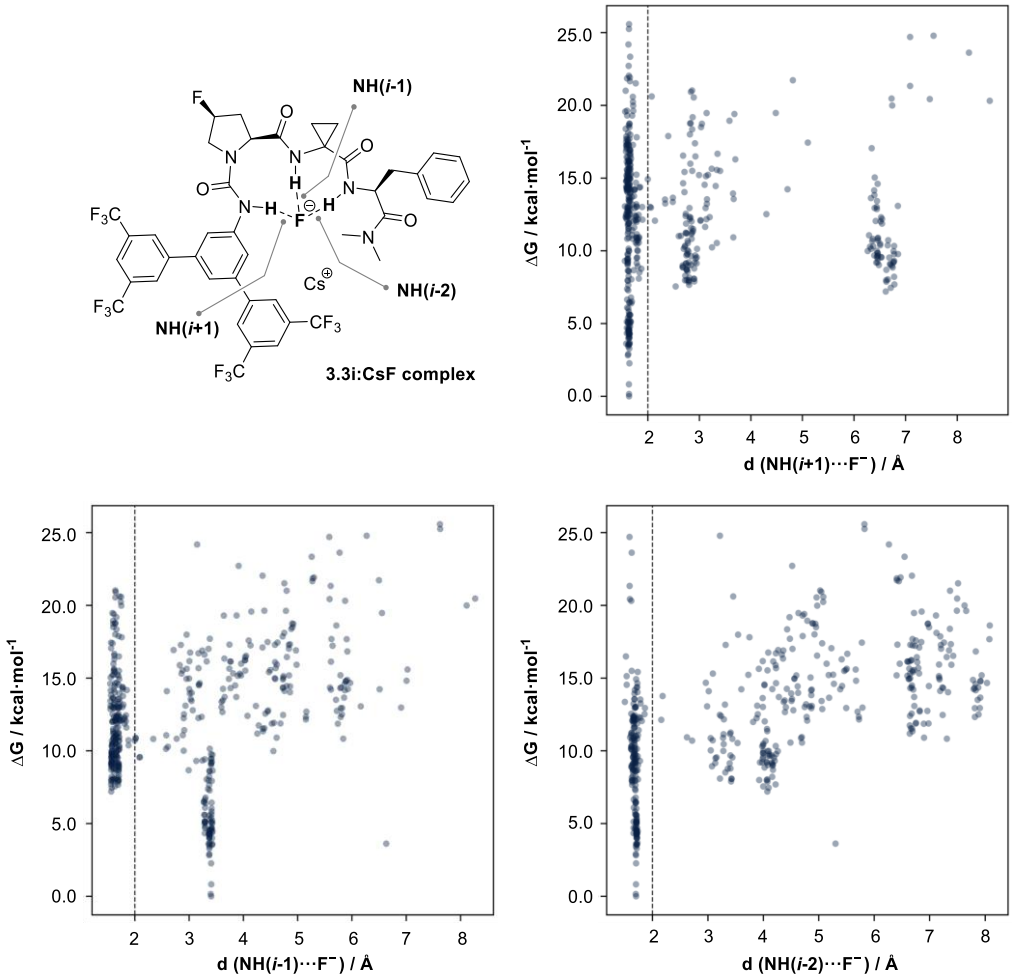

Figure 5.6.1. Relative Gibbs free energies plotted against NH–F⁻ bond lengths.

5.7. Crystallographic information

The crystallographic data were obtained in collaboration with Jessica Sellar (JS), Calum Patel (CP) and Dr. Agamemnon Crumpton (AC) and their contributions are included below.

Compounds **2a**, **2b**, **2c**, **2s** and **2i** were crystalised via vapour diffusion method using EtOAc/pentane (for **2a** and **2b**), $CHCl_3$/heptane (for **2c**, by JS), CH_2Cl_2/hexane (for **2s**) and 1,2-dichloroethane/pentane (for **2i**) solvent systems. Data for crystals **2a** and **2b** were collected at a wavelength of 1.54184 Å using a Rigaku XtaLAB Synergy-R DW diffractometer with a HyPix-Arc 150 detector, while data for **2c** and **2s** were collected at λ = 1.54184 Å using a Rigaku XtaLAB SuperNovae A diffractometer with an Atlas CCD (charge-coupled device) detector (by CP). Crystals were selected under perfluoropolyether oil, mounted on MiTeGen Micromount loop and quench-cooled using an Oxford Cryosystems open flow N_2 cooling device.[37]

Single crystal diffraction data for **2i** was collected at beamline I19, Diamond Light Source (by AC).[38] The data were collected using Zr K-edge radiation (λ = 0.6889 Å) with a Pilatus 2M detector. The crystals were mounted on MiTeGen micromounts using a paratone oil, where they were cooled for data collection by a Cryostream nitrogen-gas stream. Crystal sustained significant beam damage limiting experiment to two runs.

All data were reduced using the CrysAlisPro package,[39] including unit cell parameter refinement and inter-frame scaling (which was carried out using SCALE3 ABSPACK within CrysAlisPro). Equivalent reflections were merged, and corrected; crystal faces were indexed and used to apply an absorption and illuminated volume correction with the CrysAlisPro suite. Structures were solved *ab initio* from the integrated intensities using SuperFlip[40] and refined using full-matrix least-squares on F2 using CRYSTALS.[41] The Flack parameter was refined to determine the enantiomer.[42] Hydrogen atoms were included in the refinement with soft restraints.[43] Structures for **2c** and **2s** were solved by CP and AC, and for **2i** by AC. Selected details of data collection are given in **Table 5.7.1.**

Table 5.7.1. Selected X-ray data collection and refinement parameters.

	2b	**2a**	**2c**	**2s**	**2i**
Formula	$C_{31}H_{47}N_5O_6$	$C_{31}H_{47}N_5O_6$	$(C_{27}H_{29}F_6N_5O_4)_2$ $(H_2O)_6$	$C_{45}H_{37}F_{12}N_5O_4$ C_6H_{14}	$(C_{41}H_{34}F_{13}N_5O_4)_2$ $C_2H_4Cl_2$
Mw (g mol^{-1})	585.74	585.74	1311.20	1025.96	1914.41
Cell system	monoclinic	orthorhombic	monoclinic	tetragonal	monoclinic
Space group	$P2_1$	$P2_12_12_1$	$I2_1$	$P4_3$	$P2_1$
a (Å)	10.6739(1)	9.46823(3)	22.5238(9)	16.6079(3)	13.8398(6)
b (Å)	9.4321(1)	10.80840(3)	7.53079(18)	16.6079(3)	18.5943(6)
c (Å)	16.1917(1)	31.10510(9)	36.9807(12)	19.1207(9)	16.6416(6)
α (°)	90	90	90	90	90
β (°)	95.5259(4)	90	104.541(4)	90	92.305(4)
γ (°)	90	90	90	90	90
V (Å^{-3})	1622.56(3)	3183.184(16)	6071.8(4)	5273.9(3)	4279.1(3)
Z	2	4	8	4	2
ϱ_{calc} (g cm^{-3})	1.199	1.222	1.434	1.292	1.486
Radiation, λ (Å)	CuKα (λ = 1.54184)	CuKα (λ = 1.54184)	CuKα (λ = 1.54184)	CuKα (λ = 1.54184)	Synchrotron (λ = 0.6889)
μ (mm^{-1})	0.679	0.692	1.111	0.961	0.180
F(000)	2692	2626	2736	2128	1956
$R_{(int)}$	0.0265	0.0262	0.0658	0.0606	0.0640
Parameters	392	392	1011	901	1334
R_1 (all data /I >2σ(I))	0.0265 /0.0259	0.0262 /0.0256	0.0658 /0.0463	0.0606 /0.0490	0.0640 /0.0406
Ωr$_2$ (all data /I >2σ(I))	0.0687 /0.0682	0.0665 /0.0662	0.1255 /0.1121	0.1348 /0.1239	0.0947 /0.0908
GooF	0.985	1.016	1.032	1.051	0.850
T (K)	100.15	100.15	150.01	150.01	100
Largest diff. peak/hole (e Å^{-3})	0.14/−0.15	0.11/−0.13	0.20/−0.22	0.24/−0.20	0.29/−0.21
Flack	−0.04(9)	0.02(9)	−0.04(9)	−0.03(6)	-0.01(8)

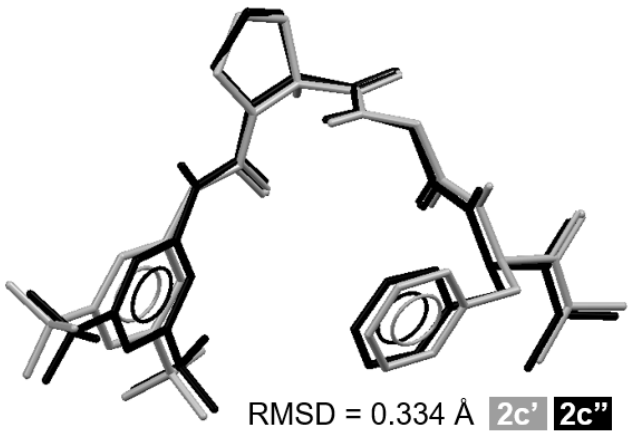

Figure 5.7.1. Overlay of **2c** conformers: **2c'** and **2c"**.

The data that was used to analyse various structural features of peptide crystal structures is provided. Measurements were extracted from the crystallographic information files (.cif) using Mercury 2022.1 CSD[44] and were subsequently tabulated (**Table 5.7.2**).

Table 5.7.2. Structural features of conformers **2a**, **2b**, **2c'**, **2c"**, **2s**, **2i'** and **2i"** extracted from X-ray crystals structures.

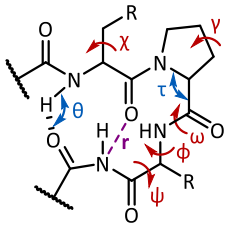

	2a	**2b**	**2c'**	**2c"**
ω(*i*+*1*) (°)	178.68(8)	-176.02(9)	-176.02(9)	n/a
φ(*i*+*1*) (°)	-153.58(9)	-116.3(1)	-116.3(1)	n/a
ψ(*i*+*1*) (°)	74.7(1)	169.5(1)	169.5(1)	175.8(4)
τ(*i*+*1*) (°)	107.63(8)	109.40(9)	109.40(9)	n/a
ω(*i*) (°)	174.78(9)	-169.24(9)	-169.24(9)	-175.4(3)
φ(*i*) (°)	64.8(1)	-58.6(1)	-58.6(1)	-83.7(4)
ψ(*i*) (°)	-125.28(9)	127.5(1)	127.5(1)	-16.2(5)
τ(*i*) (°)	109.96(8)	111.82(9)	111.82(9)	113.8(3)
ω(*i*−*1*) (°)	172.85(9)	-178.1(1)	-178.1(1)	-178.1(4)
φ(*i*−*1*) (°)	-73.1(1)	61.0(1)	61.0(1)	-89.5(5)
ψ(*i*−*1*) (°)	-9.5(1)	17.8(1)	17.8(1)	-160.7(4)
τ(*i*−*1*) (°)	116.65(8)	117.0(1)	117.0(1)	112.6(4)
ω(*i*−*2*) (°)	174.9(1)	-174.0(1)	-174.0(1)	171.5(4)
φ(*i*−*2*) (°)	-91.1(1)	-161.8(1)	-161.8(1)	90.6(5)
ψ(*i*−*2*) (°)	137.9(1)	71.4(1)	71.4(1)	-160.7(4)
τ(*i*−*2*) (°)	109.79(8)	107.46(9)	107.46(9)	111.7(4)
Bend (°)	60.26	52.98	52.98	n/a
Twist (°)	-0.61(4)	-11.69(4)	-11.69(4)	
γ(*i*) (°)	37.0(1)	41.5(1)	41.5(1)	*distorted pucker*
Pro Cγ Pucker	*exo*	*exo*	*exo*	
Cα(*i*+*1*)—Cα(*i*−*2*) (Å)	4.933(1)	5.164(2)	5.164(2)	7.566(6)
Cβ(*i*+*1*)—Cβ(*i*−*2*) (Å)	4.043(1)	5.151(2)	5.151(2)	8.794(6)
N(*i*−*2*) —O(*i*+*1*) *r* (Å)	2.900(1)	2.838(1)	2.838(1)	5.913(5)
NH(*i*−*2*)—O(*i*+*1*) θ (°)	160(1)	163(1)	163(1)	43.3(1)
N(*i*+*1*) —O(*i*−*2*) *r* (Å)	2.896(1)	3.096(1)	3.096(1)	n/a
NH(*i*+*1*)—O(*i*−*2*) θ (°)	163(1)	164(1)	164(1)	n/a
N(*i*−*1*)—O(*i*+*1*) *r* (Å)	3.196(1)	3.114(1)	3.114(1)	3.529(5)
NH(*i*−*1*)—O(*i*+*1*) θ (°)	89.6(8)	84.3(9)	84.3(9)	94.3
χ(*i*+*1*) (°)	-169.88(8)	-70.8(1)	-70.8(1)	n/a
χ(*i*−*2*) (°)	-86.6(1)	-154.85(9)	-154.85(9)	63.2(7)
β-turn type	type II'	type II	type II	n/a

n.a. = not applicable

Table 4.7.2. (continued) Structural features of conformers **2a**, **2b**, **2c'**, **2c"**, **2s**, **2i'** and **2i"** extracted from X-ray crystals structures.

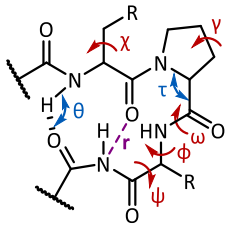

	2s	**2i'**	**2i"**
ω(*i*+1) (°)	n/a	n/a	n/a
φ(*i*+1) (°)	n/a	n/a	n/a
ψ(*i*+1) (°)	176.6(3)	175.6(4)	179.8(4)
τ(*i*+1) (°)	n/a	n/a	n/a
ω(*i*) (°)	178.3(3)	-172.1(4)	-170.4(4)
φ(*i*) (°)	-59.9(4)	-69(6)	-78.5(6)
ψ(*i*) (°)	122.1(3)	-14.3(7)	-9.4(7)
τ(*i*) (°)	110.1(3)	114.4(4)	114.1(4)
ω(*i*−1) (°)	-178.2(3)	173.1(4)	-179.7(4)
φ(*i*−1) (°)	73.8(4)	-104.6(6)	69.8(6)
ψ(*i*−1) (°)	7.3(5)	14.6(7)	14.5(7)
τ(*i*−1) (°)	116.5(3)	115.5(4)	114.3(4)
ω(*i*−2) (°)	-178.2(3)	179.5(4)	-168.8(5)
φ(*i*−2) (°)	-65.5(4)	-70.5(6)	-114.3(5)
ψ(*i*−2) (°)	134.0(3)	135.9(5)	153.7(5)
τ(*i*−2) (°)	109.5(3)	108.5(4)	108.4(4)
Bend (°)	n/a	n/a	n/a
Twist (°)	-2.5(1)	46.4(2)	
γ(*i*) (°)	40.4(4)	-21.5(5)	-36.1(5)
Pro C$^{\gamma}$ Pucker	exo	endo	endo
Cα(*i*+1)—Cα(*i*−2) (Å)	4.956(4)	5.244(7)	7.985(7)
Cβ(*i*+1)—Cβ(*i*−2) (Å)	3.517(5)	4.208(7)	9.277(8)
N(*i*−2) —O(*i*+1) *r* (Å)	2.920(4)	2.978(5)	5.928(5)
NH(*i*−2)—O(*i*+1) θ (°)	167.3	163.7	122.1(1)
N(*i*+1) —O(*i*−2) *r* (Å)	n/a	n/a	n/a
NH(*i*+1)—O(*i*−2) θ (°)	n/a	n/a	n/a
N(*i*−1)—O(*i*+1) *r* (Å)	3.052(4)	3.078(4)	3.260(5)
NH(*i*−1)—O(*i*+1) θ (°)	81.4	89.0	96
χ(*i*+1) (°)	n/a	n/a	n/a
χ(*i*−2) (°)	-175.4(7)	-171.7(4)	-167.1(5)
β-turn type	type II	type I	n/a

n.a. = not applicable

5.8. References

(1) Pupo, G.; Vicini, A. C.; Ascough, D. M. H.; Ibba, F.; Christensen, K. E.; Thompson, A. L.; Brown, J. M.; Paton, R. S.; Gouverneur, V. Hydrogen Bonding Phase-Transfer Catalysis with Potassium Fluoride: Enantioselective Synthesis of β-Fluoroamines. *J. Am. Chem. Soc.* **2019**, *141* (7), 2878–2883.

(2) Metrano, A. J.; Abascal, N. C.; Mercado, B. Q.; Paulson, E. K.; Hurtley, A. E.; Miller, S. J. Diversity of Secondary Structure in Catalytic Peptides with β-Turn-Biased Sequences. *J. Am. Chem. Soc.* **2017**, *139* (1), 492–516.

(3) Leggio, A.; Belsito, E. L.; De Luca, G.; Di Gioia, M. L.; Leotta, V.; Romio, E.; Siciliano, C.; Liguori, A. One-pot synthesis of amides from carboxylic acids activated using thionyl chloride. *RSC Adv.* **2016**, *6* (41), 34468–34475.

(4) Inman, M.; Dexter, H. L.; Moody, C. J. Total Synthesis of the Cyclic Dodecapeptides Wewakazole and Wewakazole B. *Org. Lett.* **2017**, *19* (13), 3454–3457.

(5) Vicini, A. C.; Pupo, G.; Ibba, F.; Gouverneur, V. Multigram synthesis of *N*-alkyl *bis*-ureas for asymmetric hydrogen bonding phase-transfer catalysis. *Nat. Protoc.* **2021**, *16* (12), 5559–5591.

(6) Lenstra, D. C.; Damen, E.; Leenders, R. G. G.; Blaauw, R. H.; Rutjes, F. P. J. T.; Wegert, A.; Mecinović, J. Structure–Activity Relationship Studies on (*R*)-PFI-2 Analogues as Inhibitors of Histone Lysine Methyltransferase SETD7. *ChemMedChem* **2018**, *13* (14), 1405–1413.

(7) (a) Trost, B. M.; Donckele, E. J.; Thaisrivongs, D. A.; Osipov, M.; Masters, J. T. A New Class of Non-C_2-Symmetric Ligands for Oxidative and Redox-Neutral Palladium-Catalyzed Asymmetric Allylic Alkylations of 1,3-Diketones. *J. Am. Chem. Soc.* **2015**, *137* (7), 2776–2784; (b) Aubry, C.; Oulyadi, H.; Dutheuil, G.; Leprince, J.; Vaudry, H.; Pannecoucke, X.; Quirion, J.-C. New synthesis of *cis* 5-*tert*-butyl-L-proline via cuprate. Evaluation as a cis proline mimetic in a biological active octapeptide. *J. Pept. Sci.* **2006**, *12* (2), 154–160.

(8) Flavell, R. R.; von Morze, C.; Blecha, J. E.; Korenchan, D. E.; Van Criekinge, M.; Sriram, R.; Gordon, J. W.; Chen, H.-Y.; Subramaniam, S.; Bok, R. A.; Wang, Z. J.; Vigneron, D. B.; Larson, P. E.; Kurhanewicz, J.; Wilson, D. M. Application of Good's buffers to pH imaging using hyperpolarized ^{13}C MRI. *Chem. Commun.* **2015**, *51* (74), 14119–14122.

(9) Degerbeck, F.; Fransson, B.; Grehn, L.; Ragnarsson, U. Synthesis of ^{15}N-labelled chiral Boc-amino acids from triflates: enantiomers of leucine and phenylalanine. *J. Chem. Soc., Perkin Trans. 1* **1993**, (1), 11–14.

(10) Peura, L.; Malmioja, K.; Laine, K.; Leppänen, J.; Gynther, M.; Isotalo, A.; Rautio, J. Large Amino Acid Transporter 1 (LAT1) Prodrugs of Valproic Acid: New Prodrug Design Ideas for Central Nervous System Delivery. *Mol. Pharmaceutics* **2011**, *8* (5), 1857–1866.

(11) Budke, B.; Tueckmantel, W.; Miles, K.; Kozikowski, A. P.; Connell, P. P. Optimization of Drug Candidates That Inhibit the D-Loop Activity of RAD51. *ChemMedChem* **2019**, *14* (10), 1031–1040.

(12) Wallén, E. A. A.; Christiaans, J. A. M.; Saarinen, T. J.; Jarho, E. M.; Forsberg, M. M.; Venäläinen, J. I.; Männistö, P. T.; Gynther, J. Conformationally rigid *N*-acyl-5-alkyl-L-prolyl-pyrrolidines as prolyl oligopeptidase inhibitors. *Biorg. Med. Chem.* **2003**, *11* (17), 3611–3619.

(13) Vicini, A. Hydrogen bonding phase-transfer catalysis with alkali metal fluorides: enantioselective synthesis of β-fluoroamines from reaction development to scale-up. University of Oxford, 2020.

(14) Haruyama Takuya, O. N., Seo Satoshi. Compound, light-emitting device, light-emitting apparatus, electronic device, and lighting device. US2021/61753, 2021.

(15) (a) Askari, M. S.; Orio, M.; Ottenwaelder, X. Controlled nitrene transfer from a tyrosinase-like arylnitroso–copper complex. *Chem. Commun.* **2015**, *51* (56), 11206–11209; (b) Sharma, V.; De, D.; Saha, R.; Das, R.; Chattaraj, P. K.; Bharadwaj, P. K. A Cu(II)-MOF capable of fixing CO_2 from air and showing high capacity H_2 and CO_2 adsorption. *Chem. Commun.* **2017**, *53* (100), 13371–13374; (c) Rozsar, D.; Farley, A. J. M.; McLauchlan, I.; Shennan, B. D. A.; Yamazaki, K.; Dixon, D. J. Bifunctional Iminophosphorane-Catalyzed Enantioselective Nitroalkane Addition to Unactivated α,β-Unsaturated Esters. *Angew. Chem., Int. Ed.* **2023**, *62* (21), e202303391.

(16) Rasheed, S.; Rao, D. N.; Reddy, A. S.; Shankar, R.; Das, P. Sulphuric acid immobilized on silica gel (H_2SO_4–SiO_2) as an eco-friendly catalyst for transamidation. *RSC Adv.* **2015**, *5* (14), 10567–10574.

(17) Bagheri Natanzi, M.; Kazemi, F.; Zand, Z.; Kaboudin, B. Highly chemoselective and fast practical visible photoreduction of nitroaromatic compounds to aromatic amines and amides using a self-assembled triad TiO_2-TEOA-NC (LMCT/EDA) complex system. *Green Chem.* **2024**, *26* (3), 1637–1652.

(18) Gavinolla, V.; Thangalipalli, S.; Bandalla, S. G.; Panduga, R.; Neella, C. K. A thermo-regulated highly regioselective mono and dihalogenations of phenols and anilines in water employing new Lewis base

adducts (LBAs) [DBUBr]$^+$Br$^-$ and [DBUI]$^+$I$^-$ as green reagents: a simple approach. *New J. Chem.* **2023**, *47* (45), 20777–20784.

(19) Li, X.; Deng, X.; Coyne, A. G.; Srinivasan, R. *meta*-Nitration of Arenes Bearing *ortho*/*para* Directing Group(s) Using C−H Borylation. *Chem. – Eur. J.* **2019**, *25* (34), 8018–8023.

(20) Martinez, G. E.; Nugent, J. W.; Fout, A. R. Simple Nickel Salts for the Amination of (Hetero)aryl Bromides and Iodides with Lithium Bis(trimethylsilyl)amide. *Organometallics* **2018**, *37* (18), 2941–2944.

(21) Monaco, M. R.; Poladura, B.; Diaz de Los Bernardos, M.; Leutzsch, M.; Goddard, R.; List, B. Activation of Carboxylic Acids in Asymmetric Organocatalysis. *Angew. Chem., Int. Ed.* **2014**, *53* (27), 7063–7067.

(22) Monaco, M. R.; Prévost, S.; List, B. Organocatalytic Asymmetric Hydrolysis of Epoxides. *Angew. Chem., Int. Ed.* **2014**, *53* (31), 8142–8145.

(23) Hansen, S. U.; Bols, M. 1-Azaribofuranoside analogues as designed inhibitors of purine nucleoside phosphorylase. Synthesis and biological evaluation. *Acta Chem. Scand.* **1998**, *52* (10), 1214–1222.

(24) Yamasaki, M.; Lu, P.-P.; Morgan, B. P.; Garard, M.; Collibee, S.; Koganemaru, Y.; Sami, Y.; Negoro, K.; Imada, S.; Kamikubo, T.; Ishikawa, N.; Inagi, Y.; Ohnuki, K.; Sato, S.; Tanaka, H.; Ishida, J.; Abe, T. Slow Skeletal Troponin Activators. WO2023/245137, 2023.

(25) (a) Abraham, M. H.; Abraham, R. J.; Byrne, J.; Griffiths, L. NMR Method for the Determination of Solute Hydrogen Bond Acidity. *J. Org. Chem.* **2006**, *71* (9), 3389–3394; (b) Abraham, M. H.; Whiting, G. S.; Doherty, R. M.; Shuely, W. J. Hydrogen bonding: XVI. A new solute salvation parameter, π_2^H, from gas chromatographic data. *J. Chromatogr. A* **1991**, *587* (2), 213–228.

(26) Abraham, M. H.; Abraham, R. J. A simple and facile NMR method for the determination of hydrogen bonding by amide N–H protons in protein models and other compounds. *New J. Chem.* **2017**, *41* (14), 6064–6066.

(27) Ibba, F.; Pupo, G.; Thompson, A. L.; Brown, J. M.; Claridge, T. D. W.; Gouverneur, V. Impact of Multiple Hydrogen Bonds with Fluoride on Catalysis: Insight from NMR Spectroscopy. *J. Am. Chem. Soc.* **2020**, *142* (46), 19731–19744.

(28) Shaka, A. J.; Barker, P. B.; Freeman, R. Computer-optimized decoupling scheme for wideband applications and low-level operation. *J. Magn. Reson.* **1985**, *64* (3), 547–552.

(29) Vidal-Ferran, A.; Mon, I.; Bauzá, A.; Frontera, A.; Rovira, L. Supramolecularly Regulated Ligands for Asymmetric Hydroformylations and Hydrogenations. *Chem. – Eur. J.* **2015**, *21* (32), 11417–11426.

(30) (a) *Gaussian 16 Rev. C.01*; Gaussian Inc.: Wallingford, CT, 2016; (b) Zhao, Y.; Truhlar, D. G. A new local density functional for main-group thermochemistry, transition metal bonding, thermochemical kinetics, and noncovalent interactions. *J. Chem. Phys.* **2006**, *125* (19); (c) Weigend, F.; Ahlrichs, R. Balanced basis sets of split valence, triple zeta valence and quadruple zeta valence quality for H to Rn: Design and assessment of accuracy. *Phys. Chem. Chem. Phys.* **2005**, *7* (18), 3297–3305; (d) Grimme, S.; Antony, J.; Ehrlich, S.; Krieg, H. A consistent and accurate *ab initio* parametrization of density functional dispersion correction (DFT-D) for the 94 elements H-Pu. *J. Chem. Phys.* **2010**, *132* (154104).

(31) Marenich, A. V.; Cramer, C. J.; Truhlar, D. G. Universal Solvation Model Based on Solute Electron Density and on a Continuum Model of the Solvent Defined by the Bulk Dielectric Constant and Atomic Surface Tensions. *J. Phys. Chem. B* **2009**, *113* (18), 6378–6396.

(32) (a) Neese, F. The ORCA program system. *WIREs Comput. Mol. Sci.* **2012**, *2* (1), 73–78; (b) Neese, F. Software update: The ORCA program system—Version 5.0. *WIREs Comput. Mol. Sci.* **2022**, *12* (5), e1606; (c) Zhao, Y.; Truhlar, D. G. The M06 suite of density functionals for main group thermochemistry, thermochemical kinetics, noncovalent interactions, excited states, and transition elements: two new functionals and systematic testing of four M06-class functionals and 12 other functionals. *Theor. Chem. Acc.* **2008**, *120* (1), 215–241.

(33) Luchini, G.; Alegre-Requena, J. V.; Funes-Ardoiz, I.; Paton, R. S. GoodVibes: automated thermochemistry for heterogeneous computational chemistry data *F1000Research* **2020**, *9* (291).

(34) Grimme, S. Supramolecular Binding Thermodynamics by Dispersion-Corrected Density Functional Theory. *Chem. – Eur. J.* **2012**, *18* (32), 9955–9964.

(35) (a) de Souza, B. GOAT: A Global Optimization Algorithm for Molecules and Atomic Clusters. *Angew. Chem., Int. Ed.* **2025**, *64* (18), e202500393; (b) Bannwarth, C.; Ehlert, S.; Grimme, S. GFN2-xTB—An Accurate and Broadly Parametrized Self-Consistent Tight-Binding Quantum Chemical Method with Multipole Electrostatics and Density-Dependent Dispersion Contributions. *J. Chem. Theory Comput.* **2019**, *15* (3), 1652–1671.

(36) Stahn, M.; Ehlert, S.; Grimme, S. Extended Conductor-like Polarizable Continuum Solvation Model (CPCM-X) for Semiempirical Methods. *J. Phys. Chem. A* **2023**, *127* (33), 7036–7043.

(37) Cosier, J.; Glazer, A. M. A nitrogen-gas-stream cryostat for general X-ray diffraction studies. *J. Appl. Crystallogr.* **1986**, *19* (2), 105–107.

(38) Allan, D. R.; Nowell, H.; Barnett, S. A.; Warren, M. R.; Wilcox, A.; Christensen, J.; Saunders, L. K.; Peach, A.; Hooper, M. T.; Zaja, L.; Patel, S.; Cahill, L.; Marshall, R.; Trimnell, S.; Foster, A. J.; Bates, T.; Lay, S.; Williams, M. A.; Hathaway, P. V.; Winter, G.; Gerstel, M.; Wooley, R. W. A Novel Dual Air-Bearing Fixed-χ Diffractometer for Small-Molecule Single-Crystal X-ray Diffraction on Beamline I19 at Diamond Light Source. *Crystals* **2017**, *7* (11), 336.

(39) Rigaku Oxford Diffraction. **2021**.

(40) Palatinus, L.; Chapuis, G. SUPERFLIP - a computer program for the solution of crystal structures by charge flipping in arbitrary dimensions. *J. Appl. Crystallogr.* **2007**, *40* (4), 786–790.

(41) Betteridge, P. W.; Carruthers, J. R.; Cooper, R. I.; Prout, K.; Watkin, D. J. CRYSTALS version 12: software for guided crystal structure analysis. *J. Appl. Crystallogr.* **2003**, *36* (6), 1487.

(42) Flack, H. On enantiomorph-polarity estimation. *Acta Crystallogr. Sect. A* **1983**, *39* (6), 876–881.

(43) Cooper, R. I.; Thompson, A. L.; Watkin, D. J. CRYSTALS enhancements: dealing with hydrogen atoms in refinement. *J. Appl. Crystallogr.* **2010**, *43*, 1100–1107.

(44) Macrae, C. F.; Sovago, I.; Cottrell, S. J.; Galek, P. T. A.; McCabe, P.; Pidcock, E.; Platings, M.; Shields, G. P.; Stevens, J. S.; Towler, M.; Wood, P. A. Mercury 4.0: from visualization to analysis, design and prediction. *J. Appl. Crystallogr.* **2020**, *53* (1), 226–235.